

DISS. ETH NO. 26688

**TOWARDS RELIABLE OPERATION OF
CONVERTER-DOMINATED POWER
SYSTEMS: DYNAMICS, OPTIMIZATION
AND CONTROL**

A dissertation submitted to attain the degree of
DOCTOR OF SCIENCES of ETH ZURICH
(Dr. sc. ETH Zurich)

presented by

UROŠ MARKOVIĆ

MSc D-ITET ETH Zurich

born on 20 September 1990
citizen of Serbia

accepted on the recommendation of

Prof. Dr. Gabriela Hug, examiner
Prof. Dr. Petros Aristidou, co-examiner
Prof. Dr. Florian Dörfler, co-examiner
Prof. Dr. David J. Hill, co-examiner

2020

Uroš Marković: *Towards reliable operation of converter-dominated power systems: Dynamics, optimization and control*, © 2020

DOI: 10.3929/ethz-b-000432013

ISBN: 978-3-907234-14-3

To my family and friends.

ABSTRACT

The environmental and sustainability concerns related to burning of fossil fuels and nuclear waste disposal have led to drastic changes in the global energy mix over the past few decades, primarily stemming from massive integration of Renewable Energy Sources (RES). As a result, the electric power system is currently undergoing a major transition from bulk synchronous generation towards integration of large shares of distributed renewable generation. Due to intermittent nature and physical characteristics of these resources, as well as the fact that they are typically connected to the system via Power Electronics (PE), their interaction with the grid is substantially different from the one of Synchronous Machines (SMs). While the rotating parts of SMs inherently provide physical inertia to the system, the PE interface electrically decouples the kinetic energy stored in the rotating masses from the network. This results in larger and more frequent frequency deviations and could jeopardize the stability of the power grid. Moreover, power converters introduce faster dynamics, which implies that the timescale separation traditionally assumed in control and operation of power systems may not hold. Likewise, measurement or communication delays can destabilize the complex cascaded converter controls and hinder their performance. In order to tackle the aforementioned problems, new ancillary services and novel control algorithms are needed to exploit the flexibility and fast actuation of power converters. In addition, an important question is how to optimally place such devices in a power system to ensure robust and resilient operation.

The main goal of this thesis is to develop control and optimization methods for reliable and resilient operation of power systems with high share of RES. The thesis particularly focuses on transmission-level networks hosting large shares of converter-interfaced RES and is comprised of three parts.

The first part presents the modeling, stability and hierarchical control of PE-dominated power systems with detailed SM, converter and transmission network dynamics. The compatibility of novel grid-forming control strategies in systems with 100 % converter-interfaced generation is investigated and the mathematical equivalence between the methods is discussed. Motivated by the timescale separation between the fast and slow dynamics in a converter-based power system, a model-order reduction method based on singular perturbation is proposed that preserves the slow system dynamics of the

full-order converter model and captures the impact of the removed fast states on slow variables. Moreover, novel insights into stability properties of power systems with large-scale integration of RES are provided by characterizing the maximum permissible penetration levels of converter-based generation as well as the nature of the associated unstable modes and the underlying dynamics.

The second part studies the frequency dynamics and fast frequency control applications in low-inertia grids. In particular, a frequency response model of a generic low-inertia system is developed and analytical expressions for frequency metrics of interest are derived. Subsequently, several adaptive Virtual Synchronous Machine (VSM) controllers are proposed in order to adjust the emulated inertia and damping constants according to the frequency disturbance in the system, while simultaneously preserving a trade-off between the critical frequency limits and the required control effort. Furthermore, two MPC controllers for converter-interfaced generators operating in a grid-forming mode are introduced with the goal of exploiting their responsiveness and providing fast frequency control. In order to ensure sufficient energy and power capacity for providing such services, a uniform method for combined sizing of DC-side storage capacity and tuning of controller gains of grid-forming converters is developed.

Finally, the third part provides various methods for improving reliability and performance of networks with high converter penetration. More specifically, a novel control strategy for synchronization of grid-connected converters based on emulating the physical properties of an induction machine is proposed. We also deal with the topic of time delay in low-inertia power systems, taking into consideration both the constant and time-varying delays. The problem of allocation of inertia and damping in an inverter-dominated power system is tackled by developing an iterative eigensensitivity-based optimization framework with a comprehensive multi-objective formulation that takes into account several performance metrics. The economic impact of ancillary services such as fast frequency and inertial response is studied by proposing a two-stage stochastic unit commitment formulation that accounts for wind power and equipment contingency uncertainties. Subsequently, the model is employed for investigating the procurement and pricing of inertial response. Three novel pricing and payment schemes that reimburse inertia providers in a transparent and fair manner according to their individual participation are proposed. The thesis closes with the study on the impact of inverter-based generation on islanding detection schemes. To this end, an improved analytical formulation for estimating the non-detection zone of loss

of mains protection devices in the presence of different converter operation modes is presented.

ZUSAMMENFASSUNG

Die Umwelt- und Nachhaltigkeitsbedenken im Zusammenhang mit der Verbrennung fossiler Brennstoffe und der Entsorgung nuklearer Abfälle haben in den letzten Jahrzehnten zu drastischen Veränderungen im globalen Energiemix geführt, und eine massive Integration Erneuerbarer Energiequellen (EE) hervorrufen. Infolgedessen befindet sich das Stromnetz derzeit im Umbruch von der synchronen Massenerzeugung hin zur Integration großer Anteile dezentraler erneuerbarer Energieerzeugung. Aufgrund der volatilen Natur und der physikalischen Eigenschaften dieser Ressourcen sowie dem üblichen Anschluss der Anlagen per Leistungselektronik (LE), unterscheidet sich ihre Interaktion mit dem Netz erheblich von den traditionellen Synchronmaschinen (SM). Während die Turbinen und Rotoren in SMs dem System von Natur aus physikalische Trägheit verleihen, entkoppelt die LE-Schnittstelle erneuerbarer Energieeinspeisung die in den rotierenden Massen gespeicherte kinetische Energie elektrisch vom Stromnetz. Dies resultiert nicht nur in signifikanteren und häufigeren Frequenzabweichungen, sondern kann die Stabilität des Stromnetzes gefährden. Darüber hinaus führen Stromrichter eine schnellere Dynamik ein, wodurch die klassische Zeitskalentrennung die für den Betrieb und die Steuerung von Stromversorgungssystemen üblicherweise angenommen wird möglicherweise ihre Gültigkeit verliert. Ebenso können Verzögerungen in der Mess- oder Kommunikationstechnik die komplexen, kaskadierten Inverterregelung destabilisieren und deren Leistung beeinträchtigen. Um die oben genannten Probleme anzugehen und die Flexibilität und schnelle Aktivierung von Stromrichtern zu nutzen, sind neue Netzdienstleistungen und neuartige Regelalgorithmen erforderlich. Weiterhin, stellt sich die Frage wie diese Systeme optimal in einem Stromversorgungssystem platziert werden können, um einen robusten und belastbaren Betrieb zu gewährleisten.

Das Hauptziel dieser Thesis ist die Entwicklung von Regel- und Optimierungsmethoden für den zuverlässigen und belastbaren Betrieb von Stromversorgungssystemen mit einem hohem Anteil an erneuerbaren Energien. Die Arbeit konzentriert sich insbesondere auf Übertragungsnetze, die hohe Anteile von EE mit Inverterschnittstelle beherbergen und besteht aus drei Teilen.

Der erste Teil präsentiert die Modellierung, Stabilität und hierarchische Regelung von LE-dominierten Stromversorgungssystemen mit detaillierter

dynamischer Beschreibung von SMs, Invertern und Übertragungsnetzen. Die Kompatibilität neuartiger netzunterstützender und formender Steuerungsstrategien in Systemen mit 100 % Inverterschnittstellenerzeugung wird untersucht und die mathematische Äquivalenz zwischen den Methoden diskutiert. Motiviert durch die zeitliche Trennung zwischen schneller und langsamer Dynamik in einem inverterbasierten Stromversorgungssystem wird eine auf singulärer Störungstheorie basierende Methode zur Reduzierung der Modellordnung vorgeschlagen. Diese behält die langsame Systemdynamik des Invertermodells in voller Ordnung bei und überträgt die Auswirkungen der signifikant schnelleren Zustände auf langsamere Variablen. Darüber hinaus werden neue Einblicke in die Stabilitätseigenschaften von Stromversorgungssystemen mit großflächiger Integration von erneuerbaren Energiequellen erlangt, indem die maximal zulässigen Durchdringungsniveaus der inverterbasierten Erzeugung sowie die Art der damit verbundenen instabilen Modi und die zugrunde liegende Dynamik charakterisiert werden.

Der zweite Teil untersucht die Frequenzdynamik und Anwendungen zur schnellen Frequenzregelung in Netzen mit geringer Massträgheit. Insbesondere wird ein Frequenzantwortmodell eines generischen Systems mit geringer Trägheit entwickelt und analytische Beschreibungen für wichtige Frequenzmetriken hergeleitet. Anschließend werden mehrere adaptive virtuelle Synchronmaschinen (VSM)-Steuerungen vorgeschlagen, um die emulierten Trägheits- und Dämpfungskonstanten entsprechend der Frequenzstörung im System anzupassen und gleichzeitig einen Kompromiss zwischen den kritischen Grenzen der Frequenz und dem erforderlichen Steuerungsaufwand aufrechtzuerhalten. Darüber hinaus werden zwei MPC-Steuerungen für Generatoren mit Inverterschnittstelle eingeführt, die in einem systemformenden Modus arbeiten, um ihre Reaktionsfähigkeit zu nutzen und eine schnelle Frequenzregelung bereitzustellen. Um eine ausreichende Energie- und Stromkapazität für die Bereitstellung solcher Dienste sicherzustellen, wird ein einheitliches Verfahren zur kombinierten Dimensionierung der gleichstromseitigen Speicherkapazität und zur Auslegung der Regelparameter von netzbildenden Invertern entwickelt.

Schließlich enthält der dritte Teil verschiedene Methoden zur Verbesserung der Zuverlässigkeit und Leistungsfähigkeit von Netzwerken mit hoher Inverterdurchdringung. Insbesondere wird eine neuartige Regelstrategie zur Synchronisation von netzgekoppelten Invertern vorgeschlagen, die auf der Emulation der physikalischen Eigenschaften einer Induktionsmaschine basiert. Wir beschäftigen uns auch mit dem Thema Zeitverzögerung in Stromversorgungssystemen mit geringer Trägheit, wobei sowohl die konstanten als auch

die zeitlich variierenden Verzögerungen berücksichtigt werden. Das Problem der Zuweisung von Trägheit und Dämpfung in einem von Wechselrichtern dominierten Stromversorgungssystem wird durch die Entwicklung eines iterativen, auf Eigenempfindlichkeit basierenden Optimierungsrahmens mit einer umfassenden Formulierung mit mehreren Zielsetzungen gelöst. Gleichzeitig werden mehrere Leistungsmetriken berücksichtigt. Die wirtschaftlichen Auswirkungen von Netzdienstleistungen wie schnelle die Frequenzregelung und die Trägheitsreaktion werden untersucht, indem eine zweistufige stochastische Unit-Commitment-Formulierung vorgeschlagen wird, die die Unsicherheiten in Bezug auf Windkraft und Kontingenzunsicherheiten technischer Assets berücksichtigt. Anschließend wird das Modell zur Untersuchung der Bereitstellung und Preisgestaltung von Trägheitsreaktionen verwendet. Es werden drei neuartige Preis- und Zahlungsschemata vorgeschlagen, die Trägheitsbereitsteller auf transparente und faire Weise entsprechend ihrer individuellen Beteiligung erstatten. Die Arbeit schließt mit einer Untersuchung der Auswirkungen von leistungselektronisch gesteuerten Erzeugung auf klassische Mechanismen zur Inselerkennung. Zu diesem Zweck wird eine verbesserte analytische Formulierung zur Schätzung der Nichterfassungszone für den Verlust von Netzschutzgeräten bei Vorhandensein verschiedener Umrichterbetriebsarten vorgestellt.

ACKNOWLEDGEMENTS

This doctoral thesis summarizes the research activities conducted during my time as a PhD student at the Power Systems Laboratory (PSL) of ETH Zurich from March 2016 to February 2020. There are many people to thank for their help and support during this time.

First and foremost, I would like to express my deepest gratitude to my advisor Prof. Gabriela Hug for giving me the opportunity to pursue my PhD at PSL. She has been an exemplary advisor who provided me with a lot of support, guidance and freedom in my research. My gratitude also goes to Prof. Göran Andersson for allowing me to be an active part of PSL during my master studies.

My next thanks goes to Prof. Petros Aristidou for his immense support during my first year at PSL, which helped me better define the goals of my research. He was of incredible importance to me, both as a mentor, an office mate and a partner on the MIGRATE project.

Special thanks go to Prof. Florian Dörfler from the Automatic Control Laboratory of ETH Zurich for being effectively my second advisor for a significant part of the PhD studies, and for accepting to be a co-examiner of this thesis. I benefited a lot from the inspiring discussions we had during the meetings of the MIGRATE project.

Another special thanks goes to Prof. David Hill from the University of Hong Kong for being a co-examiner of this thesis. I appreciate the time he spent on reading the thesis and providing valuable comments that helped me improve the quality of the final manuscript.

I would also like to thank Dr. Marcello Colombino and Prof. Dominic Groß from the Automatic Control Laboratory of ETH Zurich for the fruitful collaboration and the good working environment throughout the project.

I extend my thanks to all members of the MIGRATE consortium, both the research and industry partners. In particular, I would like to thank our close collaborators at RTE, Lille University of Science and Technology and University College Dublin, as well as all members of the project management team. In particular, I appreciate the constructive discussions during the project meetings with Thibault Prevost, Dr. Marie-Sophie Debry, Dr. Guillaume Denis, Prof. Xavier Guillaud, Dr. Frédéric Colas, Dr. François Gruson, Prof. Xavier Kestelyn, Dr. Quentin Cossart, Dr. Taoufik Qoria and

Prof. Damian Flynn, as well as the inputs and feedback from several transmission system operators which were pivotal in making our work practically relevant. Furthermore, I acknowledge the financial support from the European Union's Horizon 2020 research and innovation program.

During the final year of my PhD studies, I spent three amazing months as a visiting researcher at the Energy and Resources Group, University of California, Berkeley, and the Grid Integration Group at the Lawrence Berkeley National Laboratory (LBNL). I would like to thank Prof. Duncan Callaway, Dr. Evangelos Vrettos and Ciaran Roberts for being the hosts and providing me with this opportunity. I sincerely enjoyed our insightful discussions on various topics and great collaboration during my stay there.

Throughout my PhD, I have been fortunate to supervise a number of semester and master thesis projects. My appreciation goes to all of my former students, namely Andreas Venzke, Lakshmi Srinivasan, Arsam Aryandoust, Ron Ofir, Johanna Vorwerk, David Roman Kayanan, Zhongda Chu, Body Nasef, Matthieu Paturet, Simon Hobi, David Rodriguez Flores, Ivo Caduff, Ognjen Stanojev, Baudouin Vandebussche, Jialun Zhang, Nicolas Früh, Verena Häberle, Ashwin Venkatraman and Demetris Chrysostomou for their efforts and hard work. These projects have tremendously helped me in exploring different ideas and contributed to some of the results included in this thesis.

My PhD experience would not be the same if it hadn't been for the atmosphere and enthusiasm of the people at the PSL. As it is hard to name everyone individually, I would simply like to thank every member of the PSL for motivating discussions and collaborations, ski trips, conferences, excursions and overall great time over the past 4 years. A special thanks goes to my office mates in G29, Aleksandar Jovičić, Ognjen Stanojev and Conor O'Malley, for putting up with me and my frequent meetings and Skype calls, and also for being my main lunch partners in my favorite ETH mensa. It was an inspiring and friendly working environment that I always looked forward returning to. Additionally, I would like to thank Dr. Stavros Karagiannopoulos for constantly boosting my creativity with his amazing ice coffees and unique and often underrated sense of humor, as well as Johanna Vorwerk for helping me improve the translation of the abstract into German.

Last, but certainly not the least, I would like to thank my family and friends. I am deeply grateful to my parents and grandmother for their guidance, love and support throughout my whole academic life. Without them I would never be where I am today. My friends were an endless source of energy, happiness and heartwarming moments, always making sure to remind me that I was "just a student". Finally, my sincere thank you goes to Nina for

her unconditional love and support during my whole PhD studies, from the first to the final publication (which she often reminds me of). She was an important companion on this journey, helping me along the way and sharing the experiences with me, be it on conferences, PSL excursions or ski trips. Nina was a true partner in crime from day one and deserves a special place in this thesis as well as in my heart.

Uroš Marković

February 2020

CONTENTS

List of Acronyms	xxi
List of Figures	xxiv
List of Tables	xxxv
1 INTRODUCTION	1
1.1 Background and Motivation	1
1.2 Contributions	3
1.3 Thesis Outline	4
1.4 Publications	7
1.5 Mathematical Notation	12
I MODELING AND STABILITY OF INVERTER-DOMINATED POWER SYSTEMS	
2 MODELING AND CONTROL OF INVERTER-DOMINATED GRIDS	17
2.1 Introduction	17
2.2 Modeling and Control of Power Converters	19
2.3 Grid-Following System-level Control	28
2.4 Grid-Forming System-Level Control	30
2.5 Overcurrent Protection	36
2.6 Comparison of System-Level Controls	38
2.7 Uniform Converter Model	47
2.8 Synchronous Generator Model	52
2.9 Network and System Modeling	56
2.10 Conclusion	60
3 REDUCED-ORDER MODELING OF INVERTER-BASED GENERATION	63
3.1 Introduction	63
3.2 Singular Perturbation Principles	67
3.3 Hybrid Reduction Method	72
3.4 Results	77
3.5 Conclusion	83
4 UNDERSTANDING STABILITY OF LOW-INERTIA SYSTEMS	85
4.1 Introduction	85
4.2 Timescales in Low-Inertia Systems	90
4.3 Unit Interactions in a Two-Generator System	93

4.4	Stability Properties of Large Multi-Machine Systems	102
4.5	Conclusion	109
II FREQUENCY DYNAMICS AND FAST FREQUENCY CONTROL IN LOW-INERTIA GRIDS		
5	INTERVAL-BASED ADAPTIVE INERTIA AND DAMPING CON- TROL	115
5.1	Introduction	115
5.2	Frequency Dynamics in Low-Inertia Networks	117
5.3	Interval-Based Adaptive Control Design	121
5.4	Model Validation and Control Performance	126
5.5	Conclusion	132
6	LQR-BASED ADAPTIVE VIRTUAL SYNCHRONOUS MACHINE	135
6.1	Introduction	135
6.2	Theoretical Concept and Control Design	136
6.3	Parametrization and Implementation	145
6.4	Control Performance	149
6.5	Conclusion	155
7	MODEL PREDICTIVE CONTROL FOR FREQUENCY REGULA- TION IN LOW-INERTIA SYSTEMS	157
7.1	Introduction	157
7.2	MPC-Based Fast Frequency Control for VSCs	159
7.3	Decentralized Control Design	161
7.4	Centralized Control Design	167
7.5	Model Validation and Control Performance	170
7.6	Conclusion	178
8	SIZING AND TUNING OF DC-SIDE STORAGE FOR FFC PRO- VISION	181
8.1	Introduction	181
8.2	Theoretical Preliminaries	183
8.3	Problem Formulation	184
8.4	Results	191
8.5	Conclusion	196
III IMPROVING RELIABILITY AND PERFORMANCE OF NET- WORKS WITH HIGH INVERTER PENETRATION		
9	VIRTUAL INDUCTION MACHINE STRATEGY FOR POWER CONVERTER SYNCHRONIZATION	201
9.1	Introduction	201

9.2	Theoretical Concept	204
9.3	Formulation and Implementation	210
9.4	Simulation Results	214
9.5	Stability Analysis	219
9.6	Conclusion	223
10	ANALYSIS AND CONTROL OF INVERTER-BASED GRIDS UNDER COMMUNICATION AND MEASUREMENT DELAYS	225
10.1	Introduction	226
10.2	Small-Signal Analysis of DDAEs	230
10.3	Robust Control Principles under Delay Uncertainty	239
10.4	Delay-Robust Device-Level Control Design	246
10.5	Delay-Robust Wide-Area Control Design	251
10.6	Conclusion	260
11	IMPROVING PERFORMANCE OF LOW-INERTIA SYSTEMS VIA EIGENVALUE OPTIMIZATION	261
11.1	Introduction	261
11.2	Control Theory Preliminaries	264
11.3	Objectives and Theoretical Principles	270
11.4	Problem Formulation	273
11.5	Results	282
11.6	Conclusion	294
12	STOCHASTIC UNIT COMMITMENT FORMULATION FOR LOW-INERTIA SYSTEMS	297
12.1	Introduction	297
12.2	Formulation of Frequency Constraints	300
12.3	Equipment Failure and Wind Power Uncertainty	304
12.4	Stochastic Unit Commitment	306
12.5	Case Study	311
12.6	Conclusion	316
13	ECONOMIC VALUATION AND PRICING OF INERTIA IN INVERTER-DOMINATED GRIDS	319
13.1	Introduction	319
13.2	Frequency-Constrained Unit Commitment	323
13.3	Economic Valuation of Inertia	327
13.4	Inertia Pricing and Payment Methods	329
13.5	Case Studies	335
13.6	Conclusion	345
14	IMPACT OF INVERTER-BASED GENERATION ON ISLANDING DETECTION SCHEMES IN DISTRIBUTION NETWORKS	347

14.1	Introduction	347
14.2	Theoretical Preliminaries and Existing Practice	350
14.3	Analytical Approximation of NDZ	354
14.4	Modeling and Implementation	360
14.5	Validation of NDZ Approximation	363
14.6	Conclusion	367
15	CONCLUSIONS AND OUTLOOK	371
15.1	Summary	371
15.2	Conclusions	372
15.3	Outlook	373
A	APPENDIX A - PROOFS	377
A.1	Proof of Proposition 6.3.1	377
A.2	Proof of Proposition 5.3.1	379
A.3	Proof of Proposition 10.3.1	381
A.4	Proof of Proposition 10.5.2	381
B	APPENDIX B - EXAMPLES AND DERIVATIONS	387
B.1	Vector Formulation of Circuit Dynamics	387
B.2	Mathematical Equivalence between Droop and VSM Control	388
B.3	Frequency Control Loop of a Grid-Forming Converter in a Multi-Machine System	388
B.4	Derivation of Saturated Frequency Slip	390
B.5	Clarification of PWL Formulation	391
B.6	Monotonic Properties of NDZ Bounds	392
	BIBLIOGRAPHY	395

LIST OF ACRONYMS

AC	Alternating Current
AGC	Automatic Generation Control
APC	Active Power Controller
AVR	Automatic Voltage Regulator
DAE	Differential-Algebraic Equation
DC	Direct Current
DDAE	Delay Differential-Algebraic Equation
DDE	Delay Differential Equation
DFIG	Doubly-Fed Induction Generator
dVOC	dispatchable Virtual Oscillator Control
EMF	Electro-Magnetic Field
EMT	Electro-Magnetic Transients
ENTSO-E	European Network of Transmission System Operators for Electricity
EOM	Energy-Only Market
ERCOT	Electric Reliability Council of Texas
FFC	Fast Frequency Control
FFR	Fast Frequency Response
FOSP	First-Order Singular Perturbation
FRR	Frequency Response Reserve
GS	Gain Scheduling
HIL	Hardware-In-the-Loop
HVDC	High-Voltage Direct Current
IM	Induction Machine
IP	Inertia Payments
LFT	Linear Fractional Transformation
LMI	Linear Matrix Inequality
LMS	Linear Multi-Step

LoM	Loss of Mains
LP	Linear Program
LPV	Linear Parameter-Varying
LQR	Linear-Quadratic Regulator
LTl	Linear Time-Invariant
MILP	Mixed-Integer Linear Program
MINLP	Mixed-Integer Non-Linear Program
MISOCP	Mixed-Integer Second-Order Cone Program
MOR	Model-Order Reduction
MPC	Model Predictive Control
mp-LP	multi-parametric Linear Program
MTTF	Mean Time To Failure
MTTR	Mean Time To Repair
NDZ	Non-Detection Zone
ODE	Ordinary Differential Equation
OF	Over-Frequency
OV	Over-Voltage
PCC	Point of Common Coupling
PDE	Partial Differential Equations
PE	Power Electronics
PFC	Primary Frequency Control
PLL	Phase-Locked Loop
PMU	Phasor Measurement Unit
PFA	Participation Factor Analysis
PSS	Power System Stabilizer
PWL	Piece-Wise Linearization
RC	Robust Control
RES	Renewable Energy Sources
RMS	Root Mean Square
RMSE	Root Mean Square Error
RoCoF	Rate-of-Change-of-Frequency
RRS	Responsive Reserve Service

RRS	Responsive Reserve Services
SCR	Short-Circuit Ratio
SG	Synchronous Generator
SIR	Synchronous Inertial Response
SM	Synchronous Machine
SMIB	Single-Machine Infinite-Bus
SoC	State-of-Charge
SRF	Synchronously-rotating Reference Frame
SVM	Support Vector Machine
TIO	Time Integration Operator
TSO	Transmission System Operator
TVI	Threshold Virtual Impedance
UC	Unit Commitment
UF	Under-Frequency
UFLS	Under-Frequency Load Shedding
UV	Under-Voltage
VCG	Vickrey-Clarke-Groves
VI	Virtual Inertia
VIM	Virtual Induction Machine
VOC	Virtual Oscillator Control
VSC	Voltage Source Converter
VSM	Virtual Synchronous Machine
WAC	Wide-Area Control
WAMC	Wide-Area Monitoring and Control
WAMS	Wide Area Monitoring Systems
WSCC	Western System Coordinating Council
ZOSP	Zero-Order Singular Perturbation

LIST OF FIGURES

Figure 2.1	Traditional (simplified) representation of system-level controls of grid-connected power converters, with characteristic setpoint input and internally computed reference output: (a) grid-forming; (b) grid-feeding; (c) voltage-source-based grid-supporting; and (d) current-source-based grid-supporting. Dashed lines indicate less prioritized control requirements.	20
Figure 2.2	Representation of the VSC model: (a) two-level VSC connected through a transformer to the grid; (b) general input-output block structure of the power converter model and its control scheme.	22
Figure 2.3	Simplified MIMO structure of the device model.	24
Figure 2.4	Simplified, general MIMO structure of the system-level control: (a) grid-following operation mode; (b) grid-forming operation mode.	26
Figure 2.5	Simplified, general MIMO structure of the device-level control.	28
Figure 2.6	Simplified, general MIMO structure of the system-level control for different grid-forming control methods.	30
Figure 2.7	Simplified representation of the grid-forming converter model with inclusion of overcurrent protection.	37
Figure 2.8	Single-line diagram of a single converter connected to an infinite bus via two parallel transmission lines used for the case study in Section 2.6.1.	39
Figure 2.9	Reference tracking of a single converter connected to a strong grid.	40
Figure 2.10	Converter performance during islanding from the main grid.	42
Figure 2.11	Response of a single converter during a short circuit fault and subsequent line opening.	43
Figure 2.12	Single-line diagram of a three-bus test case used for analyzing the compatibility of different converter controls in Section 2.6.2.	44

Figure 2.13	Simulation results for the three-bus case study comprised solely of droop-based converters.	45
Figure 2.14	Simulation results for the three-bus case study comprised of converters regulated through three different system-level control schemes.	46
Figure 2.15	General configuration of the implemented VSC control structure.	48
Figure 2.16	Vector diagram representing the alignment of different SRFs.	51
Figure 2.17	SCR influence on small-signal stability of a converter under different operation modes.	51
Figure 2.18	Block diagram of a synchronous generator equipped with a prime mover, a governor and a voltage excitation system. The internal state variables are denoted by red color.	53
Figure 2.19	Generic network model with line dynamics and respective dq -frame alignment.	57
Figure 2.20	Time-domain performance of nonlinear and linear model representation of a two-generator system after a load step change.	60
Figure 3.1	Test case system comprising a single-line diagram of a converter connected to an infinite bus via two parallel transmission lines.	77
Figure 3.2	Time-domain response of different model orders after line opening: grid-following control mode (top) and grid-forming control mode (bottom). Dashed lines denote the corresponding reduction using the hybrid approach.	78
Figure 3.3	Run time and RMSE for different model orders of grid-following (left) and grid-forming (right) inverter using zero-order and hybrid approach.	79
Figure 3.4	Root loci spectrum of interest for different model orders using zero-order reduction of a grid-following inverter.	81
Figure 3.5	Stability maps corresponding to different model orders of grid-following inverter in Fig. 3.4; the system is stable within the shaded region.	82
Figure 4.1	Characteristic timescales of different physical and control dynamics in a low-inertia system.	91

Figure 4.2	Configuration of the investigated system comprising two generators and one load connected via a transmission line.	93
Figure 4.3	Impact of inverter penetration on system stability for different unit configuration.	94
Figure 4.4	Impact of different controllers on system stability under high grid-following inverter penetration in Scenario I.	95
Figure 4.5	Stability maps in $K_s - \eta$ and $D_g - \eta$ planes indicating the effect of PSS stabilization gain and SG damping on admissible penetration of grid-following inverter units in Scenario I.	96
Figure 4.6	Impact of different controllers on system stability under high grid-forming inverter penetration in Scenario II.	97
Figure 4.7	Impact of different controllers on system stability under high grid-following inverter penetration in Scenario III.	98
Figure 4.8	Stability map in the $K_p^s - \eta$ plane indicating the effect of proportional PLL gain on admissible penetration of grid-following inverter units in Scenario III.	99
Figure 4.9	Impact of inverter penetration on system stability for different unit configuration, with inclusion of transmission line dynamics. Transparent dashed lines indicate results for scenarios without line dynamics from Fig. 4.3.	100
Figure 4.10	Root loci spectrum of interest for different system operating points: general mode movement (top) and the most critical modes (bottom). In the bottom figure, the edge color of the mode corresponds to the color of the respective arrow indicating the direction of the movement. The size of the symbol scales down with the increase in converter power setpoint p_c^*	101
Figure 4.11	Stability margins of the IEEE 9-bus test case: network diagram, with blue and red lines indicating the additionally incorporated transmission lines (left) and stability mapping under different levels of network connectivity (right). Colored arrows indicate the appropriate reading direction on the respective axes.	103

Figure 4.12	Maximum permissible inverter penetration under different system portfolios (\mathcal{P}) and levels of network connectivity (ε_g).	105
Figure 4.13	Modified South-East Australian power system line diagram.	106
Figure 4.14	Time-domain response of individual generators in South-East Australian network within first 10 s after initialization. The results correspond to the default system configuration presented in Fig. 4.13, with a substitution of a grid-following VSC at node 501 by a grid-forming one.	107
Figure 5.1	Uniform system frequency dynamics model.	118
Figure 5.2	Frequency response of a traditional power system. Shaded areas indicate the respective <i>accelerating</i> (green) and <i>decelerating</i> (red) intervals of the response.	122
Figure 5.3	Transient energy trajectory after a step disturbance.	125
Figure 5.4	Topology of the investigated three-area test system; the converter-based generation is placed at nodes 2, 6 and 10.	126
Figure 5.5	Frequency response after a 350 MW step increase in load.	127
Figure 5.6	Error distribution of frequency nadir computation.	128
Figure 5.7	system response under different VSM control designs: (i) CoI frequency; (ii) CoI RoCoF; (iii) aggregate inertia; and (iv) aggregate damping.	129
Figure 5.8	system response under different VSM control designs, retuned such that they meet the prescribed ENTSO-E criteria: (i) CoI frequency; (ii) CoI RoCoF; (iii) aggregate inertia; and (iv) aggregate damping.	130
Figure 5.9	Energy utilization for containing the frequency within limits: (a) activation of individual control components over time; and (b) total contribution of additional control effort.	131
Figure 5.10	Time-domain response with and without adaptive control when applied to a detailed EMT model: (i) individual generator frequencies; (ii) aggregate inertia; and (iii) aggregate damping.	133
Figure 6.1	State feedback control for adaptive VSM approach.	137
Figure 6.2	Multi-LQR control design in <i>Method A</i>	140

Figure 6.3	Application of a multi-LQR scheme in <i>Method A</i> . . .	140
Figure 6.4	Signal logic scheme for LQR detection in <i>Method A</i> . .	141
Figure 6.5	Multi-LQR control design in <i>Method B</i>	142
Figure 6.6	Iterative progress of feedback control gains in Algorithm 2.	145
Figure 6.7	System-level control design algorithm.	146
Figure 6.8	Stability analysis of the adaptive VSM control design: (a) stability region of inertia feedback gains; and (b) transient energy trajectory after a step disturbance. .	148
Figure 6.9	Individual control scheme for optimal gain selection.	149
Figure 6.10	System response under different VSM control designs: (i) CoI frequency; (ii) CoI RoCoF; (iii) aggregate inertia; and (iv) aggregate damping.	151
Figure 6.11	Energy utilization for containing a loss of generator: (a) components of the additional control effort; and (b) total energy content.	152
Figure 6.12	System frequency response after a loss of synchronous generator in the detailed EMT model: <i>Method B</i> vs. open-loop.	153
Figure 6.13	Configuration of the investigated HIL setup: a 2-bus system comprising the VSC supplying an <i>RL</i> load over a transmission line.	154
Figure 6.14	Response of the single converter supplying a varying load in HIL setup: (i) frequency measurement; (ii) filtered active power measurement; and (iii) output voltage measurement.	155
Figure 7.1	Simplified diagram of the implemented control structure with the MPC-based supervisory layer.	161
Figure 7.2	IEEE 39-bus New England test system. Inverter-based generation is placed at nodes 1, 2 and 3. Disturbance locations under consideration are indicated by red symbols.	171
Figure 7.3	Comparison of decentralized MPC performance under two frequency prediction models. Anticipated frequency evolution and adjusted power injections are used for evaluation.	172
Figure 7.4	Accuracy of the frequency prediction model: sensitivity to model parameters (top) and CoI-model verification (bottom).	173

Figure 7.5	Individual frequency and power response for the decentralized (top two figures) and centralized (bottom two figures) FFC scheme following a disturbance at bus 16. Uncontrolled response reflects the worst-case generator frequency without the use of FFC.	175
Figure 7.6	Individual frequency and power response for the decentralized (top two figures) and centralized (bottom two figures) FFC scheme following a disturbance at bus 26.	176
Figure 7.7	Individual frequency and power response for the decentralized (top two figures) and centralized (bottom two figures) FFC scheme following a disturbance at bus 38.	177
Figure 8.1	An exemplar feasible region in the $M - D$ plane. Colored arrows indicate feasible half-planes of respective frequency constraints.	185
Figure 8.2	Linear approximation of frequency and RoCoF signals.	189
Figure 8.3	Graphical illustration of the “worst-case” frequency deviation signal. Red and blue shaded areas reflect the over- and under-approximated battery energy content, respectively.	190
Figure 8.4	Graphical representation of the nature of the optimization problem and the activation of respective binding constraints for different input parameters ΔP , η_b and R_{g_i}	192
Figure 8.5	Correlation between M_b , D_b and η_b for $R_{g_i} = 4.6\%$	195
Figure 8.6	Approximation of energy content associated with integral constraint in Scenario I (top) and Scenario II (bottom). Colored and gray-shaded segments indicate the respective over- and under-approximations.	196
Figure 8.7	Utilization of battery’s power and energy during a disturbance in Scenario I (top) and Scenario II (bottom); shaded lines refer to Case A (without iterative improvement).	197
Figure 9.1	Simplified equivalent circuit of an induction machine.	205
Figure 9.2	Control structure of different synchronization units of a power converter: (a) type-2 SRF-PLL; (b) virtual induction machine.	211

Figure 9.3	Transient behavior of the VIM-based unit during start-up: (i) voltages; (ii) current and its dq -components; (iii) active and reactive power; (iv) frequencies; and (v) VIM frequency terms.	216
Figure 9.4	VIM response to the variation of controller setpoints: (a) Variation of the voltage setpoint. (b) Variation of the active power setpoint.	217
Figure 9.5	Impact of initial rotor frequency term on the synchronization process of a VIM during start-up: synchronous VIM frequency (top) and converter output voltage (bottom).	218
Figure 9.6	Behavior of different synchronization units after grid disconnection.	219
Figure 9.7	Stability maps of different converter modes in the $R_c^p - R_c^q$ plane.	220
Figure 9.8	SCR influence on system stability for different converter modes.	221
Figure 9.9	Impact of penetration of inverter-based generation on system stability for different converter operation modes.	221
Figure 9.10	Stability surface of a VIM-based converter in the $R_r - L_r - L_m$ space. The shaded area below the surface indicates a stable operating region.	222
Figure 10.1	Eigenvalue spectrum computed using both Padé approximation (denoted by circles) and Chebyshev discretization (denoted by triangles): full spectrum (top) and critical spectrum around the imaginary axis (bottom).	236
Figure 10.2	Stability maps in $\tau - K_p^v$ and $\tau - K_p^i$ planes. The system is stable within the shaded region.	237
Figure 10.3	Critical eigenvalue spectrum around the imaginary axis for the simplified converter control model.	238
Figure 10.4	Equivalent representation of the delay function $F_\tau(s)$: (a) original delay function $F_\tau(s)$; (b) time delay function with LFT-based representation of the delay block τ^{-1} ; (c) LFT formulation of the delay block τ^{-1} ; (d) LFT formulation of the delay function $F_\tau(s)$	240
Figure 10.5	General control plant of the investigated system: (a) LFT general plant; (b) LPV general plant.	242
Figure 10.6	Mixed sensitivity \mathcal{H}_∞ design.	243

Figure 10.7	Proposed control design strategies: (a) robust active damping control ($\mathcal{K}_1, \mathcal{K}_2$); (b) uniform robust inner control (\mathcal{K}_3). Delayed signals are denoted by red color.	247
Figure 10.8	Response to a step change in active power setpoint under constant time delay for different inner control designs: (i) $\tau = 150 \mu\text{s}$; (ii) $\tau = 500 \mu\text{s}$; and (iii) $\tau = 1 \text{ ms}$;	249
Figure 10.9	Response to a step change in active power setpoint under varying time delay for different inner control designs: varying time delay signal (top) and converter power output (bottom).	250
Figure 10.10	Topology of the investigated Kundur two-area system with WAC; Area 1 is on the left and Area 2 is on the right-hand side.	255
Figure 10.11	Mode shape of underdamped modes. Configuration I: (a) mode 1, (b) mode 2, (c) mode 3; (d) Configuration II; (e) Configuration III. Note that VSC_i and SG_i denote the respective generator types connected at node i .	256
Figure 10.12	Configuration I - frequency response of a traditional power system after a step change in load for two different scenarios: uncontrolled system (top) and controlled system with communication delays (bottom).	257
Figure 10.13	Configuration II - frequency response of a low-inertia system after a step change in load for two different scenarios: uncontrolled system (top) and controlled system with communication delays (bottom).	258
Figure 10.14	Configuration III - frequency response of a low-inertia system after a step change in load for two different scenarios: uncontrolled system (top) and controlled system with communication delays (bottom).	259
Figure 11.1	Flowchart of the employed iterative procedure in the second step of the multi-step approach.	281
Figure 11.2	Eigenvalue spectrum close to imaginary axis of the reduced- and full-order models for the identical inertia and damping allocation.	283
Figure 11.3	Optimal distribution of inertia and damping through uniform formulation when applied to full- and reduced-order models.	284

Figure 11.4	Optimal distribution of inertia and damping through multi-step optimization.	285
Figure 11.5	Comparison of uniform and multi-step formulation applied to a low-inertia system: critical eigenvalue spectrum (top) and allocation of inertia and damping (bottom).	286
Figure 11.6	Comparison of uniform and multi-step formulation applied to a no-inertia system: critical eigenvalue spectrum (top) and allocation of inertia and damping (bottom).	288
Figure 11.7	Impact of frequency constraints on allocation in the low-inertia system: critical eigenvalue spectrum (top) and distribution of inertia and damping (bottom). . .	290
Figure 11.8	Impact of frequency constraints on allocation in the no-inertia system: critical eigenvalue spectrum (top) and distribution of inertia and damping (bottom). . .	291
Figure 11.9	Comparison of frequency response after a disturbance for the cases with and without frequency constraints; thin lines represent individual generator frequencies, whereas thick lines denote the respective CoI frequency response.	292
Figure 11.10	Sensitivity evolution of the worst-case damping ratio to virtual inertia and damping parameters of individual converters over iterations.	293
Figure 11.11	Evolution of the worst-case damping ratio and system \mathcal{H}_2 norm over iterations.	294
Figure 12.1	PWL of the nadir constraint for $M = 9$ s.	302
Figure 12.2	All possible values of frequency nadir after a generator loss.	303
Figure 12.3	Scenario tree for the two-stage stochastic UC problem.	306
Figure 12.4	Modified IEEE RTS-96 system diagram comprising 2 areas, 16 wind farms and 20 synchronous generators [308].	312
Figure 12.5	UC dispatch of synchronous generation for respective load and wind profiles.	313
Figure 12.6	Impact of frequency constraints on the aggregate level of system inertia.	314
Figure 12.7	Constraint gaps for different frequency metrics. Dashed lines refer to the case without frequency constraints.	315

Figure 12.8	Frequency evolution of the uniform CoI model with and without FC for 20 seconds after the fault instance at $t = 67$ h.	315
Figure 13.1	Cost curve of additional inertia provision.	329
Figure 13.2	Proposed methodology for determining inertia payments.	332
Figure 13.3	EOM price with and without frequency constraints.	339
Figure 13.4	Impact of virtual inertia on total inertia payments under different bid-in prices and payment mechanisms: (i) <i>ex-post</i> calculation; (ii) utility function; and (iii) uplift payments.	340
Figure 14.1	Generic system for studying anti-islanding detection schemes. Both switches are originally closed, with the opening of switch S_2 reflecting the islanding operation and activation of the LoM protection.	351
Figure 14.2	Graphical illustration of the (traditional) NDZ approximation widely used in the literature.	353
Figure 14.3	Simplified representation of grid-connected power converters with characteristic setpoint input and internally computed reference output: (a) grid-forming mode; and (b) grid-following mode.	355
Figure 14.4	Single-line diagram of the test system under investigation.	363
Figure 14.5	Comparison of analytical and simulated NDZs in case of grid-following converters: grid-feeding mode (top) and grid-supporting mode (bottom). Dark rectangular region represents an NDZ of the grid-feeding inverter obtained through a traditional approximation.	364
Figure 14.6	Analytical NDZ in case of grid-supporting converters for a wide range of frequency droop gains $R_f \in [0 - 25]$ p.u.	365
Figure 14.7	Analytical NDZ in case of grid-supporting converters for different LoM protection settings.	366
Figure 14.8	Analytical NDZ in case of grid-forming converters with conventional droop gain tuning of $(R_P, R_Q) = (0.05, 0.005)$ p.u.	367

- Figure 14.9 Comparison of analytical and simulated NDZs in case of grid-forming converters with unconventional droop gain tuning: scenario $(R_P, R_Q) = (0.125, 0.75)$ p.u. (top) and scenario $(R_P, R_Q) = (0.05, 0.1)$ p.u. (bottom).368
- Figure B.1 Illustration of the PWL method on a 2-D function. . 392

LIST OF TABLES

Table 2.1	Converter control parameters.	52
Table 2.2	Synchronous generator parameters.	54
Table 3.1	Small-scale factors of the inverter model.	75
Table 3.2	Modal analysis of the inverter model.	76
Table 4.1	Scenario configuration based on the generation portfolio in the system.	108
Table 5.1	Parameters for sensitivity analysis.	127
Table 7.1	Fault scenarios at different buses with indicated applied disturbance magnitudes and estimated imbalances for each VSC located at nodes 1, 2 and 3, respectively.	174
Table 8.1	Optimal sizing and tuning for $\Delta P = 620$ MW.	194
Table 9.1	Simulation parameters of the proposed VIM controller.	215
Table 9.2	State participation [%] in the unstable modes.	222
Table 10.1	State participation [%] in the most critical conjugate pair $\lambda_{1,2}$	237
Table 10.2	Stability performance of different control designs.	248
Table 10.3	Underdamped modes of the Kundur two-area system.	256
Table 11.1	Comparison of system performance metrics for the low-inertia test system and loss of synchronous generation at node 1.	292
Table 12.1	Computational cost of the linearization methods.	304
Table 12.2	Unit commitment nomenclature of Chapter 12.	307
Table 12.3	Parameters of the conventional and converter-interfaced generation.	312
Table 12.4	Comparison of the total number of dispatched synchronous generators through UC for each hour.	313
Table 12.5	Unit commitment costs [\$] breakdown on day 3.	316
Table 13.1	Breakdown of UC costs [€] with and without inertia requirements.	327
Table 13.2	Small test system description.	336
Table 13.3	Parameters of VI battery units in the large system.	337
Table 13.4	Breakdown of hourly UC costs [€] for <i>Method 1</i>	338
Table 13.5	Hourly SG profits [€] under <i>Method 1</i> pricing scheme.	339

Table 13.6	Breakdown of hourly UC costs [€] for <i>Method 2</i>	341
Table 13.7	Hourly SG profits [€] under <i>Method 2</i> pricing scheme.	342
Table 13.8	Hourly SG profits [€] under <i>Method 3</i> pricing scheme.	343
Table 13.9	Comparison of different inertia payment methods.	344
Table 13.10	Comparison of total inertia payments [€] under different levels of VI installation in the system.	345
Table 13.11	Policy implications of proposed payment methods with distinctive advantages (green) and disadvantages (red).	346
Table 14.1	Frequency and voltage protection settings prescribed by the operators of different European countries.	362
Table 14.2	Employed frequency and voltage protection settings.	362
Table A.1	Values of ν_M and ν_D throughout the response.	380

INTRODUCTION

The world as we have created it is a process of our thinking. It cannot be changed without changing our thinking.

— Albert Einstein

1.1 BACKGROUND AND MOTIVATION

With the convergence of economic and policy drivers, electric power systems are hosting rapidly increasing shares of wind and solar generation in an effort to replace traditional thermal generation based on fossil fuel and nuclear power. Due to intermittent nature of these Renewable Energy Sources (RES) and the fact that they are typically connected to the power system via Power Electronics (PE), their interaction with the power system is substantially different from Synchronous Machines (SMs). While curtailment or energy storage can be used to overcome the lack of controllability of renewable sources, today's renewable, converter-interfaced generation does not provide the same level of grid support (e.g., inertia, primary frequency control) that is traditionally provided by conventional generation and SMs. This jeopardizes the system's reliability [1] and already resulted in wide-area outages [2].

Large-scale low-inertia power systems have been a theoretical concept up until recently, but have now become a reality and Transmission System Operators (TSOs) around the world are facing challenges caused by high penetration of PE-based RES [2–4]. Moreover, some countries already have solar and/or wind generation capacity capable of covering more than 100% of the demand, leading to the questions on how to control and operate a large-scale power systems almost entirely based on converter-interfaced generation [5, 6]. The challenges related to replacing SMs in legacy power systems are primarily related to the loss of rotational inertia [7], frequency stability [8, 9], and adverse interactions between the fast response of power converters and components of the legacy systems [10–12]. The last aspect also poses an obstacle for modeling and simulation of large-scale networks [8, 13], and requires appropriate reduced-order models of power converters in order to achieve scalability [14, 15].

On the other hand, the challenges in 100% converter-based systems are similar in nature but broader in scope. In particular, an underlying issue in such systems is that the grid-forming devices are needed to even establish a well-defined system frequency [6]. Moreover, in conventional bulk generation based on SMs, the high levels of inertia are inherent in the machine design and compensate for the relatively large response time of primary control caused by the slow response of steam and hydro turbines. In contrast, power converters introduce faster dynamics, which implies that the timescale separation traditionally assumed in control and operation of power systems may not hold, resulting in unexpected oscillations and even instability [12, 16, 17]. For instance, converter-based generation that provides fast frequency control can excite oscillations in the transmission grid and destabilize the entire system [17]. Likewise, measurement or communication delays can destabilize the control of power converters [18–20]. Moreover, for conventional generation, the stability at the *device-level* (i.e., the level of a synchronous machine) directly implies transient stability of the power system, whereas standard control architectures for power converters comprise a *system-level* control layer that generates a desired behaviour (e.g., frequency and voltage reference signals) and a *device-level* control layer that tracks these references.

From an ancillary service perspective, novel control algorithms can be used to provide both existing system services as well as novel services that exploit the flexibility and fast actuation of power converters. In particular, primary frequency control can be provided faster, and both the primary frequency control as well as inertial response of converter-interfaced generation can be adapted according to the state of the grid. On the other hand, the PE-based renewable generation typically requires some form of energy storage to provide ancillary services and the impact of physical storage limitations on such services must be considered. Moreover, given converter-interfaced generation providing aforementioned ancillary services, an important question is how to optimally place such devices in a power system to ensure robust and resilient operation.

The goal of this thesis is to improve the modeling and understanding of dynamical interactions in inverter-dominated grids, as well as to develop new control and optimization methods for reliable and resilient operation of such systems. In the first part of the thesis, we focus on modeling and stability of PE-dominated power systems, taking into account the most promising system-level converter control schemes and detailed SM and network dynamics. In the second part, frequency dynamics in low-inertia systems and advanced converter control schemes for fast frequency provision are studied.

Finally, the third part presents various methods for improving reliability and performance of networks with high converter penetration, addressing topics such as synchronization, measurement and communication delays, valuation and pricing of inertia, and placement of virtual inertia and damping.

1.2 CONTRIBUTIONS

We focus on improving reliability and resilience of transmission-level networks hosting large shares of converter-interfaced RES. Specifically, the main contributions of this thesis are:

- A detailed mathematical representation of a realistic low-inertia power system, with different system-level converter controls subsumed under a general dynamical form.
- A reduced-order power converter model that provides a more accurate time-domain performance during transients.
- Novel insights into stability properties of power systems with large-scale integration of RES, especially in terms of characterizing the maximum permissible penetration levels of converter-based generation.
- A uniform frequency response model of a generic low-inertia system and several adaptive Virtual Synchronous Machine (VSM) controllers that ensure the frequency metrics are kept within bounds prescribed by the TSO.
- A *centralized* and a *decentralized* Model Predictive Control (MPC) approach for converter-interfaced generators operating in grid-forming mode, with the goal of exploiting their responsiveness and providing fast frequency control to the system.
- A method for combined sizing of DC-side storage capacity and tuning of controller gains of grid-forming converters, which ensures sufficient energy and power capacity for containing a predefined active power imbalance and preserving frequency within prescribed limits.
- A control strategy for synchronization of grid-connected converters based on emulating the physical properties of an induction machine and taking advantage of its inherent grid-friendly properties such as self-synchronization, oscillation damping and standalone capabilities.

- A device-level controller of a power converter robust to uncertainty in local measurement delays, and a delay-robust wide-area oscillation damping controller for inverter-dominated power systems capable of dealing with time-varying communication delays.
- A multi-objective method for allocation of inertia and damping in a low-inertia power system based on eigensensitivity optimization, considering several performance metrics such as small-signal stability, minimum damping ratio, frequency response and system norms.
- A stochastic unit commitment problem formulation for a power network with low levels of rotational inertia, accounting for frequency-related constraints and wind power and equipment contingency uncertainties.
- Three novel pricing and payment schemes that reimburse inertia providers in a transparent and fair manner according to their individual participation in the ancillary service market.
- An improved analytical approximation of the non-detection zone of islanding detection schemes in the presence of PE-interfaced distributed generation operating in various control modes.

1.3 THESIS OUTLINE

The thesis is organized into three parts. The first part focuses on modeling, stability and hierarchical control of PE-dominated power systems, the second part studies the frequency dynamics and fast frequency control applications in low-inertia grids, whereas the third part provides various methods for improving reliability and performance of networks with high converter penetration. The content of each part is divided into the following chapters:

Part I

- **Chapter 2** presents the modeling and control of low-inertia power systems comprising SM, converter and transmission network dynamics. A detailed mathematical representation of the converter model and the most promising control strategies in the literature are introduced, with different system-level controls subsumed under a general model describing the controller's internal dynamics. The compatibility of novel grid-forming control strategies in systems with 100% converter-interfaced generation is investigated and the mathematical equivalence between the methods is discussed.

- **Chapter 3** proposes a *hybrid* model-order reduction method based on singular perturbation, motivated by the timescale separation between the fast and slow dynamics in an inverter-based power system. Such technique preserves the slow system dynamics of the full-order model, while simultaneously capturing the impact of the removed fast states on slow variables. The simulations showcase an improved time-domain performance during transients, while having only a negligible increase in computational requirements.
- **Chapter 4** presents novel insights into stability properties of power systems with large-scale integration of RES. This work characterizes the maximum permissible penetration levels of inverter-based generation as well as the nature of the associated unstable modes and the underlying dynamics. Moreover, potential directions for improving the system stability margin under different generation portfolios are proposed.

Part II

- **Chapter 5** develops a uniform frequency response model of a generic low-inertia system and derives analytical expressions for frequency metrics of interest. This information is then applied to the control design, where the VSM inertia and damping constants are adjusted according to the frequency disturbance and the respective VSM acceleration interval, while preserving the frequency within prescribed thresholds.
- **Chapter 6** proposes two adaptive VSM controllers based on a linear-quadratic regulator. The optimal state feedback gains are determined to adaptively adjust the emulated inertia and damping constants according to the frequency disturbance in the system, while simultaneously preserving a trade-off between the critical frequency limits and the required control effort.
- **Chapter 7** develops a *centralized* and a *decentralized* MPC controller for converter-interfaced generators operating in grid-forming mode, with the goal of exploiting their responsiveness and providing fast frequency control. The controller adapts converter power injection to limit the frequency excursion after a disturbance.
- **Chapter 8** introduces a method for combined sizing of DC-side storage capacity and tuning of controller gains of grid-forming converters, which accounts for the coupling between installation planning and operation parameters of the storage unit. It ensures sufficient energy

and power capacity for containing a predefined active power imbalance and preserving frequency within prescribed limits.

Part III

- **Chapter 9** presents a novel control strategy for synchronization of grid-connected converters based on emulating the physical properties of an induction machine and taking advantage of its inherent grid-friendly properties such as self-synchronization, oscillation damping and standalone capabilities. The subsequent small-signal analysis provides guidelines for appropriate control tuning and reveals some interesting properties pertaining to the nature of the underlying operation mode.
- **Chapter 10** deals with the topic of time delay in low-inertia power systems, taking into consideration both the constant and time-varying delays. The focus is set on two different problem setups: (i) the problem of constant local measurement delay, its impact on the stability of a single inverter control scheme, and the design of a device-level controller robust to uncertainty in such measurement delays; and (ii) the design of the delay-robust wide-area oscillation damping controller for inverter-dominated power systems capable of dealing with time-varying communication delays.
- **Chapter 11** proposes a method for allocation of inertia and damping in an inverter-dominated power system. The approach combines a detailed system representation from Chapter 2 with an iterative eigensensitivity-based optimization framework. A comprehensive multi-objective formulation is presented, considering several performance metrics such as small-signal stability, minimum damping ratio, frequency response and system norms.
- **Chapter 12** studies the unit commitment problem in a power network with low levels of rotational inertia. Frequency-related constraints derived in Chapter 5 are included into a two-stage stochastic formulation that accounts for wind power and equipment contingency uncertainties using a scenario-tree approach.
- **Chapter 13** investigates the procurement and pricing of inertial response using a frequency-constrained unit commitment formulation, which co-optimizes the provision of energy and inertia services while accounting for their complementary properties. Three novel pricing and payment schemes that reimburse inertia providers in a transparent and fair manner according to their individual participation are proposed.

- **Chapter 14** studies the impact of inverter-based generation on islanding detection schemes. An improved analytical formulation for estimating the non-detection zone of loss of mains protection devices in the presence of grid-feeding inverters is proposed, as well as novel NDZ approximations for grid-supporting and grid-forming inverter-based services.

Finally, **Chapter 15** summarizes the key findings of this thesis and suggests directions for future work.

1.4 PUBLICATIONS

The work presented in this thesis has been reported in the following publications:

Articles in peer-reviewed journals:

- [1] **U. Markovic**, D. Chrysostomou, P. Aristidou, and G. Hug. “Impact of Inverter-Based Generation on Islanding Detection Schemes in Distribution Networks”. In: *Electric Power Systems Research* 190 (Jan. 2021), 106610.
- [2] I. Caduff, **U. Markovic**, C. Roberts, G. Hug, and E. Vrettos. “Reduced-Order Modeling of Inverter-Based Generation using Hybrid Singular Perturbation”. In: *Electric Power Systems Research* 190 (Jan. 2021), 106773.
- [3] S. Alghamdi, **U. Markovic**, O. Stanojev, J. Schiffer, G. Hug, and P. Aristidou. “Wide-Area Oscillation Damping in Low-Inertia Grids under Time-Varying Communication Delays”. In: *Electric Power Systems Research* 189 (Dec. 2020), 106629.
- [4] **U. Markovic**, O. Stanojev, E. Vrettos, P. Aristidou, D. Callaway, and G. Hug. “Understanding Stability of Low-Inertia Systems”. In: *IEEE Transactions on Power Systems* (Nov. 2020).
- [5] M. Paturet, **U. Markovic**, S. Delikaraoglou, E. Vrettos, P. Aristidou, and G. Hug. “Stochastic Unit Commitment in Low-Inertia Grids”. In: *IEEE Transactions on Power Systems* 35.5 (Sept. 2020), 3448.
- [6] O. Stanojev, **U. Markovic**, P. Aristidou, G. Hug, D. Callaway, and E. Vrettos. “MPC-Based Fast Frequency Control of Voltage Source Converters in Low-Inertia Power Systems”. In: *IEEE Transactions on Power Systems* (June 2020), 1.

- [7] **U. Markovic**, Z. Chu, P. Aristidou, and G. Hug. “LQR-Based Adaptive Virtual Synchronous Machine for Power Systems with High Inverter Penetration”. In: *IEEE Transactions on Sustainable Energy* 10.3 (July 2019), 1501.
- [8] M. Paturet, **U. Markovic**, S. Delikaraoglou, E. Vrettos, P. Aristidou, and G. Hug. “Economic Valuation and Pricing of Inertia in Inverter-Dominated Power Systems”. In: *IEEE Transactions on Power Systems* (under review).
- [9] **U. Markovic**, J. Zhang, D. Rodriguez Flores, O. Stanojev, P. Aristidou, and G. Hug. “Impact of Measurement Delays on Stability and Performance of Inverter-Dominated Power Systems”. In: *IEEE Transactions on Power Systems* (under review).
- [10] **U. Markovic**, O. Stanojev, P. Aristidou, and G. Hug. “Improving Frequency Stability of Low-Inertia Systems using Virtual Induction Machine”. In: *IEEE Transactions on Power Systems* (under review).
- [11] A. Venkatraman, **U. Markovic**, D. Shchetinin, E. Vrettos, P. Aristidou, and G. Hug. “Improving Dynamic Properties of Low-Inertia Systems through Eigensensitivity Optimization”. In: *IEEE Transactions on Power Systems* (under review).
- [12] **U. Markovic**, D. Groß, P. Aristidou, F. Colas, T. Qoria, T. Prevost, G. Denis, M. Debry, X. Guillaud, and G. Hug. “Compatibility of Grid-Forming Control Strategies in 100% Converter-Based Power Systems”. In: *IEEE Transactions on Power Delivery* (under review).

Conference contributions:

- [13] **U. Markovic**, D. Chrysostomou, P. Aristidou, and G. Hug. “Impact of Inverter-Based Generation on Islanding Detection Schemes in Distribution Networks”. In: *2020 PSCC*. June 2020.
- [14] I. Caduff, **U. Markovic**, C. Roberts, G. Hug, and E. Vrettos. “Reduced-Order Modeling of Inverter-Based Generation using Hybrid Singular Perturbation”. In: *2020 PSCC*. June 2020.
- [15] S. Alghamdi, **U. Markovic**, O. Stanojev, J. Schiffer, G. Hug, and P. Aristidou. “Wide-Area Oscillation Damping in Low-Inertia Grids under Time-Varying Communication Delays”. In: *2020 PSCC*. June 2020.

- [16] **U. Markovic**, V. Häberle, D. Shchetinin, G. Hug, D. Callaway, and E. Vrettos. “Optimal Sizing and Tuning of Storage Capacity for Fast Frequency Control in Low-Inertia Systems”. In: *2019 SEST. (Best Paper Award)*. Sept. 2019.
- [17] D. Rodriguez Flores, **U. Markovic**, P. Aristidou, and G. Hug. “Robust Converter Control Design under Time-Delay Uncertainty”. In: *2019 PowerTech*. June 2019.
- [18] **U. Markovic**, N. Früh, P. Aristidou, and G. Hug. “Interval-Based Adaptive Inertia and Damping Control of a Virtual Synchronous Machine”. In: *2019 PowerTech. (Finalist for Basil Papadias Best Paper Award - 3rd Prize)*. June 2019.
- [19] **U. Markovic**, J. Vorwerk, P. Aristidou, and G. Hug. “Stability Analysis of Converter Control Modes in Low-Inertia Power Systems”. In: *2018 ISGT-Europe*. Oct. 2018.
- [20] **U. Markovic**, O. Stanojev, P. Aristidou, and G. Hug. “Partial Grid Forming Concept for 100% Inverter-Based Transmission Systems”. In: *2018 PES General Meeting*. Aug. 2018.
- [21] R. Ofir, **U. Markovic**, P. Aristidou, and G. Hug. “Droop vs. Virtual Inertia: Comparison from the Perspective of Converter Operation Mode”. In: *2018 ENERGYCON*. June 2018.
- [22] **U. Markovic**, Z. Chu, P. Aristidou, and G. Hug. “Fast Frequency Control Scheme through Adaptive Virtual Inertia Emulation”. In: *2018 ISGT-Asia*. May 2018.
- [23] **U. Markovic**, P. Aristidou, and G. Hug. “Virtual Induction Machine Strategy for Converters in Power Systems with Low Rotational Inertia”. In: *2017 IREP*. Aug. 2017.
- [24] **U. Markovic**, P. Aristidou, and G. Hug. “Stability Performance of Power Electronic Devices with Time Delays”. In: *2017 PowerTech. (Finalist for Basil Papadias Best Paper Award - 2nd Prize)*. June 2017.

Other publications:

- [25] **U. Markovic**, T. Jouini, and D. Groß. *MIGRATE WP3 - Control and Operation of a Grid with 100% Converter-Based Devices*. Tech. rep. Horizon 2020 - LCE-6, Dec. 2018.
- [26] T. Qoria, **U. Markovic**, T. Jouini, D. Groß, G. Denis, and T. Prevost. *Data underlying the research of a 3 bus model for full inverter system - Migrate WP3*. 2018.

The following papers have been published in the course of the PhD studies, but their content is not included in the thesis:

Articles in peer-reviewed journals:

- [27] A. M. Nakiganda, S. Dehghan, **U. Markovic**, G. Hug, and P. Aristidou. “A Stochastic-Robust Approach for Resilient Microgrid Investment Planning Under Static and Transient Islanding Security Constraints”. In: *IEEE Transactions on Smart Grid* (under review).
- [28] J. Vorwerk, **U. Markovic**, P. Aristidou, E. Vrettos, and G. Hug. “Modeling of Variable-Speed Refrigeration for Fast Frequency Control in Low-Inertia Systems”. In: *IET Smart Grid* (Sept. 2020).
- [29] Z. Chu, **U. Markovic**, G. Hug, and F. Teng. “Towards Optimal System Scheduling with Synthetic Inertia Provision from Wind Turbines”. In: *IEEE Transactions on Power Systems* 35.5 (Apr. 2020), 4056.
- [30] A. Venzke, L. Halilbasic, **U. Markovic**, G. Hug, and S. Chatzivasileiadis. “Convex Relaxations of Chance Constrained AC Optimal Power Flow”. In: *IEEE Transactions on Power Systems* 33.3 (May 2018), 2829.
- [31] T. Borsche, **U. Markovic**, and G. Andersson. “A New Algorithm for Primary Frequency Control with Cooling Appliances”. In: *Computer Science - Research and Development Springer Journal* 31.1–2 (May 2016), 89.

Conference contributions:

- [32] O. Stanojev, **U. Markovic**, E. Vrettos, P. Aristidou, D. Callaway, and G. Hug. “Enhanced MPC for Fast Frequency Control in Inverter-Dominated Power Systems”. In: *2020 SEST. (Best Paper Award)*. Sept. 2020.
- [33] O. Stanojev, O. Kundacina, **U. Markovic**, E. Vrettos, P. Aristidou, and G. Hug. “A Reinforcement Learning Approach for Fast Frequency Control in Low-Inertia Power Systems”. In: *2020 North American Power Symposium (NAPS)*. Sept. 2020.
- [34] L. Srinivasan, **U. Markovic**, M. G. Vayá, and G. Hug. “Provision of Frequency Control by a BESS in Combination with Flexible Units”. In: *2018 ENERGYCON*. June 2018.

- [35] **U. Markovic**, E. Kaffe, D. Mountouri, F. Kienzle, S. Karagiannopoulos, and A. Ulbig. “The Future Role of a DSO in Distribution Networks with High Penetration of Flexible Prosumers”. In: *CIREN Workshop 2016*. June 2016.

In addition to aforementioned publications, the content of this thesis is also based on the following semester and master theses conducted in the Power Systems Laboratory of ETH Zurich:

Master theses:

- [1] Ashwin Venkatraman. *Improving Dynamic Performance of Low-Inertia Systems through Eigensensitivity Optimization*. Dec. 2019.
- [2] Ognjen Stanojev. *MPC-Based Fast Frequency Control of Voltage Source Converters in Low-Inertia Systems*. Sept. 2019.
- [3] Matthieu Paturet. *Economic Valuation and Pricing of Inertia in Inverter-Dominated Power Systems*. June 2019.
- [4] Ivo Caduff. *Model-Order Reduction Methods for High-Fidelity Low Inertia Systems*. Mar. 2019.
- [5] David Rodriguez Flores. *Robust Converter Control Design under Time-Delay Uncertainty*. Oct. 2018.
- [6] Zhongda Chu. *Provision of Adaptive Inertia and Damping in a Multi-Inverter Low-Inertia Power System*. Mar. 2018.
- [7] Arsam Aryandoust. *Modeling and Optimization-Based Control of a Dynamic Demand Response System for Active Distribution Networks*. Oct. 2017.
- [8] Lakshmi Srinivasan. *Provision of Secondary Control by a Battery Energy Storage System in Combination with a Pool of Flexible Units*. Sept. 2017.
- [9] Andreas Venzke. *Convex Relaxations for Optimization of AC and HVDC Grids under Uncertainty*. Mar. 2017.

Semester theses:

- [10] Demetris Chrysostomou. *Impact of Low-Inertia systems on Distribution Grid Protection*. Oct. 2019.
- [11] Verena Häberle. *Optimal Sizing, Placement and Tuning of Converters with Inclusion of Dynamic Stability Constraints*. Jan. 2019.

- [12] Nicolas Früh. *Interval-based Adaptive Inertia and Damping Control of a Virtual Synchronous Machine*. Mar. 2018.
- [13] Jialun Zhang. *Impact of Time-Delays on Stability of Inertia-less Power Systems*. Mar. 2018.
- [14] Baudouin Vandebussche. *Optimal Placement of Grid-Forming Converters in a 100% PE-based Power System*. Mar. 2018.
- [15] Body Nasef. *Small-Signal Modeling and Stability of a Virtual Induction Machine*. Mar. 2018.
- [16] Matthieu Paturet. *Unit Commitment Problem with Inclusion of Inertia Constraints*. Mar. 2018.
- [17] Zhongda Chu. *Adaptive Provision of Virtual Inertia on a Transmission System Level*. Mar. 2018.
- [18] Simon Hobi. *Comparison of a Synchronous Machine and a Matching DC-AC Converter Model*. Feb. 2018.
- [19] Ognjen Stanojev. *Partial Grid Forming Concept for 100% Inverter-Based Transmission Systems*. Jan. 2018.
- [20] Johanna Vorwerk. *Small-Signal Analysis of Power Systems with No Rotational Inertia*. Jan. 2018.
- [21] David Roman Kayanan. *Comparing Droop Control Variations on a Grid-Interfaced VSC via Virtual HIL*. Sept. 2017.
- [22] Ron Ofir. *Modelling and Transient Analysis of Small-Scale Power Systems with No Inertia*. Aug. 2017.

1.5 MATHEMATICAL NOTATION

We use \mathbb{R} to denote the set of real and natural numbers and, e.g., $\mathbb{R}_{\geq a} := \{x \in \mathbb{R} | x \geq a\}$. Given an angle $\theta \in [-\pi, \pi)$, the 2-D rotation matrix is given by

$$\mathcal{R}(\theta) := \begin{bmatrix} \cos \theta & -\sin \theta \\ \sin \theta & \cos \theta \end{bmatrix} \in \mathbb{R}^{2 \times 2}.$$

Moreover, we define the 90° rotation matrix $j := \mathcal{R}(\pi/2)$ that can be interpreted as an embedding of the complex imaginary unit $\sqrt{-1}$ into \mathbb{R}^2 . For column vectors $x \in \mathbb{R}^n$ and $y \in \mathbb{R}^m$ we use $(x, y) = [x^\top, y^\top]^\top \in \mathbb{R}^{n+m}$ to denote a stacked vector. Furthermore, I_n denotes the identity matrix of dimension n , \otimes denotes the Kronecker product, and $\|x\|$ denotes the Euclidean

norm. Matrices of zeros of dimension $n \times m$ are denoted by $\mathbb{0}_{n \times m}$, and $\mathbb{0}_n$ and $\mathbb{1}_n$ denote column vectors of zeros and ones of length n .

Part I

MODELING AND STABILITY OF
INVERTER-DOMINATED POWER
SYSTEMS

MODELING AND CONTROL OF INVERTER-DOMINATED GRIDS

This chapter discusses the modeling and control of low-inertia power systems. For that purpose, a detailed mathematical representation of the converter model is introduced. The most prevalent control strategies in the literature are described, with different system-level controls subsumed under a general model describing the controller's internal dynamics. Subsequently, the compatibility of novel grid-forming control strategies in systems with 100% converter-interfaced generation is investigated and the mathematical equivalence between the methods is discussed. In addition, the overcurrent limitation schemes are also taken into consideration in order to fully capture the flexibility and fast actuation capabilities of grid-forming power converters. Furthermore, we propose a high-fidelity formulation of a generic low-inertia system comprising detailed models of synchronous and converter-interfaced generation as well as the transmission network dynamics. The accuracy of the developed model is validated through time-domain simulations. This chapter is based on [21–24].

2.1 INTRODUCTION

The dynamics of a conventional power system are dominated by synchronous machines and their controls, and have been thoroughly modeled and studied in the literature [25–27]. In order to achieve a similar level of detail in modeling of low-inertia systems, we need an accurate representation of power electronic converters and their control schemes. While very elaborate models of power converters and the primary energy sources behind them have been proposed [28–37], such level of detail is not practical for analysis and control design in large-scale transmission systems. In contrast, the microgrid literature tends to abstract the power converters as controllable voltage sources with outer (i.e., system-level) control loops [38–41], and even further simplify them by exploiting the singular perturbation techniques [42] and applying model reduction methods based on the premise of timescale separation [15, 43–45]. However, recent studies have shown that such abstract modeling approach cannot be used for transmission networks as it might not be able to

capture potentially adverse interference between controllers of synchronous and converter-interfaced generation [12, 17, 46, 47].

From a viewpoint of the power system, the Voltage Source Converter (VSC) can be seen as a black box that modulates an AC voltage and injects active and reactive power into the grid. In terms of VSC control, two components represent a foundation of every converter control scheme: the device-level control and the system-level control. The former (inner) control layer tracks the reference signals provided by the latter (outer) control layer, which aims at meeting certain system-level specifications. These can range from injecting a pre-specified amount of power to providing services such as electrical inertia (i.e., an inertial response generated by power converters) and primary frequency control. Several concepts for outer control design have been proposed based on the analogy between Synchronous Generators (SGs) and converter-interfaced generation, most notably droop control [48], synchronous machine emulation [49–51], Virtual Oscillator Control (VOC) [52], and dispatchable VOC (dVOC) [17, 53]. In addition, the machine matching control [54–58] combines the aspects of outer and inner control by exploiting the duality of DC voltage and mechanical frequency of an SM. Moreover, an additional synchronization layer (e.g., a phase-locked loop) may be used to detect the frequency at the Point of Common Coupling (PCC) and enhance initial synchronization to the grid, but subsequently stays inactive during regular operation.

Despite numerous proposed techniques, the existing literature is very convoluted in terms of converter control and individual operation modes, with unclear boundaries between various control strategies. The issue particularly stems from inconsistent terminology used for describing the converter functions from the system-level perspective, resulting in similar terms assigned to completely different control designs [59]. In particular, the most common definitions of converter operation modes have been proposed in the context of AC microgrids [60–62], with their predefined input-output control structures becoming outdated, i.e., incompatible with novel control methods such as VOC and machine matching. Furthermore, these classifications do not distinguish between the employed synchronization principles (e.g., synchronization methods based on power, current or DC voltage imbalance).

Finally, from a device-level perspective, aspects such as overcurrent protection and limited energy storage within the power converter play an important role. These aspects are typically ignored in the system-level analysis. However, unlike the overcurrent protection of SMs, that tends to be relatively slow due to machines being capable of withstanding significant overcurrents for a short

period of time, the importance of current saturation limits in converter-based power system is much higher [35, 36, 63]. In this chapter, we aim to bridge the gap and analyze the interplay between the device-level control, including overcurrent protection, and the grid-forming (i.e., system-level) control strategies.

The contribution of this chapter is twofold. Firstly, we introduce the mathematical representation of a detailed converter model as well as the basic design principles of its control scheme. Moreover, we present different system-level control techniques and define a general formulation that subsumes them into a single model describing the controller's internal dynamics. The focus is primarily on the compatibility of novel grid-forming control strategies in systems with 100 % converter-interfaced generation that fully exploit the flexibility and fast actuation capabilities of power converters, while accounting for their stringent overcurrent limits. Secondly, we propose a detailed Differential-Algebraic Equation (DAE) formulation of a generic low-inertia system comprising detailed models of synchronous and converter-interfaced generation as well as the transmission network dynamics, and validate its accuracy and time-domain performance.

The rest of the chapter is structured as follows. In Section 2.2, technical requirements and general control architecture of a two-level voltage source converter are introduced. A particular focus is set on system-level control, with Section 2.3 describing the traditional grid-following control and Section 2.4 focusing on the most promising grid-forming control strategies. The most common overcurrent protection techniques are introduced in Section 2.5, followed by a study in Section 2.6 that investigates the compatibility of novel grid-forming control strategies employing such current limits in a 100 % inverter-based power system. Subsequently, a uniform representation of a droop-based VSC encompassing both the grid-forming and the grid-following operation mode is presented in Section 2.7, together with the detailed dynamical model of a synchronous generator in Section 2.8. Finally, Section 2.9 describes the network dynamics and completes the model formulation of a generic low-inertia system, whereas Section 2.10 concludes the chapter.

2.2 MODELING AND CONTROL OF POWER CONVERTERS

2.2.1 *Drawbacks of Existing Control Classification*

From a system-level perspective, the overall behaviour of the controlled power converter is of interest and not the internal structure of its controls. Due

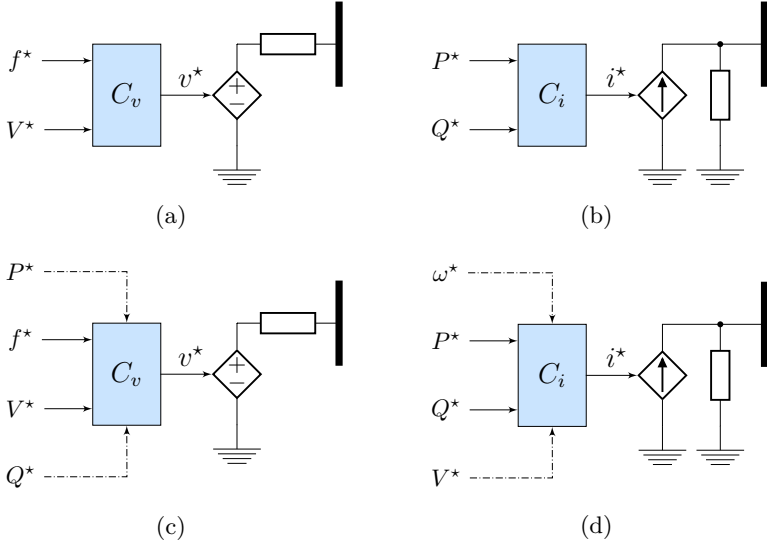


FIGURE 2.1: Traditional (simplified) representation of system-level controls of grid-connected power converters, with characteristic setpoint input and internally computed reference output: (a) grid-forming; (b) grid-feeding; (c) voltage-source-based grid-supporting; and (d) current-source-based grid-supporting. Dashed lines indicate less prioritized control requirements.

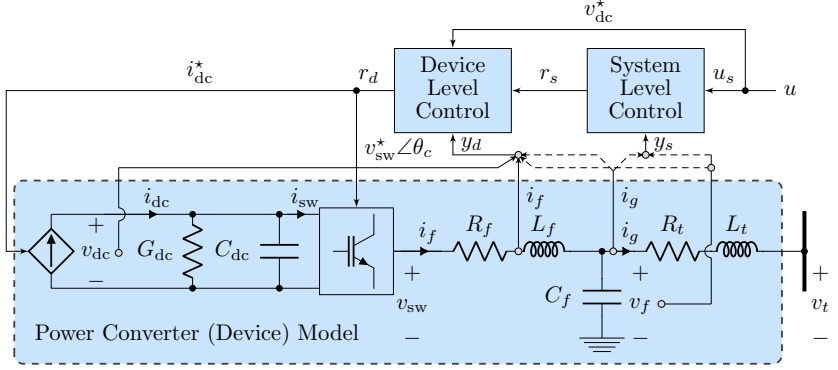
to their initial applications, the earliest definitions of converter operation modes have been proposed in the context of AC microgrids, classified into *grid-forming*, *grid-feeding* and *grid-supporting* category [60–62]. These system-level controls are often represented using a simplified control block structure illustrated in Fig. 2.1, showcasing the characteristic setpoint input and internally computed reference output. In particular, the grid-forming converters are represented as an ideal AC voltage source with a low-output impedance (see Fig. 2.1a), setting the voltage amplitude ($V^* \in \mathbb{R}_{>0}$) and frequency ($f^* \in \mathbb{R}_{>0}$) of the local grid, whereas the grid-feeding converters are mainly designed to deliver predefined power $(P^*, Q^*) \in \mathbb{R}_{\geq 0}^2$ to an energized grid and represented as an ideal current source connected to the grid in parallel with high impedance (see Fig. 2.1b). Finally, the grid-supporting power converters are in between the two aforementioned classes, with the main objective to deliver proper values of active and reactive power (i.e., adjust their output current and voltage) to contribute to the regulation of the grid frequency and

voltage. The last category can have both a controllable voltage source (see Fig. 2.1c) and a controllable current source (see Fig. 2.1d) implementation, with the former one resembling more the grid-forming operation and the latter one being closer to the grid-feeding control.

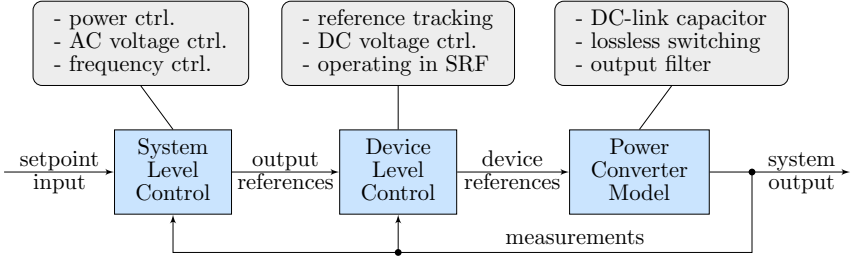
While useful for microgrid applications, the aforementioned classification might be impractical and lead to counter intuitive conclusions when applied to transmission systems [24]. For instance, a grid-forming converter without dispatchable power setpoints is not suitable for transmission-level services, whereas a grid-supporting mode of operation lacks a universally accepted definition and tends to be applied to units both with and without standalone capabilities. Moreover, grid codes are now imposing the provision of frequency and voltage support as a requirement for grid-connected power converters, thus rendering the existing grid-feeding category obsolete. As a result, a more universal and common terminology has emerged in power electronics, control, and power systems, differentiating only between *grid-forming* and *grid-following* operation mode, i.e., power converters that can form a stable frequency and voltage and ones that can only operate when connected to a stiff power grid, respectively. Depending on the control design, both converter types can provide specific system-level services, hence encompassing the grid-feeding and grid-supporting categories as well. Nevertheless, guided by the traditional practice of droop-based control schemes, such classification also characterizes the system-level control by its input-output characteristic, therefore neglecting the underlying control dynamics. However, as will be shown in this chapter, the transparency of the internal control design is the key component towards providing an insightful representation of the system-level control and addressing the multifaceted nature of the problem.

2.2.2 General Control Structure

The prevalent control architecture for power converters is the two-level VSC shown in Fig. 2.2a. In this setup, an outer *system-level* control - that may also include an *overcurrent protection* scheme - provides a reference for the converter's terminal voltage that is subsequently tracked by a cascaded *device-level* controller. We first present the model of a two-level voltage source converter and subsequently discuss the individual control blocks depicted in Fig. 2.2b.



(a)



(b)

FIGURE 2.2: Representation of the VSC model: (a) two-level VSC connected through a transformer to the grid; (b) general input-output block structure of the power converter model and its control scheme.

2.2.3 Three-Phase Two-Level Voltage Source Converter

The model of a voltage source converter (i.e., the device model in Fig. 2.2a) used throughout this thesis consists of a DC-link capacitor, a lossless switching block which modulates the DC-capacitor voltage $v_{dc} \in \mathbb{R}_{>0}$ into a three-phase AC voltage $v_{sw}^{abc} \in \mathbb{R}^3$, and an output filter. Throughout this work, we assume that the DC-source current $i_{dc} \in \mathbb{R}_{>0}$ is supplied by a controllable source (e.g., an energy storage or a curtailed renewable generation) and can be used as a control input. Averaging the dynamics (in SI) over one switching period yields

$$C_{dc}\dot{v}_{dc} = -G_{dc}v_{dc} - i_{sw} + i_{dc}, \quad (2.1a)$$

$$L_f \dot{i}_f^{abc} = -R_f i_f^{abc} + v_{\text{sw}}^{abc} - v_f^{abc}, \quad (2.1b)$$

$$C_f \dot{v}_f^{abc} = +i_f^{abc} - i_g^{abc}, \quad (2.1c)$$

where $C_{\text{dc}} \in \mathbb{R}_{>0}$ and $G_{\text{dc}} \in \mathbb{R}_{>0}$ denote the DC capacitance and conductance, and $C_f \in \mathbb{R}_{>0}$, $L_f \in \mathbb{R}_{>0}$, $R_f \in \mathbb{R}_{>0}$ represent the AC filter capacitance, inductance and resistance, respectively. The converter is controlled by the modulation signal $m^{abc} \in [-1_3, 1_3]$ that controls the modulated three-phase voltage $v_{\text{sw}}^{abc} = \frac{1}{2} m^{abc} v_{\text{dc}}$ and the current $i_{\text{sw}} = \frac{1}{2} m^{abc \top} i_f^{abc}$ flowing into the switching block. Moreover, we use $i_f^{abc} \in \mathbb{R}^3$, $v_f^{abc} \in \mathbb{R}^3$, and $i_g^{abc} \in \mathbb{R}^3$ to denote the three-phase filter current, three-phase converter voltage, and three-phase current injection into the system.

For control design purposes, the complete converter model is often described in per-unit, which transform (2.1) into

$$\frac{C_{\text{dc}}}{\omega_b} \dot{v}_{\text{dc}} = -g_{\text{dc}} v_{\text{dc}} - i_{\text{sw}} + i_{\text{dc}}, \quad (2.2a)$$

$$\frac{\ell_f}{\omega_b} \dot{i}_f^{abc} = -r_f i_f^{abc} + v_{\text{sw}}^{abc} - v_f^{abc}, \quad (2.2b)$$

$$\frac{C_f}{\omega_b} \dot{v}_f^{abc} = +i_f^{abc} - i_g^{abc}, \quad (2.2c)$$

with $\omega_b \in \mathbb{R}_{>0}$ being the base frequency and lowercase symbols reflecting the per-unit values of respective circuit parameters, i.e.,

$$r_f = \frac{R_f}{Z_b}, \quad \ell_f = \frac{\omega_b L_f}{Z_b}, \quad c_f = \omega_b Z_b C_f, \quad (2.3a)$$

$$g_{\text{dc}} = G_{\text{dc}} Z_b, \quad c_{\text{dc}} = \omega_b Z_b C_{\text{dc}}. \quad (2.3b)$$

Here, $Z_b = \omega_b L_b = (\omega_b C_b)^{-1}$ represents the base impedance. This thesis will deal strictly with per-unit formulation of converter models and controls, unless explicitly stated otherwise. Therefore, the explicit per-unit declaration of system variables in (2.2) and the rest of the chapter is omitted for brevity.

We assume that the three-phase signals are balanced and, given a reference angle $\theta_r \in [-\pi, \pi)$, the converter variables can be defined in a rotating dq -reference frame by applying the power-variant dq -transform (see e.g., [64, Chapter 6.1])

$$T(\theta_r) := \frac{2}{3} \begin{bmatrix} \cos \theta_r & \cos(\theta_r - \frac{2\pi}{3}) & \cos(\theta_r + \frac{2\pi}{3}) \\ \sin \theta_r & \sin(\theta_r - \frac{2\pi}{3}) & \sin(\theta_r + \frac{2\pi}{3}) \end{bmatrix} \quad (2.4)$$

to the three-phase converter signals (e.g., $v_f^{dq} = T(\theta_r) v_f^{abc}$). For reasons similar to the ones pertaining to per-unit notation, the dq superscript will

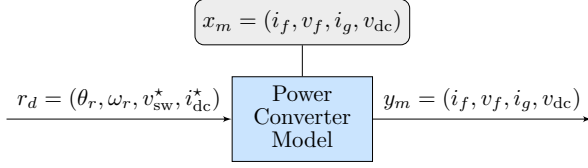


FIGURE 2.3: Simplified MIMO structure of the device model.

not be used in the remainder of the chapter, i.e., the presented converter model will be described in dq -vector form $x := x^{dq} := (x^d, x^q)$ and per-unit. Therefore, guided by the practice commonly employed in power electronics (see Appendix B.1), we rewrite filter dynamics in (2.2b)-(2.2c) as

$$\dot{i}_f = \frac{\omega_b}{\ell_f} (v_{sw} - v_f) - \left(\frac{r_f}{\ell_f} \omega_b + j\omega_b \omega_r \right) i_f, \quad (2.5a)$$

$$\dot{v}_f = \frac{\omega_b}{c_f} (i_f - i_g) - j\omega_b \omega_r v_f. \quad (2.5b)$$

The converter is usually interfaced to the grid through a transformer, with the dynamics of transformer current (i.e., current injected into the grid) described by

$$\dot{i}_g = \frac{\omega_b}{\ell_t} (v_f - v_t) - \left(\frac{r_t}{\ell_t} \omega_b + j\omega_b \omega_r \right) i_g, \quad (2.5c)$$

where $r_t \in \mathbb{R}_{>0}$ and $\ell_t \in \mathbb{R}_{>0}$ denote the transformer's per-unit resistance and inductance, $v_t \in \mathbb{R}^2$ is the voltage at the connection terminal, and $\omega_r \in \mathbb{R}_{>0}$ is the normalized reference for the angular velocity of the dq -frame.

Expressions in (2.5) represent the AC-side dynamics of the power converter and, together with DC-side dynamics in (2.2a), complete the 7th-order converter model described by $x_m = (i_f, v_f, i_g, v_{dc}) \in \mathbb{R}^7$ and depicted in Fig. 2.3. The input vector comprises device-level references¹ $r_d = (\theta_r, \omega_r, v_{sw}^*, i_{dc}^*) \in \mathbb{R}^5$ and the measurement output y_m encompasses full state feedback for system- and device-level control (i.e., $x_m \subset y_m$), as well as the converter's AC-voltage magnitude $V_c \in \mathbb{R}_{>0}$ and instantaneous active and reactive power injection $(p_c, q_c) \in \mathbb{R}^2$ given by

$$V_c := \|v_f\|, \quad p_c := v_f^\top i_g, \quad q_c := v_f^\top j^\top i_g. \quad (2.6)$$

The latter three measurements are directly obtained from converter's output voltage v_f and current i_g and are therefore not explicitly included in $y_m := x_m$

¹ We assume perfect tracking of the DC-current reference, i.e., $i_{dc} = i_{dc}^*$ in (2.2a).

for brevity. However, these measurements will be considered available to the system-level control. In fact, this control layer often includes processing of v_f and i_g such that the quantities in (2.6) are internally obtained. Moreover, note that we assume $v_{sw} := v_{sw}^*$, i.e., the modulation voltage reference v_{sw}^* is perfectly transformed to the AC side. Due to high modeling complexity and very fast underlying dynamics [65], the converter switching is not included in the model nor will it be considered throughout this thesis.

2.2.4 System-Level Control

The desired dynamic behavior of the power converter as seen from the system point of view is commonly prescribed by a dynamic controller of the form

$$\dot{x}_s = \kappa(x_s, y_s, u_s), \quad (2.7a)$$

$$r_s = h(x_s, y_s, u_s), \quad (2.7b)$$

where $x_s \in \mathbb{R}^n$ is a vector of internal controller states, $y_s \in \mathbb{R}^m$ are the measured converter outputs, $u_s \in \mathbb{R}^p$ are the prescribed control setpoints, and $r_s \in \mathbb{R}^q$ is a vector of computed references sent to the device-level control. A simplified representation of the general MIMO structure for both grid-forming and grid-following operation mode is illustrated in Fig. 2.4, with the former mode differentiating between four representative classes of control, namely droop control, VSM, VOC and matching control.

The two converter modes are fundamentally different. In the context of grid-following control, the measurements $y_s = (v_f, p_c, q_c) \in \mathbb{R}^4$ are commonly the output voltage and the active and reactive power. Moreover, (2.7) models a synchronization device that estimates the phase angle $\theta_s \in [-\pi, \pi)$ of the voltage v_f as well as the synchronous (grid) frequency $\omega_s \in \mathbb{R}_{>0}$ at the PCC, and provides them as reference $\hat{r}_s = (\theta_s, \omega_s)$ to the device-level control (see Fig. 2.3). Additionally, the so-called outer control loop is used to calculate the current reference $i_f^* \in \mathbb{R}^2$ based on the mismatch between measured signals y_s and prescribed setpoints u_s . Hence, the system-level controller is described by $x_s^{\text{follow}} = (\theta_s, \varepsilon, \tilde{p}_c, \tilde{q}_c) \in \mathbb{R}^4$, where $\tilde{p}_c \in \mathbb{R}$ and $\tilde{q}_c \in \mathbb{R}$ are the internal states corresponding to active and reactive power, respectively. Since the angle (θ_s) and frequency (ω_s) references are “only” measured and passed through to device-level control (i.e., they are not regulated by an appropriate control law), we do not include them into the main output reference vector r . Instead, we denote them by an auxiliary reference vector \hat{r} in order to make a better distinction between the control tasks of grid-forming and grid-following

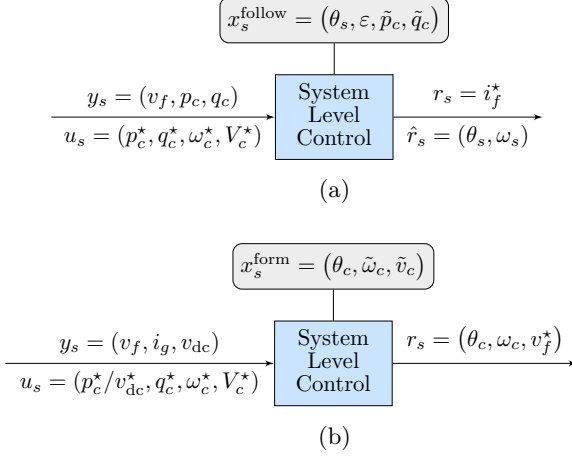


FIGURE 2.4: Simplified, general MIMO structure of the system-level control: (a) grid-following operation mode; (b) grid-forming operation mode.

operation modes. A detailed system-level control structure of a grid-following converter will be presented in Section 2.3

On the other hand, grid-forming control can broadly be categorized into three main groups based on the principles upon which the synchronization is achieved. In particular: (i) controls that measure power (i.e., $y_s = (p_c, q_c)$, subsumed under $y_s = (v_f, i_g)$ in Fig. 2.4b for clarity) and achieve synchronization through power imbalance, namely droop- and VSM-based methods; (ii) controls that measure current (i.e., $y_s = i_g$) and provide synchronization through current flows such as VOC and dVOC; and (iii) controls based on DC-voltage measurement (i.e., $y_s = v_{dc}$) and synchronization through DC-voltage/energy imbalance, e.g., indirect matching control. Independent of the measured signals, all these controllers have a common objective, which is to provide a reference angle $\theta_c \in [-\pi, \pi)$, reference frequency $\omega_c \in \mathbb{R}_{>0}$, and output voltage reference $v_f^* := v_c \in \mathbb{R}^2$ (i.e., $r_s = (\theta_c, \omega_c, v_f^*) \in \mathbb{R}^4$) in the corresponding dq -frame to the device-level control. Understandably, in addition to various measurements, these grid-forming strategies also employ different control inputs and internal state variables. Nevertheless, all aforementioned controllers can be subsumed under the state vector $x_s^{\text{form}} = (\theta_c, \tilde{\omega}_c, \tilde{v}_c) \in \mathbb{R}^4$, with angle θ_c , frequency $\tilde{\omega}_c \in \mathbb{R}_{>0}$ and voltage $\tilde{v}_c \in \mathbb{R}^2$ being internal states of the control and not measured (unlike for the grid-following approach). Section 2.4 will focus in depth on all aforementioned grid-forming control

methods, especially in terms of controller dynamics in (2.7a), and provide insightful analogies between them.

By comparing the reference output vectors r_s of two converter modes in Fig. 2.4, we can observe that the grid-following controller regulates the converter as a controllable current source (hence $r_s = i_f^*$), whereas the grid-forming method takes full advantage of VSC capabilities and controls the converter as a voltage source, i.e., provides a voltage reference v_f^* . As such, the definition of the system-level control output aligns with traditional classification in Section 2.2.1. However, different reference signals also imply that the structure of the device-level control has to differ between the two control modes. The fundamental principles of this control layer are described in the following section.

2.2.5 Device-Level Control

We start off this section by analyzing the device-level control of grid-forming converters, with a general structure presented in Fig. 2.5. As previously pointed out in Section 2.2.2, this control layer provides both AC and DC-side reference signals for the VSC device. The AC-side controller operates in a synchronously-rotating dq -frame, with the reference angle θ_c and velocity ω_c provided by the system-level control (2.7). In particular, given a voltage reference $v_f^* \in \mathbb{R}^2$ in dq -coordinates defined by (θ_c, ω_c) , the device-level control is described by a cascade of voltage and current controllers (also called inner control loops) computing a switching voltage reference $v_{sw}^* \in \mathbb{R}^2$ [51, 66]. More precisely, it encompasses a PI voltage controller

$$\dot{\xi} = v_f^* - v_f, \quad (2.8a)$$

$$i_f^* = K_P^v(v_f^* - v_f) + K_I^v\xi + K_F^v i_g + j\omega_c c_f v_f, \quad (2.8b)$$

that provides an internal current reference i_f^* for a current PI controller

$$\dot{\gamma} = i_f^* - i_f, \quad (2.9a)$$

$$v_{sw}^* = K_P^i(i_f^* - i_f) + K_I^i\gamma + K_F^i v_f + j\omega_c \ell_f i_f, \quad (2.9b)$$

where $(K_P^v, K_I^v) \in \mathbb{R}_{>0}^2$, $(K_I^v, K_F^v) \in \mathbb{R}_{\geq 0}^2$ and $(K_F^v, K_F^i) \in \mathbb{Z}_{\{0,1\}}^2$ are the respective proportional, integral, and feed-forward gains, $\xi \in \mathbb{R}^2$ and $\gamma \in \mathbb{R}^2$ represent the integrator states, and superscripts v and i denote the voltage and current controllers [22, 37, 67]. Note that the angular velocity of a Synchronously-rotating Reference Frame (SRF) ω_c is reflected in the last terms of (2.8b) and (2.9b).

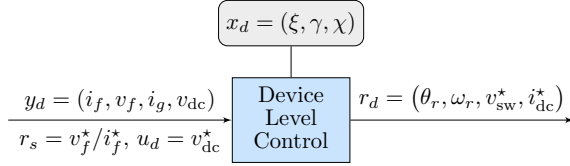


FIGURE 2.5: Simplified, general MIMO structure of the device-level control.

Finally, the DC voltage is controlled through the DC-current source and a PI controller, as follows:

$$\dot{\chi} = v_{\text{dc}}^* - v_{\text{dc}}, \quad (2.10\text{a})$$

$$i_{\text{dc}} = K_P^{\text{dc}}(v_{\text{dc}}^* - v_{\text{dc}}) + K_I^{\text{dc}}\chi + K_F^{\text{dc}}i_{\text{dc}}^*, \quad (2.10\text{b})$$

with DC-voltage setpoint $u_d = v_{\text{dc}}^* \in \mathbb{R}_{>0}$ being an external control input, $\chi \in \mathbb{R}$ the internal state variable, and proportional, integral, and feed-forward gains denoted by $K_P^{\text{dc}} \in \mathbb{R}_{>0}$, $K_I^{\text{dc}} \in \mathbb{R}_{\geq 0}$, and $K_F^{\text{dc}} \in \{0, 1\}$, respectively. The DC current reference $i_{\text{dc}}^* \in \mathbb{R}_{>0}$ at a nominal operating point (V_c^*, p_c^*, q_c^*) , including DC and AC converter losses, is given by

$$i_{\text{dc}}^* := v_{\text{dc}}^*{}^{-1} \left(p_c^* + r_f \frac{p_c^{*2} + q_c^{*2}}{V_c^{*2}} \right) + g_{\text{dc}} v_{\text{dc}}^*, \quad (2.10\text{c})$$

which indicates that for $v_{\text{dc}} = v_{\text{dc}}^*$ the DC-side current will be $i_{\text{dc}} = i_{\text{dc}}^*$.

Having computed the AC current and voltage (i_f^*, v_{sw}^*) and DC current (i_{dc}^*) reference signals, the device-level control output $r_d = (\theta_r, \omega_r, v_{\text{sw}}^*, i_{\text{dc}}^*)$ is sent to the power converter, with $(\theta_r, \omega_r) = (\theta_c, \omega_c)$ being the angular reference adopted from the system-level control. The state vector of the controller is described by $x_d = (\xi, \gamma, \chi) \in \mathbb{R}^5$. In contrast, the system-level controller of a grid-following converter provides filter current reference. Therefore, the device-level control only comprises AC and DC-current computation given by (2.9)-(2.10) (i.e., $x_d = (\gamma, \chi) \in \mathbb{R}^3$), thus bypassing the inner voltage controller. The output reference vector $r_d = (\theta_s, \omega_s, v_{\text{sw}}^*, i_{\text{dc}}^*)$ is provided to the power converter model, with $(\theta_r, \omega_r) = (\theta_s, \omega_s)$ being the measured angle and frequency references obtained by a synchronization unit within the system-level control.

2.3 GRID-FOLLOWING SYSTEM-LEVEL CONTROL

As mentioned previously in Section 2.2.4, the grid-following system-level control employs measurements of the output voltage and power (i.e., $y_s =$

(v_f, p_c, q_c)), and (2.7) models a synchronization device - usually a Phase-Locked Loop (PLL) - that acts as an observer and estimates the synchronous (grid) frequency ω_s and phase angle $\theta_s \in [-\pi, \pi)$ of the voltage $v_f \angle \theta_s$ at the PCC. The most common PLL implementation is a so-called type-2 SRF PLL [68], which achieves synchronization by diminishing the q -component $v_f^q \in \mathbb{R}$ of the voltage via PI control, thus aligning the d -axis of the SRF with the output voltage vector v_f [22, 24, 69]:

$$\dot{\varepsilon} = v_f^q, \quad (2.11a)$$

$$\omega_s = \omega_0 + K_P^s v_f^q + K_I^s \varepsilon, \quad (2.11b)$$

$$\dot{\theta}_s = \omega_b \omega_s. \quad (2.11c)$$

Here, (K_P^s, K_I^s) are the proportional and integral control gains of the synchronization unit, $\omega_0 = 1$ p.u. is the nominal angular frequency, and $\varepsilon \in \mathbb{R}$ is the integrator state. Note that the grid-following converters require an established three-phase voltage at the connection terminal in order to obtain a reasonable frequency (i.e., angle) signal. Therefore, they do not possess standalone nor black start capabilities.

Having determined the synchronous angle and frequency (θ_s, ω_s) , the outer control loop subsequently computes the current reference $i_f^* \in \mathbb{R}^2$. By employing frequency and voltage droop control ($R_c^\omega \in \mathbb{R}_{\geq 0}$, $R_c^v \in \mathbb{R}_{\geq 0}$) in combination with integral controllers $K_{I,f}^d \in \mathbb{R}_{>0}$ and $K_{I,f}^q \in \mathbb{R}_{>0}$, the outer control loop, described by internal states variables $(\tilde{p}_c, \tilde{q}_c)$, regulates the power output (p_c, q_c) to its respective setpoint (p_c^*, q_c^*) , as follows:

$$\dot{\tilde{p}}_c = K_{I,f}^d (p_c^* - p_c - R_c^\omega (\omega_s - \omega_c^*)), \quad (2.12a)$$

$$\dot{\tilde{q}}_c = K_{I,f}^q (q_c^* - q_c - R_c^v (\|v_f\| - V_c^*)). \quad (2.12b)$$

Due to the $P - f$ and $Q - V$ droop characteristics, the active power reference is adjusted in response to a deviation of the measured frequency ω_s with respect to the frequency setpoint ω_c^* , whereas the reactive power reference is modified according to the mismatch between the magnitude of the output voltage $\|v_f\|$ and the converter voltage setpoint V_c^* . Hence, the internal state vector of the system-level controller is $x_s^{\text{follow}} = (\theta_s, \omega_s, \tilde{p}_c, \tilde{q}_c) \in \mathbb{R}^4$, with \tilde{p}_c and \tilde{q}_c representing the power (i.e., dq -current) references. It should be pointed out that the controller (2.12) can take different forms, varying from a traditional frequency/AC-voltage droop control [70] and droop control with a low-pass filter [24] to DC-energy/reactive power droop control [71].

The computed power references are then transformed into the corresponding current reference signal $r_s = i_f^*$, with two commonly used implementations

for balanced systems: a constant current and a constant power mode. The first approach directly feeds the power references to the device-level control $i_f^* = (\tilde{p}_c, \tilde{q}_c)$, while the second mode adjusts them based on output voltage measurement such that the converter's power output is kept constant:

$$i_f^{*d} = \frac{v_f^d \tilde{p}_c + v_f^q \tilde{q}_c}{\|v_f\|}, \quad i_f^{*q} = \frac{v_f^q \tilde{p}_c - v_f^d \tilde{q}_c}{\|v_f\|}. \quad (2.13)$$

Note that the presented control strategy represents the *grid-supporting* version of the grid-following control (see Section 2.2.1). In other words, apart from respecting the given power setpoints p_c^* and q_c^* , this converter mode also provides voltage and frequency support through droop control (R_c^ω, R_c^v) and additional setpoints (ω_c^*, V_c^*). This formulation also subsumes the *grid-feeding* mode, which can be easily obtained by setting $R_c^\omega = R_c^v = 0$ in (2.12) and $u_s = (p_c^*, q_c^*)$ in Fig. 2.4a.

2.4 GRID-FORMING SYSTEM-LEVEL CONTROL

This section focuses solely on grid-forming control, i.e., different synchronization strategies and controller implementation described by (2.7) and Fig. 2.4b. Furthermore, the comparison between the traditional droop control and the recently proposed novel control strategies (i.e., VSM, dVOC and indirect matching control) as well as the underlying conditions for equivalence will be discussed. For clarity, we extend the block diagram in Fig. 2.4b such that it reflects internal control states of each individual grid-forming control approach (see Fig. 2.6). As explained previously in Section 2.2.4, for this mode of operation the output vector $r_s = (\theta_c, \omega_c, v_c) \in \mathbb{R}^4$ comprises angle, frequency and voltage references, with the computed voltage v_c corresponding to the converter's output voltage reference, i.e., $v_f^* := v_c$.

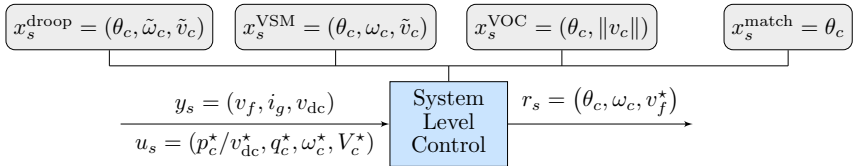


FIGURE 2.6: Simplified, general MIMO structure of the system-level control for different grid-forming control methods.

2.4.1 Synchronization through Power Imbalance

We first discuss grid-forming control strategies that achieve synchronization through measuring power imbalance. The focus is set on an inverter-based transmission system with the standard assumption that active power and frequency, i.e., reactive power and voltage, are fully decoupled². Under such circumstances, the grid-forming control strategies that respond to power imbalances are of the form

$$\omega_c = \omega_c^* + \underbrace{\lambda_\theta(s)(p_c^* - p_c)}_{\tilde{\omega}_c}, \quad v_c^d = V_c^* + \underbrace{\lambda_v(s)(q_c^* - q_c)}_{\tilde{v}_c}, \quad (2.14)$$

with $\lambda_\theta(s)$ and $\lambda_v(s)$ representing the controller's transfer functions, $\dot{\theta}_c = \omega_b \omega_c$ and $v_c^q = 0$. We emphasize that, unlike for the grid-following operation mode, in this case the angle θ_c , frequency $\tilde{\omega}_c \in \mathbb{R}$, and voltage $\tilde{v}_c \in \mathbb{R}$ are internal states of the control. In contrast, the active active and reactive power injections p_c and q_c are measured, i.e., $y_s = (p_c, q_c) \in \mathbb{R}^2$. The two main control techniques employing power imbalance-based synchronization are droop control and VSM control.

2.4.1.1 Droop Control

Droop control is inspired by the traditional primary frequency control of a synchronous machine and is the prevalent control scheme for parallel grid-forming converters [48, 73, 74]. By appropriately adjusting the individual droop factors, it enables self-synchronization through the power grid and power sharing in proportion to the converter rating, while using only local measurements. Droop control is given by (2.14) and

$$\lambda_\theta(s) = R_c^p \frac{\omega_z}{\omega_z + s}, \quad \lambda_v(s) = R_c^q \frac{\omega_z}{\omega_z + s}, \quad (2.15)$$

with $R_c^p \in \mathbb{R}_{>0}$ and $R_c^q \in \mathbb{R}_{\geq 0}$ being the droop gains and $\omega_z \in \mathbb{R}_{>0}$ denoting the cut-off frequency of a low-pass filter applied to the power measurements. Therefore, the control state vector can be defined as $x_s^{\text{droop}} = (\theta_c, \tilde{\omega}_c, \tilde{v}_c)$, where

$$\dot{\tilde{\omega}}_c = -\omega_z \tilde{\omega}_c + R_c^p \omega_z (p_c^* - p_c), \quad (2.16a)$$

$$\dot{\tilde{v}}_c = -\omega_z \tilde{v}_c + R_c^q \omega_z (q_c^* - q_c). \quad (2.16b)$$

² To address potential power coupling in distribution grids and microgrids, reverse droop [60] and adaptive droop [72] can be used.

2.4.1.2 *Virtual Synchronous Machine*

An alternative system-level control approach aims to reproduce the stabilizing effects of synchronous machines by emulating³ their physical properties, in particular the physical aspects pertaining to frequency dynamics. Numerous VSM implementations have been presented in the literature [34, 49, 51, 75–77], that differ both in the level of detail of SM dynamics as well as in their role within the converter control scheme. Nonetheless, assuming small frequency deviations around the nominal value (i.e., $\omega_c \approx 1$ p.u.), they can all be represented by an explicit model of the swing equation in per-unit:

$$M_c \dot{\omega}_c = p_c^* - p_c - D_c(\omega_c - \omega_c^*), \quad (2.17)$$

where $M_c \in \mathbb{R}_{>0}$ and $D_c \in \mathbb{R}_{>0}$ denote the *virtual* inertia and damping constants, and $\omega_c \in \mathbb{R}_{>0}$ is the internally computed reference frequency and state of the system-level controller. The reactive power control is often preserved in the droop control form given by $\lambda_v(s)$ in (2.15), and hence the state vector comprises $x_s^{\text{VSM}} = (\theta_c, \omega_c, \tilde{v}_c)$. Comparing active power droop control and (2.17), one can observe that both approaches employ droop-like proportional control. While in the former case it is imposed on the power imbalance, in the latter case the frequency deviation is used. In fact, the two control architectures are mathematically equivalent for small frequency deviations around the nominal value and constant active power and frequency reference inputs [23, 50] (see Appendix B.2 for more detail). Specifically, with R_c^p and ω_z given by

$$R_c^p = D_c^{-1}, \quad \omega_z = D_c M_c^{-1}, \quad (2.18)$$

the dynamical system in (2.14)-(2.15) implements the same transfer function as (2.17), but with different internal state variable (i.e., $\tilde{\omega}_c$ instead of ω_c). Therefore, for brevity of the presentation, throughout the remainder of this chapter we will focus only on droop control implementation with a low-pass filter given by (2.15).

2.4.2 *Synchronization through Current Flows*

In this section, we briefly introduce the virtual oscillator control as a method for decentralized synchronization and control of parallel inverters through electrical coupling between them. Moreover, we review recent results on

³ Hence the name *virtual* synchronous machine.

dispatchable VOC for 100% converter-based power systems, for which insightful analytic stability certificates are available and have been validated experimentally [17, 53, 78].

2.4.2.1 Virtual Oscillator Control

Inspired by the phenomenon of synchronization in networks of coupled oscillators, this method controls the inverters to behave like virtual Liénard-type oscillators [52, 79]. As such, VOC is a promising approach because it can globally synchronize an inverter-based power system and achieve load sharing in proportion to their ratings. However, the nominal power injection cannot be specified in the original VOC approach [52, 79], i.e., it cannot be dispatched. For passive loads it can be shown that power is delivered to the loads [79], but the power sharing by the inverters and their voltage magnitudes are determined by the load and network parameters.

2.4.2.2 Dispatchable Virtual Oscillator Control

The following section describes the dynamics of a dVOC in SI. For that purpose, we introduce the matrix $K \in \mathbb{R}^{2 \times 2}$ and function $\Phi(v)$ that depend on the setpoints for active power, reactive power and voltage magnitude (p_c^*, q_c^*, V_c^*) , and are defined as

$$K = \frac{1}{V_c^{*2}} \mathcal{R}(\kappa) \begin{bmatrix} p_c^* & q_c^* \\ -q_c^* & p_c^* \end{bmatrix}, \quad \Phi(v) = \frac{V_c^{*2} - \|v\|^2}{V_c^{*2}}. \quad (2.19)$$

Moreover, $\kappa = \tan^{-1}(\rho\omega_b)$ is a function of the inductance to resistance ratio $\rho = \ell/r$ of the transmission network. The closed-loop dynamics of the dVOC reference voltage $v_c^{\alpha\beta} \in \mathbb{R}^2$ in stationary $\alpha\beta$ -coordinates are given by

$$\dot{v}_c^{\alpha\beta} = \omega_c^* j v_c^{\alpha\beta} + \eta \left(K v_c^{\alpha\beta} - \mathcal{R}(\kappa) i_g^{\alpha\beta} + \alpha \Phi(v_c^{\alpha\beta}) v_c^{\alpha\beta} \right), \quad (2.20)$$

where $\eta \in \mathbb{R}_{>0}$ is the *synchronization* gain and $\alpha \in \mathbb{R}_{>0}$ is the *voltage* control gain. The reference values for the device-level control are obtained by measuring the grid current (i.e., $y_s = i_g^{\alpha\beta}$ is the measurement input) and subsequently computing the angle $\theta_c = \angle v_c^{\alpha\beta}$ and magnitude $v_f^* = (\|v_c^{\alpha\beta}\|, 0)$ of $v_c^{\alpha\beta}$ at runtime. Note that $\Phi(v_c^{\alpha\beta}) v_c^{\alpha\beta}$ can be interpreted as a normalized quadratic voltage error that scales the voltage reference vector $v_c^{\alpha\beta}$ up or down. Furthermore, the term $K v_c^{\alpha\beta} - \mathcal{R}(\kappa) i_g^{\alpha\beta}$ can be interpreted either in terms of tracking power setpoints or in terms of phase synchronization, and

vanishes when the converter operates at the nominal operating point [17, Section II-D].

To establish the connection to power setpoint tracking, we assume a purely inductive network (i.e., $\kappa = \pi/2$) and rewrite the control law (2.20) in polar dq -coordinates, which yields

$$\omega_c = \omega_c^* + \eta \left(\frac{p_c^*}{V_c^{*2}} - \frac{p_c}{(v_c^d)^2} \right), \quad (2.21a)$$

$$\dot{v}_c^d = \frac{\eta}{V_c^*} \left(\frac{q_c^*}{V_c^{*2}} - \frac{q_c}{(v_c^d)^2} \right) v_c^d + \frac{\eta\alpha}{V_c^{*2}} \left(V_c^{*2} - (v_c^d)^2 \right) v_c^d. \quad (2.21b)$$

Approximating the dynamics for small voltage magnitude deviations (i.e., $\|v_c\| = v_c^d \approx V_c^*$), and considering the steady state of the voltage magnitude (i.e., $\dot{v}_c^d \approx 0$) transforms (2.21) into

$$\omega_c = \omega_c^* + \frac{\eta}{V_c^{*2}} (p_c^* - p_c), \quad (2.22a)$$

$$v_c^d = V_c^* + \frac{\eta}{\alpha V_c^*} (q_c^* - q_c). \quad (2.22b)$$

This is precisely the definition of droop control in (2.14), where

$$\lambda_\theta = \frac{\eta}{V_c^{*2}}, \quad \lambda_v = \frac{\eta}{\alpha V_c^*}. \quad (2.23)$$

In other words, (2.21) corresponds to droop control without the low-pass filter, with (2.23) defining the droop gains $R_c^p := \lambda_\theta$ and $R_c^q := \lambda_v$. The device-level references are therefore $r_s = (\theta_c, \omega_c, v_f^*) \in \mathbb{R}^4$, where ω_c and $v_f^* := (v_c^d, 0)$ are given by (2.22) and converted into per-unit for uniform formulation, and $\dot{\theta}_c = \omega_b \omega_c$, whereas the controller's state vector comprises $x_s^{\text{VOC}} = (\theta_c, \|v_c\|) \in \mathbb{R}^2$. In contrast, under assumptions typically made in the control of microgrids such as purely resistive lines (i.e., $\kappa = 0$), small deviations of voltage magnitudes (i.e., $\|v_c\| = v_c^d \approx V_c^*$) and $p_c^* = q_c^* = 0$, dVOC coincides with the (averaged) virtual oscillator control [80, Section III-C].

2.4.3 Synchronization through DC Voltage/Energy Imbalance

This class of grid-forming system-level controls is based on the observation that the DC-link voltage - similar to the synchronous machine's frequency - indicates power imbalances. Several controllers have been proposed that exploit this observation to structurally match the dynamics of a power

converter to that of a synchronous machine by driving the converter frequency based on the DC voltage or the DC-voltage deviation [15, 58, 81, 82]. This section will primarily focus on a so-called indirect machine matching method, described and mathematically formulated in SI.

2.4.3.1 Indirect Matching Control

In [58], the angle θ_c computed as

$$\dot{\theta}_c = \omega_c^* \frac{v_{\text{dc}}^*}{v_{\text{dc}}} \quad (2.24)$$

is directly used as the angle of the modulation signal (i.e., $\angle m^{abc} = \theta_c$), and the resulting converter model has the same structure as that of a 5th-order synchronous machine model [58]. While this analogy is interesting in its own right, the parameters of the controlled converter differ from those of a machine by an order of magnitude. Therefore, the converter does not replace SMs one to one. Instead, the main feature of matching control is that it makes the power imbalance between generation (i.e., the DC source) and the AC side of the converter transparent.

In this study, we use the matching control proposed in [15]:

$$\dot{\theta}_c = \omega_c^* + K_\theta(v_{\text{dc}} - v_{\text{dc}}^*), \quad (2.25)$$

where $K_\theta \in \mathbb{R}$ is a control gain that adjusts the mapping between frequency deviation and DC-voltage deviation, i.e., from (2.25) it follows that

$$\omega_c - \omega_c^* = K_\theta(v_{\text{dc}} - v_{\text{dc}}^*). \quad (2.26)$$

Furthermore, the controller is adapted in order to meet the general block structure in Fig. 2.2. Precisely, the device-level references $r_s = (\theta_c, \omega_c, v_f^*)$ are generated by combining the angle θ_c from (2.25) with frequency ω_c in (2.26) and the voltage magnitude $v_f^* := V_c^*$. Note that the presented control design does not incorporate explicit reactive power regulation. Hence, $y_s = v_{\text{dc}}$ and $u_s = (v_{\text{dc}}^*, \omega_c^*, V_c^*) \in \mathbb{R}^3$ are the only needed measurement and setpoint input signals, whereas $x_s^{\text{match}} = \theta_c$ is the state vector of the controller.

With DC-side regulation subsumed under the system-level control in this case, some necessary changes must be made to the device-level control in order to account for these modifications. When employing matching control, the DC voltage is controlled by a proportional controller with feed-forward (i.e., $K_I^{\text{dc}} = 0$ and $K_F^{\text{dc}} = 1$ in (2.10b)). We note that the feed-forward term delivers the required power to the DC-link capacitor, and the angle dynamics

in (2.25) adjust the angle until the power inflow and outflow of the DC link capacitor are balanced and $p_c = p_c^*$. Moreover, using the controller (2.25), frequency imbalance is proportional to DC-voltage imbalance and hence the proportional DC-voltage regulation provides frequency drooping. To clarify the role of the parameters, let us apply the change of coordinates

$$v_{dc} - v_{dc}^* = K_\theta^{-1}(\omega_c - \omega_c^*) \quad (2.27)$$

to (2.1a) and (2.10)⁴. Furthermore, we assume

$$v_{dc}^* i_{sw} \approx p_c + p_{loss}^*, \quad (2.28)$$

with $p_{loss}^* \in \mathbb{R}_{>0}$ denoting the AC-side converter losses at nominal operating conditions (V_c^*, p_c^*, q_c^*) . This results in

$$M_c \dot{\omega}_c = p_c^* - \frac{v_{dc}^*}{v_{dc}} p_c - D_c (\omega_c - \omega_c^*), \quad (2.29)$$

where

$$M_c = \frac{C_{dc}}{K_\theta} v_{dc}^*, \quad D_c = \frac{K_P^{dc} + G_{dc}}{K_\theta} v_{dc}^*, \quad (2.30)$$

and resembles the swing equation (2.17) for $v_{dc}^* \approx v_{dc}$. In other words, matching control explicitly links the inertia and damping provided by the grid-forming converter to its internal energy storage and stiffness of the DC voltage regulation. In contrast, droop control and dVOC assume stiff DC-voltage regulation and collapse the DC voltage if the capabilities of the DC source are exceeded [10]. Finally, we note that K_θ needs to be chosen such that the DC voltage deviation stays within acceptable limits for the expected frequency deviations in the system.

2.5 OVERCURRENT PROTECTION

Unlike synchronous machines, which can withstand overcurrents several (up to five) times higher than their nominal current rating [83], the converter-interfaced generation is much more vulnerable to high currents due to the presence of temperature-sensitive power electronic components [84]. Furthermore, the fault current withstand of VSCs - usually in the range of 50-60% percent above the nominal current rating - is significantly lower than that of thyristor-based converters (typically twice the nominal current rating of the converter) [85]. Hence, faults on a line fed by the VSCs must be limited and interrupted much faster than those in a conventional HVDC system.

⁴ Described in SI instead of per-unit.

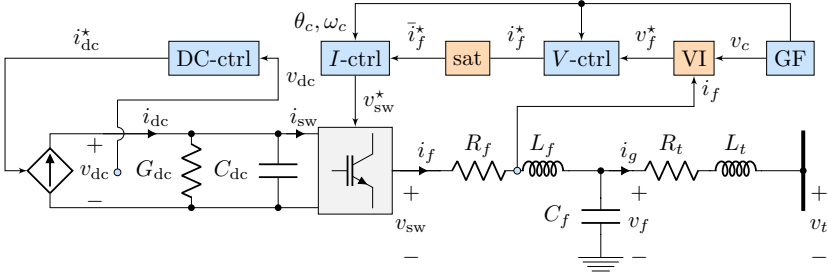


FIGURE 2.7: Simplified representation of the grid-forming converter model with inclusion of overcurrent protection.

Since grid-following control regulates the converter as a controllable current source and provides current reference signal to device-level control, the respective current can easily be limited in both balanced and unbalanced system conditions [86]. However, this is not the case for grid-forming operation mode, as the system-level control computes the voltage vector at the PCC, whereas the current injection is determined internally by the device-level control. Moreover, due to their responsive characteristic in terms of frequency and voltage regulation, grid-forming VSCs might lead to significantly higher current spikes immediately after the disturbance. While grid-following control subject to current limits has been well studied [86, 87], only few works consider the converter’s AC-current limits in the analysis of grid-forming control [88–92]. In this section, we will discuss the two prevalent approaches in the literature, namely limitation of the reference current i_f^* and virtual impedance methods. Nevertheless, it should be noted that some more advanced and potentially more efficient methods have been proposed recently (see e.g., [93]).

A simplified diagram of the grid-forming converter model with inclusion of the overcurrent protection is illustrated in Fig. 2.7, with system-level control represented by the “GF” block and device-level control split into individual components pertaining to AC-voltage and current and DC-current regulation. For simplicity, the measurement signals for the device- and system-level control are not depicted in Fig. 2.7, as they are already provided in Fig. 2.2a. Note that the two overcurrent controllers are placed differently in the control scheme, i.e., the virtual impedance (“VI” block) modifies the system-level reference signal sent to the device-level control, whereas the current limitation (“sat” block) saturates the current reference computed internally within the device-level control. In order to meet the control block representation in Fig. 2.2, the former controller will be assigned to the system-level control.

2.5.1 Reference Current Limitation

Conceptually, the converter's AC current can be regulated by limiting the reference i_f^* of the AC-current controller (2.9) within the device-level control:

$$\bar{i}_f^* = \frac{1}{\|i_f^*\|} \min \{ \|i_f\|, \bar{i}_{\text{lim}} \} i_f^*, \quad (2.31)$$

where $\bar{i}_{\text{lim}} \in \mathbb{R}_{>0}$ is the prescribed threshold and \bar{i}_f^* is the saturated reference provided to the inner current control loop. To this end, various methods for limiting the reference current have been proposed in the literature [88]. However, this approach typically results in integrator windup, both in the AC-voltage controller (2.8) and the system-level control (2.7), and can ultimately cause a loss of synchronization or synchronous instability [89]. While anti-windup feedback can be used to prevent integrator windup in the AC voltage controller, this approach severely degrades the performance of AC voltage control (see [14, Section III-2]).

2.5.2 Threshold Virtual Impedance (TVI)

To limit the converter current while avoiding integrator windup, the system-level reference v_c can be modified instead of directly feeding it through (i.e., $v_f^* = v_c$) to the AC voltage controller (2.8). Such procedure emulates an increased filter impedance when the current magnitude $\|i_f\|$ exceeds a predefined threshold, thus avoiding saturation of the reference current and improving controllability [90–92]. As the transient current depends on the grid reactance, increasing the output impedance of the inverter reduces its post-fault current overshoot. Specifically, given a virtual resistance and inductance $r_v \in \mathbb{R}_{\geq 0}$ and $\ell_v \in \mathbb{R}_{\geq 0}$, the TVI control

$$v_f^* = v_c - \rho_v \max \{ \|i_f\| - \bar{i}_{\text{lim}}, 0 \} z_v i_f \quad (2.32)$$

modifies the grid-forming voltage reference v_c by linearly increasing the emulated impedance $z_v = r_v I_2 + j\omega_0 \ell_v$ if the current i_f is above a given threshold, with $\rho_v \in \mathbb{R}_{>0}$ denoting a tuning parameter and $I_2 = \text{diag}(\mathbb{1}_2)$.

2.6 COMPARISON OF SYSTEM-LEVEL CONTROLS

In this section, an Electro-Magnetic Transients (EMT) model developed in MATLAB Simulink [94] is used to evaluate the proposed system-level control

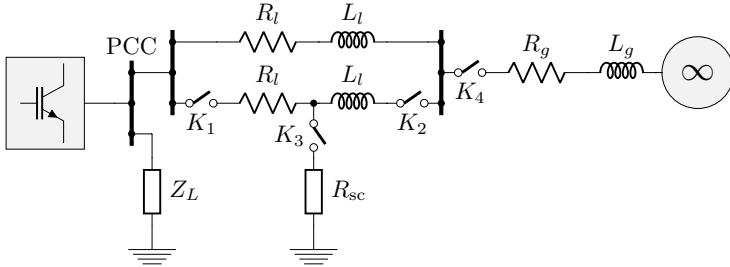


FIGURE 2.8: Single-line diagram of a single converter connected to an infinite bus via two parallel transmission lines used for the case study in Section 2.6.1.

strategies in combination with a device-level controller and a TVI-based current limitation scheme. For each test case we consider a standard cascaded device-level control (2.8)-(2.9) comprised of an inner and outer PI control loop for regulating the output current and voltage (i_f, v_f) respectively, whereas the DC-side voltage regulation varies between different control schemes (see Section 2.4). Finally, all parameters of the system-level control have been adapted to approximately obtain a steady-state frequency deviation of 0.1 Hz for an active power deviation of 0.1 p.u.

2.6.1 Single-Converter Infinite-Bus

A first set of test cases is based on a single converter with a $\bar{P}_c = 1000$ MW rating connected to an infinite bus⁵ through two parallel transmission lines, as depicted in Fig. 2.8, and is used to study: (i) tracking of power and voltage references when connected to a strong grid; (ii) converter islanding; and (iii) the response to grid events, i.e., disconnection of a line and short-circuit faults. For the purposes of the first two case studies, the transmission lines are bypassed, i.e., the inverter is directly connected to the infinite bus. The TVI current threshold is set to $\bar{i}_{lim} = 1.2$ p.u.

2.6.1.1 Reference Tracking

In this case the switch K_4 is closed and converter setpoints for the terminal voltage as well as the active power are varied in order to test the reference tracking performance. Starting from $V_c^* = 1$ p.u. and $P_c^* = 500$ MW, the

⁵ The impedance of the infinite bus is computed based on a short-circuit ratio of 20.

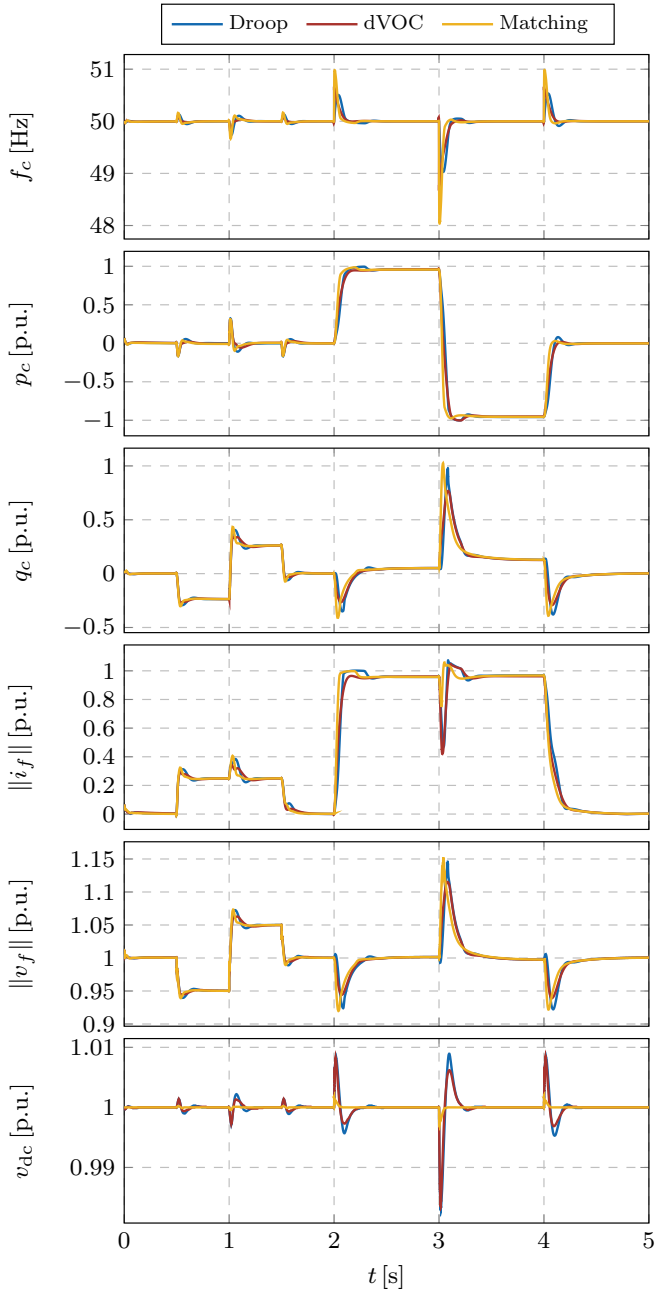


FIGURE 2.9: Reference tracking of a single converter connected to a strong grid.

voltage reference is set to $V_c^* = 0.95$ p.u. at $t = 0.5$ s, $V_c^* = 1.05$ p.u. at $t = 1$ s, and $V_c^* = 1$ p.u. at $t = 1.5$ s. Moreover, the active power reference is changed to $P_c^* = 1000$ MW at $t = 2$ s, $P_c^* = -1000$ MW at $t = 3$ s, and $P_c^* = 0$ MW at $t = 4$ s. The respective simulation results are shown in Fig. 2.9.

All three controls reach the voltage and active power reference roughly within 100 ms and 200 ms after the change, respectively. We notice that a reversal of the power reference at $t = 3$ s leads to a large overshoot of the output voltage. However, in a real-world system this effect would have been limited due to several factors, for instance the reference slope would have been less steep. In general, the controls experience qualitatively similar behaviour and reference tracking, as no significant differences can be observed on the AC side. In particular, droop control and dVOC exhibit nearly identical response. The only notable distinction is that the indirect matching control results in smaller fluctuations in the DC voltage because it explicitly considers the DC voltage in the control of the converter's AC side.

2.6.1.2 *Islanding*

In this scenario, the converter is supplying a local impedance load of 500 MW and the switch K_4 opens at $t = 0.5$ s, thus islanding the converter and the load. Furthermore, a constant power load of 100 MW is enabled at $t = 1.5$ s. The frequency response of all three control strategies illustrated in Fig. 2.10 is qualitatively similar, with droop control showing a slower response than indirect matching control and dVOC. Moreover, all control strategies result in exactly the same behaviour on the AC side of the converter and regulate the output voltage to its reference value within 100 ms after the disturbance. On the DC side, droop control and dVOC are indistinguishable. In contrast, indirect matching control again results in a different behaviour of the DC voltage. More specifically, the fluctuations in the DC voltage are smaller and, analogously to a synchronous machine, a power imbalance on the AC side results in an energy imbalance on the DC side, i.e., a deviation of the voltage of the DC-link capacitor proportional to the frequency deviation. In other words, while the corresponding timescales are much faster for a power converter, the qualitative behaviour is identical to that of a synchronous machine.

2.6.1.3 *Short-Circuit Fault and Line Opening*

Next, a three-phase short-circuit fault on one of the lines is simulated at $t = 1.5$ s via closing the switch K_3 and subsequently cleared by disconnecting

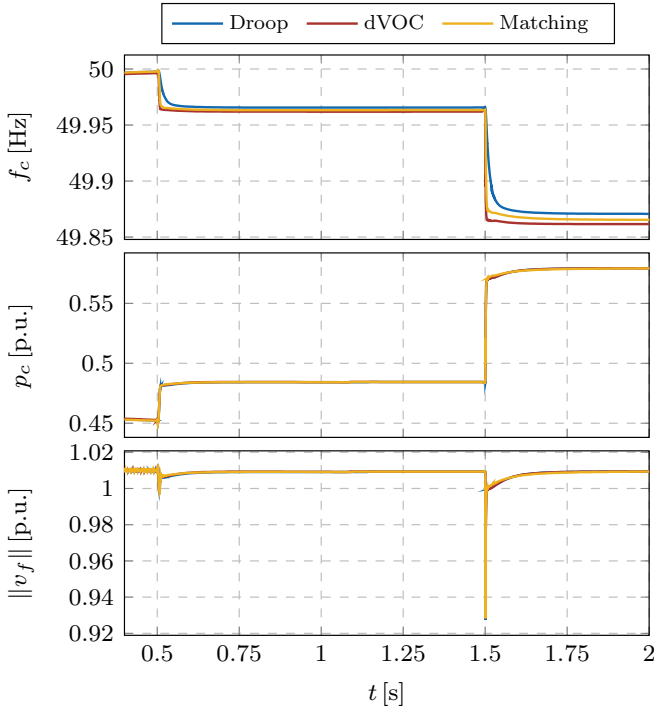


FIGURE 2.10: Converter performance during islanding from the main grid.

the line (opening of switches K_1 and K_2) after 150 ms; switch K_4 is in the closed position the whole time. The simulation results presented in Fig. 2.11 indicate that all three control algorithms recover in stable manner and reach the initial references within 250 ms. The current limitation of the device-level control exhibits the same behaviour with all three system-level controls and, after an initial transient, limits the current to below 1.2 p.u. During the fault, the frequency increase is limited but significant enough so that the angle of the converter output voltage diverges compared to the angle of the infinite bus. Even though all three controls have the same static droop characteristic at nominal voltage, dVOC couples the frequency and voltage response, resulting in a lower frequency deviation during fault compared to the other two control schemes, which in turn enables dVOC to return faster to steady state. Compared to droop control and dVOC, indirect matching control again results in a different response of the DC voltage as previously discussed. Interestingly, droop control experiences the least amount of oscillations in the

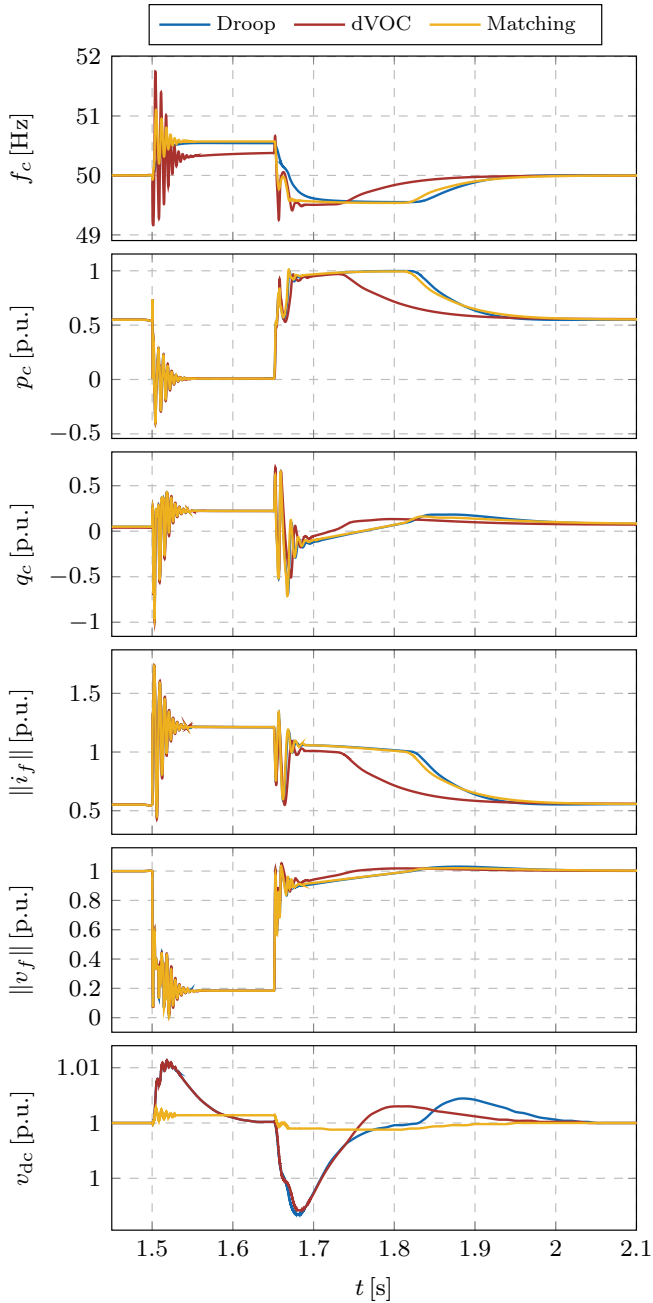


FIGURE 2.11: Response of a single converter during a short circuit fault and subsequent line opening.

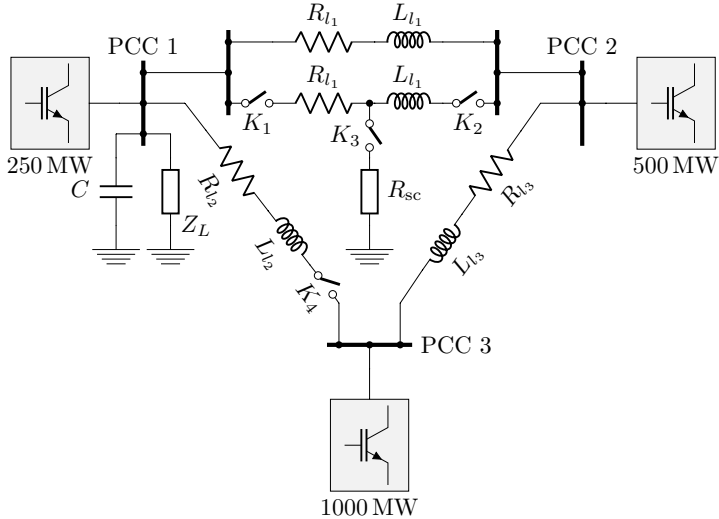


FIGURE 2.12: Single-line diagram of a three-bus test case used for analyzing the compatibility of different converter controls in Section 2.6.2.

DC signals. It should be noted however that the current limitation scheme of the underlying controller was tuned using droop as system-level controller. Finally, we note that the response on the AC side immediately after the fault, as well as after the fault clearance, is identical for all controls because it is governed by the physics of the system (i.e., the capacitor resonance with the line inductance) and the current limitation scheme. It is expected that the voltage resonance and current overshoot can be improved by more efficient overcurrent protection methods.

2.6.2 Multi-Converter System

In the future power system, grid-forming converters of various ratings will be interconnected via transmission grids with diverse topologies. Therefore, a three-bus system comprised of 400 kV overhead lines and 1125 MW of resistive load illustrated in Fig. 2.12 is used to investigate the compatibility of different system-level control algorithms and the response to grid events in a 100% converter-based system. The switch K_4 opens at $t = 0.5$ s corresponding to a sudden line trip between the smallest and largest VSC units (Inverter 1 and Inverter 3 respectively). At $t = 1.5$ s, a large three-phase fault is applied

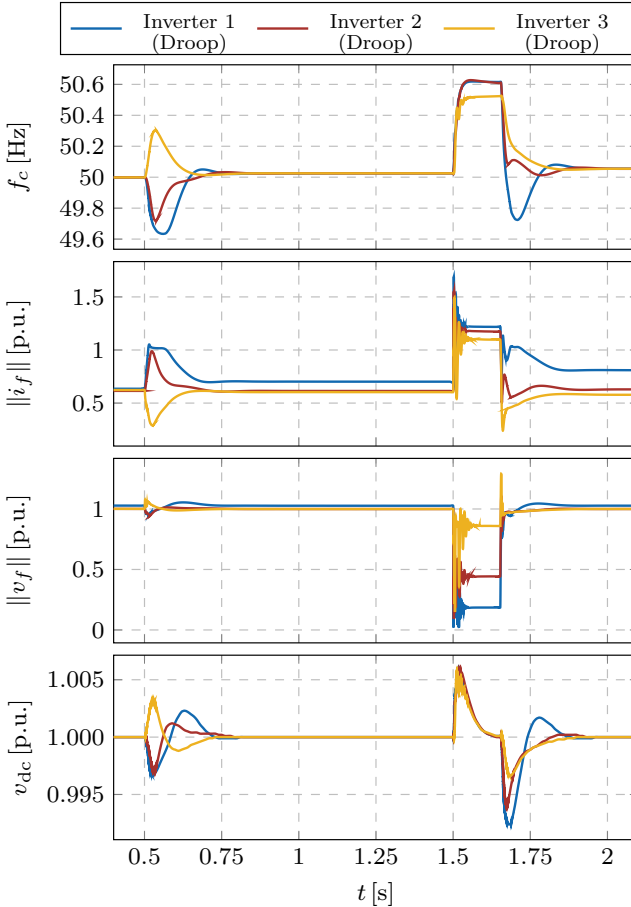


FIGURE 2.13: Simulation results for the three-bus case study comprised solely of droop-based converters.

on one of the two lines connecting the first and the second converter (in the vicinity of PCC 1) and the line is opened 150 ms after the fault, similar to the scenario described in Section 2.6.1.3.

First, we investigate the response of a power system with only droop-controlled converters. As shown in Fig. 2.13, the system recovers a stable operating point as all converters converge to the same frequency in less than 250 ms after each event. While different ratings and electrical distance of converters from the events lead to different individual responses, even

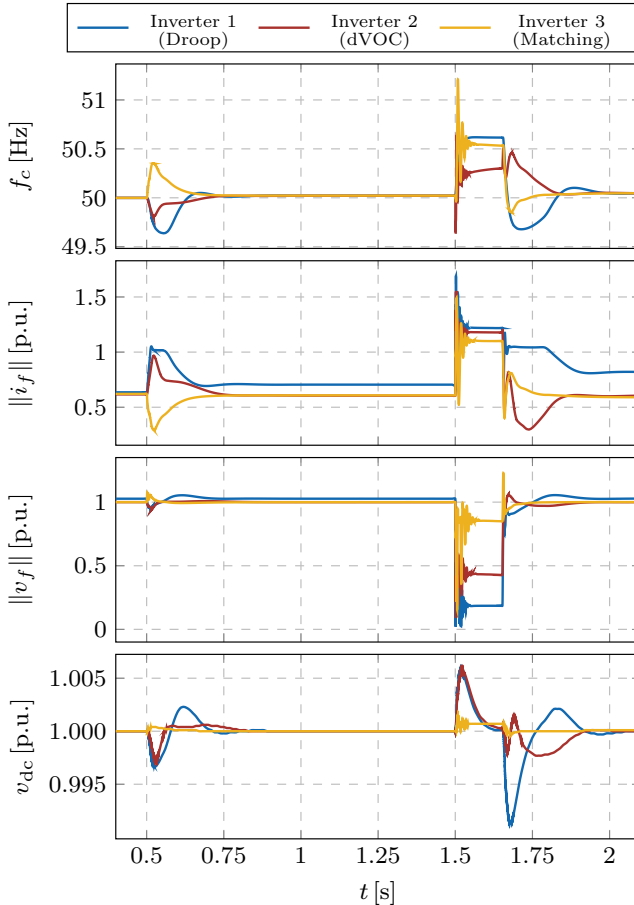


FIGURE 2.14: Simulation results for the three-bus case study comprised of converters regulated through three different system-level control schemes.

the converter with the lowest rating (Inverter 1) is well protected by the action of the TVI, despite supplying a major part of the load during the transients. Nonetheless, its output current exceeds the permissible limit of 1.2 p.u. for a very short period of time (< 5 ms). Similarly, the converter with the highest rating (Inverter 3) briefly exhibits a large overvoltage (≈ 1.3 p.u.) after the fault clearance. Further investigations are required to determine if the overcurrents and overvoltages observed in this study are withstood by

the hardware, or if they are prevented by the low-level protections of the valves (which have been ignored in this study) without affecting the system stability. Otherwise, the implemented protection strategy must be enhanced.

Compared to the previous (uniform control) case, the system with three different controllers settles to a similar steady state but only within 400 ms after each event, as indicated in Fig. 2.14. Other distinctions mainly concern the frequency behavior which depends strongly on the control strategy. Notably, the maximum frequency deviation and Rate-of-Change-of-Frequency (RoCoF) are high for indirect matching control. However, fast frequency oscillations will not be seen by other devices as frequency measurements usually act as a low-pass filter. Moreover, they should not have any impact on the converter itself as there are no rotating parts. Since the frequency is less homogeneous during the fault, the frequency transients after fault clearing are longer. On the other hand, all control schemes result in identical AC-voltage behavior. Such compatibility of different system-level control strategies is not surprising considering that they all exhibit similar behavior independently. However, adverse interactions might still arise in different grid configurations or may be excited by other events. Therefore, no rigorous conclusions on the overall stability of a system using a mix of different grid-forming controls can be made at this stage.

2.7 UNIFORM CONVERTER MODEL

In previous sections, we have shown both analytically (Section 2.4) and through simulations (Section 2.6) that the different grid-forming control strategies can be subsumed under a droop-based controller under certain assumptions. Therefore, the rest of this chapter as well as the thesis will focus only on droop control as a mean of system-level regulation. Moreover, due to its mathematical equivalence to droop control under small frequency deviations (see Section 2.2.4), the VSM control approach will also be considered throughout this work.

In order to facilitate a DAE form of an arbitrary, generic low-inertia system, we propose a uniform converter model that comprises both grid-forming and grid-following mode of operation within a single control structure. More precisely, we modify the latter control design (both in terms of system- and device-level control) such that it fits the input-output characteristic of a grid-forming VSC while still preserving its dynamical properties. The general configuration of the implemented control scheme is illustrated⁶ in Fig. 2.15,

⁶ Colored blocks in Fig. 2.15 indicate the presence of internal control dynamics.

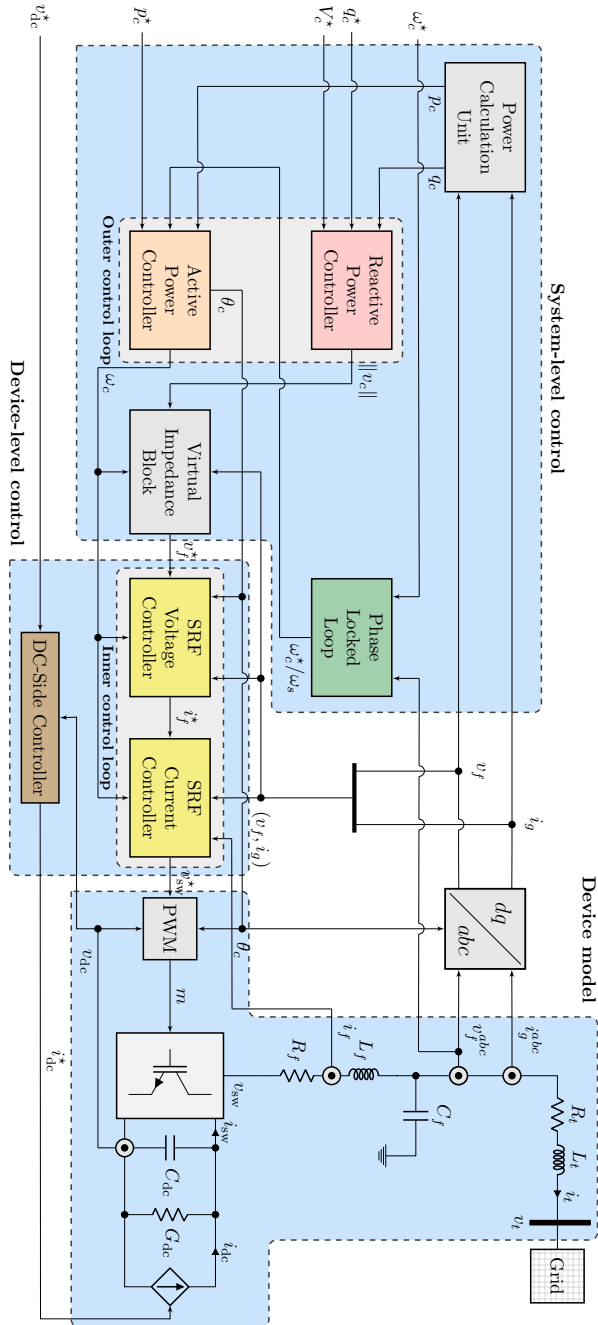


FIGURE 2.15: General configuration of the implemented VSC control structure.

with three main segments (i.e., system-level control, device-level control and device model) corresponding to the block diagram in Fig. 2.2. By closely studying the proposed control structure, one can observe that it very much resembles the grid-forming control design from Section 2.2. In fact, beside the inclusion of the PLL in Fig. 2.15, the two models are identical. However, the PLL has no function in the grid-forming operation, as it is bypassed and the frequency setpoint ω_c^* is directly fed to the Active Power Controller (APC). Note that the virtual impedance can be employed in two ways. On the one hand, it can act as a current limitation strategy in the form of a TVI controller (2.32). On the other hand, it can be embedded as a traditional virtual impedance, i.e., an additional degree of freedom for active stabilization and disturbance rejection by providing a minor cross-coupling between d - and q -components via the resistive and inductive elements r_v and ℓ_v . In such case, (2.32) is simplified into

$$v_f^* = v_c - (r_v I_2 + j\omega_0 \ell_v) i_f. \quad (2.33)$$

In terms of grid-following operation, the main distinction lies in the system-level control design, i.e., the droop implementation of the outer control loop. Instead of applying the controller (2.12) and drooping the frequency and voltage imbalance in order to determine the power (i.e., current) references, we employ a grid-forming control law given by (2.14) and (2.15). However, the frequency and voltage setpoint inputs ω_c^* and V_c^* are replaced by measurements ω_s and $\|v_f\|$, respectively, resulting in

$$\omega_c = \omega_s + \lambda_\theta(s) (p_c^* - p_c), \quad v_c^d = \|v_f\| + \lambda_v(s) (q_c^* - q_c), \quad (2.34)$$

with $\lambda_\theta(s)$ and $\lambda_v(s)$ provided in (2.15). Furthermore, we introduce the terms for low-pass filtered active and reactive power

$$\tilde{p}_c = \frac{\omega_z}{\omega_z + s} p_c, \quad \tilde{q}_c = \frac{\omega_z}{\omega_z + s} q_c, \quad (2.35)$$

and, by neglecting the low-pass filtering of constant setpoints p_c^* and q_c^* , rewrite (2.34) as

$$\omega_c = \omega^* + R_c^p (p_c^* - \tilde{p}_c), \quad v_c^d = V^* + R_c^q (q_c^* - \tilde{q}_c), \quad (2.36)$$

where $\omega^* \in \{\omega_c^*, \omega_s\}$ and $V^* \in \{V_c^*, \|v_f\|\}$, depending on the converter mode. The control in (2.36) provides a uniform formulation for system-level regulation and encompasses both operation modes, with $(\omega^*, V^*) := (\omega_c^*, V_c^*)$ for grid-forming and $(\omega^*, V^*) := (\omega_s, \|v_f\|)$ for grid-following case. Note that in

theory the controller (2.36) can take any of the four combinations for (ω^*, V^*) . However, the stability and performance of such system highly depends on the network configuration and control design of other converter-based generators in the grid, as shown in [24] under the concept of partial grid-forming control.

While not meeting the input-output criteria depicted in Fig 2.4a, the presented grid-following control still achieves power reference tracking while simultaneously supporting the voltage and frequency at the PCC. In contrast to the controller (2.12), where the active power setpoint is adjusted according to the frequency mismatch, the droop control in (2.36) ensures that the power output meets its predefined setpoint by adjusting the reference frequency and voltage accordingly. It should be pointed out that the same implementation could have been achieved for a VSM controller. Furthermore, such uniform structure implies that the same cascaded device-level control can be used for both converter modes. Therefore, the proposed uniform model can be described by (2.5),(2.8)-(2.10) and (2.36) for the grid-forming mode and (2.5),(2.8)-(2.11) and (2.36) for the grid-following mode of operation, resulting in the 14th and 16th-order models, respectively, represented by the state vectors

$$x_c^{\text{form}} = (i_f, v_f, i_g, \xi, \gamma, \chi, \tilde{p}_c, \tilde{q}_c, \theta_c) \in \mathbb{R}^{14}, \quad (2.37)$$

$$x_c^{\text{follow}} = (i_f, v_f, i_g, \xi, \gamma, \chi, \varepsilon, \theta_s, \tilde{p}_c, \tilde{q}_c, \theta_c) \in \mathbb{R}^{16}. \quad (2.38)$$

Clearly, the only difference between the two models is the presence of PLL dynamics (i.e., controller states ε and θ_s).

Another important aspect of the proposed grid-following control scheme is the presence of two SRFs within the same model. More precisely, the synchronization unit is implemented as a PLL, which measures the three-phase output voltage v_f^{abc} and transforms it into an internal dq -frame. Therefore, a second SRF defined by θ_s is introduced in addition to the converter's SRF with a reference angle θ_c , as illustrated in Fig. 2.16. Note that $\omega_g \in \mathbb{R}_{>0}$ and $\theta_g \in [-\pi, \pi)$ represent the actual frequency and angle of output voltage v_f , whereas $\vartheta_c \in \mathbb{R}$ and $\vartheta_s \in \mathbb{R}$ are the angular displacements of the individual SRFs compared to that voltage vector. As a result, the PLL controller (2.11) is redefined as

$$\dot{\varepsilon} = \hat{v}_f^q, \quad (2.39a)$$

$$\omega_s = \omega_0 + K_P^s \hat{v}_f^q + K_I^s \varepsilon, \quad (2.39b)$$

$$\dot{\theta}_s = \omega_b \omega_s, \quad (2.39c)$$

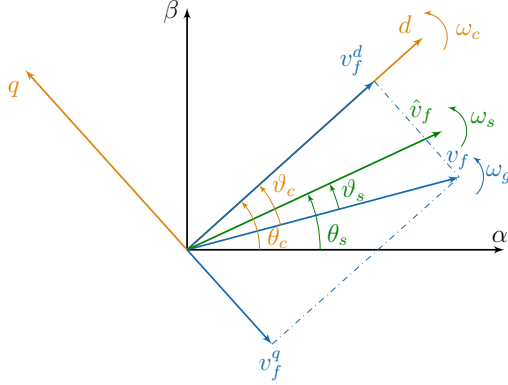


FIGURE 2.16: Vector diagram representing the alignment of different SRFs.

where $\hat{v}_f = \mathcal{R}(\theta_c - \theta_s) v_f$ represents the output voltage vector v_f expressed in the PLL's internal SRF, i.e.,

$$\hat{v}_f^q = v_f^d \sin(\theta_c - \theta_s) + v_f^q \cos(\theta_c - \theta_s). \quad (2.40)$$

By substituting (2.40) in (2.39), we obtain a uniform control scheme implemented in a single SRF defined by the APC (i.e., by the reference angle θ_c). Finally, the most relevant model and control tuning parameters are provided in Table 2.1. However, the system-level control tuning might vary throughout this thesis.

The conceptual differences between the two converter modes can be observed by studying the effect of grid strength on converter's small-signal stability. In particular, different Short-Circuit Ratios (SCRs) expressed as

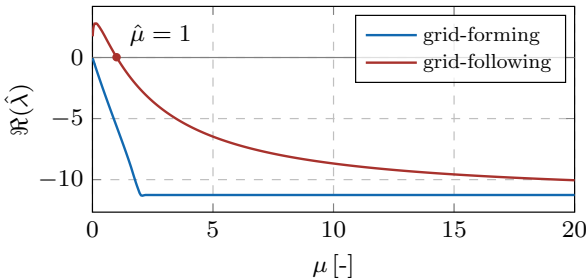


FIGURE 2.17: SCR influence on small-signal stability of a converter under different operation modes.

Parameter	Symbol	Value	Unit
Active power droop gain	R_c^p	2	%
Reactive power droop gain	R_c^q	0.1	%
LPF cut-off frequency	f_z	5	Hz
RLC filter resistance	r_f	0.03	p.u.
RLC filter inductance	ℓ_f	0.08	p.u.
RLC filter capacitance	c_f	0.074	p.u.
P-gain of SRF current control	K_P^i	0.74	-
I-gain of SRF current control	K_I^i	1.19	-
FF-gain of SRF current control	K_F^i	0	-
P-gain of SRF voltage control	K_P^v	0.52	-
I-gain of SRF voltage control	K_I^v	1.16	-
FF-gain of SRF voltage control	K_F^v	1	-
PLL proportional gain	K_P^s	0.4	-
PLL integral gain	K_I^s	4.69	-
Virtual impedance resistance	r_v	0.001	p.u.
Virtual impedance inductance	ℓ_v	0.2	p.u.

TABLE 2.1: Converter control parameters.

$\mu = x_g^{-1} \in [0, 20]$ are considered by changing the reactance $x_g \in \mathbb{R}_{>0}$ and resistance $r_g \in \mathbb{R}_{>0}$ of the grid equivalent such that the transmission system ratio $X_g/R_g \approx 10$ is preserved. The movement of the most critical eigenvalue $\hat{\lambda}$ illustrated in Fig. 2.17 suggests that the grid-following inverter faces instability when connected to a relatively weak grid (corresponding to the critical SCR $\hat{\mu} = 1$). In contrast, the grid-forming inverter does not impose any requirements on the stiffness of the voltage at the PCC, justified by the fact that it can establish its own terminal voltage by the nature of the control design.

2.8 SYNCHRONOUS GENERATOR MODEL

In this thesis, we consider a traditional two-pole synchronous generator equipped with a prime mover and a governor. Additionally, a voltage excitation system comprised of an Automatic Voltage Regulator (AVR) and a Power System Stabilizer (PSS) is incorporated into the model. A detailed block diagram of the SG model and control scheme is illustrated in Fig. 2.18,

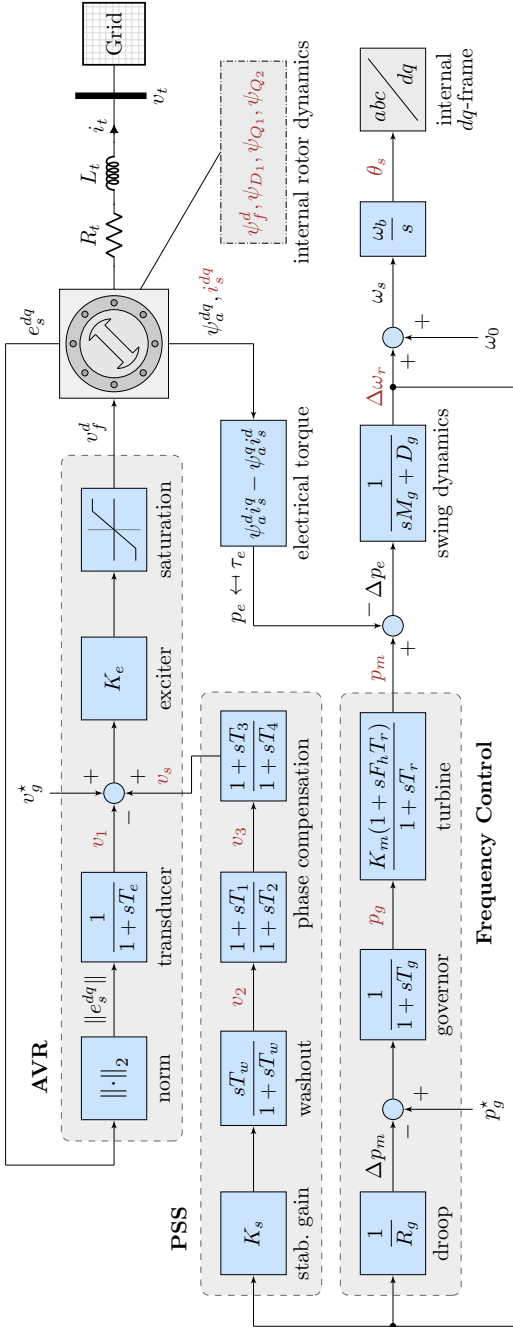


FIGURE 2.18: Block diagram of a synchronous generator equipped with a prime mover, a governor and a voltage excitation system. The internal state variables are denoted by red color.

Parameter	Symbol	Value	Unit
Droop control gain	R_g	2	%
Governor time constant	T_g	0.5	s
Reheat time constant	T_r	10	s
Mechanical power gain factor	K_m	0.85	-
Turbine power fraction factor	F_h	0.1	-
Normalized inertia constant	M_g	13	s
Normalized damping factor	D_g	1	p.u.
Transducer time constant	T_e	0.05	s
AVR exciter control gain	K_e	200	-
Saturation minimum output	V_f^{\min}	0	p.u.
Saturation maximum output	V_f^{\max}	4	p.u.
PSS stabilization gain	K_s	5	-
Washout time constant	T_w	2	s
1 st lead-lag derivative time constant	T_1	0.25	s
1 st lead-lag delay time constant	T_2	0.03	s
2 nd lead-lag derivative time constant	T_3	0.15	s
2 nd lead-lag delay time constant	T_4	0.015	s

TABLE 2.2: Synchronous generator parameters.

where the generator is connected to the grid through a transformer modeled as a series impedance. This is a well-established configuration used both for academic and industrial purposes [26, 46, 95]. The complete model is described in an SRF defined by generator's synchronous velocity and expressed in per-unit, with the main parameters provided in Table 2.2.

2.8.1 Internal Machine Dynamics

The internal machine dynamics are characterized by the swing dynamics of the rotor as well as the transients in the rotor circuits, as transients in the stator windings decay rapidly and can thus be neglected. The swing dynamics are traditionally represented by the swing equation

$$M_g \Delta \dot{\omega}_r = \Delta p_e - D_g \Delta \omega_r, \quad (2.41)$$

with $M_g \in \mathbb{R} > 0$ and $D_g \in \mathbb{R} > 0$ being the normalized inertia and damping constants, $\Delta \omega_r \in \mathbb{R}$ denoting the deviation of rotor's angular velocity from the

nominal value, and $\Delta p_e \in \mathbb{R}$ describing the mismatch between the mechanical power generated by the turbine and the electrical power at the SG's output.

On the other hand, rotor circuit dynamics originate in the armature reaction, i.e., in the effect of the stator field on the rotor currents, which can be described through flux linkage dynamics:

$$\dot{\psi}_f^d = \frac{\omega_0 r_f}{x_{a,u}^d} v_f^d - \frac{\omega_0 r_f}{x_f} (\psi_f^d - \psi_a^d), \quad (2.42a)$$

$$\dot{\psi}_{D_1} = -\frac{\omega_0 r_{D_1}}{x_{D_1}} (\psi_{D_1} - \psi_a^d), \quad (2.42b)$$

$$\dot{\psi}_{Q_1} = -\frac{\omega_0 r_{Q_1}}{x_{Q_1}} (\psi_{Q_1} - \psi_a^q), \quad (2.42c)$$

$$\dot{\psi}_{Q_2} = -\frac{\omega_0 r_{Q_2}}{x_{Q_2}} (\psi_{Q_2} - \psi_a^q). \quad (2.42d)$$

Here, subscripts f , D_1 , Q_1 and Q_2 stand for the quantities of the field circuit, d -axis damping circuit and two q -axis damping circuits respectively, whereas $\psi \in \mathbb{R}^2$, $r \in \mathbb{R}_{>0}$ and $x \in \mathbb{R}_{>0}$ denote the respective flux linkage, resistance and reactance of a circuit. Moreover, $v_f \in \mathbb{R}^2$ is the exciter's output voltage with zero q -component (i.e., $\|v_f\| = v_f^d$), $\omega_0 \in \mathbb{R}_{>0}$ designates the synchronous angular velocity, and $x_{a,u}^d \in \mathbb{R}_{>0}$ stands for the unsaturated mutual reactance. Superscripts d and q are omitted from damping circuit quantities for simplicity, i.e., $\psi_{D_1} \in \mathbb{R}$, $\psi_{Q_1} \in \mathbb{R}$ and $\psi_{Q_2} \in \mathbb{R}$. The dq -components of the armature flux linkage $\psi_a \in \mathbb{R}^2$ are expressed as

$$\psi_a^d = \hat{x}_{a,s}^d \left(-i_s^d + \frac{\psi_f^d}{x_f} + \frac{\psi_{D_1}}{x_{D_1}} \right), \quad (2.43a)$$

$$\psi_a^q = \hat{x}_{a,s}^q \left(-i_s^q + \frac{\psi_{Q_1}}{x_{Q_1}} + \frac{\psi_{D_1}}{x_{Q_2}} \right), \quad (2.43b)$$

with the subtransient, saturated, mutual reactances $\hat{x}_{a,s}^d \in \mathbb{R}_{>0}$ and $\hat{x}_{a,s}^q \in \mathbb{R}_{>0}$ defined by

$$\hat{x}_{a,s}^d = \left(\left(x_{a,s}^d \right)^{-1} + x_f^{-1} + x_{D_1}^{-1} \right)^{-1}, \quad (2.43c)$$

$$\hat{x}_{a,s}^q = \left(\left(x_{a,s}^q \right)^{-1} + x_{Q_1}^{-1} + x_{Q_2}^{-1} \right)^{-1}. \quad (2.43d)$$

Finally, the inclusion of stator's circuit balance completes the internal generator model:

$$e_s^d = -r_a i_s^d + x_l i_s^q - \psi_a^q, \quad (2.44a)$$

$$e_s^q = -r_a i_s^q + x_l i_s^d - \psi_a^d. \quad (2.44b)$$

In (2.44), stator voltage and current vectors are denoted by $e_s \in \mathbb{R}^2$ and $i_s \in \mathbb{R}^2$, while $r_a \in \mathbb{R}_{>0}$ and $x_l \in \mathbb{R}_{>0}$ represent the armature resistance and leakage reactance respectively. Expressions (2.41)-(2.44) yield a 6th-order dynamical model described by the state vector $x_g^{\text{int}} := (\theta_s, \omega_s, \psi_f^d, \psi_{D1}, \psi_{Q1}, \psi_{D2}) \in \mathbb{R}^6$, where $\dot{\theta}_s = \omega_b \omega_s$. For more details regarding the generator modeling and internal parameter computation we refer the reader to [26].

2.8.2 Control Design and Electrical Interface

The proposed control scheme comprises two independent loops for frequency and voltage regulation [95]. The former one consists of droop control and governor and turbine dynamics (see Fig. 2.18), described respectively by state variables $p_g \in \mathbb{R}$ and $p_m \in \mathbb{R}$ (i.e., a state vector $x_g^{\text{freq}} = (p_g, p_m) \in \mathbb{R}^2$). On the other hand, voltage control includes an AVR with a transducer and a saturated exciter, and a PSS combining a washout filter and a lead-lag phase compensation, with vectors $x_g^{\text{AVR}} := v_1 \in \mathbb{R}$ and $x_g^{\text{PSS}} := (v_2, v_3, v_s) \in \mathbb{R}^3$ describing the underlying controller states respectively. For brevity, we will omit a detailed derivation of the control dynamics pertaining to frequency control, AVR and PSS, as it can be easily deduced from the control block diagram in Fig. 2.18. Note that all state variables are denoted by red color in Fig. 2.18.

As mentioned previously, a synchronous generator is interfaced to the grid through a transformer modeled as a series impedance $r_t \in \mathbb{R}_{>0}$ and $\ell_t \in \mathbb{R}_{>0}$. The dynamics of the current $i_t \in \mathbb{R}^2$ flowing through a transformer can be expressed in an SRF defined by (θ_s, ω_s) as

$$\dot{i}_t = \frac{\omega_b}{\ell_t} (e_s - v_t) - \left(\frac{r_t}{\ell_t} \omega_b + j \omega_b \omega_s \right) i_s, \quad (2.45)$$

where $v_t \in \mathbb{R}^2$ denotes the terminal voltage and terminal current corresponds to stator current (i.e., $i_s := i_t$). Finally, by combining (2.41)-(2.45) with the dynamics of frequency and voltage control loops, we obtain a 14th-order SG model described by the state vector $x_g = (x_g^{\text{int}}, x_g^{\text{freq}}, x_g^{\text{AVR}}, x_g^{\text{PSS}}, i_t) \in \mathbb{R}^{14}$.

2.9 NETWORK AND SYSTEM MODELING

2.9.1 Transmission Network Dynamics

Modeling of the transmission network is described for a generic system depicted in Fig. 2.19, composed of generators supplying local RL loads and the

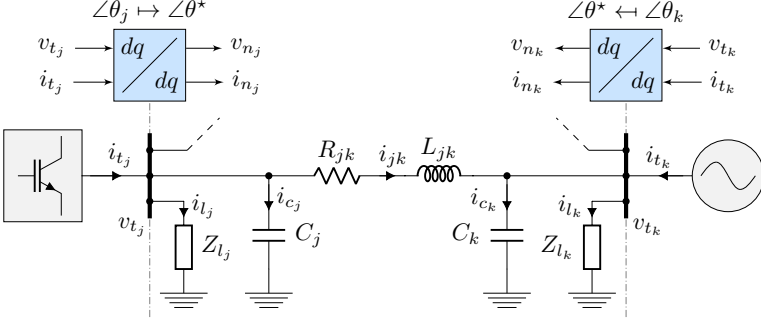


FIGURE 2.19: Generic network model with line dynamics and respective dq -frame alignment.

interconnecting transmission lines modeled as π -sections; long transmission lines with lengths above 250 km are represented by distributed line parameters. In order to establish a consistent mathematical formulation, all variables have to be defined within a single SRF, including the reference frame of the network. Neglecting grid dynamics has been a general assumption for SG-dominated power systems, based on the premise of grid and generator's armature dynamics being much faster than those of the excitation and governor systems [96, 97]. Alternatively, studies often oversimplify the problem and assume that the grid's SRF rotates at constant nominal angular velocity, as pointed out in [98]. For this purpose however, we introduce a transformation $f_n : \mathbb{Z}_{>0} \mapsto \mathbb{Z}_{>0}$ that maps the set of generator indices $g \in \mathcal{G} \subset \mathbb{Z}_{>0}$ to the subset of nodal indices of the network with generator connection $j \in \mathcal{N}_g \subset \mathcal{N}$, with $\mathcal{N} \subset \mathbb{Z}_{>0}$ being the index set of network nodes. Hence, the terminal currents⁷ $i_{t_g} \in \mathbb{R}^2$ and voltages $v_{t_g} \in \mathbb{R}^2$ of each generator unit $g \in \mathcal{G}$ are mapped to vectors $i_{t_j} \in \mathbb{R}^2$ and $v_{t_j} \in \mathbb{R}^2$ corresponding to the terminal currents and voltages of the network nodes $j \in \mathcal{N}_g$, where $j = f_n(g)$. The nodal vectors are subsequently aligned to the SRF of an arbitrary synchronous generator or a grid-forming converter $r \in \mathcal{G}$, rotating at angular speed $\omega^* := \omega_{s_r}$, i.e., $\omega^* := \omega_{c_r}$, as follows:

$$x_{n_j} = \mathcal{R}(\theta^* - \theta_j) x_{t_j}, \quad \forall j \in \mathcal{N}. \quad (2.46)$$

Here, $x_{n_j} \in \{i_{n_j}, v_{n_j}\}$ denotes the “nodal” metrics described in the nominal reference frame, the uniform SRF angle is computed as $\dot{\theta}^* = \omega_b \omega^*$, and

⁷ Note that the terminal currents correspond to stator currents i_s of SGs (see Fig. 2.18) or to grid injection currents i_g of VSCs (see Fig. 2.15).

$\theta_j \in [-\pi, \pi)$ corresponds to the internal SRF angle of the respective unit, i.e., $\theta_j := \theta_{s_j}$ for the synchronous and $\theta_j := \theta_{c_j}$ for the converter-based generator. According to [96], such approach provides a good trade-off between the computational complexity and model accuracy.

The nodal voltage and current dynamics can now be expressed $\forall j \in \mathcal{N}$ as

$$\dot{v}_{n_j} = \frac{\omega_b}{c_{l_j}} i_{c_j} - j\omega_b \omega^* v_{n_j}, \quad (2.47a)$$

$$\dot{i}_{l_j} = \frac{\omega_b}{l_{l_j}} v_{n_j} - \left(\frac{r_{l_j}}{l_{l_j}} \omega_b + j\omega_b \omega^* \right) i_{l_j}, \quad (2.47b)$$

thus capturing the load and shunt phenomena at each node, with $r_{l_j} \in \mathbb{R}_{>0}$ and $l_{l_j} \in \mathbb{R}_{>0}$ being the load's resistance and inductance, and $c_j \in \mathbb{R}_{>0}$ reflecting the aggregate shunt capacitance. Finally, the line dynamics are represented using a conventional RL circuit formulation

$$\dot{i}_{jk} = \frac{\omega_b}{l_{jk}} (v_{n_j} - v_{n_k}) - \left(\frac{r_{jk}}{l_{jk}} \omega_b + j\omega_b \omega^* \right) i_{jk}, \quad \forall j \in \mathcal{N}, k \in \mathcal{K}_j, \quad (2.48)$$

with $i_{jk} \in \mathbb{R}^2$ being the current and $(r_{jk}, l_{jk}) \in \mathbb{R}_{>0}^2$ the respective parameters of a transmission line connecting nodes $j \in \mathcal{N}$ and $k \in \mathcal{K}_j$, and $\mathcal{K}_j \subset \mathcal{N}$ denoting the subset of nodes adjacent to node j . Combining (2.46)-(2.48) with the algebraic expressions for current balance at each node $j \in \mathcal{N}$ in the system concludes the network model.

2.9.2 Complete Model Formulation

Having defined models of different generation units and the network, we can complete the general Ordinary Differential Equation (ODE) formulation of the system. Let us consider a large-scale, low-inertia system with nodal and generation index sets \mathcal{N} and \mathcal{G} defined previously. Furthermore, let $\mathcal{S} \subset \mathbb{Z}_{>0}$ and $\mathcal{C} \subset \mathbb{Z}_{>0}$ ($\mathcal{S} \cup \mathcal{C} = \mathcal{G}$) be the index sets of synchronous and converter-interfaced generators, with the second set differentiating between the subsets $\mathcal{C}_F \subset \mathcal{C}$ and $\mathcal{C}_f \subset \mathcal{C}$ of grid-forming and grid-following units, respectively. Furthermore, let $\mathcal{B} \subset \mathbb{Z}_{>0}$ denote the index set of network branches, where elements of the branch current vector $i_b \in \mathbb{R}^{|\mathcal{B}|}$ are mapped to the currents i_{jk} in (2.48) using the transformation $f_i : \mathbb{Z}_{>0}^2 \mapsto \mathbb{Z}_{>0}$ such that $\forall j \in \mathcal{N}, \forall k \in \mathcal{K}_j, \exists m \in \mathcal{B} \mid m = f_i(j, k) \wedge i_{b_m} := i_{jk}$.

The dynamical model of such system can be expressed by

$$\dot{x} = f(x, u), \quad (2.49a)$$

where

$$x = \left(x_{c_1}^F, \dots, x_{c_{|\mathcal{C}_F|}}^F, x_{c_1}^f, \dots, x_{c_{|\mathcal{C}_f|}}^f, x_{g_1}, \dots, x_{g_{|\mathcal{S}|}}, x_n \right), \quad (2.49b)$$

$$u = \left(u_{c_1}^F, \dots, u_{c_{|\mathcal{C}_F|}}^F, u_{c_1}^f, \dots, u_{c_{|\mathcal{C}_f|}}^f, u_{g_{|\mathcal{S}|}} \right). \quad (2.49c)$$

The state and control input vectors of grid-forming and grid-following converters (denoted by superscripts F and f respectively) in (2.49b)-(2.49c) are defined $\forall p \in \mathcal{C}_F$ and $\forall q \in \mathcal{C}_f$ as

$$x_{c_p}^F = (i_f, v_f, i_g, \xi, \gamma, \chi, \tilde{p}_c, \tilde{q}_c, \theta_c) \in \mathbb{R}^{14}, \quad (2.49d)$$

$$x_{c_q}^f = (i_f, v_f, i_g, \xi, \gamma, \chi, \varepsilon, \theta_s, \tilde{p}_c, \tilde{q}_c, \theta_c) \in \mathbb{R}^{16}, \quad (2.49e)$$

$$u_{c_p}^F = (p_c^*, q_c^*, V_c^*, \omega_c^*, v_{dc}^*) \in \mathbb{R}^5, \quad (2.49f)$$

$$u_{c_q}^f = (p_c^*, q_c^*, v_{dc}^*) \in \mathbb{R}^3. \quad (2.49g)$$

Moreover, the SGs in (2.49b)-(2.49c) are described $\forall r \in \mathcal{S}$ by

$$x_{g_r} = \left(\theta_s, \omega_s, \psi_f^d, \psi_{D_1}, \psi_{Q_1}, \psi_{D_2}, i_s, v_1, v_2, v_3, v_s, p_g, p_m \right) \in \mathbb{R}^{14}, \quad (2.49h)$$

$$u_{g_r} = (p_g^*, v_g^*) \in \mathbb{R}^2, \quad (2.49i)$$

and the state vector of network dynamics is expressed in the form

$$x_n = \left(v_{n_1}, \dots, v_{n_{|\mathcal{N}|}}, i_{l_1}, \dots, i_{l_{|\mathcal{N}|}}, i_{b_1}, \dots, i_{b_{|\mathcal{B}|}} \right) \in \mathbb{R}^{4|\mathcal{N}|+2|\mathcal{B}|}. \quad (2.49j)$$

The final model order is therefore $N = 14|\mathcal{C}_F| + 16|\mathcal{C}_f| + 14|\mathcal{S}| + 4|\mathcal{N}| + 2|\mathcal{B}|$, whereas the control input vector comprises $M = 5|\mathcal{C}_F| + 3|\mathcal{C}_f| + 2|\mathcal{S}|$ setpoints. Note that for a VSM-based converter the state \tilde{p}_c in (2.49d)-(2.49e) is replaced by ω_c (see Section 2.4).

The nonlinear ODE model (2.49) can also be represented in a linear form

$$\Delta \dot{x} = A \Delta x + B \Delta u \quad (2.50)$$

by linearizing (2.49a) around the steady-state point (x_0, u_0) , with $A \in \mathbb{R}^{N \times N}$ and $B \in \mathbb{R}^{N \times M}$ being the state-space matrices, and Δ denoting small deviations around the equilibrium (x_0, u_0) . Nevertheless, while providing accurate dynamical representation of the system, such linear model also leads to a minor steady-state error compared to its nonlinear counterpart. The mismatch can be seen in Fig. 2.20, showcasing a time-domain response of a two-generator system after a step increase in load demand. The steady-state error arises due to the linearization of the alignment, i.e., the approximation

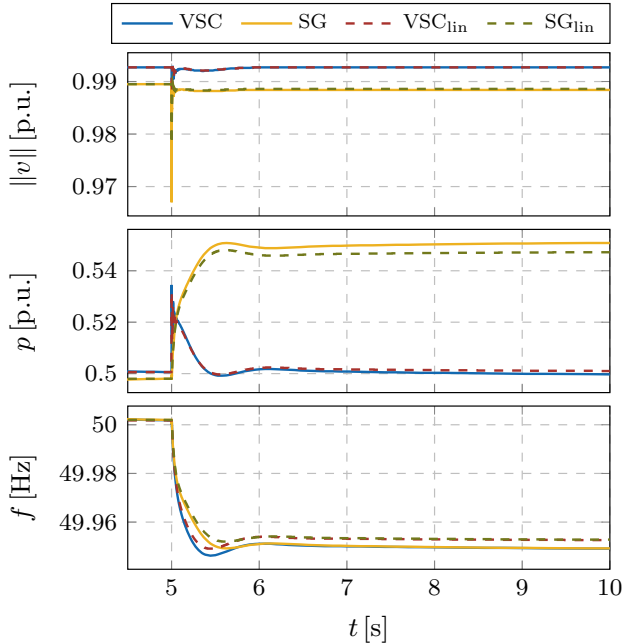


FIGURE 2.20: Time-domain performance of nonlinear and linear model representation of a two-generator system after a load step change.

of trigonometric terms within the rotation matrix $\mathcal{R}(\cdot)$ in (2.46). This also explains why power, and hence the frequency, experience the highest mismatch, as they cumulatively absorb the errors pertaining to alignment of each individual voltage and current vector. Note that for a global SRF rotating at constant angular velocity ω^* , the formulation (2.50) is not feasible, i.e., the obtained linear model is unstable. This is again justified by the linearization of (2.46), which cannot accurately capture the alignment. It should be pointed out that both the nonlinear model in (2.49) as well as its linear counterpart in (2.50) will be used throughout this thesis for analysis, control design and validation of various optimization methods.

2.10 CONCLUSION

This chapter presents the methodology for detailed modeling of low- and no-inertia power systems. A mathematical representation of the averaged power converter device is introduced, together with the state-of-the-art converter

control schemes. Moreover, the most promising grid-forming control strategies are described and subsumed under a general model describing the controller's internal dynamics, hence resolving the ambiguities pertaining to traditional classification of converter operation modes. The compatibility of novel grid-forming control strategies in systems with 100% converter-interfaced generation is investigated and the mathematical equivalence between the methods is discussed. In addition, the overcurrent limitation schemes are also taken into consideration in order to fully capture the flexibility and fast actuation capabilities of grid-forming power converters. Simulation results indicate a similar AC-side converter response under all control strategies, therefore validating the mathematical equivalence between the methods. Nevertheless, the indirect machine matching shows notable distinctions on the DC side as it explicitly considers the DC voltage in the control of the converter's AC side.

Furthermore, we derive a high-fidelity formulation of a generic low-inertia system comprising different types of synchronous and converter-interfaced generation. For that purpose, a 14th-order SG model comprising internal machine dynamics as well as voltage and frequency regulation has been presented. Moreover, a uniform converter model subsuming both grid-forming and grid-following mode of operation within a single control scheme is proposed, with a 14th-order model describing a grid-forming converter and a 16th-order model corresponding to a grid-following VSC unit. Transmission line dynamics are also included in the model, with the dynamics of the whole system aligned to the SRF rotating at the angular velocity of an arbitrary SG or a grid-forming VSC. Such modeling approach is necessary in order to obtain a feasible state-space representation of the system. Finally, the accuracy of the proposed ODE model is validated through time-domain simulations.

REDUCED-ORDER MODELING OF INVERTER-BASED GENERATION

This chapter contributes to the field of inverter modelling for large-scale simulations by introducing a new Model-Order Reduction (MOR) method based on singular perturbation. Motivated by the timescale separation between the fast and slow dynamics in an inverter-based power system, the proposed nonlinear MOR concept extends on the existing zero- and first-order reduction methods by combining the low computational burden of the former approach with the higher accuracy of the latter one. As a result, such hybrid MOR technique preserves the slow system dynamics of the full-order model, while simultaneously capturing the impact of the removed fast states on slow variables. Moreover, we introduce several improvements to the existing first-order MOR in order to make it tractable and more efficient when applied to a realistic full-order inverter model. The novel hybrid approach is applied to both grid-forming and grid-following inverter control schemes and compared against existing reduction methods from the literature. The results showcase a better time-domain performance of the hybrid method during transients, while having only a negligible increase in computational requirements compared to the traditional zero-order approach. This chapter is based on [99].

3.1 INTRODUCTION

With increasing shares of inverter-interfaced renewable energy resources such as photovoltaics and variable-speed wind turbines, the dynamic power system simulations are facing new challenges [6]. One of these challenges consists of finding the appropriate amount of detail for individual inverter models depending on the application. For microgrid applications there exists a commonly used inverter model that captures both the outer and inner cascaded control loops and has been used in various studies in the literature [22–24, 46, 51, 67]. Applications include stability analyses [22, 51, 67], comparison of different active power control algorithms [22–24], as well as the evaluation of dynamic interactions between inverters and synchronous machines [46]. Nonetheless, the existing model is too complex for use in large-scale sim-

ulations due to the large number of dynamic variables, which motivates employing MOR methods to enhance scalability.

A commonly used MOR approach in power system modeling is singular perturbation, which is based on timescale separation of fast and slow dynamics and assumes that the fast states reach a quasi steady-state solution instantaneously [100]. Several MOR methods based on singular perturbation have been recently proposed to simplify inverter models [15, 44, 101–104]. The authors in [101] employ a direct truncation approach and compare it against reduction models based on particle swarm optimization. However, they focus on reducing a simplified sixth-order inverter model that initially does not encapsulate all of the underlying control dynamics. Similarly, the inverter models used in [102] and [103] for stability assessment of the reduced-order islanded microgrid are too simplistic, with the former study ignoring the effect of filter dynamics and the latter neglecting the fast inner loop controllers essential for stable converter operation. This is improved in [104], where a detailed 15th-order model is considered, both in the islanded and grid-connected mode, and subsequently reduced to an eighth-order model by neglecting the fast dynamics of states associated with the voltage and current measurements in the *RLC* filter as well as the filter state of the PLL. Interestingly enough, the dynamics of the traditionally “fast” inner control loops are preserved in the reduced model due to unconventional parametrization of the associated PI controllers which might not be justified in real-world applications. While the computational benefits and steady-state tracking of the proposed low-order model are validated on an IEEE-37 bus distribution test system, the fast transients are not captured. Moreover, all aforementioned studies deal with linearized inverter models limited to an operating region close to the equilibrium, which implies that the obtained reduced-order models might not have a satisfactory performance during large disturbances.

In contrast, [44] and [15] focus on large-scale, nonlinear dynamic models of low-inertia systems. The work in [44] applies singular perturbation and Kron reduction to the model of a 100% inverter-based islanded microgrid with the aim of reducing its model order in temporal and spatial aspects, respectively. In particular, Kron reduction is utilized to eliminate internal, non-inverter buses and isolate the mutual inverter interactions, whereas individual inverters are reduced to a fifth-order model by eliminating the dynamical equations for the voltage and current controllers through means of singular perturbation. MOR is taken a step further in this study by also proposing the third- and first-order models in the context of different applications such as design

and verification of secondary and tertiary-level controllers and long-term performance and reliability evaluation, respectively. However, the inverter model used in [44] excludes the filter capacitors and the case studies are solely confined to small-signal disturbances in the form of load resistance step changes (corresponding to active power mismatch), and are therefore not reflective of transient capabilities of the given inverter models. On the other hand, [15] proposes a reduced-order model of a low-inertia system comprising power converters, synchronous generators and their interactions with the power grid (i.e., network dynamics). Using arguments from singular perturbation theory, the authors obtain a tractable model for control design and subsequently use the insights gained to bridge the gap between grid-level objectives and device-level control by introducing an internal model and matching controller that exploits structural similarities between power converters and synchronous generators. In addition, they propose a nonlinear droop control that stabilizes the power system. Nevertheless, the employed converter control scheme does not include inner controllers and PLL dynamics, and it does not study the accuracy of the reduced model during large disturbances.

Guided by a standard practice in singular perturbation, all previous MOR strategies exploit *small parameters* to identify the fast and slow states. More precisely, the states “to be removed” are determined based on the time constants of their respective differential equations. Such approach is meaningful when capturing slow system dynamics, as it preserves stability properties of the original system within the reduced-order model [42, 105]. However, it discards the dynamics of the fast states and therefore some potentially important phenomena during transients, as indicated by the results in [104, 106]. Nevertheless, depending on the model application, some relevant fast dynamics might be of interest (e.g., internal PLL dynamics during active power transients) and should not be completely neglected. This idea is partially addressed in [106] where, instead of employing small parameters, singular perturbation is performed based on modal analysis and participation factors. Such approach investigates a timescale separation between different modes in the system and identifies the states to be removed by their contribution to the fast modes. The authors obtain several reduced-order inverter control designs in nonlinear form and demonstrate that even the models of very low order suffice when analyzing steady-state performance. However, the time-domain responses after a line opening reveal a significant loss in model accuracy when subjected to a large disturbance, independent of the model order.

Alternatively, the work in [16] takes into account transmission line dynamics when performing singular perturbation of an inverter-based microgrid, justified by the fact that the line and simplified inverter dynamics are on similar timescales. The study even suggests that the timescale separation is not large enough to apply the standard singular perturbation method. Therefore, a new approach called *first-order singular perturbation* is introduced and demonstrated on a small test system. As opposed to neglecting the dynamics of fast variables altogether, this method allows for a more accurate inclusion of possible effects that the fast states could have on slow modes. This is justified by the presence of several clusters of modes in the eigenvalue spectrum, indicating a strong timescale separation between different dynamics in the system. Nevertheless, the proposed approach relies on small parameters and uses an oversimplified, linear, fifth-order inverter model as an initial full-order benchmark. As a result, the authors propose a reduced third-order model that could be of interest for the purposes of small-signal analysis, but cannot track transients under large disturbances.

This study continues the previous line of research and extends it by proposing a novel *hybrid* method for singular perturbation-based MOR. Specifically, the presented method combines the classical approach used in [15, 44, 101–104, 106] (called *Zero-Order Singular Perturbation (ZOSP)* hereinafter) with the first-order approach of [16] in order to achieve a trade-off between the transient performance and model complexity. Furthermore, we introduce two additional improvements to [16]. First, we apply the *First-Order Singular Perturbation (FOSP)* method directly to the detailed nonlinear model instead of a simplified linear model, resulting in more accurate lower-order inverter representation; and second, we use modal analysis (i.e., participation factors) instead of small parameters to determine the order of the dynamic variables to be removed. However, unlike the approach in [106], where the linearization and modal analysis have been conducted only once on the level of the full-order model, we repeat modal analysis in an iterative fashion after the removal of each dynamic state. Hence, the proposed hybrid method enables separation of the nonlinear model at hand into three timescales, thereby increasing flexibility in the reduction process and achieving a better trade-off between complexity and performance. Moreover, such procedure also allows us to mitigate the MOR sensitivity to underlying model parameters. Unlike the previous studies, we evaluate the effectiveness of our model-reduction approach on both the grid-forming and grid-following converter control schemes, due to the differences in system dynamics in the presence of a PLL.

The rest of the chapter is structured as follows. In Section 3.2, the theoretical preliminaries of singular perturbation are introduced together with the analytical formulation of both the zero- and first-order approach in linear and nonlinear form, respectively. The mathematical concept of the proposed hybrid singular perturbation method is described in Section 3.3, including the modifications to the first-order method and the iterative participation factor analysis. Moreover, the timescale separation pertaining to the state-of-the-art converter control design is presented and discussed. Section 3.4 showcases different model orders obtained via the hybrid approach and compares them against the traditional zero-order-reduced models in terms of time-domain performance and small-signal stability. Finally, Section 3.5 draws the main conclusions and discusses the outlook of the study.

3.2 SINGULAR PERTURBATION PRINCIPLES

3.2.1 *Primer on Singular Perturbation Theory*

For better understanding of the employed MOR method, we first introduce basic theoretical preliminaries of singular perturbation adopted from [105]. Let us consider a standard singular perturbation model of a nonlinear, time-invariant system

$$\dot{x}_s = f(x_s, x_f, u), \quad x_s(t_0) = x_s^0, \quad (3.1a)$$

$$\epsilon \dot{x}_f = g(x_s, x_f, u), \quad x_f(t_0) = x_f^0, \quad (3.1b)$$

where $x_s \in \mathbb{R}^n$, $x_f \in \mathbb{R}^m$ and $u \in \mathbb{R}^r$ are the state vectors describing the “slow” and “fast” states and the control input vector, respectively, and $f(\cdot)$ and $g(\cdot)$ are assumed to be sufficiently many times continuously differentiable functions of their arguments. The small positive scalar $\epsilon \in \mathbb{R}_{>0}$ in (3.1b) multiplies the derivatives of the fast states - representing the small parameters - to be neglected. Let $(x_s^0, x_f^0) \in \mathbb{R}^{n+m}$ be the equilibrium state of the nonlinear singularly perturbed system (3.1) and $u^0 \in \mathbb{R}^r$ be a constant control input such that

$$f(x_s^0, x_f^0, u^0) = \mathbb{0}_n, \quad (3.2a)$$

$$g(x_s^0, x_f^0, u^0) = \mathbb{0}_m, \quad (3.2b)$$

and linearize the system around (x_s^0, x_f^0, u^0) , as follows:

$$\Delta \dot{x}_s = A_{ss} \Delta x_s + A_{sf} \Delta x_f + B_s \Delta u, \quad (3.3a)$$

$$\epsilon \Delta \dot{x}_f = A_{fs} \Delta x_s + A_{ff} \Delta x_f + B_f \Delta u. \quad (3.3b)$$

Here, $A_{ss} \in \mathbb{R}^{n \times n}$, $A_{sf} \in \mathbb{R}^{n \times m}$, $A_{fs} \in \mathbb{R}^{m \times n}$, $A_{ff} \in \mathbb{R}^{m \times m}$, $B_s \in \mathbb{R}^{n \times r}$, $B_f \in \mathbb{R}^{m \times r}$ is the respective state-space representation, and Δ denotes a small deviation

$$\Delta x_s = x_s - x_s^0, \quad \Delta x_f = x_f - x_f^0, \quad \Delta u = u - u^0 \quad (3.4)$$

about the equilibrium (x_s^0, x_f^0, u^0) .

In this chapter, we focus on the analysis of two-timescale properties of the model (3.3) and hence disregard the control input by assuming $\Delta u = \mathbb{0}_r$. Moreover, we introduce a set of coordinates in which the system appears in a distinct block-triangular form. In this so-called actuator form, the fast block, defined by the state vector $\eta \in \mathbb{R}^m$, “drives” the slow block with the original state vector x_s . The actuator form is therefore the result of the change of variables (see [105, Section 1.4]) given by

$$\eta = \Delta x_f + L(\epsilon)\Delta x_s, \quad (3.5)$$

i.e., the similarity transformation (assuming $I = \text{diag}(\mathbb{1}_n)$ and $\mathbb{0}$ representing zero matrices of appropriate dimensions)

$$\begin{bmatrix} \Delta \dot{x}_s \\ \dot{\eta} \end{bmatrix} = \begin{bmatrix} I & \mathbb{0} \\ L(\epsilon) & I \end{bmatrix} \begin{bmatrix} \Delta x_s \\ \Delta x_f \end{bmatrix}. \quad (3.6)$$

We can now transform (3.3) into

$$\begin{bmatrix} \Delta \dot{x}_s \\ \epsilon \dot{\eta} \end{bmatrix} = \begin{bmatrix} A_{ss} - A_{sf}L & A_{sf} \\ R(L, \epsilon) & A_{ff} + \epsilon LA_{sf} \end{bmatrix} \begin{bmatrix} \Delta x_s \\ \eta \end{bmatrix}, \quad (3.7)$$

which can be represented in an upper-triangular form

$$\begin{bmatrix} \Delta \dot{x}_s \\ \epsilon \dot{\eta} \end{bmatrix} = \begin{bmatrix} A_{ss} - A_{sf}L & A_{sf} \\ \mathbb{0} & A_{ff} + \epsilon LA_{sf} \end{bmatrix} \begin{bmatrix} \Delta x_s \\ \eta \end{bmatrix}, \quad (3.8)$$

provided that the matrix $L(\epsilon) \in \mathbb{R}^{m \times n}$ satisfies the algebraic equation

$$R(L, \epsilon) = A_{fs} - A_{ff}L + \epsilon LA_{ss} - \epsilon LA_{sf}L = \mathbb{0}. \quad (3.9)$$

By obtaining the actuator form in (3.8), we have partially decoupled (3.7) to provide a separate fast subsystem

$$\epsilon \dot{\eta} = (A_{ff} + \epsilon LA_{sf})\eta. \quad (3.10)$$

Note that the feedback loop of the fast subsystem is a high-gain loop, i.e., its gain tends to infinity as $\epsilon \rightarrow 0$. This is a characteristic of the fast part of every singularly perturbed system in the standard form (i.e., when A_{ff} is nonsingular), and would not hold if A_{ff} was singular [105]. Lemma 3.2.1 establishes that $L(\epsilon)$ satisfying (3.9) exists.

Lemma 3.2.1. *If A_{ff} is nonsingular, there is a $\epsilon^* > 0$ such that for all $\epsilon \in [0, \epsilon^*]$, there exists a solution $L(\epsilon)$ to (3.9) which is approximated according to*

$$L(\epsilon) = A_{ff}^{-1}A_{fs} + \epsilon A_{ff}^{-2}A_{fs}A_0 + \mathcal{O}(\epsilon^2), \quad (3.11)$$

where

$$A_0 = A_{ss} - A_{sf}A_{ff}^{-1}A_{fs}. \quad (3.12)$$

Proof. The proof is given in [105, Section 2 (Lemma 2.1)]. □□□

The “big \mathcal{O} ” notation $\mathcal{O}(\epsilon)$ in (3.11) represents the order of magnitude relation valid for sufficiently small ϵ . Furthermore Lemma 3.2.2 provides an upper bound on the value of ϵ^* for which the approximation (3.11) holds.

Lemma 3.2.2. *Under the conditions of Lemma 3.2.1, the approximation (3.11) is valid for all ϵ in the interval $0 \leq \epsilon < \epsilon_1$, where*

$$\epsilon_1 = \frac{1}{\|A_{ff}^{-1}\|(\|A_0\| + \|A_{sf}\|\|A_{ff}^{-1}A_{fs}\| + 2(\|A_0\|\|A_{sf}\|\|A_{ff}^{-1}A_{fs}\|^{1/2})}. \quad (3.13)$$

Proof. The proof is given in [105, Section 2 (Lemma 2.2)]. □□□

Separating the system (3.3) into two lower-order subsystems of different timescales allows us to infer the stability of the original system.

Corollary 3.2.3. *If A_{ff} exists, and if A_0 and A_{ff} are Hurwitz matrices, then there exists $\epsilon^* > 0$ such that for all $\epsilon \in (0, \epsilon^*]$ the system (3.3) is asymptotically stable.*

The fact that the stability of the actual system (3.3) can be inferred from the analysis of lower-order systems in separate timescales is of great practical significance for control analysis and design. In particular, assuming asymptotic stability conditions given by Corollary 3.2.3 have been met, we can approximate the $\epsilon\Delta\dot{x}_f$ term in (3.3b) through means of Taylor representation and reduce the order of the system. The remainder of this section discusses two such approximations.

3.2.2 Zero-Order Singular Perturbation

The idea of ZOSP is to completely disregard the fast state dynamics, justified by the fact that they are occurring on a much shorter timescale compared to the slow dynamics. In other words, the changes in the fast variables can be seen as instantaneous from the perspective of slow variables. The two-timescale linear system (3.3) can thus be rewritten as

$$\Delta \dot{x}_s = A_{ss} \Delta x_s + A_{sf} \Delta x_f + B_s \Delta u, \quad (3.14a)$$

$$\mathbb{0}_m \approx Y \Delta \dot{x}_f = A_{fs} \Delta x_s + A_{ff} \Delta x_f + B_f \Delta u, \quad (3.14b)$$

with $Y = \text{diag}(\epsilon_1, \dots, \epsilon_m)$ denoting a diagonal matrix comprised of small parameters. Note that unlike the formulation in (3.3b), where first derivatives of the fast states were multiplied by a common scalar ϵ , in (3.14b) each state variable has its own scaling factor reflecting the characteristic time constant of the respective differential equation.

As stated previously, the zero-order model reduction is performed by assuming that the fast states reach steady state immediately, thus neglecting their dynamics. As a result, corresponding differential equations (3.14b) are transformed into algebraic ones. In order to bring the system to its final (reduced) ODE form, the algebraic expressions are solved for their respective variables

$$\Delta x_f = -A_{ff}^{-1} A_{fs} \Delta x_s - A_{ff}^{-1} B_f \Delta u, \quad (3.15)$$

and subsequently substituted into (3.14a), which yields

$$\Delta \dot{x}_s = \left(A_{ss} - A_{sf} A_{ff}^{-1} A_{fs} \right) \Delta x_s + \left(B_s - A_{sf} A_{ff}^{-1} B_f \right) \Delta u. \quad (3.16)$$

In comparison to the initial system (3.14), the formulation in (3.16) reveals that the formerly fast states are no longer present in the reduced-order model. Nevertheless, the relations between fast and slow states act as algebraic constraints for the remaining differential states and are represented by submatrices A_{sf} , A_{ff} and A_{fs} of the initial state space. Moreover, the state matrix of the reduced-order model is $(A_{ss} - A_{sf} A_{ff}^{-1} A_{fs})$ and corresponds to A_0 in (3.12). Understandably, A_{ff} is considered to be nonsingular.

The same ZOSP approach can also be applied directly to nonlinear systems. Similar to the linear case, the two-timescale, nonlinear ODE system (3.1) can be approximated by

$$\dot{x}_s = f(x_s, x_f, u), \quad (3.17a)$$

$$\mathbb{0}_m \approx Y \dot{x}_f = g(x_s, x_f, u), \quad (3.17b)$$

by assuming a quasi steady-state of the fast states. Therefore, original ODEs are converted into a set of DAEs, with algebraic equations given by the right-hand side of (3.17b). Depending on the complexity of the newly formed algebraic equations, it might or might not be possible to solve (3.17b) for the fast states and substitute the acquired expressions into (3.17a) in order to obtain a reduced-order ODE set. Note that a pure ODE system would be favorable for most numerical solvers, since the presence of algebraic constraints introduces additional iterations and may significantly increase computational time.

3.2.3 First-Order Singular Perturbation

We demonstrate the principles of FOSP on a linear system (3.3) by following the derivation provided in [16]. Unlike in the traditional zero-order approach, where fast dynamics are completely neglected by converting the corresponding differential equations into algebraic ones, the first-order method removes the fast states by stating that the first derivative of Δx_f is non-zero, whereas its second derivative is negligible. This property is especially useful in systems with several distinctive timescales and has a potential of better capturing the impact of fast states on slow system dynamics. Mathematically speaking, this corresponds to a Taylor series expansion of the vector of the fast states and hence the name first-order reduction.

Let us again start from a general two-timescale representation

$$\Delta \dot{x}_s = A_{ss} \Delta x_s + A_{sf} \Delta x_f + B_s \Delta u, \quad (3.18a)$$

$$Y \Delta \dot{x}_f = A_{fs} \Delta x_s + A_{ff} \Delta x_f + B_f \Delta u, \quad (3.18b)$$

where, in contrast to (3.14), $Y \Delta \dot{x}_f \neq 0_m$. Taking the derivative of (3.18b) with respect to time and equating it to zero yields

$$0_m \approx Y \Delta \ddot{x}_f = A_{fs} \Delta \dot{x}_s + A_{ff} \Delta \dot{x}_f + B_f \Delta \dot{u}. \quad (3.19)$$

Assuming time-invariant control inputs ($\Delta \dot{u} = 0_r$) and solving (3.19) for $\Delta \dot{x}_f$ results in

$$\Delta \dot{x}_f = -A_{ff}^{-1} A_{fs} \Delta \dot{x}_s. \quad (3.20)$$

Substituting the intermediate result (3.20) into (3.18b) gives the following expression for Δx_f :

$$\Delta x_f = -A_{ff}^{-1} Y A_{ff}^{-1} A_{fs} \Delta \dot{x}_s - A_{ff}^{-1} A_{fs} \Delta x_s - A_{ff}^{-1} B_f \Delta u. \quad (3.21)$$

Finally, by substituting (3.21) into (3.18a) and separating the terms for Δx and $\Delta \dot{x}$, a linear first-order ODE form is obtained:

$$\dot{x}_s = A_0 \Delta x_s + B_0 \Delta u, \quad (3.22a)$$

with the reduced-order state space (A_0, B_0) defined by

$$A_0 := \left(I + A_{sf} A_{ff}^{-1} \Upsilon A_{ff}^{-1} A_{fs} \right)^{-1} \left(A_{ss} - A_{sf} A_{ff}^{-1} A_{fs} \right), \quad (3.22b)$$

$$B_0 := \left(I + A_{sf} A_{ff}^{-1} \Upsilon A_{ff}^{-1} A_{fs} \right)^{-1} \left(B_s - A_{sf} A_{ff}^{-1} B_f \right). \quad (3.22c)$$

A comparison between (3.22) and the corresponding ZOSP formulation in (3.16) reveals an addition of a new term $(I + A_{sf} A_{ff}^{-1} \Upsilon A_{ff}^{-1} A_{fs})^{-1}$ to matrices A_0 and B_0 . On one hand, it results in a more accurate reduced-order model, but on the other hand leads to a model representation of higher complexity which might increase computational time. Note that the reduced model is only attainable and valid if the aforementioned inverse exists.

3.3 HYBRID REDUCTION METHOD

3.3.1 *Modification to the First-Order Approach*

The work in [16] confined the FOSP application solely to linear systems, since obtaining an appropriate reduced-order ODE form of a nonlinear system is not straightforward. We address this problem by proposing an alternative implementation of the FOSP method, which follows the similar principles as its linear counterpart in Section 3.2.3. In particular, given the nonlinear system (3.17), the second derivative of fast states is considered negligible (corresponding to $\ddot{x}_f = \mathbb{0}_m$) by taking the first derivative of (3.17b) and equating its left-hand side to zero:

$$\mathbb{0}_m = \frac{\partial g(x_s, x_f, u)}{\partial x_s} \dot{x}_s + \frac{\partial g(x_s, x_f, u)}{\partial x_f} \dot{x}_f. \quad (3.23)$$

Instead of replicating the approach from [16] and attempting to solve (3.23) for \dot{x}_f directly¹, we observe that the differential terms \dot{x}_s and \dot{x}_f are already given by (3.17a) and (3.17b) respectively, and can thus be substituted. This results in the following DAE form:

$$\dot{x}_s = f(x_s, x_f, u), \quad (3.24a)$$

¹ Note that such procedure might not be computationally feasible, depending on the system.

$$\mathbb{0}_m = \frac{\partial g(x_s, x_f, u)}{\partial x_s} f(x_s, x_f, u) + \frac{\partial g(x_s, x_f, u)}{\partial x_f} g(x_s, x_f, u), \quad (3.24b)$$

where now x_s denotes the vector of state variables and x_f stands for the vector of algebraic variables.

As previously stated in Section 3.2, functions $f(\cdot)$ and $g(\cdot)$ are assumed to be sufficiently many times continuously differentiable with respect to their arguments. Therefore, the computation of the first derivatives in (3.24b) is feasible. While potentially convoluted, the final mathematical expressions in (3.24b) are strictly algebraic and the DAE system (3.24) can be handled by an off-the-shelf solver. This however is not the case when dealing with (3.23).

3.3.2 Hybrid Singular Perturbation

The main idea of the proposed hybrid method is to combine ZOSP and FOSP in systems with more than two distinctive timescales and potentially better capture the dynamical performance during transients. Specifically, we consider a three-timescale, nonlinear ODE system of the form

$$\dot{x}_s = f(x, u), \quad (3.25a)$$

$$\dot{x}_f = g(x, u), \quad (3.25b)$$

$$\dot{x}_v = h(x, u), \quad (3.25c)$$

where $x := (x_s, x_f, x_v) \in \mathbb{R}^{n+m+p}$ represents the state vector comprised of slow states $x_s \in \mathbb{R}^n$, fast states $x_f \in \mathbb{R}^m$ and very fast states $x_v \in \mathbb{R}^p$, and $f(\cdot)$, $g(\cdot)$ and $h(\cdot)$ are the respective functions. Based on the discussion in Section 3.2, the dynamics of the slow states remain intact, the dynamics of the fast states are reduced using FOSP ($\ddot{x}_f = 0$), and the dynamics of the very fast states are reduced using ZOSP ($\dot{x}_v = 0$), which yields the following DAE system:

$$\dot{x}_s = f(x, y, u), \quad (3.26a)$$

$$\mathbb{0}_m = \frac{\partial g(x, y, u)}{\partial x_s} f(x, y, u) + \frac{\partial g(x, y, u)}{\partial x_f} g(x, y, u) + \frac{\partial g(x, y, u)}{\partial x_v} h(x, y, u), \quad (3.26b)$$

$$\mathbb{0}_p = h(x, y, u). \quad (3.26c)$$

It can be seen that the hybrid method introduces two separate sets of algebraic constraints, namely (3.26b) and (3.26c), correlating the algebraic variables $y := (x_f, x_v)$ that comprise the original fast and very fast states to the

preserved slow differential states $x := x_s$ in (3.26a). Hence, the final model order is n , i.e., it is reduced by $m + p$ compared to the original system. Note that the values of n and m do not necessarily correspond to the values of the same parameters in Section 3.2.

By applying the hybrid approach one clearly assumes a three-timescale separation, i.e., the fact that the state dynamics can be split into slow, fast and very fast. For systems comprising two distinctive timescales, such classification is traditionally done based on the small parameters. However, a tri-level categorization is more complex and it might not be clear how to conduct it *a priori*. Moreover, the goal of this study is not only to preserve the slow variables but also to determine the most relevant dynamics to be preserved in order to capture the transient oscillations and overshoot. Therefore, the employed method is not based on small parameters but rather on performing an iterative Participation Factor Analysis (PFA), as explained in the next section.

3.3.3 Iterative Participation Factor Analysis

PFA is an established method for quantifying the influence of a state on a mode and vice versa [107]. The knowledge of timescales gained through eigenvalue analysis, in combination with the acquired information about the coupling of states and modes, allows for classification (i.e., separation) of state variables based on the respective timescales. For a linear, time invariant ODE system

$$\dot{x} = Ax + Bu, \quad (3.27)$$

the participation of state k (x_k) in mode i (λ_i) is defined as

$$P_{ki} = u_{ki}v_{ki}, \quad (3.28)$$

where u_{ki} is the i^{th} entry of the k^{th} left eigenvector and v_{ki} is the i^{th} entry of the k^{th} right eigenvector of the state-space matrix A . More details on theoretical preliminaries of the eigenvalue analysis and the computation of the underlying eigenvectors are provided in Section 11.3.2.

As stated in Section 3.1, the PFA has been used in the literature to distinguish the fast from the slow states [106]. Note that the full-order model is linearized only once at the beginning of the MOR process in [106]. As a result, the participation factors are computed only once and based on their values the order of the states to be removed is determined in a single step. In contrast, this work proposes an alternative, iterative approach to PFA that involves sequential computation of participation factors as the order of

the model is being reduced. More precisely, after removing each state, the newly obtained nonlinear model is linearized, PFA is performed, and the next fastest state to be removed is determined. This procedure is repeated until the desired model order is reached.

The benefit of iterative PFA is better tracking of changes in the model structure due to reduction, which can influence the systems modes in subsequent reduction steps. In other words, re-linearization of the nonlinear model at each reduction step allows for obtaining a more accurate linear model approximation. It should be noted though that, as the model order progressively decreases, it becomes more likely that the state matrix of a reduced model becomes singular (due to one or more eigenvalues being zero), which of course means that the iterative process has to be stopped and the lowest possible model order has been reached.

3.3.4 Timescale Separation

A traditional approach in singular perturbation is to employ small parameters as an indicator of timescale separation within a dynamical system, since these factors are reflective of the time constants of individual state variables. In order to obtain such parameters, the differential equations describing the system dynamics must be reformulated such that the observed quantity is isolated on the left-hand side of the equation in the first-order form $\epsilon_i \dot{x}_i = x_i + \dots$, with $\epsilon_i \in \mathbf{Y}$ representing the respective time constant of the dynamics pertaining to the state variable x_i . The values of small parameters for the grid-connected

State variables	Small-scale factors \mathbf{Y}	
	analytical expression	numerical value
ξ^d, ξ^q	K_P^v/K_I^v	0.0008
v_f^d, v_f^q	$\omega_b \frac{\ell_f (\ell_g + \ell_t)}{r_d (\ell_f + \ell_g + \ell_t)}$	0.0152
\tilde{p}_c, \tilde{q}_c	$1/\omega_z$	0.0318
i_g^d, i_g^q	$\omega_b (\ell_g + \ell_t)/(r_g + r_t)$	0.0637
i_f^d, i_f^q	$\omega_b \ell_f / r_f$	0.0849
γ^d, γ^q	K_P^i/K_I^i	0.089
$\varepsilon, \theta_s, \theta_c$	1	1

TABLE 3.1: Small-scale factors of the inverter model.

Eigenvalues	ω_k [Hz]	Main variables	Model order ^a
$-759.4 \pm j3684$	598.58	v_f^d, v_f^q	13
$-649.4 \pm j3603$	582.67	i_g^d, i_g^q	11
$-3530 \pm j348.2$	564.52	i_f^d, i_f^q	9
$-32.6 \pm j194$	31.31	ξ^d, ξ^q	7
-61.7	9.82	θ_s	6
-31.5	5.01	\tilde{q}_c	5
$-10.1 \pm j29.2$	4.92	\tilde{p}_c, θ_c	4, 3
-12.6	2.01	ε	2
-11.3^b	1.79	γ^d, γ^q	0

a After the removal of the corresponding state variables.

b A conjugate pair of eigenvalues with an imaginary part equal to zero.

TABLE 3.2: Modal analysis of the inverter model.

inverter² from Section 2.7 operating in a grid-following mode are given in Table 3.1, ordered respectively from the fastest to the slowest state variable. For mathematical validity, a small resistance $r_d = 0.02$ p.u. is added in series with the filter capacitor c_f . It should be noted that the grid-forming VSC experiences the same small parameters, with PLL states (θ_s, ε) being omitted from the model.

In contrast, through the PFA approach the modes of the system are sorted by their natural frequency (i.e., the distance from the origin in the complex plane), defined as $\omega_k = \sqrt{\Re(\lambda_k)^2 + \Im(\lambda_k)^2}$. Subsequently, the states with the highest participation in the fastest mode (or conjugate pair of modes) are reduced, as indicated in Table 3.2. Such method suggests that the electrical states of the *RLC* filter within the device model, i.e., (v_f^d, v_f^q) , (i_g^d, i_g^q) and (i_f^d, i_f^q) respectively, contribute the most to the fast modes and should be removed first in the given order. This is significantly different from the results in Table 3.1, where the integrator states of the SRF voltage control are prioritized over (v_f^d, v_f^q) and the dynamics of the outer control loop are faster than (i_g^d, i_g^q) and (i_f^d, i_f^q) . The observed discrepancies between the two approaches indicate that the fastest states are not necessarily in direct correlation with the fastest modes, and removing them would not fully eliminate the less relevant modes. Similarly, the impact of fast variables on slower system dynamics might not be negligible, which is directly addressed through application of the FOSP methodology in the proposed hybrid approach.

² We do not consider DC-side dynamics in this case study, i.e., controller (2.10) is omitted.

The modal decomposition given in Table 3.2 shows that there are three modes of the system whose natural frequency is two orders of magnitude greater than the frequency of the slowest modes. Therefore, these modes can be considered very fast and the state variables with the highest participation should be removed using ZOSP. The dominant states contributing to the aforementioned modes are (v_f^d, v_f^q) , (i_g^d, i_g^q) and (i_f^d, i_f^q) . The remaining modes are separated at most by one order of magnitude and therefore are candidates for either ZOSP or FOSP. The time-domain performance for various combinations of ZOSP/FOSP reduction methods applied to the remaining state variables will be examined in Section 3.4.1.

3.4 RESULTS

3.4.1 Time-Domain Performance during Transients

In order to capture and compare the dynamic behavior and performance of different model orders and reduction methods during transients, we consider the test case illustrated in Fig. 3.1. It comprises a single inverter connected to a stiff grid (infinite bus) via two parallel transmission lines, developed in MATLAB Simulink according to the design presented in Chapter 2. In particular, this test case represents the disconnection of one of two parallel lines, effectively modeled through the opening of switches K_1 and K_2 . The time-domain responses of different model orders for both grid-forming and grid-following operation mode are presented in Fig. 3.2, with full and dashed lines denoting the corresponding reductions using the zero-order and hybrid approach, respectively. The more oscillatory behavior of the grid-following unit is a consequence of the PLL. Additionally, in order to quantitatively

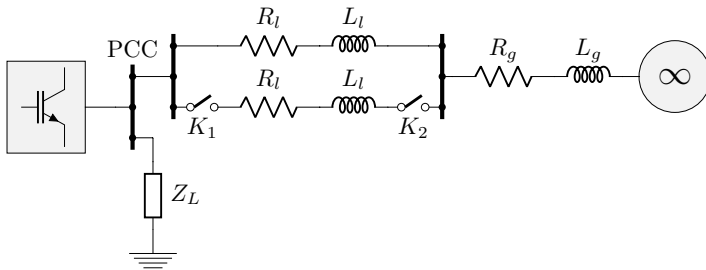


FIGURE 3.1: Test case system comprising a single-line diagram of a converter connected to an infinite bus via two parallel transmission lines.

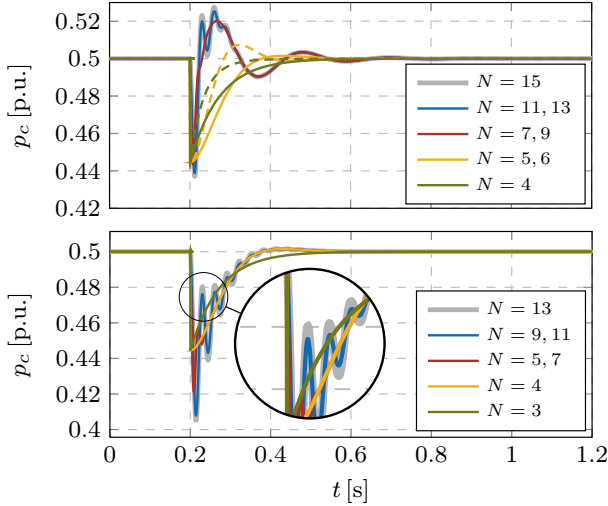


FIGURE 3.2: Time-domain response of different model orders after line opening: grid-following control mode (top) and grid-forming control mode (bottom). Dashed lines denote the corresponding reduction using the hybrid approach.

benchmark the performance of each model, their run time and Root Mean Square Error (RMSE) in terms of active power and voltage magnitude mismatch are computed and compared. For the purpose of generating a statistically relevant sample, the run time is computed as mean computational time over 100 iterations. On the other hand, the RMSE calculation is achieved by re-running the simulations for all model orders with a fixed-step solver and comparing the mismatch between signals at each discrete time step. Moreover, the RMSE metric is applied only to the period during transients, i.e., between the fault instance and the point at which the system reaches steady state, with the results depicted in Fig. 3.3.

It is immediately noticeable from Fig. 3.2 that dropping the very fast electrical states does not have much impact on the overall response. Indeed, after removing v_f and i_g the performance is unchanged for both operation modes, whereas only the very fast oscillations are not mapped by removing i_f . These findings therefore justify the use of zero-order reduction for the removal of very fast variables. Interestingly enough, dropping the integrator states (ξ^d, ξ^q) as next in line in Table 3.2 has no effect on the overall performance. While the corresponding mode is rather classified as fast than very fast, this

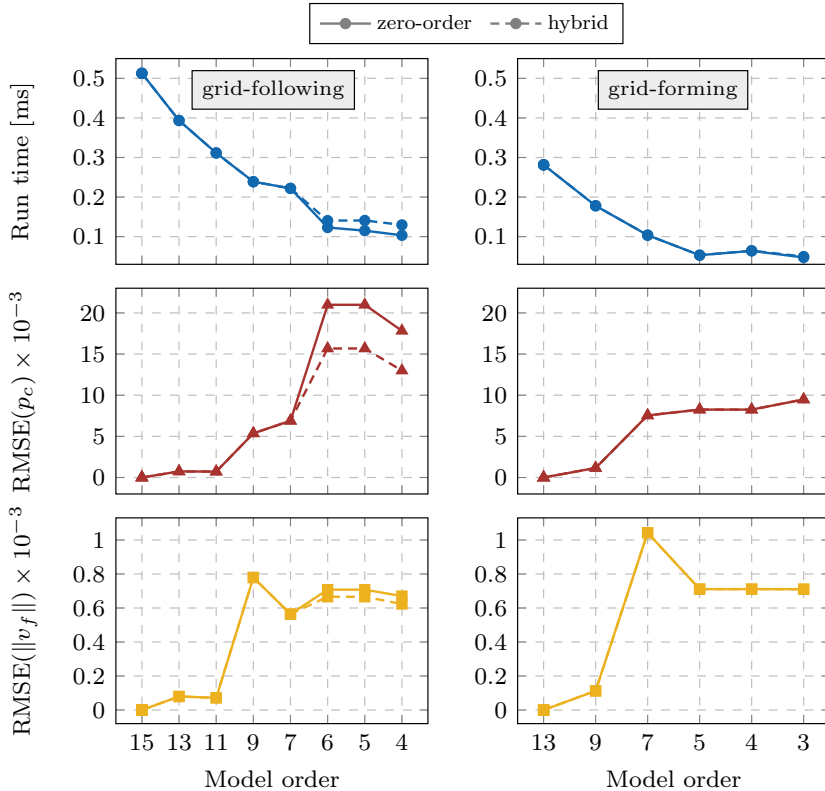


FIGURE 3.3: Run time and RMSE for different model orders of grid-following (left) and grid-forming (right) inverter using zero-order and hybrid approach.

effect might be explained by the fact that the time constant of the underlying state dynamics is very small (see Table 3.1). Moreover, as mathematical expressions for inner control loops are convoluted and nested, the elimination of state variables (ξ^d, ξ^q) was not possible using FOSP and resulted in numerical issues. This is an important aspect and a potential drawback of a FOSP application to nonlinear systems, which has not been reported previously in [16]. Hence, the first 8 states are all removed using ZOSP, irrelevant of the inverter operation mode.

Going for lower-order models, we now tackle the relatively fast states, i.e., variables that could potentially be removed both using zero- and first-order reduction, with the use of the latter method resulting in the proposed hybrid

MOR approach. For the grid-forming mode of operation there is a negligible difference in both the time-domain response and the computational time when removing the remaining states with either ZOSP or FOSP. This can be seen both qualitatively in Fig. 3.2 and quantitatively in Fig. 3.3. In both cases the fourth- and third-order models were derived by removing \tilde{q}_c and \tilde{p}_c , respectively, with the hybrid model using FOSP method. In general, applying either ZOSP or FOSP to the remaining two states does not pose a major factor, as all models experience a rather similar trajectory response, with the higher-order models showing initially larger deviation and oscillatory behavior. Thus, FOSP appears to offer no measurable improvement in this case; a somewhat understandable outcome considering that the zero-order approach already achieves a very accurate approximation of the full-order model, as previously observed in [106].

While there is a negligible difference in the transient performance of a grid-forming inverter between the zero-order and hybrid approach, there is a significant improvement in the run time when reducing to fifth-order model and below. Despite an inevitable increase in RMSE, the significant reduction in run time makes these reduced order models appealing from the perspective of large-scale system simulations. Indeed, similar model orders have also been proposed in [44, 101–104, 106] using ZOSP.

For the case of grid-following operation, however, the reduced-order models below $N = 7$ presented in Fig. 3.2 show distinctly different behavior immediately following the disturbance. Any further reduction using ZOSP results in a lagged response and is incapable of reproducing the overshoot response of the full-order model. Although a seventh-order model may be sufficient for microgrid or small-scale analysis, it may be necessary to further reduce the model order for large-scale EMT simulations, particularly given the order of SG models and the relative capacity of converters and synchronous machines. For further reduction we consider two cases: the first, where we continue to reduce all states using ZOSP; and the second, where we adapt a hybrid approach by first removing θ_s using FOSP and all subsequent states using ZOSP. In both cases, the order of reduction is shown in Table 3.2. Namely, we see that the hybrid model, indicated by a dashed line, outperforms its corresponding ZOSP model as illustrated in Fig. 3.2. The hybrid model is better at reproducing the fast response of the full-order model, with both the hybrid sixth- and fifth-order models capturing the overshoot to a certain extent as well as the initial oscillatory behavior.

For the case of grid-following operation, there is a noticeable RMSE difference between the zero-order and the hybrid method, with ZOSP having

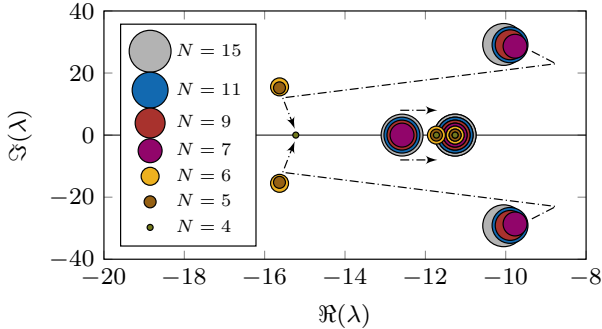


FIGURE 3.4: Root loci spectrum of interest for different model orders using zero-order reduction of a grid-following inverter.

$\approx 33\%$ higher RMSE in terms of active power response for the sixth-order and below (see Fig. 3.3). On the other hand, the run time is rather similar, especially for $N = 6$; a small difference is justified by the more complex nature of the first-order algebraic constraints in FOSP. Similarly to the grid-forming mode, a significant and steady reduction in the computational run time is observed when going for lower-order models, with sixth-order and lower being almost 50% faster than the model orders $N = 7$ and $N = 9$. This is again particularly advantageous when considering large system-scale simulations, where both computational time and memory allocation become a concern as the number of individual models scales up.

3.4.2 Eigenvalue Analysis and Stability Properties

Some interesting observations can be made by studying the most critical modes of the root loci spectrum for different model orders of the zero-order approach, depicted in Fig. 3.4. Understandably, removing states associated with very fast dynamics has no impact on the slow modes, reflected in the preserved eigenvalue spectrum close to the imaginary axes for $N \geq 7$. Nevertheless, dropping the dynamics of the outer control loop (i.e., \tilde{q}_c and \tilde{p}_c respectively) and PLL (i.e., θ_s) has a massive impact on the slow modes. In particular, the most critical pair of eigenvalues is significantly shifted to the left, whereas other slow modes now become more critical. This “movement” is indicated by the dashed lines in Fig. 3.4. Such massive changes in the root loci spectrum might also justify the changes in the transient performance

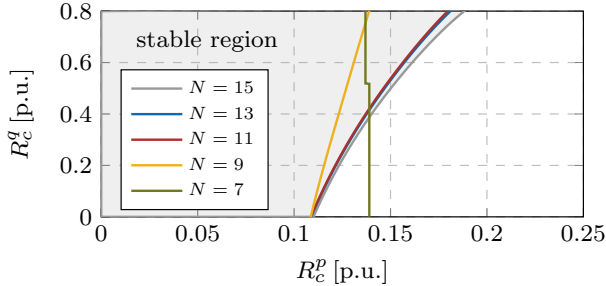


FIGURE 3.5: Stability maps corresponding to different model orders of grid-following inverter in Fig. 3.4; the system is stable within the shaded region.

and drastic increase in RMSE (see Fig. 3.3) when going for $N < 7$, especially in the case of a grid-following inverter due to the presence of a PLL.

These conclusions are substantiated by the stability maps provided in Fig. 3.5, defining a stable region in the $R_c^p - R_c^q$ plane. Different lines³ indicate a change in the boundary of the stable region for the corresponding model order. It should be noted that for lower orders ($N \leq 6$), the whole region of interest is stable and the lines are therefore not graphically illustrated. These results are in direct correlation with Fig. 3.4. More precisely, the mismatch between the slow modes of the full- and reduced-order models is mapped to the accuracy of the approximation of the stable region boundary, with a massive shift in the critical modes for $N = 6$ reflected by a very large stable region. Such change is not surprising, considering that the removed states affect the dynamics of active and reactive power control, and the stability region of interest is analyzed in the $R_c^p - R_c^q$ plane. It however highlights that both ZOSP and FOSP might not be applicable to stability studies when reaching lower-order inverter models (especially with the use of PFA), which was not reported in [16] as this study dealt with a very low full-order model. Furthermore, the discrepancies in the approximation of the stability region suggest that different modeling approaches and model orders should be employed when dealing with small-signal analysis compared to the simulations of large-signal disturbances (e.g., line openings and short circuits). In particular, while PFA seems promising in terms of defining the most relevant states for preserving the dynamical response of the original

³ Note that the colors of individual model orders in Fig. 3.5 do not correspond to the same colors in Fig. 3.2 and Fig. 3.4.

model, it does not respect the timescales of the system and could potentially diminish the assumptions necessary for singular perturbation theory and the underlying stability guarantees. On the other hand, the traditionally used small parameters fail to capture the fast transients of the full-order model. Therefore, alternative metrics such as controllability and observability of the modes and their respective residues (see Section 11.2) could be employed in determining the optimal reduced model order.

3.5 CONCLUSION

This chapter presents a hybrid model-order reduction method, which takes advantage of different timescales in a dynamical model and can be applied to nonlinear systems. In particular, it combines the low computational burden of the traditional zero-order singular perturbation with the higher accuracy of the first-order approach. In order to determine the order of the state removal, the conventional method based on small parameters is replaced by an iterative participation factor analysis. The novel hybrid approach is applied to both grid-forming and grid-following inverter control schemes, and compared against the traditional zero-order reduction. While the improvement in the performance of the lower-order models of the grid-forming inverter is insignificant, the results for the grid-following operation mode showcase a better time-domain performance during transients, while having only a negligible increase in computational requirements.

Future work will focus on the performance of the hybrid reduction method in a large-scale network with a high penetration of inverter-interfaced generation. In such power systems, the slower dynamics of conventional generation as well as the very fast dynamics of transmission lines are expected to have a significant influence on the acceptable model order. The mix of different system dynamics can be effectively tackled by the proposed reduction technique and presents an interesting path for future studies.

UNDERSTANDING STABILITY OF LOW-INERTIA SYSTEMS

This chapter presents novel insights into stability properties of power systems with large-scale integration of renewable generation. The focus is set on a high-fidelity representation of a generic low-inertia system comprising full-order control schemes of both synchronous and converter-based generators, with the latter differentiating between grid-forming and grid-following mode of operation. Furthermore, the dynamics of transmission lines and loads are captured in the model formulation. Using modal analysis techniques such as participation factors and parameter sensitivity, the most vulnerable segments of the system are determined and the adverse effects of timescale coupling and control interference are investigated. More precisely, this work characterizes the maximum permissible penetration levels of inverter-based generation as well as the nature of the associated unstable modes and the underlying dynamics. Finally, potential directions for improving the system stability margin under different generation portfolios are proposed. The content of this chapter is based on [12].

4.1 INTRODUCTION

Due to convergence of economic and policy drivers, large-scale electric power grids are hosting rapidly increasing amounts of wind and solar generation as well as battery storage. These sources often interface with the grid via power electronic devices, whose interactions with the grid are substantially different from synchronous machines and pose many challenges to power system modeling, analysis and control [6]. Moreover, a high penetration of fast-acting VSCs may create unexpected couplings and existing control approaches based on timescale separation may become less valid, thus adversely affecting frequency and voltage stability. With the aim of providing solutions to the underlying problems, detailed and accurate models of low-inertia systems, usually in the form of DAEs, are needed for the purpose of small-signal analysis.

The field of small-signal analysis is well established for conventional power systems [26, 27, 108]. With the increasing integration of renewables, a number of publications addressing modeling and stability of 100% inverter-based microgrids has emerged, varying from the analysis of individual converter operation modes in a single-machine infinite-bus equivalent [22–24, 51, 69, 109] to operation of small and real-size distribution grids [39, 67, 70, 98, 103, 110–115]. The former studies mostly emphasize the validation of the proposed small-signal models and provide insights into the stability characteristics and modes of individual inverter control schemes by analyzing their sensitivities with respect to system parameters. In particular, [51] and [109] investigate stability properties of grid-supporting inverters operating as virtual synchronous machines with dynamic and quasi-stationary machine models, [69] compares dynamic characteristics of droop-based grid-feeding and grid-supporting VSCs in terms of power control tuning and operating point, whereas [22–24] extend these analyses to different types of grid-forming and grid-following converter control schemes. While providing valuable insights into the operation of individual converter-interfaced generation units, all aforementioned studies consider single-generator models and a stiff grid equivalent, which oversimplifies the problem.

The interconnected multi-inverter configurations have also been thoroughly investigated in the literature. Studies in [103, 110, 111] propose various state-space models for small systems consisted of two or three inverters connected through constant impedance lines, followed by stability analyses such as droop gain parameter sweeps and the impact of R/X ratio of the interconnecting cables. However, the authors use simplified inverter models comprising only droop control and LCL filter dynamics, thus neglecting inner control loops and line dynamics in the process. Moreover, they only consider grid-forming operation and do not take into account a potentially adverse impact of PLLs on system stability. Alternatively, [70] focuses on interactions between a virtual synchronous generator and a converter-interfaced load by considering small-signal stability under different operating conditions. While the authors include a dynamic model of the load and the interconnecting line, they analyze stability solely via parameter sweeps of the virtual inertia constant and load impedance, which does not provide enough insight into the nature of potential instabilities. A more general and rigorous approach towards synchronization and stability analysis of droop-based microgrids is taken in [39, 112, 113], where the appropriate conditions for synchronization, power sharing and voltage stability of droop-controlled inverters in islanded microgrids have been derived. Nevertheless, the aforementioned simplifications in terms of model

complexity, network and load dynamics, and converter operation modes are still present.

In contrast, the studies in [67, 98, 114, 115] focus on detailed system models which include both low and high inverter frequency dynamics as well as the network and load dynamics, and propose accurate small-signal representation of real-size microgrids. The work in [67] provides analysis in terms of system eigenvalues and their sensitivity to different states. It was observed that the dominant low-frequency modes are highly sensitive to network configuration and the parameters of the power sharing controller, whereas the high frequency modes are largely sensitive to the inverter inner loop controllers, network dynamics, and load dynamics. However, only grid-forming mode of operation has been taken into consideration. Alternatively, the authors in [98] present a new methodology for forming, augmenting, and modifying the state-space matrices of large microgrids comprising both grid-forming and grid-following inverter control schemes, and investigate a 100% inverter-based 69-bus distribution system. The emphasis is however on model validation, state matrix partitioning and optimal control tuning for improving the oscillatory modes in the system, but not on the stability analysis. Furthermore, [114] sets a particular focus on inner cascade loops and the differences in small-signal stability of a three-inverter microgrid utilizing conventional PI-based and internal model-based control approaches. Eigenvalue sensitivity analysis with respect to power droop gains and filter inductance again reveals that the low-frequency modes are highly sensitive to the parameters of the power sharing controllers for both methods. On the other hand, [115] proposes an approximation method based on critical clusters for assessing the droop gain stability margins of medium-scale islanded microgrids that takes advantage of the fact that the contribution of inverters to the small-signal stability may depend on their location and the interactions with each other. Both [114] and [115] are however solely restricted to grid-forming VSCs and do not investigate the adverse interactions between different converter control schemes. The latter aspect is partially tackled in [116] by analyzing stability issues between a grid-feeding VSC and an inverter operating as a virtual synchronous generator, with a focus on virtual inertia characteristics and interaction between power converters and the AC grid. Moreover, [116–118] highlight some conceptual differences between a traditional and an inverter-based power system in terms of associated control timescales. Nonetheless, they all confine the analysis only to 100% inverter-based microgrids.

While the aforementioned studies provide various perspectives on stability of microgrids and zero-inertia systems, less emphasis has been placed on performance of large-scale systems with a mixture of synchronous machines and VSCs. Having in mind that operators in Ireland [119], Texas [4] and South Australia [2] are already facing obstacles regarding high wind penetration during certain periods of the day, the fundamental understanding of low-inertia systems and their stability properties is of crucial importance. Nevertheless, simulation and analysis of large power systems with a mix of synchronous and converter-based generation involves a significant computational burden. To this end, commercial software packages such as PSLF [120], DSATools [121] and PSS/E [122] are widely employed, both for industrial and academic purposes. While these software tools incorporate detailed dynamic models of different generator types and provide means for large-scale time-domain simulations, they are restricted in terms of analytical capabilities and flexibility. This mostly stems from underlying modeling assumptions valid for traditional SG-based power networks, which are however not applicable to inverter-dominated systems. For instance, the widely employed dynamic models for wind and photovoltaic plants, originally proposed by WECC renewable energy modeling task force [123], do not consider dynamics of high-frequency converter controls and PLLs, which can have a detrimental impact on small-signal stability. Furthermore, the transmission line dynamics are traditionally neglected in power system studies due to drastically shorter timescales compared to SG dynamics. With the introduction of fast-acting power electronic devices, such assumptions are not valid anymore [6].

In turn, the existing literature tends to neglect important aspects of system dynamics and confine the analytical analysis to simplified mathematical models and state-space formulations. More precisely, [124–127] study the impact of large-scale wind power generation on power system oscillation, transient and small-signal stability. However, the authors either use oversimplified synchronous generator models (i.e., not equipped with governors and exciters) [124], neglect inner control loops of inverter-interfaced wind generation [125, 126] or focus on high-level probabilistic frameworks [127], which obstructs them from capturing some important dynamic interactions and phenomena. On the other hand, [128] and [129] employ systematic nonlinear simulations and off-the-shelf small-signal analysis tools to assess the impact of increased penetration of wind and photovoltaic generation on stability of the Kundur two-area and the western North American power system, respectively. Both studies are however restricted solely to investigation of inter-area oscillations and the nature of underlying oscillatory modes.

Alternatively, a two-bus microgrid comprising a grid-following VSC and a synchronous generator was investigated in [130] and [46] through eigenvalue analysis. Both studies point out that the PLL can be a source of oscillatory modes and instability. The work in [130] incorporates relatively detailed control structures of both units, but mostly focuses on model validation and sensitivity analysis to determine the optimal ranges of relevant control parameters. On the other hand, the authors in [46] provide insightful remarks regarding the permissible penetration levels of grid-following inverters, as well as the relevance of different controllers on small-signal stability. However, they employ an inverter scaling method that complicates DAE implementation on a larger system and omit the PSS and important flux dynamics from the SG model. Furthermore, neither of the aforementioned studies explore the deeper causes of instability, nor consider the impact of different converter operation modes. Finally, the focus is primarily on distribution networks and microgrids, thus neglecting the potential impact of transmission line dynamics.

The work presented in this chapter improves on the existing literature in several ways. In contrast to [67, 98, 114–118], we include several converter operation modes and investigate their interactions in a 100% inverter-dominated transmission network. The analysis is also extended to low-inertia systems and the adverse interference between different components of synchronous and converter-based generation. However, unlike the work in [46, 124–130], we employ a more detailed representation of a generic, low-inertia system (see Section 2.9) that captures all relevant physical properties and associated dynamics, including various generation models and control schemes as well as line and load dynamics. Moreover, unlike most of the existing studies, we are not primarily concerned with parameter sensitivity but rather with investigating maximum permissible penetrations of PE-interfaced generation under various system configurations. In particular, the critical levels of installed inverter-based generation and the key modes of arising instability are identified and mapped back to the respective controller dynamics. It is shown that the root cause of instability cannot be associated solely with the aggregate power injection of VSC units, as it varies depending on the installed capacity and operating setpoints of renewable generation. Additionally, the problems arising from underlying timescale coupling of converter and transmission line dynamics, as well as the timescale separation between the respective VSC and SG controllers regulating the same system quantities have been observed. As a result, new insights into the overall stability of low- and no-inertia systems are presented, together with potential directions for improving the

system stability margin under different generation portfolios. Furthermore, some of the widely common premises in terms of stability and overall system dynamics have been debunked solely as an artifact of inadequate modeling and system representation, which justifies the importance of high level of detail when studying the dynamics of low-inertia systems.

The rest of the chapter is structured as follows. In Section 4.2, the characteristic timescales of low-inertia systems and the potential impact of transmission line dynamics are discussed. In Section 4.3, a detailed small-signal analysis of a two-generator system with various unit configurations is conducted. Some insightful observations regarding permissible penetration of inverter-interfaced generation have been made, and the most vulnerable and instability prone segments of the system have been determined. These assumptions are further validated in Section 4.4 by conducting a similar analysis on the IEEE 9-bus and the South-East Australian Grid. Finally, Section 4.5 draws the most important conclusions on qualitative properties and small-signal stability of future low-inertia systems and concludes the study.

4.2 TIMESCALES IN LOW-INERTIA SYSTEMS

The overall complexity of dynamics pertaining to low-inertia systems is well described through their characteristic timescales illustrated in Fig. 4.1. Conventional power systems based on synchronous generators have a distinct difference in time constants¹ for frequency and voltage regulation, with turbines ($T_r \approx 10$ s) and governors ($T_g \approx 1$ s) operating on much longer timescales than the exciter ($T_e \approx 50$ ms) [95]. Moreover, swing and flux dynamics reflect the time constants of the swing equation and synchronous machine flux linkages, respectively. Considering that the time constants of line dynamics vary in the $T_l \in [1 - 30]$ ms range, depending on the network type, it is clear that the conventional control schemes would ensure system stability. However, with the inclusion of fast-acting, converter-based generation, the system dynamics become more complex and convoluted and may lead to unexpected couplings [6]. For instance, the traditional assumption of neglecting fast line dynamics is not valid anymore, since the underlying dynamics are of the same order of magnitude as the ones of converter voltage control. On the other hand, the time constants of PI controllers and low-pass filters associated with the system- and device-level inverter control are one or two orders of magnitude smaller than the ones of synchronous machines, potentially resulting in adverse control interference and instability, especially

¹ The time constant notation is adopted from Chapter 2.

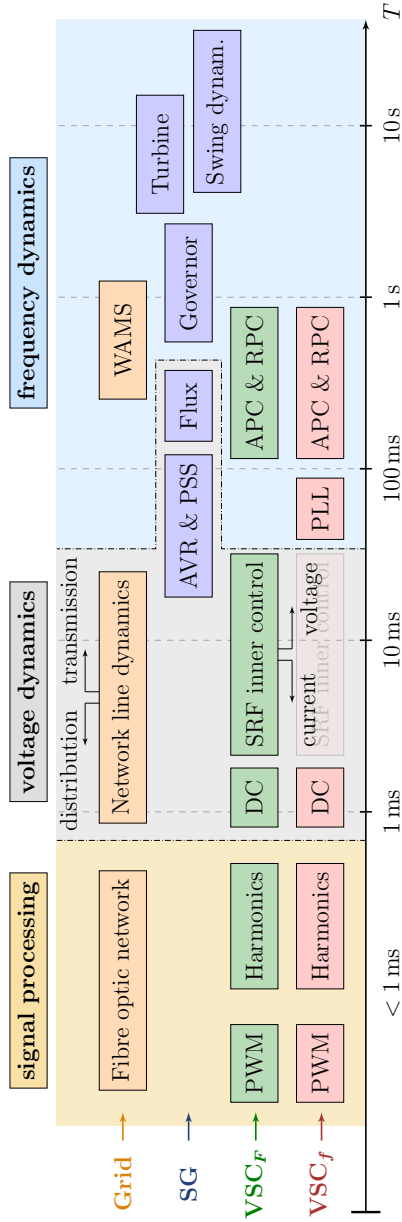


FIGURE 4.1: Characteristic timescales of different physical and control dynamics in a low-inertia system.

in networks with high installation shares of renewables. Moreover, the time delays associated with Wide Area Monitoring Systems (WAMS) would make any type of emergency regulation without the use of high-speed fibre optics obsolete [131].

It should be noted that by voltage and frequency dynamics in Fig. 4.1 we refer to the controllers associated with voltage and frequency regulation, respectively. While somewhat related, these notions are not in direct correlation with the traditional voltage and frequency stability terms [132], especially considering the complex dynamics of low-inertia systems and a timescale separation between the controls of different unit types regulating the same system metric (voltage magnitude or frequency).

We also note that the impact of network line dynamics becomes more profound in *inertialess* systems. Its effect on frequency stability can be illustrated by analyzing a general frequency control loop of an individual grid-forming inverter $j \in \mathcal{N}_g$ connected to $|\mathcal{K}_j|$ VSC units $k \in \mathcal{K}_j$ adjacent to inverter j , as follows:

$$\tau_z \ddot{\theta}_{c_j} + (1 - \omega_b R_c^p B'_j) \dot{\theta}_{c_j} + \omega_b R_c^p B_j \theta_{c_j} + C_j = 0, \quad (4.1a)$$

with

$$C_j = \omega_b \omega_{c_j}^* + \omega_b R_c^p p_{c_j}^*, \quad (4.1b)$$

$$B_j = \sum_{k \in \mathcal{K}_j} \frac{\omega_0 \ell_{jk}}{\omega_b (r_{jk}^2 + \omega_0^2 \ell_{jk}^2)^2}, \quad B'_j = \sum_{k \in \mathcal{K}_j} \frac{2r_{jk} \ell_{jk}^2}{\omega_b (r_{jk}^2 + \omega_0^2 \ell_{jk}^2)^2}. \quad (4.1c)$$

The notation is adopted from Chapter 2, with the declaration of additional variables as well as the derivation of expressions in (4.1) provided in Appendix B.3.

In order to preserve system synchronization, the natural negative feedback terms for θ_{c_j} and $\dot{\theta}_{c_j}$ must be positive, indicating an upper limit on the active power droop gain $R_c^p < (\omega_b B'_j)^{-1}$. Such threshold is even more restrictive for distribution networks, due to shorter node distances and a lower ℓ_{jk}/r_{jk} line impedance ratio. Furthermore, the impact of the power network also pertains to inverter synchronization through θ_{c_j} term, since very high feedback control gains $\kappa_j = \omega_b R_c^p B_j$ might lead to inverter frequency oscillations exciting the oscillatory modes of the transmission lines. In other words, the inverters achieve synchronization by inferring information about the phase angle differences through local measurements of currents and voltages. Therefore, the time constant of transmission lines can be interpreted as a propagation delay of the information on the phase angles, and the controllers cannot act

faster than the time needed to observe information through the network. Hence, larger time constants require a lower feedback gain, which implies that reducing transmission line impedance ratio or increasing network connectivity can make a low-inertia system unstable. Similar remarks have been pointed out for microgrids comprising solely inverters based on droop [133] and dispatchable virtual oscillator control [17]. While we only focus on frequency dynamics in this example, it should be noted that the voltage dynamics could also be assessed using the proposed approach, as indicated in [16, 17, 133].

4.3 UNIT INTERACTIONS IN A TWO-GENERATOR SYSTEM

For the first case study we consider a simple two-bus system illustrated in Fig. 4.2, with two generators connected through a transmission line and an RL load supplied at the first node. The goal is to incorporate different types of generation units into the system and investigate their dynamic interactions and the respective stability margins. In order to confine the observed phenomena solely to the generators under study, the transmission line dynamics are neglected at this point, i.e., line connections are represented only by algebraic equations.

We investigate three different scenarios based on the generator type configuration: (i) a synchronous generator and a grid-following VSC; (ii) a synchronous generator and a grid-forming VSC; and (iii) a grid-forming and a grid-following VSC. Furthermore, we introduce a penetration ratio $\eta \in \mathbb{R}_{\geq 0}$, which describes the installed penetration level of inverter-based units. In the first two cases this corresponds to

$$\eta = \frac{\bar{P}_c}{\bar{P}_g + \bar{P}_c}, \quad (4.2)$$



FIGURE 4.2: Configuration of the investigated system comprising two generators and one load connected via a transmission line.

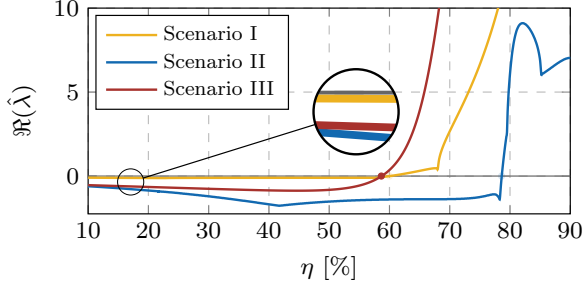


FIGURE 4.3: Impact of inverter penetration on system stability for different unit configuration.

whereas in the last scenario this factor describes the penetration of grid-following generation, i.e.,

$$\eta = \frac{\bar{P}_{c_f}}{\bar{P}_{c_F} + \bar{P}_{c_f}}, \quad (4.3)$$

with $\bar{P}_g \in \mathbb{R}_{\geq 0}$ and $\bar{P}_c \in \mathbb{R}_{\geq 0}$ denoting the installed powers of synchronous and converter-interfaced generation, and subscripts F and f representing the grid-forming and grid-following converters respectively. Note that all generators operate at 50% of the installed capacity, i.e., $p_g^* = p_{c_f}^* = p_{c_F}^* = 0.5$ p.u..

The small-signal stability margins of different system configurations are presented in Fig. 4.3, where the stability is assessed through real-part movement of the most critical eigenvalue $\hat{\lambda}$. Understandably, the system comprising both synchronous generators and grid-forming inverters can withstand higher levels of PE-based devices ($\approx 79\%$), as the voltage phasors at both nodes are fully established and controlled by local generators. Additionally, the synchronization and power sharing properties are inherently provided by both units. On the other hand, the penetration of grid-following generation adversely affects the system balance and significantly reduces the maximum admissible ratio to $\eta_{\max} \approx 60\%$ and $\eta_{\max} \approx 59\%$ for Scenarios I and III, respectively. Scenario III also has a steeper progression of $\hat{\lambda}$, indicating that it is difficult to achieve a noticeable improvement of the critical penetration ratio.

As a second step, we thoroughly explore the fundamental components contributing to the aforementioned instability. This is achieved by determining the critical modes of the system, employing participation factor and parameter sensitivity analyses, and determining the states (i.e., controllers) that mainly

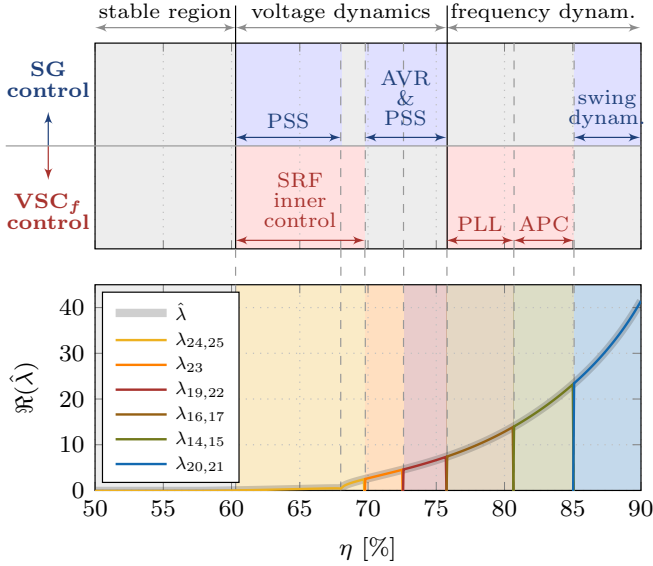


FIGURE 4.4: Impact of different controllers on system stability under high grid-following inverter penetration in Scenario I.

contribute to such modes. Each of the proposed scenarios comprises a unique DAE system with specific dynamics. Therefore, all three system configurations are individually investigated and discussed in detail in the following sections.

4.3.1 Scenario I: Interaction between the SG and Grid-Following VSC

It is observed that the inverter penetration above 60% leads to system collapse. Interestingly, the instability initially originates in the voltage dynamics due to incompatibility of the VSC's inner control loop and the generator's PSS, as illustrated in Fig. 4.4. Subsequently, the vulnerability spreads across the whole excitation system including the AVR. At this point the system is heavily unstable. This phenomena comes from the time constants of the inner loops being drastically smaller than the ones of the exciter. More specifically, once the system becomes predominantly PE-based the “non-forming” aspect of the inverter's voltage phasor counteracts and diminishes the firm voltage at the SG terminal, thus weakening the system. For even higher VSC penetration levels (> 75%) the network faces frequency stability issues, as the PLL, and subsequently the active power controller, cannot provide

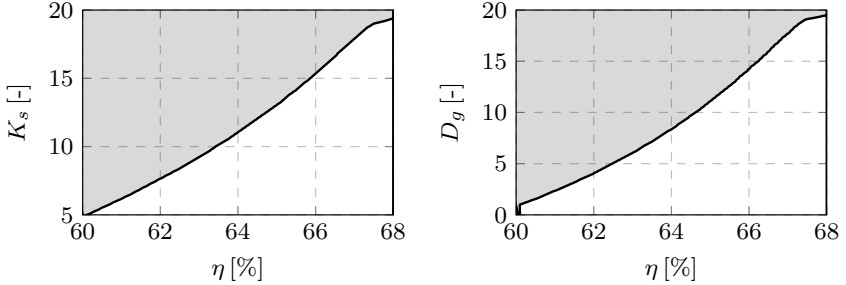


FIGURE 4.5: Stability maps in $K_s - \eta$ and $D_g - \eta$ planes indicating the effect of PSS stabilization gain and SG damping on admissible penetration of grid-following inverter units in Scenario I.

adequate synchronization of the grid-following units due to an insufficiently stiff global frequency signal.

By studying the movement of the critical eigenvalue spectrum in Fig. 4.4 we notice that the real part $\Re(\hat{\lambda})$ significantly increases for inverter shares above 68%. Considering that PSS and inner SRF controllers largely participate in critical modes for $\eta \in [60, 68]$ %, one can assume that re-tuning the respective control gains could restore system stability within this range. While the increase in stabilization gain K_s shown in Fig. 4.5 proves to be beneficial for the system, the adjustment of inner loop's PI controllers has no impact on the eigenvalue spectrum. This is an expected outcome due to a large timescale separation between the two feedback loops, which in turn hinders the synchronous generation from providing a stiff voltage at the terminal. Furthermore, the tuning of the device-level control is often predefined by the manufacturer and optimally designed for providing fast and accurate voltage and power reference tracking, implying that any parameter change would distort its original purpose and effectiveness. Beside the SG voltage regulators, the dynamics of the swing equation also prove to be relevant to a certain extent for the overall stability. However, in contrast to the popular belief that low inertia levels lead to vulnerability, it is in fact the insufficient damping that propagates the problem. Similar to the PSS stabilization gain, the higher damping constant D_g facilitates the integration of converters, whereas the inertia constant has no impact on the overall penetration (see Fig. 4.5); an observation that was also made in [46]. Nonetheless, damping is related to physical properties of synchronous generators, while droop gains - essentially corresponding to damping - are prescribed within narrow ranges by the grid codes. This suggests that the most viable and practical solution

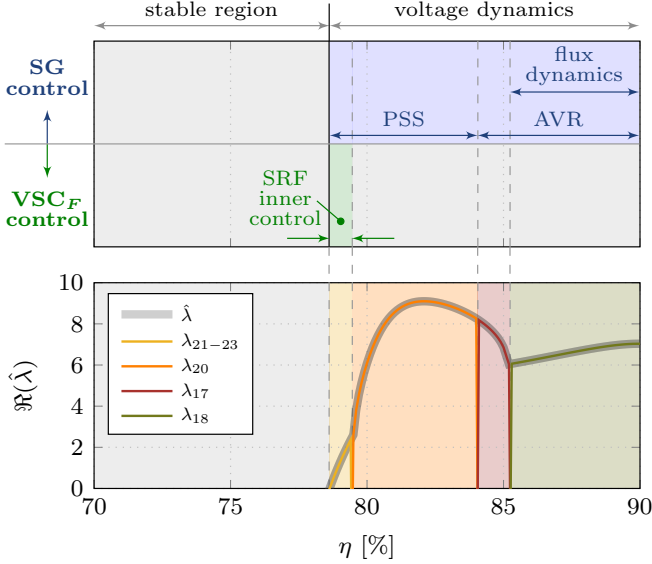


FIGURE 4.6: Impact of different controllers on system stability under high grid-forming inverter penetration in Scenario II.

would be to improve the PSS design (i.e., increase its responsiveness) in order to accommodate a high penetration of grid-following inverter-based generation.

4.3.2 Scenario II: Interaction between the SG and Grid-Forming VSC

The issues pertaining to timescale separation between different voltage controllers, already highlighted in the previous scenario, remain also in this scenario. It can be noticed that the “forming” inverter property bolsters the voltage vector at the respective bus and drastically improves the stability margin of the system. Nonetheless, for $\eta > 78\%$ the AVR and PSS controllers cannot achieve adequate voltage stabilization, as the eigenvalues depicted in Fig. 4.6 are located deeply into the right-hand side of the root loci spectrum. Hence, the maximum feasible penetration of VSCs can hardly be improved. Another important observation is that the frequency dynamics are not contributing to instability anymore, since both units independently establish an adequate frequency signal and subsequently synchronize.

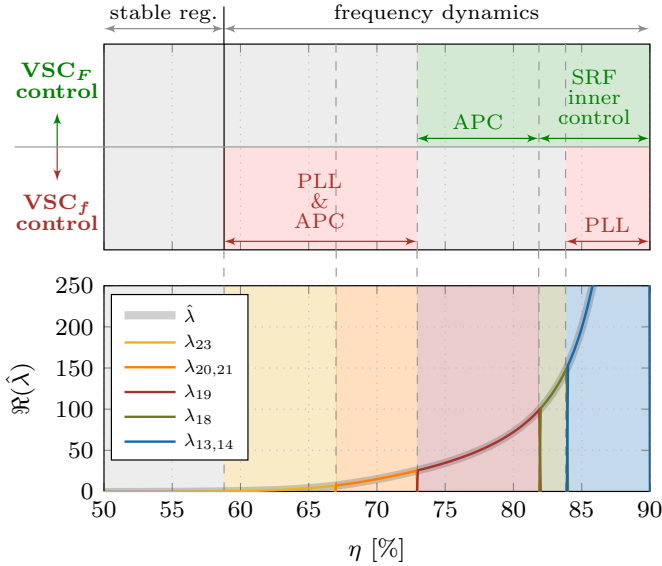


FIGURE 4.7: Impact of different controllers on system stability under high grid-following inverter penetration in Scenario III.

4.3.3 Scenario III: Interaction between Different VSC Operation Modes

We tackle the 100% PE-based scenario by increasing the share of grid-following units reflected in an increasing factor η , as shown in Fig. 4.7. The main distinction of this scenario is the elimination of voltage control issues in the presence of SGs and inverters, as both VSCs regulate voltage on the same timescale. In spite of improving the voltage dynamics in the system, the synchronization problems are aggravated due to an exclusion of a synchronous generator. In other words, the dedicated “forming” capability of a grid-forming converter is inferior to the one of a traditional generator. As a result, for penetration levels above $\approx 59\%$ the PLL units of grid-following inverters cannot accurately estimate the frequency signal, leading to failure in the active power control and preventing system-level synchronization. Similar properties are also reflected in Fig. 4.8 when analyzing η as a function of the proportional PLL gain K_p^s , with a more responsive PLL potentially facilitating a higher penetration factor. However, this approach does not solve the fundamental problem at hand and provides only a marginal improvement of a few percent. It should be noted that the integral gain of the respective

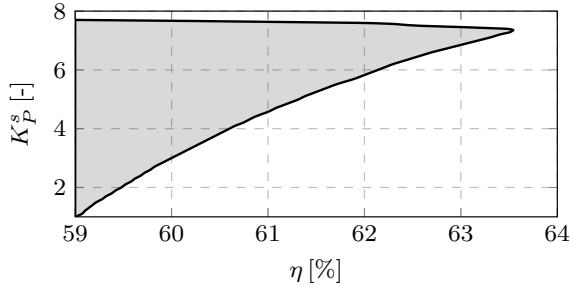


FIGURE 4.8: Stability map in the $K_P^s - \eta$ plane indicating the effect of proportional PLL gain on admissible penetration of grid-following inverter units in Scenario III.

PI controller does not affect the system stability margin, indicating that the original PLL time constant could be maintained in the process.

Note that scenarios comprising two identical generator types will not be considered in this chapter for simplicity. More precisely, the stability of an all SG-based network has been thoroughly studied in the literature [26, 27, 132], whereas a system with only grid-following inverters would not be capable of standalone operation. Finally, the stability issues of an all-forming, transmission-level inverter system are confined mostly to synchronization and generation of a stable angle reference, and hence cannot be studied through small-signal analysis. Furthermore, such systems are only confined to theoretical analysis and have no existing real-world application thus far.

4.3.4 Inclusion of Transmission Line Dynamics

We broaden the scope of our analysis by explicitly including transmission line dynamics, i.e., modeling line connections via differential equations described in Section 2.9. The same three scenarios are re-evaluated and compared against the previous case studies, with the results given in Fig. 4.9. A noticeable difference in the stability margin of a 100% inverter-based system can be observed, where the inclusion of line dynamics significantly increases the maximum penetration ratio η . This can be explained by the inductive and capacitive components of the lines acting as energy buffers and augmenting the synchronization between the two units. More precisely, the frequency issues associated with a large proportion of PLL-based generation are alleviated through interactions with the LC segments of transmission lines, which

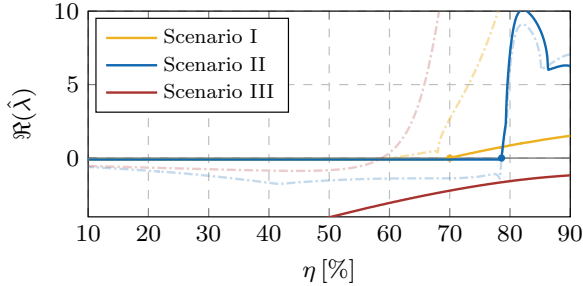


FIGURE 4.9: Impact of inverter penetration on system stability for different unit configuration, with inclusion of transmission line dynamics. Transparent dashed lines indicate results for scenarios without line dynamics from Fig. 4.3.

slows down the frequency dynamics and enables the grid-following VSCs to more accurately detect the weak global frequency signal. Similar conclusions have been drawn for autonomous microgrids [134] and networks comprised of a specific class of grid-forming inverters [17], as well as in [27] using a mechanical analogue of swings in a multi-machine system.

On the other hand, the scenarios experiencing instability related to voltage dynamics are for the most part unaffected by the transmission line dynamics. The voltage control interaction between the synchronous and PE-based generation is somewhat mitigated, due to the time constants of the line dynamics and the inner SRF controls being of the same order of magnitude. However, the line dynamics do not have any impact on the slower modes associated with synchronous machines. Therefore, the stability in Scenario I cannot be preserved for a grid-following penetration above 70 %, as the issues lie within the AVR and PSS control design. The predominant impact of SGs on system stability is even higher in Scenario II, with grid-forming inverters only marginally affecting the critical modes within a narrow range of $\eta \in [78, 79]$ %. Hence, the maximum admissible VSC penetration after the inclusion of transmission line dynamics remains the same in this case.

4.3.5 Impact of System Operating Point

In addition to the total installed capacity of PE-interfaced generation, the actual dispatch (i.e., operating power setpoints) of converter-based units can have a detrimental effect on small-signal stability. In fact, it can completely

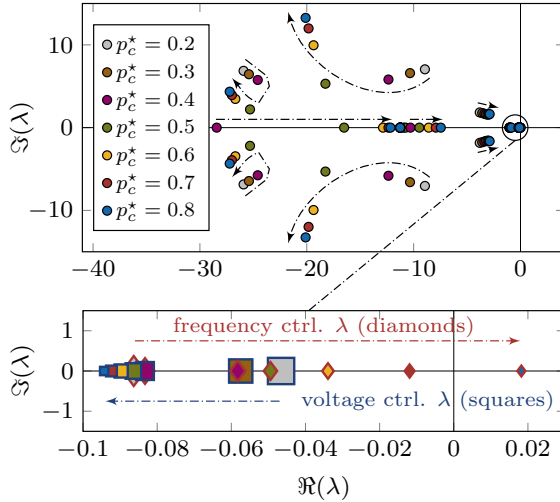


FIGURE 4.10: Root loci spectrum of interest for different system operating points: general mode movement (top) and the most critical modes (bottom). In the bottom figure, the edge color of the mode corresponds to the color of the respective arrow indicating the direction of the movement. The size of the symbol scales down with the increase in converter power setpoint p_c^* .

change the nature of the unstable modes and the controllers contributing to such modes and instability. One such example is illustrated in Fig. 4.10, depicting a root loci spectrum of the system from Scenario II. The SG and grid-forming VSC have identical installed power capacities $\bar{P}_g = \bar{P}_c$, suggesting that $\eta = 0.5$. Note that for such configuration and $p_g^* = p_c^* = 0.5$ p.u., the system in Scenario II is stable (see Fig. 4.6). The original unit dispatch (set at 50% for each unit) is modified by gradually changing the power setpoints while holding the total generation output constant, which corresponds to redistribution of the load demand between the two generators.

Under SG-dominated operation the most critical mode (denoted by blue-edged squares in Fig. 4.10) is associated with voltage control dynamics. This is also identified as the same mode becoming unstable for increased installed VSC capacity, previously pointed out in Section 4.3.2. However, when increasing the converter dispatch point p_c^* , the aforementioned mode moves to the left-hand side (indicated by the blue arrow), whereas another mode (denoted by red-edged diamonds) shifts to the right-hand side (indicated by the red arrow) and eventually becomes unstable for $p_c^* > 0.7$ p.u. An interesting

observation is that the instability arises from synchronization issues, i.e., it is a consequence of adverse interactions between the two frequency controllers. Such finding confirms a very complex nature of potentially unstable modes in a PE-dominated power system, and implies that a single metric of inverter penetration might not be sufficient to prescribe reliable stability margins. Another insightful remark can be made regarding the nature of the most critical modes, as they all have zero imaginary part. This implies that the underlying instability is not oscillatory, and one should not be thinking of “fast” and “slow” second-order dynamics but rather of just simple first-order dynamics when referring to these modes.

4.4 STABILITY PROPERTIES OF LARGE MULTI-MACHINE SYSTEMS

4.4.1 *Stability Margins of IEEE 9-bus System*

In order to investigate the simultaneous interactions between all three unit types, as well as to increase network complexity, the IEEE 9-bus system given in Fig. 4.11 is considered in this case study. It represents a simple approximation of the Western System Coordinating Council (WSCC) to an equivalent system with nine buses and three generators. A grid-following VSC is placed at node 2 and a grid-forming VSC at node 3. The transmission line dynamics are also included in the model.

The stability mapping for the IEEE 9-bus system shown in the form of a triangular plot in Fig. 4.11 considers various installation capacities of each generation unit, together with different levels of network connectivity. Each triangular axis denotes a penetration of the respective unit type, more precisely $\eta_{SG} \in \mathbb{R}_{>0}$ refers to synchronous generators, $\eta_F \in \mathbb{R}_{>0}$ to grid-forming and $\eta_f \in \mathbb{R}_{>0}$ to grid-following inverter-based units; colored areas indicate a predominant penetration ($\geq 50\%$) of a single generation type. It should be noted that the system is always comprised of three generation units, i.e., axes points indicating a 0% penetration of a single generator type are not considered, and the individual penetration levels are varied in discrete steps of 1%. We modify the original system by gradually adding transmission lines, first between the generator buses and subsequently between the load buses, as indicated by the red and blue lines, respectively, in the network diagram in Fig. 4.11. Such procedure allows us to increase the network connectivity, defined for a system comprising $N_n = |\mathcal{N}|$ nodes and $N_b = |\mathcal{B}|$ branches hereinafter as

$$\varepsilon_g := \frac{2N_b}{N_n^2 - N_n}, \quad (4.4)$$

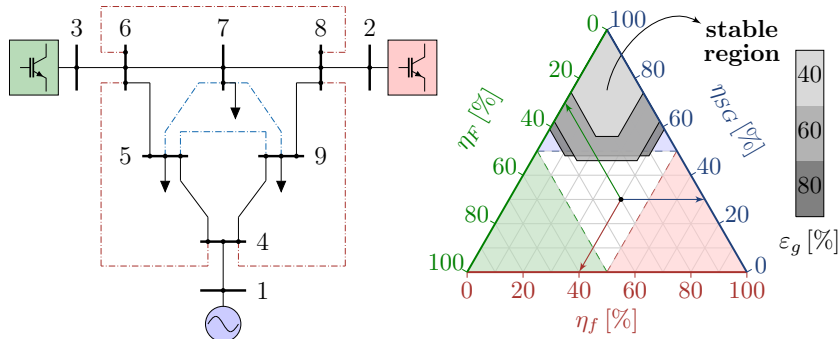


FIGURE 4.11: Stability margins of the IEEE 9-bus test case: network diagram, with blue and red lines indicating the additionally incorporated transmission lines (left) and stability mapping under different levels of network connectivity (right). Colored arrows indicate the appropriate reading direction on the respective axes.

from 40% in the original model to 60% and 80% in the modified system.

The stability map in Fig. 4.11 reveals that, for the generator configuration in this test case, system stability cannot be maintained with less than 47% synchronous generation. Reducing connectivity (in particular removing generator bus network connections) makes the system even more reliant on synchronous generation. It is clear that stability erodes at high VSC penetration levels independent of the grid-forming share, which is consistent with our previous findings in Section 4.3. Interestingly, the permissible converter installation margin significantly reduces when the η_F/η_f ratio diverges from 1, as the maximum value of $\eta = \eta_F + \eta_f$ drops from 44% to 27% in case of $\eta_F \approx 0\%$ or $\eta_f \approx 0\%$. This is due to different instabilities occurring between various unit types, specifically voltage issues for a system comprised of synchronous and inverter-based generators (Scenarios I and II) and synchronization obstacles related to a 100% PE-based system (Scenario III), as described in Section 4.3. For a rather balanced portfolio, all of these problems are somewhat confined within reasonable limits, while an imbalance in the η_F/η_f ratio tends to emphasize the voltage dynamics issues and endanger the whole network. Another valid point can be made regarding the beneficial impact of transmission line dynamics. As previously indicated in Section 4.3.4, a direct network connection between units experiencing frequency instability mitigates the synchronization issues, thus facilitating a higher permissible

share of PE-based devices. Nonetheless, this is not the case for transmission lines between the load nodes, as increasing connectivity from 60 % to 80 % has a negligible impact on the stability margin.

We extend this analysis by differentiating between three different generation portfolios: (i) \mathcal{P}_0 - a mix of all three unit types, as previously discussed; (ii) \mathcal{P}_f - a system comprising only synchronous generators and grid-following VSCs; and (iii) \mathcal{P}_F - a system comprising only synchronous generators and grid-forming VSCs; in the latter two cases the portfolio consists of two synchronous and one inverter-based generator, i.e., one of the VSCs from the original portfolio \mathcal{P}_0 is replaced by SG, whereas the total inverter penetration ratio is either $\eta = \eta_f$ or $\eta = \eta_F$. The results for the IEEE 9-bus system presented in Fig. 4.12 suggest that more homogeneous portfolios, such as \mathcal{P}_f and \mathcal{P}_F , can withstand drastically higher penetrations of renewables, with η_{\max} reaching up to 75 % and 82 % respectively. Understandably, portfolio \mathcal{P}_F has a higher η_{\max} margin due to less accentuated voltage instability compared to the \mathcal{P}_f scenario. However, increasing network connectivity balances these penetration ratios out, as direct transmission line connections resolve the timescale separation between the voltage controllers of synchronous and converter-based generators (see Fig. 4.1). As a result, the system can facilitate up to $\eta_{\max} = 88\%$ of PE-interfaced units; an increase of approximately 70 % compared to the original portfolio \mathcal{P}_0 .

Alternatively, a different configuration with a less heterogeneous portfolio comprised of two grid-forming and one grid-following inverter is investigated. For higher levels of network connectivity the system faces no stability issues under any share of installed powers, whereas in case of $\varepsilon_g = 40\%$ the maximum permissible penetration of grid-following generation is 93 %. This highlights the fact that the small-signal stability of low-inertia systems is drastically more vulnerable compared to the one of 100 % PE-based systems.

4.4.2 *Stability Characteristics of South-East Australian Network*

Having gained fundamental understanding of dynamic interactions between different types of generators in a simplistic test environment, we extend the analysis to a 14-generator, 59-bus South-East Australian system [135, 136] shown in Fig. 4.13. This network represents a long, linear system as opposed to the more tightly meshed networks found in Europe and the United States. For convenience, it has been divided into 5 areas, with areas 1 and 2 being closely electrically coupled. Therefore, there are in essence 4 main regions, namely South Australia (area 5), Queensland (area 4), Victoria (area 3) and

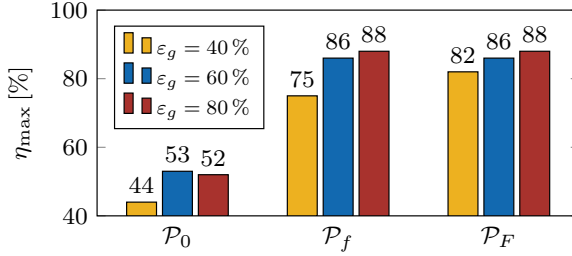


FIGURE 4.12: Maximum permissible inverter penetration under different system portfolios (\mathcal{P}) and levels of network connectivity (ε_g).

New South Wales (subsuming areas 1 and 2), and hence 3 inter-area modes are present. Beside its string topology, the system is characterized by the weak coupling between South Australia and the rest of the system. The model employed in this chapter considers the light loading scenario provided in [136, 137].

Moreover, for the purpose of this work, the model presented in [137] was modified to obtain a low-inertia case study by replacing synchronous generators located at buses 101, 202, 301, 302, 501, 502 and 503 by grid-following VSCs of identical power rating. In addition, we install 4 more grid-following units, two in each of the area 2 and 3, at nodes 212 and 214, i.e., 308 and 314 respectively. This yields a total of 11 converter-interfaced generators operating in grid-following mode and 7 conventional synchronous generators, representing the default test case for our analysis. Such modeling choice is based on the high penetration of renewable generation in the real-world system, particularly in area 5, that does not provide standalone frequency support [138, 139]. Note that the default system comprises all-inverter-based areas 5, 3 and 1, corresponding to South Australia, Victoria and the far south region of New South Wales. The time-domain response of the proposed system during initialization is depicted in Fig. 4.14, with all generators synchronizing within 5 s. In order to illustrate the conceptual differences between grid-forming and grid-following devices, the VSC at node 501 has been assigned with a grid-forming mode of operation. This is reflected in the frequency performance in Fig. 4.14, as the grid-forming DG experiences a significantly faster frequency response compared to other generators. In contrast, the remaining grid-following converters have slower frequency dynamics, similar to the synchronous generators, justified by the fact that this type of VSC-based generation employs PLLs for synchronization.

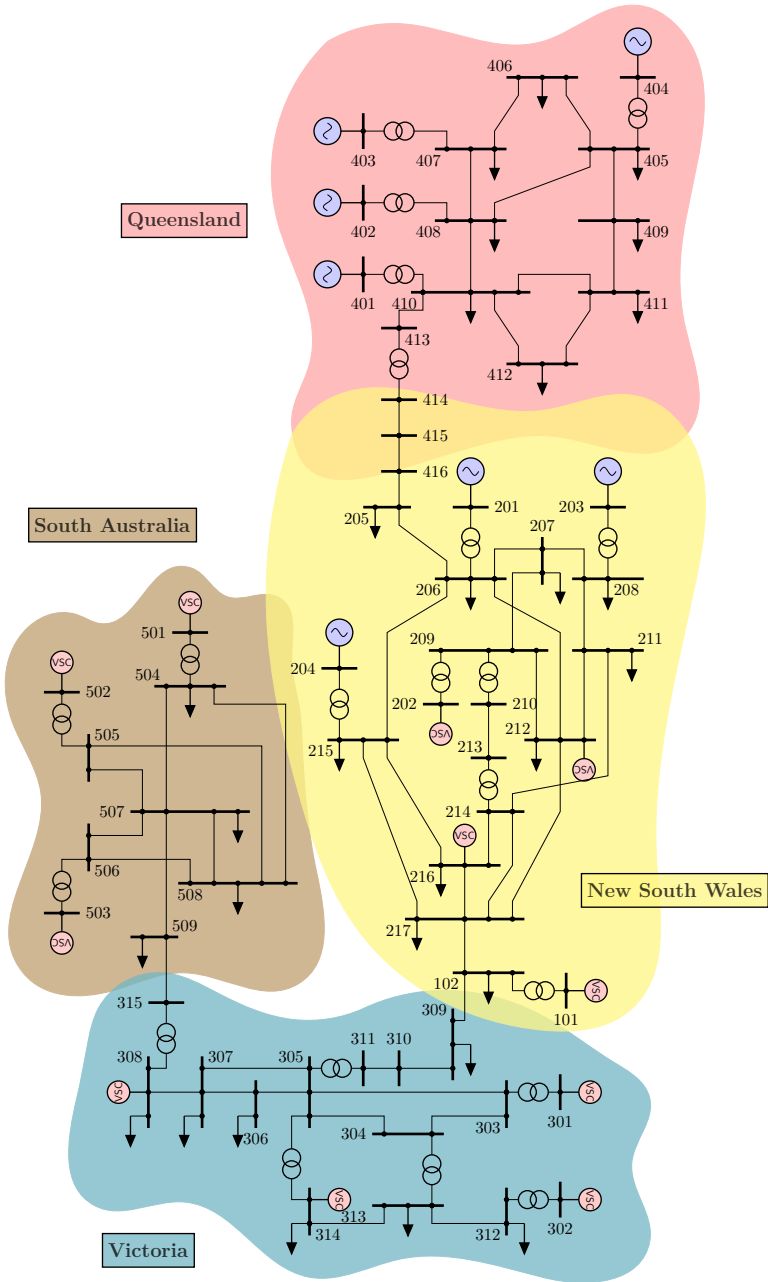


FIGURE 4.13: Modified South-East Australian power system line diagram.

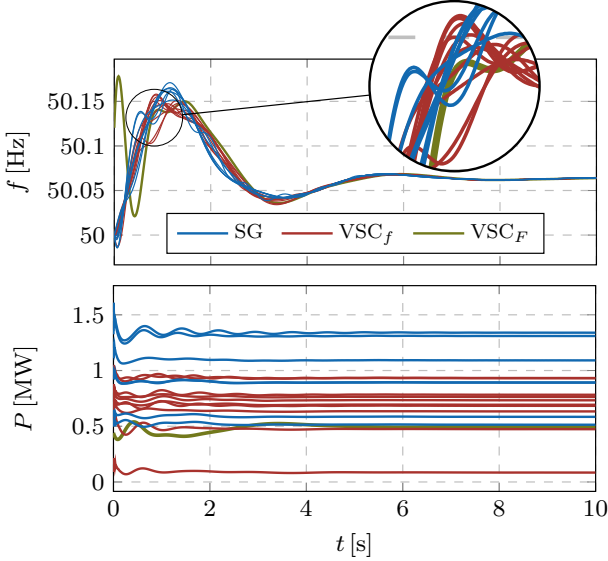


FIGURE 4.14: Time-domain response of individual generators in South-East Australian network within first 10s after initialization. The results correspond to the default system configuration presented in Fig. 4.13, with a substitution of a grid-following VSC at node 501 by a grid-forming one.

In the following step, we analyze the stability margins of the South-East Australian network for 33 different configuration scenarios categorized into 6 groups given in Table 4.1. The first set of 8 scenarios (\mathcal{G}_1), including the default system setup in Scenario 1, is generated by successively replacing one of the existing SGs in Queensland and New South Wales (areas 2 and 4) of the default system by an equivalent grid-following inverter. Similarly, set \mathcal{G}_2 considers 6 scenarios where two of the aforementioned SGs are simultaneously converted into converter-interfaced units. In contrast, \mathcal{G}_3 restores South Australia to its original condition (i.e., makes area 5 SG-based) and presents 9 scenarios with a substantially higher level of inverter penetration in areas 2 and 4, with Scenario 23 only having one SG in Queensland and New South Wales combined. The two scenarios in \mathcal{G}_4 are the only instances with grid-forming VSC installation in the system and represent 100% inverter-based configurations, whereas sets \mathcal{G}_5 and \mathcal{G}_6 restore original synchronous generation in areas 1, 3 and 5 and study the impact of PE-based generators in areas 2

Scenario	Generation type at the respective node																			η [%]	stab.	
	501	502	503	308	314	302	301	101	214	212	204	203	201	401	402	403	404	202				
G_1	1	f	f	f	f	f	f	f	f	f	f	f	f	f	f	f	f	f	f	56.97	yes	
	2	f	f	f	f	f	f	f	f	f	f	f	f	f	f	f	f	f	f	f	61.96	no
	3	f	f	f	f	f	f	f	f	f	f	f	f	f	f	f	f	f	f	f	66.35	no
	4	f	f	f	f	f	f	f	f	f	f	f	f	f	f	f	f	f	f	f	64.68	no
	5	f	f	f	f	f	f	f	f	f	f	f	f	f	f	f	f	f	f	f	63.36	yes
	6	f	f	f	f	f	f	f	f	f	f	f	f	f	f	f	f	f	f	f	60.83	yes
G_2	7	f	f	f	f	f	f	f	f	f	f	f	f	f	f	f	f	f	f	f	63.36	yes
	8	f	f	f	f	f	f	f	f	f	f	f	f	f	f	f	f	f	f	f	61.3	yes
	9	f	f	f	f	f	f	f	f	f	f	f	f	f	f	f	f	f	f	f	67.68	no
	10	f	f	f	f	f	f	f	f	f	f	f	f	f	f	f	f	f	f	f	67.21	no
	11	f	f	f	f	f	f	f	f	f	f	f	f	f	f	f	f	f	f	f	67.21	no
	12	f	f	f	f	f	f	f	f	f	f	f	f	f	f	f	f	f	f	f	65.16	yes
G_3	13	f	f	f	f	f	f	f	f	f	f	f	f	f	f	f	f	f	f	f	69.74	yes
	14	f	f	f	f	f	f	f	f	f	f	f	f	f	f	f	f	f	f	f	67.68	yes
	15	f	f	f	f	f	f	f	f	f	f	f	f	f	f	f	f	f	f	f	57.98	yes
	16	f	f	f	f	f	f	f	f	f	f	f	f	f	f	f	f	f	f	f	70.74	no
	17	f	f	f	f	f	f	f	f	f	f	f	f	f	f	f	f	f	f	f	63.02	yes
	18	f	f	f	f	f	f	f	f	f	f	f	f	f	f	f	f	f	f	f	65.75	yes
G_4	19	f	f	f	f	f	f	f	f	f	f	f	f	f	f	f	f	f	f	f	61.36	yes
	20	f	f	f	f	f	f	f	f	f	f	f	f	f	f	f	f	f	f	f	65.69	yes
	21	f	f	f	f	f	f	f	f	f	f	f	f	f	f	f	f	f	f	f	72.07	yes
	22	f	f	f	f	f	f	f	f	f	f	f	f	f	f	f	f	f	f	f	78.45	yes
	23	f	f	f	f	f	f	f	f	f	f	f	f	f	f	f	f	f	f	f	82.31	no
	24	f	f	f	f	f	f	f	f	f	f	f	f	f	f	f	f	f	f	f	91.95	yes
G_5	25	F	f	f	f	f	f	f	f	f	f	f	f	f	f	f	f	f	f	f	96.27	no
	26	f	f	f	f	f	f	f	f	f	f	f	f	f	f	f	f	f	f	f	22.47	yes
	27	f	f	f	f	f	f	f	f	f	f	f	f	f	f	f	f	f	f	f	27.45	yes
	28	f	f	f	f	f	f	f	f	f	f	f	f	f	f	f	f	f	f	f	31.84	yes
	29	f	f	f	f	f	f	f	f	f	f	f	f	f	f	f	f	f	f	f	58.97	yes
	30	f	f	f	f	f	f	f	f	f	f	f	f	f	f	f	f	f	f	f	63.95	yes
G_6	31	f	f	f	f	f	f	f	f	f	f	f	f	f	f	f	f	f	f	f	68.28	yes
	32	f	f	f	f	f	f	f	f	f	f	f	f	f	f	f	f	f	f	f	74.66	no
	33	f	f	f	f	f	f	f	f	f	f	f	f	f	f	f	f	f	f	f	70.34	yes

TABLE 4.1: Scenario configuration based on the generation portfolio in the system.

and 4. The main distinction between the latter two sets is the substantially higher inverter penetration in the second case.

By closely studying the inverter penetration levels and system configurations² in Table 4.1, we can make several insightful observations that validate the claims raised in Section 4.3 and Section 4.4.1. First of all, there is a clear upper bound on the level of grid-following inverter penetration that a traditional power system can withstand. For sets \mathcal{G}_1 and \mathcal{G}_2 this limit corresponds to $\eta_{\max} \in [60 - 70]$ %, while for \mathcal{G}_3 , \mathcal{G}_5 and \mathcal{G}_6 the maximum permissible penetration increases to $\eta_{\max} \in [60 - 70]$ %. Understandably, the network configuration and unit placement play a role. This justifies the lower VSC installation margins for former scenarios (sets \mathcal{G}_1 and \mathcal{G}_2) where South Australia (area 5) is inverter-based, since the electrical distances between the synchronous and inverter-interfaced generation are the longest and hence the system is more vulnerable. We also showcase that the operator should not aim at enforcing a single margin for maximum VSC penetration, as Scenario 22 is stable for $\eta = 78.5$ % while Scenario 2 is unstable for $\eta = 62$ %; again, solely due to the outline of the system and placement of the grid-following DGs in the network.

Finally, we validate the notion that an all-inverter network is significantly less prone to instability, as Scenario 24 can withstand a share of ≈ 92 % grid-following inverters while having only two grid-forming units in the grid. However, removing one of those grid-forming DGs leads to frequency instability (Scenario 25). Note that in Scenario 24 the grid-forming VSCs are placed at the end nodes of the system (node 501 in South Australia and node 404 in Queensland), thus capable of covering wide areas affected by their “forming” property and facilitating a high grid-following inverter penetration. By replacing the grid-forming unit at node 404 with a grid-following one, the electrical distance between this converter and the grid-forming VSC in South Australia becomes too large and the system cannot preserve small-signal stability. We can therefore conclude that the problem of placement of grid-forming inverters in a low-inertia system could be of high importance in the future. This topic is addressed in Chapter 11.

4.5 CONCLUSION

This chapter presents a comprehensive small-signal analysis of a realistic low-inertia system, with inclusion of detailed control schemes of both synchronous

² Synchronous generators are denoted by “S”, whereas grid-forming and grid-following converter-interfaced DGs are denoted by “F” and “f” respectively.

and converter-based generators as well as the dynamics of loads and transmission lines. Using modal analysis techniques we expose the most vulnerable segments of the system under different penetration levels of inverter-based units, various generation portfolios and system operating points, and investigate the adverse effects of the underlying control interference. As a result, some new insights into the overall stability of low- and no-inertia systems are presented, together with the proposed directions for improving the system stability margin under different scenarios and configurations. While presented results may vary between systems of different sizes and complexity and should be taken with caution from a quantitative perspective, they highlight some important qualitative properties of future low-inertia systems. Therefore, several key conclusions can be drawn from this study:

Transition might be hard: The existing literature focuses mostly on 100% inverter-based power systems and the associated frequency stability and synchronization issues, assuming an easy transition along the way. While this might be the case from the perspective of stiff frequency signal in the network, the overall stability of the interim low-inertia system is significantly more vulnerable and harder to ensure.

Need for a uniform regulation: Throughout this study we assume a perfectly balanced converter control design, i.e., compatible control schemes and parameter tuning which ensure stable synchronization and safe operation of the system. However, this might not be the case in the future, especially considering current grid codes and lack of a uniform regulation for VSC manufacturers. As a matter of fact, the portfolios \mathcal{P}_f and \mathcal{P}_F in Section 4.4.1 could have even underperformed compared to \mathcal{P}_0 under such circumstances. Furthermore, even the sole definition and classification of converter operation modes, e.g., *grid-forming*, *grid-following* and *grid-supporting*, lacks foundation and tends to drastically differentiate between different operators and industries.

Adverse effects of timescale separation: One of the main contrasts between traditional and low-inertia systems is a timescale separation between the respective controllers of synchronous and inverter-based generators regulating the same control variable (voltage or frequency). Due to significantly faster dynamics of VSCs, the power systems are facing voltage and frequency instability under high penetration of renewables, especially in the case of very heterogeneous³ production portfolios. Nevertheless, such effects can only be observed under sufficiently detailed modeling of underlying control schemes.

³ By heterogeneous we consider portfolios comprised of both grid-forming and grid-following VSCs, in addition to synchronous generators.

Premise of line dynamics must be changed: Transmission line dynamics have traditionally been neglected in power system studies, since their fast dynamics did not influence the dynamic behavior of the overall slower generation side. However, with the introduction of fast-acting PE devices, the aforementioned interactions become drastically more profound in networks with low rotational inertia. Interestingly enough, they can have both positive and adverse effects on the system depending on the generation portfolio. On the one hand, the time constants of transmission lines enable them to act as a buffer and “bypass” the gap between fast inverter and slow SG dynamics, thus aiding stability of systems with large shares of grid-following DGs. Furthermore, direct line connections improve synchronization between generators. On the other hand, they impose strict upper bounds on droop feedback gains of grid-forming VSCs in order to ensure both voltage and frequency stability, which are not necessarily met by today’s manufacturers. The latter property is especially pronounced in distribution networks, due to shorter node distances and a lower X/R line impedance ratio.

“Missing” inertia is not the key problem: Contrary to popular belief, low inertia on its own does not have a major impact on the small-signal stability of power systems. It does however affect frequency dynamics and associated fast transients, which in turn can adversely trigger numerous protection schemes based on frequency measurements such as frequency deviation and RoCoF.

DG penetration cannot be quantified with a single metric: The operators seek to find the maximum permissible penetration levels of converter-interfaced DGs that still ensure stable system operation. This metric is usually based on the ratio between the installed DG and conventional SG capacity. However, in addition to the sheer capacity of PE-interfaced generation, the system operating points have a crucial impact on overall stability. In fact, they can drastically change the nature of the unstable modes and the underlying dynamics, which in turn could affect the optimal power flow dispatch. Hence, obtaining a unique system metric that can provide stability certificates under any system operating point is a rather challenging task.

Future research could include, among other things, a thorough analysis of potentially adverse effects of incompatible converter control strategies, impact of unit placement on transient and small-signal stability, as well as the overall system capability for frequency regulation (e.g., limiting frequency nadir and RoCoF) under high inverter penetration.

Part II

FREQUENCY DYNAMICS AND FAST
FREQUENCY CONTROL IN LOW-INERTIA
GRIDS

INTERVAL-BASED ADAPTIVE INERTIA AND DAMPING CONTROL

This chapter proposes a novel active power controller for converter-based generation. For that purpose, a uniform frequency response model of a generic low-inertia system is developed and the analytical expressions for frequency metrics of interest such as frequency nadir, RoCoF and steady-state frequency deviation are derived. This information is then applied to the control design, where the emulated inertia and damping constants of a VSM are adjusted according to the frequency disturbance and the respective VSM acceleration interval, while keeping the frequency within limits prescribed by the system operator. Furthermore, the sufficient stability conditions for control tuning are determined. A comparative study against the existing approaches in the literature verifies the control effectiveness. The work in this chapter is based on [19, 140].

5.1 INTRODUCTION

The loss of rotational inertia can have devastating effects on system dynamics, with large frequency deviations potentially triggering undesirable events such as load-shedding and large-scale blackouts, as indicated in [141]. However, this study also shows that grid-scale energy storage devices can be employed for providing fast frequency support in isolated systems with high shares of renewables; such support can be incorporated within a control scheme of a grid-forming VSC [62]. Despite numerous approaches in the literature, almost all grid-forming VSC control strategies can be formulated as a VSM (i.e., droop) equivalent, an emulation technique based on a swing equation of a synchronous machine [23, 49, 142] (see Section 2.4). However, a vast majority of such designs assumes an infinite amount of power and energy on the converter's DC side, thus neglecting the dynamical limitations of the capacitor, which might be an issue for real-world applications [143]. This problem was addressed in [144] with a distributed virtual inertia approach that regulates the DC-link voltages such that the capacitors are aggregated into a large unit

for frequency support. However, it is implemented using a basic proportional frequency controller that limits its responsiveness. Such obstacle is usually resolved with inclusion of a derivative control term corresponding to RoCoF measurement. The addition of derivative control for containing excessive frequency excursions has been suggested in several studies [145–147]. In [145], a RoCoF measurement contributes as an input to the traditional droop-like primary frequency control of a wind turbine; [146] proposes a droop controller in the form of a heuristic RoCoF exponential function, while [147] suggests the respective measurement as an input for an optimization-based online tuning of a VSM. Regardless of the employed technique, all aforementioned studies focus solely on the overall frequency improvement and disregard the costs and energy resources required for such regulation.

Motivated by the same approach, a subgroup of so-called *interval-based* controllers emerged [148, 149], where a sign of the trigger signal $\varrho = (\Delta\omega)(d\omega/dt)$ is used to indicate whether the unit is in the *accelerating* or *decelerating* mode. The nature of the mode would then heuristically determine the level of virtual inertia and/or damping in a gain-scheduling fashion. Nonetheless, all concepts mentioned above focus solely on the overall frequency improvement, while disregarding the costs and energy resources required for such regulation. We tackle this issue by proposing an *adaptive* VSM control design that simultaneously keeps the frequency within prescribed limits and minimizes the needed control effort.

The contribution of this work is twofold. Firstly, we derive a Center-of-Inertia (CoI) frequency response model of a simplified low-inertia system that preserves relevant frequency dynamics of conventional and inverter-interfaced generation. The accuracy of the simplified CoI model is validated against the individual frequencies obtained through time-domain simulations of a detailed model developed in Chapter 2. Secondly, an adaptive frequency-constrained VSM controller is proposed using an interval-based approach and the sufficient tuning conditions for ensuring stable system operation are determined. Moreover, the proposed VSM strategy is implemented within a state-of-the-art converter control scheme (see Section 2.7) and compared against the existing concepts in the literature.

The remainder of the chapter is structured as follows. In Section 5.2, the CoI frequency dynamics of a generic low-inertia system are derived analytically. Section 5.3 describes the interval-based adaptive VSM design as well as the existing approaches in the literature. Subsequently, a novel control concept is proposed together with the respective tuning conditions for preserving stability. Section 5.4 showcases the results of time-domain simulation and

compares the methods, whereas Section 5.5 draws the main conclusions and discusses future work.

5.2 FREQUENCY DYNAMICS IN LOW-INERTIA NETWORKS

5.2.1 *Inertial Response and Primary Frequency Control*

The goal of this section is to derive a simplified, but sufficiently accurate, CoI frequency response model of a generic low-inertia system. Note that the complete mathematical formulation throughout the chapter is described in per-unit. For clarity and better understanding of mathematical representation, the index set notation is changed compared to the one introduced in Chapter 2. For similar reasons, the per-unit parameters are represented by uppercase symbols. Moreover, since we work primarily with aggregate (CoI) system parameters in this study, certain parameters of individual units, namely inertia, damping and droop gain constants, are denoted by $(\tilde{\cdot})$.

Let us observe a generic system comprising multiple *traditional* (subscript g) and *converter-interfaced* (subscript c) generators, as depicted in Fig. 5.1. The SG dynamics are described by the swing equation, with $M_g \in \mathbb{R}_{\geq 0}$ and $D_g \in \mathbb{R}_{\geq 0}$ denoting the normalized aggregate inertia and damping constants of the generators:

$$M_g := \frac{\sum_{i \in \mathcal{N}_g} \tilde{M}_{g_i} P_{g_i}}{P_{b_g}}, \quad D_g := \frac{\sum_{i \in \mathcal{N}_g} \tilde{D}_{g_i} P_{g_i}}{P_{b_g}}. \quad (5.1)$$

Here, $\mathcal{N}_g \subset \mathbb{Z}_{>0}$ is the index set of $m = |\mathcal{N}_g|$ traditional synchronous generators, $P_g \in \mathbb{R}_{>0}^m$ is the vector of their nominal powers, $\tilde{M}_g \in \mathbb{R}_{>0}^m$ and $\tilde{D}_g \in \mathbb{R}_{>0}^m$ are the individual SG inertia and damping constants, and $P_{b_g} \in \mathbb{R}_{>0}$ refers to the base power of the generators, i.e., a sum of nominal powers of all connected generation units. The low-order model proposed in [25] is used for modelling the governor droop and turbine dynamics; $T_g \in \mathbb{R}_{>0}^m$ are the turbine time constants, $\tilde{R}_g \in \mathbb{R}_{\geq 0}^m$ and $K_g \in \mathbb{R}_{>0}^m$ are the respective frequency droop and mechanical power gain factors, while $F_g \in \mathbb{R}_{\geq 0}^m$ denotes the fraction of total power generated by the turbines of synchronous machines.

Furthermore, we incorporate the impact of grid-forming converters, as they are the only type of PE-interfaced units providing frequency support [62]. A particular focus is set on droop and VSM-based control schemes, as two of the currently most prevalent frequency control techniques in the literature [142]. As previously described in Section 2.2.4 (see also Appendix B.2), under certain conditions these two system-level controls have equivalent small-

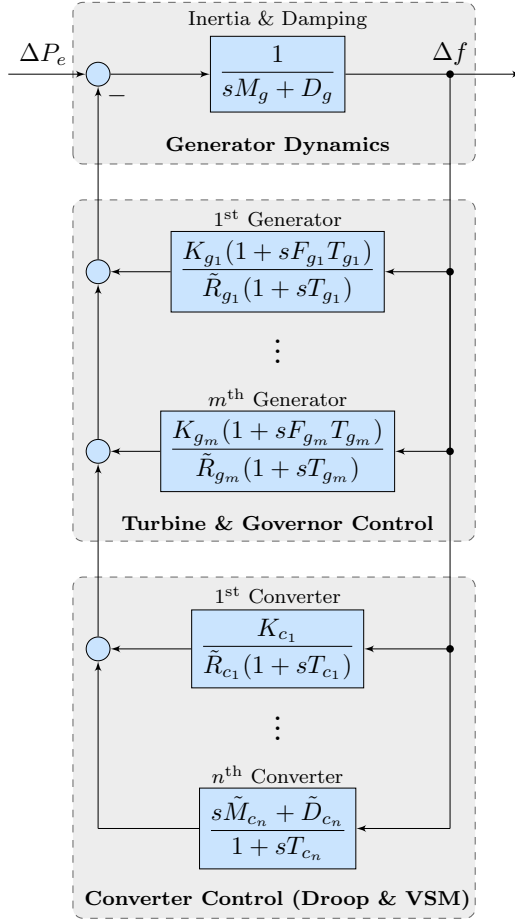


FIGURE 5.1: Uniform system frequency dynamics model.

signal properties in the grid-forming mode of operation. Hence, the index set of grid-forming converters providing either droop ($\mathcal{N}_d \subset \mathbb{Z}_{>0}$, $n_d = |\mathcal{N}_d|$) or VSM ($\mathcal{N}_v \subset \mathbb{Z}_{>0}$, $n_v = |\mathcal{N}_v|$) regulation is represented by $\mathcal{N}_c \subset \mathbb{Z}_{>0}$, where $\mathcal{N}_c = \mathcal{N}_d \cup \mathcal{N}_v$ and $n = n_d + n_v$. In Fig. 5.1, $T_c \in \mathbb{R}_{>0}^n$ is the vector of time constants of converter-based generation, $\tilde{R}_c \in \mathbb{R}_{>0}^{n_d}$ and $K_c \in \mathbb{R}_{>0}^{n_d}$ are the respective vectors of droop and mechanical power gain factors of droop-based VSCs, whereas $\tilde{M}_c \in \mathbb{R}_{\geq 0}^{n_v}$ and $\tilde{D}_c \in \mathbb{R}_{>0}^{n_v}$ denote the normalized virtual inertia and damping constants of VSM-controlled converters.

5.2.2 Analytic Formulation of Frequency Metrics

Based on the control diagram in Fig. 5.1, we can now derive a transfer function $G(s)$ of general-order system dynamics from the electrical power disturbance input ($\Delta P_e \in \mathbb{R}$) to the CoI frequency deviation output ($\Delta f \in \mathbb{R}$), as follows:

$$G(s) = \frac{\Delta f}{\Delta P_e} = \left(\underbrace{\left(sM_g + D_g + \sum_{i \in \mathcal{N}_g} \frac{K_{g_i}(1 + sF_{g_i}T_{g_i})}{\tilde{R}_{g_i}(1 + sT_{g_i})} \right)}_{\text{traditional synchronous generators}} + \underbrace{\sum_{j \in \mathcal{N}_d} \frac{K_{c_j}}{\tilde{R}_{c_j}(1 + sT_{c_j})}}_{\text{droop-based converters}} + \underbrace{\sum_{k \in \mathcal{N}_v} \frac{s\tilde{M}_{c_k} + \tilde{D}_{c_k}}{1 + sT_{c_k}}}_{\text{VSM-based converters}} \right)^{-1}. \quad (5.2)$$

The sensitivity of the frequency response to governor parameters can be computed through means of modal analysis or linear curve-fitting. The latter approach was employed in [150] on a simplified, low-order frequency model proposed in [25]. It was shown that the frequency nadir of the traditional SG-based system is the least sensitive to inertia and governor time constants. Nevertheless, the time instance of frequency nadir and the rate of frequency decay are highly sensitive to inertia, as will be shown later. Hence, assuming equal time constants $T_{g_i} := T, \forall i \in \mathcal{N}_g$ of all synchronous machines is a reasonable simplification. Additionally, the inverter time constants are approximately 2-3 orders of magnitude lower than the ones of synchronous generators, which justifies the approximation $T \gg T_{c_l} \approx 0, \forall l \in \mathcal{N}_c$. Now we can transform (5.2) into

$$G(s) = \frac{1}{MT} \frac{1 + sT}{s^2 + 2\zeta\omega_n s + \omega_n^2}, \quad (5.3)$$

where the natural frequency $\omega_n \in \mathbb{R}_{>0}$ and damping ratio $\zeta \in \mathbb{R}_{>0}$ are described by

$$\omega_n := \sqrt{\frac{D + R_g}{MT}}, \quad \zeta := \frac{M + T(D + F_g)}{2\sqrt{MT(D + R_g)}}, \quad (5.4)$$

and the respective aggregate parameters are defined as follows:

$$M := \frac{M_g P_{b_g} + M_c P_{b_c}}{P_{b_g} + P_{b_c}}, \quad D := \frac{D_g P_{b_g} + D_c P_{b_c} + R_c P_{b_c}}{P_{b_g} + P_{b_c}}, \quad (5.5a)$$

$$F_g := \sum_{i \in \mathcal{N}_g} \frac{K_{g_i} F_{g_i} P_{g_i}}{\tilde{R}_{g_i} P_{b_g}}, \quad R_g := \sum_{i \in \mathcal{N}_g} \frac{K_{g_i} P_{g_i}}{\tilde{R}_{g_i} P_{b_g}}, \quad (5.5b)$$

$$R_c := \sum_{j \in \mathcal{N}_d} \frac{K_{c_j} P_{c_j}}{\tilde{R}_{c_j} P_{b_c}}, \quad M_c := \sum_{k \in \mathcal{N}_v} \tilde{M}_{c_k} \frac{P_{c_k}}{P_{b_c}}, \quad D_c := \sum_{k \in \mathcal{N}_v} \tilde{D}_{c_k} \frac{P_{c_k}}{P_{b_c}}. \quad (5.5c)$$

It should be noted that the P_{g_i}/P_{b_g} , P_{c_j}/P_{b_c} and P_{c_k}/P_{b_c} terms in (5.5) come from per-unit normalization, with $P_{b_c} \in \mathbb{R}_{>0}$ being the base power of converter-interfaced generation units. The expressions in (5.5a) indicate that the equivalent inertia and damping constants $M_c \in \mathbb{R}_{>0}$ and $D_c \in \mathbb{R}_{>0}$ as well as the aggregate droop $R_c \in \mathbb{R}_{>0}$ contribute proportionally to the overall inertia and damping of the system $M \in \mathbb{R}_{>0}$ and $D \in \mathbb{R}_{>0}$, respectively. Interestingly enough, (5.5c) reveals that R_c is inversely proportional to individual VSC droop gains \tilde{R}_{c_j} , suggesting that the lower frequency droop factors would lead to higher damping in the system. Needless to say, the opposite implies to active power droop applications.

Assuming a stepwise disturbance in the electrical power $\Delta P_e(s) = -\Delta P/s$, the time-domain expression for frequency deviation can be derived as

$$\Delta f(t) = -\frac{\Delta P}{MT\omega_n^2} - \frac{\Delta P}{M\omega_d} e^{-\zeta\omega_n t} \left(\sin(\omega_d t) - \frac{1}{\omega_n T} \sin(\omega_d t + \phi) \right), \quad (5.6)$$

with the introduction of new variables

$$\omega_d := \omega_n \sqrt{1 - \zeta^2}, \quad \phi := \sin^{-1} \left(\sqrt{1 - \zeta^2} \right). \quad (5.7)$$

The time instance $t_m \in \mathbb{R}_{>0}$ of frequency nadir can be determined by observing the RoCoF, i.e., finding the instance at which the frequency derivative is equal to zero. Taking a first derivative of the right-hand side in (5.6) and solving $\Delta \dot{f}(t_m) = 0$ for t_m results in an infinite number of solutions of the form

$$t_m^{(k)} = \frac{1}{\omega_d} \tan^{-1} \left(\frac{\omega_d}{\zeta\omega_n - T^{-1}} \right) + \frac{k\pi}{\omega_d}, \quad (5.8)$$

where $k \in \mathbb{Z}_{\geq 0}$. Substituting $t_m^{(k)}$ into (5.6) and conducting a set of trivial mathematical transformations yields the analytical expression for every local frequency extremum

$$\Delta f_{\max}^{(k)} = -\frac{\Delta P}{D + R_g} \left(1 + (-1)^k \sqrt{\frac{T(R_g - F_g)}{M}} e^{-\zeta\omega_n t_m^{(k)}} \right). \quad (5.9)$$

Since frequency nadir corresponds to the first and largest deviation (assuming a stable, underdamped system), we will consider $\Delta f_{\max} := \Delta f_{\max}^{(0)}$ throughout this thesis. The maximum RoCoF occurs at the instance of the disturbance $t_r = 0^+$ and is equal to

$$\dot{f}_{\max} = \dot{f}(t_r) = -\frac{\Delta P}{M}, \quad (5.10)$$

whereas the steady-state frequency deviation settles at

$$\Delta f_{\text{ss}} = -\frac{\Delta P}{D + R_g}. \quad (5.11)$$

By analyzing expressions (5.9)-(5.11) we can conclude that the frequency metrics of interest (frequency nadir, RoCoF and steady-state frequency deviation) are directly dependent on total inertia and damping constants, all of which can be regulated via droop and VSM control gains: RoCoF and steady-state deviation explicitly through $\dot{f}_{\max} \sim M^{-1}$ and $\Delta f_{\text{ss}} \sim (D + R_g)^{-1}$ respectively, and nadir through a highly nonlinear function $\Delta f_{\max} = F_{\text{nadir}}(M, D, R_g)$ given in (5.9). The system operators enforce strict requirements for all aforementioned aspects of frequency response in order to preserve system stability and avoid unwanted activation of load shedding and tripping of protection relays [151]. Having that in mind, it becomes clear that by actively controlling converter control gains one can effectively preserve frequency within prescribed bounds. This notion will be applied throughout several chapters of the thesis, including this one.

5.3 INTERVAL-BASED ADAPTIVE CONTROL DESIGN

In this section, we explain general concepts of the interval-based, adaptive VSM method. Moreover, the existing control approaches in the literature are discussed and a new controller with an improved performance is proposed, together with the sufficient stability conditions for control tuning.

5.3.1 Theoretical Concept

Let us observe a frequency response to a step disturbance described in (5.6) and illustrated in Fig 5.2. For brevity, we shall denote frequency deviation by $\omega := \Delta f$ in the remainder of this chapter. The system response consists of alternating *accelerating* and *decelerating* intervals, similar to the power-angle

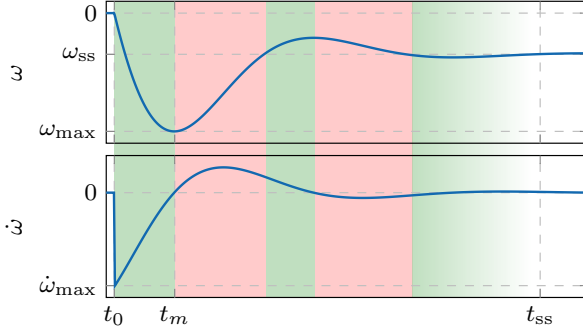


FIGURE 5.2: Frequency response of a traditional power system. Shaded areas indicate the respective *accelerating* (green) and *decelerating* (red) intervals of the response.

curve of a typical synchronous machine. These phases are determined by the sign of the product $\varrho \in \mathbb{R}$ defined by

$$\varrho(t) := \underbrace{(\omega(t) - \omega_{\text{ss}})}_{\Delta\omega(t)} \dot{\omega}(t) \begin{cases} > 0 & \mapsto \text{accelerating phase,} \\ < 0 & \mapsto \text{decelerating phase,} \end{cases} \quad (5.12)$$

which suggests that the same direction of frequency deviation and RoCoF would lead to an acceleration of the virtual machine and vice versa. Therefore, signal ϱ can be employed as a control input for adaptive regulation of the converter control gains, more specifically M_c and D_c for converters employing VSM regulation and R_c for droop-controlled converters. For simplicity, we will solely focus on the former control strategy in this study.

5.3.2 Existing Control Schemes

The beneficial aspects of the interval approach have first been emphasized in [148], with the proposition of a *bang-bang* (\mathcal{K}_{BB}) inertia control strategy. This approach is based on alternating the inertia constant of the VSM between two discrete values: the high value $\bar{M}_c \in \mathbb{R}_{>0}$ and the low value $\underline{M}_c \in \mathbb{R}_{\geq 0}$, while preserving the default pre-disturbance damping $D_c^* \in \mathbb{R}_{>0}$:

$$M_c(t) := \begin{cases} \bar{M}_c, & \forall t : \varrho(t) > 0, \\ \underline{M}_c, & \forall t : \varrho(t) \leq 0, \end{cases} \quad D_c(t) := D_c^*. \quad (5.13a)$$

However, a single degree of freedom restricts the controller's performance and the bang-bang characteristic leads to an oscillatory behavior. These issues have been addressed in [149], which extends the concept by including the adaptive damping and a more practical control algorithm. Governed by the aforementioned notions of $\dot{\omega} \sim M^{-1}$ and $\Delta\omega \sim D^{-1}$, the so-called *self-adaptive* inertia and damping controller (\mathcal{K}_{SA}) improves the previously proposed \mathcal{K}_{BB} control by adjusting M_c and D_c proportionally to the respective RoCoF and frequency deviation:

$$M_c(t) := \begin{cases} M_c^* + k_M |\dot{\omega}(t)|, & \forall t : \varrho(t) > 0 \wedge |\dot{\omega}(t)| > \varepsilon_M, \\ M_c^*, & \forall t : \varrho(t) \leq 0 \vee |\dot{\omega}(t)| \leq \varepsilon_M, \end{cases} \quad (5.14a)$$

$$D_c(t) := \begin{cases} D_c^* + k_D |\Delta\omega(t)|, & \forall t : \varrho(t) \leq 0 \wedge |\dot{\omega}(t)| > \varepsilon_D, \\ D_c^*, & \forall t : \varrho(t) > 0 \vee |\dot{\omega}(t)| \leq \varepsilon_D, \end{cases} \quad (5.14b)$$

with $k_M \in \mathbb{R}$ and $k_D \in \mathbb{R}$ being the virtual inertia and damping feedback gains, and $M_c^* \in \mathbb{R}_{>0}$ and $D_c^* \in \mathbb{R}_{>0}$ denoting the inertia and damping constants prior to the disturbance. Thresholds $\varepsilon_M \in \mathbb{R}_{\geq 0}$ and $\varepsilon_D \in \mathbb{R}_{\geq 0}$ are used to cancel out the adaptive components as soon as the system approaches equilibrium, thus preventing unwanted oscillations and instability. Nonetheless, while drastically better than the bang-bang approach, this strategy still preserves several inherent flaws such as: (i) the individual adaptive control of either inertia or damping, which is suboptimal for regulating the frequency nadir in (5.9); and (ii) a discontinuous response resulting from a combination of the control scheme and a RoCoF-based threshold trigger.

5.3.3 Optimal Frequency-Constrained Control (\mathcal{K}_{OFC})

In this work, we improve the existing strategies by simultaneously regulating the VSM control gains, justified by the fact that both inertia and damping contribute to the limitation of frequency nadir during a disturbance. Furthermore, we aim at minimizing the necessary control effort, more precisely the energy utilization of the associated DC-side buffer, in order to keep the frequency within prescribed ENTSO-E thresholds $\omega_{\text{lim}} \in \mathbb{R}_{>0}$ and $\dot{\omega}_{\text{lim}} \in \mathbb{R}_{>0}$ [152].

This is achieved by employing a gain-scheduling approach, where the optimal VSM feedback gains $(\Delta M_c^*, \Delta D_c^*)$ for the first *accelerating* phase are selected based on the measured disturbance ΔP , with $T_c \in \mathbb{R}_{>0}$ being a given time constant of the virtual machine. A detailed iterative procedure

Algorithm 1 Iterative computation of optimal control gains in (5.16)

- 1: Set $k = 0$
 - 2: Initialize the algorithm $\triangleright M_c^{(0)} = -\Delta P / \dot{\omega}_{\text{lim}}, D_c^{(0)} = M_c^{(0)} / T_c$
 - 3: **while** $\omega_{\text{max}}^{(k)} < \omega_{\text{lim}}$ **do**
 - 4: $k = k + 1$
 - 5: Update frequency nadir threshold in (5.9) $\triangleright \omega_{\text{max}}^{(k)}$
 - 6: Apply marginal gain increase $\triangleright M_c^{(k)} = M_c^{(k-1)} + \delta M_c$
 $\triangleright D_c^{(k)} = D_c^{(k-1)} + \delta D_c$
 - 7: **end while**
 - 8: Return $\Delta M_c^* = M_c^{(k)} - M_c^*, \Delta D_c^* = D_c^{(k)} - D_c^*$
-

is given in Algorithm 1. Subsequently, during the *decelerating* interval, the adaptive inertia component is neutralized whereas the adaptive damping is set to decay with time as

$$\Delta D_c(t) := \frac{\Delta \omega(t)}{\omega_{\text{max}} - \omega_{\text{ss}}} \Delta D_c^* + k_D \dot{\omega}(t), \quad (5.15)$$

and is limited within a range $\Delta D_c(t) \in [-D_c^*, \Delta D_c^*]$ such that the total damping $D_c(t)$ preserves a positive decaying trend throughout the whole interval. Finally, the proposed adaptive VSM strategy is of the form:

$$M_c(t) := \begin{cases} M_c^* + \Delta M_c^*, & \forall t : \varrho(t) > 0 \wedge \mathcal{C}(\dot{\omega}(t), \ddot{\omega}(t)), \\ M_c^*, & \forall t : \varrho(t) \leq 0 \vee \neg \mathcal{C}(\dot{\omega}(t), \ddot{\omega}(t)), \end{cases} \quad (5.16a)$$

$$D_c(t) := \begin{cases} D_c^* + \Delta D_c^*, & \forall t : \varrho(t) > 0 \wedge \mathcal{C}(\dot{\omega}(t), \ddot{\omega}(t)), \\ D_c^* + \Delta D_c(t), & \forall t : \varrho(t) \leq 0 \vee \neg \mathcal{C}(\dot{\omega}(t), \ddot{\omega}(t)), \end{cases} \quad (5.16b)$$

with

$$\mathcal{C}(\dot{\omega}(t), \ddot{\omega}(t)) := |\dot{\omega}(t)| > \varepsilon_1 \wedge |\ddot{\omega}(t)| > \varepsilon_2 \quad (5.17)$$

representing the logical threshold based on RoCoF and its first derivative that ensures a smooth control transition. Although obtaining an accurate $\ddot{\omega}(t)$ measurement introduces time delay in the controller's response, it does not hinder the control performance as both maximum RoCoF and frequency nadir occur before the respective trigger activation. Nevertheless, it should be pointed out that the logical circuitry for such switching might pose an obstacle for real-world hardware applications and should be considered a drawback of the proposed approach. This issue is addressed in Chapter 6.

5.3.4 Stability Assessment

In this section, we focus on deriving the sufficient stability conditions for the proposed adaptive VSM controller \mathcal{K}_{OFC} .

Proposition 5.3.1. *Consider the second-order system in (5.3). Assume that the virtual inertia and damping gains of VSM-based converters can be controlled according to the law given by (5.16). The asymptotic stability of the system is guaranteed if the following tuning conditions are included in Algorithm 1:*

$$\Delta M_c^* \leq 2M + 2(D + F_g)T, \quad (5.18a)$$

$$\Delta D_c^* \geq 2\frac{M}{T} - 2(D + F_g). \quad (5.18b)$$

Proof. The proof is given in Appendix A.2. □□□

To validate the theoretical analysis, the energy trajectory of the Lyapunov function (see Appendix A.2 for more details) is analyzed and compared between the adaptive controller \mathcal{K}_{OFC} and the traditional non-adaptive VSM control (denoted hereinafter by \mathcal{K}_0). The simulation results in Fig. 5.3 confirm that $V(\omega, \dot{\omega})$ remains positive, with both energy trajectories preserving a decaying trend throughout the disturbance period and converging to the same equilibrium. Note that the inherent switching instances of \mathcal{K}_{OFC} can be clearly seen in Fig. 5.3. Nevertheless, the effectiveness of the adaptive controller is reflected in the shorter energy trajectory compared to the non-adaptive method.

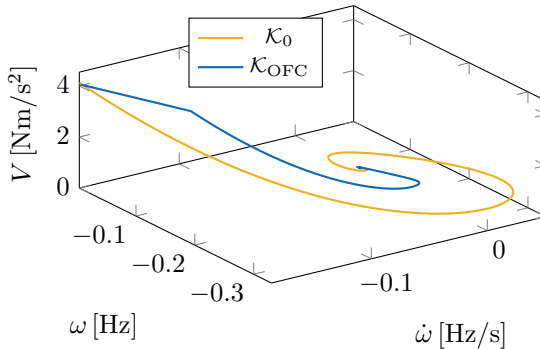


FIGURE 5.3: Transient energy trajectory after a step disturbance.

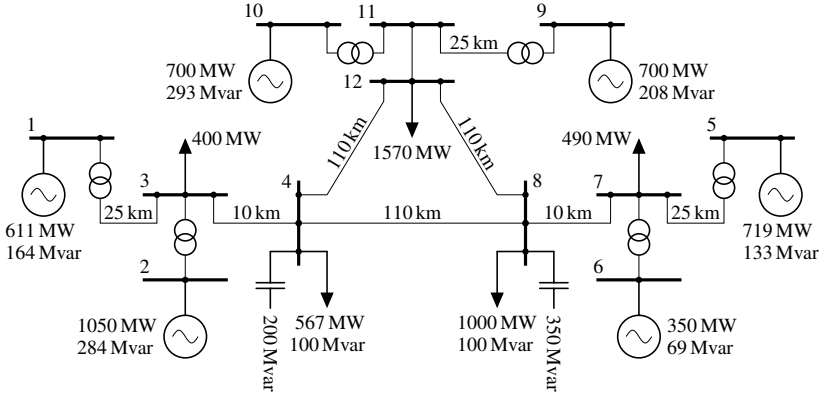


FIGURE 5.4: Topology of the investigated three-area test system; the converter-based generation is placed at nodes 2, 6 and 10.

5.4 MODEL VALIDATION AND CONTROL PERFORMANCE

5.4.1 Frequency Model Validation

As proof of concept, we test the proposed frequency model from Section 5.2 on a modified version of the well-known Kundur two-area system, with an addition of one more area forming a triangle illustrated in Fig. 5.4. The modified system comprises six generators, with the network, generation and load parameters adapted from the original two-area system in [26]. The same test case has been previously used in other relevant studies on placement and effects of inertia and damping in low-inertia systems [140, 153, 154]. Furthermore, we consider a scenario where three traditional generators at nodes 2, 6 and 10 are replaced by converter-interfaced units.

In order to validate the analytical expressions from Section 5.2.2, a 350 MW active power load increase at node 12 is simulated using an EMT model from Chapter 2 developed in MATLAB Simulink [94]. The obtained individual generator frequencies are compared against the analytical CoI frequency expression (5.6). The resulting response depicted in Fig. 5.5 clearly verifies the accuracy of the proposed formulation, with a negligible mismatch being a consequence of the time constant approximation $T \gg T_{c_l} \approx 0, \forall l \in \mathcal{N}_c$. Understandably, the fast swings arising from frequency oscillations of individual generators cannot be captured using a CoI-based frequency model.

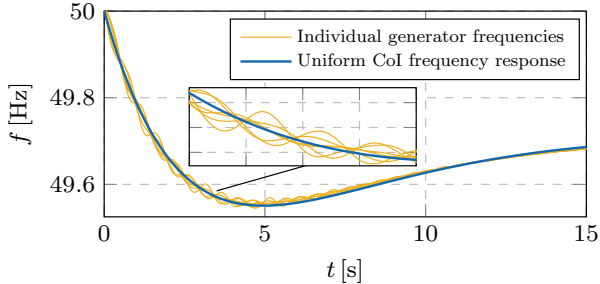


FIGURE 5.5: Frequency response after a 350 MW step increase in load.

Nonetheless, it only leads to a marginal under-approximation of frequency nadir and does not hinder the effectiveness of the reduced-order model.

Having in mind that the vast majority of studies and control design applications are done offline, a risk of inadequate system information pertains to overall error propagation, especially regarding the expressions for frequency metrics in (5.9)-(5.11). This potential issue is investigated using a rigorous parametric sensitivity analysis, with all relevant unit parameters arbitrarily selected from a wide range around the nominal values given in Table 5.1. We study a generic large-scale system consisted of 1000 synchronous and inverter-based generators, and consider 10^5 different configuration scenarios. In each scenario, a set of 100 generator units is randomly removed in order to account for the generators that could potentially be offline. Subsequently, the frequency nadir is analytically computed and compared to its respective value in the full system (i.e., a system with all 1000 units online). The distribution of the computational error shown in Fig. 5.6 verifies the robustness of the

Parameter	Symbol	Range
Nominal active power	P_g/P_c	[100 – 2000] MW
Frequency droop control gain	\tilde{R}_g/\tilde{R}_c	[1 – 5] %
Normalized inertia constant	\tilde{M}_g/\tilde{M}_c	[1 – 20] s
Normalized damping constant	\tilde{D}_g/\tilde{D}_c	[1 – 30] p.u.
Mechanical power gain factor	K_g/K_c	[0.85 – 1] p.u.
Turbine power fraction factor	F_g	[0.05 – 0.2] p.u.
Turbine time constant	T_g	[1 – 10] s

TABLE 5.1: Parameters for sensitivity analysis.

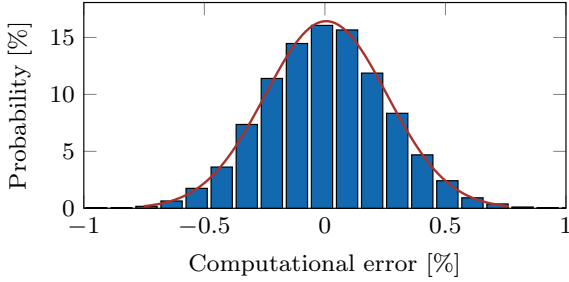


FIGURE 5.6: Error distribution of frequency nadir computation.

modeling approach, as the worst-case mismatch is kept below 1%, and 95% of the scenario set is within a 0.5% error range. In order to account for any potential model discrepancies, a small margin corresponding to the maximum computational error could be added to Δf_{\max} , \dot{f}_{\max} and Δf_{ss} terms in (5.9)-(5.11), such that the frequency response of the system always meets the predefined criteria.

5.4.2 Control Performance

The control performance is investigated on the same three-area test system, with the thresholds for frequency nadir and RoCoF set at $\Delta f_{\text{lim}} = 0.2$ Hz, $\dot{f}_{\text{lim}} = 1$ Hz/s, respectively¹. A noticeably low nadir limit is enforced in order to provide a reasonable comparison between different control schemes, as tuning of \mathcal{K}_{BB} and \mathcal{K}_{SA} has been adapted from the respective studies in [148] and [149]. In contrast to the previous analysis, a 250 MW load increase at node 12 is considered as a disturbance. For clarity and better understanding of the individual control designs, the majority of the analysis in this section focuses on the CoI frequency response.

The system response under different VSM control designs is depicted in Fig. 5.7. Understandably, the investigated contingency leads to unacceptable frequency excursion under the open-loop control \mathcal{K}_0 , indicated by the frequency nadir of 0.33 Hz. While \mathcal{K}_{BB} and \mathcal{K}_{SA} reduce this deviation, it is still kept above the admissible threshold. On the other hand, \mathcal{K}_{OFC} ensures that the frequency nadir is preserved within given bounds and provides the smoothest response; \mathcal{K}_{BB} has a high settling time due to insufficient damping, whereas \mathcal{K}_{SA} is characterized by a discontinuity at the instance of frequency

¹ Corresponding to the per-unit counterparts $\omega_{\text{lim}} = 0.004$ p.u., $\dot{\omega}_{\text{lim}} = 0.02$ p.u. in Section 5.3.

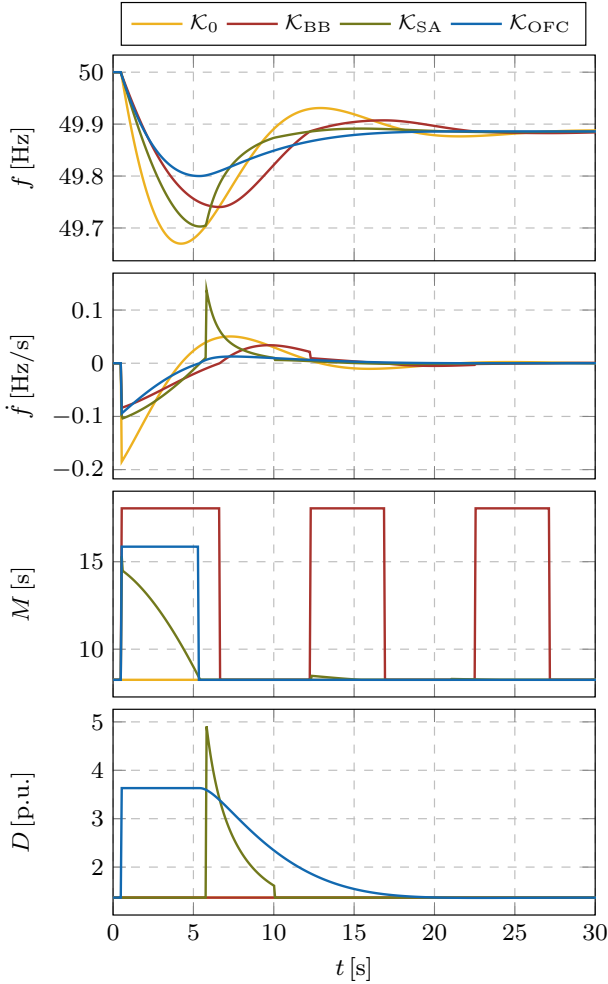


FIGURE 5.7: system response under different VSM control designs: (i) CoI frequency; (ii) CoI RoCoF; (iii) aggregate inertia; and (iv) aggregate damping.

nadir. Moreover, the latter designs are inherently suboptimal, as they presume independent and inefficient temporal regulation of either inertia or damping. More precisely, \mathcal{K}_{BB} tends to activate high levels of inertia at wrong time instances leading to a sluggish response, whereas \mathcal{K}_{SA} control strategy increases damping when ω is at its peak, resulting in the aforementioned

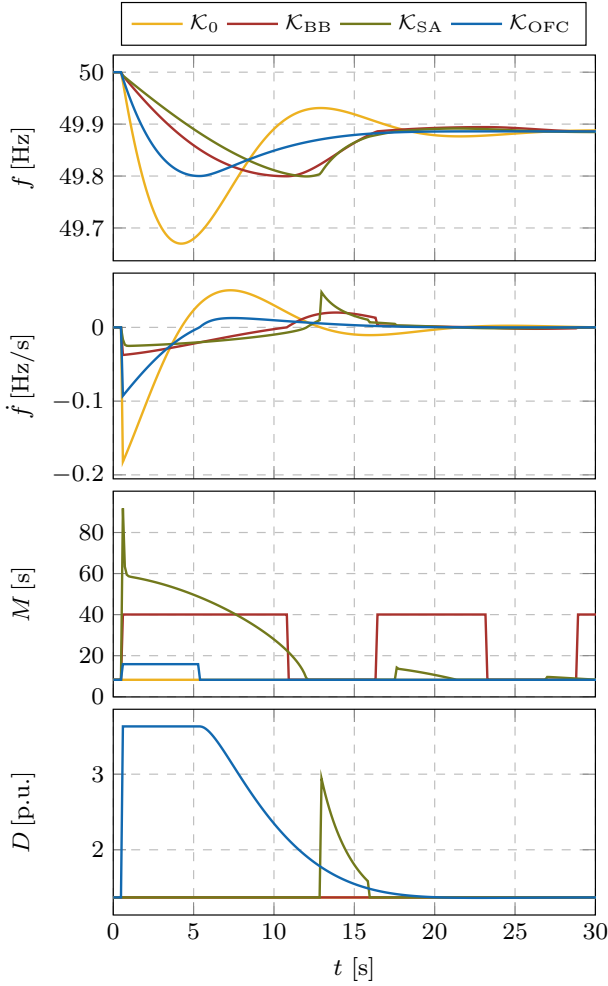


FIGURE 5.8: system response under different VSM control designs, retuned such that they meet the prescribed ENTSO-E criteria: (i) CoI frequency; (ii) CoI RoCoF; (iii) aggregate inertia; and (iv) aggregate damping.

power spike. In contrast, the proposed VSM approach immediately employs both the proportional (D) and derivative (M) control gains for preserving frequency within the given bounds. The efficiency of such approach can be observed in Fig. 5.8, with the inertia gains of \mathcal{K}_{BB} and \mathcal{K}_{SA} retuned such that $\Delta f_{\max} = 0.2$ Hz. As a result, the swing time constant $T = M/D$ increases,

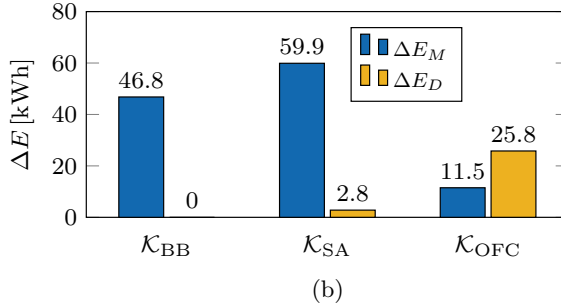
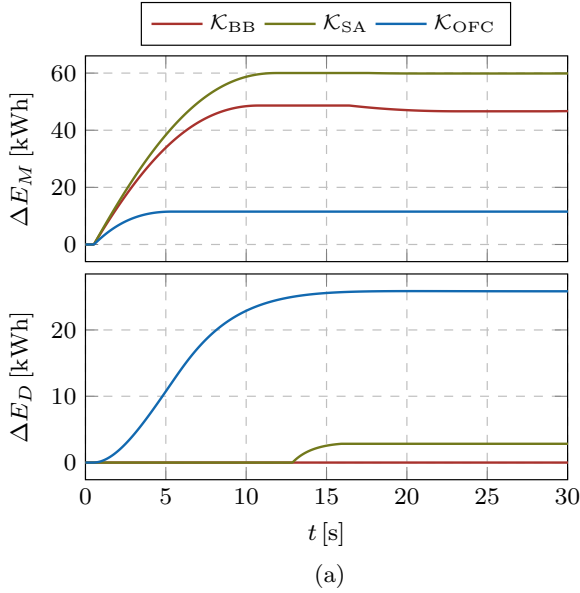


FIGURE 5.9: Energy utilization for containing the frequency within limits: (a) activation of individual control components over time; and (b) total contribution of additional control effort.

which makes up for a very high control effort and an unacceptably slow response.

Some insightful conclusions regarding the performance of the described control schemes can be drawn from the energy content of the control effort presented in Fig. 5.9, with respective energy terms computed as $\Delta E_M = \int \Delta M \dot{\omega} dt$ and $\Delta E_D = \int \Delta D \omega dt$. First of all, it justifies the proposed concept of compensating inertia with damping during high RoCoF instances, since the

ΔE_M term would have a predominant impact on the total energy utilization. Moreover, it can be observed that \mathcal{K}_{OFC} reduces the total energy of the adaptive control by 20% and 40% compared to \mathcal{K}_{BB} and \mathcal{K}_{SA} , respectively. In fact, it predominantly employs the proportional droop-like response, with ΔE_D contributing to 70% of the total energy. The activation of individual control components in Fig. 5.9a reveals the distinctive nature of the three algorithms. The existing interval-based controllers are restricted solely to adaptive inertia as a mean of frequency regulation during the initial response, which directly acts on RoCoF through explicit $M\dot{\omega}$ term. The effectiveness of such approach is however limited, since the impact of inertia decays over time, together with $\dot{\omega}$. As a result, the inertia gain is overdimensioned, leading to high depletion of energy. In contrast, the combined effort of inertia and damping under the \mathcal{K}_{OFC} control strategy achieves a qualitatively similar system performance with a more natural frequency response and less energy consumption. We therefore conclude that \mathcal{K}_{OFC} is the most effective and practical control approach of the three for adaptive VSM design.

Furthermore, the proposed controller is incorporated into a detailed EMT model (see Chapter 2 for more detail) of the three-area test system by assigning the adaptive VSM capabilities to all three converter-interfaced generators. The control effort is split between units proportionally to their installed power capacity, whereas the iterative computation of optimal control gains in Algorithm 1 is completed offline for a wide range of disturbance magnitudes and subsequently assigned to each VSC as a look-up table in MATLAB. Simulation results depicted in Fig (5.10) showcase a similar performance as the CoI model. However, an important distinction can be observed in the evolution of the inertia gain M , with the ripple occurring at the switching instance between the two control intervals. This is for the most part a consequence of the switching trigger $\mathcal{C}(\dot{\omega}(t), \ddot{\omega}(t))$ defined by (5.17), suggesting that a further improvement might be needed; either by optimizing the values of ε_1 and ε_2 or by completely redesigning the implemented circuit logic.

5.5 CONCLUSION

The presented chapter introduces a decentralized VSM concept for converter-interfaced DGs in power systems with high shares of renewable resources. Using an interval-based approach, the emulated inertia and damping constants are adaptively adjusted according to the frequency disturbance in the system, while simultaneously preserving stable operation and frequency

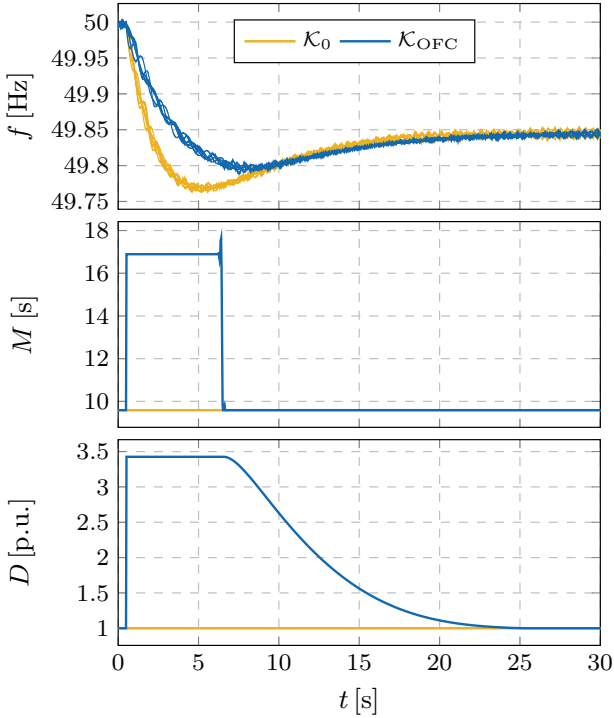


FIGURE 5.10: Time-domain response with and without adaptive control when applied to a detailed EMT model: (i) individual generator frequencies; (ii) aggregate inertia; and (iii) aggregate damping.

within prescribed limits. The proposed control design is integrated into a state-of-the-art converter control scheme and compared against the existing VSM approaches, showcasing a superior performance in terms of frequency regulation and energy utilization. It is verified that the simultaneous control of both inertia and damping throughout the course of system response achieves a drastically smoother frequency characteristic at a lower cost.

The future work will focus on improving the optimality of the control design, as well as extending the methodology onto 100% inverter-based power systems. In particular, a somewhat heuristic nature of the presented controller could potentially be improved upon through more advanced control applications. Moreover, the need for sensitive switching circuit might pose an obstacle for real-world implementation. These and other challenges are tackled in Chapter 6.

LQR-BASED ADAPTIVE VIRTUAL SYNCHRONOUS MACHINE

This chapter presents a novel VSM controller for converter-interfaced generation in power systems with high shares of renewable energy. Using an optimization technique based on a Linear-Quadratic Regulator (LQR), the optimal state feedback gains are determined to adaptively adjust the emulated inertia and damping constants according to the frequency disturbance in the system, while simultaneously preserving a trade-off between the critical frequency limits and the required control effort. Two adaptive control designs are proposed and validated through time-domain simulations, showcasing a drastically improved performance compared to traditional VSM control. The work in this chapter is based on [140, 155].

6.1 INTRODUCTION

The work presented in this chapter builds on the study previously conducted in Chapter 5. Hence, the underlying problems pertaining to frequency control in low-inertia systems, as well as the relevant existing literature addressing the topic, have already been pointed out and can be found in Section 5.1. In particular, the goal is to design an adaptive, local VSM controller for converter-interfaced DGs in PE-dominated power systems that ensures reliable system operation in terms of frequency dynamics. While the adaptive VSM methods based on the interval stage of the post-fault response (i.e., the acceleration mode of the VSM) in [148, 149] address the topic, they have inherent design flaws and suboptimal performance (see Section 5.3). The approach proposed in Chapter 5 resolves some of the issues and showcases improvements both in terms of frequency response and depletion of energy on the converter's DC side. This stems from a more balanced utilization of both control gains (i.e., virtual inertia and virtual damping), guided by the notion of minimizing the control effort and energy resources required for preserving frequency within prescribed bounds. However, similarly to [148, 149], the given controller is mostly based on heuristics and therefore prone to error and suboptimal performance under different grid conditions. Moreover, due to the interval characteristic of

the algorithm, the transition between intervals requires complex switching sequences and could experience overshoots during transients.

In contrast, this chapter focuses on improving the “optimality” of the adaptive control design and addressing the aforementioned drawbacks of the interval-based methods. The problem was first tackled in [155] with an LQR-based adaptive VSM controller that adjusts the virtual inertia gain to achieve a trade-off between the two objectives, namely the frequency performance and the control effort. However, it was implemented on a simplified single-inverter test case and the adaptive damping capabilities were not taken into account. This study extends the work in [155] in several directions by: (i) employing the uniform frequency dynamics model from Section 5.2; (ii) including adaptive damping and proposing two novel LQR-based control strategies; (iii) providing a formulation for decentralized multi-inverter control scheme; and (iv) incorporating controllers into a detailed EMT model and verifying the theoretical concepts through time-domain simulations.

The remainder of the chapter is structured as follows. Section 6.2 describes the adaptive VSM formulation and proposes two novel control designs. Section 6.3 discusses means of control implementation, parametrization and multi-inverter application, as well as the sufficient control tuning conditions for stable operation. Finally, Section 6.4 showcases the simulation results and compares the methods, whereas Section 6.5 draws the main conclusions and discusses future work.

6.2 THEORETICAL CONCEPT AND CONTROL DESIGN

6.2.1 *Nonlinear State Feedback Model*

Let us recall the uniform frequency model and its respective notation from Chapter 5, in particular the transfer function (5.3) of the form

$$G(s) = \frac{\Delta f}{\Delta P_e} = \frac{1}{MT} \frac{1 + sT}{s^2 + 2\zeta\omega_n s + \omega_n^2}. \quad (6.1)$$

As in the previous chapter, we shall denote frequency deviation by $\omega := \Delta f$ throughout this study. After the active power disturbance $\Delta P_e = -\Delta P/s$ has been applied, $\Delta P \in \mathbb{R}$ can be considered a constant on the interval $t \in [0^+, +\infty)$, thus transforming (6.1) into

$$\ddot{\omega} = -2\zeta\omega_n \dot{\omega} - \omega_n^2 \omega + \frac{\Delta P}{MT}. \quad (6.2)$$

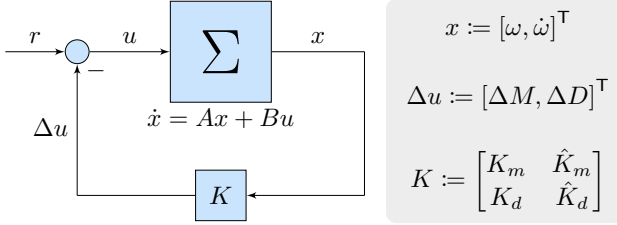


FIGURE 6.1: State feedback control for adaptive VSM approach.

Combining (5.4) and (6.2) yields a state-space representation

$$\begin{bmatrix} \dot{\omega} \\ \dot{\omega} \end{bmatrix} = \begin{bmatrix} 0 & I \\ -\frac{D+R_g}{MT} & -\left(\frac{D+F_g}{M} + \frac{1}{T}\right) \end{bmatrix} \begin{bmatrix} \omega \\ \dot{\omega} \end{bmatrix} + \begin{bmatrix} 0 \\ \frac{\Delta P}{TM} \end{bmatrix}, \quad (6.3)$$

with $x = (\omega, \dot{\omega}) \in \mathbb{R}^2$ being the state vector and $x_0 = (0, \dot{\omega}(0^+)) \in \mathbb{R}^2$ denoting the respective initial conditions. Note that the state vector represents the frequency nadir and RoCoF of the CoI response.

It was previously suggested in Section 5.2 that the frequency metrics of interest can be effectively kept within predefined bounds by actively regulating the aggregate inertia and damping of the system. Guided by this notion, let us consider a system depicted in Fig. 6.1 with the addition of state feedback in (6.3). More precisely, the normalized inertia and damping constants of the system are adjusted through a full state feedback control of the form

$$\underbrace{\begin{bmatrix} M \\ D \end{bmatrix}}_u = \underbrace{\begin{bmatrix} M^* \\ D^* \end{bmatrix}}_{u^*} + \underbrace{\begin{bmatrix} \Delta M \\ \Delta D \end{bmatrix}}_{\Delta u} = \begin{bmatrix} M^* \\ D^* \end{bmatrix} - \underbrace{\begin{bmatrix} K_m & \hat{K}_m \\ K_d & \hat{K}_d \end{bmatrix}}_K \underbrace{\begin{bmatrix} \omega \\ \dot{\omega} \end{bmatrix}}_x, \quad (6.4)$$

where $M^* \in \mathbb{R}_{>0}$ and $D^* \in \mathbb{R}_{>0}$ denote the total inertia and damping constants of the system before the disturbance, and $K_M := (K_m, \hat{K}_m) \in \mathbb{R}^2$ and $K_D := (K_d, \hat{K}_d) \in \mathbb{R}^2$ represent the proportional feedback control gains for inertia and damping, respectively. The steady-state equilibrium of such system can be easily derived from (6.3)-(6.4) by solving $\dot{x} = 0_2$ for x , which yields a solution $x_{ss} := (\omega_{ss}, \dot{\omega}_{ss}) = \left(\frac{\Delta P}{D^* + R_g}, 0\right)$.

The main objective of this study is to obtain a control gain matrix $K := [K_M, K_D]^\top \in \mathbb{R}^{2 \times 2}$ that would guarantee an optimal balance between the frequency regulation and the required energy use through adaptive inertia and damping control. Such balance can be achieved by minimizing the

quadratic objective function, with separate cost terms for frequency deviation ($Q \in \mathbb{R}^{2 \times 2}$) and overall control effort ($R \in \mathbb{R}^{2 \times 2}$), i.e.,

$$\min_{x,u} \int_0^\infty (x^\top Q x + u^\top R u) dt, \tag{6.5}$$

while simultaneously subjected to system dynamics in (6.3) and state feedback control in (6.4). This problem formulation resembles the one of an LQR, which requires a linear system model and a state feedback control in order to compute the optimal control gains. The substitution of (6.4) in (6.3) yields a nonlinear system of the form $\dot{x} = f_0(x, u)$. Therefore, we need to linearize it around an appropriate linearization point, which should intuitively be one of the two equilibrium points $x_1^* = (0, 0)$ and $x_2^* = (\omega_{ss}, 0)$, before and after the disturbance. However, since $\frac{\partial f_0}{\partial D} \Big|_{x_1^*, u^*} = 0$ and $\frac{\partial f_0}{\partial M} \Big|_{x_2^*, u^*} = 0$, a single linearization does not provide a model that could sufficiently capture the adaptive nature of the proposed controller. Furthermore, an LQR based on the system linearized around a non-equilibrium operating point would tend to drive the system back to the same unstable point, which is not desirable. Hence, we propose two different linearization and control design methods in order to implement a *multi-LQR* scheme and overcome this issue.

6.2.2 Method A: Two Independent Controllers

The first method is based on the assumption that the system damping has little effect in the initial stages of frequency response, whereas the system inertia has low impact in the later stages. These two phases are separated by the time instance of frequency nadir, thus dividing the response time into $[0, t_m)$ and $[t_m, +\infty)$ intervals, with $u_M = M$ and $u_D = D$ being the only control input, respectively. The initial stage of system response, i.e., $t \in [0, t_m)$, can be characterized by linearizing the system (6.3) around (x_1^*, u_M^*) , while assuming $D = D^*$ throughout the sequence, which yields

$$\underbrace{\begin{bmatrix} \dot{\omega} \\ \dot{\omega} \end{bmatrix}}_{\dot{x}_M} = \underbrace{\begin{bmatrix} 0 & I \\ -\frac{D^* + R_g}{TM^*} & -\left(\frac{D^* + F_g}{M^*} + \frac{1}{T}\right) \end{bmatrix}}_A \begin{bmatrix} \omega \\ \dot{\omega} \end{bmatrix} + \underbrace{\begin{bmatrix} 0 \\ \frac{-\Delta P}{TM^{*2}} \end{bmatrix}}_{B_M} \Delta M, \tag{6.6}$$

$$\underbrace{\begin{bmatrix} \omega_0 \\ \dot{\omega}_0 \end{bmatrix}}_{x_{M0}} = \begin{bmatrix} 0 \\ \dot{\omega}(0^+) \end{bmatrix}, \quad \Delta M = -\underbrace{\begin{bmatrix} K_m & \hat{K}_m \end{bmatrix}}_{K_M^\top} \begin{bmatrix} \omega \\ \dot{\omega} \end{bmatrix}.$$

Similarly, the period $t \in [t_m, +\infty)$ is described using the linearization around (x_2^*, u_D^*) and a no-feedback inertia control, resulting in

$$\underbrace{\begin{bmatrix} \dot{\hat{\omega}} \\ \ddot{\hat{\omega}} \end{bmatrix}}_{\dot{x}_D} = \underbrace{\begin{bmatrix} 0 & I \\ -\frac{D^*+R_g}{TM^*} & -\left(\frac{D^*+F_g}{M^*} + \frac{1}{T}\right) \end{bmatrix}}_A \begin{bmatrix} \hat{\omega} \\ \dot{\hat{\omega}} \end{bmatrix} + \underbrace{\begin{bmatrix} 0 \\ \frac{-\omega_{ss}}{TM^*} \end{bmatrix}}_{B_D} \Delta D, \quad (6.7)$$

$$\underbrace{\begin{bmatrix} \hat{\omega}_0 \\ \dot{\hat{\omega}}_0 \end{bmatrix}}_{x_{D_0}} = \begin{bmatrix} \omega_m - \omega_{ss} \\ 0 \end{bmatrix}, \quad \Delta D = -\underbrace{\begin{bmatrix} K_d & \hat{K}_d \end{bmatrix}}_{K_D^\top} \begin{bmatrix} \hat{\omega} \\ \dot{\hat{\omega}} \end{bmatrix},$$

where $\omega_m := \omega(t_m)$ and $\hat{\omega} := \omega - \omega_{ss}$.

In order to achieve a trade-off between the frequency response and the control effort, the following general form of a twofold optimization problem is used to derive the controllers:

$$\min_{x_i, \Delta u_i} \int_{t_{1,i}}^{t_{2,i}} \left(x_i^\top Q x_i + \Delta u_i^\top R_i \Delta u_i \right) dt \quad (6.8a)$$

$$\text{s.t.} \quad \dot{x}_i = A x_i + B_i \Delta u_i, \quad (6.8b)$$

$$\Delta u_i = -K_i^\top x_i. \quad (6.8c)$$

Here, $Q = \text{diag}(Q_1, Q_2)$ and $R_i \in \mathbb{R}$, with $Q_1 \in \mathbb{R}$, $Q_2 \in \mathbb{R}$ reflecting the cost factors for excessive frequency deviation and RoCoF, whereas index $i \in \{M, D\}$ denotes the corresponding multi-LQR formulation, from now on termed M-LQR and D-LQR respectively. The two controllers have different state-space models, state vectors and control inputs, but also the weight R_i in the objective function corresponding to the control effort penalty differs. This allows to distinguish between the different nature of energy utilization in the two stages. Furthermore, the integral spans over different time intervals, corresponding to the aforementioned two stages of the frequency response. For a given set of cost penalties Q and R_i , the optimization in (6.8) yields the optimal feedback control gains $K_i^* = R_i^{-1} B_i^\top P_i$, where $P_i \in \mathbb{R}^{2 \times 2}$ is the solution to the algebraic Riccati equation

$$A^\top P_i + P_i A - P_i B_i R_i^{-1} B_i^\top P_i + Q = \mathbb{0}_2. \quad (6.9)$$

The two control designs can be completed independently, as shown in Fig. 6.2, with the control effort factorization providing cost penalties $R_M \in \mathbb{R}$ and $R_D \in \mathbb{R}$ under the following ratio:

$$\eta = \frac{R_D}{R_M} = \left(\frac{\Delta M_{\max}}{\Delta D_{\max}} \right)^2 \approx \left(\frac{\omega_{\max}}{\dot{\omega}_{\max}} \right)^2. \quad (6.10)$$

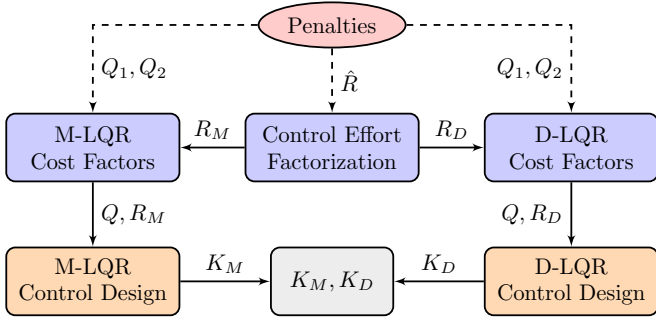


FIGURE 6.2: Multi-LQR control design in *Method A*.

The approximation is based on equating the energy content of the two controllers during peak power injection, which according to the dynamics of the swing equation corresponds to the ratio of frequency nadir and maximum RoCoF. Hence, using the given penalty input $\hat{R} \in \mathbb{R}$, the control effort costs can be determined as $R_M = \hat{R}$ and $R_D = \eta \hat{R}$.

The application of a multi-LQR scheme in *Method A* consists of a continuous alternation between the two algorithms, with D-LQR being initialized at the instance of frequency nadir ($\varrho = 1$) and remaining active until the frequency stabilization threshold $\varepsilon_\omega \in \mathbb{R}_{>0}$ has been met. As soon as the system reaches equilibrium the M-LQR control mode is deployed ($\varrho = 0$), as depicted in Fig. 6.3, where blue and red dots refer to the respective linearization points. The *idle* mode corresponds to a pre-disturbance period, where the control gains are kept the same as for the previous M-LQR sequence. Once the fault is detected through a RoCoF threshold $\bar{\varepsilon}_\omega \in \mathbb{R}_{>0}$, the new K_M gains are computed and the *active* M-LQR mode is initiated. In order to generate an adequate trigger signal $\varrho \in \{0, 1\}$, the signal logic scheme incorporates three

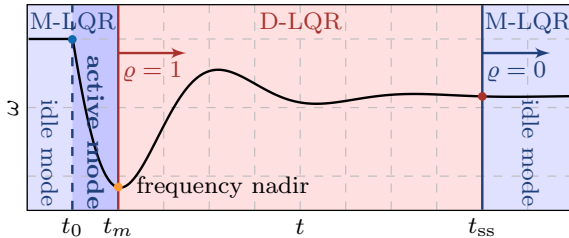


FIGURE 6.3: Application of a multi-LQR scheme in *Method A*.

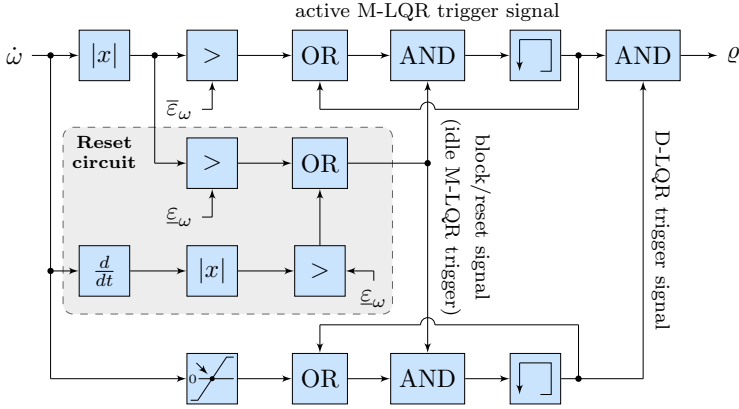


FIGURE 6.4: Signal logic scheme for LQR detection in *Method A*.

main circuits illustrated in Fig. 6.4: (i) a fault detection block that employs a RoCoF threshold ($\bar{\varepsilon}_\omega$) to ignite the active M-LQR mode; (ii) a D-LQR trigger signal using zero-crossing of RoCoF; and (iii) a block/reset signal based on frequency stabilization (idle M-LQR trigger).

It can be noticed that *Method A* resembles the adaptive controller \mathcal{K}_{OFC} from Chapter 5 (see Section 5.3) in several aspects. First of all, both methods make certain assumptions in terms of frequency response, i.e., the correlation between the frequency nadir and VSM parameters over the course of the response, thus introducing heuristics into the control design. Moreover, both approaches employ interval-based regulation and therefore require complex switching circuitry. Such control technique could also lead to flickering and overshoot during the switching instance, as previously experienced in Section 5.4. Hence, *Method A* does not resolve the issues raised in Section 6.1 and should not be considered a viable alternative to interval-based control.

6.2.3 *Method B: Two Dependent Controllers*

The second approach attempts to fully capture the properties of both control inputs by designing a cooperative control of the two LQR-based controllers. This is achieved through an iterative exchange of optimal control gains between the two consecutive LQR computations visualized in Fig. 6.5. The linearization practice is kept the same as for *Method A*.

Let us start with the M-LQR design, while preserving the notation from Section 6.2.2. Unlike the previous method, where an assumption $D = D^*$

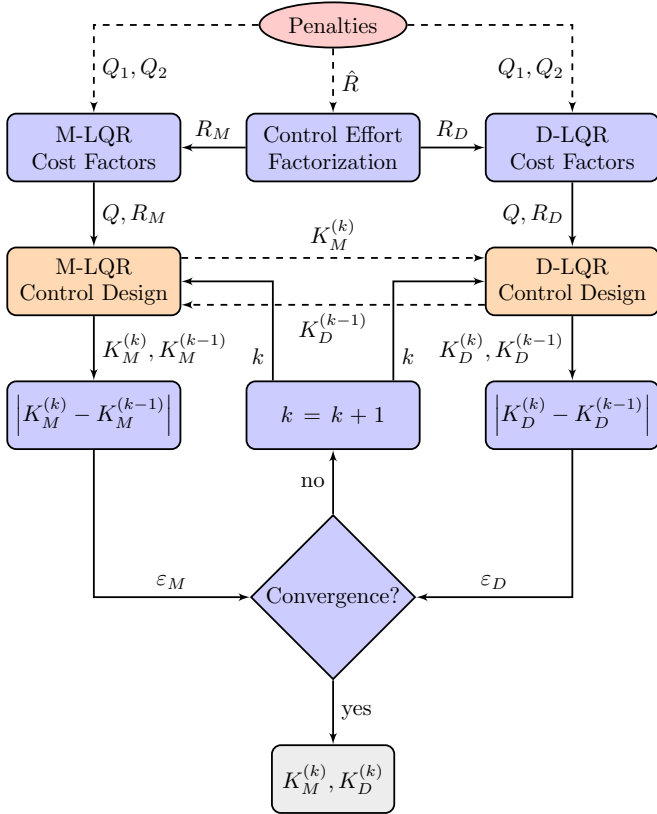


FIGURE 6.5: Multi-LQR control design in *Method B*.

was made, here we include the adaptive damping control from (6.7) of the form

$$D = D(\omega, \dot{\omega}) = D^* - \underbrace{\begin{bmatrix} K_d & \hat{K}_d \end{bmatrix}}_{K_D^\top} \begin{bmatrix} \omega - \omega_{ss} \\ \dot{\omega} \end{bmatrix}, \quad (6.11)$$

with K_D being a known parameter obtained in the previous update of D-LQR. The system in (6.3) can now be transformed into

$$\begin{aligned} \begin{bmatrix} \dot{\omega} \\ \ddot{\omega} \end{bmatrix} &= \begin{bmatrix} 0 & I \\ -\left(\frac{D(\omega, \dot{\omega}) + R_g}{TM}\right) & -\left(\frac{D(\omega, \dot{\omega}) + F_g}{M} + \frac{1}{T}\right) \end{bmatrix} \begin{bmatrix} \omega \\ \dot{\omega} \end{bmatrix} + \begin{bmatrix} 0 \\ \frac{\Delta P}{TM} \end{bmatrix} \\ &= f_1(\omega, \dot{\omega}, M, D(\omega, \dot{\omega})), \end{aligned} \quad (6.12)$$

which, after the linearization around (x_1^*, u_M^*) , yields

$$\underbrace{\begin{bmatrix} \dot{\omega} \\ \ddot{\omega} \end{bmatrix}}_{\dot{x}_M} = \underbrace{\begin{bmatrix} 0 & I \\ -\frac{D^*+R_g+K_d\omega_{ss}}{TM^*} & -\left(\frac{D^*+F_g+K_d\omega_{ss}}{M^*} + \frac{1}{T}\right) \end{bmatrix}}_{A_M} \begin{bmatrix} \omega \\ \dot{\omega} \end{bmatrix} + \underbrace{\begin{bmatrix} 0 \\ -\frac{\Delta P}{TM^{*2}} \end{bmatrix}}_{B_M} \Delta M$$

$$= A_M(K_d) \begin{bmatrix} \omega \\ \dot{\omega} \end{bmatrix} + B_M \Delta M. \quad (6.13)$$

Similarly, we can assume K_M as a known parameter and define the adaptive inertia control for D-LQR as

$$M = M(\omega, \dot{\omega}) = M^* - \underbrace{\begin{bmatrix} K_m & \hat{K}_m \end{bmatrix}}_{K_M^\top} \begin{bmatrix} \omega \\ \dot{\omega} \end{bmatrix}, \quad (6.14)$$

which gives us the closed-loop nonlinear system

$$\begin{bmatrix} \dot{\omega} \\ \ddot{\omega} \end{bmatrix} = \begin{bmatrix} 0 & I \\ -\frac{D+R_g}{TM(\omega, \dot{\omega})} & -\left(\frac{D+F_g}{M(\omega, \dot{\omega})} + \frac{1}{T}\right) \end{bmatrix} \begin{bmatrix} \omega \\ \dot{\omega} \end{bmatrix} + \begin{bmatrix} 0 \\ \frac{\Delta P}{TM(\omega, \dot{\omega})} \end{bmatrix} \quad (6.15)$$

$$= f_2(\omega, \dot{\omega}, M(\omega, \dot{\omega}), D).$$

Finally, the expression for the linearized model around (x_2^*, u_D^*) can be computed as

$$\begin{bmatrix} \dot{\hat{\omega}} \\ \ddot{\hat{\omega}} \end{bmatrix} = \underbrace{\begin{bmatrix} 0 & I \\ -\frac{D^*+R_g}{\kappa T} & -\left(\frac{D^*+F_g}{\kappa} + \frac{1}{T}\right) \end{bmatrix}}_{A_D} \begin{bmatrix} \hat{\omega} \\ \dot{\hat{\omega}} \end{bmatrix} + \underbrace{\begin{bmatrix} 0 \\ \frac{-\omega_{ss}}{\kappa T} \end{bmatrix}}_{B_D} \Delta D$$

$$= A_D(K_m) \begin{bmatrix} \hat{\omega} \\ \dot{\hat{\omega}} \end{bmatrix} + B_D(K_m) \Delta D, \quad (6.16)$$

where $\kappa := M^* - K_m\omega_{ss}$.

Understandably, the multi-LQR optimization problem in *Method B* resembles the one in (6.8), with the two main exceptions: (i) both LQRs are infinite, i.e., $[t_{1,i}, t_{2,i}] = [0, +\infty)$; and (ii) the state-space model (6.8b) is replaced by $\dot{x}_i = A_i x_i + B_i \Delta u_i$. However, due to numerical interdependence between the matrices $A_M(K_d)$, $A_D(K_m)$ and $B_D(K_m)$, the two LQR systems cannot be solved independently as in *Method A*. Instead, they are iterated until the

Algorithm 2 Iterative computation of optimal control gains in *Method B*

-
- | | |
|---|--|
| 1: Set $k = 0$ and $\varepsilon^{(0)} = 0$ | |
| 2: Initialize system in open-loop | $\triangleright K_M^{(0)} = K_D^{(0)} = \mathbb{0}_2$ |
| 3: while $\varepsilon^{(k)} > \epsilon$ or $k = 0$ do | |
| 4: $k = k + 1$ | |
| 5: Run <i>M-LQR</i> = $f_1 \left(K_D^{(k-1)} \right)$ | \triangleright derive $K_M^{(k)}$ |
| 6: Run <i>D-LQR</i> = $f_2 \left(K_M^{(k)} \right)$ | \triangleright derive $K_D^{(k)}$ |
| 7: Compute error terms | $\triangleright \varepsilon_M^{(k)} = \left K_M^{(k)} - K_M^{(k-1)} \right $ |
| | $\triangleright \varepsilon_D^{(k)} = \left K_D^{(k)} - K_D^{(k-1)} \right $ |
| 8: Determine convergence error | $\triangleright \varepsilon^{(k)} = \varepsilon_M^{(k)} + \varepsilon_D^{(k)}$ |
| 9: end while | |
| 10: Return $K_M^{(k)}, K_D^{(k)}$ | |
-

convergence between consecutive steps dictated by the threshold $\epsilon \in \mathbb{R}^2$ is achieved, as proposed in Algorithm 2. As a result, a single uniform controller is obtained, which simplifies the implementation compared to the previous method.

The performance of Algorithm 2 is presented in Fig. 6.6, which showcases the iterative progress of the optimal control gain computation. Due to the complexity of a closed-form solution of the combined Riccati equations, the possibility for deriving an analytic convergence criterion is restricted. However, the fast convergence can be justified by analyzing the mathematical properties of the control design in *Method B*. Since the algorithm is initialized at $K_M^{(0)} = K_D^{(0)} = \mathbb{0}_2$, the computation of the first M-LQR is done inefficiently without inclusion of adaptive damping. With adaptive inertia control in place, the damping feedback can be reasonably determined for $k = 1$. The inaccuracy of $\hat{K}_m^{(1)}$ and $\hat{K}_d^{(1)}$ is a sole consequence of linearization, i.e., the fact that the LQR design stabilizes the inverter around the equilibrium where the influence of $\dot{\omega}$ is negligible. This problem is resolved in the second iteration, as both $\hat{K}_m^{(2)}$ and $\hat{K}_d^{(2)}$ are appropriately readjusted, with feedback gains corresponding to ω remaining constant. Therefore, the convergence is guaranteed within three iterations. This sequence also explains the gradual reduction of convergence error: the first iteration computes all four control gains initially set to zero, whereas the second one only tunes the two gains corresponding to the state feedback $\dot{\omega}$.

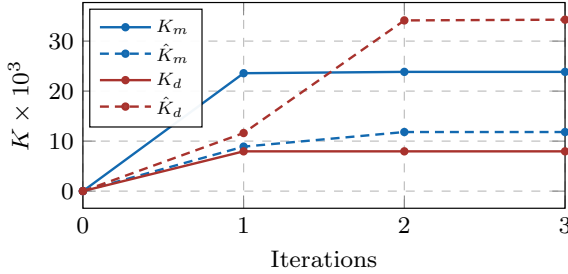


FIGURE 6.6: Iterative progress of feedback control gains in Algorithm 2.

6.3 PARAMETRIZATION AND IMPLEMENTATION

6.3.1 LQR Cost Parametrization

The expression in (6.9) implies that the selection of cost factors Q and R_i comprehensively determines the optimal control gains, thus highlighting the importance of cost parametrization. One of the most common first choices for LQR tuning is given by the Bryson’s rule [156], which considers all objective costs equally and selects the respective weights such that

$$Q_1 = \frac{1}{(\omega_{\text{lim}})^2}, \quad Q_2 = \frac{1}{(\dot{\omega}_{\text{lim}})^2}, \quad R_i = \frac{1}{(\Delta u_{i,\text{lim}})^2}, \quad (6.17)$$

with subscript “lim” denoting the maximum acceptable value of a specific variable. While permissible limits for frequency nadir and RoCoF are prescribed by the operator, the maximum allowed control gains for virtual inertia and damping as well as their correlation to the aforementioned frequency metrics are unclear. This problem is resolved by fixing one penalty factor, in our case the frequency penalties $Q = \text{diag}(Q_1, Q_2)$ by setting $Q_1 = (\omega_{\text{lim}})^{-2}$ and $Q_2 = (\dot{\omega}_{\text{lim}})^{-2}$, and adjusting the cost of control accordingly. Since the optimal selection of $\Delta u_{i,\text{lim}}$ (i.e., ΔM_{lim} and ΔD_{lim}) is inconclusive, we propose an iterative procedure within the optimal control design scheme presented in Fig. 6.7. Starting from the nominal penalty input $\hat{R}^{(0)} \approx 0$, the algorithm yields a maximum penalty and thus a minimum control effort that still ensures maintaining the frequency and RoCoF within the given bounds. As a result, a unique 1-D look-up table of the form $K^* = T_{PK}(\Delta P)$ is generated offline, which provides the optimal feedback gain scheduling for any given system-level disturbance ΔP .

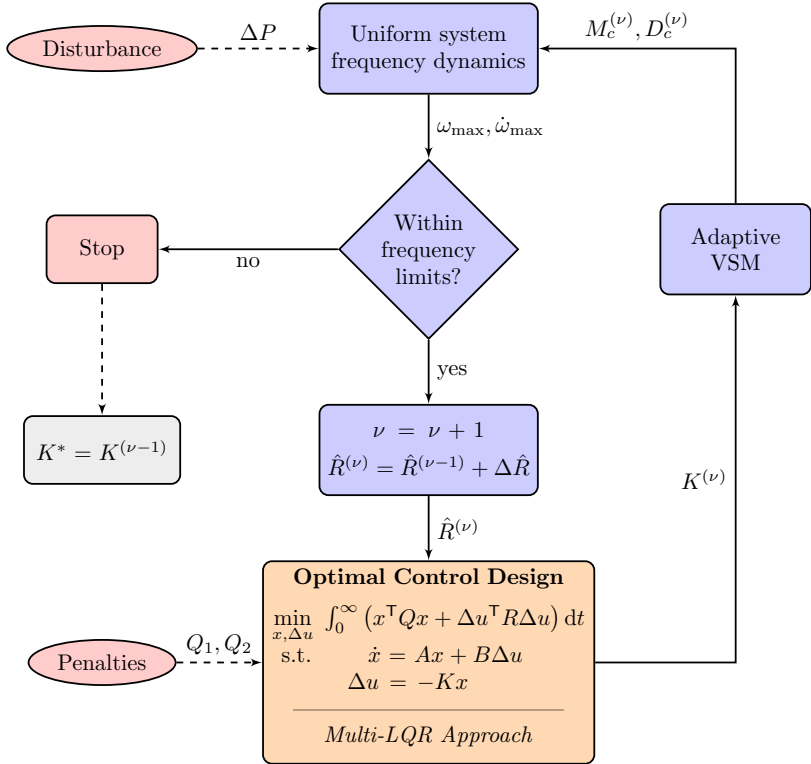


FIGURE 6.7: System-level control design algorithm.

Note that the “optimal control design” block in Fig. 6.7 corresponds to the proposed multi-LQR schemes for *Method A* and *Method B* in Fig. 6.2 and Fig. 6.5, respectively. In other words, the LQR computation of optimal control gains presented in Section 6.2 is embedded in the iterative procedure in Fig. 6.7 and done at each iteration of the main algorithm. Furthermore, in case of *Method B*, this sequence comprises two nested algorithms, with the lower-level one providing correlation between the two LQR controllers (see Algorithm 2) and the upper-level procedure determining the optimal cost factors. Nevertheless, the computational requirements of such sequential setup are not high, partly due to the fast convergence of Algorithm 2 discussed in Section 6.2.3 and partly due to the low computational burden of the upper-level algorithm. Moreover, the latter aspect can be further regulated by adjusting the incremental increase $\Delta \hat{R} \in \mathbb{R}_{>0}$ of the control cost.

6.3.2 Stability Assessment

This section discusses stability properties and provides sufficient stability conditions for the proposed adaptive VSM design.

Proposition 6.3.1. *Consider the system in (6.3) with the closed-loop state feedback from (6.4). Assuming a justifiable approximation $R_M K_M \approx R_D K_D$, the asymptotic stability of the system is guaranteed under the following tuning condition of the adaptive VSM controller:*

$$\frac{M^*}{T} + D^* + F_g \leq \frac{M^* - \sqrt{M^{*2} - 4\hat{K}_m \Delta P}}{4\hat{K}_m / K_m}. \quad (6.18)$$

Proof. The proof is given in Appendix A.1. □□□

The aforementioned condition also has a physical interpretation. Since M^*/T term corresponds to damping, this stability margin indicates that the system damping has to be higher than the maximum rate of change of inertia. In other words, the proportional inertia feedback gains K_m and \hat{K}_m are bounded by the shaded stability region depicted in Fig. 6.8a. Furthermore, as proof of concept, the energy content of the proposed Lyapunov function (see Appendix A.1) is analyzed based on the obtained simulation results. Both the adaptive VSM concept and the traditional “open-loop” implementation (corresponding to controller \mathcal{K}_0 in Chapter 5) have been investigated, with the performance shown in Fig. 6.8b. One can notice that $V(\omega, \dot{\omega})$ remains positive in both cases, with transient energy trajectory preserving a decaying trend throughout the disturbance period and converging to zero, thus verifying stability of the system. Nonetheless, the effectiveness of the adaptive controller is reflected in the shorter energy trajectory compared to the open-loop method, implying that the system reaches steady state faster. Moreover, we can observe that the final equilibrium point is x_2^* , as previously discussed in Section 6.2.

It should be noted that the suggested stability assessment applies only to *Method B*, since gains M and D vary discontinuously in *Method A* due to explicit switching actions. However, this can be resolved by approximating the derivative terms $\partial M/\partial t$ and $\partial D/\partial t$ by their average values at the points of switching instances and conducting a similar analysis. Such approach resembles the technique used in Appendix A.2 and once again suggests a correlation between *Method A* and the interval-based control in Section 5.3. As we consider *Method B* to be the more sophisticated and efficient approach of the two, the other stability analysis is omitted for brevity.

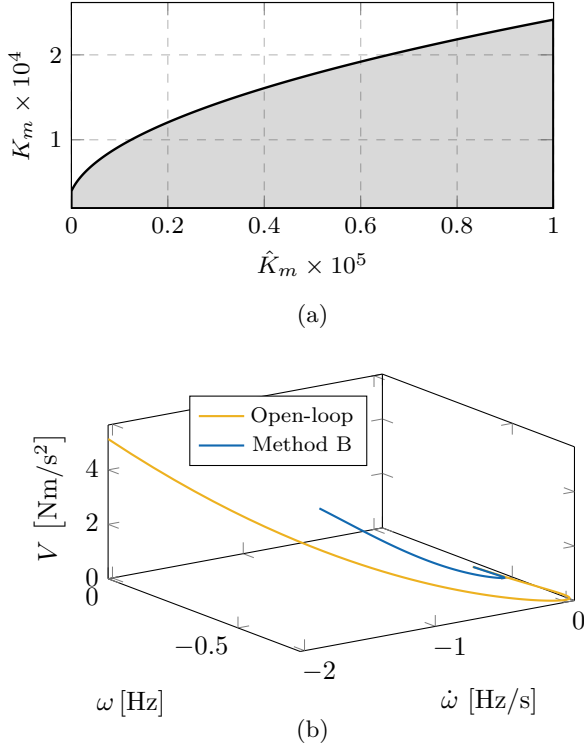


FIGURE 6.8: Stability analysis of the adaptive VSM control design: (a) stability region of inertia feedback gains; and (b) transient energy trajectory after a step disturbance.

6.3.3 Implementation and Multi-Inverter Application

In order to implement the proposed adaptive control design in a large-scale, multi-inverter system, the information of the global power imbalance ΔP should be extracted from a locally measured disturbance $\Delta P_{c_i} \in \mathbb{R}$ at the terminal of each grid-forming converter unit $i \in \mathcal{N}_c$. One potential way of describing the relationship between the two signals is by mimicking the system stiffness of a traditional power system, i.e., the composite frequency

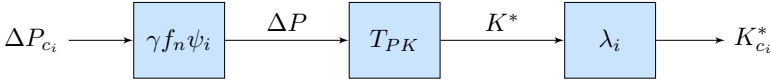


FIGURE 6.9: Individual control scheme for optimal gain selection.

response characteristic $\beta \in \mathbb{R}_{>0}$ of conventional synchronous generators, and designing a low-inertia equivalent

$$\gamma = D_l P_{l_0} + \frac{1}{f_n} \sum_{i \in \mathcal{N}_c} \frac{P_{c_i}}{R_{c_i}^p}. \quad (6.19)$$

The nominal frequency is denoted by $f_n \in \mathbb{R}_{>0}$, $P_{l_0} \in \mathbb{R}_{>0}$ and $D_l \in \mathbb{R}$ are the load power at nominal frequency and its sensitivity to frequency changes, whereas $R_{c_i}^p = D_{c_i}^{-1}$ is the respective frequency droop equivalent of a VSM-based active power controller (see Section 2.4). We can now derive the expression for the disturbance magnitude by extrapolating the locally measured active power mismatch at the VSC terminal [26], which yields

$$\Delta P = \gamma f_n R_{c_i} \frac{\Delta P_{c_i}}{P_{c_i}} = \gamma f_n \underbrace{(D_{c_i} P_{c_i})^{-1}}_{\psi_i} \Delta P_{c_i}. \quad (6.20)$$

Traditional generators are omitted from the computation of γ due to large time constants and significantly slower frequency regulation compared to converter-interfaced generation. Once the system-level disturbance ΔP is determined, the optimal feedback gain of the combined VSM control action can be obtained from the look-up table T_{PK} , as illustrated in Fig. 6.9. A sharing property of the control effort is achieved via proportional scaling factors $\lambda_i = P_{c_i} / \sum_i P_{c_i}$, assuming unit participation proportional to the installed power capacity. By assigning feedback control gains $K_{c_i,i}^* \in \mathbb{R}^{2 \times 2}$ to respective converters we ensure a non-interfering operation and a sufficiently large adaptive VSM response for preserving the frequency stability of the system. Moreover, the adaptive state feedback of individual inertia and damping constants can easily be incorporated within the conventional system-level control scheme described in Section 2.2.4.

6.4 CONTROL PERFORMANCE

We investigate the same three-area test case previously introduced in Chapter 5, comprising three synchronous and three converter-interfaced generators. In order to simplify the analysis, all converter units are operating in

grid-forming mode and are equipped with adaptive VSM controllers. As a disturbance, a loss of synchronous generator at node 5 (i.e., $\Delta P = 719$ MW) is considered. The overall system performance under the two proposed controllers is compared against the non-adaptive open-loop approach. For better understanding of the system response, the first part of the analysis is confined to the CoI frequency model, and the second part focuses on simulation results obtained using a detailed EMT model in MATLAB Simulink [94] as well as a Single-Machine Infinite-Bus (SMIB) model developed on the virtual Hardware-In-the-Loop (HIL) platform [157].

6.4.1 Performance on a Simplified CoI Model

Understandably, a major contingency such as a loss of synchronous generator leads to unacceptable frequency excursion under the open-loop VSM control, indicated by the frequency nadir of ≈ 0.7 Hz in Fig. 6.10. In contrast, the adaptive VSM schemes fulfill their purpose of alleviating the disturbance and improve the frequency response in terms of nadir and maximum RoCoF. The impact of the cost penalty selection is reflected in the frequency nadir reaching the prescribed Under-Frequency Load Shedding (UFLS) threshold of $\Delta f_{\text{lim}} = 0.5$ Hz. *Method A* achieves a marginally faster convergence rate due to an explicit switch from M-LQR to D-LQR control mode at the instance of reaching the frequency nadir, which is also the reason for the discontinuity in the RoCoF curve due to a sudden step change in M . On the contrary, the additional damping during the initial stages of the response in *Method B* aids the control of the frequency nadir, thus activating less inertia compared to the previous method. This however leads to a slightly higher maximum RoCoF, which is a well-justified trade-off considering that the RoCoF is significantly below the predefined limit $\dot{f}_{\text{lim}} = 1$ Hz/s. Nonetheless, the characteristics are reversed in the second stage, as more inertia and less damping is provided by *Method B* than by *Method A*. Another interesting observation is the initial undershoot of damping in *Method B*; a consequence of the D-LQR trying to effectively reach its linearization point x_2^* . This “non-minimum phase” characteristic occurs however only for very large disturbances, with the steady-state frequency well below the 50 Hz mark.

The activation of M and D reveals the distinctive nature of the two algorithms. *Method A* is restricted solely to adaptive inertia as a mean of frequency regulation during the initial response (M-LQR), which directly acts on RoCoF through the explicit $M\dot{\omega}$ term. The effectiveness of such approach is however limited, since the impact of inertia decays over time together with

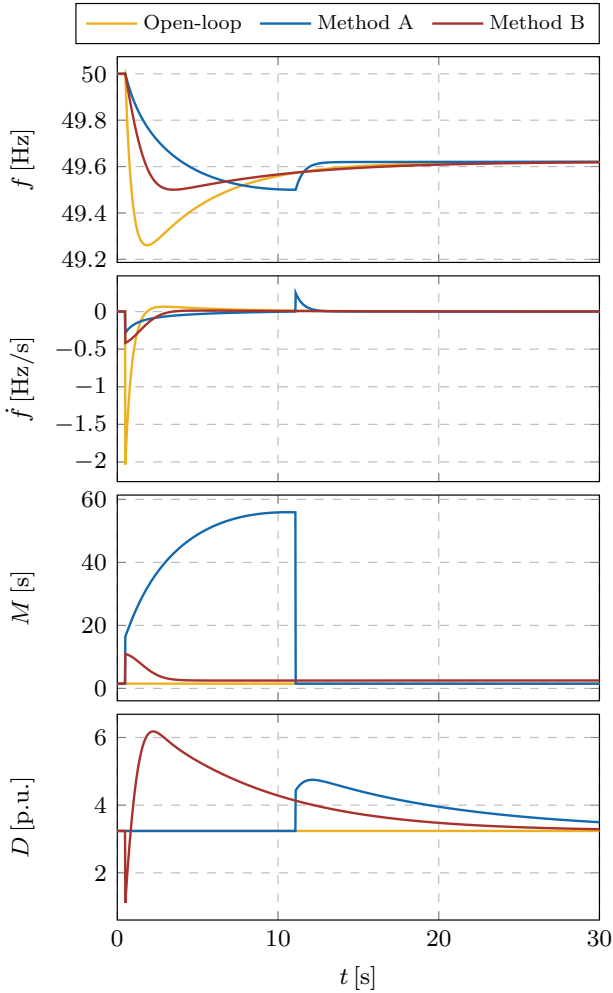
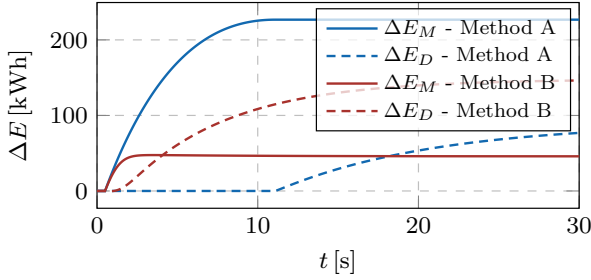
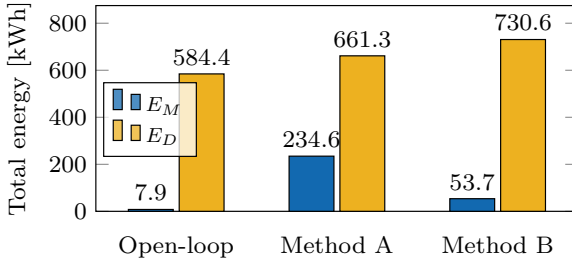


FIGURE 6.10: System response under different VSM control designs: (i) CoI frequency; (ii) CoI RoCoF; (iii) aggregate inertia; and (iv) aggregate damping.

$\hat{\omega}$. As a result, the inertia gain is overdimensioned, leading to high depletion of energy and a noticeable spike at the switching instance between the two LQRs. In contrast, the combined effort of inertia and damping in *Method B* achieves a qualitatively similar system performance with a more natural frequency response and less energy consumption, as indicated in Fig. 6.11.



(a)



(b)

FIGURE 6.11: Energy utilization for containing a loss of generator: (a) components of the additional control effort; and (b) total energy content.

We therefore conclude that, in addition to being more practical for real-world implementation compared to *Method A*, *Method B* is also the more effective approach for adaptive VSM design.

Some insightful conclusions regarding the two control concepts can be drawn from the energy content of the control effort, with respective energy terms computed as described in Section 5.4. First of all, it clarifies the decision in the latter approach to compensate inertia with damping during high RoCoF instances, since ΔE_M term would have a predominant impact on the total costs. Moreover, it can be observed that *Method B* reduces the total energy use of the adaptive control by $\approx 12.5\%$. The increase in total battery utilization compared to the open-loop VSM can be justified by the small size of the test system that makes it highly vulnerable to a loss of generator which accounts for 20% of total base power. Nonetheless, this is just a fraction ($\approx 1\%$) of the total energy capacity of a 100 MW/129 MWh lithium-ion Hornsdale Power Reserve battery in South Australia (better

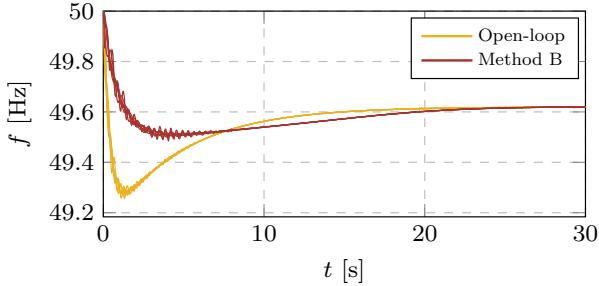


FIGURE 6.12: System frequency response after a loss of synchronous generator in the detailed EMT model: *Method B* vs. open-loop.

known as “Tesla Big Battery”), which was recently installed and successfully used for similar fast regulation purposes [158]. Considering that the installed power of the aforementioned system is an order of magnitude higher than in the observed test case, the application of proposed LQR control is well justified.

6.4.2 Performance on a Detailed EMT Model

The previous case study has verified the mathematical assumptions made in Section 6.2 and concluded that *Method B* is the more prominent control method of the two. Therefore, only this adaptive scheme will be investigated in the remainder of the chapter. As a next step, the developed controller is assigned to all three converter-interfaced generators and simulated on a detailed EMT model. The individual frequency response of all generators depicted in Fig. 6.12 confirms that under the adaptive VSM method the synchronization is preserved and frequency metrics (frequency nadir in particular) are kept within predefined bounds, unlike for the open-loop approach. Furthermore, it validates the accuracy of the proposed multi-machine frequency modeling from Section 5.2 and suggests that the control performance is not hindered in the presence of detailed SG, VSC and transmission line dynamics.

6.4.3 Hardware-in-the-Loop Setup

For the purposes of evaluating the proposed converter controller in real-world applications, the adaptive VSM has been implemented on the HIL setup. We employ a 4-core Typhoon HIL402 hardware device together with the

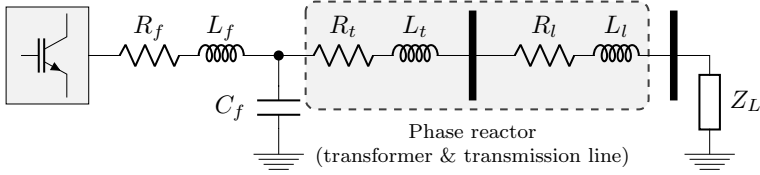


FIGURE 6.13: Configuration of the investigated HIL setup: a 2-bus system comprising the VSC supplying an RL load over a transmission line.

virtual HIL platform [157]. Virtual HIL is a software toolbox within a HIL toolchain that enables development of HIL models on a local computer and communicates in real time with the same HIL toolchain [159]. Therefore, it provides a high degree of accuracy regarding the performance of the developed VSM strategies.

The configuration of the investigated HIL setup is presented in Fig. 6.13, comprising a single VSC supplying an RL load over a transmission line. Similarly to the design described in Section 2.2, the converter is interfaced to the network through a filter and a transformer. Despite such system being a simplification of the previously studied three-area network, it is still sufficient for testing of high-fidelity PE controllers in closed loop, as it captures the real-time signal processing as well as the associated switching and time delay.

We select a switching frequency of $f_{sw} = 10$ kHz and analyze a step change in active load power at $t_f = 5$ s with a sample time of $T_s = 100$ μ s. In order to trigger the adaptive controller, a more restrictive frequency nadir threshold of $\Delta f_{lim} = 200$ mHz has been imposed. *Method B* again prevails as a drastically better control design compared to the open-loop approach, indicated by the improved frequency response in Fig. 6.14. However, one can notice a first-order response of the system, which is a consequence of neglecting synchronous generators and the corresponding turbine dynamics. Nonetheless, the adaptive VSM controller responds appropriately by increasing the power output in order to keep the frequency within limits. Note that the signal provided in Fig. 6.14 represents the filtered converter power \tilde{p}_c and not the original measurement p_c ; hence, the lack of noise and oscillations. On the other hand, the output voltage v_f is measured and the frequency f_c is subsequently computed using a PLL. One can observe that, as a result of the closed-loop state feedback, the oscillations in frequency and voltage are slightly propagated. However, frequency stability is preserved and the system reaches new equilibrium as converter's response settles down and the adaptive gains decay to zero.

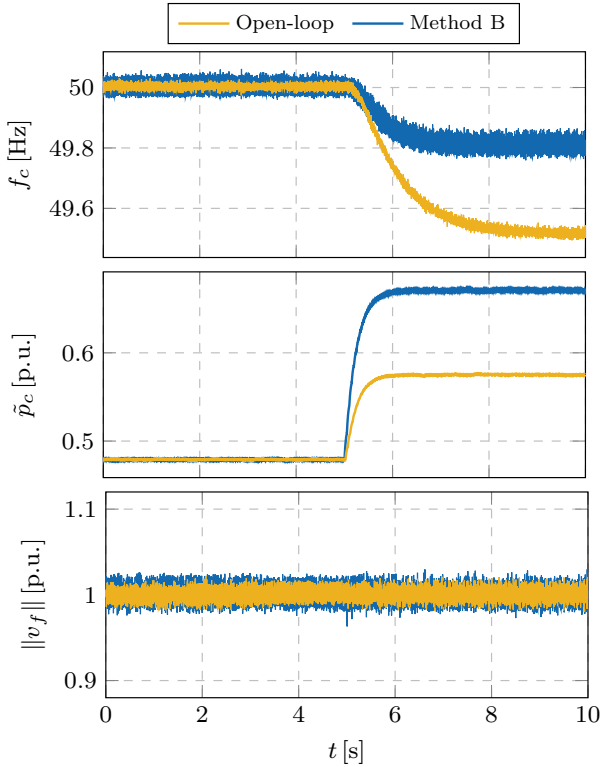


FIGURE 6.14: Response of the single converter supplying a varying load in HIL setup: (i) frequency measurement; (ii) filtered active power measurement; and (iii) output voltage measurement.

6.5 CONCLUSION

This chapter presents a decentralized VSM controller for converter-interfaced generation in power systems with high share of renewable resources. An LQR-based optimization procedure is employed in order to determine the state feedback gains that adaptively adjust the emulated inertia and damping constants according to the frequency disturbance in the system. The proposed control design preserves a trade-off between violating the frequency limits and minimizing the control effort, achieved by defining the LQR cost factors through an additional iterative algorithm. Moreover, the implementation and tuning for a decentralized, multi-inverter application are described.

Two methods have been proposed in order to tackle the issues pertaining to inadequate single linearization point of the system. As a result, two conceptually different control designs, namely *Method A* and *Method B*, have been introduced and compared against the open-loop concept using several simulation platforms. The results indicate an overall better frequency response of adaptive controllers, with a reasonable increase in energy consumption compared to the open-loop VSM. Nonetheless, *Method A* shares several common characteristics (and therefore drawbacks) with the interval-based controllers discussed in Chapter 5. Therefore, due to its conceptually superior design and a more effective performance in terms of frequency response, *Method B* is determined to be the more prominent approach of the two. Future work could potentially consider adapting and improving the aforementioned controllers in order to cope with more severe system-level disturbances (e.g., short circuits and line faults).

MODEL PREDICTIVE CONTROL FOR FREQUENCY REGULATION IN LOW-INERTIA SYSTEMS

This chapter proposes a novel control scheme based on model predictive control for converter-interfaced generators operating in a grid-forming mode, with the goal of exploiting their responsiveness and providing Fast Frequency Control (FFC) to the system. The controller adapts converter power injection to limit the frequency nadir and RoCoF after a disturbance. Both centralized and decentralized MPC approaches are considered and compared in terms of performance and practical implementation. Special attention is given to the decentralized controller by generating an explicit MPC solution to enhance computational efficiency and reduce hardware requirements. Simulation results obtained from a detailed DAE representation of the IEEE 39-bus system demonstrate the effectiveness of proposed control schemes. The chapter is based on [160].

7.1 INTRODUCTION

A large-scale integration of converter-interfaced generation imposes new challenges on real-time power system control and operation, as the lack of rotational inertia and governor droop control (i.e., damping) leads to faster dynamics and larger frequency deviations [6]. In order to mitigate potential stability issues and improve the resilience of low-inertia systems, new ancillary services such as FFC are needed [8]. As previously pointed out in Chapters 5 and 6, these requirements can be fulfilled by grid-forming (i.e., grid-supporting) VSCs and the associated DC-side energy buffers, as they can effectively adjust the power output in response to frequency deviations. Nevertheless, the majority of proposed control strategies focuses solely on the converter's AC-side, disregarding the DC-link dynamics in the process and making the simplifying assumption that an infinite amount of power and energy is available at the DC-side capacitor [143]. Moreover, while specifying a constant droop gain leads to satisfactory VSC performance under small

frequency deviations, it prevents the converter from utilizing its maximum power capacity in emergency cases.

MPC, an optimization-based, discrete-time control scheme, appears to be promising for incorporating all of the aforementioned aspects into a uniform problem formulation [161]. The capability to compute optimal control inputs based on predictions of future state evolution using a state-space system model and disturbance forecasts, while taking operational constraints into consideration, has made MPC attractive for frequency regulation in power systems.

In recent years several studies have considered the application of MPC in Automatic Generation Control (AGC). Centralized [162], hierarchical [163] and distributed [164] approaches have been proposed and shown to improve frequency regulation and robustness to uncertainty when compared to standard PI control. In contrast, only a few studies have addressed the application of MPC to fast frequency control [165–167]. A real-time optimal control scheme based on *explicit* MPC for regulating frequency and providing inertial response was presented in [165]. Although the advantages of an explicit MPC scheme in fast frequency regulation were illustrated, this study used a simplified power system model and did not include converter-based generation.

The drawbacks of the aforementioned study were addressed in [166] and [167], where MPC-based frequency support through HVDC grids was investigated. In [166], a *decentralized* MPC control scheme for frequency containment in emergency situations was proposed. Frequency predictions are made based on RoCoF measurements and the VSC output is adjusted if constraint violations are detected or expected. Despite being decentralized, this approach requires global information about the grid topology and HVDC converter locations to calculate sensitivity factors corresponding to DC-voltage droop. Tuning of such parameters as well as the increased computational burden (due to solving the MPC problem online) are the limitations of this approach. Alternatively, stabilization of large power systems using VSC-based HVDC links equipped with a *centralized* MPC controller was analyzed in [167]. Based on global measurements, the VSC injections are manipulated to damp out oscillations in the system. However, fast communication links are required to leverage MPC benefits and resolve potential stability issues arising from communication delays.

This chapter presents both a centralized and a decentralized MPC-based FFC strategy that can be incorporated as an additional layer to the primary frequency control (droop or VSM-based). While not active in normal opera-

tion, the MPC is triggered in case of large disturbances to keep the frequency deviation and RoCoF within limits prescribed by the operator. We start by introducing improvements to the frequency prediction in [166] by applying a CoI frequency dynamics model of a low-inertia system from Section 5.2. Subsequently, model identification methods are employed to estimate the parameters of the frequency response model based on historical data. Furthermore, improvements in computational efficiency of the decentralized MPC approach by means of an offline explicit solution scheme are assessed. Finally, in contrast to the studies in [165–167], the proposed control design is verified through time-domain simulations using a detailed DAE model of a low-inertia system described in Chapter 2.

The rest of the chapter is structured as follows. In Section 7.2, a general overview of MPC application to FFC is provided and the MPC-based supervisory layer is introduced in the converter control scheme. Sections 7.3 and 7.4 elaborate on the design of decentralized and centralized controllers, respectively, as well as the underlying prediction models. Additionally, in Section 7.3, an explicit MPC solution and the model identification procedure for estimating the prediction model parameters are presented. Simulation results from different case studies are illustrated in Section 7.5, whereas Section 7.6 draws the main conclusions and discusses future work.

7.2 MPC-BASED FAST FREQUENCY CONTROL FOR VSCS

7.2.1 MPC Application to Fast Frequency Control

Traditionally, primary frequency control together with system’s rotational inertia was sufficient for containing frequency excursions in emergency cases. However, as the system inertia and hence the time constants of frequency dynamics decrease, the primary control response times fail to meet the requirements for maintaining the frequency within limits in the immediate aftermath of a disturbance. This raises the need for control schemes operating on shorter timescales [168]; a service that could be ideally provided through rapid active power delivery of the VSC interfacing the renewable generation or battery storage unit to the network.

The basic MPC concept can be outlined as follows. At the current discrete time step $k \in \mathbb{Z}_{\geq 0}$, the controller receives the latest available measurements and uses state-space-based predictions to compute the optimal control sequence $u^*(k), u^*(k+1), \dots, u^*(k+N-1)$ over a horizon of $N \in \mathbb{Z}_{\geq 0}$ future time steps to satisfy the required constraints at the minimum cost. Subse-

quently, only the control action for the first time sample is applied to the system and the rest of the sequence is discarded. The procedure is repeated for every following sample time step with the inclusion of updated process measurements.

An MPC-based FFC scheme for converter-interfaced generators can be developed according to the following approach. After a large disturbance, sufficient information is promptly collected by observing changes in system variables in order to predict frequency evolution for the next time period. Optimal control actions are then computed based on the state-space predictions to prevent critical threshold violations (e.g., frequency nadir or RoCoF), while respecting device-level constraints. Subsequently, each converter unit participating in FFC attempts to counteract a part of the estimated disturbance. The frequency control scheme needs to be compatible with and complementary to all grid-forming controllers and is therefore designed as a supervisory control layer. Without loss of generality, this chapter focuses solely on droop-based grid-forming converters, but the same application can be easily applied to VSM operation mode based on a well-known small-signal equivalence between the two models (see Section 2.4).

7.2.2 VSC-Level Implementation

The proposed converter control design, outlined in Fig. 7.1, is based on a traditional two-level control scheme comprising an outer control loop for active and reactive power regulation and an inner cascade of voltage and current controllers, previously described in Section 2.7. Moreover, an MPC-based supervisory control layer is included, with the purpose of providing FFC by adjusting the active power setpoint in response to a disturbance. The modeling and mathematical notation are taken from Chapter 2.

The addition of MPC affects the active power output, with the new control design of the form

$$\omega_c := \omega_c^* + R_c^p(p_c^* + \Delta p_c^* - \tilde{p}_c), \quad \dot{\tilde{p}}_c := \omega_z(p_c - \tilde{p}_c). \quad (7.1)$$

The controller provides output frequency and angle references $(\omega_c, \theta_c) \in \mathbb{R}^2$ by adjusting the predefined setpoints according to the low-pass filtered power measurement $\tilde{p}_c \in \mathbb{R}$, droop control gain $R_c^p \in \mathbb{R}_{>0}$, and the setpoint change $\Delta p_c^* \in \mathbb{R}$ generated by the supervisory layer. Assuming constant Δp_c^* , the RoCoF state $\dot{\omega}_c$ can be computed from (7.1) as

$$\dot{\omega}_c = R_c^p \omega_z(\tilde{p}_c - p_c). \quad (7.2)$$

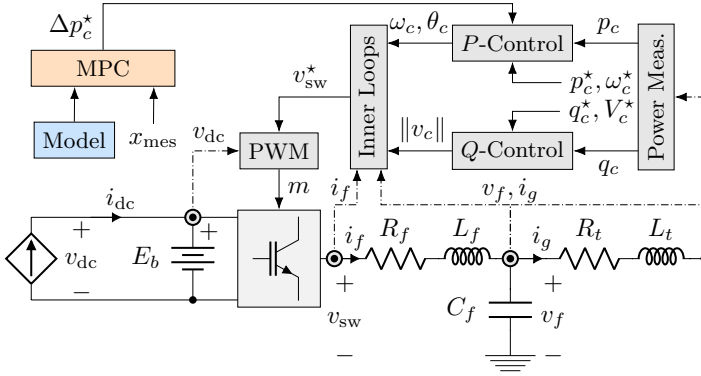


FIGURE 7.1: Simplified diagram of the implemented control structure with the MPC-based supervisory layer.

With the assumption of a lossless converter, a simple model¹ for the battery State-of-Charge (SoC) $\chi \in \mathbb{R}_{\geq 0}$ can be derived based on the power balance between the converter's DC-side input power $p_{dc} := v_{dc}i_{dc} \in \mathbb{R}$ and the AC-side output power $p_{sw} := v_{sw}^T i_f$ before the filter. The SOC dynamics are described by

$$\dot{\chi} := \frac{p_{dc} - p_{sw}}{E_b}, \quad (7.3)$$

with $E_b \in \mathbb{R}_{>0}$ denoting the total energy capacity of the battery. The supervisory control layer employs an MPC which, based on a frequency prediction model and the newest available measurements $x_{mes} \in \mathbb{R}^m$, generates a signal Δp_c^* to modulate the active power setpoint in response to a disturbance. Whereas inactive during normal operation, the supervisory layer is triggered in emergency cases and remains active until the new steady state is reached.

7.3 DECENTRALIZED CONTROL DESIGN

The main goal of the decentralized approach is to design an FFC scheme where each VSC relies solely on local measurements and proportionally participates in disturbance mitigation based on its location in the system. Optimally, the converters closer to the fault shall provide more support in order to avoid stress on the transmission lines and losses. Communication among converters is avoided and each individual VSC can be included in FFC support in a *plug-and-play* fashion.

¹ Note that we are not employing the DC-side control (2.10) from Chapter 2.

Since there is no need for provision of FFC in normal operation, the controller remains inactive until a disturbance is detected. As a disturbance indicator, internally obtainable RoCoF estimates defined by (7.2) are used. As long as the RoCoF stays within a predefined deadband the controller remains idle. Once the threshold is violated, the FFC is activated and kept in operation until the average RoCoF returns below prescribed margins. A benefit of such approach lies in the simultaneous activation and synchronous action of all VSCs participating in FFC, without the need for communication and independent of converter location.

In the remainder of this section, the derivation of an accurate frequency prediction model is presented together with mathematical formulation of the decentralized MPC problem. Moreover, a data-driven approach for estimating the prediction model parameters is described as well as the explicit MPC solution scheme for efficient computation of the optimal control inputs.

7.3.1 Frequency Prediction Model

The work in [166] proposes a simple RoCoF-based frequency prediction model, where at each discrete time step $k \in \mathbb{Z}_{\geq 0}$ an instantaneous RoCoF measurement $r_f(k) \in \mathbb{R}$ is obtained and used to estimate the frequency deviation $\Delta f(k+j) \in \mathbb{R}$ for N future time steps $j \in \{1, 2, \dots, N\}$ of the prediction horizon, as follows:

$$\Delta f(k+j) = r_f(k)T_s + \frac{\Delta p_c(k+j)}{2H}T_s. \quad (7.4)$$

Here, $T_s \in \mathbb{R}_{>0}$ denotes the length of a single time step, $H \in \mathbb{R}_{>0}$ is the aggregate inertia constant, and $\Delta p_c(k+j) \in \mathbb{R}$ represents the VSC power adjustment at the respective time step. Although simple and convenient for MPC implementation, the proposed model predicts a linear frequency decay based on the instantaneous RoCoF at the onset of the disturbance, and hence leads to large errors when estimating the frequency nadir.

We improve the prediction accuracy by employing a CoI frequency model of a generic low-inertia system introduced in Section 5.2, accounting for the inertial response and primary frequency control of SGs as well as the frequency support of converter-based generators. In Laplace domain, it can be represented by a simplified, yet sufficiently accurate, transfer function $G(s)$ relating the CoI frequency deviation $\Delta f(s) \in \mathbb{C}$ to a change in power $\Delta p(s) \in \mathbb{C}$:

$$G(s) = \frac{\Delta f(s)}{\Delta p(s)} = \frac{1}{MT} \frac{1+sT}{s^2 + 2\zeta\omega_n s + \omega_n^2}. \quad (7.5)$$

The definitions and analytical expressions for natural frequency $\omega_n \in \mathbb{R}_{>0}$, damping ratio $\zeta \in \mathbb{R}_{>0}$, and aggregate inertia and damping constants $M \in \mathbb{R}_{>0}$ and $D \in \mathbb{R}_{>0}$ are given by (5.4)-(5.5) and can be found in Section 5.2, together with the verification of the proposed frequency model; $T \in \mathbb{R}_{>0}$ stands for the generator time constant, assumed to be equal for all SGs in the system.

Transfer function (7.5) can now be transformed into a controllable canonical state-space model

$$\underbrace{\begin{bmatrix} \dot{q}_1(t) \\ \dot{q}_2(t) \end{bmatrix}}_{\dot{x}(t)} = \underbrace{\begin{bmatrix} 0 & I \\ -\omega_n^2 & -2\zeta\omega_n \end{bmatrix}}_A \begin{bmatrix} q_1(t) \\ q_2(t) \end{bmatrix} + \underbrace{\begin{bmatrix} 0 \\ I \end{bmatrix}}_B \Delta p(t), \quad (7.6a)$$

$$\Delta f(t) = \underbrace{\begin{bmatrix} \frac{1}{MT} & \frac{1}{M} \end{bmatrix}}_C \begin{bmatrix} q_1(t) \\ q_2(t) \end{bmatrix}, \quad (7.6b)$$

where $A \in \mathbb{R}^{2 \times 2}$, $B \in \mathbb{Z}_{\geq 0}^2$ and $C \in \mathbb{R}_{\geq 0}^{2 \times 1}$ denote the state-space matrices, and $x := (q_1, q_2) \in \mathbb{R}^2$ represents the state vector that does not correspond to any physical variables in the system. A zero-order hold equivalent of the state-space model is used to obtain a discrete-time form suitable for MPC application.

Since $\Delta p(t)$ is a control input in (7.6), it is necessary to measure the disturbance signal prior to predicting the frequency evolution. By applying a stepwise disturbance $\Delta p(s) = \Delta P/s$ to the model in (7.5), a relationship between the maximum instantaneous RoCoF $\dot{\omega}_{\max} \in \mathbb{R}$ and the disturbance magnitude $\Delta P \in \mathbb{R}$ is known, and yields $\dot{\omega}_{\max} := -\Delta P/M$ (see Section 5.2.2). Note that the formulation is presented in per-unit, i.e., $\dot{\omega}_{\max} = \dot{f}_{\max}/f_b$. Considering that the RoCoF measurements are internally available at each grid-forming VSC, the magnitude of the system disturbance can be locally estimated and subsequently used for frequency evolution prediction in (7.6).

7.3.2 Decentralized MPC Formulation

Let us denote by $\mathcal{H} = \{k, k+1, \dots, k+N\}$ the MPC prediction horizon of length N , including k as the current time step. The proposed optimization problem aims at minimizing the total control effort over the full horizon, i.e., $\forall k \in \mathcal{H}$, as follows:

$$\min_u \sum_{k \in \mathcal{H}} C_P(k) \|\Delta p_c^*(k)\| + C_H (\|\eta_f\|_\infty + \|\eta_r\|_\infty) \quad (7.7a)$$

$$\text{s.t. } x(k+1) = A_d x(k) + B_d (\Delta p_c^*(k) + \Delta P), \quad (7.7b)$$

$$f(k) = C_d x(k) + f_0, \quad (7.7c)$$

$$\dot{f}(k) = \frac{f(k) - f(k-1)}{T_s}, \quad (7.7d)$$

$$p_c(k) = p_c^* + \sum_{r=1}^k \Delta p_c^*(r) + R_c^p (\omega_c^* - \omega_c(k)), \quad (7.7e)$$

$$\chi(k+1) = \chi(k) + T_s \frac{p_c^* - p_c(k)}{E_b}, \quad (7.7f)$$

$$\underline{p}_c, \text{lim} \leq p_c(k) \leq \bar{p}_c, \text{lim}, \quad (7.7g)$$

$$\underline{\chi} \text{lim} \leq \chi(k) \leq \bar{\chi} \text{lim}, \quad (7.7h)$$

$$\underline{f} \text{lim} \leq f(k) + R_c^p \Delta p_c^*(k) \leq \bar{f} \text{lim}, \quad (7.7i)$$

$$\underline{f} \text{lim} - \eta_f(k) \leq f(k) \leq \bar{f} \text{lim} + \eta_f(k), \quad (7.7j)$$

$$\underline{\dot{f}} \text{lim} - \eta_r(k) \leq \dot{f}(k) \leq \bar{\dot{f}} \text{lim} + \eta_r(k), \quad (7.7k)$$

$$\eta_f(k) \geq 0, \eta_r(k) \geq 0, \quad (7.7l)$$

with $x(k) \in \mathbb{R}^2$ denoting a state vector at a discrete time step k and $u \in \mathbb{R}^{N+1}$ being the vector of setpoint changes $\Delta p_c^*(k)$. The coefficients $C_P(k) \in \mathbb{R}_{\geq 0}$ in the objective function (7.7a) represent the cost of the converter action at each time step k . Values of the coefficients are chosen such that $C_P(k) \leq C_P(k+1)$ holds, which incentivizes the use of control resources at earlier time steps in order to prevent late reactions and frequency oscillations near the frequency limit resulting from the converter setpoint alteration. Slack variables $\eta_f \in \mathbb{R}_{\geq 0}^{N+1}$ and $\eta_r \in \mathbb{R}_{\geq 0}^{N+1}$, in conjunction with a large penalty factor $C_H \in \mathbb{R}_{> 0}$, are used to relax the respective frequency and RoCoF constraints and avoid potential feasibility issues.

The prediction model described in (7.7b)-(7.7d) aims at anticipating the system frequency evolution for future time steps. For that purpose, the discrete-time counterpart of the frequency prediction model (7.6) is used, with $A_d \in \mathbb{R}^{2 \times 2}$, $B_d \in \mathbb{Z}_{\geq 0}^2$ and $C_d \in \mathbb{R}_{\geq 0}^{2 \times 1}$ describing the respective state space, $\Delta P \in \mathbb{R}$ denoting the estimated disturbance magnitude, $T_s \in \mathbb{R}_{> 0}$ designating the length of a single discrete time step, and $f_0 \in \mathbb{R}_{> 0}$ representing the frequency linearization point (i.e., the nominal frequency). Equality (7.7d) augments the frequency model with the prediction of average RoCoF over a single time step.

Constraints (7.7e)-(7.7i) take into account the physical limitations of the converter such as the upper and lower bounds on power output $p_c(k)$ and bat-

tery SoC $\chi(k)$. The second term in (7.7e) accumulates the setpoint changes from previous time steps and the third term accounts for the contribution of droop control; (7.7f) is a discrete formulation of the dynamics pertaining to battery SoC, with $p_{dc} = p_c^*$. Expression (7.7i) captures the impact of droop control on system frequency, thus anticipating excessive frequency spikes coming from fast setpoint changes at the converter nodes and preventing potential converter tripping. Finally, constraints (7.7j)-(7.7k) impose upper and lower bounds on system variables, with subscript “lim” indicating the respective threshold, whereas (7.7l) stands for trivial non-negativity constraints of slack variables.

Each VSC participating in FFC is expected to compensate for a portion of the total disturbance. Hence, the computed optimal setpoint change $\Delta p_{c_i}^*$ of each converter² $i \in \mathcal{N}_c$ is weighted by the participation coefficient $k_{p_i} := \bar{P}_i/P_t$ before being applied to the VSC, with $\bar{P}_i \in \mathbb{R}_{>0}$ being its rated power and $P_t \in \mathbb{R}_{>0}$ representing the net installed power of all converters participating in FFC.

7.3.3 Model Identification

Reliable performance of predictive control largely depends on the accuracy of the prediction model. The parameters in (7.5)-(7.6) vary with generator dispatch changes and require information regarding the specifications of every online generator. Hence, a methodology to obtain accurate model parameters needs to be developed. Combining the known mathematical structure of the prediction model with available measurement data, the *grey-box* modelling approaches can be exploited for online estimation of model parameters.

A grey-box model is mathematically formulated as a set of continuous stochastic differential equations. It can be derived by extending the state-space model (7.6) to account for measurement errors and process uncertainty, which yields

$$\dot{x}(t) = A(\Omega)x(t) + B(\Omega)\Delta p(t) + \mu, \quad (7.8a)$$

$$\Delta f(t) = C(\Omega)x(t) + \varepsilon, \quad (7.8b)$$

with $\Omega \in \mathbb{R}^p$ representing the vector of unknown parameters, $\mu \in \mathbb{R}^2$ denoting a Wiener process and $\varepsilon \in \mathbb{R}$ being the measurement error. The prediction error method [169] is an efficient grey-box identification approach for parameter estimation using a linear state estimator and minimizing the square of

² The index set notation is also adopted from Chapter 5.

prediction residuals over all measurement samples $m \in \mathcal{M} \subset \mathbb{Z}_{\geq 0}$. The optimization problem can be formulated as

$$\min_{\Omega} \sum_{m \in \mathcal{M}} \|\Delta f(m) - \Delta \hat{f}(m)\|_2^2 \quad (7.9a)$$

$$\text{s.t. } \hat{x}(m+1) = A(\Omega)\hat{x}(m) + B(\Omega)\Delta p(m) + K(\Omega) (\Delta f(m) - \Delta \hat{f}(m)), \quad (7.9b)$$

$$\Delta \hat{f}(m) = C(\Omega)\hat{x}(m), \quad (7.9c)$$

$$\hat{x}(0) = x_0, \quad (7.9d)$$

where $K(\Omega) \in \mathbb{R}^2$ is the parametrized Kalman gain, $x_0 \in \mathbb{R}^2$ represents the initial state vector, and symbol $\hat{x}(m) \in \mathbb{R}^2$ denotes the vector of estimated state variables from a measurement sample m .

The data required for system identification process ($\Delta f(t)$ and $\Delta p(t)$ in particular) can be obtained by means of load step-change tests carried out at the converter terminal. However, to ensure observability, the disturbance magnitude needs to be significant. Another approach is to use disturbance data acquired by the operator, but would require occasional communication and result in the loss of a plug-and-play feature. Nevertheless, note that this communication will be on a much longer timescale, which preserves the controller's decentralized aspect. The optimization problem (7.9) is solved using the MATLAB System Identification Toolbox [170], which also ensures stability by preserving the eigenvalues of $A - KC$ inside the unit circle.

7.3.4 Explicit MPC

Explicit MPC offers an alternative approach for computing optimal control actions without the need for executing an optimization algorithm in real time. The basis for such application lies in multi-parametric programming, whose solution yields a complete map of all optimal solutions for different operating conditions, and hence the effort needed to obtain the optimal control inputs reduces to function evaluation. The embedded control system can in turn be designed with low hardware and software requirements.

Deriving explicit MPC formulation of (7.7) transforms the given optimization problem into a *multi-parametric Linear Program* (mp-LP) by treating $l_k = (x(k), \chi(k), p_c(k)) \in \mathcal{P}$ as a parameter vector at current time step k , within a predefined feasible polyhedral set $\mathcal{P} \subset \mathbb{R}^4$. The solution of mp-LP gives an explicit MPC control law

$$\Delta p_c^*(l_k) = J_i(l_k) + q_i, \quad (7.10)$$

where $J_i(l_k) \in \mathbb{R}$ and $q_i \in \mathbb{R}$ define a piecewise affine function for all parameter vectors $l_k \in \mathcal{P}_i$ belonging to a polyhedral subspace partition $\mathcal{P}_i \subseteq \mathcal{P}$ of the original set [171]. The number of subspace partitions mostly depends on the number and complexity of constraints, whereas the required offline computational time depends on the length of the prediction horizon.

7.4 CENTRALIZED CONTROL DESIGN

The aim of the centralized grid controller is to provide fast frequency response by manipulating the active power setpoints of all converter-interfaced generators simultaneously. In contrast to decentralized control, which relies only on locally available measurements, an estimate of the dynamical system state can be globally obtained using a wide-area system of Phasor Measurement Units (PMUs), thus improving the regulation accuracy. A benefit of these additional measurements is that FFC can be provided while taking line power flow limits into consideration. In this study we assume the communication links to be reliable and high-speed, therefore neglecting any communication failure scenarios and delays and focusing solely on the underlying control problem.

Similarly to the decentralized MPC, the centralized grid controller is triggered by a large power imbalance. More precisely, PMU measurements at every bus are compared to the scheduled power injections in order to detect the disturbance. Once detected, the power imbalance is used as an input for the MPC problem. Upon activation, the MPC solver runs on a constant clock until average RoCoF values at every bus over a predefined time period fall below a given threshold. The remainder of this section presents the derivation of an appropriate prediction model and formulation of the centralized MPC problem.

7.4.1 Simplified System Model

Following the work in [154], we derive a prediction model that captures frequency dynamics of individual units as well as network line flows, while being simple enough for practical MPC implementation. Each VSC-interfaced unit $i \in \mathcal{N}_c$, where $n_c = |\mathcal{N}_c|$, can be modeled with two dynamic states $x_{c_i} = (\theta_{c_i}, \tilde{p}_{c_i}) \in \mathbb{R}^2$, reflecting the voltage angle $\theta_{c_i} \in [-\pi, \pi)$ and filtered active power $\tilde{p}_{c_i} \in \mathbb{R}$ from (7.1). Using droop control, the angle dynamics can be expressed by

$$\dot{\theta}_{c_i} = R_{c_i}^p (\Delta p_{c_i}^* - \tilde{p}_{c_i}), \quad (7.11)$$

thus capturing the frequency response of the converter linearized around a steady-state operating point.

For synchronous generation, a third-order SG model of the form

$$M_{s_j} \dot{\omega}_{s_j} = -D_{s_j} \omega_{s_j} + p_{m_j}^* - p_{s_j}, \quad (7.12)$$

$$T_{g_j} \dot{\tilde{p}}_{s_j} = -\tilde{p}_{s_j} - K_{g_j} \omega_{s_j}, \quad (7.13)$$

$$\dot{\theta}_{s_j} = \omega_{s_j} \quad (7.14)$$

is employed, where $x_{s_j} = (\theta_{s_j}, \omega_{s_j}, \tilde{p}_{s_j}) \in \mathbb{R}^3$ is the state vector describing the rotor angle $\theta_{s_j} \in [-\pi, \pi)$, rotor speed $\omega_{s_j} \in \mathbb{R}_{\geq 0}$, and dynamics of governor control $\tilde{p}_{s_j} \in \mathbb{R}$ of each synchronous generator $j \in \mathcal{N}_g$, with $n_g = |\mathcal{N}_g|$; $p_{s_j} \in \mathbb{R}$ indicates changes in the electrical power output, $M_{s_j} \in \mathbb{R}_{>0}$ and $D_{s_j} \in \mathbb{R}_{>0}$ denote generator inertia and damping constants, whereas $T_{g_j} \in \mathbb{R}_{>0}$ and $K_{g_j} \in \mathbb{R}_{>0}$ represent the governor time constant and control gain respectively. The swing equation (7.12) is linearized around steady state and assumes constant mechanical input $p_{m_j}^* \in \mathbb{R}_{\geq 0}$ over the timescales of interest. A first-order low-pass filter given by (7.13) models the governor dynamics and droop control of the generator [26].

A DC power flow approximation is used to model the network comprising $n_n = |\mathcal{N}_n|$ nodes and $n_b = |\mathcal{N}_b|$ branches, described by the graph Laplacian $L \in \mathbb{R}^{n_n \times n_n}$ (i.e., the bus susceptance matrix of the grid). Under small-signal DC power flow assumptions, the vector $p \in \mathbb{R}^{n_n}$ representing the active power injection at each node can be linearized as

$$p = L\theta + p_l, \quad (7.15)$$

with $\theta \in \mathbb{R}^{n_n}$ being the vector of nodal voltage angles and $p_l \in \mathbb{R}^{n_n}$ denoting the vector of load power changes at every bus. Line flows $p_b \in \mathbb{R}^{n_b}$ across branches are subsequently computed as $p_b = \hat{X}_b G \theta$, where $\hat{X}_b = \text{diag}(\hat{x}_1^{-1}, \dots, \hat{x}_{n_b}^{-1}) \in \mathbb{R}^{n_b \times n_b}$ denotes the line susceptance matrix³ and $G \in \mathbb{Z}^{n_b \times n_n}$ is the graph incidence matrix.

Finally, a uniform representation of the network comprising n_n nodes, n_b branches, n_g synchronous and n_c converter-interfaced generators can be established by combining (7.1) with (7.11)-(7.15), resulting in the linear system

$$\dot{x} = \hat{A}x + \hat{B}u, \quad (7.16a)$$

$$y = \hat{C}x + \hat{D}u, \quad (7.16b)$$

³ \hat{x}_k represents the series reactance of branch $k \in \mathcal{N}_b \subseteq \mathbb{Z}_{\geq 0}$.

where matrices $\hat{A} \in \mathbb{R}^{(2n_c+3n_g) \times (2n_c+3n_g)}$, $\hat{B} \in \mathbb{R}^{(2n_c+3n_g) \times (n_c+n_n)}$, $\hat{C} \in \mathbb{R}^{(n_c+n_g+n_b) \times (2n_c+3n_g)}$ and $\hat{D} \in \mathbb{R}^{(n_c+n_g+n_b) \times (n_c+n_n)}$ describe the respective state space, and system vectors are defined as

$$x = \left(x_{c_1}, \dots, x_{c_{n_c}}, x_{s_1}, \dots, x_{s_{n_g}} \right) \in \mathbb{R}^{2n_c+3n_g}, \quad (7.17a)$$

$$u = \left(\Delta p_{c_1}^*, \dots, \Delta p_{c_{n_c}}^* \right) \in \mathbb{R}^{n_c+n_n}, \quad (7.17b)$$

$$y = \left(f_{c_1}, \dots, f_{c_{n_c}}, f_{s_1}, \dots, f_{s_{n_g}}, p_{b_1}, \dots, p_{b_{n_b}} \right) \in \mathbb{R}^{n_c+n_g+n_b}. \quad (7.17c)$$

In (7.17c), $f_{s_i} = f_b \omega_{s_i}$ and $f_{c_i} = f_b \omega_{c_i}$ represent individual frequencies of SG and VSC units converted into SI, with $f_b = 50$ Hz being the base frequency.

7.4.2 Centralized MPC Formulation

The proposed optimization problem resembles the one presented in Section 7.3. Nonetheless, there are few key distinctions, as the centralized controller determines the power output of each converter participating in FFC. The objective function therefore aims at minimizing the total control effort over the full horizon $k \in \mathcal{H}$ and over all converter units $i \in \mathcal{N}_c$:

$$\min_u \sum_{k \in \mathcal{H}} \sum_{i \in \mathcal{N}_c} C_{P_i}(k) \|\Delta p_{c_i}^*(k)\| + C_H (\|\eta_f\|_\infty + \|\eta_r\|_\infty) \quad (7.18a)$$

$$\text{s.t. } \forall k \in \mathcal{H}, \forall i \in \mathcal{N}_c, \forall j \in \mathcal{N},$$

$$x(k+1) = \hat{A}_d x(k) + \hat{B}_d u(k), \quad (7.18b)$$

$$y(k) = \hat{C}_d x(k) + \hat{D}_d u(k) + \begin{bmatrix} f_0 \\ p_{b_0} \end{bmatrix}, \quad (7.18c)$$

$$\dot{f}_j(k) = \frac{f_j(k) - f_j(k-1)}{T_s}, \quad (7.18d)$$

$$p_{c_i}(k) = p_{c_i}^* + \sum_{r=1}^k \Delta p_{c_i}^*(r) + R_{c_i}^p (\omega_{c_i}^* - \omega_{c_i}(k)), \quad (7.18e)$$

$$\chi_i(k+1) = \chi_i(k) + T_s \frac{p_{c_i}^* - p_{c_i}(k)}{E_{b_i}}, \quad (7.18f)$$

$$\underline{p}_{c_i, \text{lim}} \leq p_{c_i}(k) \leq \bar{p}_{c_i, \text{lim}}, \quad (7.18g)$$

$$\underline{\chi}_i, \text{lim} \leq \chi_i(k) \leq \bar{\chi}_i, \text{lim}, \quad (7.18h)$$

$$\underline{f}_{\text{lim}} \leq f_i(k) + R_{c_i}^p \Delta p_{c_i}^*(k) \leq \bar{f}_{\text{lim}}, \quad (7.18i)$$

$$\underline{p}_b, \text{lim} \leq p_b \leq \bar{p}_b, \text{lim}, \quad (7.18j)$$

$$\underline{f}_{\text{lim}} - \eta_f(k) \leq f_j(k) \leq \bar{f}_{\text{lim}} + \eta_f(k), \quad (7.18k)$$

$$\underline{\dot{f}}_{\text{lim}} - \eta_r(k) \leq \dot{f}_j(k) \leq \bar{\dot{f}}_{\text{lim}} + \eta_r(k), \quad (7.18l)$$

$$\eta_f(k) \geq 0, \eta_r(k) \geq 0, \quad (7.18m)$$

where $\mathcal{N} = \mathcal{N}_g \cup \mathcal{N}_c$ denotes the index set of all generators (including both synchronous and converter-interfaced ones) in the system, and $u(k) \in \mathbb{R}^{n_c+n_n}$ is the vector comprising setpoint changes $\Delta p_{c_i}^*(k)$ of all VSCs and nodal load injections $p_l(k)$ at time step k . The prediction model in (7.18b)-(7.18c) represents the discrete-time counterpart (denoted by subscript d) of the state space given by (7.16)-(7.17), with the vector of load injections p_l in (7.17b) being populated by PMU measurements of system disturbances and remaining constant throughout the prediction horizon. Vectors $f_0 \in \mathbb{R}^{n_c}$ and $p_{b_0} \in \mathbb{R}^{n_b}$ define the linearization point for individual converter frequencies and network line flows. The RoCoF is calculated for all generators in (7.18d) and branch flows are kept within permissible limits in (7.18j). Constraints on each individual VSC (7.18e)-(7.18i) are imposed to keep the SoC, power output and frequency spikes within limits, with the notation adapted from (7.7). Frequency and RoCoF constraints are enforced on all generators in (7.18k)-(7.18l), whereas non-negativity constraints are imposed on slack variables in (7.18m).

7.5 MODEL VALIDATION AND CONTROL PERFORMANCE

The two proposed FFC schemes have been implemented and evaluated on the IEEE 39-bus test system depicted in Fig. 7.2. This is a well-known 10-machine representation of the New England power system, with generator at node 1 representing the aggregation of a large number of generators. The relevant network, load and generation parameters can be found in [172, 173]. The simulations have been performed in MATLAB using a DAE model described in Section 2.9 that encompasses detailed representation of generator and transmission line dynamics. The investigated system comprises seven conventional generators, as three SGs from the original system (precisely at nodes 1, 2 and 3) have been replaced by converter-interfaced units of 1000 MW installed power for the purposes of this analysis. The respective power ratings and output limits of the remaining SGs have been preserved. All VSCs operate in grid-forming mode, parametrized according to Table 2.1, and are equipped with the supervisory FFC layer.

The disturbances are generated through step changes in active power at network buses of interest, thus emulating either a loss of generator or a loss of

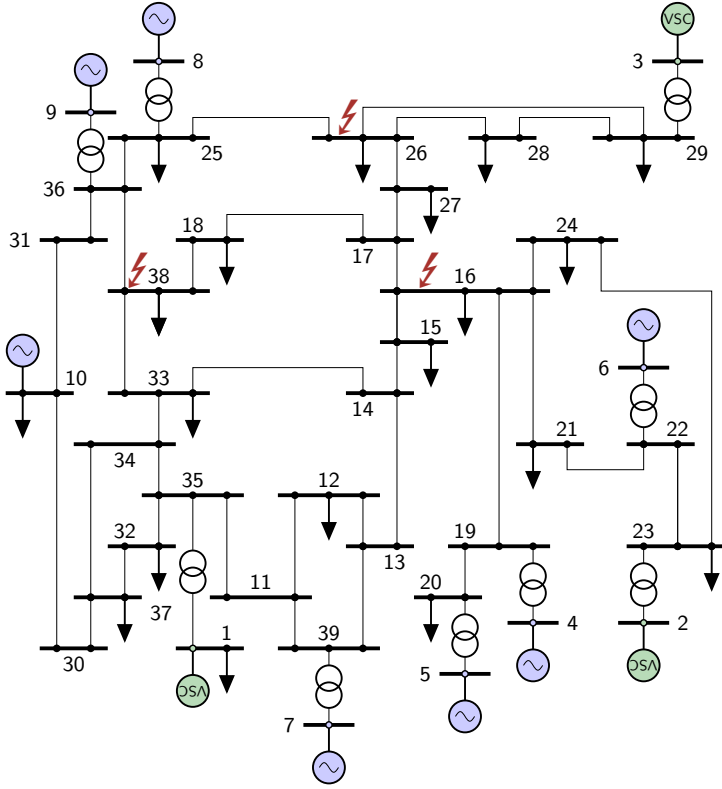


FIGURE 7.2: IEEE 39-bus New England test system. Inverter-based generation is placed at nodes 1, 2 and 3. Disturbance locations under consideration are indicated by red symbols.

load. In this study we assume that the first stage of automatic load-shedding is initiated in case of frequency deviation beyond ± 0.5 Hz, whereas the RoCoF protection is triggered at ± 1 Hz/s for RoCoF measurements averaged over a 250 ms cycle. Therefore, the frequency-related thresholds in (7.7) and (7.18) are set as follows: $\underline{f}_{\text{lim}} = 49.5$ Hz, $\bar{f}_{\text{lim}} = 50.5$ Hz, $\underline{\dot{f}}_{\text{lim}} = -1$ Hz/s and $\bar{\dot{f}}_{\text{lim}} = 1$ Hz/s.

The prediction horizon of the MPC-based controller is set to three time steps with a sampling period of 250 ms. On the one hand, the prediction horizon length of 750 ms reflects a trade-off between controller performance and computational effort. On the other hand, the MPC sampling period is selected such that it exceeds all delays associated with the converter and

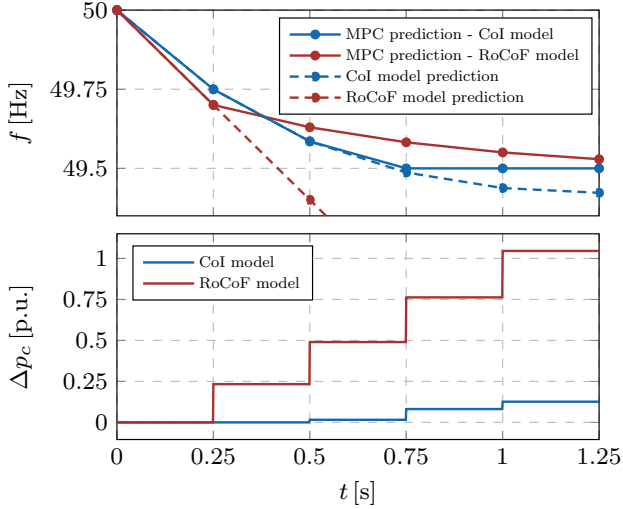


FIGURE 7.3: Comparison of decentralized MPC performance under two frequency prediction models. Anticipated frequency evolution and adjusted power injections are used for evaluation.

supervisory layer, as well as the time needed to compute the optimal control decisions.

The following sections will first analyze the impact of parametrization on the accuracy of the frequency prediction model in (7.6), and compare it against the RoCoF-based approach in (7.4). Subsequently, the controller performance for different disturbance locations and magnitudes is evaluated, followed by a discussion on the battery storage requirements and explicit MPC formulation.

7.5.1 Prediction Model Validation

The controller operation for $N = 5$ time steps is shown in Fig. 7.3, comparing the performance of the proposed frequency prediction model against the RoCoF-based one. Predicted frequency evolution in case of no corrective actions (indicated by the dashed lines) demonstrates the conservative nature of the RoCoF-based approach. In particular, due to constant RoCoF estimate throughout the whole prediction horizon, the anticipated frequency nadir is well below the actual value. As a result, the control effort is significantly higher

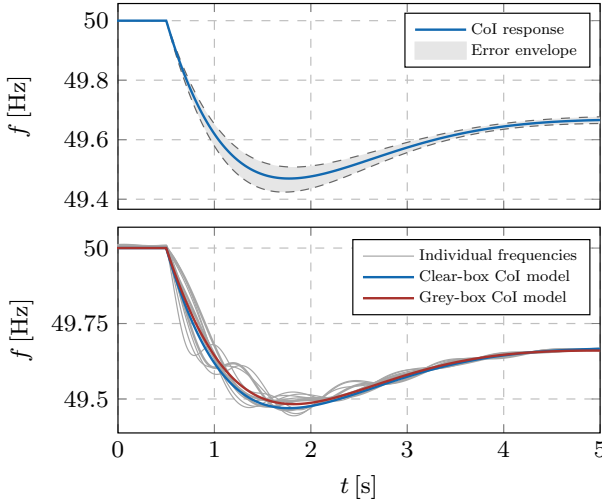


FIGURE 7.4: Accuracy of the frequency prediction model: sensitivity to model parameters (top) and CoI-model verification (bottom).

than with the CoI model. Being proven advantageous and more efficient, only the CoI model is considered hereinafter.

It was noted previously that inaccurate knowledge of system parameters in the CoI model could lead to degradation of response quality and potential control failure. To investigate the severity of this problem, a parametric sensitivity analysis was performed for an arbitrary disturbance by considering all possible combinations of two SGs in the IEEE 39-bus system going offline. The error envelope around the median frequency response, derived from simulations and illustrated in the upper plot of Fig. 7.4, indicates the maximum nadir error of $\approx 0.01\%$ for the considered generator sets.

The aforementioned issue with parameter uncertainty can be mitigated through the grey-box system identification procedure outlined in Section 7.3. To illustrate the efficiency of such approach, an active power step change of 1575 MW at bus 16 is simulated, with generator frequencies presented in Fig. 7.4. The individual frequencies are compared to the frequency prediction of the CoI model, once parametrized using the exact generator parameters (clear-box) and once through the grey-box model identification procedure. The individual generator frequencies are matched well by the CoI model response in both cases, with a negligible difference between the two parametrization methods. The data used for system identification process were retrieved by

simulating a different load step disturbance and collecting VSC frequency measurements at node 1. Parameter fitting was subsequently employed using the MATLAB System Identification Toolbox with an RMSE of 2%.

7.5.2 Control Performance and Comparison

Performance of the decentralized control depends on how well the power imbalance can be estimated through internal RoCoF state of the active power controller. It is well known that frequencies, and correspondingly the instantaneous RoCoF values, will vary significantly at different nodes of a large power system following a disturbance. For this reason, a symmetrical placement of converters providing FFC support is crucial for coverage of disturbances at as many system nodes as possible. Since power ratings of all VSCs are the same, each unit is expected to participate equally in disturbance mitigation. Unlike the decentralized approach, the centralized grid controller obtains an accurate disturbance estimate through wide-area measurements, independent of the disturbance location, and hence operates with low error margins.

In the following, we evaluate and compare the performance of both control approaches by analyzing the system response for different disturbance locations indicated in Fig. 7.2. The values of applied and estimated disturbance magnitudes for every considered bus and for each VSC are presented in Table 7.1.

First, let us consider a power disturbance of 1575 MW at node 16. Fig. 7.5 shows the frequencies of individual generators for both FFC approaches. The dashed line represents the lowest (i.e., “worst-case”) frequency nadir of any SG in the system when the FFC is disabled. The VSC at node 3 remains inactive due to the large electrical distance to the fault location

Bus	Disturbance [MW]	Estimated disturbance [MW]		
		VSC 1	VSC 2	VSC 3
16	1575	1550	1955	835
26	1430	1100	790	3860
38	1850	1390	520	650

TABLE 7.1: Fault scenarios at different buses with indicated applied disturbance magnitudes and estimated imbalances for each VSC located at nodes 1, 2 and 3, respectively.

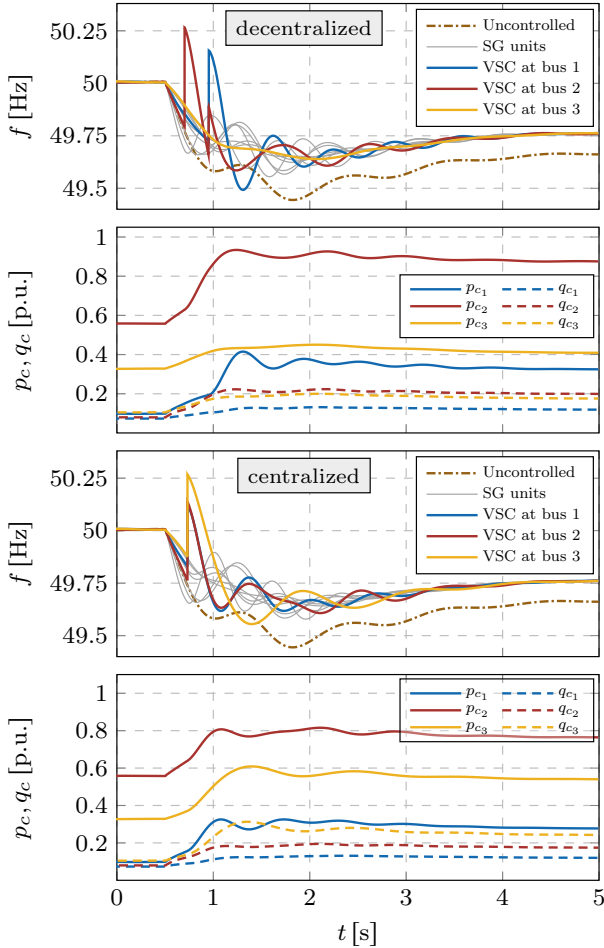


FIGURE 7.5: Individual frequency and power response for the decentralized (top two figures) and centralized (bottom two figures) FFC scheme following a disturbance at bus 16. Uncontrolled response reflects the worst-case generator frequency without the use of FFC.

and consequent underestimation of the disturbance. However, the support from the other two converters is sufficient to compensate the disturbance and prevent load-shedding. On the other hand, the global MPC-based grid controller dispatches all three units equally, with the identical total control effort for both MPC approaches.

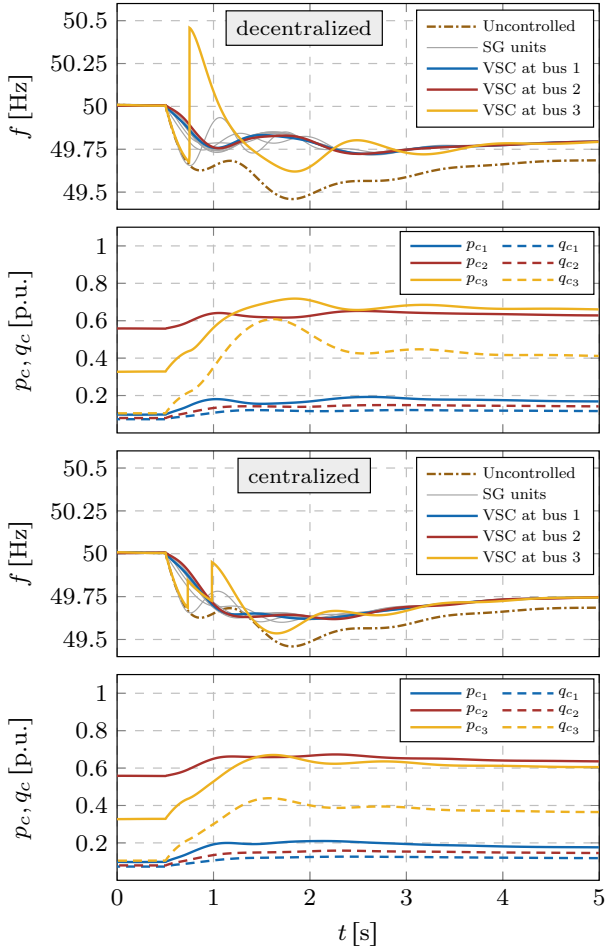


FIGURE 7.6: Individual frequency and power response for the decentralized (top two figures) and centralized (bottom two figures) FFC scheme following a disturbance at bus 26.

In contrast, Fig. 7.6 illustrates the control performance for a disturbance at bus 26, in the vicinity of converter-interfaced DG at node 3. Hence, this VSC unit overestimates the disturbance and increases its power output to the saturation limit, whereas the other two converters remained idle. Similarly, the centralized controller increases only the power output of the VSC at node 3, which due to its location has the most influence on the relevant frequency

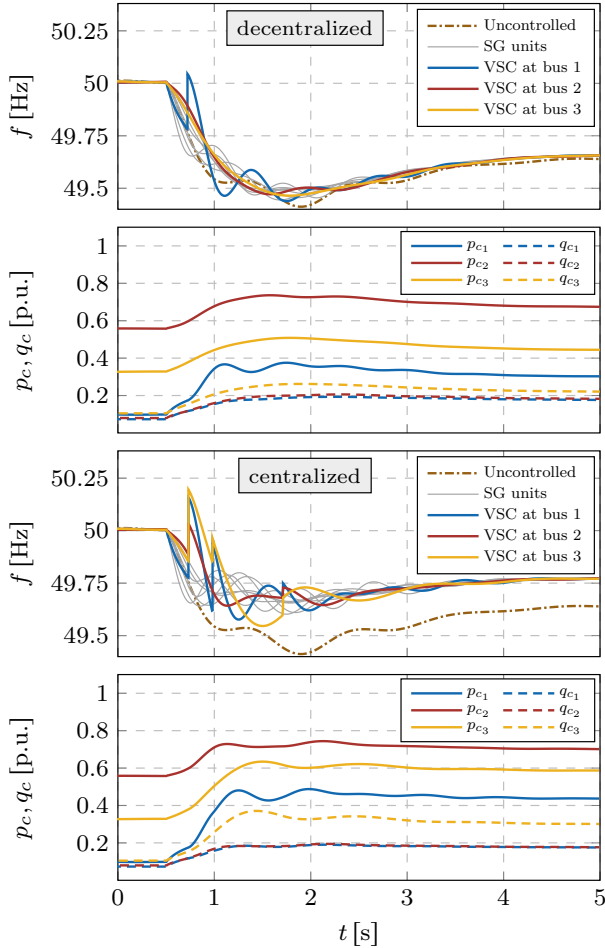


FIGURE 7.7: Individual frequency and power response for the decentralized (top two figures) and centralized (bottom two figures) FFC scheme following a disturbance at bus 38.

dynamics. An overall lower control effort is employed in the centralized approach.

Lastly, we consider a disturbance at bus 38, located such that it exhibits a large electrical distance between all three VSCs. The individual frequency response of all generators is given in Fig. 7.7. Understandably, decentralized controllers underestimate the disturbance due to a large electrical distance

from the fault location. VSC-based DG at bus 1 is the only one to react, though insufficiently to compensate for the disturbance and prevent load-shedding. Having accurate global measurements, the centralized grid controller detects the disturbance and reacts appropriately and timely through all available converter-interfaced units.

7.5.3 Analysis of Computational Efficiency

The solution of the linear MPC optimization problems (7.7) and (7.18) was performed using the CPLEX solver, an LP solver based on interior point algorithms, for numerical computation and YALMIP [174] for high-level modeling. The computational time required for solving the decentralized MPC problem is 182.35 ms, whereas the centralized MPC problem is solved in 342.43 ms on average. The computational efficiency for the decentralized controller can further be improved by generating an explicit solution, as discussed in Sec. 7.3. The explicit MPC solution was generated using YALMIP for modeling and the MPT3 toolbox [175] for low-level numerical solution of the multi-parametric optimization problem. The solution partitions the parameter space in 452 regions and takes 1.295 s to be generated. In this case, the time required to obtain the optimal control inputs reduces to 15.86 ms.

7.6 CONCLUSION

This chapter presents a novel FFC scheme for converter-interfaced DGs in low-inertia systems, which exploits their fast response to prevent load-shedding scenarios. An MPC-based supervisory control layer is added to the traditional converter control scheme, which in response to a large disturbance manipulates converter setpoints to contain the frequency within predefined bounds. Both centralized and decentralized control approaches were considered and compared. Novel prediction models were developed and compared to the state-of-the-art, which showcased improvements in prediction accuracy.

The centralized approach has proven to be advantageous in several cases indicating the value of fast communication infrastructure. On the other hand, the decentralized controller proves to be efficient for containing frequency excursions for disturbances occurring in the vicinity of at least one or few converter-interfaced generators. Advantages of this approach are a simple, plug-and-play architecture, as well as a low-cost and computationally efficient implementation. Simulation results do not suggest any potential frequency

instabilities arising from the control actions of the MPC-based supervisory layer, but we leave a theoretical proof of stability for future work.

7.6.1 *Outlook and Future Work*

An interesting avenue for future work is a distributed approach, where controllers of individual VSCs carry out their calculations in separate processors, but efficiently cooperate using only communication links between different local controllers. The extension of this study will focus on applying the uniform frequency model from Section 5.2 to machine learning frameworks, such as data-driven Support Vector Machine (SVM), to accurately predict system frequency evolution in the aftermath of a disturbance.

The quality of frequency prediction depends on the accuracy of the estimated disturbance magnitude. In Section 7.3, individual inverters use local instantaneous RoCoF measurements to compute the disturbance magnitude. However, it was observed that the instantaneous RoCoF values at different nodes of a large power system can vary significantly following a disturbance, thus resulting in inaccurate magnitude estimates. With the distributed control scheme, the existing communication infrastructure would allow the individual units to exchange local RoCoF measurements and obtain a more reliable disturbance estimate. In this sense, a distributed observer is used for providing a reliable and accurate disturbance magnitude estimation for the CoI model.

The distributed observer could be designed by collecting data from offline simulations and subsequently employing SVM regression to develop a predictor model, which would provide far more accurate estimates of the disturbance magnitude according to provided measurements. Moreover, converters can exchange information about the setpoint changes they are about to apply. Hence, each converter acquires the same disturbance estimation as well as the knowledge about future corrective actions, which would eventually ensure a synchronized and cooperative response of all VSCs providing FFC support.

SIZING AND TUNING OF DC-SIDE STORAGE FOR FFC PROVISION

This chapter discusses a method for combined sizing of DC-side storage capacity and tuning of controller gains of grid-forming converters, which accounts for the coupling between installation planning and operation parameters of the storage unit. Furthermore, it ensures sufficient energy and power capacity for containing a predefined active power imbalance and preserving frequency within prescribed limits. For this purpose, the analytic expressions of relevant frequency metrics as well as the energy utilization of the associated converter storage are incorporated into a non-convex optimization problem, which is then simplified by constructing and utilizing linear approximations of some of the nonlinear constraints. As a result, the optimal installed power/energy capacity can be determined, together with the virtual inertia and damping gains of the associated converter control scheme. The chapter is based on [176].

8.1 INTRODUCTION

As previously explained in Chapters 5-7, the majority of advanced VSC control strategies assumes an infinite amount of power and energy on the converter's DC side, thus neglecting its dynamical limitations [23, 49, 141, 142, 144–149]. In fact, the problem of storage sizing is typically overlooked, as all of the above mentioned studies focus solely on improving the frequency response. While the control aspect of this problem is addressed in Chapters 5-7 through more intelligent and responsive FFC schemes, the actual sizing of storage capacity is determined *a priori* and not taken into analysis.

Complementary works that take storage aspects into consideration usually involve strong simplifying assumptions regarding the AC-side dynamics and control, which obscures the complexity of the problems pertaining to low-inertia systems. More precisely, the work in [177] improves the ability of batteries to provide frequency control by introducing two heuristics that offset their frequency response in order to respond only to fast and zero-mean frequency deviations. While this method provides quantitative insights from the storage unit and TSO perspectives, it mostly focuses on battery degra-

dation and disregards the sizing aspect. On the other hand, [178, Section III] considers novel ancillary services that leverage the flexibility and fast response of converter-interfaced generation, more precisely the impact of the associated energy storage. A control scheme for power converters with energy storage system is proposed that provides services such as electrical inertia and Primary Frequency Control (PFC), while explicitly accounting for limited energy storage capacity. A similar perspective pertains to the problem analyzed in [139] where, given a set of converter-interfaced generators providing similar ancillary services, an optimization-based approach is developed to optimally allocate such devices in a power system to ensure robust operation. However, both [178] and [139] assume a given size of installed battery capacity and focus on optimal control tuning and regulation of the provided resources.

With drastic changes to the power system generation portfolio and the overall system dynamics, requirements on frequency regulation are changing. While the distinction between different ancillary services might be clear on the system-level, it is not the case for actual device-level implementation and control of the associated energy buffer. Moreover, the physical properties of existing storage units impose additional constraints on the design. We tackle this issue by proposing a novel approach that combines sizing of the DC-side storage and tuning of the VSM controller gains of grid-forming converters. The proposed approach accounts for the coupling between the sizing of the storage and the tuning of the control parameters of the converter, namely the dependence of energy drawn from or fed to the storage on the VSM controller gains. Furthermore, the method ensures sufficient energy and power capacity for containing a prescribed active power imbalance and preserving frequency within limits given by the operator [152]. Such comprehensive and multifaceted design approach has not been taken in the literature thus far.

The contribution of this work is twofold. First, the relationships between frequency and power/energy storage capacity are derived analytically and, together with closed-form CoI frequency expressions, incorporated into an optimization problem. Second, we propose approximations and an iterative solution scheme that render the problem reliably solvable by commercial nonlinear solvers. The proposed methods are demonstrated in an exemplar case study to determine the optimal sizing and controller tuning parameters, which are then incorporated into detailed converter control schemes and verified through time-domain simulations.

The rest of the chapter is structured as follows. Section 8.2 discusses theoretical preliminaries, namely the derivation of frequency and damping ratio-related constraints. The problem formulation is presented in Section 8.3,

where the proposed optimization problem and the necessary approximations are described. The optimization results in terms of storage sizing and VSM tuning are provided in Section 8.4, whereas Section 8.5 concludes the chapter.

8.2 THEORETICAL PRELIMINARIES

Let us recall from Section 5.2 that the expressions for relevant frequency metrics, namely frequency nadir, RoCoF and steady-state deviation, can be obtained analytically as follows:

$$\Delta f_{\max}^{(k)} := -\frac{\Delta P}{D + R_g} \left(1 + (-1)^k \sqrt{\frac{T(R_g - F_g)}{M}} e^{-\zeta \omega_n t_m^{(k)}} \right), \quad (8.1a)$$

$$\dot{f}_{\max} := -\frac{\Delta P}{M}, \quad (8.1b)$$

$$\Delta f_{\text{ss}} := -\frac{\Delta P}{D + R_g}, \quad (8.1c)$$

with the time instances of local frequency extremum given by

$$t_m^{(k)} := \frac{1}{\omega_d} \tan^{-1} \left(\frac{\omega_d}{\zeta \omega_n - T^{-1}} \right) + \frac{k\pi}{\omega_d}, \quad (8.2)$$

and the underlying variables defined as

$$\omega_n := \sqrt{\frac{D + R_g}{MT}}, \quad \zeta := \frac{M + T(D + F_g)}{2\sqrt{MT(D + R_g)}}, \quad \omega_d := \omega_n \sqrt{1 - \zeta^2}. \quad (8.3)$$

Note that the inertia $M \in \mathbb{R}_{>0}$ and damping $D \in \mathbb{R}_{>0}$ constants represent weighted system averages and that the formulation is given in per-unit. In case of decaying oscillations (i.e., an underdamped response), the maximum frequency nadir occurs at the instance of first frequency extremum $\Delta f_{\max} := \Delta f_{\max}^{(0)}$. More details on the notation and derivation of the expressions in (8.1)-(8.3) are provided in Section 5.2.2.

It can clearly be deduced from (8.1) that the frequency response is highly dependent on inertia and damping, both of which can be modified through appropriate *sizing* of the converter DC-side storage and *tuning* of the associated VSM control gains. In particular, by optimizing the installed power/energy capacity of the converter's storage unit and the virtual inertia and damping gains of a VSM controller, one can regulate the aggregate inertia and damping accordingly. Therefore, RoCoF and steady-state frequency deviation can be controlled explicitly via respective M and D adjustment, and nadir through

a highly nonlinear function given by (8.1a) for $k = 0$. We highlight that, unlike the previous concepts in Chapter 5 and Chapter 6, we do not consider adaptive VSM control designs in this study. In other words, while defined as decision variables and optimally computed for the problem at hand, the inertia and damping constants are not to be changed in real time once the VSM control is tuned and implemented. This is justified by the fact that such methodology has a higher potential for real-world applications.

Moreover, the expressions (8.2)-(8.3) suggest that variables ω_d and $t_m^{(k)}$ are not necessarily real numbers. To ensure that $\omega_d \in \mathbb{R}$ and hence $t_m^{(k)} \in \mathbb{R}$, we only consider an underdamped frequency response, i.e.,

$$\zeta = \frac{M + T(D + F_g)}{2\sqrt{MT(D + R_g)}} < 1, \quad (8.4)$$

which imposes an upper bound on damping as a function of system inertia: $D < \bar{D}(M)$. Moreover, in order for $t_m^{(0)} > 0$ to hold, the argument of the arctan expression in (8.2) needs to be strictly positive, thus preventing the discontinuity at $\zeta\omega_n = T^{-1}$. In mathematical terms, the inequality

$$0 < \frac{\omega_d}{\zeta\omega_n - T^{-1}} \quad (8.5)$$

must be satisfied, which is equivalent to

$$\underline{D}(M) = \frac{M}{T} - F_g < D. \quad (8.6)$$

Expression (8.6) provides a lower bound on average system damping, again as a function of system inertia. Finally, by imposing the limits on aforementioned frequency metrics in (8.1), and combining them with (8.4), (8.6) and the trivial non-negativity conditions for M and D , one obtains a feasible region in the $M - D$ plane. An example of such region is illustrated in Fig. 8.1 for an arbitrary set of online generation units. Noticeably, the addition of maximum limits on frequency metrics (denoted by subscript “lim”) imposes minimum requirements on inertia and damping constants, thus reducing the fundamental feasible region defined by $\underline{D}(M) < D < \bar{D}(M)$.

8.3 PROBLEM FORMULATION

8.3.1 Objectives and Problem Description

The goal of this study is to compute the minimum storage capacity sufficient for providing adequate frequency support in a low-inertia system. Such storage

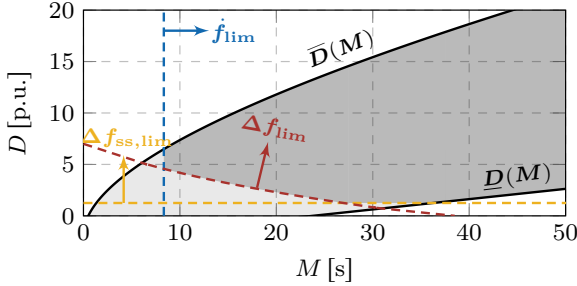


FIGURE 8.1: An exemplar feasible region in the $M - D$ plane. Colored arrows indicate feasible half-planes of respective frequency constraints.

device is interfaced to the grid through a fully controllable VSC employing a VSM regulation presented in Section 2.2.4. Having the battery as the only source of energy, the VSM controller must efficiently use the available resources in order to preserve frequency within given bounds and not exceed the physical storage limitations, namely energy and power capacity. The tuning of VSM parameters is therefore of crucial importance and, as such, explicitly included in the analysis.

In order for the VSM to provide FFC, the converter must be operating in a grid-forming mode (see Section 2.2.4 for more details). This implies that its integration into the network will increase the total grid-forming capacity of the system. Mathematically speaking, the aggregate inertia and damping constants defined in (5.5a) will now be transformed into

$$M := \frac{M_g P_{b_g} + M_c P_{b_c} + M_b P_b}{P_{b_g} + P_{b_c} + P_b}, \quad D := \frac{D_g P_{b_g} + D_c P_{b_c} + D_b P_b}{P_{b_g} + P_{b_c} + P_b}, \quad (8.7)$$

with $P_b \in \mathbb{R}_{>0}$, $M_b \in \mathbb{R}_{>0}$ and $D_b \in \mathbb{R}_{>0}$ representing the installed battery power and the emulated inertia and damping gains of the battery's VSM controller, respectively. The remaining parameters in (8.7) reflect the base powers (P_{b_g}, P_{b_c}) and normalized inertia (M_g, M_c) and damping (D_g, D_c) constants of synchronous and converter-interfaced generation in the network, respectively. The appropriate definitions and analytical derivations can be found in Section 5.2. The expressions in (8.7) clearly show that, in addition to the VSM control gains, the installed power capacity of the battery will also have a decisive impact on frequency performance of the system. Therefore, it must also be considered a decision variable in the problem formulation.

8.3.2 Optimization Problem

The task of computing the installed battery capacity (P_b, E_b) and respective VSM parameters (M_b, D_b) is tackled through a single optimization problem of the form:

$$\min_{M_b, D_b, P_b} C_{\text{inst}}(P_b) \quad (8.8a)$$

$$\text{s.t.} \quad |\Delta f_{\text{max}}| f_0 \leq \Delta f_{\text{lim}}, \quad (8.8b)$$

$$\left| \dot{f}_{\text{max}} \right| f_0 \leq \dot{f}_{\text{lim}}, \quad (8.8c)$$

$$|\Delta f_{\text{ss}}| f_0 \leq \Delta f_{\text{ss,lim}}, \quad (8.8d)$$

$$\underline{D}(M) < D < \bar{D}(M), \quad (8.8e)$$

$$F(M_b, D_b, P_b) \leq 0, \quad (8.8f)$$

$$\left| M_b \dot{f}(t) + D_b \Delta f(t) \right| \leq \frac{P_b}{P_0}, \quad \forall t, \quad (8.8g)$$

$$\left| \int_0^{t_{\text{ss}}} \left(M_b \dot{f}(t) + D_b \Delta f(t) \right) dt \right| \leq \frac{E_b}{\eta_b P_0}, \quad (8.8h)$$

where $E_b \in \mathbb{R}$ denotes the storage energy capacity and $C_{\text{inst}} \in \mathbb{R}$ is the total battery installation cost of the form $C_{\text{inst}}(P_b) = aP_b^2 + bP_b$. The negative quadratic cost factor $a = -500 \text{ \$/MW}^2$ and the positive linear factor $b = 1000 \text{ \$/MW}$ reflect the economies of scale [179]. Only P_b accounts for the installation costs of the battery, whereas the virtual control gains are essentially “cost-free”. Note that the average system parameters $M = f_M(M_b, P_b)$ and $D = f_D(D_b, P_b)$ in (8.7) are weighted functions of the respective decision variables. Moreover, $E_b = \eta_b P_b$ is linked to installed battery power using the energy-to-power ratio $\eta_b \in \mathbb{R}_{>0}$, and therefore only P_b is declared as a decision variable in (8.8a).

Constraints (8.8b)-(8.8d) reflect the enforced frequency limits, more precisely the under-frequency load-shedding trigger ($\Delta f_{\text{lim}} = 0.5 \text{ Hz}$), the maximum permissible RoCoF ($\dot{f}_{\text{lim}} = 0.6 \text{ Hz/s}$) and the maximum allowed steady-state deviation ($\Delta f_{\text{ss,lim}} = 0.2 \text{ Hz}$); the frequency expressions are converted into SI through multiplication by nominal (i.e., base) frequency $f_0 = 50 \text{ Hz}$. Furthermore, inequality (8.8e) captures the fundamental feasible region required for validity of analytical expressions pertaining to frequency metrics in (8.8b)-(8.8d). Constraint (8.8f) stands for some trivial non-negativity and variable constraints, e.g., $M_b \geq 0$. Finally, (8.8g)-(8.8h) describe the battery power and energy capacity constraints. According to the swing equation of the battery’s VSM, the maximum absolute value of the instantaneous power

in (8.8g) is constrained by P_b . As we are working in per-unit, the right-hand side of (8.8g)-(8.8h) is normalized by the base power $P_0 \in \mathbb{R}_{>0}$ and base energy $E_0 = \eta_b P_0$, respectively.

Optimization problem (8.8) is non-convex due to the non-convex quadratic objective function (8.8a) and the nonlinear constraints. Specifically, the maximum absolute value of the swing equation representing the battery's VSM control in (8.8g) and the energy capacity integral in (8.8h) can be both computed analytically, however this results in highly nonlinear and nested trigonometric expressions. Removing (8.8g) and (8.8h) results in a problem (8.8a)-(8.8f) that can be solved to a local minimum with off-the-shelf solvers such as IPOPT, despite the remaining non-convexity due to the concave objective function (8.8a). Nevertheless, introducing complicated constraints (8.8g) and (8.8h) raises numerical issues and prevents state-of-the-art solvers from reliably finding a local optimum. To work around this issue, we propose to approximate both (8.8g) and (8.8h). The left-hand side of the former constraint is split into two terms referring to frequency-related and RoCoF-related power injection, and conservatively bounded using a triangular inequality of the form

$$\left| M_b \dot{f}(t) + D_b \Delta f(t) \right| \leq \left| M_b \dot{f}(t) \right| + \left| D_b \Delta f(t) \right| \leq \left| M_b \dot{f}_{\max} \right| + \left| D_b \Delta f_{\max} \right|, \forall t, \quad (8.9)$$

which transforms (8.8g) into

$$\left| M_b \dot{f}_{\max} \right| + \left| D_b \Delta f_{\max} \right| \leq \frac{P_b}{P_0}. \quad (8.10)$$

Having previously obtained closed-form expressions for Δf_{\max} and \dot{f}_{\max} , incorporating (8.10) into (8.8) is trivial.

On the other hand, constraint (8.8h) is linearized by approximating the frequency deviation and its first derivative using four linear segments (denoted by Δf_{lin} and \dot{f}_{lin} hereinafter) and the respective frequency thresholds, as outlined in the following section. The resulting approximation of the energy capacity constraint would thus be given by

$$\left| \int_0^{t_{\text{ss}}} \left(M_b \dot{f}_{\text{lin}}(t) + D_b \Delta f_{\text{lin}}(t) \right) dt \right| \leq \frac{E_b}{\eta_b P_0}. \quad (8.11)$$

8.3.3 Approximation of Frequency Deviation and RoCoF

A piecewise linear approximation of frequency deviation $\Delta f(t)$ and its derivative $\dot{f}(t)$ after a disturbance is achieved by dividing the respective time-domain

signals into linear intervals specified by the time instances $t_p, t_m^{(0)}, t_m^{(1)}$ and t_{ss} ; $t_m^{(0)} \in \mathbb{R}_{>0}$ and $t_m^{(1)} \in \mathbb{R}_{>0}$ correspond to the first two local frequency extrema given by (8.2), while $t_p \in \mathbb{R}_{>0}$ is defined by the intersection point of the maximum permissible nadir and RoCoF limits, i.e., $t_p = \Delta f_{lim} / \dot{f}_{lim}$. The integration time $t_{ss} \in \mathbb{R}_{>0}$ is set to a fixed value of 30 s, which is analytically validated as a sufficient period for the decay of frequency oscillations, precisely $\dot{f}(t_{ss}) \approx 0$ and $\ddot{f}(t_{ss}) \approx 0$. Moreover, it also coincides with the requirements for PFC regulation, i.e., it ensures that the fast frequency control of VSCs does not interfere with the activation of primary reserves across the system [151].

The approximated frequency deviation $\Delta f_{lin}(t) \in \mathbb{R}$ is therefore segmented into the following four time intervals:

$$\Delta f_{lin}(t) = \begin{cases} \Delta f_{lin,0}(t) = k_0 t, & 0 \leq t < t_p, \\ \Delta f_{lin,1}(t) = k_1, & t_p \leq t < t_m^{(0)}, \\ \Delta f_{lin,2}(t) = k_1 + k_2 (t - t_m^{(0)}), & t_m^{(0)} \leq t < t_m^{(1)}, \\ \Delta f_{lin,3}(t) = k_3, & t_m^{(1)} \leq t \leq t_{ss}, \end{cases} \quad (8.12)$$

with the respective parameters $k_0 \in \mathbb{R}, k_1 \in \mathbb{R}, k_2 \in \mathbb{R}, k_3 \in \mathbb{R}$ defined by

$$k_0 = -\frac{\Delta f_{lim}}{f_0 t_p}, \quad k_1 = -\frac{\Delta f_{lim}}{f_0}, \quad (8.13a)$$

$$k_2 = \frac{\Delta f_{lim} - \Delta f_{ss,lim}}{f_0 (t_m^{(1)} - t_m^{(0)})}, \quad k_3 = -\frac{\Delta f_{ss,lim}}{f_0}. \quad (8.13b)$$

Similarly, the RoCoF signal approximation $\dot{f}_{lin}(t) \in \mathbb{R}$ employs three linear segments by combining the first two time intervals from (8.12) into one, i.e.,

$$\dot{f}_{lin}(t) = \begin{cases} \dot{f}_{lin,1}(t) = c_1, & 0 \leq t < t_m^{(0)}, \\ \dot{f}_{lin,2}(t) = c_2, & t_m^{(0)} \leq t < t_m^{(1)}, \\ \dot{f}_{lin,3}(t) = c_3, & t_m^{(1)} \leq t \leq t_{ss}, \end{cases} \quad (8.14)$$

where the constants $c_1 \in \mathbb{R}, c_2 \in \mathbb{R}, c_3 \in \mathbb{Z}$ are determined as follows:

$$c_1 = -\frac{\dot{f}_{lim}}{2f_0}, \quad c_2 = \frac{\Delta f_{lin}(t_m^{(1)}) - \Delta f_{lin}(t_m^{(0)})}{f_0 (t_m^{(1)} - t_m^{(0)})}, \quad c_3 = 0. \quad (8.15)$$

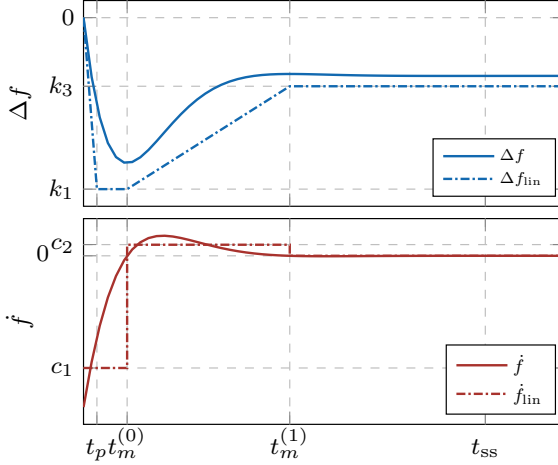


FIGURE 8.2: Linear approximation of frequency and RoCoF signals.

The resulting piecewise linear approximations are illustrated in Fig. 8.2. It can be noticed that the proposed linearization approaches in (8.12) and (8.14) are conceptually different. On the one hand, the frequency deviation signal in (8.12) is bounded in a conservative way by the predefined frequency thresholds. On the other hand, the linearization of RoCoF is not necessarily conservative (indicated by both under- and over-approximated segments), but is motivated by approximating the battery's energy content associated with such signal, which also justifies the choice of $c_1 = 0$ and $c_2 = k_2$ in (8.15). In other words, the RoCoF approximation is aimed at accurately estimating the integral of the signal and not the signal itself. Nonetheless, for validity of the given linearization, we need to ensure that the integral in (8.8h) is upper-bounded by the approximated integral in (8.11). More precisely, the net integration area of the piecewise linear segments must be greater than the one of the original nonlinear signals. To verify this, we consider the theoretical “worst-case” scenario, i.e., a highly underdamped frequency response that reaches all prescribed frequency thresholds. Moreover, the analysis focuses on individual validation of the respective energy content associated with Δf and \dot{f} terms. A graphical illustration of frequency deviation for a presumable “worst-case” scenario is depicted in Fig. 8.3, with the signal reaching maximum permissible nadir and experiencing slowly decaying oscillations around the steady-state threshold.

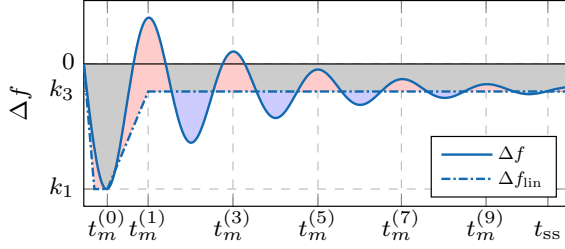


FIGURE 8.3: Graphical illustration of the “worst-case” frequency deviation signal. Red and blue shaded areas reflect the over- and under-approximated battery energy content, respectively.

Having in mind that the following inequalities hold:

$$\Delta f_{\max}^{(0)} = \Delta f(t_m^{(0)}) \geq \Delta f_{\text{lin}}(t_m^{(0)}) = -\Delta f_{\text{lim}}, \quad (8.16)$$

$$\Delta f_{\max}^{(1)} = \Delta f(t_m^{(1)}) \geq \Delta f_{\text{lin}}(t_m^{(1)}) = -\Delta f_{\text{ss,lim}}, \quad (8.17)$$

one can confirm that the first swing, i.e., the first two local extrema of the frequency response, are conservatively approximated by the proposed linearization, as indicated by the shaded regions in Fig. 8.3. As the oscillations decay over time, so does the mismatch between the actual and approximated energy content of the battery. Therefore, the approximated net integral of Δf_{lin} serves as an upper bound on the net integration area of the nonlinear signal Δf . A similar analysis can be used for graphically demonstrating the conservativeness of \hat{f}_{lin} , but is omitted for brevity.

While the proposed integral approximation is shown to be conservative, it does not ensure sufficient accuracy due to its heuristic nature. More precisely, the nonlinear battery energy content might be drastically over-approximated, thus imposing unnecessarily strict requirements on the installed energy capacity of the storage unit. Hence, the proposed linear approximation in (8.11) serves only as a starting point, and the iterative algorithm described in Section 8.3.4 evaluates the respective approximation error and minimizes it in order to ensure the desired accuracy of the solution of optimization problem (8.8).

8.3.4 Iterative Improvement of Linear Integral Approximation

The approach towards improving the accuracy of the linear approximation in Section 8.3.3 consists of two main steps, as described in Algorithm 3. First,

Algorithm 3 Improvement of linear integral approximation

- | | | |
|----|---|---|
| 1: | while ($ \epsilon_1 \geq \epsilon^* \vee \epsilon_2 \geq \epsilon^*$) do | |
| 2: | Solve optimization problem (8.8) | $\triangleright P_b, M_b, D_b$ |
| 3: | Compute frequency metrics | $\triangleright \Delta f_{\max}, \dot{f}_{\max}, \Delta f_{\text{ss}}$ |
| 4: | Update linear coefficients in (8.12)-(8.15) | $\triangleright \Delta f'_{\text{lim}} = \Delta f_{\max}$
$\triangleright \dot{f}'_{\text{lim}} = \dot{f}_{\max}$
$\triangleright \Delta f'_{\text{ss,lim}} = \Delta f_{\text{ss}}$ |
| 5: | Compute integral approximation errors | $\triangleright \epsilon_1, \epsilon_2$ |
| 6: | Adjust linear coefficients for RocoF in (8.15) | $\triangleright c_1 = c_1 + \Delta c_1(\epsilon_1)$
$\triangleright c_2 = c_2 + \Delta c_2(\epsilon_2)$ |
| 7: | end while | |
| 8: | Return final optimal solution | $\triangleright P_b^*, M_b^*, D_b^*$ |
-

at each iteration, for every non-binding frequency constraint (8.8b)-(8.8d) the respective frequency limit in (8.13) and (8.15) is updated by the actual value of the appropriate frequency metric (nadir, RoCoF or steady-state deviation), denoted by $(\cdot)'$ in Algorithm 3. This significantly reduces the over-approximation of the total energy content in (8.11), especially associated with the Δf_{lin} term. Second, a fine adjustment of the approximated net integration area corresponding to \dot{f}_{lin} is conducted. Let us quantify the numerically computed integral approximation error $\epsilon_i \in \mathbb{R}$ as follows:

$$\epsilon_i = \frac{\left| \int_{t \in T_i} M_b \dot{f}_{\text{lin},i}(t) dt \right| - \left| \int_{t \in T_i} M_b \dot{f}(t) dt \right|}{\left| \int_{t \in T_i} M_b \dot{f}(t) dt \right|}, \quad (8.18)$$

where $i \in \{1, 2\}$ and $T_1 = \left[0, t_m^{(0)}\right)$ and $T_2 = \left[t_m^{(0)}, t_m^{(1)}\right)$ represent the first two time intervals from (8.14). The error associated with interval $\left[t_m^{(1)}, t_{\text{ss}}\right]$ is rather negligible due to small RoCoF oscillations around zero and is therefore neglected in the algorithm. Based on the sign and magnitude of ϵ_i , the parameters c_1 and c_2 in (8.15) are iteratively adjusted by marginal terms $\Delta c_i(\epsilon_i) \in \mathbb{R}$ until the condition $|\epsilon_i| < \epsilon^*$ is satisfied, with $\epsilon^* \in \mathbb{R}_{>0}$ being the maximum acceptable approximation error.

8.4 RESULTS

We apply the proposed methodology to the three-area system described in Section 5.4 (see Fig. 5.4), comprising six synchronous generators. All SGs

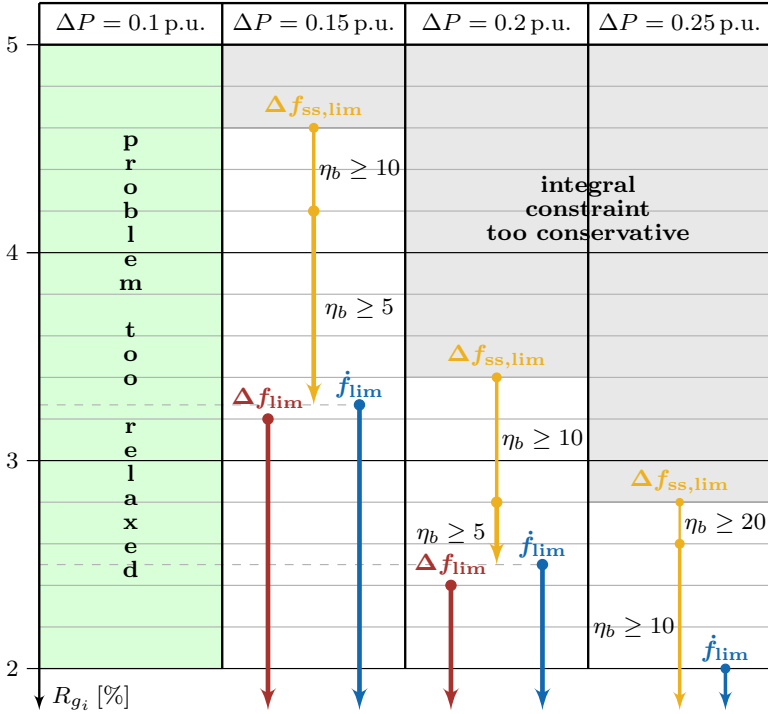


FIGURE 8.4: Graphical representation of the nature of the optimization problem and the activation of respective binding constraints for different input parameters ΔP , η_b and R_{g_i} .

but the one placed at node 1 are replaced by converter-based units operating in a grid-following mode¹, thus leading to an overall inverter penetration of $\approx 85\%$ and insufficient provision of fast frequency response. Therefore, the objective is to design the storage unit, i.e., compute its minimum power and energy capacity, and assign it to one of the inverters, effectively transforming it into a grid-forming VSC. Moreover, the optimal tuning of the associated VSM controller that guarantees satisfactory transient performance has to be obtained.

For better understanding of the optimization performance, we will consider ΔP , η_b and R_{g_i} to be adjustable input parameters for the proposed optimization problem in (8.8) throughout the course of this study. The first term describes the magnitude of the disturbance that must be contained

¹ Converter-based generation is placed at nodes 2, 5, 6, 9 and 10 of the three-area system.

by FFC; the second is associated with the power-to-energy capability of installed energy storage technology at the DC side; the last one denotes the individual droop gains of synchronous generators (see Section 5.2 for more detail), potentially regulated by system operators to accommodate high penetration of inverter-based generation. The selection of these parameters can drastically affect the nature of the problem at hand, with the optimization problem potentially being too relaxed or infeasible. The underlying characteristics are illustrated in Fig. 8.4 for different combinations of input variables ΔP , η_b and R_{g_i} . We consider four different disturbance magnitudes $\Delta P \in \{0.1, 0.15, 0.2, 0.25\}$ p.u., energy-to-power ratios with unity steps (i.e., 1 s increments) in the range $\eta_b \in [1, 20]$ s, and SG droop gains changed by 0.2% increments on the interval $R_{g_i} \in [2, 5]$ %.

The shaded regions in Fig. 8.4 indicate the set of parameters for which the previously discussed issues occur. In fact, even the set of feasible problems varies in nature, having different frequency-related constraints as binding depending on the given inputs. Each of the three constraints in (8.8b)-(8.8d) is denoted by a different color, with the arrow line thickness indicating the value of the energy-to-power ratio². For instance, the value of droop gains has a decisive impact on the bounds of the feasible region as well as the permissible range of energy-to-power ratio, with smaller droop coefficients allowing for lower values of η_b (suggested by thicker lines in Fig. 8.4). Indeed, the SG frequency droop gains are inversely proportional to system damping (see Section 5.2), which justifies the aforementioned flexibility in terms of η_b . It also explains the order of the binding constraints. More precisely, the steady-state frequency constraint in (8.8d) can be satisfied by achieving a sufficient aggregate damping constant, which is the case for low values of R_{g_i} . However, this is more pronounced for larger disturbances, where the minimum damping (and hence the maximum SG droop gain) requirement is significantly more strict, resulting in steady-state constraint being the binding one. In contrast, the remaining two inequalities (8.8b)-(8.8c) are partially or completely affected by system inertia and therefore easier to comply by for high droop factors.

For simplicity, we assume a maximum disturbance of 620 MW ($\Delta P \approx 0.15$ p.u.) in the remainder of the study, corresponding to the installed power of a single SG, and consider solely the droop gains of 2.6% and 4.6% as two distinctive benchmark cases (see dashed lines in Fig. 8.4). The optimization results with and without the use of iterative Algorithm 3 are presented in

² The arrow line thickness in Fig. 8.4 is inversely proportional to the value of the energy-to-power ratio. More precisely, the thickest line corresponds to $\eta_b \geq 5$ whereas the thinnest lines reflect the scenario with $\eta_b \geq 20$.

Case A: Without iterative improvement in Algorithm 3

η_b [s]	R_{g_i} [%]	P_b [MW]	E_b [MWh]	M_b [s]	D_b [p.u.]	ε_g [%]
1-6	4.6	-	-	-	-	
7	4.6	2745.74	5.34	53.23	15.39	43.83
8	4.6	2058.63	4.57	55.56	12.00	36.91
9	4.6	1664.90	4.16	57.77	10.06	32.12
10	4.6	1408.80	3.91	59.87	8.80	28.59
11	4.6	1228.35	3.75	61.87	7.91	25.87
12	4.6	1094.02	3.65	63.79	7.24	23.72
13-20	4.6	1007.69	3.64-5.60	65.29	6.82	22.26
1-20	2.6	661.78	0.18-3.68	12.63	1.46	15.83

Case B: With iterative improvement in Algorithm 3

η_b [s]	R_{g_i} [%]	P_b [MW]	E_b [MWh]	M_b [s]	D_b [p.u.]	ε_g [%]
1-3	4.6	-	-	-	-	
4	4.6	2614.36	2.90	53.58	14.74	42.63
5	4.6	1378.72	1.91	60.16	8.65	28.15
6-20	4.6	1007.69	1.68-5.60	65.29	6.82	22.26
1-20	2.6	661.78	0.18-3.68	12.63	1.46	15.83

TABLE 8.1: Optimal sizing and tuning for $\Delta P = 620$ MW.

Table 8.1 for various η_b values. Interestingly enough, for $R_{g_i} = 4.6\%$ there is a noticeable threshold in η_b after which the additional energy capacity does not contribute to frequency response and the optimizer returns the same battery size and VSM tuning. This is illustrated in Fig. 8.5 for the case without iterative improvement. The use of Algorithm 3 leads to a noticeable reduction in battery installation costs for the higher droop gain. Furthermore, the identical optimal solutions for $\eta_b \in [6, 20]$ suggest that the installed energy capacity is not a binding factor in the optimization problem. On the other hand, neither the energy-to-power ratio nor the iterative adjustment have an impact on the cases with lower droop gains, which is a consequence of the precision of the initial integral approximation, as will be further elaborated. Consequently, the necessary share³ of inverter capacity with grid-forming capabilities can vary drastically, from 16% up to 44%.

³ The grid-forming share $\varepsilon_g \in \mathbb{R}_{\geq 0}$ is based on the installed converter powers.

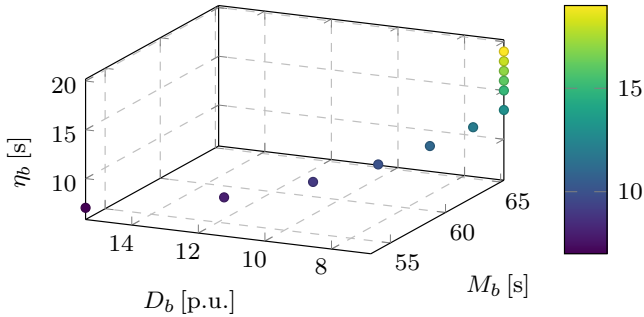


FIGURE 8.5: Correlation between M_b , D_b and η_b for $R_{g_i} = 4.6\%$.

Let us now focus on the following two scenarios: (i) ($R_{g_i} = 4.6\%$, $\eta_b = 10$ s) and (ii) ($R_{g_i} = 2.6\%$, $\eta_b = 15$ s). In Scenario I, the steady-state frequency constraint is binding and the integral approximation is thus very conservative. In contrast, the maximum permissible nadir and RoCoF requirements impose tight constraints in Scenario II, with the integral approximation being significantly less conservative. This is justified by the conceptually different linearization of frequency deviation and RoCoF signals in Section 8.3.3, i.e., the latter approximation capturing better the battery's energy content. The shaded blue and red regions in Fig. 8.6 reflect the over-approximation of the integral constraint associated with Δf and \dot{f} terms respectively, while the gray areas represent the under-approximated energy content. As a result, a 28.5% reduction in the installed battery power can be achieved in Scenario I when applying the iterative adjustment method, whereas no improvement is needed in Scenario II due to sufficiently accurate initial approximation.

Similar characteristics can be observed in Fig. 8.7 by analyzing the power (P_c) and energy (E_c) activation of a grid-forming converter interfacing the battery storage, as well as comparing the installed battery power before (P_b^0) and after (P_b) the iterative improvement. Moreover, the results suggest that the installed power capacity is sufficient for containing the predefined disturbance, with the maximum converter power injection never exceeding the battery limit. However, the DC-side energy content is vastly under-utilized due to insufficiently low energy-to-power ratio, which suggests a need for a more suitable energy storage technology (e.g., ultracapacitors, flywheels, etc.). Alternatively, the existing sodium-sulfur and lithium-ion batteries could potentially be considered for such applications as they have sufficiently low energy-to-power ratios and are capable of providing fast power responses [180].

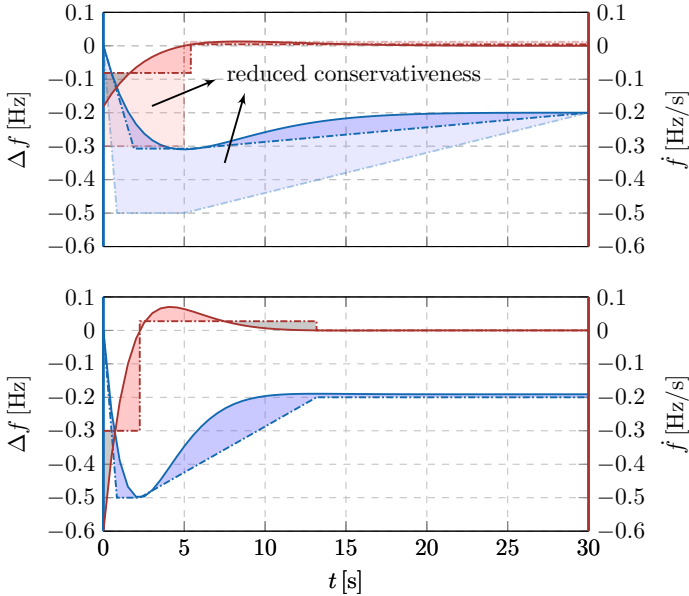


FIGURE 8.6: Approximation of energy content associated with integral constraint in Scenario I (top) and Scenario II (bottom). Colored and gray-shaded segments indicate the respective over- and under-approximations.

8.5 CONCLUSION

The presented chapter introduces a method for combined sizing of the storage capacity and tuning of the associated controller gains of a grid-forming converter interfacing the storage unit to the grid. For this purpose, the analytic expressions of relevant system frequency metrics as well as the energy utilization of the associated converter storage device were incorporated into a non-convex optimization problem, which is then simplified by approximating the nonlinear constraints that render the problem too complex to be solved by standard solvers. By accounting for the coupling between installation planning and operation parameters of the storage unit, the proposed method ensures sufficient energy and power capacity for containing a predefined active power imbalance and preserving frequency within prescribed ENTSO-E limits. Furthermore, the optimal virtual inertia and damping gains of the associated VSM-based converter control scheme are determined.

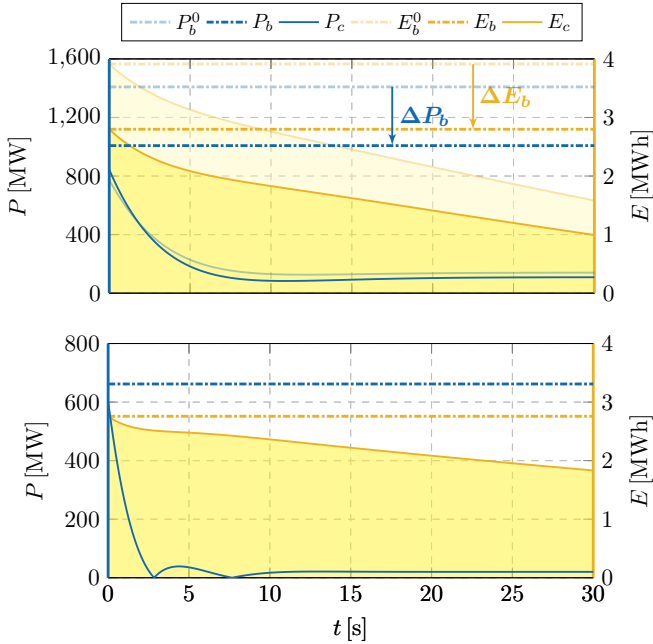


FIGURE 8.7: Utilization of battery's power and energy during a disturbance in Scenario I (top) and Scenario II (bottom); shaded lines refer to Case A (without iterative improvement).

The converter performance after a disturbance validates the accuracy of the proposed approach. However, one should keep in mind that various system and individual unit properties (e.g., possible disturbance magnitudes, SG droop gains, available energy storage technologies) could have a drastic impact on the final outcome and should be studied more thoroughly. As potential directions for future work, the placement of grid-forming inverters and the impact of different energy storage technologies including cost and performance models should be investigated. The former topic is comprehensively addressed in Chapter 11.

Part III

IMPROVING RELIABILITY AND
PERFORMANCE OF NETWORKS WITH
HIGH INVERTER PENETRATION

VIRTUAL INDUCTION MACHINE STRATEGY FOR POWER CONVERTER SYNCHRONIZATION

This chapter presents a novel control strategy for synchronization of grid-connected VSCs in power systems with low rotational inertia. The proposed model is based on emulating the physical properties of an induction machine and taking advantage of its inherent grid-friendly properties such as self-synchronization, oscillation damping and standalone capabilities. For that purpose, a detailed mathematical model of its working principles is derived, which includes the possibility of obtaining the unknown grid frequency without a dedicated synchronization unit, but rather via processing of the voltage and current measurements at the converter output. This eliminates the need for an inherently nonlinear PLL, traditionally employed in grid-following converter control schemes, while simultaneously preserving the conventional system-level and device-level control. Furthermore, the appropriate steps for obtaining an index-1 DAE representation of such converter control model are provided. The EMT simulations validate the mathematical principles of the proposed controller, whereas a small-signal analysis provides guidelines for appropriate control tuning and reveals some interesting properties pertaining to the nature of the underlying operation mode. The chapter is based on [181, 182].

9.1 INTRODUCTION

The primary frequency control of synchronous machines is naturally based on the measure of the rotor angular speed of the machine itself. Since the dynamic response of synchronous machines imposes frequency variations, the rotor speed is clearly the correct measurement to use for frequency control [6]. However, the situation changes substantially when it comes to defining the frequency signal for converter-interfaced generation. Unlike synchronous machines, and depending on the respective mode of operation, PE-interfaced DGs do not necessarily impose the frequency at the point of connection (see Section 2.3). In particular, for the purposes of grid-following power converter

control, a brittle local bus frequency signal has to be estimated by means of available measurements, usually AC voltages and/or currents at the point of connection.

In order to regulate a grid-connected VSC in a grid-following mode, a control sequence comprising a synchronization unit, an outer power-control loop and a cascade of inner voltage and current controls has become an industry standard for providing adequate voltage, active and reactive power outputs [183] (see Section 2.2). Furthermore, the norm of having a PLL as a synchronization unit has been established [184], together with its numerous variants [185–188]. However, despite being widely utilized for frequency estimation, this additional, inherently nonlinear outer loop introduces complexity in the system. As its input signal undergoes fast electromagnetic transients, the PLL can show numerical issues and be affected by jumps and discontinuities following discrete events in the system such as faults or line outages [6]. Moreover, by the nature of its design, it introduces a non-negligible delay which can limit the performance of controllers depending on the frequency estimation, and in addition may be extremely difficult to tune [34, 189]. Several publications have recognized the impact of PLLs in operation of non-synchronous generation [190, 191], but also highlighted the potential instabilities arising from high penetration of power converters employing these synchronization devices [12, 192, 193].

Recent studies have addressed some of the aforementioned issue and concepts of PLL-less converter regulation in the form of power-synchronization [194], virtual oscillator control [52, 78] and self-synchronizing *synchronverters* [34] have emerged. While seemingly providing synchronization properties, the proposed methods also have some drawbacks. The power-synchronization is mostly oriented towards VSC-HVDC applications and faces challenges with weak AC system connections, virtual oscillator control faces obstacles in terms of reference tracking, whereas the synchronverter concept still requires a back-up PLL and improvements in operation under unbalanced and distorted grid voltages. Furthermore, all aforementioned controls apply to grid-forming operation mode. While grid-forming and grid-supporting DGs are an integral part of a future low-inertia power grid, the exiting systems are primarily composed of renewable generation interfaced to the network via grid-following inverters.

On the other hand, a recently proposed VSC control method under the name of *inducverter* introduces the idea of a grid-connected converter operating under Induction Machine (IM) working principles and no dedicated PLL unit [195]. Although the concept is still at its early stages, it can potentially

resolve the issues associated with the conventional PLL-based synchronization loop. However, [195] proposes a control design that integrates the system-level controller and synchronization unit into one compact structure. As a result, the true function of the emulated induction machine and its potential value and applications in VSC control are misinterpreted, as the authors of [195] state that the induverter participates in power system frequency regulation and stabilization by introducing virtual inertia, whereas such properties are a sole function of the implemented PI-based droop power control. Additionally, the controller is implemented in a hybrid abc - dq frame, where dq -axis current references are obtained according to the real and reactive power errors and translated to abc voltage references through an adaptive virtual impedance in the abc frame. This significantly complicates the analytical representation of the model and its analysis, reflected by the fact that the authors do not propose a reasonable tuning procedure and suggest that the parameters should be simply adopted from an existing induction machine. Finally, the fact that the cascaded inner control loop is replaced by a simple adaptive lead or lag compensator raises concerns in terms of fast voltage reference tracking and overcurrents during transients.

We improve the aforementioned design flaws by incorporating the Virtual Induction Machine (VIM) framework in [181] as an independent synchronization unit into a detailed converter model and analyzing the time-domain performance of a grid-connected VSC through EMT simulations. Nevertheless, no improvements have been made in terms of analytical analysis and advanced tuning. This chapter reformulates the mathematical principles of an emulated induction machine from [181, 195] and extends them by deriving an appropriate index-1 DAE representation of such grid-connected VSC control scheme. This allows for a detailed small-signal analysis, which in turns helps improve the control tuning and reveals that replacing PLL by a VIM results in a hybrid operation mode with both grid-forming and grid-following properties. It also enables us to draw accurate conclusions regarding the overall emulation properties and the system response.

The remainder of the chapter is structured as follows. In Section 9.2, the mathematical model of an induction machine and the VIM control principles are presented. Section 9.3 describes the VIM control design and its implementation into a state-of-the-art VSC controller, as well as the model formulation as an index-1 DAE system. Section 9.4 showcases the EMT simulation results and model validation, whereas Section 9.5 provides an insightful small-signal stability analysis. Finally, Section 9.6 discusses the outlook of the study and concludes the chapter.

9.2 THEORETICAL CONCEPT

9.2.1 *Induction vs Synchronous Machine: Working Principles*

One of the main differences between the synchronous and induction machine is the physical concept behind the rotor movement and the subsequent synchronization to the grid. While the SM always operates at synchronous speed, the IM requires a mismatch between the synchronous speed $\omega_s \in \mathbb{R}_{\geq 0}$ and the machine's rotor speed $\omega_r \in \mathbb{R}_{\geq 0}$ to operate, a so-called slip $\nu \in \mathbb{R}_{> 0}$:

$$\nu := \frac{\omega_s - \omega_r}{\omega_s} = \frac{\omega_\nu}{\omega_s}, \quad (9.1)$$

with $\omega_\nu := \omega_s - \omega_r$ denoting the slip frequency. Furthermore, unlike synchronous generators, induction machines do not have an excitation system in the rotor. This means that the ElectroMagnetic Field (EMF) induced in the rotor of an IM is a consequence of its rotation and the subsequent change of the magnetic flux linkage through the circuit. Since the rotor is closed through either an external resistance or a short-circuit ring, the induced EMF generates a current flow in the rotor conductor. Therefore, the machine can never be operating at synchronous speed, since there would be no EMF in the rotor frame to initiate its movement.

Based on the previously described properties, one can observe that the IM with an arbitrary initial rotor speed somewhat close to the synchronous speed has a self-start capability, i.e., has the potential to synchronize with a grid of an unknown frequency and voltage magnitude. This implies that the PLL units, together with their inherent drawbacks in the form of time delay and stability margins, could be omitted from the converter control scheme and replaced by a VIM-based synchronization unit. However, such implementation should not be confused with system-level regulation, e.g., droop control, VSM or VOC, as it does not inherently yield emulation of inertia or frequency oscillation damping (also one of the misconceptions of [195]). Nevertheless, those services could easily be provided by an appropriate outer control loop, as will be shown later.

9.2.2 *Induction Machine Emulation Strategy*

For the purpose of emulating the operating principles of an IM through VSC control, let us observe a dynamical model¹ of an IM in a synchronously-

¹ Unlike the formulation in Chapter 2, the mathematical model introduced in this section is described completely in SI.

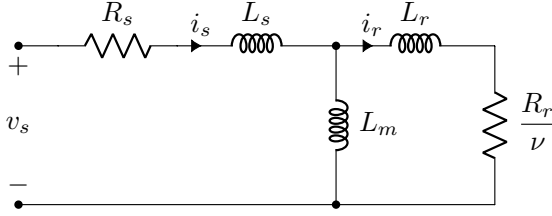


FIGURE 9.1: Simplified equivalent circuit of an induction machine.

rotating dq -frame, according to the equivalent circuit representation illustrated in Fig. (9.1) [196]:

$$v_s^d = R_s i_s^d + \dot{\psi}_s^d - \omega_s \psi_s^q, \quad (9.2a)$$

$$v_s^q = R_s i_s^q + \dot{\psi}_s^q + \omega_s \psi_s^d, \quad (9.2b)$$

$$v_r^d = 0 = R_r i_r^d + \dot{\psi}_r^d - \omega_\nu \psi_r^q, \quad (9.2c)$$

$$v_r^q = 0 = R_r i_r^q + \dot{\psi}_r^q + \omega_\nu \psi_r^d, \quad (9.2d)$$

where $v_s = (v_s^d, v_s^q) \in \mathbb{R}^2$, $v_r = (v_r^d, v_r^q) \in \mathbb{R}^2$, $\psi_s = (\psi_s^d, \psi_s^q) \in \mathbb{R}^2$ and $\psi_r = (\psi_r^d, \psi_r^q) \in \mathbb{R}^2$ are the vectors of stator and rotor voltages and flux linkages, respectively, and $R_s \in \mathbb{R}_{>0}$ and $R_r \in \mathbb{R}_{>0}$ are the stator and rotor circuit resistances. The superscripts d and q refer to the vector component in the corresponding axis of the dq -reference frame, rotating at the time-variant synchronous speed ω_s . The first two expressions in (9.2) describe the stator voltage, whereas the latter two reflect the voltage circuit balance of a short-circuited rotor, hence $v_r = \mathbf{0}_2$. Note that the slip frequency ω_ν is involved in the last terms of (9.2c)-(9.2d). Moreover, the stator and rotor flux linkages can be described by

$$\psi_s = L_s i_s + L_m i_r, \quad (9.3a)$$

$$\psi_r = L_r i_r + L_m i_s, \quad (9.3b)$$

with $i_s = (i_s^d, i_s^q) \in \mathbb{R}^2$ and $i_r = (i_r^d, i_r^q) \in \mathbb{R}^2$ denoting the vectors comprising stator and rotor current components in different axes, and $L_s \in \mathbb{R}_{>0}$, $L_r \in \mathbb{R}_{>0}$, $L_m \in \mathbb{R}_{>0}$ being the stator, rotor and mutual inductance respectively.

The electric power passing between stator and rotor can now be expressed in terms of currents and flux linkages, either on the stator or on the rotor side:

$$p_e = \omega_s \frac{3}{2} \left(\psi_s^d i_s^q - \psi_s^q i_s^d \right) = \omega_s \frac{3}{2} \left(\psi_r^q i_r^d - \psi_r^d i_r^q \right), \quad (9.4)$$

which yields the virtual electrical torque

$$\tau_e = \frac{p_e}{\omega_s} = \frac{3}{2} \left(\psi_s^d i_s^q - \psi_s^q i_s^d \right) = \frac{3}{2} L_m \left(i_r^d i_s^q - i_r^q i_s^d \right). \quad (9.5)$$

It can be observed that the expression for τ_e in (9.5) is the same as for a synchronous machine [196].

Considering the fact that the converter model will not involve a PLL (and hence the synchronous and slip speed are unknown to the controller), the presence of ω_s and ω_ν terms in (9.2a)-(9.2b) and (9.2c)-(9.2d), respectively, poses an obstacle for the control design. In other words, ω_s and ω_ν are unknown variables and need to be computed internally based on available measurement signals. For that purpose, a field-oriented IM control first presented in [197] is employed. Since the direction of the dq -frame is arbitrary, it is assumed that in steady state the virtual rotor flux is aligned with the d -axis, resulting in a simplified model with $\psi_r^q = 0$. The described procedure is similar to ones used in conventional PLLs (see Section 2.3), where the calculation of the voltage angle is based on aligning the voltage vector with the d -axis of a synchronously-rotating reference-frame [198].

According to the suggested approximation, (9.3b) is reformulated as

$$i_r^d = \frac{\psi_r^d - L_m i_s^d}{L_r}, \quad (9.6a)$$

$$i_r^q = -\frac{L_m}{L_r} i_s^q, \quad (9.6b)$$

and the expressions for rotor voltage components in (9.2c) and (9.2d) can now be rewritten:

$$0 = R_r i_r^d + \dot{\psi}_r^d, \quad (9.7a)$$

$$0 = R_r i_r^q + \omega_\nu \psi_r^d. \quad (9.7b)$$

Substituting (9.6a) into (9.7a) yields

$$\dot{\psi}_r^d = -R_r i_r^d = -\frac{R_r}{L_r} \left(\psi_r^d - L_m i_s^d \right), \quad (9.8)$$

which in frequency domain² can be expressed as

$$\psi_r^d = \frac{R_r L_m}{R_r + s L_r} i_s^d = K_\psi(s) i_s^d. \quad (9.9)$$

² The notation (s) next to the complex variable term $x(s)$ in frequency domain is omitted for brevity.

In a similar fashion, the slip frequency of induction machine is computed by combining (9.6b) and (9.7b), i.e.,

$$\omega_\nu = -\frac{R_r}{\psi_r^d} i_r^q = -\frac{R_r L_m}{L_r} \frac{i_s^q}{\psi_r^d}, \quad (9.10)$$

and subsequently substituting ψ_r^d from (9.9), which gives

$$\omega_\nu = \left(\frac{R_r}{L_r} + s \right) \frac{i_s^q}{i_s^d} = K_\nu(s) \frac{i_s^q}{i_s^d}. \quad (9.11)$$

The expression (9.11) describes the dynamics of the slip frequency as a PD controller $K_\nu(s)$ applied to the ratio of dq -components of the stator current. As such, this term is clearly adaptable to the variations in grid frequency and machine power output. Nevertheless, in order to complete the PLL-less control design, one needs to determine the synchronous speed. Having in mind that $\omega_s = \omega_r + \omega_\nu$, an exact estimation of the rotor angular velocity is sufficient for achieving the targeted objective.

Let us observe the power balance of an induction machine via the swing equation and the mechanical dynamics of the rotor:

$$J\dot{\omega}_r = \tau_m - \tau_e - \tau_d. \quad (9.12)$$

Here, $J \in \mathbb{R}_{>0}$ is the rotor's momentum of inertia, and $\tau_m \in \mathbb{R}$, $\tau_e \in \mathbb{R}$ and $\tau_d \in \mathbb{R}$ correspond to the mechanical, electrical and damping torque. By declaring $\Delta\omega_r \in \mathbb{R}$ as a deviation of ω_r from an initial (nominal) rotor speed³ $\omega_0^* \in \mathbb{R}_{>0}$, the expression (9.12) becomes

$$\Delta\dot{\omega}_r = \frac{1}{J} (\tau_m - \tau_e - \tau_d). \quad (9.13)$$

By expressing all three torque components in (9.13) as functions of converter input signals, one could finalize the closed-form VIM formulation. We elaborate on mathematical details and derivations in the remainder of this section.

The electrical torque component is defined by (9.5), but can be further simplified by substituting the following expressions for stator flux linkage components:

$$\psi_s^d = \left(L_s - \frac{L_m^2}{L_r} \right) i_s^d + \frac{L_m}{L_r} \psi_r^d, \quad (9.14a)$$

$$\psi_s^q = \left(L_s - \frac{L_m^2}{L_r} \right) i_s^q, \quad (9.14b)$$

³ We denote the initial (nominal) rotor speed by $(\cdot)^*$ as it will later serve as an input setpoint to the VIM controller.

previously obtained from (9.3). The electrical torque in time domain is therefore of the form

$$\tau_e = \frac{3}{2} \frac{L_m}{L_r} \psi_r^d i_s^q, \tag{9.15}$$

whereas in frequency domain it yields

$$\tau_e = \frac{3}{2} \frac{L_m}{L_r} K_\psi(s) i_s^d i_s^q = K_e(s) i_s^d i_s^q. \tag{9.16}$$

In (9.16), $K_e(s)$ represents a first-order transfer function

$$K_e(s) = \frac{3}{2} \frac{L_m}{L_r} K_\psi(s) = \frac{3}{2} \frac{R_r L_m^2}{R_r L_r + s L_r^2}, \tag{9.17}$$

defined by the circuit parameters of the underlying induction machine, namely the rotor resistance and reactance as well as the mutual inductance.

On the other hand, the mechanical torque is determined by the machine’s mechanical power input and the angular speed of the rotor. Assuming a lossless converter, the mechanical input power of IM can be approximated by the output power measured at the converter terminal (denoted by p_c), and the mechanical torque is therefore given by

$$\tau_m = \frac{p_m}{\omega_r} \approx \frac{p_c}{\omega_r}. \tag{9.18}$$

Since the terminal current and voltage measurements of the converter - corresponding to stator current and voltage of a virtual induction machine⁴ - are available and actively employed in both system- and device-level control, the active power output can be expressed as $p_c := v^T i_g := v_s^T i_s$, thus transforming (9.18) into

$$\tau_m = \frac{v_s^T i_s}{\omega_0^* + \Delta\omega_r}. \tag{9.19}$$

Finally, the damping torque $\tau_d = D\Delta\omega_r$ is proportional to the rotor frequency deviation, which yields the following low-pass filter characteristic of the induction machine in frequency domain:

$$\Delta\omega_r = \frac{1}{J_s + D} (\tau_m - \tau_e), \tag{9.20}$$

where $D \in \mathbb{R}_{>0}$ denotes the damping constant. Substituting (9.16) and (9.19) into (9.21) results in a closed-form expression for $\Delta\omega_r$ of the form

$$\Delta\omega_r = \frac{1}{J_s + D} \left(\frac{v_s^T i_s}{\omega_0^* + \Delta\omega_r} - \frac{3}{2} \frac{R_r L_m^2}{R_r L_r + s L_r^2} i_s^d i_s^q \right), \tag{9.21}$$

⁴ In other words, $v_f := v_s$ and $i_g := i_s$, using the notation from Chapter 2

which corresponds to $\Delta\omega_r = F_r(u, p)$, with the control input vector $u \in \mathbb{R}^4$ and parameter vector $p \in \mathbb{R}_{>0}^6$ defined by

$$u = (v_s^d, v_s^q, i_s^d, i_s^q), \quad (9.22a)$$

$$p = (J, D, R_r, L_r, L_m, \omega_0^*). \quad (9.22b)$$

Unlike the widely used VSM control [49, 66], and in contrast to the claims made in [195], the inertia and damping in (9.21) will not be reflected in the converter's frequency response and oscillation damping performance. They do however contribute to a more robust and resilient frequency estimation technique, as will be shown later in Section 9.4.

Having obtained desired analytical expressions for all frequency components, the synchronous speed can now be computed from the frequency slip ω_ν in (9.11) and $\Delta\omega_r$ in (9.21), as follows:

$$\omega_s = \omega_r + \omega_\nu = \underbrace{\omega_0^* + F_r(u, p)}_{\omega_r} + \underbrace{\left(\frac{R_r}{L_r} + s\right) \frac{i_s^q}{i_s^d}}_{\omega_\nu} = F_s(u, p). \quad (9.23)$$

Similarly to any PLL, the angle reference is determined by integrating the frequency signal, i.e., $\theta_s = \omega_s$. The resulting expression in (9.23) clearly shows that the closed-loop controller $F_s(u, p)$ emulates the synchronous speed and thus the synchronization properties of an IM based solely on the voltage and current measurements v_f and i_g at the converter terminal, therefore fully replacing the conventional PLL-based synchronization. On the downside, the difference between the true synchronous speed and initial rotor speed setpoint can have an impact on synchronization accuracy. In particular, a proper selection of ω_0^* prior to the grid connection of VSC reduces $\Delta\omega_r$ and the subsequent transients. This concept resembles the behavior of an induction generator in a similar operation mode [195]. Nevertheless, it can be reasonably assumed that the VSC is connected to the grid during steady-state operation. Thus, a very basic PLL can be used only to estimate ω_0^* . However, even if this functionality is not available, any reasonable ω_0^* guess will still allow the VIM to synchronise at the cost of some minor transients. A sensitivity analysis addressing the underlying phenomena is provided in Section 9.4.2.

Another potential drawback of the controller (9.23) is the fact that the slip frequency ω_ν is computed using a PD controller imposed on the quotient of the current components in dq -frame. On the one hand, the derivative control is sensitive to fast signal changes. As the quotient i_s^q/i_s^d can experience high oscillations during transients, the PD controller might be prone to overshoots

and even instability. On the other hand, the given input-output structure of the PD controller might lead to an index-2 DAE form⁵, which in turn increases the computational burden and imposes restrictions on the selection of the DAE solver. The aspects of DAE formulation will be discussed in detail in Section 9.3.2.

9.3 FORMULATION AND IMPLEMENTATION

9.3.1 Control Implementation: PLL vs VIM

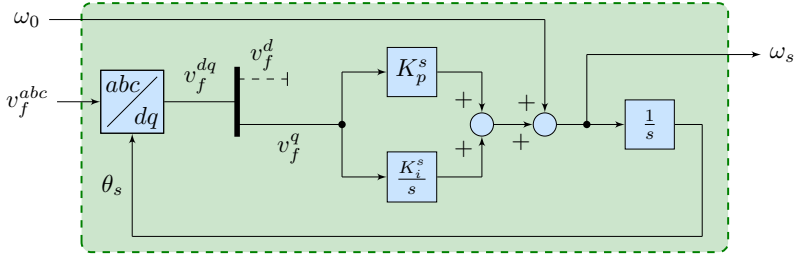
The proposed VIM controller is integrated into a detailed VSC control scheme presented in Section 2.7. More precisely, the traditional PLL unit is replaced by the VIM, with the system-level and device-level control structure preserved. For comparison and clarity, the control-block implementation of both synchronization units (i.e., a type-2 SRF-PLL and a VIM) is depicted in Fig. 9.2.

A basic structure and operating principles of a type-2 SRF-PLL [68] have already been presented in Section 2.3. This synchronization device acts as an observer and tracks the synchronous speed by measuring the stationary output voltage v_f^{abc} , transforming it into an internal dq -SRF (i.e., v_f^{dq}), and passing it through a PI-controller (K_P^s, K_I^s) that acts on the phase angle difference:

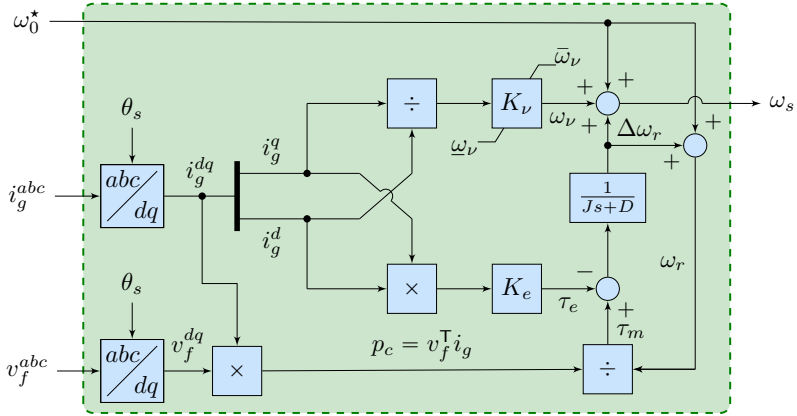
$$\omega_s = \omega_0 + \left(K_P^s + \frac{K_I^s}{s} \right) v_f^q, \quad (9.24)$$

with $\omega_0 \in \mathbb{R}_{>0}$ denoting the nominal angular velocity. The synchronization is achieved by aligning the d -axis of the internal SRF with the stationary abc -frame and diminishing the q -component, as described in [22, 24, 68] and illustrated in Fig. 9.2a. It should be pointed out that the combined Clarke and Park transformation within the PLL is completely independent of the transformation defined by the angle and frequency of the active power controller used for the rest of the VSC control scheme, and therefore introduces a second SRF into the system. Hence, the internally computed filter voltage \hat{v}_f must be aligned with the corresponding voltage vector in the main SRF (see Section 2.3 for more detail). Since in this chapter we only present the

⁵ Index is a notion used in the theory of DAEs for measuring the distance from a DAE to its related ODE (i.e., the number of differentiations needed to obtain the ODE form). It is a non-negative integer that provides useful information about the mathematical structure and potential complications in the analysis and the numerical solution of the DAE. In general, the higher the index of a DAE, the more difficulties one can expect for obtaining its numerical solution [199].



(a)



(b)

FIGURE 9.2: Control structure of different synchronization units of a power converter: (a) type-2 SRF-PLL; (b) virtual induction machine.

DAE formulation of a synchronization unit and not of the complete converter model, (·) notation for the internal SRF variables is omitted for brevity.

The VIM control design illustrated in Fig. 9.2b is based on (9.23). Similarly to other synchronization methods including the PLL, the unknown grid frequency can be obtained by simply measuring the three-phase current and voltage at the filter output (i_g^{abc}, v_f^{abc}). Note that the VIM also operates in a separate SRF defined by the internally computed synchronization angle θ_s , and requires alignment of the transformed dq -quantities with the main SRF. As previously explained in Section 9.2, another necessary input for the controller is the initial rotor frequency ω_0^* , which determines the VIM's oscillation level at start-up. However, the requirement for the initial guess of

ω_0^\star is not very strict, as it should only be “close enough” to the synchronous speed and subsequently let the emulated physical machine bring the VSC to synchronism. Moreover, in order to cope with potential frequency slip spikes during transients, induced by the PD control $K_\nu(s)$ acting on the quotient i_g^q/i_g^d in (9.11), the frequency slip is constrained by the saturation limits $\omega_\nu \in [\underline{\omega}_\nu, \bar{\omega}_\nu]$.

9.3.2 DAE Formulation

The DAE formulation of a conventional converter control scheme has been presented in detail in Chapter 2 and will not be included in this chapter. In case of a DG operating in a grid-following mode, a synchronization unit is needed for obtaining the grid frequency at the connection terminal. As previously shown in Section 2.3, the PLL controller (9.24) can be expressed as a second-order dynamic system

$$\dot{\varepsilon} = v_f^q, \tag{9.25a}$$

$$\omega_s = \omega_0 + K_P^s v_f^q + K_I^s \varepsilon, \tag{9.25b}$$

$$\dot{\theta}_s = \omega_s, \tag{9.25c}$$

with $x_{\text{pll}} := (\varepsilon, \theta_s) \in \mathbb{R}^2$ being the state vector and $y_{\text{pll}} := \omega_s$ an algebraic output vector.

In contrast, obtaining an appropriate (i.e., index-1) DAE representation of the VIM controller is not straightforward due to aforementioned issues pertaining to the computation of slip frequency in (9.11), as well as the fact that the electrical torque is described by a first-order transfer function $K_e(s)$ applied to the product of state variables i_g^d and i_g^q in (9.16). As such the existing DAE model is incomplete, since the number of algebraic equations does not correspond to the number of algebraic variables. More precisely, the algebraic equation describing the slip frequency is missing and must be derived by transforming (9.11) accordingly.

We tackle this issue by introducing a new variable $\varphi \in \mathbb{R}$ such that

$$\varphi := \frac{d}{dt} \left(\frac{i_g^q}{i_g^d} \right). \tag{9.26}$$

Moreover, we define $\varphi_d := i_g^d$ and $\varphi_q := i_g^q$, and apply a quotient rule to (9.26), which yields

$$\varphi = \frac{i_g^q i_g^d - i_g^q i_g^d}{(i_g^d)^2} = \frac{1}{i_g^d} \varphi_q - \frac{i_g^q}{(i_g^d)^2} \varphi_d. \tag{9.27}$$

Note that the terms $(\varphi_d, \varphi_q) \in \mathbb{R}^2$ correspond to the differential equation (2.5c) in Chapter 2, describing the dynamics of the current flowing through a transformer. Redefining (2.5c) in SI yields

$$\varphi_d = \frac{\omega_b I_b}{\ell_t} \left(v_f^d - v_t^d \right) - I_b \left(\frac{r_t}{\ell_t} \omega_b i_g^d + \omega_b \omega_c i_g^q \right), \quad (9.28a)$$

$$\varphi_q = \frac{\omega_b I_b}{\ell_t} \left(v_f^q - v_t^q \right) - I_b \left(\frac{r_t}{\ell_t} \omega_b i_g^q + \omega_b \omega_c i_g^d \right). \quad (9.28b)$$

Here, $\omega_b \in \mathbb{R}_{>0}$ and $I_b \in \mathbb{R}_{>0}$ denote the base angular velocity and current used for conversion between the per unit and SI. The rest of notation is adopted from Chapter 2. By rewriting (9.16) and (9.21) as

$$\dot{\tau}_e = -\frac{R_r}{L_r} \tau_e + \frac{3R_r L_m^2}{2L_r^2} i_g^d i_g^q, \quad (9.29a)$$

$$\Delta \dot{\omega}_r = \frac{1}{J} \left(\frac{v_f^\top i_g}{\omega_0^* + \Delta \omega_r} - \tau_e \right) - D \Delta \omega_r, \quad (9.29b)$$

and transforming (9.11) and (9.23) respectively into

$$\tilde{\omega}_\nu = \frac{R_r}{L_r} \frac{i_g^q}{i_g^d} + \varphi, \quad (9.30a)$$

$$\omega_s = \omega_0^* + \Delta \omega_r + \tilde{\omega}_\nu, \quad (9.30b)$$

we obtain an index-1 DAE form comprising (9.29) as differential equations and (9.27)-(9.28), (9.30) as algebraic equations⁶. The state vector representing the VIM dynamics is thus $x_{\text{vim}} = (\tau_e, \Delta \omega_r) \in \mathbb{R}^2$, and is of the same order as the PLL controller, whereas the vector of algebraic variables consists of $y_{\text{vim}} = (\varphi, \varphi_d, \varphi_q, \tilde{\omega}_\nu, \omega_s) \in \mathbb{R}^5$. The newly defined variable $\tilde{\omega}_\nu \in \mathbb{R}$ represents the unsaturated frequency slip.

In order to include the frequency slip saturation limits into the DAE model, we employ the well-known expressions for the minimum and maximum of two variables:

$$\min\{a, b\} = \frac{a + b - |b - a|}{2}, \quad (9.31a)$$

$$\max\{a, b\} = \frac{a + b + |b - a|}{2}, \quad (9.31b)$$

⁶ The state vectors v_f, i_g and v_t are included in the dynamical model of the converter control in Section 2.7 and hence do not contribute to the model order of the synchronization unit.

and re-declare $\omega_\nu \in [\underline{\omega}_\nu, \bar{\omega}_\nu]$ as the saturated slip counterpart of $\tilde{\omega}_\nu$, determined by the following algebraic equation:

$$\omega_\nu = \frac{1}{2} \left(\frac{1}{2} (\tilde{\omega}_\nu + \underline{\omega}_\nu + |\underline{\omega}_\nu - \tilde{\omega}_\nu|) + \bar{\omega}_\nu - \left| \bar{\omega}_\nu - \frac{1}{2} (\tilde{\omega}_\nu + \underline{\omega}_\nu + |\underline{\omega}_\nu - \tilde{\omega}_\nu|) \right| \right). \quad (9.32)$$

The derivation of (9.32) is given in Appendix B.4.

By including ω_ν into y_{vim} we complete the DAE formulation of the VIM controller. Combining it with the internal dynamics of converter's system- and device-level control, as well as with the the network-side dynamics pertaining to the device model representation, results in a 16th-order converter model for both the PLL and VIM-based synchronization principle.

9.4 SIMULATION RESULTS

9.4.1 System Setup and VIM Tuning

In this section, the performance of the proposed control scheme is studied for various transient scenarios using the detailed EMT model of a grid-following VSC connected to a stiff grid, developed in MATLAB Simulink and described in Chapter 2. We focus on real-time operation events such as start-up and synchronization, response to setpoint variation (i.e., voltage and power reference tracking) and islanding (i.e., converter disconnection from the main grid). Finally, the impact of the initial rotor speed estimate ω_0^* on the converter's synchronization process with the grid is studied.

Understandably, the VIM's response is highly dependent on the selection of tuning parameters, in particular the parameters of the equivalent physical induction machine. This mainly refers to the rotor resistance and inductance, but also to the mutual inductance included in the transfer function $K_e(s)$. Additionally, proper values for the moment of inertia and damping are crucial for the dynamics of the rotor frequency, which in turn affects the sinusoidal nature of the voltage and current at the converter terminal. The initial parameters used in this case study have been obtained from a physical induction generator of a 1.5 MW type-1 wind turbine, with the most relevant parameters for VIM design listed in Table 9.1. Note that the VIM input frequency is set at $f_0^* = 50$ Hz.

The dynamics of the frequency slip are described by a PD controller $K_\nu(s)$ in (9.11), with the proportional gain $K_\nu^P = R_r/L_r$ given by the IM parameters and a unity derivative gain $K_\nu^D = 1$. Nevertheless, such high value of the derivative gain can destabilize converter control during transients.

Parameter	Symbol	Value
Nominal rated power	P_n	1.5 MW
Total moment of inertia ^a	J	152.14 kg m ²
Damping constant	D	10 N m/s
Rotor resistance	R_r	0.0005 p.u.
Rotor inductance	L_r	0.05 p.u.
Mutual inductance	L_m	0.6 p.u.
Initial frequency setpoint ^b	f_0^*	50 Hz

^a Corresponding to the normalized inertia constant $H = 5$ s.

^b Corresponding to $\omega_0^* = 314.16$ rad/s in Section 9.3.

TABLE 9.1: Simulation parameters of the proposed VIM controller.

This problem is overcome by re-tuning the PD controller via Ziegler-Nichols method [200], i.e., determining the optimal K_ν^D component while assuming the existing proportional gain K_ν^P , which results in $K_\nu^D = 0.001$. The parameters of the system-level control (i.e., droop gains and cut-off frequency of the low-pass filter included in the power control) and the device-level control (i.e., PI gains of the cascaded voltage and current controllers) have been adopted from Chapter 2 (see Table 2.1) in order to test the plug-n-play properties of the VIM.

9.4.2 Case Studies

First, the connection and synchronization of a VIM-based converter to the grid is studied. The VSC is connected to the grid at $t = 0$ s, with the initial input frequency $f_0^* = 50$ Hz set equal to the grid frequency. The voltage reference is initialized at $V_c^* = 1$ p.u., whereas the active and reactive power setpoints are set to $p_c^* = 0.5$ p.u. and $q_c^* = 0$ p.u., respectively.

The transient response illustrated in Fig. 9.3 confirms the soft-start and self-synchronization capabilities of the VIM as well as an adequate oscillation damping characteristic. The setpoints are correctly tracked and the voltage and current overshoots during start-up are acceptable. Note that the initial overcurrents are in accordance with the characteristic response of an induction generator, but can also be assigned to numerical initialization of the model. The initial transients are better understood by observing the estimated synchronous frequency f_s and its time-variant components f_ν and Δf_r . The frequency slip is very volatile during the first 300 ms, unlike the rotor's

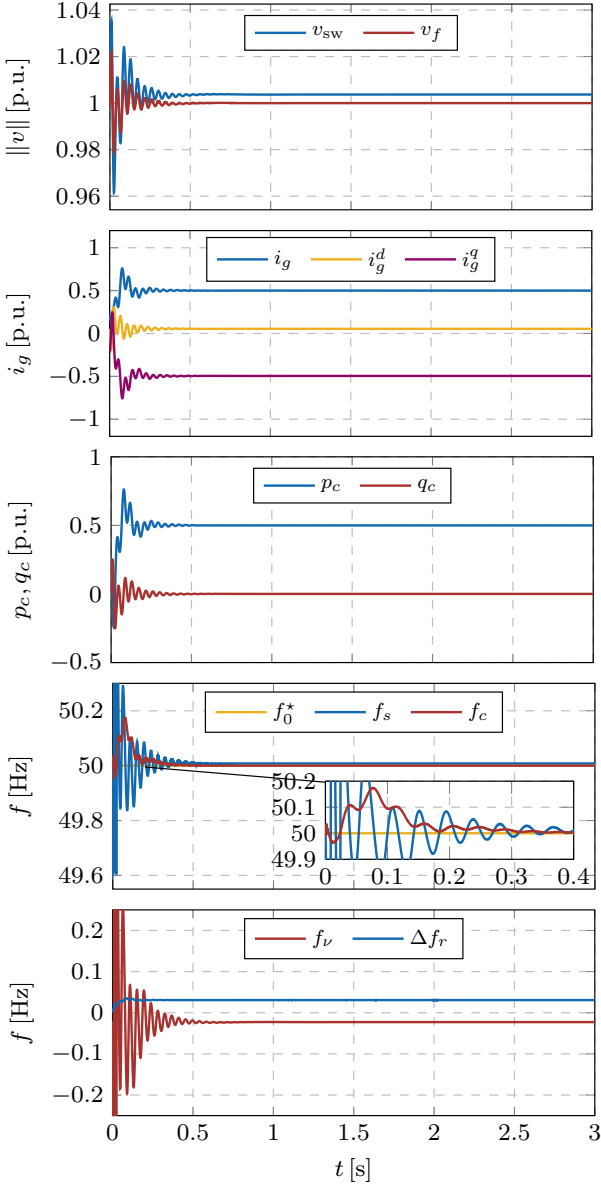


FIGURE 9.3: Transient behavior of the VIM-based unit during start-up: (i) voltages; (ii) current and its dq -components; (iii) active and reactive power; (iv) frequencies; and (v) VIM frequency terms.

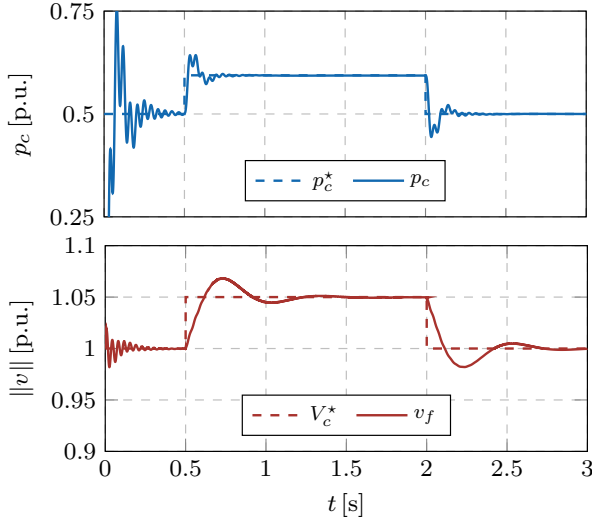


FIGURE 9.4: VIM response to the variation of controller setpoints: (a) Variation of the voltage setpoint. (b) Variation of the active power setpoint.

frequency dynamics term Δf_r , which can be associated with two aspects: (i) frequency slip is proportional to the quotient i_g^q/i_g^d , which can reach very high values when $i_g^d \approx 0$; (ii) $K_\nu(s)$ behaves as a PD controller, with its derivative actions (K_ν^D) being mostly utilized throughout the first 300 ms of the start-up. After 500 ms, both frequency components stabilize and the synchronous and converter output frequency reach a steady state value of $f_s \approx f_c \approx 50.008$ Hz.

Another important aspect of control performance is the reference tracking, i.e., converter's ability to follow sudden changes in voltage and power setpoints. Both scenarios are simulated independently, with setpoint changes occurring at $t = 0.5$ s in each case. The voltage reference exhibits a step increase of 5%, whereas the active power reference increases by 20%. Both step changes last for 1.5 s before setpoints returning to their original values.

The results depicted in Fig. 9.4 indicate that power and voltage reference tracking is achieved within reasonable time, as both the output voltage (i.e., the voltage v_f after the filter) and active power follow closely the respective setpoints. This is an expected outcome, as the reference tracking capability comes from the proper design of system- and device-level controls, which remain intact compared to the model presented in Chapter 2. Nevertheless,

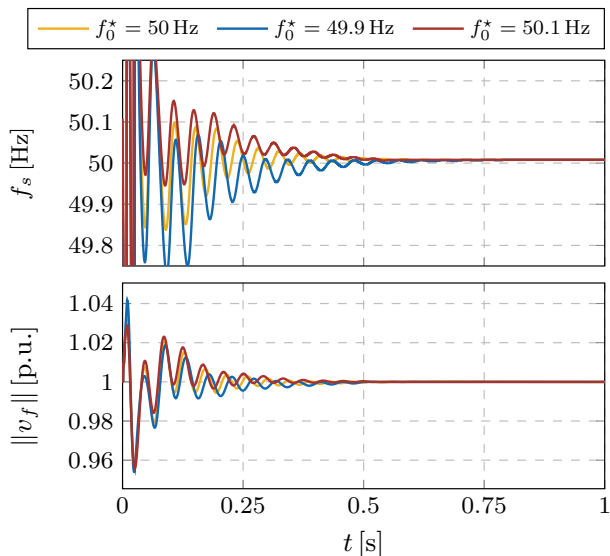


FIGURE 9.5: Impact of initial rotor frequency term on the synchronization process of a VIM during start-up: synchronous VIM frequency (top) and converter output voltage (bottom).

an inefficient synchronization device would have deteriorated the performance, which is clearly not the case for the VIM. A somewhat delayed response and excessive overshoot in the voltage output is solely an artifact of the employed PI tuning of the inner control loops, since the selected tuning favors the power tracking over the voltage tracking, and can easily be addressed with a different set of PI control gains.

Let us recall that one of the control inputs to the VIM is the so-called “estimated” initial rotor frequency f_0^* . Previous examples have shown that under the $f_s \approx f_0^*$ condition the system experiences a satisfactory performance with good synchronization and damping properties. However, having knowledge of the exact grid frequency prior to the connection of the VSC might not be achievable in real-world applications. Thus, the impact of inaccurate f_0^* guess on converter synchronization is investigated by studying the frequency and voltage response for $f_0^* = 49.9$ Hz and $f_0^* = 50.1$ Hz, and comparing it against the results presented in Fig. 9.3 for the “ideal” case where $f_0^* = 50$ Hz. The analysis is set on the first second of the response after start-up, with The frequency and voltage response presented in Fig. 9.5. We can conclude

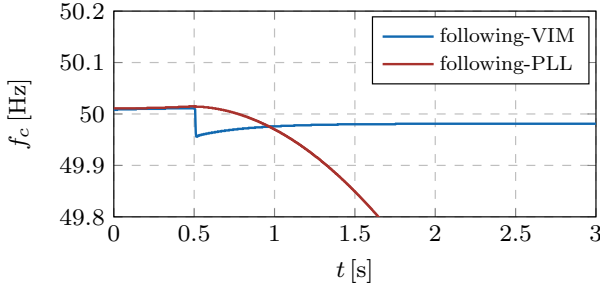


FIGURE 9.6: Behavior of different synchronization units after grid disconnection.

that the synchronization is successfully achieved within 500 ms for all three scenarios, with no distinctive differences between the three initialization points. Hence, as stated previously in Section 9.2, the VIM will experience fast synchronization for any reasonable guess of the initial rotor frequency prior to the grid connection.

Finally, we investigate the behavior of the VIM-controlled converter after the disconnection from the network. One of the main benefits of employing a VIM synchronization scheme is its standalone capability, i.e., the ability to stay in synchronism and operate even after being disconnected from the main grid; a characteristic of a physical induction machine. Such property is not attainable by traditional grid-following VSCs employing a phase-locked loop. The islanding is simulated⁷ at $t = 0.5$ s and the inverter response is showcased in Fig. 9.6. The PLL-based unit loses synchronism immediately after the disconnection, with frequency plummeting below 49 Hz within 3 s of the disconnection. On the other hand, after some negligible initial transients, the VIM restores the converter to a new steady-state point and proceeds with normal operation.

9.5 STABILITY ANALYSIS

Having validated the theoretical concept of VIM through EMT simulations, we dedicate this section to small-signal analysis of the DAE model presented in Section 9.3. Moreover, we consider three different converter operation modes: (i) a grid-following VSC with a PLL; (ii) a grid-following VSC with a VIM; and (iii) a grid-forming VSC. Some very insightful observations can

⁷ We assume $t = 0$ to be the time instance at which the initialization transients have decayed and the system is in synchronism.

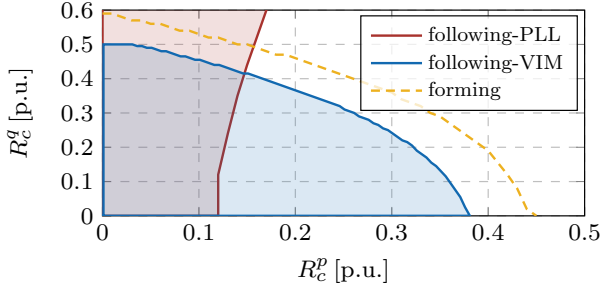


FIGURE 9.7: Stability maps of different converter modes in the $R_c^p - R_c^q$ plane.

be made by studying the stability maps in the $R_c^p - R_c^q$ plane of a single inverter connected to a stiff grid. One such map is illustrated in Fig 9.7 for a wide range of active and reactive power droop gains. Clearly, the two grid-following controllers have significantly different stability regions. However, for a reasonable tuning range considered in practice (i.e., $R_c^p < 0.1$ p.u. and $R_c^q < 0.05$ p.u.), the two regions are identical. Nevertheless, a very interesting observation can be made by comparing the aforementioned stability maps to the corresponding map of a grid-forming unit. Indeed, the stable region of a grid forming VSC closely resembles the one of a VIM-based inverter for the whole parameter range, suggesting that replacing a PLL with a VIM-based synchronization device might provide some “forming-like” properties to the grid-following VSCs. A notion that could be substantiated by the fact that the VIM has standalone capabilities.

We continue this line of investigation by comparing the stability margins of all three converter modes depending on the strength (i.e., the short-circuit ratio) of the grid at the connection terminal. As previously shown in Section 2.7 (see Fig. 2.17), the critical SCR for a PLL-based inverter is $\hat{\mu} = 1$, whereas the grid-forming VSC does not impose any requirements on the minimum grid strength. In that sense, the VIM-controlled inverter again resembles the grid-forming one, since it can withstand any SCR level as illustrated in Fig. 9.8. Moreover a similar analysis is done with respect to the maximum permissible penetration of inverter-interfaced generation, corresponding to the study presented in Chapter 4. The movement of the most critical eigenvalue, i.e., the evolution of its real part with the increase in VSC installation level, is depicted in Fig. 9.9 for the two-bus test case comprising one synchronous and one inverter-interfaced generator from Fig. 4.2. While the maximum permissible installed capacity of PLL-based units is slightly

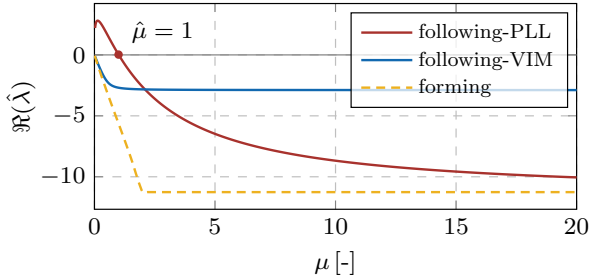


FIGURE 9.8: SCR influence on system stability for different converter modes.

below 70 %, this level can be increased by $\approx 7\%$ by substituting the PLL with the VIM, therefore almost reaching the maximum permissible penetration of grid forming VSCs of $\eta_{\max} = 78.5\%$. Note that the eigenvalue movement for scenarios SG – VSC_{pll} and SG – VSC_{form} is taken from Fig. 4.9. This just goes to show that, despite not being able to provide black start and independently generate stable frequency reference, the VIM-based grid-following converters clearly share conceptual similarities with the grid-forming mode of operation. Furthermore, it should be pointed out that the instabilities arising at the maximum converter installation levels obtained from Fig. 9.9 are solely associated with device-level control, with the highest state participation given in Table 9.2. Hence, the instability is related to the inner voltage and current control and is not affected by the selection of the synchronization unit.

Finally, we briefly address the topic of control tuning pertaining to the proposed VIM design. As previously pointed out in Section 9.2, the tuning of a VIM can be based on the parameters of a physical induction machine.

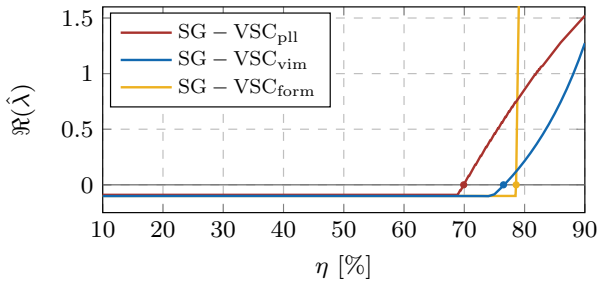


FIGURE 9.9: Impact of penetration of inverter-based generation on system stability for different converter operation modes.

State	i_f^d	i_f^q	v_f^d	v_f^q	ξ^d	ξ^q	i_g^d	i_g^q	other
PF	30.2	30.5	8.1	8.4	6.2	6.8	4.5	4.1	1.2

TABLE 9.2: State participation [%] in the unstable modes.

This particularly applies to the selection of resistance and inductance values involved in the PD controller $K_\nu(s)$ in (9.11) and the transfer function $K_e(s)$ in (9.17). However, emulating the existing machine has its drawbacks, as it does not guarantee an optimal control performance. This was already discussed in Section 9.3, as the derivative gain K_ν^D had to be re-tuned in order to achieve a satisfactory response during transients. Moreover, some induction generators might simply result in an unstable system. One such example is provided in Fig. 9.10 with the stability surface of a VIM-based converter illustrated in the $R_r - L_r - L_m$ space. It reflects the possible obstacles one could face when applying heuristic methods for VIM tuning, as the surface in Fig. 9.10 has distinctively nonlinear segments. Nevertheless, since VIM is an emulation of a physical machine, the tuning process does not have to incorporate exact physical parameters, but can rather use them as an initial starting point when designing the controller. Therefore, the multi-dimensional stability mapping, such as the one illustrated in Fig. 9.10, can be of great importance when optimizing the VIM performance.

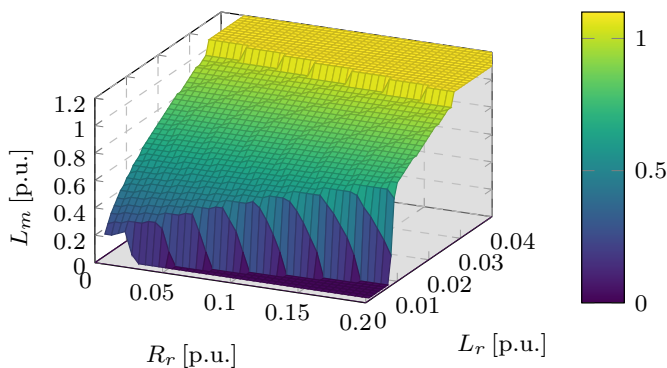


FIGURE 9.10: Stability surface of a VIM-based converter in the $R_r - L_r - L_m$ space. The shaded area below the surface indicates a stable operating region.

9.6 CONCLUSION

This chapter proposes a novel control strategy for synchronization of grid-connected VSCs based on the emulation of induction generator principles. For that purpose, a detailed mathematical model of an induction machine was derived and implemented within a detailed converter control scheme. It therefore eliminates the need for a dedicated PLL unit, while also providing additional services such as standalone operation after an islanding event. Moreover, similar to the the PLL, the VIM also has plug-n-play properties and can be combined with any system-level and device-level control method. The EMT simulations showcase smooth start-up and synchronization to the grid and an accurate computation of grid frequency, independent of the initial rotor speed input. The proposed synchronization device does not hinder the performance of other converter controls and preserves accurate voltage and power setpoint tracking. Finally, it was shown that a VIM-based grid-following converter resembles a grid-forming unit in certain operational aspects, therefore allowing for a higher penetration of VIM-controlled DGs compared to the PLL-based ones. A path for future work should go in a similar direction and further explore the dynamical properties of a VIM, as well as its interactions with conventional SGs and different converter control schemes.

ANALYSIS AND CONTROL OF INVERTER-BASED GRIDS UNDER COMMUNICATION AND MEASUREMENT DELAYS

This chapter deals with the topic of time delay in low-inertia power systems, taking into consideration both the constant and time-varying delays. The focus is set on two different problem setups: (i) the problem of constant local measurement delay, its impact on the stability of a single inverter control scheme, and the design of a device-level controller robust to uncertainty in such measurement delays; and (ii) the design of the delay-robust wide-area oscillation damping controller for inverter-dominated power systems capable of dealing with time-varying communication delays.

In the first case, the small-signal stability and robust converter control design under time delay uncertainty have been investigated. For this purpose, a delay DAE model of the VSC control scheme is developed, with the transcendental nature of the characteristic equation resolved by implementing the Padé approximation and Chebyshev discretization scheme and observing a finite number of critical low-frequency eigenvalues. Moreover, two approaches for time delay modeling are proposed using linear fractional transformations and linear parameter-varying systems, respectively. Subsequently, two output-feedback synthesis methods are implemented based on \mathcal{H}_∞ control theory and formulated using linear matrix inequalities, namely a norm-bounded parametric \mathcal{H}_∞ controller and a gain-scheduled \mathcal{H}_∞ controller. These robust control principles are then employed to improve the performance of VSCs under varying measurement delays. In particular, three novel control strategies are proposed in order to redesign the conventional inner control loop and improve converter performance when dealing with measurement signal uncertainty.

The second aspect of this chapter focuses on Wide-Area Control (WAC) for oscillation damping under time-varying communication delays that, if not appropriately considered in the control design, can destabilise the system, especially under shorter timescales of low-inertia systems. To this end, we propose a design procedure for a delay-robust WAC that successfully improves the oscillation damping while ensuring robustness against time-varying

communication delays in a system comprising both synchronous and converter-interfaced generation. All proposed methods and controllers have been tested and validated on detailed EMT model described in Chapter 2. The first part of this chapter is based on [18, 20, 201], whereas the second part is adapted from [202].

10.1 INTRODUCTION

10.1.1 *Stability and Control under Local Measurement Delays*

The ongoing energy transition is accompanied by a loss of rotational inertia, which can have adverse effects on system stability margins [6]. This problem is dealt with through advanced converter control schemes such as droop control [39], VSM [76], machine matching [58] and dVOC [53] discussed in Section 2.4. However, all of the proposed approaches involve local signal measurements, which are often subjective to time delays. The impact of local measurement delays is often ignored in traditional power systems due to large time constants of synchronous generators and governor controls. Nonetheless, with significantly shorter timescales in low-inertia systems, the local converter control measurements might play an important role in the overall system stability [12].

In order to properly analyze stability of power systems with inclusion of signal delays, their conventional mathematical representation based on DAEs should be extended to Delay Differential-Algebraic Equations (DDAEs). The variations of this concept have been investigated in [203–206], but only for traditional power systems comprising synchronous machines with signal delays in the terminal voltage measurement. The studies in [203, 204] analyze the impact of large measurement delays on the boundary of the small-signal stability region via a “predictor–corrector” framework, employing an optimization problem as the algorithm’s corrector. The results suggest that the small delays (< 10 ms) can be ignored, whereas the larger ones (> 100 ms) could significantly impact the dynamic characteristics of the system. Nevertheless, the downsides of the proposed approach are the imprecise time delay approximation as well as poor scalability onto larger systems. On the other hand, [205, 206] employ four techniques for approximating the numerical solutions of a subset of the roots of the characteristic matrix pertaining to the original DDAE set. Moreover, they include additional delays in transducers of AVR and PSS. The authors conclude that the Padé approximants and Chebyshev discretization are the most accurate and robust

methods of those considered. However, the focus of the studies is set solely on constant measurement delays with no uncertainty.

In contrast, a probabilistic approach for modelling the delays as a random variable and employing Monte Carlo simulations was used in [207], while [208] proposes a use of Lyapunov functions for deriving the delay-dependent stability criteria. The studies in [209] and [210] employ classical \mathcal{H}_∞ methods to deal with fixed delays, and [211] suggests a parameter-dependent \mathcal{H}_∞ gain-scheduling for delays within a certain tolerance. Other approaches in the literature consider a use of Smith predictors [212], adaptive control schemes [213] and lead-lag compensators [214]. Nonetheless, all aforementioned studies focus on conventional power systems and the underlying delays in local and wide-area measurements, thus neglecting the impact of time delays coming from measurement or communication in the PE components which can play an important role in system stability. While some concerns regarding the impact of local converter delays in low-inertia systems have already been raised in [18], it was done for a simplistic system and without considering the delay uncertainty.

This chapter contributes in several ways to the existing literature. Firstly, we introduce a mathematical framework for studying the impact of measurement delays on small-signal stability of inverter-based power systems. The critical eigenvalues of the system - corresponding to the solutions of the characteristic equation of the representative DDAE set - are determined using Padé approximation and Chebyshev discretization scheme, and adequate stability margins are assessed based on bifurcation analysis. Secondly, we propose two methods for modelling the delay uncertainty, namely using Linear Fractional Transformations (LFTs) and Linear Parameter-Varying (LPV) systems, and incorporate them into the Robust Control (RC) design. As a result, two output-feedback synthesis methods are implemented based on \mathcal{H}_∞ control theory and formulated using Linear Matrix Inequalities (LMIs), each employing a different delay uncertainty model. Finally, three novel control strategies are proposed in order to redesign the conventional device-level control of VSC-interfaced generators and improve the performance under constant measurement delays and uncertainty.

10.1.2 *Wide-Area Control under Time-Varying Communication Delays*

Electric power systems are frequently subjected to low-frequency inter-area oscillations caused by SGs, or coherent groups of generators, oscillating against each other in an interconnected system [26]. Insufficient damping of such

oscillations can lead to increased losses, excessive strain on the mechanical components of generators, and in extreme cases instability. Traditionally, these underdamped oscillations have been addressed by deploying decentralized PSSs at units participating in the power swing modes. Various control strategies for tuning of PSS parameters have been proposed in the literature, such as pole placement [215], root locus [216], \mathcal{H}_2 [217] and \mathcal{H}_∞ [218] norm. In particular, PSS can improve oscillation damping by adjusting the reference signal of the exciter, thus counteracting a high-gain fast response of the AVR. Nevertheless, relying solely on decentralized control might sometimes be inadequate for providing sufficient damping of inter-area modes, or even worsen the performance of the overall system [219, 220]. Recently, with the advancements in Wide-Area Monitoring and Control (WAMC), new methods have been proposed that exploit WAMC capabilities to improve damping by coordinating multiple units through a wide-area controller [221, 222].

The deployment of a communication network to enable WAMC is however not problem-free and can introduce additional vulnerabilities to the system, one of the most prominent being communication delays. The latter arise in the form of transmission delays, propagation delays, processing delays and queuing delays [223, 224]. Since the presence of communication delays influences the system performance and can even lead to instability [225], taking such delays into account is necessary in order to design a well-functioning WAMC.

While this problem has already been investigated for constant delays in the frequency domain [226, 227], the proposed analyses are not applicable to the case of time-varying delays. Yet, the latter are ubiquitous in sampled data networked control systems such as WAMC [228, 229]. The reasons for this are the joint presence of digital controls and continuous physical dynamics, as well as the fact that the network access and propagation delays typically depend on the communication network congestion and are hence time-varying [230]. Therefore, following a standard practice in sampled-data and networked control systems, in the second part of the chapter the communication delays are represented by bounded, time-dependent functions [228, 229]. As a consequence, the resulting dynamical system is non-autonomous, which implies that an eigenvalue-based stability analysis is inconclusive [231]. A standard alternative is to employ the Lyapunov-Krasovskii theory in combination with an LMI approach [228, 229]. This has been pursued for WAC synthesis in power systems with purely conventional generation in [232–235].

With the displacement of conventional SGs by inverter-interfaced renewable generation, the voltage and frequency dynamics as well as the respective control interaction in power systems become more complex and harder

to analyze [12]. Moreover, the number of PSS units providing oscillation damping is also reduced. This issue was partially addressed in [167], with the development of a global MPC for providing power-oscillation damping and stabilization of large AC power systems using VSC-based HVDC links. On the other hand, employing DGs for participation in the inter-area oscillation damping has been considered in [236–238]. However, none of the above studies considers time-varying communication delays in the WACs.

The main contribution of the chapter on this end is a design procedure for a delay-robust, wide-area output feedback controller that regulates both conventional and converter-based generators to enhance oscillation damping in a detailed low-inertia system with and under the consideration of time-varying delays. Compared to the existing work on WAC, where full state feedback controllers were used [221, 222, 239], we propose a static output feedback controller which eases its practical implementation. Moreover, the proposed control synthesis ensures damping of low-frequency modes by minimizing the upper bound of the \mathcal{L}_2 -gain, which is equivalent to the \mathcal{H}_∞ norm of a linear time-invariant system [229, 231] and has been proven to be effective in improving the damping of inter-area modes [218, 222, 232, 240, 241]. For this purpose, and since in any practical WAMC there will inevitably be a minimum nonzero communication delay, we model the delays as interval time-varying delays, i.e., assuming non-zero constant upper and lower bounds [229]. The control synthesis is derived by applying the augmented Lyapunov-Krasovskii functional in [242] together with the descriptor method. Subsequently, the variable transformation from [243] is employed to formulate the control design problem as a convex optimization problem with LMI constraints.

The remainder of the chapter is structured as follows. In Section 10.2, the analytical methods for investigating the small-signal analysis of delayed power systems are introduced and applied to a detailed converter control scheme with constant measurement delays. Section 10.3 describes the modeling of delay uncertainty and the employed control analysis and synthesis methods for robust control design. Furthermore, Section 10.4 proposes three novel device-level control strategies robust to uncertain constant measurement delays and investigates their time-domain performance. The topic of WAC is addressed in Section 10.5, where a control synthesis approach for designing the WAC that ensures robustness with respect to time-varying communication delays is presented and validated on the Kundur two-area system. Finally, Section 10.6 discusses the outlook of the studies and concludes the chapter.

10.2 SMALL-SIGNAL ANALYSIS OF DDAES

10.2.1 General DDAE Form for Power Systems

The dynamic behavior of electric power systems is usually described by a set of DAEs [205, 244]

$$\dot{x} = f(x, y, z), \tag{10.1a}$$

$$\mathbb{0}_m = g(x, y, z), \tag{10.1b}$$

where $f : \mathbb{R}^{n+m+k} \mapsto \mathbb{R}^n$ and $g : \mathbb{R}^{n+m+k} \mapsto \mathbb{R}^m$ are sets of differential and algebraic equations, $x \in \mathbb{R}^n$ and $y \in \mathbb{R}^m$ are column vectors of state and algebraic variables, and $z \in \mathbb{R}^k$ is a column vector of the discrete event variables. Despite being widely used in power system studies, representation (10.1) fails to accurately capture the time delays and their potential impact on the overall system stability. Assuming a single constant time delay $\tau \in \mathbb{R}_{>0}$ affecting the measurements, the DAE model (10.1) can be transformed into a set of DDAEs of the form

$$\dot{x} = f(x, y, x_\tau, y_\tau, z), \tag{10.2a}$$

$$\mathbb{0}_m = g(x, y, x_\tau, y_\tau, z), \tag{10.2b}$$

with $x_\tau \in \mathbb{R}^n$ and $y_\tau \in \mathbb{R}^m$ denoting the vectors of delayed state and algebraic variables, i.e., $x_\tau(t) \equiv x(t - \tau)$ and $y_\tau(t) \equiv y(t - \tau)$, and $t \in \mathbb{R}_{\geq 0}$ representing the current simulation time. For practical models of power systems it is often assumed that g does not depend on y_τ , thus simplifying the general set of DDAEs to an index-1 Hessenberg form (see [199] for more details), which yields

$$\dot{x} = f(x, y, x_\tau, y_\tau, z), \tag{10.3a}$$

$$\mathbb{0}_m = g(x, y, x_\tau, z). \tag{10.3b}$$

However, there is no loss of generality between (10.3) and the initial system model [205].

10.2.2 Characteristic Equation of General DDAE

Let us linearize the DDAE system (10.3) around the presumably known stationary solution $(x_0, y_0) \in \mathbb{R}^{n+m}$:

$$\Delta \dot{x} = f_x \Delta x + f_{x_\tau} \Delta x_\tau + f_y \Delta y + f_{y_\tau} \Delta y_\tau \tag{10.4a}$$

$$\mathbb{0}_m = g_x \Delta x + g_{x_\tau} \Delta x_\tau + g_y \Delta y, \tag{10.4b}$$

where $f_x \in \mathbb{R}^{n \times n}$, $f_{x_\tau} \in \mathbb{R}^{n \times n}$, $f_y \in \mathbb{R}^{n \times m}$, $f_{y_\tau} \in \mathbb{R}^{n \times m}$, $g_x \in \mathbb{R}^{m \times n}$, $g_{x_\tau} \in \mathbb{R}^{m \times n}$, $g_y \in \mathbb{R}^{m \times m}$ are the respective Jacobian matrices of first-order partial derivatives, and Δ reflects a small deviation around the equilibrium. By deriving Δy from (10.4b) and substituting it in (10.4a), one can obtain

$$\Delta \dot{x} = (f_x - f_y g_y^{-1} g_x) \Delta x + (f_{x_\tau} - f_y g_y^{-1} g_{x_\tau}) \Delta x_\tau + f_{y_\tau} \Delta y_\tau. \quad (10.5)$$

Understandably, a usual assumption of a non-singular characteristic of g_y must be made in order to ensure feasibility of (10.5).

In order to obtain a meaningful expression from (10.5), the vector Δy_τ must be eliminated, i.e., substituted by a linear form of actual or delayed state variables. This is done by considering the set of algebraic equations g at time step $(t - \tau)$:

$$0_m = g(x(t - \tau), y(t - \tau), x_\tau(t - \tau)). \quad (10.6)$$

Having in mind that the equalities

$$x_\tau = x(t - \tau), \quad y_\tau = y(t - \tau), \quad x_\tau(t - \tau) = x(t - 2\tau) \quad (10.7)$$

hold, it is possible to differentiate (10.6) and obtain

$$0_m = g_x \Delta x_\tau + g_y \Delta y_\tau + g_{x_\tau} \Delta x(t - 2\tau). \quad (10.8)$$

It should be noted that the Jacobian matrices in (10.4) and (10.8) are the same, since variables x and y meet the steady-state conditions $x(t_0) = x(t_0 - \tau)$, $y(t_0) = y(t_0 - \tau)$ at any instance $t_0 \in \mathbb{R}_{\geq 0}$. Moreover, this work focuses on systems where it can be justifiably assumed that only one type of time delay is present. More precisely, the delayed variables correspond to local measurement delays, which can be expected to be very similar for different devices. Therefore, we can simplify (10.8) by eliminating its last term and substituting the obtained expression for Δy_τ in (10.5), which yields

$$\Delta \dot{x} = (f_x - f_y g_y^{-1} g_x) \Delta x + (f_{x_\tau} - f_y g_y^{-1} g_{x_\tau} - f_{y_\tau} g_y^{-1} g_x) \Delta x_\tau. \quad (10.9)$$

The final form of (10.9) can be declared as

$$\Delta \dot{x} = A_0 \Delta x + A_1 \Delta x(t - \tau), \quad (10.10)$$

where

$$A_0 = f_x - f_y g_y^{-1} g_x, \quad (10.11a)$$

$$A_1 = f_{x_\tau} - f_y g_y^{-1} g_{x_\tau} - f_{y_\tau} g_y^{-1} g_x. \quad (10.11b)$$

Equation (10.11a) denotes a standard DAE state matrix $A_0 \in \mathbb{R}^{n \times n}$, whereas $A_1 \in \mathbb{R}^{n \times n}$ in (10.11b) is a consequence of time delays. The formulation in (10.10) represents a special case of the standard Delay Differential Equation (DDE) form

$$\dot{x} = A_0 x(t) + \sum_{i=1}^{\nu} A_i x_i(t - \tau_i), \quad (10.12)$$

whose characteristic matrix can be defined by

$$\Delta(\lambda) = \lambda I_n - A_0 - \sum_{i=1}^{\nu} A_i e^{-\lambda \tau_i}. \quad (10.13)$$

The matrix $I_n = \text{diag}(\mathbf{1}_n)$ is the identity matrix of order n , while $\tau_i \in \mathbb{R}_{>0}$ represents the respective time delay for $i \in [1, \nu]$; in this specific case $\nu = 1$ and $\tau_1 = \tau$. Despite (10.13) being transcendental, the number of its right-half plane solutions is finite and therefore can be used for small-signal stability studies [245]. Furthermore, the stability properties of the respective root loci spectrum are applicable to the DDAE system (10.10). More details regarding the derivation of expressions (10.10)-(10.13) for multiple-delay systems as well as the theoretical background behind the eigenvalue properties of (10.13) can be found in [205].

Since the explicit solution of (10.13) is unknown, certain numerical approximations have to be employed in order to find a finite subset of the initial roots which reflect the same stability characteristics. The study in [206] compared four different approaches to approximate the spectrum of large power systems modelled as a set of DDAE, notably: (i) a Padé approximation [246]; (ii) a Chebyshev discretization scheme of an equivalent set of Partial Differential Equations (PDEs) that resembles the original DDAEs [247–249]; (iii) a discretization of the Time Integration Operator (TIO) [250–252]; and (iv) a Linear Multi-Step (LMS) discretization [253–255]. It was shown that the Padé approximants and Chebyshev discretization are the most accurate and robust methods of those considered, with Chebyshev discretization performing well for both small (5–250 ms) and large (1–10 s) delays and Padé approximants working efficiently only for small delays. The poor results shown by the TIO and LMS methods compared to the first two techniques come from the fact that Chebyshev discretization and Padé approximation methods work directly with (10.13) and are concerned solely with approximating the $e^{-\lambda \tau_i}$ terms, whereas the TIO and LMS methods work with (10.12) and require approximations of both the \dot{x} term and the delay terms [206]. As the delays involved with local measurements in power electronic converters are in the order of tens and hundreds of microseconds, both Padé approximants and

Chebyshev discretization scheme appear to be viable methods for small-signal analysis and will therefore be considered and compared in this chapter.

10.2.3 Padé Approximation

Instead of addressing the transcendental property of the characteristic matrix in time domain given by (10.13), Padé approximation models the delay as a time shift in Laplace domain using a well-known property of the Laplace transform \mathcal{L} :

$$f(t - \tau)u(t - \tau) \xrightarrow{\mathcal{L}} e^{-\tau s}F(s), \quad (10.14)$$

where s is the complex frequency in Laplace domain, $u(t - \tau)$ is the delayed unit step function, and $F(s)$ is the Laplace transform of the function $f(t)$. Such formulation allows for converting the original DDAE problem into a set of DAEs, with delayed variables approximated by algebraic functions of multiple new state variables. In particular, this approach consists of defining a rational polynomial transfer function that approximates the exponential time shift term $e^{-\tau s}$ through Taylor's expansion:

$$e^{-\tau s} = 1 - \tau s + \frac{(\tau s)^2}{2!} - \frac{(\tau s)^3}{3!} + \dots \approx \frac{b_0 + b_1\tau s + \dots + b_q(\tau s)^q}{a_0 + a_1\tau s + \dots + a_p(\tau s)^p}, \quad (10.15)$$

and subsequently applies an inverse Laplace transform in order to obtain the approximated DAE form. The coefficients $(a_1, \dots, a_p) \in \mathbb{R}^p$ and $(b_1, \dots, b_q) \in \mathbb{R}^q$ in (10.15) are calculated by dividing the right-hand side polynomials and equating them to the first $p + q$ counterparts of Taylor's expansions, with generally $p \geq q$ and $(p, q) \in \mathbb{Z}_{>0}^2$ [246]. Nonetheless, $p = q$ is a noteworthy and common case for which the coefficients can be obtained using the following iterative formula:

$$a_0 := 1, \quad a_i := a_{i-1} \frac{p - i + 1}{i(2p - i + 1)}, \quad b_i := (-1)^i a_i. \quad (10.16)$$

While the approximation accuracy increases with the order of Padé approximants, the actual value of p cannot be too high as the polynomial coefficients also depend on time delay τ , which in turn can lead to coefficient $a_p\tau^p$ being critically close to the single-precision floating-point in case of small time delays [206]. Hence, $p = q = 6$ is a common choice in numerical simulations for power systems. Using the inverse Laplace transform, the time domain expression of the p^{th} -order approximant u_τ of the delayed unit step function $u(t - \tau)$ can be determined:

$$u_\tau := \tilde{x}_1 + b_1\tau\tilde{x}_2 + \dots + b_{p-1}\tau^{p-1}\tilde{x}_p + b_p\tau^p\dot{\tilde{x}}_p, \quad (10.17)$$

where

$$\begin{aligned} \dot{\tilde{x}}_i &:= \tilde{x}_{i+1}, \quad i = 1, 2, \dots, p-1, \\ a_p \tau^p \dot{\tilde{x}}_p &:= u - (a_0 \tilde{x}_1 + a_1 \tau \tilde{x}_2 + \dots + a_{p-1} \tau^{p-1} \tilde{x}_p). \end{aligned} \tag{10.18}$$

In other words, the delayed variable u_τ is replaced by a linear combination of p new state variables $(\tilde{x}_1, \dots, \tilde{x}_p) \in \mathbb{R}^p$. For more details we refer the reader to [206, 246].

10.2.4 Chebyshev Discretization Scheme

This technique is based on recasting (10.12) as an abstract Cauchy problem, i.e., transforming the initial eigenvalue analysis of a DDE system into computing roots of an infinite dimensional set of PDEs, without any loss of information. A finite element-based discretization method is then employed in order to make the PDE problem computationally tractable [205, 247].

For the purposes of this study, a simplification that only state variables are subjected to time delays can be made, justified by the fact that the delays are associated only with the measurements of currents and voltages used for inverter feedback control. Therefore, assuming a single event variable, we can reformulate (10.3) into

$$\dot{x} = f(x, y, x_\tau), \tag{10.19a}$$

$$\mathbb{0}_m = g(x, y, x_\tau), \tag{10.19b}$$

for which the characteristic matrix becomes

$$\Delta(\lambda) = \lambda I_n - A_0 - A_1 e^{-\lambda \tau}, \tag{10.20}$$

and

$$A_0 = f_x - f_y g_y^{-1} g_x, \tag{10.21}$$

$$A_1 = f_{x_\tau} - f_y g_y^{-1} g_{x_\tau}. \tag{10.22}$$

According to [206], the root loci spectrum of (10.20) can be approximated by the eigenvalues of the discretization matrix

$$M := \left[\begin{array}{cccc} \hat{C} \otimes I_n & & & \\ A_1 & \mathbb{0}_{n \times n} & \dots & \mathbb{0}_{n \times n} & A_0 \end{array} \right], \tag{10.23}$$

with \otimes denoting the Kronecker product and \hat{C} indicating a matrix composed of the first $N - 1$ rows of the matrix

$$C = -\frac{2D_N}{\tau}. \quad (10.24)$$

Here, $D_N \in \mathbb{R}^{N \times (N+1)}$ represents the Chebyshev differentiation matrix of order N , interpolated over $N + 1$ Chebyshev nodes of the form $x_k = \cos\left(\frac{k\pi}{N}\right)$, $\forall k \in [0, \dots, N]$ on the normalized interval $[-1, 1]$. Each element $D_{i,j} \in D_N$ of the differentiation matrix, with indices (i, j) ranging from 0 to N , can be defined according to the following interpolation scheme:

$$D_{i,j} := \begin{cases} \frac{c_i(-1)^{i+j}}{c_j(x_i-x_j)}, & i \neq j, \\ \frac{-1}{2} \frac{x_i}{1-x_i^2}, & i = j \neq 1, N-1, \\ \frac{2N^2+1}{6}, & i = j = 0, \\ -\frac{2N^2+1}{6}, & i = j = N, \end{cases} \quad (10.25)$$

where $c_0 = c_N = 2$ and $c_2 = c_3 = \dots = c_{N-1} = 1$. More details on the differentiation matrix and the underlying interpolation scheme are provided in [205].

Similar to the order of Padé approximant, the selection of the number of nodes N defines the computational effort and precision of the proposed method; a range of $N \in [5, 10]$ is considered a good trade-off between the accuracy and computational burden [18, 206]. The logic behind approximating the spectrum of (10.20) with the eigenvalues of M lies in considering M as a discretization of a PDE system, where a continuous variable $\xi \in [-\tau, 0]$ corresponds to the time delay that is discretized along the grid of N points. The position of these points is defined by Chebyshev polynomial interpolation, with the last n rows (i.e., matrix $[A_1, \mathbb{0}_{n \times (N-2)n}, A_0]$) imposing the PDE boundary conditions $\xi = -\tau$ and $\xi = 0$ corresponding to A_1 and A_0 respectively [18, 205]. A detailed mathematical interpretation of the aforementioned method can be found in [205, 206, 249].

10.2.5 Small-Signal Analysis

The DDAE formulation from Section 10.2.1 is applied to a detailed converter control scheme described in Chapter 2 and illustrated in Fig. 2.15, together with two approximation methods presented in Section 10.2.3 and

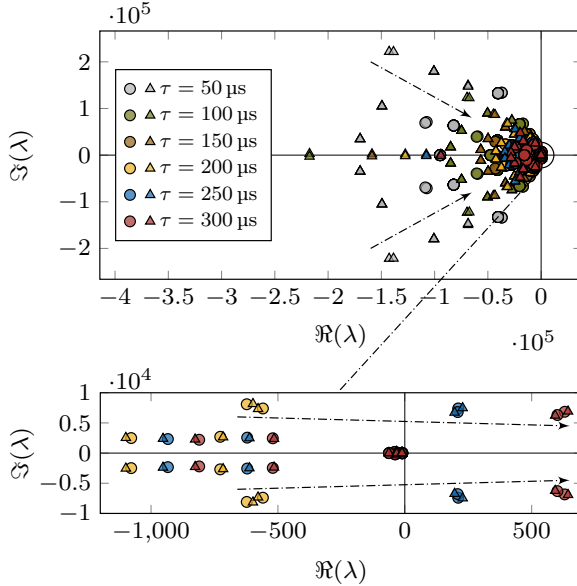


FIGURE 10.1: Eigenvalue spectrum computed using both Padé approximation (denoted by circles) and Chebyshev discretization (denoted by triangles): full spectrum (top) and critical spectrum around the imaginary axis (bottom).

Section 10.2.4. As this study is concerned with constant measurement delays and their impact on converter control, we assume that only the measurement signals of grid and filter current (i_g, i_f) as well as the voltage across the filter capacitor (v_f) are exposed to time delay. Since the converter control is designed in an SRF, in terms of DDAE formulation this corresponds to delaying the state variables expressed in a dq -frame, i.e., $x_\tau = (i_{g\tau}^d, i_{g\tau}^q, i_{f\tau}^d, i_{f\tau}^q, v_{f\tau}^d, v_{f\tau}^q) \in \mathbb{R}^6$.

The vulnerability of the system to constant measurement delays is first evaluated through small-signal analysis for a wide range of time delays (changed in $50 \mu\text{s}$ increments) and two approximations of the eigenvalue spectrum presented previously. By studying the root locus given in Fig. 10.1, one can observe that the increase in measurement delay gradually shifts the complete spectrum to the right, potentially leading to instability. Moreover, the two spectrums resulting from Padé approximation and Chebyshev discretization are distinctively different, which is understandable having in mind the different nature of the approximation involved with each method, as well as

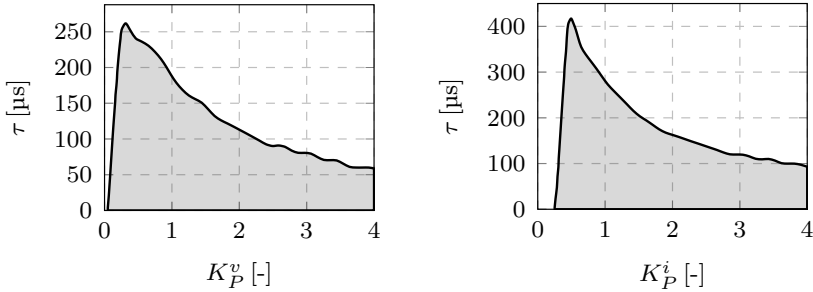


FIGURE 10.2: Stability maps in $\tau - K_p^v$ and $\tau - K_p^i$ planes. The system is stable within the shaded region.

the fact that both techniques “overapproximate” the eigenvalue spectrum by including a different number of additional artificial modes (see Section 10.2.3 and Section 10.2.4). However, the movement of the most critical modes is the same for both methods, with the respective eigenvalues being almost identical. This validates the effectiveness of both approximation techniques for the problem at hand, and justifies the claims pertaining to the accuracy in capturing the most critical modes of the original system [206].

A higher discretization of the time delay increments reveals that the critical measurement delay for both approximation approaches and a given control tuning is $\hat{\tau} = 233 \mu\text{s}$. The same value has also been obtained through sequence of EMT simulations in MATLAB Simulink for a given set of constant signal delays. Nevertheless, for higher proportional gains of the inner loop PI controllers these values can drop to a $\hat{\tau} \in [50 - 100] \mu\text{s}$ range, as indicated by the stability maps in Fig. 10.2. Having in mind that more responsive device-level controllers might be needed for voltage tracking and overcurrent protection in future inverter-dominated power systems [12], the aforementioned stability issues pertaining to measurement delay margins might become a reality. Furthermore, the participation factor analysis presented in Table 10.1 reveals that the potentially unstable modes are associated solely to the SRF

$\lambda_{1,2}$	$i_{f(\tau)}^d$	$i_{f(\tau)}^q$	$v_{f(\tau)}^d$	$v_{f(\tau)}^q$	$i_{g(\tau)}^d$	$i_{g(\tau)}^q$	ξ^d	ξ^q
λ_1	46.3	30.4	10.6	8.7	1.4	0.8	1.1	0.7
λ_2	30.1	45.8	8.9	11.3	0.8	1.4	0.8	0.9

TABLE 10.1: State participation [%] in the most critical conjugate pair $\lambda_{1,2}$.

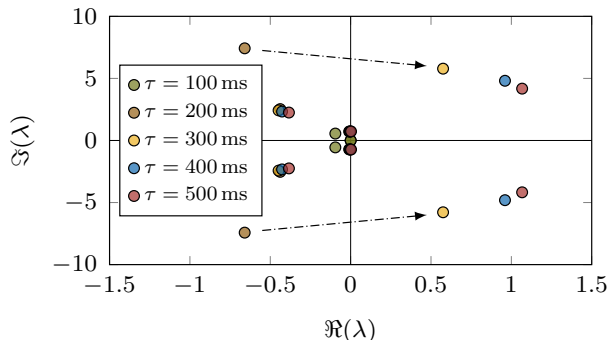


FIGURE 10.3: Critical eigenvalue spectrum around the imaginary axis for the simplified converter control model.

voltage and current controls, with filter current components (i_f^d, i_f^q) and their delayed counterparts being the predominant states. This also suggests that the current control might be the more vulnerable SRF controller of the two.

The importance of detailed converter control modeling when studying the impact of measurement delays is further emphasized by studying the stability margin of the simplified model described in [18]. The underlying converter control scheme comprises only the system-level control, i.e., the outer loop for active and reactive power regulation and the PLL, whereas the device-level control is completely neglected. The movement of the eigenvalue spectrum depicted in Fig. 10.3 suggests that the permissible time delay is approximately three orders of magnitude higher than for the detailed control case, with the critical delay of $\hat{\tau} = 234$ ms. These results validate the previous conclusions regarding the sensitivity of inner control loops to time delays, since by removing them the VSC becomes significantly more resilient to any delay in the local measurement signals. In other words, under sufficiently high delay times, the inner control - especially current controller - cannot adequately track the given reference signals, which subsequently leads to instability.

10.3 ROBUST CONTROL PRINCIPLES UNDER DELAY UNCERTAINTY

10.3.1 *Time Delay Uncertainty Modeling*

In Section 10.2 we considered a dynamical system with constant measurement delays. However, in reality the time delays can vary and are rather unpredictable, which drastically complicates a potential control design. We tackle the robust control problem by assuming a real parametric uncertainty, and model the time delays in two different ways: (i) as an LFT; and (ii) as an LPV system. In both cases the delays are modelled as exponential functions $F_\tau(s) = e^{-\tau s}$ in the Laplace domain and are approximated using a first-order Padé approximation

$$F_\tau(s) = e^{-\tau s} \approx \frac{1 - \frac{1}{2}\tau s}{1 + \frac{1}{2}\tau s}, \quad (10.26)$$

which corresponds to setting $p = q = 1$ in (10.15).

10.3.1.1 *Time Delay as LFT*

Considering the time delay between two signals of the form $z = F_\tau(s)w$, the relation between the original signal $w \in \mathbb{R}$ and its delayed counterpart $z \in \mathbb{R}$ can be expressed as

$$z = -w + \frac{2}{\tau s}(w - z), \quad (10.27)$$

which corresponds to the block diagram in Fig. 10.4a. Next, we model delay uncertainty by assuming that the measurement delay can arbitrarily change and take any value within a 1-dimensional polytope $\tau \in [\underline{\tau}, \bar{\tau}]$, where

$$a = \frac{1}{2}(\underline{\tau} + \bar{\tau}), \quad b = \frac{1}{2}(\bar{\tau} - \underline{\tau}), \quad \delta_t \in [-1, 1]. \quad (10.28)$$

One can therefore formulate such polytope as $\tau = a + b\delta_t$.

Proposition 10.3.1. *Consider a constant, uncertain time delay $\tau = a + b\delta_t$, described by (10.28). Then, τ^{-1} can be represented by an upper LFT of the form $F_u(M, \delta_t)$, where*

$$M = \begin{bmatrix} -ba^{-1} & a^{-1} \\ -ba^{-1} & a^{-1} \end{bmatrix}. \quad (10.29)$$

Proof. The proof is given in Appendix A.3. □□□

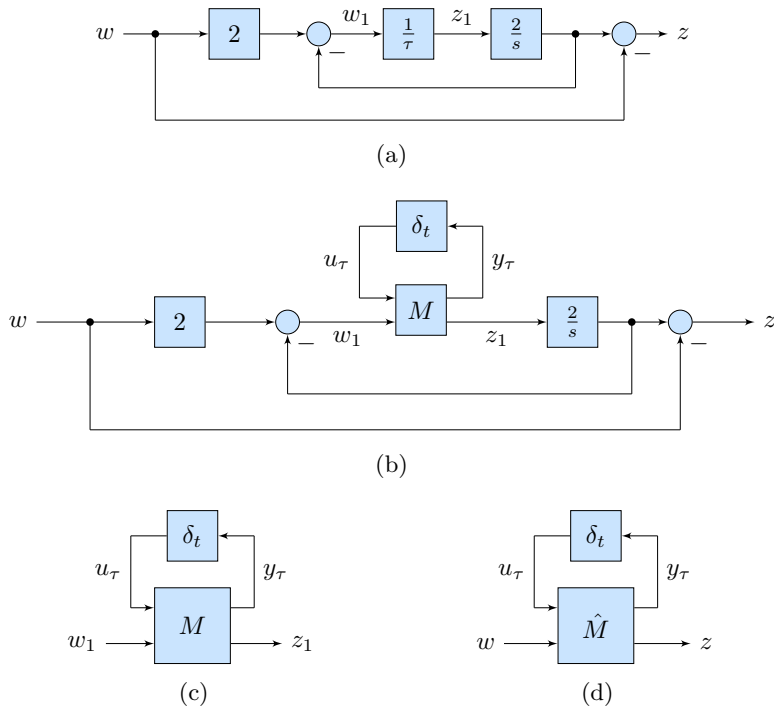


FIGURE 10.4: Equivalent representation of the delay function $F_\tau(s)$: (a) original delay function $F_\tau(s)$; (b) time delay function with LFT-based representation of the delay block τ^{-1} ; (c) LFT formulation of the delay block τ^{-1} ; (d) LFT formulation of the delay function $F_\tau(s)$.

Let us now observe a traditional feedback control system depicted in Fig. 10.4c comprising a plant M and a feedback gain δ_t , and recall that the closed-loop transfer function of such system can be represented by an upper LFT [256] of the form

$$H_{z_1 w_1} = F_u(M, \delta_t) = M_{22} + M_{21} \delta_t (I - M_{11} \delta_t)^{-1} M_{12}. \quad (10.30)$$

According to the Proposition 10.3.1, for $M = [-ba^{-1}, a^{-1}]^T \mathbb{1}_2^T$ given by (10.3.1) and $\tau = a + b\delta_t$ described by (10.28), the equality $F_u(M, \delta_t) = \tau^{-1}$ holds. Therefore, substituting the delay block τ^{-1} in Fig. 10.4a by a control system from Fig. 10.4c results in the control structure provided by Fig. 10.4b. Finally, by performing a set of trivial mathematical operations one obtains

the final LFT form presented in Fig. 10.4d, equivalent to the initial delay function $F_\tau(s)$, where

$$\hat{M} = \begin{bmatrix} \hat{M}_{11} & \hat{M}_{12} \\ \hat{M}_{21} & \hat{M}_{22} \end{bmatrix} = \frac{1}{-as + 2b} \begin{bmatrix} as + b & -2 \\ 2bs & -s \end{bmatrix}. \quad (10.31)$$

10.3.1.2 Time Delay as LPV function

Let us consider a delayed-input system without the controller. Based on the Padé approximation from (10.26), the state-space representation of the approximated delay function $F_\tau(s)$ can be derived as

$$\dot{x}_\tau = -\frac{2}{\tau}x_\tau + \frac{4}{\tau}u_\tau, \quad (10.32a)$$

$$y_\tau = x_\tau - u_\tau, \quad (10.32b)$$

where $u_\tau \in \mathbb{R}$ and $y_\tau \in \mathbb{R}$ are the delayed input and output of the system, and $x_\tau \in \mathbb{R}$ is the internal delay state. Substituting q for τ^{-1} yields

$$\begin{bmatrix} A_\tau(q) & B_\tau(q) \\ C_\tau(q) & D_\tau(q) \end{bmatrix} = \begin{bmatrix} -2q & 4q \\ 1 & -1 \end{bmatrix}. \quad (10.33)$$

The system in (10.33) can be rewritten as an affine parameter-dependent system, with the state-space matrices of the delay described as affine functions of the parameter q :

$$\begin{bmatrix} A_\tau(q) & B_\tau(q) \\ C_\tau(q) & D_\tau(q) \end{bmatrix} = \begin{bmatrix} A_{\tau_0} + qA_{\tau_1} & B_{\tau_0} + qB_{\tau_1} \\ C_{\tau_0} + qC_{\tau_1} & D_{\tau_0} + qD_{\tau_1} \end{bmatrix}. \quad (10.34)$$

10.3.2 \mathcal{H}_∞ Control Design

This section elaborates on the principles of \mathcal{H}_∞ control as well as the control analysis and synthesis methods employed in this study. For the generic linear system described by (10.36), the \mathcal{H}_∞ norm is the maximum gain of the transfer function from exogenous inputs w to exogenous outputs z over all frequencies and input directions [257]. For the purposes of \mathcal{H}_∞ control design, the system is rearranged into a so-called general control form illustrated in Fig. 10.5, where $P(s)$, $K(s)$ and Δ are the transfer function of the plant, controller and uncertainty, respectively. Note that the uncertainty transfer function is not needed for LPV system design.

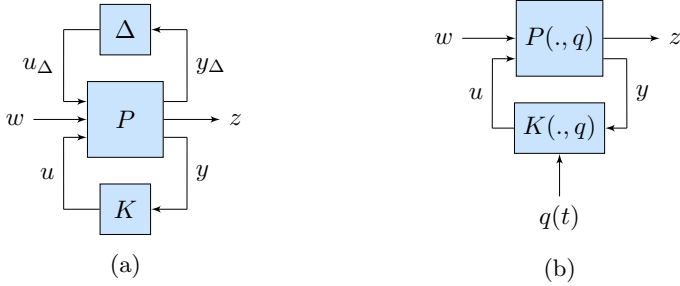


FIGURE 10.5: General control plant of the investigated system: (a) LFT general plant; (b) LPV general plant.

For simplicity of the description and without considering the uncertainty, let us decompose the state-space realization of the plant $P(s)$ as

$$P(s) = \left[\begin{array}{c|c} A & B \\ \hline C & D \end{array} \right] = \left[\begin{array}{c|cc} A & B_1 & B_2 \\ \hline C_1 & D_{11} & D_{12} \\ C_2 & D_{21} & 0 \end{array} \right], \quad (10.35)$$

in accordance with the dimensions of input and output. The system in Fig. 10.5a can now be expressed as

$$\dot{x} = Ax + B_1w + B_2u, \quad (10.36a)$$

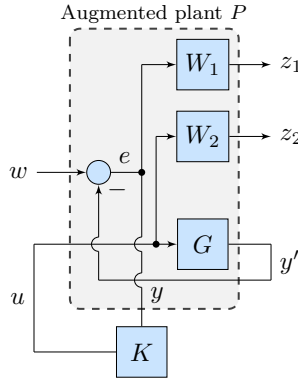
$$z = C_1x + D_{11}w + D_{12}u, \quad (10.36b)$$

$$y = C_2x + D_{21}w, \quad (10.36c)$$

with u being the control input and y the control measurement. The \mathcal{H}_∞ control problem involves designing a controller such that the generalized feedback system in Fig. 10.5 is stable and the \mathcal{H}_∞ norm of the closed-loop transfer matrix from disturbance w to performance output z is less than a given $\gamma \in \mathbb{R}_{>0}$, i.e., $\|H_{zw}\|_\infty < \gamma$. Moreover, depending on the employed control synthesis method, the closed-loop system could also guarantee a degree of robustness against model uncertainty [258].

In order to shape the sensitivity function $S(s)$ and complementary sensitivity function $K(s)S(s)$ of the closed-loop system, and achieve design targets compatible with good performance and robustness, a mixed-sensitivity \mathcal{H}_∞ design depicted in Fig. 10.6 is often used [259, 260], which minimizes

$$\left\| \left\| \begin{bmatrix} W_1(s)S(s) \\ W_2K(s)S(s) \end{bmatrix} \right\| \right\|_\infty \quad (10.37)$$

FIGURE 10.6: Mixed sensitivity \mathcal{H}_∞ design.

using pre- and post-compensators $W_1(s)$ and $W_2(s)$ respectively. The weight transfer function $W_1(s)$ is usually a low-pass filter with the purpose of improving the output disturbance rejection or reference tracking, whereas $W_2(s)$ is a high-pass filter used for minimizing the control effort at high frequencies [257, 261]. The mixed-sensitivity design is then solved by computing the augmented plant $P(s)$ from the open-loop transfer function $G(s)$ and aforementioned weighting functions.

10.3.3 Control Analysis and Synthesis

For control analysis, the robustness of the system is calculated through the concepts of robust and quadratic stability [262]. The former guarantees stability for the whole uncertainty range and can be determined either through a structural singular value function (μ) for LFT systems [257], or via a parameter-dependent Lyapunov function in the case of an LPV system [263]. Quadratic stability, on the other hand, is a fundamentally stronger concept of stability since it guarantees robust stability, as well as the resilience to arbitrary fast parameter changes [258]. However, it is also more conservative due to a single Lyapunov function being used for the whole uncertainty range.

Two control synthesis methods are employed, in particular \mathcal{H}_∞ control for norm-bounded parametric systems in case of LFT modeling and Gain-Scheduled (GS) \mathcal{H}_∞ control for LPV system design. Both methods are defined using LMIs and are based on the concept of quadratic stability [258, 264]. Additional constraints are specified to place the poles of the closed-loop system in a specific region of the left-half plane in order to ensure the

prescribed damping ratio requirements [265]. Both control synthesis problems are solved in MATLAB using the Yalmip interface [266] and SeDuMi/SDPT3 solvers [267, 268].

10.3.3.1 \mathcal{H}_∞ Control for Norm-Bounded Parametric Systems

We aim to solve the \mathcal{H}_∞ performance problem $\|H_{zw}\|_\infty < 1, \forall \|\Delta\|_2 \leq 1$, which is equivalent to the robust stability of the closed-loop system with a virtual norm-bounded uncertainty $\Delta_P(s)$ ($\|\Delta_P\|_\infty \leq 1$) inserted between the disturbance d and the error e , thus resulting in the overall uncertainty of $\text{diag}(\Delta, \Delta_P)$ [258]. A scaling matrix $L = \text{diag}(I, \sqrt{\ell}I)$ can be subsequently introduced to reduce the conservatism of the small-gain method by achieving $\|L^{1/2}H_{zw}L^{-1/2}\|_\infty < \gamma$, where L is positive definite and permutable with $\text{diag}(\Delta, \Delta_P)$.

Theorem 10.3.2. *Consider $P(s)$ given by (10.35) such that (A, B_2) is stabilizable and (C_2, A) is detectable. There are a controller $K(s)$ and a scaling matrix $L > 0$ such that the closed-loop system is stable and $\|L^{1/2}H_{zw}L^{-1/2}\|_\infty < \gamma$ iff there exist matrices $X > 0, Y > 0$ and L, J satisfying the following conditions:*

$$\begin{aligned} \begin{bmatrix} N_X^\top & 0 \\ 0 & I_{n_w} \end{bmatrix} \begin{bmatrix} AX + XA^\top & XC_1^\top & B_1 \\ C_1X & -\gamma J & D_{11} \\ B_1^\top & D_{11}^\top & -\gamma L \end{bmatrix} \begin{bmatrix} N_X & 0 \\ 0 & I_{n_w} \end{bmatrix} < 0, \\ \begin{bmatrix} N_Y^\top & 0 \\ 0 & I_{n_z} \end{bmatrix} \begin{bmatrix} YA + A^\top Y & YB_1 & C_1^\top \\ B_1^\top Y & -\gamma L & D_{11}^\top \\ C_1 & D_{11} & -\gamma J \end{bmatrix} \begin{bmatrix} N_Y & 0 \\ 0 & I_{n_z} \end{bmatrix} < 0, \quad (10.38) \\ \begin{bmatrix} X & I \\ I & Y \end{bmatrix} \geq 0, \\ LJ = I, \end{aligned}$$

where $N_X = \ker([B_2^\top D_{12}^\top])$, $N_Y = \ker([C_2 D_{21}])$, and $n_w \in \mathbb{Z}_{>0}$, $n_z \in \mathbb{Z}_{>0}$ are the number of exogenous inputs and outputs.

Proof. The proof can be found in [258, Section 16.7]. □□□

The last equality $LJ = I$ is non-convex and therefore the solvability condition cannot be solved by employing an LMI approach directly. Nevertheless, the problem can be solved using the *K-L iteration method* described in [258].

10.3.3.2 Gain-Scheduled \mathcal{H}_∞ Control for LPV Systems

Let us consider a parameter-dependent system (10.36), illustrated in Fig. 10.5b and expressed as

$$\dot{x} = A(q)x + B_1(q)w + B_2u, \quad (10.39a)$$

$$z = C_1(q)x + D_{11}(q)w + D_{12}u, \quad (10.39b)$$

$$y = C_2x + D_{21}w. \quad (10.39c)$$

This \mathcal{H}_∞ control synthesis problem seeks a parameter-dependent controller of the form

$$\dot{x}_k = A_k(q)x_k + B_k(q)u_k, \quad (10.40a)$$

$$y_k = C_k(q)x_k + D_k(q)u_k. \quad (10.40b)$$

Note that for the parameter vector $q(t)$ taking values in a box $\mathcal{B} \in \mathbb{R}^n$ with $N_{\mathcal{B}} = 2^n$ corners, the system $P(q)$ in Fig. 10.5b is confined within a matrix polytope defined by the respective vertices $P(\theta_i)$. Given the convex decomposition

$$q = \sum_{i=1}^{N_{\mathcal{B}}} \alpha_i \theta_i, \quad (10.41)$$

the controller state space can be derived as

$$\begin{bmatrix} A_k(q) & B_k(q) \\ C_k(q) & D_k(q) \end{bmatrix} = \sum_{i=1}^{N_{\mathcal{B}}} \alpha_i \begin{bmatrix} A_k(\theta_i) & B_k(\theta_i) \\ C_k(\theta_i) & D_k(\theta_i) \end{bmatrix} = \sum_{i=1}^{N_{\mathcal{B}}} \alpha_i K_i. \quad (10.42)$$

In other words, the controller state space at the operating point q is obtained through convex interpolation of the LTI vertex controllers K_i . According to Theorem 10.3.2, the gain-scheduling problem can thus be reduced to solving the following LMI problem for positive definite matrices X and Y [258]:

$$\begin{aligned} \begin{bmatrix} N_X^\top & 0 \\ 0 & I_{n_w} \end{bmatrix} & \begin{bmatrix} A(\theta_i)X + XA(\theta_i)^\top & XC_1(\theta_i)^\top & B_1(\theta_i) \\ C_1(\theta_i)X & -\gamma I & D_{11}(\theta_i) \\ B_1(\theta_i)^\top & D_{11}(\theta_i)^\top & -\gamma I \end{bmatrix} \begin{bmatrix} N_X & 0 \\ 0 & I_{n_w} \end{bmatrix} < 0, \\ \begin{bmatrix} N_Y^\top & 0 \\ 0 & I_{n_z} \end{bmatrix} & \begin{bmatrix} YA(\theta_i) + A(\theta_i)^\top Y & YB_1(\theta_i) & C_1(\theta_i)^\top \\ B_1(\theta_i)^\top Y & -\gamma I & D_{11}(\theta_i)^\top \\ C_1(\theta_i) & D_{11}(\theta_i) & -\gamma I \end{bmatrix} \begin{bmatrix} N_Y & 0 \\ 0 & I_{n_z} \end{bmatrix} < 0, \\ & \begin{bmatrix} X & I \\ I & Y \end{bmatrix} > 0, \end{aligned} \quad (10.43)$$

with the third inequality strengthened to a strict one. The designed controller K has a full order, i.e., its order is the same as that of the generalized plant, and can be derived from X , Y and γ . Note the importance of B_2 , C_2 , D_{12} , D_{21} being independent of q . If this condition is not satisfied the constraints become infinite and the problem is not easily tractable [264]. Nonetheless, such condition can be enforced by applying a pre/post filtering with high enough bandwidth to the input and output of the system.

10.4 DELAY-ROBUST DEVICE-LEVEL CONTROL DESIGN

10.4.1 Robust Control Approach

The vulnerability of the system to measurement delays was previously evaluated through small-signal analysis in Section 10.2, where we have identified the inner control loop as the most vulnerable segment of the VSC control scheme. In particular, the SRF current controller showed the lowest stability margin, with the maximum permissible measurement delay of $\hat{\tau} = 233 \mu\text{s}$ and the measurement input $(i_f, v_f) \in \mathbb{R}^4$ having the highest state participation in the unstable modes. Hence, the objective of this section is to provide a novel device-level control design that would provide resilience against the local measurement delays and the underlying uncertainty, by applying robust control principles and control synthesis methods presented in Section 10.3.

Let us recall the traditional inner control structure (2.8)-(2.9) from Chapter 2, comprising a cascade of PI controllers and feed-forward loops:

$$i_f^* = K_P^v(v_f^* - v_{f\tau}) + K_I^v\xi + K_F^v i_{g\tau} + j\omega_c c_f v_{f\tau}, \tag{10.44a}$$

$$v_{\text{sw}}^* = K_P^i(i_f^* - i_{f\tau}) + K_I^i\gamma + K_F^i v_{f\tau} + j\omega_c \ell_f i_{f\tau}, \tag{10.44b}$$

with $\dot{\xi} = v_f^* - v_{f\tau}$ and $\dot{\gamma} = i_f^* - i_{f\tau}$ being the internal integrator states, subscripts P , I and F denoting the respective proportional, integral and feed-forward gains, and superscripts v and i referring to the voltage and current control. The complete notation and mathematical details can be found in Section 2.2.3. Being measured control inputs, the voltage v_f and currents i_f and i_g are exposed to time delay and therefore incorporated in the form of delayed counterparts $v_{f\tau}$, $i_{f\tau}$ and $i_{g\tau}$ in (10.44). Moreover, we introduce the following notation to describe the deviation of a delayed measurement from its nominal/reference value:

$$\Delta v_{f\tau} = v_f^* - v_{f\tau}, \quad \Delta i_{f\tau} = i_f^* - i_{f\tau}, \quad \Delta i_{g\tau} = i_g^* - i_{g\tau}. \tag{10.45}$$

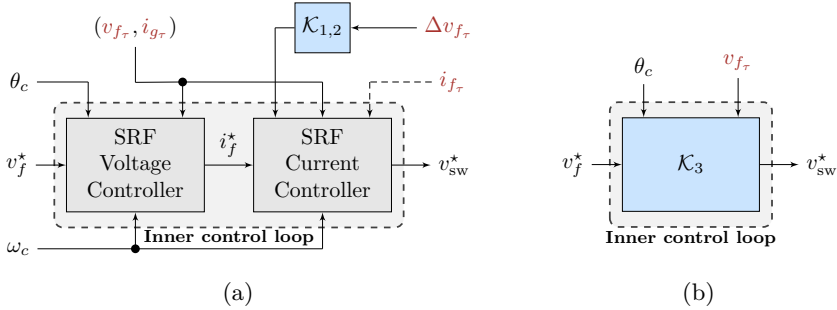


FIGURE 10.7: Proposed control design strategies: (a) robust active damping control ($\mathcal{K}_1, \mathcal{K}_2$); (b) uniform robust inner control (\mathcal{K}_3). Delayed signals are denoted by red color.

In order to improve converter performance under constant (i.e., time-invariant) but uncertain measurement delays, we propose the following three control strategies for redesigning the traditional device-level control:

$$v_{\text{sw}}^{\star(1)} = K_P^i \Delta i_{f_\tau} + K_I^i \gamma + K_F^i v_{f_\tau} + j\omega_c \ell_f i_{f_\tau} - \mathcal{K}_1(\Delta v_{f_\tau}), \quad (10.46a)$$

$$v_{\text{sw}}^{\star(2)} = K_P^i \Delta i_{g_\tau} + K_I^i \gamma + K_F^i v_{f_\tau} + j\omega_c \ell_f i_{g_\tau} - \mathcal{K}_2(\Delta v_{f_\tau}), \quad (10.46b)$$

$$v_{\text{sw}}^{\star(3)} = \mathcal{K}_3(v_f^* - v_{f_\tau}). \quad (10.46c)$$

The first two approaches depicted in Fig. 10.7a are based on including an additional damping term $\mathcal{K}_{1,2}(\Delta v_{f_\tau})$ to the current control, which depends on the deviation of the voltage across the filter capacitor. The second design also employs different current input measurement, replacing the filter current i_{f_τ} with the grid current input i_{g_τ} in order to reduce the control sensitivity to time delay. This is motivated by the high state participation of filter current in the unstable modes (see Table 10.1). Guided by the same notion, the third configuration completely redefines this cascaded control block and designs a uniform robust controller \mathcal{K}_3 that explicitly computes the modulation (i.e., switching) voltage of the converter. Such concept also eliminates the need for any current measurement input, as indicated in Fig. 10.7b, thus providing a lower controller order.

According to the control synthesis methods described in Section 10.3.3, two \mathcal{H}_∞ output feedback controllers are implemented for each design, namely

an LFT norm-bounded controller and a GS controller. The weighting transfer functions used in the mixed-sensitivity design of \mathcal{K}_1 and \mathcal{K}_2 are

$$W_1(s) = \frac{0.5s + 500}{s + 5}, \quad W_2(s) = 1. \quad (10.47)$$

Since the controller \mathcal{K}_3 tracks the voltage output of the converter, the weights are chosen such that a good integral control performance in time domain is achieved. The bandwidth of the controller is therefore set to 1000 rad/s, resulting in the weighting functions

$$W_1(s) = \frac{0.5s + 1000}{s + 0.1}, \quad W_2(s) = 1. \quad (10.48)$$

10.4.2 Controller Performance

An overview of the stability performance obtained from the proposed control designs is presented in Table 10.2. It is noticeable that the range of time delays for which the robust (denoted by RS) and quadratic (denoted by QS) stability are guaranteed as well as the order of the controllers vary significantly between different control approaches. As previously described in Section 10.3, the emphasis is put on quadratic stability since it allows for arbitrarily fast variation of measurement delays. Understandably, \mathcal{K}_3 has the lowest order due to removal of the current measurements from the control input and it provides a drastically broader stability range, both under LFT and GS implementation. This can be contributed to its conceptually superior design, which eliminates a majority of the state feedback sensitive to time delays. Moreover, the GS approach appears to be the more robust of the two, with the respective critical delay reaching millisecond range.

As a case study, we investigate the converter response to a 10% step increase in active power setpoint and evaluate its reference tracking capability under

Control	Order	QS Range	RS Range
$\mathcal{K}_{1,\text{LFT}}$	21	[0 – 370] μs	[0 – 420] μs
$\mathcal{K}_{1,\text{GS}}$	21	[0 – 750] μs	[0 – 750] μs
$\mathcal{K}_{2,\text{LFT}}$	19	[0 – 400] μs	[0 – 660] μs
$\mathcal{K}_{2,\text{GS}}$	19	[0 – 2] ms	[0 – 2] ms
$\mathcal{K}_{3,\text{LFT}}$	15	[0 – 900] μs	[0 – 1] ms
$\mathcal{K}_{3,\text{GS}}$	15	[0 – 20] ms	[0 – 50] ms

TABLE 10.2: Stability performance of different control designs.

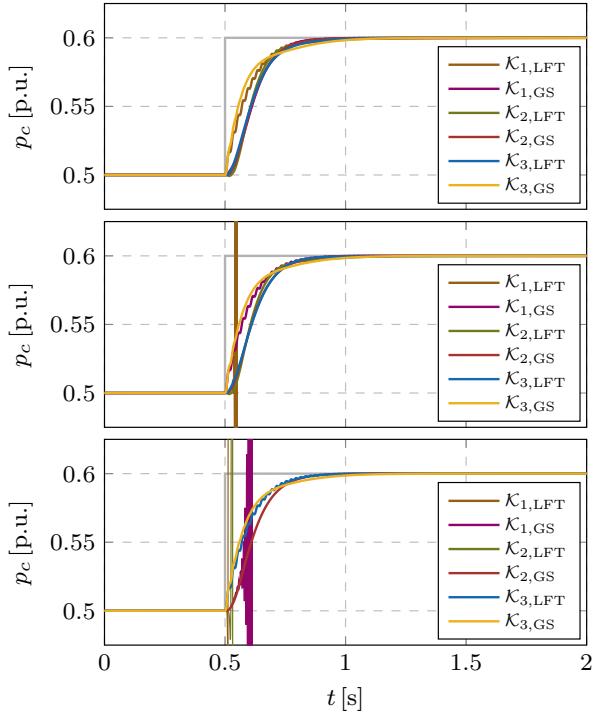


FIGURE 10.8: Response to a step change in active power setpoint under constant time delay for different inner control designs: (i) $\tau = 150 \mu\text{s}$; (ii) $\tau = 500 \mu\text{s}$; and (iii) $\tau = 1 \text{ ms}$;

different measurement delay properties. For this purpose, EMT simulations have been performed in MATLAB Simulink using the detailed model previously described in Chapter 2. A focus is first set on constant delays in the range of $[150 - 1000] \mu\text{s}$, with the results presented in Fig. 10.8. Under a reasonably small delay of $150 \mu\text{s}$ all controllers achieve good performance, with controller $\mathcal{K}_{3,\text{GS}}$ having the best overall response due to a combination of its reduced system order and gain scheduling design. Nonetheless, such level of delay could be withstood by a conventional inner control, as shown in Section 10.2.5. Alternatively, for $\tau \in [500, 1000] \mu\text{s}$ we observe that certain control designs are unstable due to insufficient robust stability range (see Table 10.2). More precisely, $\mathcal{K}_{1,\text{LFT}}$ has a critical delay threshold below $500 \mu\text{s}$, whereas $\mathcal{K}_{1,\text{GS}}$ and $\mathcal{K}_{2,\text{LFT}}$ cannot withstand a 1 ms measurement delay.

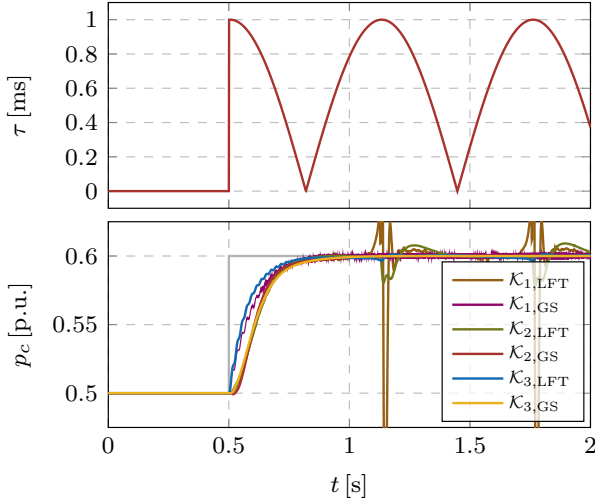


FIGURE 10.9: Response to a step change in active power setpoint under varying time delay for different inner control designs: varying time delay signal (top) and converter power output (bottom).

The aspect of quadratic stability becomes more relevant when accounting for time delay variability, as it ensures resilience to fast changes in the delay signal. Therefore, we consider an arbitrary sinusoidal delay signal $\tau = \tilde{\tau} |\sin(\omega_\tau t)|$ of amplitude $\tilde{\tau} = 1$ ms and period $T_\tau = 1.25$ s, activated at the instance of disturbance. The converter power response illustrated in Fig. 10.9 indicates that only the controllers with an acceptable quadratic stability range can tolerate such oscillatory delay nature. As a result, the LFT designs of \mathcal{K}_1 and \mathcal{K}_2 underperform whenever τ goes drastically above 370 μ s and 400 μ s, respectively. A similar characteristic is noticeable for $\mathcal{K}_{3,LFT}$, with $\hat{\tau} = 900$ μ s being slightly below the delay peak. GS configuration however reacts differently when the delays exceed the permissible range, manifested through stable but highly oscillatory behavior of $\mathcal{K}_{1,GS}$. Finally, $\mathcal{K}_{2,GS}$ and $\mathcal{K}_{3,GS}$ face no instability issues due to very broad quadratic stability ranges. Interestingly enough, even with the delay occasionally exceeding the respective permissible stability range of some inner control designs, all six controllers remain stable during the actual step response.

It can be concluded that the \mathcal{K}_3 concept clearly shows the best performance, independent of the control synthesis method. It completely replaces the inner control loop, reduces the overall control order and ensures excellent

robustness to any type of measurement delay. On the other hand, the \mathcal{K}_1 and \mathcal{K}_2 configurations have an inherent disadvantage of adding an extra controller to the existing system and increasing complexity. Furthermore, \mathcal{K}_1 achieves only a minor improvement to the original design, whereas \mathcal{K}_2 , although significantly better, is still suboptimal compared to the uniform structure of \mathcal{K}_3 .

10.5 DELAY-ROBUST WIDE-AREA CONTROL DESIGN

This section continues the line of research discussed in Section 10.1.2. More precisely, we present a design procedure for a delay-robust, wide-area output feedback controller that regulates both conventional and converter-based generators to enhance oscillation damping in a low-inertia system under time-varying delays. In contrast to Sections 10.2-10.4 that deal with constant measurement delays, this segment of the chapter focuses on power systems with time-varying communication delays between the individual controllers and the WAC.

10.5.1 Model-Order Reduction

Let us recall the detailed ODE representation of a low-inertia system from Chapter 2 (see Section 2.9), in the state-space form described by

$$\dot{\bar{x}} = \bar{A}\bar{x} + \bar{B}u, \quad (10.49)$$

where $\bar{x} \in \mathbb{R}^k$ is the state variable vector, $u \in \mathbb{R}^m$ is the input vector, and $\bar{A} \in \mathbb{R}^{k \times k}$ and $\bar{B} \in \mathbb{R}^{k \times m}$ are constant matrices.

Conventional power systems are characterized by relatively slow voltage and frequency controllers due to large turbine and governor time constants of SGs (in the range of seconds). However, with the inclusion of fast-acting, converter-based generation, the system dynamics become more complex. More precisely, the time constants of the PI controllers and low-pass filters associated with the device-level control are one or two orders of magnitude smaller than the ones of SGs (see Section 4.2 for more details). Moreover, the transmission line dynamics, traditionally neglected in SG-based power system analysis due to timescale separation, become significant in low-inertia grids [12]. As a result, such dynamical systems experience a wide range of time constants, which increases model complexity and might lead to an ill-conditioned matrix \bar{A} .

The issues pertaining to tractability are resolved by employing a model-order reduction based on a first-order singular perturbation [16, 105], previously described in Chapter 3. Such technique is especially useful in systems with several distinctive timescales and has a potential of reducing model order while capturing the impact of fast states on slow system dynamics. Let us consider a system with distinctive timescale separation between the fast and slow dynamics, which allows us to rewrite (10.49) as

$$\dot{x}_s = A_{ss}x_s + A_{sf}x_f + B_s u, \quad (10.50a)$$

$$Y\dot{x}_f = A_{fs}x_s + A_{ff}x_f + B_f u, \quad (10.50b)$$

with subscripts s and f corresponding to slow and fast states, respectively, and Y being a set of parameters designating the fast dynamics. By applying a set of mathematical operations presented in Section 3.2, one can obtain a reduced-order ODE system

$$\dot{x}_s = Ax_s + B_u u, \quad (10.51)$$

where A and B_u are the reduced state-space matrices given by (3.22b)-(3.22c), and $x_s \in \mathbb{R}^n$ denotes the preserved slow states of interest.

Such method is employed for eliminating the electrical states of the converter, corresponding to filter current and voltage dynamics, as well as the flux linkage dynamics of the synchronous generator. By removing these fast states we obtain a 10th-order VSC model and a 10th-order SG model, which compared to the original system (10.49) exhibit lower complexity and, in the authors experience, result in significantly better conditioned system matrices.

10.5.2 Controller Structure

For the purpose of our control design, we now investigate the following linear MIMO system:

$$\dot{x}_s = Ax_s + B_u u + B_w w, \quad (10.52a)$$

$$y = C_y x_s, \quad (10.52b)$$

$$z = C_z x_s + D_u u + D_w w, \quad (10.52c)$$

where $x_s \in \mathbb{R}^n$ is the reduced state variable, $u \in \mathbb{R}^m$ is the input vector, $w(t) \in \mathcal{L}_2[0, \infty)$ ¹ is the external disturbance vector, $y \in \mathbb{R}^q$ is the output

¹ A signal $u : \mathbb{R}_{\geq 0} \rightarrow \mathbb{R}^m$ is in \mathcal{L}_2 if its \mathcal{L}_2 -norm $\|u\|_{\mathcal{L}_2}$, given by $\|u\|_{\mathcal{L}_2} = \sqrt{\int_0^\infty u^\top(t)u(t) dt}$, is finite [231].

vector, $z \in \mathbb{R}^p$ is the performance output vector, $A \in \mathbb{R}^{n \times n}$, $B_u \in \mathbb{R}^{n \times m}$, $B_w \in \mathbb{R}^{n \times w}$, $C_y \in \mathbb{R}^{q \times n}$, $C_z \in \mathbb{R}^{p \times n}$, $D_u \in \mathbb{R}^{p \times m}$, and $D_w \in \mathbb{R}^{p \times w}$ are constant matrices; x_s , A and B_u correspond to the variables defined in (10.51). Moreover, we assume that the pair (A, B_u) is stabilizable.

We consider the following static output feedback controller for the system (10.52):

$$u = -Ky = -KC_y x_s, \quad (10.53)$$

where $K \in \mathbb{R}^{m \times q}$ is the controller gain to be designed. The controller (10.53) is simpler and easier for practical implementation than a full state feedback controller since it only requires the system output to be measurable.

With regard to the communication delays, it is assumed that the information flow from the i^{th} node to the WAMC center and vice versa is affected by a fast, time-varying, bounded, communication interval delay $\tau : \mathbb{R}_{\geq 0} \rightarrow [h_1, h_2]$, $h_1 \in \mathbb{R}_{\geq 0}$, $h_2 \in \mathbb{R}_{> 0}$, $h_2 > h_1$, where h_1 and h_2 are the lower and upper communication delay limits respectively. For clarity of exposition, only uniform delays are assumed to be present in the system. However, the proposed approach presented can be extended to heterogeneous delays at the expense of a more involved notation, see e.g., [269–271]. Hence, the closed-loop system is obtained by combining (10.52) with the delayed variant of (10.53), i.e.,

$$\dot{x}_s = Ax_s - B_u KC_y x_s(t - \tau(t)) + B_w w, \quad (10.54a)$$

$$z = C_z x_s - D_u KC_y x_s(t - \tau(t)) + D_w w. \quad (10.54b)$$

The objective of damping the inter-area modes is considered in our approach by minimizing the \mathcal{L}_2 -gain $\gamma \in \mathbb{R}_{> 0}$ of (10.54), which is defined as the maximum energy amplification ratio between the disturbance input signal w and the performance output signal z [229, 231]. This can be illustrated by designing the controller such that the following holds [229]:

$$J_w = \int_0^\infty \left[z^\top(t)z(t) - \gamma^2 w^\top(t)w(t) \right] dt < 0, \quad (10.55)$$

where γ is the \mathcal{L}_2 -gain of the system (10.54). For instance, defining the output performance matrix C_z in (10.54) such that z represents the frequencies of the generation units, and then minimizing the \mathcal{L}_2 -gain γ , should reduce the frequency oscillations in the system following a disturbance w . The control design objectives are summarized in the following problem statement.

Problem 10.5.1. *Consider the system (10.52). Given $h_1 \in \mathbb{R}_{\geq 0}$, $h_2 \in \mathbb{R}_{\geq 0}$ with $h_1 \leq \tau(t) \leq h_2$, design a static output feedback controller (10.53), such that the origin is a uniformly asymptotically stable equilibrium point of the resulting closed-loop system (10.54) and its \mathcal{L}_2 gain is minimized.*

10.5.3 Main Result

The main contribution of Section 10.5 is presented here by providing the following solution to Problem 10.5.1.

Proposition 10.5.2. *Consider the system given by (10.54). Fix $h_1 \geq 0$, and $h_2 > h_1$. Suppose that there exists a parameter $\bar{\gamma} > 0$ and matrices $\bar{P} \in \mathbb{R}_{>0}^{3n \times 3n}$, $\bar{R}_1 \in \mathbb{R}_{>0}^{n \times n}$, $\bar{R}_2 \in \mathbb{R}_{>0}^{n \times n}$, $\bar{S}_1 \in \mathbb{R}_{>0}^{n \times n}$, $\bar{S}_2 \in \mathbb{R}_{>0}^{n \times n}$, $M \in \mathbb{R}^{q \times q}$, $N \in \mathbb{R}^{m \times q}$, $W \in \mathbb{R}^{n \times n}$, and $\bar{X} \in \mathbb{R}^{2n \times 2n}$, such that the following problem is feasible:*

$$\min \quad \bar{\gamma} \tag{10.56a}$$

$$\text{s.t.} \quad \begin{bmatrix} \bar{\psi}_1(h_1) & \bar{\psi}_2 \\ * & -I \end{bmatrix} < 0, \quad \begin{bmatrix} \bar{\psi}_1(h_2) & \bar{\psi}_2 \\ * & -I \end{bmatrix} < 0, \tag{10.56b}$$

$$\bar{\psi}_3 = \begin{bmatrix} \bar{R}_2 & \bar{X} \\ * & \bar{R}_2 \end{bmatrix} \geq 0, \quad MC_y = C_y W, \tag{10.56c}$$

where

$$h_{12} = h_2 - h_1, \tag{10.57a}$$

$$\bar{R}_2 = \text{diag}(\bar{R}_2, 3\bar{R}_2), \tag{10.57b}$$

$$\Gamma = [G_2^T, G_3^T]^T, \tag{10.57c}$$

$$\bar{\psi}_1(\tau) = \bar{\psi}_{11} + G_0^T \bar{P} G_1(\tau) + G_1^T(\tau) \bar{P} G_0 - \Gamma^T \bar{\psi}_3 \Gamma, \tag{10.57d}$$

$$\bar{\psi}_2 = [C_z W, 0, 0, -D_u N C_y, 0, 0, 0, 0, D_w]^T, \tag{10.57e}$$

$$G_0 = \begin{bmatrix} 0 & I & 0 & 0 & 0 & 0 & 0 & 0 & 0 \\ I & 0 & -I & 0 & 0 & 0 & 0 & 0 & 0 \\ 0 & 0 & I & 0 & -I & 0 & 0 & 0 & 0 \end{bmatrix}, \tag{10.57f}$$

$$G_1(\tau) = \begin{bmatrix} I & 0 & 0 & 0 & 0 & 0 & 0 & 0 & 0 \\ 0 & 0 & 0 & 0 & 0 & h_1 I & 0 & 0 & 0 \\ 0 & 0 & 0 & 0 & 0 & 0 & (\tau - h_1) I & (h_2 - \tau) I & 0 \end{bmatrix}, \tag{10.57g}$$

$$G_2 = \begin{bmatrix} 0 & 0 & I & -I & 0 & 0 & 0 & 0 & 0 \\ 0 & 0 & I & I & 0 & 0 & -2I & 0 & 0 \end{bmatrix}, \tag{10.57h}$$

$$G_3 = \begin{bmatrix} 0 & 0 & 0 & I & -I & 0 & 0 & 0 & 0 \\ 0 & 0 & 0 & I & I & 0 & 0 & -2I & 0 \end{bmatrix}, \tag{10.57i}$$

and $\bar{\psi}_{11}$ is given by

$$\bar{\psi}_{11} = \begin{bmatrix} AW+WA^T+\bar{S}_1-4\bar{R}_1 & -W+\epsilon WA^T & -2\bar{R}_1 & -B_u NC_y & 0 & 6\bar{R}_1 & 0 & 0 & B_w \\ * & -2\epsilon W+h_1^2\bar{R}_1+h_2^2\bar{R}_2 & 0 & -\epsilon B_u NC_y & 0 & 0 & 0 & 0 & \epsilon B_w \\ * & * & -\bar{S}_1+\bar{S}_2-4\bar{R}_1 & 0 & 0 & 6\bar{R}_1 & 0 & 0 & 0 \\ * & * & * & 0 & 0 & 0 & 0 & 0 & 0 \\ * & * & * & * & -\bar{S}_2 & 0 & 0 & 0 & 0 \\ * & * & * & * & * & -12\bar{R}_1 & 0 & 0 & 0 \\ * & * & * & * & * & * & 0 & 0 & 0 \\ * & * & * & * & * & * & * & 0 & 0 \\ * & * & * & * & * & * & * & * & -\bar{\gamma}I \end{bmatrix}. \tag{10.57j}$$

Choose the controller gain as

$$K = NM^{-1}. \tag{10.58}$$

Then, $\forall \tau(t) \in [h_1, h_2]$, the origin is a uniformly asymptotically stable equilibrium point of the system (10.54) and the system has an \mathcal{L}_2 -gain less than or equal to $\gamma = \sqrt{\bar{\gamma}}$.

Proof. The proof is given in Appendix A.4. □□□

10.5.4 Case Study

The performance of the proposed WAC is assessed using the Kundur two-area system [26], which is prone to local and inter-area oscillations. The system consists of two weakly connected areas, with each comprising two generators and the parameters given in [26, Example 12.6]. Furthermore, three system configurations are considered in this work: (i) an all SG-based system serving as a benchmark for the effectiveness of the proposed WAC; (ii)

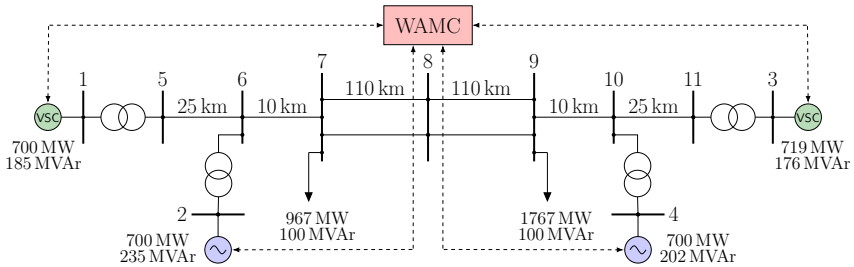


FIGURE 10.10: Topology of the investigated Kundur two-area system with WAC; Area 1 is on the left and Area 2 is on the right-hand side.

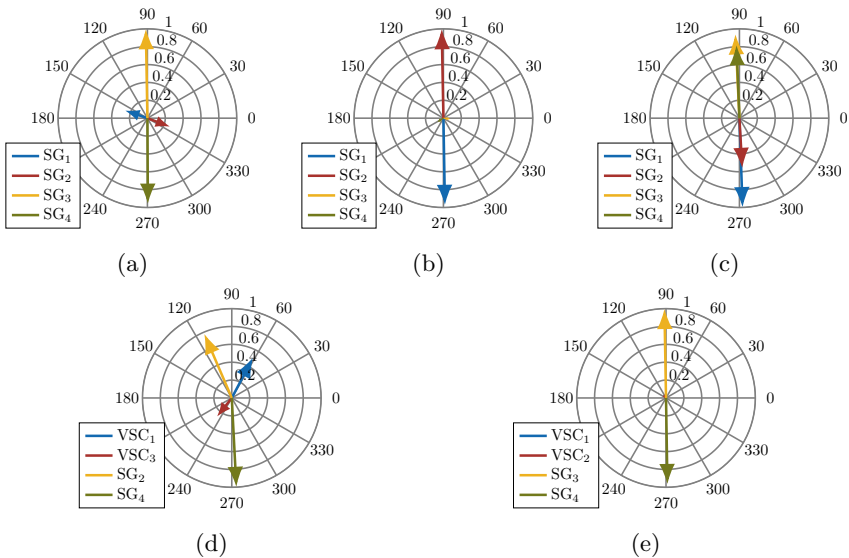


FIGURE 10.11: Mode shape of underdamped modes. Configuration I: (a) mode 1, (b) mode 2, (c) mode 3; (d) Configuration II; (e) Configuration III. Note that VSC_i and SG_i denote the respective generator types connected at node i .

a scenario where each area contains a mix of synchronous and converter-based generation, as illustrated in Fig. 10.10; and (iii) a scenario with Area 1 being all SG-based and Area 2 all converter-based.

Preliminary investigations using modal analysis show the presence of underdamped, low-frequency modes in all three configurations. Table 10.3 lists the main eigenvalues as well as the damping ratios and natural frequencies of these modes. Moreover, Fig. 10.11 illustrates the mode shape [26] of

Config.	Eigenvalues	Damping ratio	Frequency [Hz]	Mode type
I	$-0.0846 \pm 4.82i$	0.0176	0.76712	Local
	$-0.0913 \pm 4.82i$	0.019	0.76714	Local
	$-0.142 \pm 4.04i$	0.035	0.6434	Inter-area
II	$-0.228 \pm 4.46i$	0.0511	0.7098	Inter-area
III	$-0.0846 \pm 4.82i$	0.0176	0.76714	Local

TABLE 10.3: Underdamped modes of the Kundur two-area system.

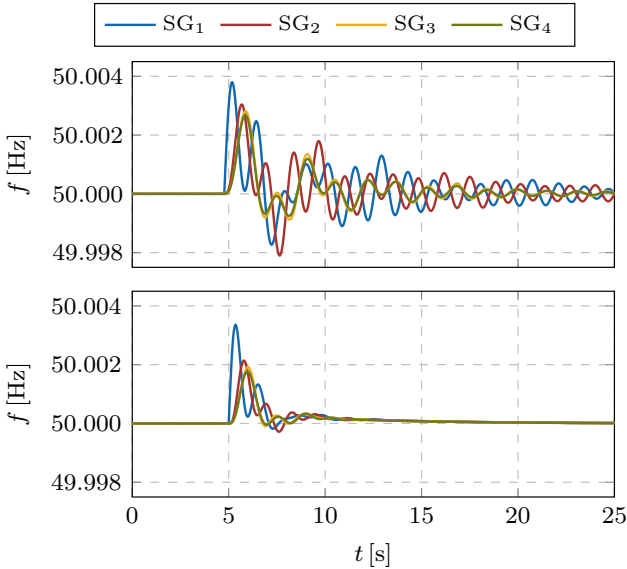


FIGURE 10.12: Configuration I - frequency response of a traditional power system after a step change in load for two different scenarios: uncontrolled system (top) and controlled system with communication delays (bottom).

these modes. It also suggests that the first configuration exhibits two local low-frequency modes and one inter-area mode, while the second and third configuration are prone to one inter-area and one local mode, respectively. All of the underdamped modes and the effectiveness of the proposed WAC are studied in the subsequent time-domain analysis.

Next, to design the WAC for all considered configurations, we solve the optimization problem (10.56). We assume that the exchanged information via a communication network is affected by fast-varying, uniform interval delays $\tau(t) \in [80, 140]$ ms, with $h_1 = 80$ ms and $h_2 = 140$ ms. Furthermore, we set $D_u = D_w = 0$ and choose C_z such that the performance output z describes the individual generator frequencies in (10.54). The implementation is done in MATLAB (R2018b), using Yalmip (version 09-02-2018) [174] and the solver MOSEK (version 8.1.0.51) [272].

We first investigate Configuration I, i.e., a power system comprised solely of SGs. This allows us to evaluate the performance of the proposed control synthesis in a conventional power system. The comparison between an

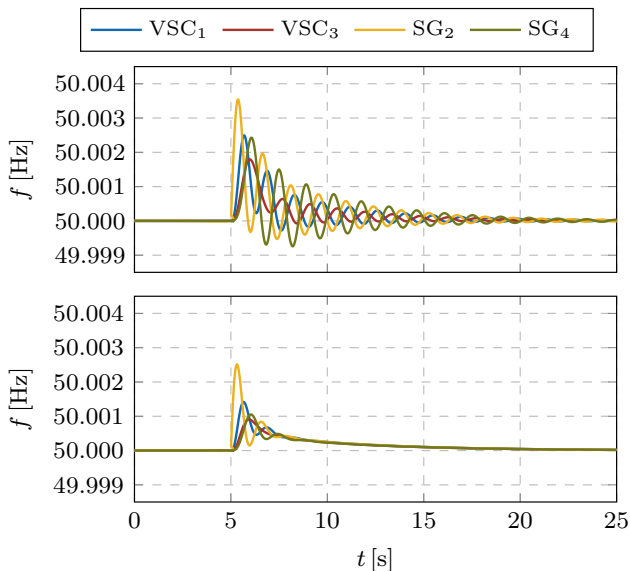


FIGURE 10.13: Configuration II - frequency response of a low-inertia system after a step change in load for two different scenarios: uncontrolled system (top) and controlled system with communication delays (bottom).

uncontrolled (open-loop) system, with only PSS participating in oscillation damping, and the system with WAC and communication delays is conducted. The simulation results given in Fig. 10.12 clearly indicate that the groups of generators in two areas oscillate against each other. On the other hand, designing the WAC using Proposition 10.5.2 reduces the system's \mathcal{L}_2 -gain from $\gamma = 2.2078$ (without the WAC) to $\gamma = 1.3425$ (with the WAC), while ensuring robustness against communication delays. As can be seen from Fig. 10.12, this also results in a significant reduction of oscillations.

Similarly, Fig. 10.13 showcases the results of the same test case for a low-inertia grid in Configuration II. We first investigate the open-loop behavior of the system, followed by the response with the WAC and including time-varying communication delays. The results confirm that the uncontrolled system exhibits oscillations between the two-areas, even if two of the generators are converter-based. The WAC implementation of the static feedback control gain K improves the system behavior by reducing the \mathcal{L}_2 -gain from $\gamma = 3.019$

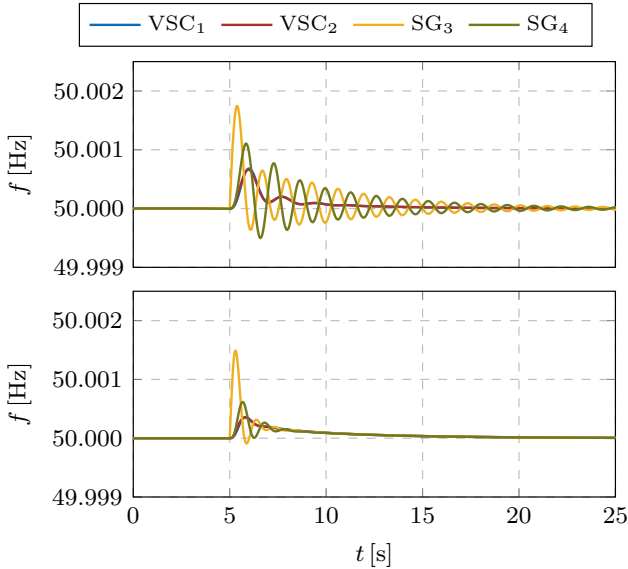


FIGURE 10.14: Configuration III - frequency response of a low-inertia system after a step change in load for two different scenarios: uncontrolled system (top) and controlled system with communication delays (bottom).

(without the WAC) to $\gamma = 1.7963$ (with the WAC), which effectively damps the oscillations and, in addition, guarantees delay-robustness.

Finally, in Configuration III we split the generation types between the two areas. As a result, there are no inter-area modes between the all inverter-based and the all SG-based areas. In fact, the grid-forming inverters are synchronized and their frequency response is very well damped. Nonetheless, the local oscillations between the SGs in Area 2 are still present, as illustrated in Fig. 10.14. Applying the WAC design can also improve these oscillation by means of reducing the system's \mathcal{L}_2 -gain. The designed WAC reduces the \mathcal{L}_2 -gain from $\gamma = 2.0628$ (without the WAC) to $\gamma = 1.0965$ (with the WAC). The frequency response in Fig. 10.14 confirms that the controller significantly improves the damping of local oscillations.

10.6 CONCLUSION

This chapter investigates the impact of time delays in inverter-dominated power networks and proposes delay-robust control designs to mitigate the stability issues pertaining to such systems. First, the topic of constant measurement delays is addressed. The critical measurement delays are determined analytically through means of Padé approximation and Chebyshev discretization applied to DDAE formulation of the VSC control scheme. Subsequently, two ways of modeling the time delay uncertainty are presented and employed for developing two output-feedback synthesis methods based on \mathcal{H}_∞ control theory. In order to improve the resilience of VSCs to uncertain delays in local measurement, three novel control strategies are proposed and combined with each of the two synthesis methods. A redesign of the conventional inner control loop is suggested, which improves converter performance when dealing with measurement uncertainty. It was found that the signal delays can have a detrimental effect on stability of inverter-dominated systems under existing control design, and that the proposed controllers could resolve the underlying issues. In particular, the uniform controller (\mathcal{K}_3) performs the best and guarantees quadratic stability for a wide range of time delays. Furthermore, the gain-scheduling synthesis appeared to be the more practical approach of the two.

The second part of the chapter deals with the impact of communication delays in wide-area measurements involved in centralized power system control schemes. In particular, the problem of wide-area oscillation damping control in low-inertia systems in the presence of time-varying communication delays is investigated. We address these challenges by proposing a design procedure for a WAC that guarantees delay-robustness and simultaneously minimizes the \mathcal{L}_2 gain of the system. More precisely, we consider a detailed model of a low-inertia system and combine an augmented Lyapunov-Krasovskii functional with the descriptor method and a change of control variables to develop a static output feedback controller synthesis. Furthermore, the proposed control design is tested on the Kundur two-area system, with results demonstrating that the proposed approach successfully improves oscillation damping and ensures robustness with respect to time-varying communication delays. The extensions of this work could focus on applying the proposed controller synthesis to large-scale low-inertia systems and introducing a sparsity-promoting feature in the control design in order to reduce the required information exchange of the WAC.

IMPROVING PERFORMANCE OF LOW-INERTIA SYSTEMS VIA EIGENVALUE OPTIMIZATION

This chapter proposes a method for allocation of inertia and damping in an inverter-dominated power system. The approach combines a detailed DAE representation of such system with an iterative, eigensensitivity-based optimization framework, in order to determine the optimal distribution of virtual gains across different VSM-based converters in the network. A comprehensive multi-objective formulation is presented, considering several performance metrics such as small-signal stability, minimum damping ratio, frequency nadir and RoCoF. Moreover, the methodology also takes system norms into account, and improves computational efficiency and adaptive regulation of incremental changes in decision variables. A computationally inexpensive and scalable problem formulation has been validated on a three-area test system. The results suggest that the low-order models commonly used in the literature do not capture the underlying dynamics of a realistic low-inertia system. Furthermore, some interesting insights pertaining to the impact of inertia and damping on different performance metrics have been gained. The chapter is based on [273].

11.1 INTRODUCTION

The electric power system is currently undergoing a major transition towards integration of large shares of distributed generation interfaced via PE converters. This is accompanied by the phase-out of conventional synchronous generators and the loss of rotational inertia. Such developments have serious effects on system dynamics, especially in terms of performance [274, 275] and larger frequency excursions and RoCoF after disturbances [2, 4, 8]. To mitigate the underlying issues, different technologies and control techniques have been proposed, primarily in terms of restoring the lost inertia by emulating an SG-like behavior through converter control. As previously discussed in Chapter 2, a number of control schemes have been designed in order to make power converters behave as closely as possible to SMs [34, 49, 51, 75–77].

These schemes can vary in the level of detail and complexity, but they all rely on replicating the dynamic behavior of a synchronous generator [66, 276], therefore providing virtual inertia and damping. Moreover, all these strategies require some sort of energy on the DC side acting as a converter's equivalent to the missing kinetic energy of the rotor; either in the form of energy storage (e.g., batteries, flywheels, supercapacitors) [277], or by employing a power source with an available kinetic energy (e.g., wind turbines and diesel generators) [145, 278].

Synthetic inertia and damping are thus becoming design parameters of the power system and could potentially serve as a foundation for an ancillary service [4, 8]. Therefore, a natural next step is to determine how much virtual inertia and damping is actually needed and where in the system would it be the most beneficial. However, even the sole definition of appropriate performance metrics is not clear. Traditionally, the total inertia and damping in the system were employed as the main metrics used for evaluating system resilience [3]. However, the authors in [7, 279] show that, in addition to aggregate inertia and damping, the distribution of these parameters in the system could be of crucial importance, with spatially heterogeneous inertia profiles resulting in worse dynamical response after a disturbance. Furthermore, performance metrics such as frequency nadir, RoCoF and minimum damping ratio are also commonly used in the literature [153, 280, 281]. In contrast, the problem of optimal tuning and placement of VSM control gains pertaining to virtual inertia and damping has recently been tackled from the perspective of system norms [139, 154, 217, 279, 282–285], namely using the \mathcal{H}_2 norm in [139, 154, 279, 282, 283], \mathcal{H}_∞ norm in [284], \mathcal{L}_2 and \mathcal{L}_∞ norms in [285], and all of the above approaches in [217].

While there is no clear path on how to approach this problem, the existing literature suggests two main research directions. On the one hand, [153, 281] analyze the sensitivity of eigenvalues with respect to inertia and damping, and subsequently maximize the critical damping ratio of the system while ensuring that frequency overshoot is limited. Although such formulation is non-convex by nature, it can be linearized and solved numerically in an iterative fashion. Nevertheless, both studies consider an oversimplified representation of the system, especially in terms of modeling of converter-interfaced generation, and employ a sequence of approximations in order to obtain a rough estimate of the frequency metrics of interest. On the other hand, [139, 154, 279, 282, 283] utilize the \mathcal{H}_2 norm as a measure of network coherency and characterization of the system frequency response, as well as for quantifying the VSM control effort. In particular, [279] and [282] aim to improve the frequency response of

the system by finding the inertia distribution that minimizes the \mathcal{H}_2 norm, with the second study specifically focusing on a network with high penetration of DFIG-based wind generation. However, neither of the studies includes the damping constant as a controllable parameter. This drawback is resolved in [139, 154, 283], where the authors argue that the performance metrics such as the damping ratio and RoCoF are not sufficient for quantifying the robustness of the system. They instead employ \mathcal{H}_2 norm not only to characterize the system response, but also to quantify the use of control effort. Furthermore, [154, 283] incorporate simplified VI devices operating in the grid-following mode as a feedback control loop, whereas [139] also includes the grid-forming VI implementation. While providing certain theoretical guarantees, the use of \mathcal{H}_2 norm is limited by the underlying assumption that the disturbance is impulsive, which is not necessarily the case in power systems (e.g., load change and generation outage yield a step-like change in active power). Another downside lies in the computational burden of solving the underlying Lyapunov equations for a detailed low-inertia system. This was not an obstacle in [139, 154, 279, 282, 283] due to simplistic representation of system dynamics based on the swing equation. However, such models are not sufficient to characterize the dynamic interactions present in a realistic system with high inverter penetration (see Chapter 4), thus raising concerns in terms of applicability of system norms.

The work proposed in this chapter aims to combine the techniques and insightful conclusions from the existing literature and provide a methodology for placement of virtual inertia and damping in a high-fidelity low-inertia system. To this end, a detailed DAE model of such system presented in Section 2.9 is used to for optimal VSM control design (i.e., control tuning) and assessing the system performance. Similarly to [153, 280, 281], we employ an iterative, eigensensitivity-based optimization framework in order to determine optimal incremental allocation of virtual gains at each step. However, unlike the approximations made in [153, 281], we include exact analytical expression for relevant frequency metrics, previously derived in Section 5.2. Moreover, improvements in terms of multi-objective nature of the problem, computational efficiency and adaptive step-size adjustments have also been made. On the other hand, motivated by [139, 154, 283], we include different VI implementations as well as the \mathcal{H}_2 and \mathcal{H}_∞ system norms in the analysis. While not computationally tractable within the iterative algorithm, the two norms are studied and taken into consideration when evaluating the system performance. As a result, we obtain a computationally inexpensive and scalable problem formulation that takes into account all

relevant aspects of the dynamic system response. Such comprehensive and multifaceted approach has not been proposed in the literature thus far.

The rest of the chapter is organized as follows. In Section 11.2, the basic concepts of linear control theory and the computation of \mathcal{H}_2 and \mathcal{H}_∞ norms are introduced. Section 11.3 discusses the principles of eigensensitivity optimization as well as different performance metrics and problem objectives. The mathematical formulation of the problem is presented in Section 11.4, followed by several case studies in Section 11.5. Finally, Section 11.6 discusses the outlook of the study and concludes the paper.

11.2 CONTROL THEORY PRELIMINARIES

Here, we introduce the basic concepts of linear control theory needed for defining and computing the two system norms of interest, namely the \mathcal{H}_2 and \mathcal{H}_∞ norms. This will also aid the later discussion in Section 11.3.3 on applicability of system norms to eigenvalue optimization. The content of the section is based on [286–291] and for the most part adapted from [287, 288, 291].

Let us consider a Linear Time-Invariant (LTI), continuous-time system

$$\dot{x}(t) = Ax(t) + Bu(t), \quad (11.1a)$$

$$y(t) = Cx(t) + Du(t), \quad (11.1b)$$

where $x \in \mathbb{R}^n$, $y \in \mathbb{R}^m$ and $u \in \mathbb{R}^p$ are the respective state, output and control input vectors, $A \in \mathbb{R}^{n \times n}$, $B \in \mathbb{R}^{n \times p}$, $C \in \mathbb{R}^{m \times n}$ and $D \in \mathbb{R}^{m \times p}$ are the state-space matrices, and $x(t_0) = x_0$.

11.2.1 Controllability and Observability

Controllability and observability are some of the fundamental ideas of control theory. We follow the discussion in [287] to introduce these concepts.

Definition 11.2.1. *The system (11.1) is said to be **controllable** if the system can be driven to any final state $x_1 = x(t_1)$, in finite time t_1 , from any initial state $x(0)$ by selecting the control $u(t)$, $0 \leq t \leq t_1$ accordingly.*

Definition 11.2.2. *The system (11.1) is called **observable** if there exists a $t_1 > 0$ such that the initial state $x(t_0)$ can be uniquely determined from knowledge of $u(t)$ and $y(t)$, $\forall t$, where $0 \leq t \leq t_1$.*

The controllability of the system (11.1) is referred to as the controllability of the pair (A, B) , whereas the observability of such system is referred to as the

observability of the pair (A, C) . Furthermore, observability and controllability of a system are dual problems. The duality implies that (A, C) is observable if (A^\top, C^\top) is controllable. Controllability and observability play important roles in the existence of positive definite and positive semidefinite solutions to Lyapunov equations.

Definition 11.2.3. *Let A be a stable matrix. The matrix*

$$C_G := \int_0^{t_1} e^{At} B B^\top e^{A^\top t} dt \quad (11.2)$$

*is called the **controllability Grammian**.*

Definition 11.2.4. *Let A be a stable matrix. The matrix*

$$O_G := \int_0^\infty e^{A^\top t} C^\top C e^{At} dt \quad (11.3)$$

*is called the **observability Grammian**.*

Theorem 11.2.5. *Let A be a stable matrix. The controllability Grammian C_G satisfies the Lyapunov equation*

$$A C_G + C_G A^\top = -B B^\top \quad (11.4)$$

and is symmetric positive definite if and only if (A, B) is controllable.

Theorem 11.2.6. *Let A be a stable matrix. The observability Grammian O_G satisfies the Lyapunov equation*

$$O_G A + A^\top O_G = -C^\top C \quad (11.5)$$

and is symmetric positive definite if and only if (A, C) is observable.

The notions of controllability and observability Grammians are of crucial importance for computing the \mathcal{H}_2 and \mathcal{H}_∞ norms of a linear time-invariant system, elaborated in more detail in the section to come.

11.2.2 $\mathcal{H}_2/\mathcal{H}_\infty$ System Norms

In order to describe system norms and their computation, one first needs to introduce the transfer function of the said system.

Definition 11.2.7. For the continuous-time state-space representation given by (11.1) and $x(0) = x_0$, the matrix

$$G(s) := \frac{y(s)}{u(s)} = C(sI - A)^{-1}B + D \quad (11.6)$$

is called the **matrix transfer function**.

The transfer function gives a relationship between the input and output of the system. It plays an important role in control theory in general and provides insights in how disturbances in the system will affect the output.

Definition 11.2.8. Let $\lambda_j(M)$ denote the j -th eigenvalue of the matrix M . For any given matrix A , the expression

$$\sigma_j(A) := \lambda_j\left(AA^T\right) \quad (11.7)$$

defines the j -th **singular value** of matrix A .

We can now introduce the following two system norms that provide a measure of the magnitude of the system output in response to a disturbance input.

Definition 11.2.9. Consider a stable, casual LTI system (11.1) with a transfer function $G(s)$. The **\mathcal{H}_2 norm** can be considered as the energy of the response of $G(s)$ to an impulse response, described by

$$\|G\|_2 := \left(\frac{1}{2\pi} \int_{-\infty}^{\infty} \text{Tr} \left(G(j\omega)^T G(j\omega) \right) d\omega \right)^{\frac{1}{2}}. \quad (11.8)$$

Alternatively, the \mathcal{H}_2 norm can be expressed as the (expected) energy of the response to white noise, computed as

$$\|G\|_2 := \sqrt{\text{Tr} \left(CPCT^T \right)}. \quad (11.9)$$

Definition 11.2.10. Consider a stable, casual LTI system (11.1) with a transfer function $G(s)$. Let $\|G(j\omega)\| = \max_i \sigma_i(G(j\omega)) = \sigma_{\max}(G(j\omega))$ be the Euclidean norm of matrix G . Then, the **\mathcal{H}_∞ norm** of the transfer function $G(s)$, denoted by $\|G\|_\infty$, is defined by

$$\|G\|_\infty := \sup_{\omega \in \mathbb{R}} \sigma_{\max}(G(j\omega)), \quad (11.10)$$

where $\sup_{\omega \in \mathbb{R}}$ denotes the supremum (i.e., least upper bound) over all real valued frequencies w .

It can be noticed that the \mathcal{H}_2 norm reflects the energy content of the performance output to a disturbance/noise, whereas the \mathcal{H}_∞ norm corresponds to the RMS gain from the disturbance to the performance output. However, while the computation of \mathcal{H}_2 norm for a given system (11.1) is explicitly given by (11.9), the approximation of \mathcal{H}_∞ norm requires computing the supremum of the frequency response over all frequencies, and hence the use of iterative algorithms. This is explained in more detail in the following section.

11.2.3 Computation of \mathcal{H}_∞ Norm

For brevity, we will only focus on \mathcal{H}_∞ computation algorithms in frequency domain, namely the *bisection* and *two-step* algorithm. However, the same conclusion apply to the state-space-based approaches. The connection between the \mathcal{H}_∞ norm of a stable transfer function and its associated Hamiltonian matrix plays an important role in the aforementioned algorithms.

Definition 11.2.11. Consider a stable, casual LTI system (11.1). From the given state-space description (A, B, C, D) , we define the **Hamiltonian matrix** M_r of the form

$$M_r := \begin{bmatrix} A + BR^{-1}D^T C & BR^{-1}B^T \\ -C^T (I + DR^{-1}D^T) C & -(A + BR^{-1}D^T C) C^T \end{bmatrix}, \quad (11.11)$$

where $R := r^2 I - D^T D$.

Now we can relate the eigenvalues of M_r to the singular values of $G(s)$.

Theorem 11.2.12. Let $G(s)$ be a stable transfer function of a casual LTI system given by (11.1) and let $r > 0$. Then $\|G\|_\infty < r$ if and only if $\sigma_{\max}(D) < r$ and M_r has no purely imaginary eigenvalues.

This theorem implies that for $r > \|G\|_\infty$, M_r will have no purely imaginary eigenvalues, and for $r < \|G\|_\infty$, M_r will have at least one purely imaginary eigenvalue. Moreover, for obtaining tighter upper and lower bounds on the approximation of the \mathcal{H}_∞ norm, one could employ Hankel singular values of the system.

Definition 11.2.13. Consider a stable, casual LTI system (11.1) with the controllability Grammian C_G and observability Grammian O_G . The square roots σH_i of the matrix $C_G O_G$ represent **Hankel singular values**.

The bisection approximation method given in Algorithm 4 is proposed by [288]. It is based on analyzing the eigenvalues of M_r at every iteration in

Algorithm 4 Iterative computation of \mathcal{H}_∞ norm via the bisection method

- 1: Initialize the algorithm by computing bounds in (11.12) $\triangleright r_{lb}, r_{ub}$
- 2: **while** $2(r_{ub} - r_{lb}) > \epsilon$ **do**
- 3: Update r according to the interval bounds $\triangleright r = \frac{r_{ub} + r_{lb}}{2}$
- 4: Compute the Hamiltonian matrix in (11.11) $\triangleright M_r$
- 5: Check for purely imaginary eigenvalues of M_r
- 6: **if** M_r has a purely imaginary eigenvalue **then**
- 7: Update the lower bound of the interval $\triangleright r_{lb} = r$
- 8: **else**
- 9: Update the upper bound of the interval $\triangleright r_{ub} = r$
- 10: **end if**
- 11: **end while**
- 12: Return r

order to determine if there exists a purely imaginary eigenvalue or not. To start the algorithm, one needs to compute the upper and lower bounds of the interval $r \in [r_{lb}, r_{ub}]$, as follows:

$$r_{lb} = \max \left\{ \sigma_{\max}(D), \sqrt{\text{Tr}(O_G C_G) / n} \right\}, \tag{11.12a}$$

$$r_{ub} = \sigma_{\max}(D) + 2\sqrt{n \text{Tr}(O_G C_G)}. \tag{11.12b}$$

It should be pointed out that obtaining the starting bounds for this algorithm might be computationally very expensive and impractical for large matrices, as it requires solving two Lyapunov equations (11.4)-(11.5), multiplying two $n \times n$ matrices and computing the eigenvalues of this product.

The extension of the bisection method came in the form of a two-step algorithm proposed by [290], in which only the lower bound r_{lb} needs to be computed. It builds on the ideas of the bisection method, but unlike the bisection algorithm that only searches at one frequency per iteration, the two-step algorithm searches over multiple frequencies per single iteration. It is important to note that the computation of the lower bound does not require finding Grammians O_G and C_G , and is thus less computationally expensive. Similarly to the bisection method, the two-step algorithm also relies on Theorem 11.2.12 as well as the following theorem.

Theorem 11.2.14. *Suppose $r > \sigma_{\max}(D)$ and $\omega \in \mathbb{R}$. Then $\det(M_r - j\omega I) = 0$ if and only if $\exists n, \sigma_n(G(j\omega)) = r$.*

As a consequence of Theorem 11.2.14, the imaginary eigenvalues of M_r are exactly the frequencies at which some singular value of $G(j\omega)$ equals r , i.e., ω_i

Algorithm 5 Iterative computation of \mathcal{H}_∞ norm via the two-step method

```

1: Compute the transfer function of the given system in (11.1)    ▷  $G(s)$ 
2: Find the poles of  $G(s)$                                        ▷  $\lambda_i$ 
3: if the poles are strictly real valued then
4:   Find  $\lambda_{\max} = \max_i |\lambda_i|$  and update  $\omega_p$                 ▷  $\omega_p = \lambda_{\max}$ 
5: else
6:   Find  $\hat{\lambda}_{\max}$  that yields  $\max_{\lambda_i} \left| \frac{\Im(\lambda_i)}{\Re(\lambda_i)} \frac{1}{\lambda_i} \right|$  and update  $\omega_p$   ▷  $\omega_p = \hat{\lambda}_{\max}$ 
7: end if
8: Compute  $r_{lb}$  using (11.13)                                       ▷  $r_{lb}$ 
9: while  $M_r$  has purely imaginary eigenvalues do
10:  Update  $r$  according to the lower interval bound                ▷  $r = (1 + 2\epsilon)r_{lb}$ 
11:  Compute the Hamiltonian matrix in (11.11)                    ▷  $M_r$ 
12:  Sort all of the purely imaginary eigenvalues of  $M_r$           ▷  $\omega_1, \omega_2, \dots, \omega_k$ 
13:  for  $i = 1, 2, \dots, k - 1$  do
14:    Compute average frequencies  $m_i$                              ▷  $m_i = \frac{1}{2} (\omega_i + \omega_{i+1})$ 
15:    Compute maximum singular valuesa                          ▷  $\sigma_{\max}(G(jm_i)) = \text{svd}_i$ 
16:    Update the lower bound of the interval                       ▷  $r_{lb} = \text{svd}_i$ 
17:  end for
18: end while
19: Return  $\|G\|_\infty = \frac{1}{2} (r_{lb} + r_{ub})$ 

```

^a svd stands for singular value decomposition.

is an eigenvalue of M_r if and only if r is a singular value of $G(j\omega)$, $\omega \in \mathbb{R}$. The underlying iterative method is given in Algorithm 5 and employs computation of the lower bound as

$$r_{lb} = \max \{ \sigma_{\max} G(0), \sigma_{\max} G(j\omega_p), \sigma_{\max}(D) \}, \quad (11.13)$$

where $\omega_p = |\lambda_i|$ and λ_i is a pole of the transfer function $G(s)$ determined according to the criteria listed in Algorithm 5. However, while computationally superior to the bisection method, the implementation of the two-step algorithm poses a need for an accurate eigenvalue solver due to its dependency on the nature of eigenvalues (i.e., finding if they are imaginary or not).

11.3 OBJECTIVES AND THEORETICAL PRINCIPLES

11.3.1 *Dynamical Properties of Low-Inertia Systems*

The level of inertia and damping present in the network largely influences the small-signal stability and frequency dynamics after a disturbance (see Chapter 4). With the increased penetration of converter-interfaced generation, the amount of inertia and damping reduces and the system becomes increasingly vulnerable to disturbances such as load fluctuations and generation outage. A few commonly used metrics for assessing the dynamic behavior of the system are listed and briefly discussed below:

- *Small-signal stability*: Defined as the ability of the system to maintain synchronism when subject to a small disturbance. The presence of an eigenvalue with a positive real part indicates that the system is small-signal unstable. It was previously shown in Chapter 4 that the system dominated by both grid-forming and grid-following power converters can face small-signal instability under insufficient levels of virtual inertia and damping (i.e., small VSM control gains).
- *Damping ratio*: Describes how fast the oscillations in the system die out. It is typically defined as the smallest or the “worst-case” damping ratio of all eigenvalues. A higher damping ratio will increase system resilience.
- *Frequency nadir*: Represents the maximum deviation of frequency from a nominal value after a disturbance. It is an important metric to consider, as a number of power system components including generators have protection elements that trip when the frequency exceeds a particular limit. Frequency nadir is a nonlinear function of both inertia and damping, given by the analytical expression in (5.9).
- *Rate-of-Change-of-Frequency*: Describes the maximum rate at which the system frequency changes and usually corresponds to the instantaneous RoCoF value after a disturbance. Similar to frequency nadir, it needs to be limited for the purposes of unwanted tripping of protection equipment. Moreover, a high value of RoCoF can also lead to an increase in frequency nadir. However, unlike frequency nadir, the RoCoF is solely a function of system inertia described by (5.10).

11.3.2 Eigensensitivity Optimization Principles

Improving the worst-case damping ratio of all modes in the system is important for ensuring an acceptable dynamic response. The damping ratios are functions of, among other parameters, individual inertia and damping constants of both synchronous and converter-based generators. However, being functions of system eigenvalues, the sensitivities of damping ratios to respective parameters are highly nonlinear and could result in a complex optimization problem [153]. This section provides a brief introduction into computation of such sensitivities and how they can be incorporated into a sequential iterative algorithm for improving the damping ratios.

Let $\lambda_i \in \mathbb{C}$ denote the i^{th} eigenvalue of the LTI system (11.1), and $\sigma_i \in \mathbb{R}$ and $\omega_i \in \mathbb{R}$ be its real and imaginary parts. The left and right eigenvectors $v_i, u_i \in \mathbb{C}^n$ of λ_i are then described by

$$Au_i = \lambda_i u_i, \quad (11.14a)$$

$$v_i^\top A = v_i^\top \lambda_i, \quad (11.14b)$$

whereas the corresponding damping ratio $\zeta_i \in \mathbb{R}$ can be defined as

$$\zeta_i := \frac{-\sigma_i}{\sqrt{\sigma_i^2 + \omega_i^2}}. \quad (11.15)$$

This value is positive for stable modes, zero for oscillatory modes and negative for unstable modes. Geometrically speaking, damping ratio is the sine of the angle between the imaginary axis and a line from the origin to the eigenvalue. Moreover, the sensitivity of eigenvalue λ_i with respect to the parameter $\alpha \in \mathbb{R}$ can be expressed as a function of eigenvectors, i.e.,

$$\frac{\partial \lambda_i}{\partial \alpha} = \frac{\partial \sigma_i}{\partial \alpha} + j \frac{\partial \omega_i}{\partial \alpha} = v_i^\top \frac{\partial A}{\partial \alpha} u_i, \quad (11.16)$$

which in turn can be used to compute the sensitivity of damping ratio ζ_i with respect to the parameter α , as follows:

$$\frac{\partial \zeta_i}{\partial \alpha} = \frac{\partial}{\partial \alpha} \left(\frac{-\sigma_i}{\sqrt{\sigma_i^2 + \omega_i^2}} \right) = \omega_i \frac{\sigma_i \frac{\partial \omega_i}{\partial \alpha} - \omega_i \frac{\partial \sigma_i}{\partial \alpha}}{(\sigma_i^2 + \omega_i^2)^{\frac{3}{2}}}. \quad (11.17)$$

Since the underlying sensitivities are nonlinear, the task of maximizing the damping ratio is performed using an iterative approach. More precisely, the sensitivities are obtained at the start of the iteration using (11.17), from which

the new parameter values that maximize the damping ratios are computed. Such iterative procedure yields

$$\zeta_i^{\nu+1} = \zeta_i^\nu + \frac{\partial \zeta_i^\nu}{\partial \alpha} (\alpha^{\nu+1} - \alpha^\nu), \quad (11.18)$$

where $\nu \in \mathbb{Z}_{\geq 0}$ denotes the iteration step and α^ν and $\alpha^{\nu+1}$, i.e., ζ^ν and $\zeta^{\nu+1}$, represent the old and new values of parameters and damping ratios, respectively. The updated damping ratios and the corresponding sensitivities are subsequently used in the next iteration step, described in more detail in Section 11.4.4.

11.3.3 *Applicability of System Norms*

Apart from the metrics presented in Section 11.3.1, system norms such as \mathcal{H}_2 and \mathcal{H}_∞ provide a measure of the magnitude of the system output after a disturbance. The system output can include performance outputs such as frequency stability and energy of the control effort, thereby making system norms a useful tool for optimization. In general, the \mathcal{H}_2 norm measures the energy of the system's impulse response, whereas the \mathcal{H}_∞ norm represents the peak gain from the disturbance to the output [286], as previously discussed in Section 11.2. Moreover, by defining a suitable performance output, the energy metrics of the VSM control effort can be directly considered in the \mathcal{H}_2 framework as the overall output energy [154]. Nevertheless, both system norms have certain drawback when it comes to computation and applicability to a detailed model of a low-inertia system presented in Chapter 2.

Mathematically speaking, the computation of the \mathcal{H}_2 norm is straightforward and given by (11.9). While tractable for small-scale systems, the computation of two Lyapunov functions pertaining to controllability and observability Grammians and subsequent multiplication of $n \times n$ matrices becomes numerically intensive on larger scale. Furthermore, the \mathcal{H}_2 norm quantifies the system performance when subjected to an impulse disturbance, which is not applicable to more common disturbances in the power system such as a loss of generator or a load demand change. On the other hand, the \mathcal{H}_∞ norm is not restrictive in terms of the nature of the disturbance signal. However, unlike the \mathcal{H}_2 norm, its computation cannot be expressed in a concise analytical form and requires the use of iterative algorithms described in Section 11.2.3. Note that the Algorithm 4 of the bisection method has similar computational drawbacks as the computation of \mathcal{H}_2 norm in (11.9). However, even the less computationally intensive Algorithm 5 is not suitable for this study, since the eigensensitivity framework presented in

Section 11.3.2 requires the computation of norm sensitivities to decision variables (specifically inertia and damping), which is not achievable under the eigenvalue analysis of the Hamiltonian matrix M_r employed in Algorithm 5. It should be noted that the computational effort for obtaining the sensitivities of aforementioned norms to system parameters is also an additional obstacle for explicitly including them into the eigensensitivity-based problem.

Finally, an important question to consider here is how important is it to minimize the system norms as much as possible. Indeed, the main concern for system operators is to ensure that the frequency metrics such as RoCoF and frequency nadir are within prescribed ENTSO-E limits in order to prevent false triggering of protection and load shedding schemes [151]. Meeting these requirements is completely sufficient for providing reliable and safe operation and any further improvement of frequency response (i.e., minimization of speed and magnitude of frequency deviation) is not necessarily of value to the operator. By minimizing system norms one imposes significantly tighter bounds on these frequency metrics, which might not be justifiable from the control effort (i.e., cost of virtual inertia and damping) perspective. Moreover, optimizing system norms is not in direct correlation with the damping ratio and does not guarantee achieving sufficient damping of oscillatory modes. In contrast, while hard to prove any formal relationship between the \mathcal{H}_∞ norm of an LTI system and the damping ratio of its eigenvalues, the intuition suggests that by improving the latter one could also reduce the former. The results presented in Section 11.5 also support these claims. Therefore, the method proposed in this chapter prioritizes the improvement of the worst-case damping ratio while ensuring that the frequency constraints are met, which simultaneously leads to a compelling reduction of system norms.

11.4 PROBLEM FORMULATION

This section describes the proposed optimization problem. The analytical expressions for frequency constraints are presented, followed by two different problem formulations, i.e., multi-step and uniform. In particular, the multi-step approach comprises three steps, each of them with a different objective function and set of constraints, whereas the uniform formulation combines all of these objectives and constraints into a single optimization problem.

11.4.1 System Frequency Metrics

In order to incorporate frequency constraints into the optimization problem, one first needs to obtain the corresponding analytical expressions in terms of decision variables (i.e., parameters of interest), namely inertia and damping. Let us recall the derivation of frequency nadir and RoCoF metrics after a step disturbance of magnitude $\Delta P \in \mathbb{R}$ described in Chapter 5. The underlying expressions in SI are defined by

$$\dot{f}_{\max} := -f_0 \frac{\Delta P}{M}, \quad (11.19a)$$

$$\Delta f_{\max} := -f_0 \frac{\Delta P}{D + R_g} \left(1 + \sqrt{\frac{T(R_g - F_g)}{M}} e^{-\zeta_s \omega_n t_m} \right), \quad (11.19b)$$

where $\dot{f}_{\max} \in \mathbb{R}$ and $\Delta f_{\max} \in \mathbb{R}$ denote the respective values of RoCoF and frequency nadir, and $f_0 = 50$ Hz represents the base frequency. All aggregate system parameters in (11.19) are described in per-unit and defined in Section 5.2. Moreover,

$$t_m := \frac{1}{\omega_n \sqrt{1 - \zeta_s^2}} \tan^{-1} \frac{\omega_n \sqrt{1 - \zeta_s^2}}{\zeta_s \omega_n - T^{-1}} \quad (11.20)$$

is the time instance of frequency nadir, with $\zeta_s \in \mathbb{R}_{>0}$ and $\omega_n \in \mathbb{R}_{>0}$ representing the damping ratio and the natural frequency of the system (i.e., its CoI) response:

$$\zeta_s := \frac{M + T(D + F_g)}{2\sqrt{MT(D + R_g)}}, \quad \omega_n := \sqrt{\frac{D + R_g}{M + T}}. \quad (11.21)$$

An additional constraint is introduced (see Chapter 8 for more details) to ensure that the time instance of frequency nadir is positive, i.e., $t_m > 0$, which corresponds to

$$\frac{M}{T} - F_g < D. \quad (11.22)$$

The expressions (11.19) and (11.22) are highly dependent on the aggregate system inertia and damping, and the ENTSO-E limits enforced on frequency metrics in (11.19) can be translated into bounds on M and D . However, frequency nadir in (11.19b) is a nonlinear function of system parameters. In order to incorporate such constraint into the iterative linear program, with in-

ertia and damping being decision variables, a first-order Taylor approximation is employed:

$$\Delta f_{\max}^{\nu+1} = \Delta f_{\max}^{\nu} + \frac{\partial \Delta f_{\max}^{\nu}}{\partial M} \Delta M^{\nu+1} + \frac{\partial \Delta f_{\max}^{\nu}}{\partial D} \Delta D^{\nu+1}, \quad (11.23)$$

where Δf_{\max}^{ν} and $\Delta f_{\max}^{\nu+1}$ are the old and new values of frequency nadir and $\Delta M^{\nu+1} \in \mathbb{R}$ and $\Delta D^{\nu+1} \in \mathbb{R}$ are the respective updates of system inertia and damping at each iteration step.

11.4.2 Multi-Step Optimization Problem

Let $\mathcal{N} \subset \mathbb{Z}_{\geq 0}$ be the index set of network buses, $\mathcal{K} \subseteq \mathcal{N}$ and $\mathcal{J} \subseteq \mathcal{N}$ represent the subset of nodes with synchronous and converter-interfaced generation respectively, and $n_k = |\mathcal{K}|$, $n_j = |\mathcal{J}|$. The individual per-unit inertia and damping constants are described by $m_j \in \mathbb{R}_{>0}$ and $d_j \in \mathbb{R}_{>0}$, whereas the incremental changes in inertia and damping computed at iteration step ν are denoted by $\Delta m^{\nu+1} \in \mathbb{R}^{n_j}$ and $\Delta d^{\nu+1} \in \mathbb{R}^{n_j}$. Note that we only consider the virtual inertia and damping gains of converter-interfaced generators as decision variables (i.e., control gains to be tuned), and parameters of synchronous generators remain intact. Moreover, $\sigma_i^{\nu} \in \mathbb{R}$ and $\zeta_i^{\nu} \in \mathbb{R}$ reflect the real part and the damping ratio of the i^{th} mode at iteration step ν .

In order to address all performance metrics listed in Section 11.3.1, we propose a sequential procedure comprising three consecutive optimization problems. More precisely, the multi-step approach first addresses the small-signal stability of the system, followed by improving the worst-case damping ratio. Finally, the inertia and damping are redistributed across the system such that the total amount of additional control effort is minimized. Three optimization steps are described in more detail below.

11.4.2.1 Step 1: Ensuring Small-Signal Stability

The first step aims at restoring the small-signal stability of the system by ensuring that the real parts of all eigenvalues become negative, i.e., $\forall i \in \mathbb{Z}_{\leq n}^+$, $\sigma_i < 0$. The problem can be formulated as

$$\min_{m,d} \quad \sigma_{\max} \quad (11.24a)$$

$$\text{s.t.} \quad \forall j \in \mathcal{J}, \forall i \in \mathbb{Z}_{\leq n}^+,$$

$$\sigma_i^{\nu+1} = \sigma_i^{\nu} + \sum_{j \in \mathcal{J}} \frac{\partial \sigma_i^{\nu}}{\partial d_j} \Delta d_j^{\nu+1} + \sum_{j \in \mathcal{J}} \frac{\partial \sigma_i^{\nu}}{\partial m_j} \Delta m_j^{\nu+1}, \quad (11.24b)$$

$$\sigma_i^{\nu+1} \leq \sigma_{\max}, \quad (11.24c)$$

$$\underline{d}_j \leq d_j^{\nu+1} \leq \bar{d}_j, \quad (11.24d)$$

$$\underline{m}_j \leq m_j^{\nu+1} \leq \bar{m}_j, \quad (11.24e)$$

$$\Delta \underline{d}_j \phi_j^d \leq \Delta d_j^{\nu+1} \leq \Delta \bar{d}_j \phi_j^d, \quad (11.24f)$$

$$\Delta \underline{m}_j \phi_j^m \leq \Delta m_j^{\nu+1} \leq \Delta \bar{m}_j \phi_j^m, \quad (11.24g)$$

$$\Delta d_j^{\nu+1} = d_j^{\nu+1} - d_j^\nu, \quad (11.24h)$$

$$\Delta m_j^{\nu+1} = m_j^{\nu+1} - m_j^\nu, \quad (11.24i)$$

with the objective to minimize the real part (σ_{\max}) of the rightmost (i.e., the most unstable) eigenvalue at each iteration step, and $(m, d) \in \mathbb{R}_{\geq 0}^{2n_j}$ being the vector of decision variables. Constraint (11.24b) iteratively computes the real parts of all modes based on their previous values and the updates arising from incremental step changes in m and d , while (11.24c) is a trivial inequality needed for achieving the aforementioned objective. Inequalities (11.24d)-(11.24e) impose upper and lower bounds on total inertia and damping at each node, whereas (11.24f)-(11.24g) place limits on the permissible changes at each iteration; $\phi^d \in \mathbb{R}^{n_j}$ and $\phi^m \in \mathbb{R}^{n_j}$ represent the normalization of step size limits based on parameter sensitivities, which will be further elaborated in Section 11.4.4. Finally, (11.24h)-(11.24i) declare the updated decision variables for the next iteration step. The optimization ends once all modes become stable, i.e., the condition $\forall i \in \mathbb{Z}_{\leq n}^+, \sigma_i < 0$ is met. Note that a similar outcome could be achieved by directly maximizing the minimum damping ratio ζ_{\min} instead of minimizing σ_{\max} in (11.24a).

11.4.2.2 Step 2: Improving Damping Ratio

Once the system is small-signal stable, the next step is to make sure that the worst-case damping ratio is above a predefined threshold $\zeta \in \mathbb{R}_{>0}$. Apart from improving the damping ratio, limits are placed on RoCoF and frequency nadir to ensure an acceptable frequency response, which leads to the problem of the form:

$$\min_{m,d} \quad -c_\zeta \zeta_{\min} + c_f (\eta_{f_1} + \eta_{f_2}) + c_f (\eta_{f_1} + \eta_{f_2}) \quad (11.25a)$$

$$\text{s.t.} \quad \forall j \in \mathcal{J}, \forall i \in \mathbb{Z}_{\leq n}^+,$$

$$(11.24d)-(11.24i),$$

$$\zeta_i^{\nu+1} = \zeta_i^\nu + \sum_{j \in \mathcal{J}} \frac{\partial \zeta_i^\nu}{\partial d_j} \Delta d_j^{\nu+1} + \sum_{j \in \mathcal{J}} \frac{\partial \zeta_i^\nu}{\partial m_j} \Delta m_j^{\nu+1}, \quad (11.25b)$$

$$\zeta_{\min} \leq \zeta_i^{\nu+1}, \quad (11.25c)$$

$$D^{\nu+1} = \frac{\sum_{k \in \mathcal{K}} P_{g_k} d_k + \sum_{j \in \mathcal{J}} P_{g_j} d_j^{\nu+1}}{\sum_{n \in \mathcal{N}} P_{g_n}}, \quad (11.25d)$$

$$M^{\nu+1} = \frac{\sum_{k \in \mathcal{K}} P_{g_k} m_k + \sum_{j \in \mathcal{J}} P_{g_j} m_j^{\nu+1}}{\sum_{n \in \mathcal{N}} P_{g_n}}, \quad (11.25e)$$

$$\Delta D^{\nu+1} = D^{\nu+1} - D^{\nu}, \quad (11.25f)$$

$$\Delta M^{\nu+1} = M^{\nu+1} - M^{\nu}, \quad (11.25g)$$

$$\Delta f_{\max}^{\nu+1} = \Delta f_{\max}^{\nu} + \frac{\partial \Delta f_{\max}^{\nu}}{\partial D} \Delta D^{\nu+1} + \frac{\partial \Delta f_{\max}^{\nu}}{\partial M} \Delta M^{\nu+1}, \quad (11.25h)$$

$$-\Delta \bar{f}_{\lim} - \eta_{f_1} \leq \Delta f_{\max}^{\nu+1} \leq \Delta \bar{f}_{\lim} + \eta_{f_2}, \quad (11.25i)$$

$$-\bar{f}_{\lim} - \eta_{f_1} \leq f_0 \frac{\Delta P}{M^{\nu+1}} \leq \bar{f}_{\lim} + \eta_{f_2}, \quad (11.25j)$$

$$\frac{M^{\nu+1}}{T} - F_g < D^{\nu+1}, \quad (11.25k)$$

$$\eta_{f_1}, \eta_{f_2}, \eta_{f_1}, \eta_{f_2} \geq 0. \quad (11.25l)$$

Here, ζ_{\min} represents the worst-case damping ratio of the system to be maximized, with $c_{\zeta} \in \mathbb{R}_{>0}$ being the corresponding cost factor. Equality (11.25b) defines the new damping ratios of all modes based on their previous values and the corresponding updates of m and k . Constraints (11.24d)-(11.24i) from the first step still apply, with additional expressions (11.25d)-(11.25l) imposing limits on frequency metrics of interest discussed in Section 11.4.1. In particular, (11.25d)-(11.25g) define the total system inertia and damping as well as the incremental changes between iterations necessary for computation of frequency margins; (11.25h) describes the Taylor approximation of the nonlinear frequency nadir constraint, (11.25j)-(11.25i) provide upper and lower bounds on permissible RoCoF and frequency nadir magnitudes and (11.25k) ensures that the time instance of frequency nadir is positive. Note that (11.25j)-(11.25i) are implemented as soft constraints, with slack variables defined by (11.25l) and included in (11.25a), together with the respective cost factors $c_f \in \mathbb{R}_{>0}$ and $c_{\bar{f}} \in \mathbb{R}_{>0}$. This optimization is completed when the the damping ratios of all modes reach a given threshold, i.e., $\zeta_{\min} \geq \underline{\zeta}$, while also ensuring that the RoCoF and nadir conditions are satisfied.

11.4.2.3 Step 3: Reducing Control Effort

After achieving a satisfactory dynamical performance in terms of metrics defined in Section 11.3.1, the goal of the final optimization step is to reduce

the total amount of inertia and damping in the system without compromising the aforementioned dynamical performance. This can be interpreted as a reduction of the VSM control effort through redistribution of virtual inertia and damping between different power converters, described by

$$\min_{m,d} \quad c_M M + c_D D \tag{11.26a}$$

$$\begin{aligned} \text{s.t.} \quad & \forall j \in \mathcal{J}, \forall i \in \mathbb{Z}_{\leq n}^+, \\ & (11.24d)-(11.24i), (11.25b)-(11.25k), \\ & \zeta_i^{\nu+1} \geq \zeta, \end{aligned} \tag{11.26b}$$

where $c_M \in \mathbb{R}_{>0}$ and $c_D \in \mathbb{R}_{>0}$ reflect the “price” of control gains, (11.24d)-(11.24i) and (11.25b)-(11.25k) encompass the system constraints from previous steps, and (11.26b) ensures that the damping ratios stay above the minimum permissible limit. In contrast to (11.25), the frequency constraints in (11.26) are implemented as hard constraints, i.e., slack variables $\eta_{f_1}, \eta_{f_2}, \eta_{j_1}, \eta_{j_2}$ are set to zero, and normalization of step sizes is neglected, i.e., $\phi_j^d = \phi_j^m = 1, \forall j \in \mathcal{J}$. The optimization ends when the incremental change in aggregate values of inertia and damping between 5 consecutive iteration steps reaches a predefined lower bound $\epsilon = 10^{-4}$.

11.4.3 Uniform Optimization Problem

An alternative approach would be to combine the objectives and constraints of all three steps into a single “uniform” formulation, which could potentially lead to a more effective allocation of virtual gains. Indeed, while employing different and independent objectives for each stage of the multi-step method effectively identifies the optimal parameters (i.e., the local optimum) for that particular step, it can also yield a suboptimal final solution compared to the uniform formulation. For instance, in the first and second step (i.e., (11.24a) and (11.25a) respectively) there is no cost associated with the amount of inertia and damping being placed, which could lead to unnecessarily high allocation of virtual inertia and damping. Despite the reduction of the control effort in the third step, the final distribution of virtual control gains can end up significantly different compared to the uniform approach.

The uniform optimization problem can be formulated as follows:

$$\min_{m,d} \quad c_\zeta \eta_\zeta + c_f (\eta_{f_1} + \eta_{f_2}) + c_j (\eta_{j_1} + \eta_{j_2}) + c_M M + c_D D \tag{11.27a}$$

$$\text{s.t.} \quad \forall j \in \mathcal{J}, \forall i \in \mathbb{Z}_{\leq n}^+,$$

(11.24d)-(11.24i), (11.25b)-(11.25l),

$$\zeta_i^{\nu+1} \geq \underline{\zeta} - \eta_\zeta, \quad (11.27b)$$

$$\eta_\zeta \geq 0. \quad (11.27c)$$

The expressions (11.24d)-(11.24i) and (11.25b)-(11.25l) include previously defined constraints, whereas (11.27b) introduces a relaxation of the minimum damping ratio requirement, with $c_\zeta \in \mathbb{R}_{>0}$ reflecting the cost of violating the respective limit and $\eta_\zeta \in \mathbb{R}_{\geq 0}$ being the new slack variable. Such formulation ensures that once the criteria for the minimum damping ratio, RoCoF and frequency nadir are met, the appropriate slack variables become zero and stop affecting the objective function. At this point, the only non-zero terms in (11.27a) pertain to the control effort (i.e., virtual inertia and damping), which corresponds to the final step of the multi-step formulation.

11.4.4 Sensitivity Computation and Solution Strategy

As mentioned previously in Section 11.3, the eigensensitivities are nonlinear and an iterative approach is used to compute the updates. The system is linearized around the current parameter values to obtain the state-space model from which the damping ratios and their sensitivities are derived. For the simplified model used in [153], it is possible to obtain the analytical expressions for the specific sensitivities of the damping ratio by studying the sensitivity $\frac{\partial A}{\partial \alpha_i}$ of the state matrix

$$A = \begin{bmatrix} \mathbb{0}_{n_m \times (n_m + n_d)} & \mathbb{1}_{n_m \times n_m} \\ -D_d^{-1} L_d & \mathbb{0}_{n_d \times n_m} \\ -M_m^{-1} L_m & -M_m^{-1} D_m \end{bmatrix} \quad (11.28)$$

to parameters $\alpha_i \in \{m_i, d_i\}, \forall i \in \mathcal{N}$. In (11.28), $M_m \in \mathbb{R}^{n_m \times n_m}$, $D_m \in \mathbb{R}^{n_m \times n_m}$ and $D_d \in \mathbb{R}^{n_d \times n_d}$ describe diagonal matrices of the state vectors, $L_m \in \mathbb{R}^{n_m \times (n_m + n_d)}$ and $L_d \in \mathbb{R}^{n_d \times (n_m + n_d)}$ represent the submatrices of the network Laplacian, and n_m and n_d denote the number of network nodes with non-zero inertia and damping respectively. Since M and D are the only submatrices with non-zero derivatives with respect to α_i , the sensitivity $\frac{\partial A}{\partial \alpha_i}$ can be determined by obtaining the respective sensitivities of M and D :

$$\left(\frac{\partial M^{-1}}{\partial m_i} \right)_{p,q} = \begin{cases} -\frac{1}{m_i^2}, & p = q = i, \\ 0, & \text{otherwise,} \end{cases} \quad (11.29a)$$

$$\left(\frac{\partial D}{\partial d_i}\right)_{p,q} = \begin{cases} 1, & p = q = i, \\ 0, & \text{otherwise.} \end{cases} \quad (11.29b)$$

A detailed derivation of the underlying expressions (11.28)-(11.29) is provided in [153].

However, when studying a realistic system with significantly higher level of detail, such as the one presented in Chapter 2, obtaining the linearized system model and the aforementioned sensitivities at each iteration is not straightforward and can result in a high computational burden. We overcome this issue by employing the Symbolic Math Toolbox in MATLAB [292] and deriving symbolic state-space representation of the system. Note that this is done only once, prior to initialization of the sequential program. The eigenvalues and their respective sensitivities are then numerically computed at each iteration and used to determine the optimal updates of virtual control gains.

A flowchart describing the concept of the proposed iterative algorithm can be found in Fig. 11.1. It should be noted that the specific flowchart reflects only the second step (i.e., improvement of the damping ratio) of the multi-step approach. At the start of each iteration, the nonlinear DAE model is linearized around the current parameter values (m^ν, d^ν) by substituting the appropriate numerical values into the symbolic state-space representation. Due to inherent nature of the problem, it is possible that during the course of optimization the update steps of the decision variables (i.e., control parameters) are too large, which would in turn imply that the linearization equilibrium and the sensitivities used to compute the updates are no longer valid. To counter this problem, the following strategy is adopted. The damping ratios $\tilde{\zeta}^\nu$ and their sensitivities are computed directly from the linear model and compared to the damping ratios obtained internally by the optimizer ζ^ν . If the difference between the two is larger than a prescribed threshold ϵ , it indicates that the changes in inertia and damping are too large for the current linearization and the step size is reduced by half. This process is repeated until the difference goes below a given threshold or until the step size becomes too small (i.e., $k = k_{\max}$). Once the linearization is validated, the acquired damping ratios $\tilde{\zeta}^\nu$ are compared against the threshold $\underline{\zeta}$. If $\tilde{\zeta}^\nu < \underline{\zeta}$, the optimizer computes the new allocation and the process continues until the damping ratios meet the given criteria; otherwise the optimization is completed.

As mentioned in Section 11.4.2, another improvement to the algorithm is introduced by continuously readjusting the upper and lower bounds on

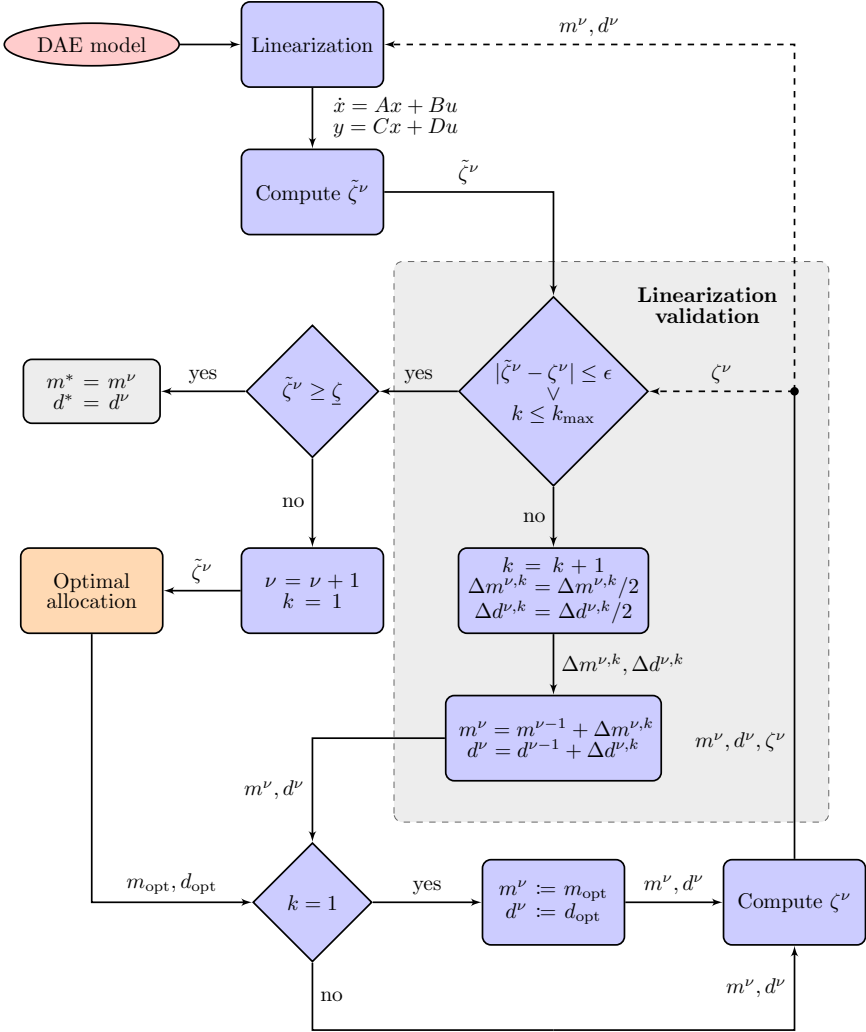


FIGURE 11.1: Flowchart of the employed iterative procedure in the second step of the multi-step approach.

incremental step changes $(\Delta m_j, \Delta \bar{m}_j, \Delta d_j, \Delta \bar{d}_j)$ between iterations, based on the damping ratio sensitivities represented by $\phi_j^d \in \mathbb{R}$ and $\phi_j^m \in \mathbb{R}$:

$$\phi_j^m = \frac{\frac{\partial \zeta_{\min}}{\partial m_j}}{\max_{j \in \mathcal{J}} \frac{\partial \zeta_{\min}}{\partial m_j}}, \quad \phi_j^d = \frac{\frac{\partial \zeta_{\min}}{\partial d_j}}{\max_{j \in \mathcal{J}} \frac{\partial \zeta_{\min}}{\partial d_j}}. \quad (11.30)$$

Such procedure assigns larger step limits to parameters with a greater impact on the damping ratio. In particular, this ensures that the virtual inertia and damping is added or removed only at converters with a substantial influence on dynamical performance of the system.

11.5 RESULTS

Similarly to previous studies on placement and effects of inertia and damping in low-inertia systems [153, 154, 282, 283], we investigate performance of the proposed optimization algorithms on a three-area system described in Chapter 5 and depicted in Fig. 5.4. In order to emulate different system conditions, two test cases are considered: (i) a *low-inertia* system with traditional SGs at nodes 1 and 5 and *grid-following* converter-interfaced generation at the remaining four generation nodes; (ii) a *no-inertia* system with a 100% inverter penetration, i.e., all six synchronous generators replaced by VSC units. Nonetheless, only converters at nodes 1 and 5 are operating in *grid-forming* mode, whereas the remaining VSCs are controlled as *grid-following* units. As previously pointed out, we assume that only the inertia and damping constants of converters are controllable, with the initial VSM parameters taken as $m_j^0 = 0.5$ s and $d_j^0 = 2$ p.u. respectively. The minimum permissible damping ratio is set at $\underline{\zeta} = 10\%$, whereas the thresholds enforced on maximum RoCoF and frequency deviation are $\bar{f}_{\max} = 1$ Hz/s and $\Delta\bar{f}_{\max} = 0.8$ Hz. The system is subjected to a disturbance ΔP , which is considered to be the worst-case power deficit caused by the loss of a single generator. For the purposes of this study it is assumed that the loss of synchronous generator occurs at node 1. Moreover, the respective upper and lower limits on incremental changes of inertia and damping at each iteration step are set at $\Delta\bar{m}_j = \Delta\bar{d}_j = 0.5$ and $\Delta\underline{m}_j = \Delta\underline{d}_j = -0.5$, respectively.

Several different case studies are conducted. Firstly, a comparison between the virtual gain allocations obtained for the simplified model of a low-inertia system employed in [154, 279, 282, 283] and the detailed model described in Chapter 2 is presented. Secondly, the performance of two proposed problem formulations on both test cases is investigated, together with the impact of frequency constraints on final distribution of virtual inertia and damping. Finally, the performance and convergence properties of the iterative algorithm from Section 11.4.4 are discussed.

11.5.1 *Simplistic vs Detailed Model*

The goal of this case study is to justify the need for a detailed system modeling when tackling the allocation of inertia and damping in a low-inertia system. First, the uniform optimization problem (11.27) is solved for the low-inertia test case described by the simplified model used in [154, 279, 282, 283]. Subsequently, the obtained allocation of inertia and damping is applied to the detailed model, with the corresponding eigenvalue spectrums of the most critical modes depicted in Fig. 11.2. The shaded region indicates the root loci area where the damping ratio is above the predefined threshold of 10%. It can clearly be seen that the dynamical properties of a full-order model are not completely preserved in a simplified model, indicated by several modes having an unsatisfactory damping ratio. In other words, while results of the proposed algorithm meet the targeted objectives when applied to a reduced-order system, the achieved dynamical characteristics do not translate to a more realistic model, therefore diminishing the effectiveness and practicality of any study employing the simplistic system representation. Moreover, similar discrepancies can be noticed between the optimal inertia and damping distribution for the two systems shown in Fig. 11.3, both in terms of total allocation of virtual gains as well as the placement in the network. Note that the allocation corresponding to the full-order model in Fig. 11.3 does not correspond to the respective eigenvalue spectrum in Fig. 11.2. More precisely, the distribution of inertia and damping in Fig. 11.3 is obtained by running the uniform optimization problem for each of the two model orders.

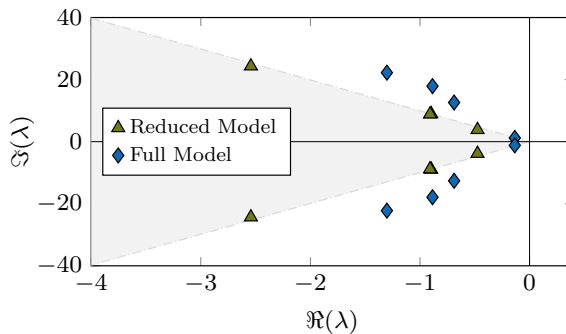


FIGURE 11.2: Eigenvalue spectrum close to imaginary axis of the reduced- and full-order models for the identical inertia and damping allocation.

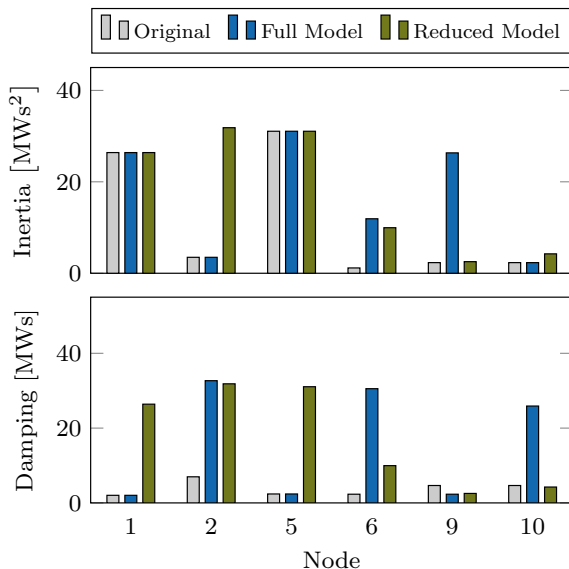


FIGURE 11.3: Optimal distribution of inertia and damping through uniform formulation when applied to full- and reduced-order models.

11.5.2 *Uniform vs Multi-Step Optimization*

Here, we analyze the performance of two optimization problems presented in Section 11.4, applied to both low- and no-inertia test cases. In order to gain better understanding of the sequential nature of the multi-step approach, we first study the outcome of each individual optimization step (11.24)-(11.26), with the respective distribution of inertia and damping illustrated in Fig. 11.4. In particular, Step 1 refers to individual VSM parameters necessary to obtain small-signal stability, Step 2 corresponds to optimal allocation ensuring the acceptable damping ratio and frequency response, whereas Step 3 minimizes the total control effort by redistributing the virtual inertia and damping across the network.

The algorithm is capable of bringing the system to stable operation by adding small amounts of inertia and damping at nodes 6 and 9, justified by the fact that controller states associated with VSCs at those nodes have the highest participation in the unstable modes. However, the dynamical performance of the system does not meet prescribed requirements due to low damping ratios and high values of RoCoF and frequency nadir. Therefore, in

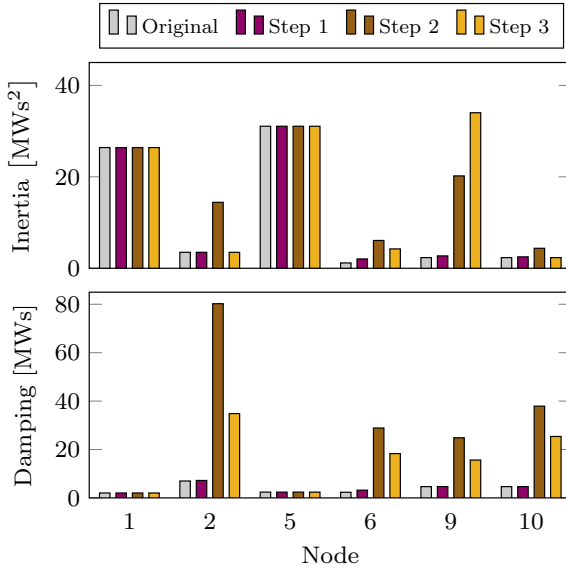


FIGURE 11.4: Optimal distribution of inertia and damping through multi-step optimization.

the next step, a considerable amount of inertia and damping is placed at every node with converter-interfaced generation, which resolves the aforementioned issues. Finally, Step 3 reduces the total amount of virtual inertia and damping by readjusting the control gains of all four VSCs, while still meeting the necessary frequency and damping ratio criteria. The optimizer reduces inertia and damping at nodes that have low or even negative sensitivities and redistributes it to nodes with a larger impact on the system damping ratio. Overall, the final step yields a more effective allocation compared to the second stage.

Having gained better understanding of the multi-step optimization approach, we can now compare its performance to the outcome of the uniform formulation. The eigenvalue spectrums in Fig. 11.5 indicate that the system is unstable at the start of the optimization (corresponding to the *original* allocation). Nevertheless, both formulations are capable of restoring stability and achieving satisfactory damping ratios and frequency response. Moreover, the total amount of virtual inertia and damping used by the two approaches remains the same, with the individual allocation differentiating between the

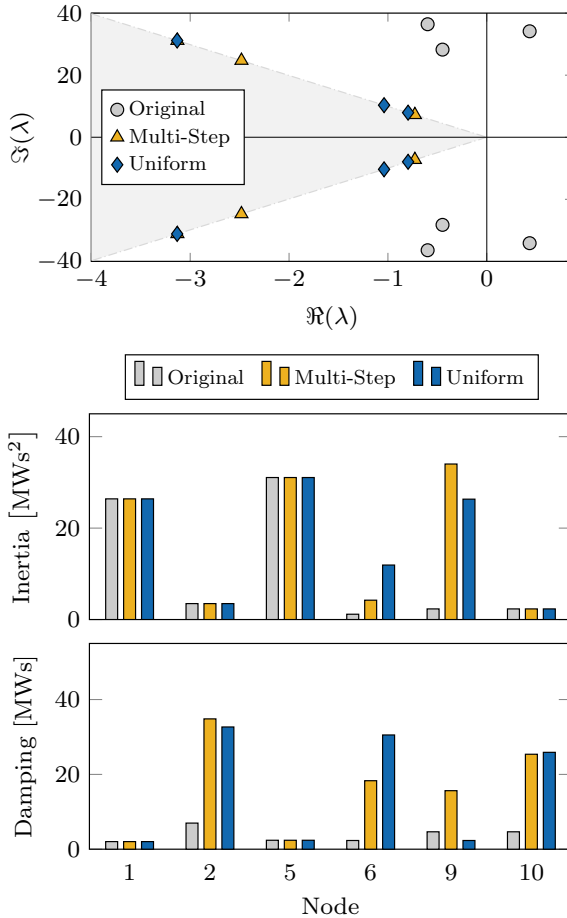


FIGURE 11.5: Comparison of uniform and multi-step formulation applied to a low-inertia system: critical eigenvalue spectrum (top) and allocation of inertia and damping (bottom).

two methods¹. This suggests that the frequency requirements, precisely RoCoF limit, act as binding constraints and impose a minimum aggregate inertia constant. Interestingly enough, in contrast to the multi-step approach and the

¹ The inertia and damping at nodes 1 and 5 remain intact due to the fact that only synchronous-generators are connected at these buses. Note that the color patterns are consistent throughout the study, i.e., yellow bars in Fig. 11.4 and Fig. 11.5 as well as blue bars in Fig. 11.3 and Fig. 11.5 are identical and correspond to the same solution.

addition of damping at all converter nodes, the uniform formulation increases virtual damping of only one VSC in each area, namely at nodes 2, 6 and 10. In general, the final inertia placement is such that the aggregate inertia in different areas is approximately the same. This qualitatively matches the results obtained in [153] and [154], where the distribution of inertia is similarly even across different areas. Nevertheless, no such correlation can be made for the allocation of virtual damping.

On the other hand, Fig. 11.6 showcases the performance of two algorithms under the no-inertia scenario, with the differences between the two allocations being more pronounced. Indeed, the multi-step approach yields a more even distribution of inertia but in turn employs more virtual damping. The underlying reason for such discrepancy lies in the problem formulation. In the multi-step approach, the cost for inertia and damping is only included in the final step, which resembles the most the optimization formulation of the uniform method. However, this also suggests that the starting point (and hence the computed sensitivities of interest) of the two algorithms will be different prior to the final step. In particular, due to no explicit cost for virtual control gains in the objective functions (11.24a) and (11.25a), the solution of the first two sequences of the multi-step approach will reach a local optimum with a substantially higher installation of inertia and damping. On the other hand, the uniform formulation ensures that at each iteration only the minimum (i.e., necessary) amount of virtual gains is added in order to meet the prescribed system-level constraints. This might result in an uneven allocation of the parameters across the system, as shown in Fig. 11.6, but it can easily be resolved by including an additional cost to promote the even distribution of inertia and damping.

Another distinction in the outcomes of two approaches is the placement of critical modes. In the multi-step approach, the critical eigenvalues are placed at the boundary of the shaded region, i.e., their damping ratios are close to the predefined threshold, whereas the uniform optimization results in critical modes being well within the shaded region. Due to the nature of the proposed problem formulation, the first few iterations of the multi-step approach focus on improving the frequency constraints, while the uniform method prioritizes the improvement of the damping ratio. Consequently, using the multi-step formulation the frequency criteria is met within fewer iterations compared to its uniform counterpart, and once the damping ratio is sufficiently high the optimization ends. In contrast, in the uniform approach the damping ratio criteria is satisfied first, with the optimization procedure continuing until the frequency limits (RoCoF in particular) are met. This results in higher

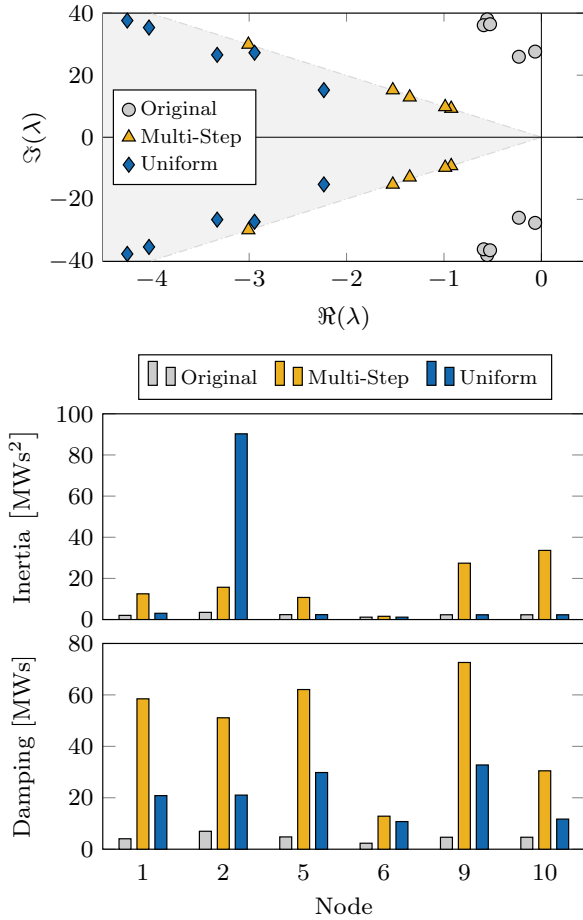


FIGURE 11.6: Comparison of uniform and multi-step formulation applied to a no-inertia system: critical eigenvalue spectrum (top) and allocation of inertia and damping (bottom).

final values of the damping ratios, as they are gradually increased over the course of remaining iterations. Nevertheless, such properties are not observed in the low-inertia test case (see Fig. 11.5) due to higher amount of inertia present in the system at the initialization stage, leading to lower RoCoF and frequency nadir values at the start of the optimization. Based on the previous analysis and due to its more generic problem formulation, we conclude that

the uniform approach is the preferred method of the two, and therefore only focus on this allocation concept in the remainder of the chapter.

11.5.3 *Impact of Frequency Constraints on Dynamical Performance*

The impact of frequency-related constraints, namely the limits on maximum permissible RoCoF and frequency nadir, on the final solution is investigated by applying the uniform optimization problem to the same two test cases, with and without the inclusion of frequency constraints in (11.25i)-(11.25k). Understandably, by removing the frequency constraints the critical modes in both scenarios are placed at the boundary of the region representing the set of acceptable damping ratios, as shown in Fig. 11.7 and Fig. 11.8. Moreover, the total amount of inertia and to some extent damping placed in the network is lower when the RoCoF and frequency nadir constraints are not considered. This effect is more pronounced in the no-inertia test case illustrated in Fig. 11.8, where the difference between the amount of inertia placed with and without taking frequency constraints into account is more significant. This is primarily due to the removal of the maximum RoCoF requirement, i.e., the minimum level of aggregate inertia needed in the network. In particular, the sensitivity of the minimum damping ratio to inertia and damping is in general of opposite sign, with the former being negative and latter being positive, which implies that the prescribed damping ratio criteria could be met by simultaneously reducing virtual inertia and damping gains at certain nodes. It goes to show that in converter-dominated power systems the allocation of inertia is mostly influenced by the RoCoF constraint, whereas the damping distribution is more relevant for preserving the frequency nadir within thresholds and improving the critical damping ratio.

Finally, the results of enforcing explicit limits on frequency metrics of interest can be observed in the system response following a disturbance, visualized in Fig. 11.9. The frequency response is significantly improved with the inclusion of frequency constraints, evidenced by lower values of RoCoF, frequency nadir and the steady-state frequency error, which is a direct consequence of the increased levels of inertia and damping present in the network. Moreover, it is noticeable that the RoCoF limit again poses as the binding constraint, with the frequency nadir being within prescribed bounds even for the optimal allocation scenario without the frequency limits.

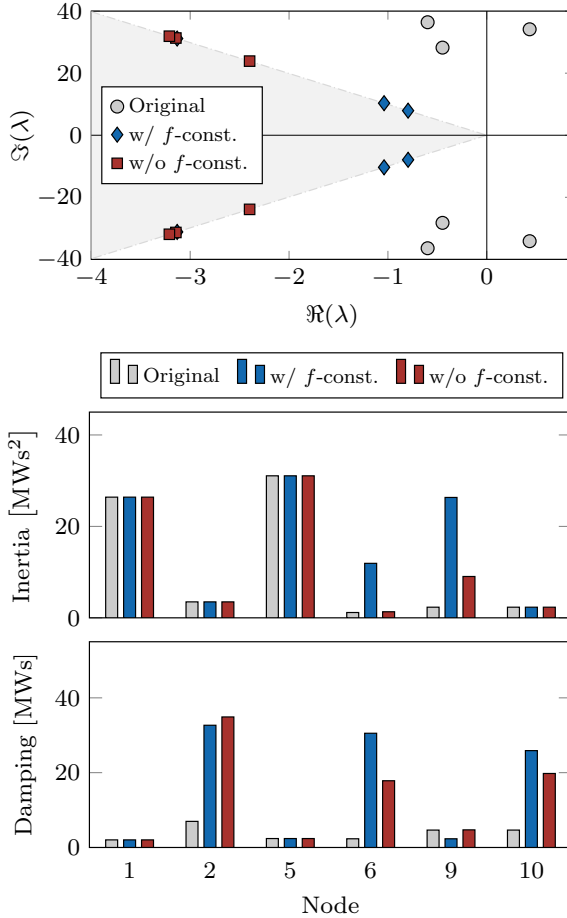


FIGURE 11.7: Impact of frequency constraints on allocation in the low-inertia system: critical eigenvalue spectrum (top) and distribution of inertia and damping (bottom).

11.5.4 Algorithm Performance and Convergence Properties

The performance of the uniform method on a low-inertia test case, as well as the impact of imposing frequency constraints, can be studied in more detail by observing the appropriate metrics given in Table 11.1. As previously discussed, the original system has low levels of aggregate inertia and damping and is small-signal unstable, indicated by the negative value of ζ_{\min} . Additionally,

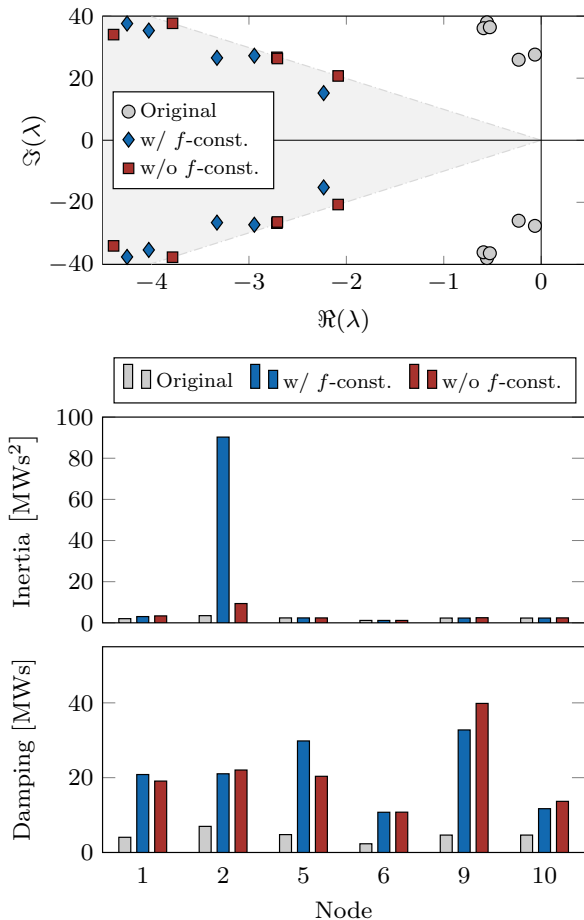


FIGURE 11.8: Impact of frequency constraints on allocation in the no-inertia system: critical eigenvalue spectrum (top) and distribution of inertia and damping (bottom).

the values of RoCoF and frequency nadir exceed the predefined thresholds and the system norms² are particularly high, suggesting an unacceptable frequency response in case of a disturbance. Note that the \mathcal{H}_∞ norm has been computed using the bisection method from Algorithm 4.

² Since the original system is unstable (resulting in $\|G\|_2 = \|G\|_\infty = \infty$), the system norms for this case are computed after employing the first stage of the multi-step formulation, i.e., bringing the system to stability.

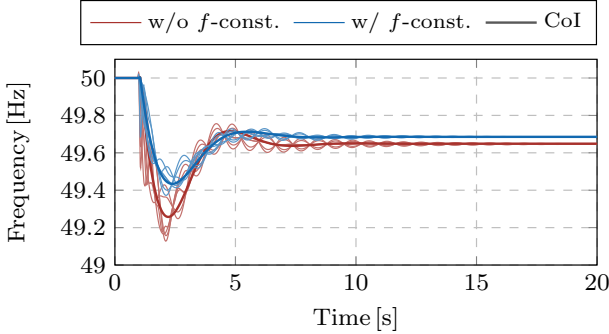


FIGURE 11.9: Comparison of frequency response after a disturbance for the cases with and without frequency constraints; thin lines represent individual generator frequencies, whereas thick lines denote the respective CoI frequency response.

By solving the optimization problem with frequency constraints, the total amount of inertia and damping in the system increases by 52 % and 316 %, respectively, which results in the worst-case damping ratio reaching the exact predefined threshold of 10 %. Moreover, the values of RoCoF and nadir are now within their acceptable limits, with RoCoF being at the prescribed boundary. As a consequence, the \mathcal{H}_2 and \mathcal{H}_∞ gains are substantially lower compared to their initial values. On the other hand, when the frequency constraints are not considered, the system inertia and damping increase by 8 % and 173 % respectively. While the total amount of employed virtual gains is lower in this case, the maximum RoCoF is unacceptably high and the

Metric	Original	w/ f -const.	w/o f -const.
Inertia [MWs ²]	66.8	101.5	72.3
Damping [MWs]	23	95.8	62.9
ζ_{\min}	-0.01	0.1	0.1
$ \dot{f}_{\max} $ [Hz/s]	1.59	1	1.4
$ \Delta f_{\max} $ [Hz]	2.17	0.58	0.76
\mathcal{H}_2 gain	18.8*	1.07	1.87
\mathcal{H}_∞ gain	3.71*	0.76	1.11

TABLE 11.1: Comparison of system performance metrics for the low-inertia test system and loss of synchronous generation at node 1.

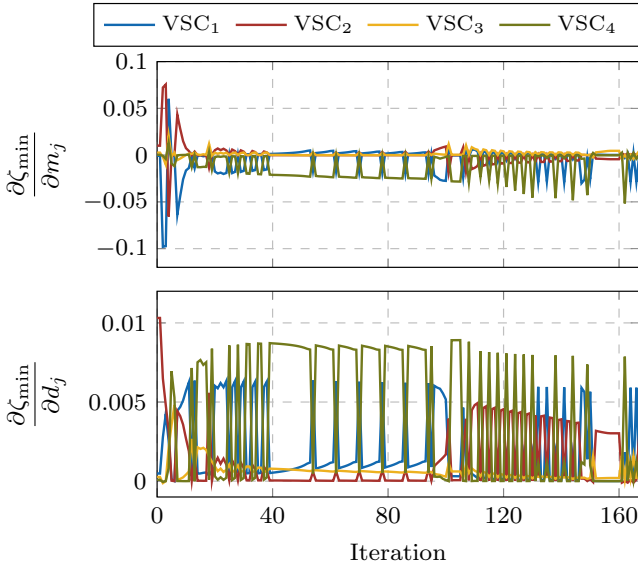


FIGURE 11.10: Sensitivity evolution of the worst-case damping ratio to virtual inertia and damping parameters of individual converters over iterations.

\mathcal{H}_2 and \mathcal{H}_∞ norms have larger values, thus suggesting a necessary trade-off between the control effort and dynamical performance.

Finally, we study numerical characteristics and convergence properties of the proposed algorithm. The sensitivities of the worst-case damping ratio with respect to virtual inertia and damping constants of converters are highly non-linear, illustrated by the evolution of respective sensitivities across iterations in Fig. 11.10. The oscillatory behavior justifies the need for adaptive step sizing of parameter updates and the techniques mentioned in Section 11.4.4. Another key inference is that the sensitivity of the damping ratio to inertia is in general negative and smaller in magnitude compared to the positive sensitivity to damping, which further supports the claim that damping is a more relevant control gain of the two for improving the damping ratios in the system.

Furthermore, the progressive iterative improvement of the worst-case damping ratio and the value of the \mathcal{H}_2 gain during the course of optimization are presented in Fig. 11.11. An important observation is that the rate-of-change of the worst-case damping ratio varies considerably as a direct consequence

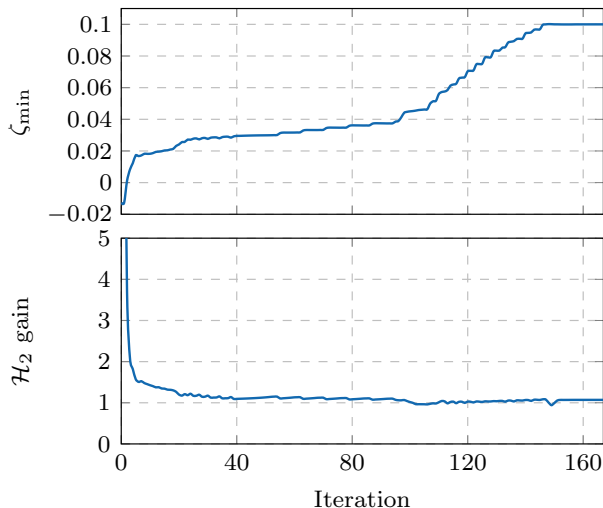


FIGURE 11.11: Evolution of the worst-case damping ratio and system \mathcal{H}_2 norm over iterations.

of the oscillatory nature of sensitivities from Fig. 11.10. Moreover, the increase in the damping ratio and the reduction of RoCoF and frequency nadir lead to a more desirable frequency response, which in turn contributes to the improvement of system norms. This validates the claims pertaining to similarities between improving the damping ratio and system norms raised in Section 11.3, since maximizing the damping ratio while simultaneously limiting the frequency response metrics achieves a similar target as directly minimizing the \mathcal{H}_2 and \mathcal{H}_∞ norms in [154]. However, the proposed approach imposes lower computational requirements and can be directly applied to realistic low-inertia systems. Further inspection of Fig. 11.11 reveals that during the last 15 iterations the worst-case damping ratio and the \mathcal{H}_2 norm are fairly constant. This segment indicates the process of inertia and damping redistribution, i.e., the minimization of the employed control effort.

11.6 CONCLUSION

In this chapter, we improve the dynamic performance of an inverter-dominated power system by optimally allocating additional virtual inertia and damping across the network. We tackle this problem by formulating an optimization problem based primarily on the sensitivities of damping ratios to inertia

and damping constants of individual generators. Moreover, we consider several additional performance metrics such as the frequency nadir, RoCoF and small-signal stability, and incorporate them as explicit constraints into two conceptually different problem formulations. To overcome the inherent nonlinearity associated with eigenvalue optimization, the sequential iterative method was employed. The improvements in terms of multi-objective nature of the problem, computational efficiency and adaptive step-size adjustments have also been made.

The results indicate that the simplified system models, commonly used in the literature, do not accurately capture the dynamics of a power system with both conventional and converter-interfaced generation. In other words, a detailed representation of low-inertia grids is needed when dealing with inertia and damping allocation problems, which poses issues for the existing methods based on minimizing the system norms. While conceptually different, both proposed formulations provide meaningful results and insightful observations in terms of the overall impact of different VSM control gains and frequency-related constraints on system dynamics. However, due to its more generic formulation and multifaceted objective function, we conclude that the uniform approach is the preferred method of the two. Moreover, we show that by improving the worst-case damping ratio and constraining the frequency metrics of interest, the algorithm also achieves a significant reduction of \mathcal{H}_2 and \mathcal{H}_∞ norms, therefore combining the objectives and targets of various studies in the literature within a single optimization problem.

STOCHASTIC UNIT COMMITMENT FORMULATION FOR LOW-INERTIA SYSTEMS

This chapter studies the Unit Commitment (UC) problem in a power network with low levels of rotational inertia. Frequency-related constraints, derived from a uniform frequency response model of such system, are included into a stochastic UC formulation that accounts for wind power and equipment contingency uncertainties using a scenario-tree approach. In contrast to the linear RoCoF and steady-state frequency error constraints, the nadir constraint is highly nonlinear. To preserve the mixed-integer linear formulation of the stochastic UC model, we propose a computationally efficient approach that allows to recast the nadir constraint by introducing appropriate bounds on relevant decision variables of the UC model. This method is shown to be generally more accurate and computationally more efficient for medium-sized networks than a piece-wise linearization method adapted from the literature. Simulation results for a modified IEEE RTS-96 system reveal that the inclusion of inertia-related constraints significantly influences the UC decisions and increases total costs, as more synchronous machines are forced to be online to provide inertial response. The chapter is based on [293].

12.1 INTRODUCTION

With increasing penetration of renewable energy sources, transmission system operators around the world face new challenges in order to ensure power grid stability under low-inertia conditions. A particular focus is set on resolving frequency stability issues due to a sudden loss of generation or a large variation of load. In the United States, the Electric Reliability Council of Texas (ERCOT) has studied the effect of low inertia on the security and reliability of the grid [4]. As the system inertia at ERCOT continues to decrease with the growth of wind generation, multiple technical solutions have been explored to mitigate the adverse impact on frequency control performance. Most notably, bringing more synchronous inertia online by committing additional units, committing different units that have higher inertia, or using synchronous

condensers, as well as slowing down the RoCoF after an event (e.g., generator trip) by increasing the rate of primary frequency response of the system. Moreover, ERCOT has recently altered the methodology for determining Responsive Reserve Service (RRS) from procuring a constant reserve for all hours to determining necessary amounts of RRS dynamically based on expected system inertia conditions. On the other hand, the Irish TSO (EirGrid) is designing new ancillary services to remunerate providers of rotational or synthetic inertia [294, 295]. EirGrid also currently imposes limits on the maximum instantaneous penetration of variable RES with respect to the total load demand at any point in time.

In systems with low rotational inertia, TSOs must impose minimum inertia requirements in order to secure frequency stability and avoid system collapse in case of a severe fault or a sudden mismatch between generation and demand. With such new requirements, the traditional UC problem, i.e., the day-ahead scheduling process to decide which generators will be committed, may be affected as more synchronous generators could be dispatched for the sole purpose of providing inertia. Nonetheless, the *ex-ante* definition of inertia and reserve requirements to cope with the sudden deviations from generation outages and renewables' forecast errors, respectively, is a challenging task due to the uncertain nature of these imbalances. To this end, we adopt a stochastic version of the UC problem that can endogenously account for the aforementioned uncertainty sources via a set of scenarios that model plausible equipment contingencies and renewables' forecast errors. In turn, this model can pre-position the flexible system resources at the day-ahead stage, without resorting to deterministic reserve requirements, in a way that improves the response to the real-time variations and minimizes the expected system cost.

Several studies have approached the problem of including inertia requirements in the UC problem. In [296–298], the authors use the CoI swing equation, which allows them to derive a RoCoF constraint and analyze its effect on the UC schedule. However, this approach oversimplifies the problem as it neglects metrics related to frequency deviation from the setpoint. This problem was addressed in [150, 299–302] with the inclusion of a constraint limiting the post-disturbance maximum frequency deviation (i.e., frequency nadir). In [150], the analytic form of frequency nadir as a function of active power disturbance is derived using a system frequency model obtained from [303]. The nadir expression is then linearized and added to the UC model, while considering a fixed sudden load increase. On the other hand, the studies in [299–302] bypass the explicit modeling of turbine and governor control as well as their impact on frequency dynamics by imposing

strict assumptions on system damping and total frequency response provision at each node. Moreover, the primary frequency response provision by SGs (essentially droop control) is approximated by a constant ramp function of time in order to decouple the governor control from frequency and simplify the analytic formulation of the problem. In addition, [302] optimizes the energy production and multi-speed allocation of frequency response services, whereas [299] looks at the impact of wind uncertainty on inertia requirements. While the proposed simplifications enable the inclusion of a nadir constraint without the explicit consideration of second-order frequency dynamics, they oversimplify the actual control implementation and disregard the aggregate impact of governor damping. Furthermore, none of the aforementioned studies incorporates the converter interface of RES and the impact of respective control schemes on the UC formulation.

The contributions of this chapter are threefold. Firstly, we improve the frequency dynamics model in [150] by including the realistic control schemes of inverter-based generation, more specifically VSM and droop control. In contrast to the existing literature, where SG inertia and damping constants are usually numerically modified in order to compensate for high RES integration, we analyze a realistic model of a low-inertia system comprising dynamic models of both synchronous and converter-based generators. This allows us to employ the analytic expressions of relevant frequency metrics (see Chapter 5) as functions of multiple system variables (e.g., inertia, damping, aggregate droop gain, etc.) to be determined by the UC model, as opposed to the approach in [299] where the inertia constant was the only decision variable of interest. Moreover, in addition to frequency nadir and RoCoF, we incorporate the limitation on quasi steady-state frequency deviation into the UC formulation. No prior work considers the dynamics and controls of virtual inertia units in the derivation of frequency constraints for inclusion in UC and hence this is the main contribution of the chapter. Secondly, a more straightforward method is proposed to extract bounds for decision variables contributing to frequency nadir, which allows us to incorporate the nonlinear nadir constraint in the UC problem in a more accurate way compared to [150], while at the same time reducing the computational burden for mid-sized systems. Finally, similar to [299], this chapter includes both the wind uncertainty and potential loss of generation in the UC model. However, we present a more comprehensive approach towards event probability computation and structuring of the scenario tree for the two-stage stochastic UC problem.

The rest of the chapter is structured as follows. In Section 12.2, the approximation of the nonlinear frequency nadir constraint for the purposes

of unit commitment is discussed. The modeling of uncertainties, namely equipment failure and wind power, in the form of probabilistic scenarios is presented in Section 12.3. Section 12.4 provides the mathematical formulation of the stochastic UC problem. Finally, Section 12.5 presents and discusses the simulation results using a modified version of the IEEE RTS-96 system, whereas Section 12.6 draws the main conclusions and discusses the outlook of the study.

12.2 FORMULATION OF FREQUENCY CONSTRAINTS

Let us recall the uniform frequency model and its respective notation from Chapter 5. The accuracy of such model has already been investigated and verified in Section 5.4.1. Moreover, it was concluded that the frequency metrics of interest are directly dependent on the average system parameters $M \in \mathbb{R}_{>0}$, $D \in \mathbb{R}_{>0}$, $R_g \in \mathbb{R}_{>0}$ and $F_g \in \mathbb{R}_{\geq 0}$, and thus they could be regulated through the UC model. In particular, RoCoF and steady-state deviation can be explicitly controlled via $\dot{f}_{\max} \sim M^{-1}$ and $\Delta f_{\text{ss}} \sim (D + R_g)^{-1}$, while nadir can be modeled using a highly nonlinear function $\Delta f_{\max}(M, D, R_g, F_g)$. Therefore, by incorporating the frequency metrics in the UC problem, we are able to make the day-ahead generator commitment decisions that ensure satisfactory real-time frequency response in case of outages.

The aforementioned frequency expressions (5.9)-(5.11) are incorporated as constraints into the stochastic UC problem, converted into SI and bounded by prescribed ENTSO-E thresholds [152], as follows:

$$\left| \frac{f_0 \Delta P}{D + R_g} \left(1 + \sqrt{\frac{T(R_g - F_g)}{M}} e^{-\zeta \omega_n t_m} \right) \right| \leq \Delta f_{\text{lim}}, \quad (12.1a)$$

$$\left| \frac{f_0 \Delta P}{M} \right| \leq \dot{f}_{\text{lim}}, \quad (12.1b)$$

$$\left| \frac{f_0 \Delta P}{D + R_g} \right| \leq \Delta f_{\text{ss,lim}}. \quad (12.1c)$$

Here, $f_0 = 50$ Hz is the base frequency, $\Delta f_{\text{lim}} = 0.4$ Hz represents the under-frequency load shedding trigger, while $\dot{f}_{\text{lim}} = 0.5$ Hz/s and $\Delta f_{\text{ss,lim}} = 0.2$ Hz are the maximum permissible RoCoF and steady-state frequency deviation.

Constraints (12.1b) and (12.1c) are linear, unlike the nonlinear frequency nadir constraint (12.1a). In order to avoid the high computational burden of a Mixed-Integer Non-Linear Program (MINLP) formulation and have a measurable optimality gap, we use a linear approximation of (12.1a) which

allows us to maintain a Mixed-Integer Linear Program (MILP) formulation of the stochastic UC problem. By integrating (12.1) in the UC problem, we are able to capture the system's real-time dynamic boundary conditions already in the day-ahead UC scheduling phase in a way that improves frequency response and minimizes the risk of load shedding.

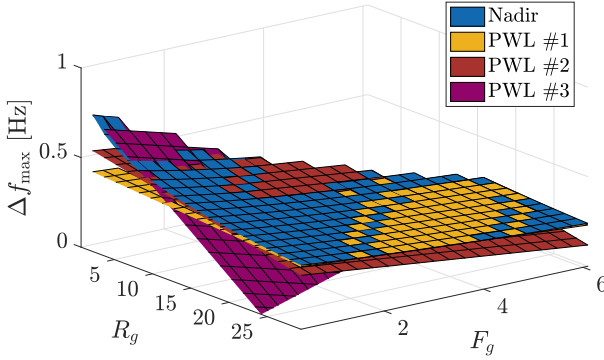
12.2.1 Piecewise Linearization of Nadir Expression

The study in [150] proposes a Piece-Wise Linearization (PWL) technique for obtaining a linearized expression for frequency nadir in order to subsequently integrate it into a UC problem. To improve clarity, this technique is outlined here before comparing its computational burden against our proposed approach introduced in Section 12.2.2. Note that the frequency nadir expression (12.1a) is a function of four UC decision variables (R_g, F_g, M, D), and as such too complicated to be directly handled by the PWL. Considering that the aggregate damping constant is of the form $D(D_{g_i}, R_{g_i}, D_{c_j}, R_{c_j})$, with respective damping (D_{g_i}, D_{c_j}) and droop (R_{g_i}, R_{c_j}) gains (see Section 5.2 for more details) usually strictly prescribed within narrow ranges by the system operator, it is justifiable to assume a constant D . Therefore, the frequency nadir becomes a function of three variables, i.e., $\Delta f_{\max}(M, R_g, F_g)$, and the PWL formulation aims to minimize the following objective function:

$$\min_{\Psi} \sum_{\eta \in \mathcal{H}} \left(\max_{\nu \in \mathcal{V}} \left\{ a_{\nu} R_g^{(\eta)} + b_{\nu} F_g^{(\eta)} + c_{\nu} M^{(\eta)} + d_{\nu} \right\} - \Delta f_{\max} \left(R_g^{(\eta)}, F_g^{(\eta)}, M^{(\eta)} \right) \right)^2, \quad (12.2)$$

with $\Psi = (\Psi_1, \dots, \Psi_{\eta}) \in \mathbb{R}^{4\eta}$ being the vector of optimization variables and $\Psi_{\nu} := (a_{\nu}, b_{\nu}, c_{\nu}, d_{\nu}) \in \mathbb{R}^4$ describing the PWL approximation of segment $\nu \in \mathcal{V} \subset \mathbb{Z}_{>0}$; $(R_g^{(\eta)}, F_g^{(\eta)}, M^{(\eta)}) \in \mathbb{R}_{>0}^3$ denotes the vector of respective evaluation points $\forall \eta \in \mathcal{H} \subset \mathbb{Z}_{>0}$. The objective function (12.2) penalizes the difference between the appropriate PWL segment and the nadir function at all evaluation points. Given the convex nature of the nadir function, the inner "max" operator chooses the appropriate PWL segment for each evaluation point by looking at which segment is closest to the curve at that specific point. To improve understanding, we elaborate on the mathematical formulation and the practical implementation of the PWL from [150] in Appendix B.5.

Upon obtaining the optimal solution of the model (12.2), the nadir constraint can be integrated into the MILP UC model by adding a set of in-

FIGURE 12.1: PWL of the nadir constraint for $M = 9$ s.

equalities, along with the nadir threshold constraint of the form $f_0 t_3 \leq \Delta f_{\text{lim}}$ (see the definition of t_3 in Appendix B.5). The results for the approximation of frequency nadir function for a test system of 20 generators described in Section 12.5 are presented in Fig. 12.1, where a loss of the largest unit is considered. Note that Fig. 12.1 showcases the surface plot for a fixed inertia constant M and thus ignores one degree of freedom. The original surface is presented in blue, whereas its PWL-approximation segments are the planes depicted in various colors. It is important to note that the optimization problem (12.2) is computationally intensive and thus, in order to obtain results within reasonable computational time, the number of PWL segments used for the approximation as well as the number of evaluation points have to be kept low.

12.2.2 Extracting Bounds on Relevant Variables

An alternative approach for linearizing the nadir constraint and integrating it into the UC problem is to confine the values of R_g , F_g , M and D within a plausible range to guarantee that the nadir threshold in (12.1a) is not violated. With this approach the damping variable D can easily be included and does not need to be set constant. The scatter plot presented in Fig. 12.2 reflects all possible values of frequency nadir after the loss of the largest generator, for the same system as in Section 12.2.1. In the general case, for a system that comprises $|\mathcal{I}|$ generators, there will be $2^{|\mathcal{I}|-1}$ possible generator commitment combinations after a generator outage. By obtaining the set of

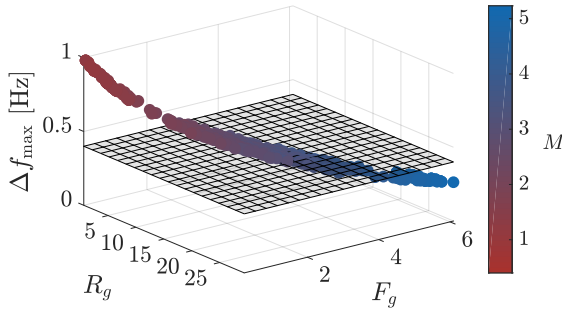


FIGURE 12.2: All possible values of frequency nadir after a generator loss.

these dispatch combinations, the values of R_g , F_g , M and D at which the UFLS threshold is not violated can be extracted, corresponding to the points below the shaded plane in Fig. 12.2. Subsequently, these values are used to substitute the nadir constraint in the unit commitment as follows:

$$F_g \geq F_g^{\text{lim}}, \quad R_g \geq R_g^{\text{lim}}, \quad M \geq M^{\text{lim}}, \quad D \geq D^{\text{lim}}. \quad (12.3)$$

The proposed method provides increased accuracy for the introduction of frequency nadir as a constraint in the UC problem. Indeed, as every possible generator combination is calculated after the loss of any single generator in the system, the exact values of frequency nadir are known and thus the constraint will not introduce any error in the optimization.

Table 12.1 provides a comparison of the proposed method to the PWL technique in terms of computational time that is needed to obtain the equivalent linear nadir expression for a single value of the disturbance magnitude ΔP . It is clear that the PWL is more computationally intensive, especially when aiming for an increased precision. In fact, running the PWL method with more than $|\mathcal{H}| = 4$ evaluation points and $|\mathcal{V}| = 4$ linear segments was not computationally possible using a standard laptop computer. It should be noted though that for very large systems, the calculation of $2^{|\mathcal{Z}|-1}$ combinations for the bound extraction method would become more computationally expensive, as the computation time increases by a factor of $2^{|\Delta\mathcal{Z}|}$ for every additional $|\Delta\mathcal{Z}|$ generators included in the system.

Nevertheless, the computational effort of the bounds extraction method could be drastically reduced through certain simplifications, therefore making it tractable on a larger scale. For instance, many combinations of committed

Linearization technique	Computational time [s]
PWL ($ \mathcal{H} = 3, \mathcal{V} = 4$)	70
PWL ($ \mathcal{H} = 4, \mathcal{V} = 4$)	7200
Bound extraction	20

TABLE 12.1: Computational cost of the linearization methods.

generation could be immediately discarded if they do not meet prescribed RoCoF limits at the instance of the disturbance. In particular, one should consider only the system dispatch with aggregate inertia above $M_{\min} = |\Delta P|/\dot{f}_{\text{lim}}$, which could easily be incorporated into the bound extraction scheme. It should also be noted that the computational burden arises solely from the sheer number of all possible generation commitment schedules, and the calculation of frequency nadir for each individual scenario can be done independently. Therefore, parallelization techniques can be readily employed to speed up the overall computation and improve the tractability of the proposed approach.

For the purposes of this chapter, the proposed bound extraction method will be used as it is significantly faster and introduces less error when applied to the 20-generator test system under investigation.

12.3 EQUIPMENT FAILURE AND WIND POWER UNCERTAINTY

This section describes the modeling of uncertainty pertaining to equipment failure and wind power production during power system operation. The uncertain nature of wind power production is modeled using a set of scenarios $\mathcal{W} \subset \mathbb{Z}_{>0}$ that captures the spatio-temporal interdependence of forecast errors, for every wind farm location and during the whole scheduling horizon. Each wind power realization scenario $\omega \in \mathcal{W}$ has the same probability of occurrence denoted by $\pi_{\omega} \in \mathbb{R}_{\geq 0}$.

In terms of equipment failure uncertainty, we consider as the set of credible contingencies the unforeseen outages of synchronous generators, whereas transmission assets are assumed to be 100% reliable. In order to reduce the computational burden, we follow the assumption from [304] considering that the generation outages happen at a discrete time period, while failed assets remain unavailable for the rest of the scheduling horizon, i.e., the Mean Time To Repair (MTTR) is greater than the scheduling horizon of the day-ahead electricity market. For the purpose of assessing the impact

of frequency constraints on the unit commitment schedule, we consider as contingency period the one in which the power system faces the highest wind power penetration, as scarcity of inertia is most likely to occur during this time due to the displacement of synchronous generators from the day-ahead schedule.

Let us define $\pi_{c_\kappa} \in \mathbb{R}_{\geq 0}$ as the probability associated with contingency scenario $c_\kappa \in \mathcal{K} \subset \mathbb{Z}_{\geq 0}$, where \mathcal{K} describes the set of credible contingencies. We denote by $A(\kappa, \tau)$ the random event of contingency c_κ happening within time period τ . Random event $B(\kappa)$ corresponds to contingency c_κ not occurring during the entire scheduling horizon. We further declare $\lambda_\kappa \in \mathbb{R}_{\geq 0}$ as the inverse of the Mean Time To Failure (MTTF) of contingency c_κ , i.e., $\lambda_\kappa := 1/\text{MTTF}_\kappa$. Considering that we are looking at only one hour during which the outages may occur, and assuming that the time between two consecutive equipment failures follows an exponential distribution [305], the probability π_{c_κ} for each contingency scenario c_κ is derived from the probabilities of occurrence of random events $A(\kappa, \tau)$ and $B(\kappa)$, calculated using the following expressions according to [306]:

$$\pi[A(1, \tau)] = \exp(-\lambda_1 \tau)(\exp(\lambda_1) - 1), \quad (12.4a)$$

$$\pi[A(1, \tau)] = \pi[A(2, \tau)] = \dots = \pi[A(|\mathcal{K}|, \tau)], \quad (12.4b)$$

$$\pi[B(1)] = \exp(-\lambda_1 \tau), \quad (12.4c)$$

$$\pi[B(1)] = \pi[B(2)] = \dots = \pi[B(|\mathcal{K}|)]. \quad (12.4d)$$

Assuming statistical independence between all contingencies, the probability π_{c_0} of the no-contingency scenario is equal to

$$\pi_{c_0} = \prod_{c_\kappa \in \mathcal{K}} \pi[B(\kappa)], \quad (12.5)$$

while the probability π_{c_κ} of losing a generator is equal to

$$\pi_{c_\kappa} = \pi[A(1, \tau)] \prod_{\substack{c_y \in \mathcal{K} \\ y \neq \kappa}} \pi[B(y)], \quad \forall c_\kappa \in \mathcal{K}. \quad (12.6)$$

It should be noted that the sum of probabilities π_{c_0} and π_{c_κ} is lower than 1, since sequential contingencies are not considered. For instance, setting MTTF equal to 1000 h for all generators yields $\pi[A(\kappa, \tau)] = 0.9995 \times 10^{-3}$ and $\pi[B(\kappa)] = 0.9990$ from (12.4). According to (12.5)-(12.6), we obtain respectively $\pi_{c_0} = 0.9960$ and $\pi_{c_\kappa} = 0.9965 \times 10^{-3}$ and thus $\sum_{\kappa=0}^4 \pi_{c_\kappa} = 0.9999 \approx 1$.

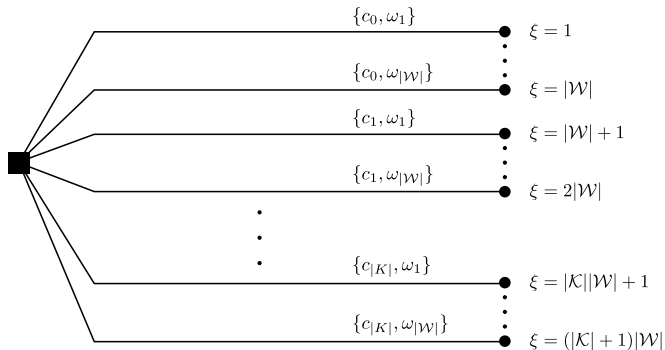


FIGURE 12.3: Scenario tree for the two-stage stochastic UC problem.

Combining the scenarios modeling the equipment failure and wind power uncertainty into a single scenario set \mathcal{E} , we define each scenario $\xi \in \mathcal{E}$ as a pair of contingency c_κ and wind power realization ω . For each $\xi = \{c_\kappa, \omega\}$ the corresponding probability of occurrence is given by $\pi_\xi = \pi_\omega \pi_{c_\kappa}$ and $\sum_{\xi \in \mathcal{E}} \pi_\xi \approx 1$, assuming that equipment outages and wind power production are statistically independent events. The structure of the scenario set \mathcal{E} used in the stochastic UC formulation is given in the form of scenario tree illustrated in Fig. 12.3, for $|\mathcal{K}|$ contingencies and $|\mathcal{W}|$ wind power scenarios.

12.4 STOCHASTIC UNIT COMMITMENT

This section provides the mathematical formulation of the stochastic unit commitment [307], with the addition of frequency-related constraints. The main notation is introduced in Table 12.2 and additional symbols are defined in the chapter where needed. All symbols are augmented by index $t \in \mathcal{T}$ when referring to different time periods.

Symbol	Unit	Description
$l \in \mathcal{L}$	-	Set of transmission lines
$\xi \in \mathcal{E}$	-	Set of scenarios with generation outages and wind uncertainty
$i \in \mathcal{I}$	-	Set of conventional generation units
$j \in \mathcal{J}$	-	Set of converter-based (i.e., wind) generation units
$n \in \mathcal{N}$	-	Set of nodes
\mathcal{I}_n	-	Set of conventional generation units located at bus n
\mathcal{J}_n	-	Set of converter-based units located at bus n
δ_n	rad	Day-ahead voltage angle at node n
$\hat{\delta}_{n\xi}$	rad	Real-time voltage angle at node n in scenario ξ
$F_{\xi t}$	-	Fraction of power generated by high-pressure turbines in scenario ξ
$k_{i\xi t}$	-	Scaled power gain factor of conventional unit i ξ
$l_{n\xi t}^{\text{shed}}$	MW	Shedding of load at node n in scenario ξ
$M_{\xi t}/D_{\xi t}$	s/p.u.	Aggregate inertia and damping of conventional generators in scenario ξ
p_{it}	MW	Day-ahead dispatch of conventional unit i
$r_{i\xi t}^{+/-}$	MW	Up-/Downward reserve deployment of unit i in scenario ξ
$R_{\xi t}$	-	Global system droop factor in scenario ξ
u_{it}	-	Commitment status of conventional unit i
w_{jt}	-	Day-ahead dispatch of wind power unit j [MW]
$w_{j\xi t}^{\text{spill}}$	MW	Wind spillage of unit j in scenario ξ
y_{it}	-	Start-up variable of conventional unit i
z_{it}	-	Shut-down variable of conventional unit i
$\alpha_{i\xi t}$	-	Outage parameter of conventional unit i in scenario ξ
$\Delta P_{\xi t}$	-	Size of power outage in scenario ξ
π_{ξ}	-	Probability of occurrence of scenario ξ
B_{nm}	S	Susceptance of transmission line (n, m)
C_i	\$/MWh	Day-ahead price offer of unit i
$C_i^{\text{SU/SD}}$	\$	Start-up/Shut-down price offer of unit i
$C_i^{+/-}$	\$/MWh	Up-/Downward reserve price offer of unit i
C^{sh}	\$/MWh	Value of lost load
L_{nt}	MW	Load demand at node n
\bar{f}_{nm}	MW	Capacity of transmission line (n, m)
P_i	MW	Active power capacity of conventional unit i
$\bar{P}_i/\underline{P}_i$	MW	Active power limits of conventional unit i
$R_i^{+/-}$	MW	Up-/Downward reserve capacity of unit i
$R_i^{\text{U/D}}$	MW/h	Ramp up/down limits of conventional unit i
$W_{j\xi t}^*$	MW	Wind power realization of unit j in scenario ξ
W_{d_j}	MW	Active power capacity of droop-controlled converter unit j
W_{v_j}	MW	Active power capacity of VSM-controlled converter unit j

TABLE 12.2: Unit commitment nomenclature of Chapter 12.

The proposed model is a two-stage stochastic optimization problem of the form:

$$\min_{\Phi} \sum_{t \in \mathcal{T}} \sum_{i \in \mathcal{I}} (C_i^{\text{SU}} y_{it} + C_i^{\text{SD}} z_{it} + C_i p_{it}) + \sum_{t \in \mathcal{T}} \sum_{\xi \in \mathcal{E}} \pi_{\xi} \left[\sum_{i \in \mathcal{I}} (C_i^+ r_{i\xi t}^+ - C_i^- r_{i\xi t}^-) + \sum_{n \in \mathcal{N}} C^{\text{sh}} l_{n\xi t}^{\text{shed}} \right] \quad (12.7a)$$

s.t. $\forall t \in \mathcal{T}, \forall i \in \mathcal{I}, \forall n \in \mathcal{N}, \forall m : (n, m) \in \mathcal{L}, \forall \xi \in \mathcal{E},$

$$\sum_{i \in \mathcal{I}_n} p_{it} + \sum_{j \in \mathcal{J}_n} w_{jt} - L_{nt} - \sum_{m: (n,m) \in \mathcal{L}} B_{nm} (\delta_{nt} - \delta_{mt}) = 0, \quad (12.7b)$$

$$B_{nm} (\delta_{nt} - \delta_{mt}) \leq \bar{f}_{nm}, \quad (12.7c)$$

$$u_{it} - u_{i(t-1)} \leq u_{i\tau_i^1}, \quad (12.7d)$$

$$u_{i(t-1)} - u_{it} \leq 1 - u_{i\tau_i^0}, \quad (12.7e)$$

$$y_{it} \geq u_{it} - u_{i(t-1)}, \quad (12.7f)$$

$$z_{it} \geq u_{i(t-1)} - u_{it}, \quad (12.7g)$$

$$\sum_{i \in \mathcal{I}_n} \left[r_{i\xi t}^+ - r_{i\xi t}^- - p_{it} (1 - \alpha_{i\xi t}) \right] + \sum_{m: (n,m) \in \mathcal{L}} B_{nm} (\hat{\delta}_{nt} - \hat{\delta}_{n\xi t} - \delta_{mt} + \hat{\delta}_{m\xi t}) \quad (12.7h)$$

$$+ \sum_{j \in \mathcal{J}_n} (W_{j\xi t}^* - w_{jt} - w_{j\xi t}^{\text{spill}}) + l_{n\xi t}^{\text{shed}} = 0, \quad (12.7i)$$

$$p_{it} + r_{i\xi t}^+ \leq \bar{P}_i u_{it}, \quad (12.7i)$$

$$p_{it} - r_{i\xi t}^- \geq \underline{P}_i u_{it}, \quad (12.7j)$$

$$p_{it} - p_{i(t-1)} + r_{i\xi t}^+ - r_{i\xi(t-1)}^+ \leq R_i^{\text{U}}, \quad (12.7k)$$

$$p_{it} - p_{i(t-1)} - r_{i\xi t}^- + r_{i\xi(t-1)}^- \geq -R_i^{\text{D}}, \quad (12.7l)$$

$$r_{i\xi t}^+ \leq R_i^+ \alpha_{i\xi t}, \quad (12.7m)$$

$$r_{i\xi t}^- \leq R_i^- \alpha_{i\xi t}, \quad (12.7n)$$

$$B_{nm} (\hat{\delta}_{n\xi t} - \hat{\delta}_{m\xi t}) \leq \bar{f}_{nm}, \quad (12.7o)$$

$$w_{j\xi t}^{\text{spill}} \leq w_{j\xi t}, \quad (12.7p)$$

$$l_{n\xi t}^{\text{shed}} \leq D_{nt}, \quad (12.7q)$$

$$k_{i\xi t} = \frac{P_i K_i}{\sum_{i \in \mathcal{I}} P_i} u_{it} \alpha_{i\xi t}, \quad (12.7r)$$

$$F_{\xi t} = \sum_{i \in \mathcal{I}} \frac{F_i k_{i\xi t}}{R_i}, \quad (12.7s)$$

$$R_{\xi t} = \sum_{i \in \mathcal{I}} \frac{k_{i\xi t}}{R_i}, \quad (12.7t)$$

$$M_{\xi t} = \sum_{i \in \mathcal{I}} \frac{2H_i k_{i\xi t}}{K_i}, \quad (12.7u)$$

$$D_{\xi t} = \sum_{i \in \mathcal{I}} \frac{D_i k_{i\xi t}}{K_i}, \quad (12.7v)$$

$$\frac{\dot{f}_{\text{lim}}}{f_0} \frac{M_{\xi t} \sum_{i \in \mathcal{I}} P_i + M_v W_v}{\sum_{i \in \mathcal{I}} P_i + W_v} \geq |\Delta P_{\xi t}|, \quad (12.7w)$$

$$F_{\xi t} \geq F_{\xi t}^{\text{lim}}, \quad R_{\xi t} \geq R_{\xi t}^{\text{lim}},$$

$$\frac{M_{\xi t} \sum_{i \in \mathcal{I}} P_i + M_v W_v}{\sum_{i \in \mathcal{I}} P_i + W_v} \geq M_{\xi t}^{\text{lim}}, \quad (12.7x)$$

$$\frac{D_{\xi t} \sum_{i \in \mathcal{I}} P_i + D_v W_v + R_d W_d}{\sum_{i \in \mathcal{I}} P_i + W_v + W_d} \geq D_{\xi t}^{\text{lim}},$$

$$\frac{\Delta f_{\text{ss,lim}}}{f_0} \frac{D_{\xi t} \sum_{i \in \mathcal{I}} P_i + D_v W_v + R_d W_d}{\sum_{i \in \mathcal{I}} P_i + W_v + W_d} \geq \Delta P_{\xi t}, \quad (12.7y)$$

$$p_{it} \geq 0, \quad w_{jt} \geq 0, \quad \delta_{nt} \geq 0, \quad \hat{\delta}_{n\xi t} \geq 0, \quad k_{i\xi t} \geq 0, \quad r_{i\xi t}^+, \quad r_{i\xi t}^- \geq 0,$$

$$l_{n\xi t}^{\text{shed}} \geq 0, \quad w_{j\xi t}^{\text{spill}} \geq 0, \quad F_{\xi t}, \quad R_{\xi t}, \quad M_{\xi t}, \quad D_{\xi t} \geq 0, \quad (12.7z)$$

$$u_{it}, \quad y_{it}, \quad z_{it} \in \{0, 1\},$$

where $\Phi = \{p_{it}, u_{it}, y_{it}, z_{it}, \forall i, t; w_{jt}, \forall j, t; \delta_{nt}, \forall n, t; \hat{\delta}_{n\xi t}, \forall n, \xi, t; r_{i\xi t}^+, r_{i\xi t}^-, \forall i, \xi, t; w_{j\xi t}^{\text{spill}}, \forall j, \xi, t; l_{n\xi t}^{\text{shed}}, \forall n, \xi, t; k_{i\xi t}, \forall i, \xi, t; F_{\xi t}, R_{\xi t}, M_{\xi t}, D_{\xi t}, \forall \xi, t\}$ is the set of optimization variables, and the time-invariant aggregate converter parameters are defined according to Chapter 5 as

$$W_d = \sum_{j \in \mathcal{J}} W_{d_j}, \quad W_v = \sum_{j \in \mathcal{J}} W_{v_j}, \quad (12.8)$$

$$M_v = \sum_{j \in \mathcal{J}} \frac{2H_{v_j} W_{d_j}}{W_d}, \quad D_v = \sum_{j \in \mathcal{J}} \frac{D_{v_j} W_{d_j}}{W_d}, \quad (12.9)$$

$$R_d = \sum_{j \in \mathcal{J}} \frac{K_j W_{d_j}}{R_{d_j} W_d}. \quad (12.10)$$

The objective function (12.7a) to be minimized is the total expected system cost that comprises the day-ahead energy and the real-time balancing costs.

The day-ahead component consists of the fuel costs $C_i \in \mathbb{R}$, start-up costs $C_i^{\text{SU}} \in \mathbb{R}$ and shut-down costs $C_i^{\text{SD}} \in \mathbb{R}$. The real-time component includes the re-dispatch cost from the deployment of upward and downward reserves based on the corresponding offer prices $C_i^+ \in \mathbb{R}$ and $C_i^- \in \mathbb{R}$, as well as the involuntary load shedding at the value of lost load $C^{\text{sh}} \in \mathbb{R}$.

Equation (12.7b) enforces the nodal power balance of the day-ahead schedule, while network power flows at the day-ahead stage are restricted by the transmission capacity limits in (12.7c). Constraints (12.7d)-(12.7e) model the minimum online and offline time of conventional units based on commitment variable $u_{it} \in \{0, 1\}$, where parameters $\tau_i^1 \in \mathbb{R}_{>0}$ and $\tau_i^0 \in \mathbb{R}_{>0}$ are defined as $\tau_i^1 = \min\{t + T_i^1 - 1, T\}$ and $\tau_i^0 = \min\{t + T_i^0 - 1, T\}$, and $T_i^1 \in \mathbb{R}_{\geq 0}$ and $T_i^0 \in \mathbb{R}_{\geq 0}$ denote the duration for which the unit $i \in \mathcal{I}$ should remain online and offline, respectively. Constraints (12.7f)-(12.7g) model the start-up and shut-down of conventional units using the binary variables $y_{it} \in \{0, 1\}$ and $z_{it} \in \{0, 1\}$, respectively.

The real-time power balance for every uncertainty realization $\xi \in \mathcal{E}$ is enforced by constraint (12.7h). Parameter $\alpha_{i\xi t} \in \{0, 1\}$ models the availability of the generators to provide reserves, i.e., $\alpha_{i\xi t} = 1$ if generator i at scenario ξ and time t is online and able to provide reserves and $\alpha_{i\xi t} = 0$ otherwise. The scheduled energy production and the deployment of upward ($r_{i\xi t}^+ \in \mathbb{R}_{\geq 0}$) and downward ($r_{i\xi t}^- \in \mathbb{R}_{\geq 0}$) reserves in each scenario ξ are bounded by the generation capacity limits of each unit via (12.7i)-(12.7j), whereas inequalities (12.7k)-(12.7l) enforce the upward and downward ramping limits accounting for the real-time reserve activation. Constraints (12.7m)-(12.7n) account for the limits of reserve capacity offers. Transmission capacity limits during real-time operation are enforced by constraint (12.7o), whereas wind spillage $w_{j\xi t}^{\text{spill}} \in \mathbb{R}_{\geq 0}$ and load shedding $l_{n\xi t}^{\text{shed}} \in \mathbb{R}_{\geq 0}$ are bounded by the wind power realization and the nodal demand through constraints (12.7p) and (12.7q), respectively.

The set of constraints (12.7r)-(12.7x) models the frequency limits of the power system. The equality constraint (12.7r) defines $k_{i\xi t} \in \mathbb{R}_{\geq 0}$ as the gain factor $K_i \in \mathbb{R}_{\geq 0}$ of generator i scaled by the ratio of its capacity over the total system capacity, which in turn is multiplied by the binary variable u_{it} and the parameter $\alpha_{i\xi t}$ to indicate that a unit can provide inertial response only if it is committed and does not face an outage. Similarly, equalities (12.7s)-(12.7v) define average system variables for power fraction, droop, inertia and damping, respectively. Constraint (12.7w) enforces the RoCoF limit, while nadir equivalent and quasi steady-state frequency bounds are

imposed by constraints (12.7x) and (12.7y). Finally, (12.7z) declares variables and provides trivial inequalities.

The main advantage of the stochastic UC model is its ability to endogenously define the reserve requirements and the number of conventional generators that should be committed at the day-ahead stage in order to contain real-time deviations of renewables and ensure sufficient frequency response in case of equipment outages. Therefore, the resulting generation schedule explicitly incorporates the frequency constraints, taking also into account the commitment status of synchronous generators.

12.5 CASE STUDY

12.5.1 *System Description*

In order to analyze the performance of the stochastic UC model presented in Section 12.4, we investigate a modified version of the IEEE RTS-96 power system from [308] depicted in Fig. 12.4, with 48 buses comprising areas 1 and 2 of the original system. Table 12.3 provides the relevant parameters of different thermal plant types as well as the tuning of droop- and VSM-based converter-interfaced generation. The studied system includes 20 generators and 16 wind farms. We assume that six wind farms are operating in grid-forming mode and providing frequency support (i.e., virtual inertia); four of them via VSM control and the remaining two through frequency droop regulation. The UC is ran for two days without frequency constraints in order to initialize the system prior to introducing the frequency constraints on days 3, 4 and 5. This is done to ensure the impact of start-up costs is well distributed and not concentrated on one day. Therefore, the total simulation horizon is five days ($T = 120$ h), whereas the UC schedule is optimized separately for each day, with the last hour of each day used as an input for the next.

As the set of possible contingencies we consider the failure of synchronous generators $i = \{1, 6, 8, 10\}$. These generators are of various capacities, ranging from the smallest to the largest unit in the system. The hour 19 of day 3 (i.e., $t = 67$ h) is selected to be the time instance of a possible contingency, as this is the hour with high wind penetration and low demand. Wind power uncertainty is modelled using ten equiprobable scenarios that are provided in [308]. For further information on the scenario generation and reduction techniques that were applied to obtain this scenario set we refer the interested reader to [309]. Combining these wind power scenarios with the set of possible

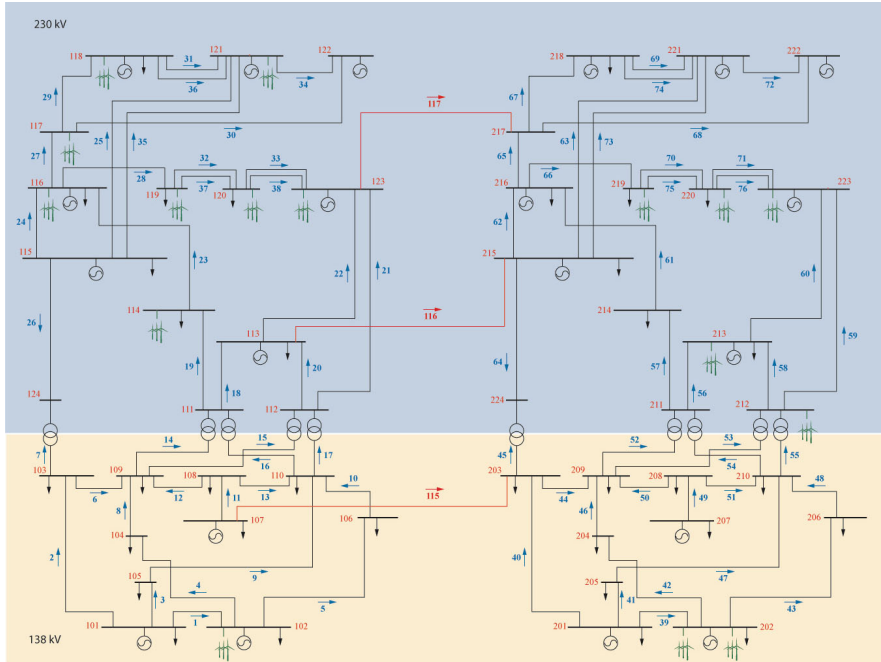


FIGURE 12.4: Modified IEEE RTS-96 system diagram comprising 2 areas, 16 wind farms and 20 synchronous generators [308].

contingencies brings the total number of scenarios considered in the stochastic UC to 50. The optimization problem is formulated in Python and uses the Gurobi solver with default parameterization. All simulations were carried out using a laptop computer with Intel Core i7 CPU with a clock rate of 2.8 GHz and 16 GB of RAM.

Type	$H_{i/j}$ [s]	$K_{i/j}$ [p.u.]	$F_{i/j}$ [p.u.]	$R_{i/j}$ [p.u.]	$D_{i/j}$ [p.u.]
Nuclear plant	4.5	0.98	0.25	0.04	0.6
CCGT plant	7.0	1.1	0.15	0.01	0.6
OCGT plant	5.5	0.95	0.35	0.03	0.6
VSM-based VSC	6.0	1.0	-	-	0.6
Droop-based VSC	-	1.0	0.001	0.05	-

TABLE 12.3: Parameters of the conventional and converter-interfaced generation.

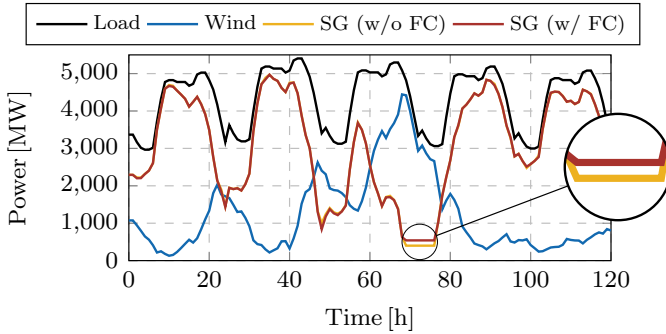


FIGURE 12.5: UC dispatch of synchronous generation for respective load and wind profiles.

12.5.2 Results

In this section, the simulation results from the stochastic UC are presented and discussed. Fig. 12.5 showcases the load and wind power profiles as well as the aggregate dispatch of synchronous generation for two UC runs: (i) without frequency constraints; and (ii) with frequency constraints, denoted by “w/o FC” and “w/ FC” respectively hereinafter. The simulation times for these two UC runs are 14 minutes 8 seconds and 14 minutes 28 seconds respectively, and thus the increase in computational time with the inclusion of frequency constraints can be considered marginal. Furthermore, Table 12.4 indicates the difference in the total number of synchronous generators committed between the two runs. Both Fig. 12.5 and Table 12.4 suggest that, although the amount of committed generators increases significantly, the total SG production is only slightly changed. This is justified by the additional generators being solely committed for the purpose of providing inertia, and thus operating at their technical minimum. The production surplus arising

Hour	65	66	67	68	69	70	71	72	73
w/o FC	6	5	4	4	4	4	4	4	4
w/ FC	6	5	10	10	10	10	10	10	10

TABLE 12.4: Comparison of the total number of dispatched synchronous generators through UC for each hour.

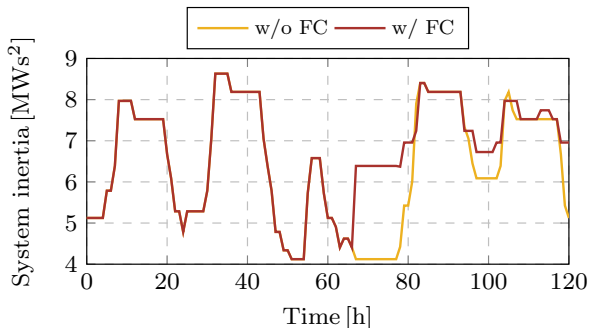


FIGURE 12.6: Impact of frequency constraints on the aggregate level of system inertia.

from the additionally committed units is compensated by wind curtailment and other generators reducing their power output.

The evolution of aggregate system inertia over the course of the whole scheduling horizon is depicted in Fig. 12.6. A noticeable step change in total system inertia at hour 67 reflects the impact of frequency constraints under contingency, which subsequently trigger a dispatch of auxiliary synchronous generators. While the inertia levels do not differentiate between the two cases during the first two days, on the days following the potential outage some carryover impacts can be observed. This is a consequence of the commitment schedule being radically changed at hour $t = 67$, thus affecting the UC schedules in the following days.

Some insightful conclusions can be drawn from Fig. 12.7, where the difference between the actual values of the frequency metrics and the respective ENTSO-E thresholds are depicted. For this purpose, we define a constraint gap $\epsilon \in \mathbb{R}$ as a measure of the relative constraint distance to its limit, e.g., $\epsilon_{\text{nadir}} = \Delta f_{\text{max}} / \Delta f_{\text{lim}} - 1$. After the completion of unit commitment, the constraints are re-evaluated using the obtained F_g , R_g , M and D values in order to determine which frequency criterion becomes binding at the instance of the fault. A negative constraint gap indicates that the specific frequency criteria is met with room to spare. It should be noted that the positive values of ϵ for $t < 67$ h suggest that the frequency threshold would be violated if a fault occurs. No action is required however, considering that in this case study we assume that the contingency can only occur at hour $t = 67$. Fig. 12.7 demonstrates that, without explicit consideration of frequency-related constraints in the stochastic UC model, all prescribed frequency limits would

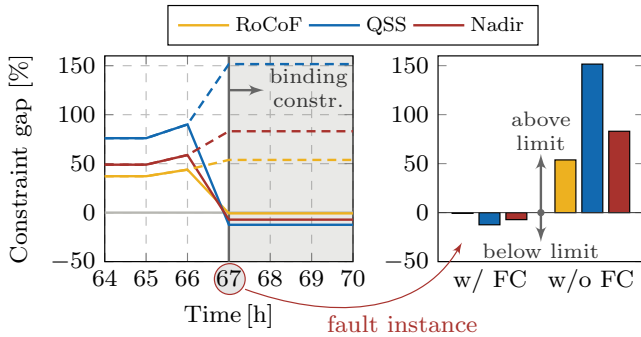


FIGURE 12.7: Constraint gaps for different frequency metrics. Dashed lines refer to the case without frequency constraints.

be violated. Moreover, it can be observed that when taking such constraints into account, the RoCoF constraint is closest to its limit - corresponding to the smallest constraint gap - and thus binding. The constraint gap difference between the two cases at hour $t = 67$ clearly highlights the importance of including frequency constraints in UC in order to avoid large frequency excursions and undesired triggering of protection and UFLS schemes. The same observations are also reflected in Fig. 12.8 through representation of the time-domain frequency response of the system following a disturbance. Understandably, the values of RoCoF, nadir and quasi steady-state frequency deviation (denoted by QSS in Fig. 12.7) are reduced compared to the case without frequency constraints such that all prescribed criteria are met.

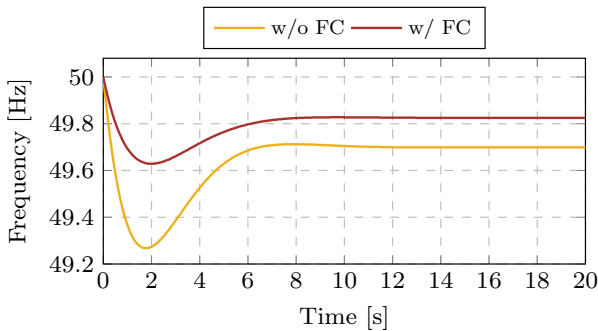


FIGURE 12.8: Frequency evolution of the uniform CoI model with and without FC for 20 seconds after the fault instance at $t = 67$ h.

Case	Total costs	Start-up	Operation	Reserves
w/o FC	410 545	788	405 561	4 196
w/ FC	432 383	2 248	420 886	9 249
Difference	5.32 %	185 %	3.78 %	120 %

TABLE 12.5: Unit commitment costs [\$] breakdown on day 3.

Finally, we investigate the economic impact of including the frequency-related constraints into the stochastic UC model, with the breakdown of operational costs for day 3 presented in Table 12.5. The addition of frequency constraints leads to a 5 % increase in total expected system costs and a significant increase in start-up costs by 185 %. This is due to six extra generators being turned on for providing inertia at the period of a potential generation failure, as shown in Table 12.4. A large increase is also seen in reserve scheduling costs, as the reserves are now not only scheduled to cover wind power uncertainty but also for possible contingencies. The change in cost is of course highly dependent on the specific system and the considered contingencies.

12.6 CONCLUSION

This chapter includes frequency constraints in the UC problem of a system with large wind power penetration in order to investigate the impact of frequency dynamics on unit scheduling in low-inertia networks. By employing the analytic expressions for post-contingency frequency response of a generic multi-machine system, we define a set of constraints reflecting the frequency nadir, RoCoF and quasi steady-state deviation. The highly non-linear frequency nadir constraint is linearized using two approaches: (i) a PWL technique adapted from the literature; and (ii) a proposed simple and efficient method for extracting bounds on decision variables of interest, which is shown to be computationally superior to PWL. Using the latter approach, the stochastic UC problem is formulated as an MILP, with an objective of minimizing the expected system costs against wind power production and generation outage uncertainties.

Our results show that the inclusion of frequency constraints in the UC model significantly affects the dispatch of synchronous generators and consequently the expected system costs. In particular, during anticipated critical events such as the loss of generation, additional synchronous machines are needed

for providing sufficient inertia and damping in the process of frequency containment. Such actions lead to a drastic increase in the UC costs, especially pertaining to start-up and reserve scheduling, which poses a new challenge as the operator must find a way to remunerate the units committed for the sole purpose of frequency regulation. This is an exciting avenue for future work and will be further addressed in Chapter 13.

ECONOMIC VALUATION AND PRICING OF INERTIA IN INVERTER-DOMINATED GRIDS

This chapter studies the procurement and pricing of inertial response using a frequency-constrained unit commitment formulation, which co-optimizes the provision of energy and inertia services while accounting for their complementary properties. The proposed approach builds on a two-step process that allows to differentiate between the units being online for energy purposes and the ones committed additionally solely for inertia provision. Subsequently, three novel pricing and payment schemes that reimburse inertia providers in a transparent and fair manner according to their individual participation are proposed. The analysis includes both synchronous and converter-based generators and provides insights into the impact of each pricing scheme on total system cost, as well as attracting new investments in the technologies capable of offering a more affordable inertial response. The results indicate that all three methods could have a beneficial impact on frequency stability and aid the operator in ensuring system reliability, whereas the policy implications to different inertia providing units might vary between the payment schemes. The content of this chapter is based on [310].

13.1 INTRODUCTION

Current strategies for power system operation and the existing market architecture were designed in a context where conventional generators (e.g., hydro, coal or gas units) were dominating. The spinning turbines of these generators are synchronized to grid frequency and their large rotating masses naturally provides the necessary physical inertia to contain frequency deviations due to sudden power imbalances. Nowadays however, increasing shares of RES with null marginal cost are displacing the more expensive synchronous generators. Considering that RES units are typically interfaced to the grid via power electronics and therefore do not provide physical inertia to the network, the ability of the power system to dampen frequency changes is diminished. In case of insufficient inertial response, large deviations from nominal frequency

in the event of a disturbance will result in fast frequency dynamics and high RoCoF, which may even lead to disconnection of generators or loads [6, 311].

In view of this new operational paradigm, inertia cannot be viewed anymore just as byproduct of the power provision from synchronous generators. In addition, existing frequency control mechanisms such as droop response by frequency containment reserves are not able to instantly reduce frequency changes following a disturbance [312]. To this end, it becomes imperative to design new market mechanisms and tailored market products that are able to adequately reward the provision of Fast Frequency Response (FFR) services from existing sources, i.e., synchronous generators, and provide correct price signals. This incentivizes new investments that can contribute to the inertial response of the power system such as fast frequency-responsive loads (e.g., heat pumps, batteries) or synthetic inertial response from wind generation. In the meantime, they should allow the system operator to express its willingness to pay for these services dynamically, depending on system conditions and the scarcity of FFR services.

Several system operators underline the need to bring more synchronous inertia online and are effectively working on designing the appropriate services and markets. This can be readily achieved if the TSO mandates additional synchronous generators to be committed during periods when economically scheduled units do not offer adequate inertia. Alternatively, the converter-interfaced units (either generation or storage devices) could be employed for providing a Virtual Inertia (VI) response. Understandably, under any potential scenario, the additionally committed units will have to be compensated with appropriate and possibly out-of-market reimbursement mechanisms.

Motivated by the above considerations, the system operator in Great Britain (National Grid) has designed new frequency regulation products to bring more fast-acting assets into the system [313]. In the same vein, a new FFR reserve will be rolled out in the Nordic synchronous area [314] in spring of 2020. These are distinct products tailored to enhance the fast frequency response of the system. However, being traded in separate markets, i.e., unbundled from energy, may fail to capture the complementarity between inertia and energy services and consequently increase the total system cost.

Following a different approach, Eirgrid in Ireland has introduced a Synchronous Inertial Response (SIR) constraint to ensure that the available inertia does not fall below a static limit of 23 000 MW s [315]. However, as this mechanism remunerates service providers based on an annual tariff, it does not reflect the instantaneous value of inertia for the system. On the other hand, the system operator in Texas (ERCOT) performs a dynamic

dimensioning of Responsive Reserve Services (RRS) that are used to maintain the reliability of the grid during low-inertia situations [4]. Since energy and RRS are co-optimized, the resulting prices account for the fact that these products compete for the same generation capacity. Nonetheless, RRS bundle various services (load resources with under-frequency relays, governor response and frequency restoration provided by generators after a frequency event) that have different contributions to frequency response and are not necessarily reflective of inertia provision. This makes the accurate definition of RRS requirements even more complex, specifically in terms of inertia, and it dilutes the price signals to the assets that truly contribute to inertial response.

Previous works in [316] and [317] have quantified the value of inertia as the decrease in total cost of a frequency-constrained unit commitment model by providing cost-free synthetic inertia. These studies showcase the benefits in terms of operational cost from enlarging the pool of inertia providers, but they disregard the costs of converter-interfaced generators and do not discuss any pricing issues. This is a non-trivial problem as the discrete nature of inertia, depending on the on/off status of the SGs, introduces pricing complexities when integrating frequency constraints. In order to circumvent the underlying issues, several studies use a linearized version of these constraints. A marginal pricing scheme is proposed in [318] based on linear constraints fitted to simulation data. Authors in [319] focus on pricing frequency response services of varying quality (i.e., with different response times) using a two-sided Vickrey-Clarke-Groves (VCG) auction, where the preferences of the system operator over each service are reflected in different utility functions. Finally, the work in [320] presents a marginal pricing scheme for frequency services based on Mixed-Integer Second-Order Cone Program (MISOCP) formulation of the frequency-security constraints. However, while the resulting prices provide reasonable incentives to the inertia providers, they do not guarantee cost recovery of all synchronous generators. Moreover, the frequency response from different unit types is characterized solely by the response time, which fails to capture the fundamental differences in inertia provision from conventional and converter-based generators.

In terms of market design, [321] presents a new PFC market model for hosting Frequency Response Reserve (FRR) offers from both generators and loads. The performance of the PFC provided by the load is benchmarked by the equivalent amount of PFC provided by the synchronous generators at each typical system inertia condition, using the network models and operation data of the ERCOT system. This information is subsequently employed in the

market design in order to accept and value the PFC offers from both generators and loads. Nonetheless, similarly to [316–320, 322], it does not guarantee generators' cost recovery and does not differentiate between the physical (i.e., rotational) inertia and the artificially emulated inertia provision. On the other hand, [323] takes virtual inertia into account and proposes an operator-agent market mechanism in which the operator aims at maximizing the social welfare and the bids are invited from agents providing virtual inertia, who in turn are compensated via a VCG payment rule. The resulting mechanism ensures truthful bidding to be the dominant bidding strategy and guarantees non-negative payoffs for the agents. However, it does not necessarily yield the minimum cost for the operator, as the net cost of providing VI as a service is based on a rather simplified economic evaluation from [324], which does not accurately reflect the true cost information. Moreover, the satisfactory frequency response in terms of ENTSO-E criteria is not ensured.

In this chapter, we study the procurement and pricing of inertial response using a frequency-constrained UC problem, which co-optimizes the provision of energy and inertia services accounting endogenously for their complementary properties. By incorporating the analytic expressions for frequency constraints in our UC model, in particular the instantaneous RoCoF constraint as it is solely reflective of system inertia, we perform a dynamic dimensioning of FFR reserve requirements instead of using exogenously defined static requirements. The proposed approach builds on a two-step process, akin to the reliability UC mechanism that is already implemented in various markets in the United States [325]. Such arrangement allows to differentiate between the units being online for energy purposes and the ones committed additionally only for inertia provision. We contribute to the ongoing discussion on FFR market design by proposing three pricing and payment schemes that reimburse inertia providers in a transparent and fair manner according to their individual participation. We analyze how these pricing schemes can lower system cost by attracting new investments in technologies capable of offering inertia at lower cost, such as grid-forming converter control schemes that employ droop and VI algorithms providing synthetic inertia and FFC services at a more competitive cost than SGs [23].

The rest of the chapter is structured as follows. In Section 13.2, we discuss the inclusion of post-contingency frequency dynamics into the traditional UC model. The economic valuation of inertia provision and the notion of inertia substitution are explained in Section 13.3. Section 13.4 presents the three proposed inertia pricing schemes and the corresponding payments to participating units. Section 13.5 analyzes the performance of each pricing

method on an illustrative system and on a larger test case with and without the inclusion of virtual inertia. Finally, Section 13.6 draws the main conclusions and discusses the outlook of the study.

13.2 FREQUENCY-CONSTRAINED UNIT COMMITMENT

13.2.1 Frequency Constraints for Inertia Valuation and Pricing

We employ the frequency response model of a generic low-inertia system, previously proposed and described in Chapter 5, that comprises both traditional and converter-interfaced generators. For clarity, let us recall the analytic expressions for frequency metrics of interest, i.e., frequency nadir (Δf_{\max}), RoCoF (\dot{f}_{\max}) and steady-state frequency deviation (Δf_{ss}), after a step disturbance $\Delta P \in \mathbb{R}$ occurring at time instance $t_0 \in \mathbb{R}_{\geq 0}$:

$$\Delta f_{\max} := -\frac{\Delta P}{D + R_g} \left(1 + \sqrt{\frac{T(R_g - F_g)}{M}} e^{-\zeta \omega_n t_m} \right), \quad (13.1a)$$

$$\dot{f}_{\max} := \dot{f}(t_0^+) = -\frac{\Delta P}{M}, \quad \Delta f_{\text{ss}} := -\frac{\Delta P}{D + R_g}. \quad (13.1b)$$

More details on mathematical formulation and variable definitions in (13.1) can be found in Section 5.2. As previously discussed in Chapter 12, the relevant frequency metrics are directly dependent on aggregate system parameters and could be regulated *a priori* through UC decisions. In particular, RoCoF and steady-state deviation can be explicitly controlled via $\dot{f}_{\max} \sim M^{-1}$ and $\Delta f_{\text{ss}} \sim (D + R_g)^{-1}$, while nadir can be modeled using a highly nonlinear function $\Delta f_{\max}(M, D, R_g, F_g)$.

With special interest in inertia, the most relevant constraint of the three presented in (13.1) is the limit on maximum instantaneous RoCoF in (13.1b), with the aggregate inertia constant $M \in \mathbb{R}_{>0}$ being the only decision variable. The quasi steady-state frequency deviation is affected solely by the damping and generator droop constants, whereas the frequency nadir depends on all aforementioned variables. The work in Chapter 12 (see Fig. 12.7) suggested that violating RoCoF threshold tends to be drastically more common than reaching the critical nadir limit, thus suggesting that the RoCoF constraint would be the binding one and therefore the most relevant when looking at the valuation and pricing of inertia. Moreover, several inertia market reports from different TSOs have focused solely on RoCoF, claiming its impact on inertia levels is more important than the one of nadir [296, 326]. Indeed, RoCoF is related to islanding and protection scheme issues, whereas nadir

affects mostly load shedding and can be regulated using proportional control (i.e., droop or virtual damping).

From the mathematical perspective, for the purpose of pricing analysis it is easier to extract meaningful information from a constraint dependent on a single variable, compared to dealing with multi-variable expressions. In particular, it would be rather difficult to determine the binding variable of a nadir constraint. Additionally, the difficulties related to linearizing the nadir expression make it not well-suited for obtaining pricing information. For the above reasons, in this chapter only the RoCoF constraint will be included into the UC formulation in order to determine the corresponding inertia prices.

13.2.2 Unit Commitment Formulation

In this section, we first provide the mathematical formulation of the frequency-constrained UC model comprising only synchronous generators, and subsequently extend it by including the VI units. The complete optimization problem is adapted from Section 12.4, together with the notation and variable declaration¹. However, unlike the method proposed in Chapter 12, where a two-stage stochastic UC model encompassing equipment (i.e., generation) failure and wind power uncertainty was developed, this study employs the traditional single-stage UC problem without considering multiple scenarios and their respective probabilities. Under such circumstances we are certain in confining the underlying conclusions pertaining to inertia valuation and pricing to the applied problem formulation and pricing mechanisms. For clarity and better elaboration of the proposed pricing methods, in the following sections we will describe the complete UC formulation for cases with and without virtual inertia.

13.2.2.1 Frequency-Constrained UC without Virtual Inertia

Similar to the stochastic UC problem in Section 12.4, a frequency-constrained unit commitment without the inclusion of VI units can be written as

$$\begin{aligned} \min_{\Phi} \quad & \sum_{t \in \mathcal{T}} \sum_{i \in \mathcal{I}} (C_i^{\text{SU}} y_{it} + C_i p_{it}) \\ \text{s.t.} \quad & \forall t \in \mathcal{T}, \forall i \in \mathcal{I}, \forall n \in \mathcal{N}, \forall m : (n, m) \in \mathcal{L}, \end{aligned} \quad (13.2a)$$

¹ The only distinction to the notation in Table 12.2 is the declaration of P_i^{cap} as the installed active power capacity of generator i (in contrast to P_i in Chapter 12).

$$\sum_{i \in \mathcal{I}} p_{it} + \sum_{j \in \mathcal{J}} W_{jt} - L_{nt} - \sum_{m: (n,m) \in \mathcal{L}} B_{nm}(\delta_{nt} - \delta_{mt}) = 0, \quad (13.2b)$$

$$B_{nm}(\delta_{nt} - \delta_{mt}) \leq \bar{f}_{nm}, \quad (13.2c)$$

$$u_{it} - u_{i(t-1)} \leq u_{i\tau^1}, \quad (13.2d)$$

$$u_{i(t-1)} - u_{it} \leq 1 - u_{i\tau^0}, \quad (13.2e)$$

$$y_{it} \geq u_{it} - u_{i(t-1)}, \quad (13.2f)$$

$$\underline{P}_i u_{it} \leq p_{it} \leq \bar{P}_i u_{it}, \quad (13.2g)$$

$$k_{it} = \frac{P_i^{\text{cap}}}{\sum_{i \in \mathcal{I}} P_i^{\text{cap}}} u_{it}, \quad (13.2h)$$

$$M_t = \sum_{i \in \mathcal{I}} 2H_i k_{it}, \quad (13.2i)$$

$$\frac{\dot{f}_{\text{lim}}}{f_0} M_t \geq |\Delta P_t|, \quad (13.2j)$$

$$p_{it}, k_{it} \geq 0, \delta_{nt} \geq 0, M_t \geq 0, u_{it}, y_{it} \in \{0, 1\}, \quad (13.2k)$$

where $\Phi = \{p_{it}, u_{it}, y_{it}, k_{it}, \forall i, t; \delta_{nt}, \forall n, t; M_t, \forall t\}$ is the set of optimization variables.

The objective function (13.2a) to be minimized is the total system cost that comprises the fuel costs and the start-up costs, denoted by $C_i \in \mathbb{R}$ and $C_i^{\text{SU}} \in \mathbb{R}$ respectively. Equality constraint (13.2b) enforces the nodal power balance, with $p_{it} \in \mathbb{R}_{\geq 0}$ being the power output of SG unit $i \in \mathcal{I}$, $W_{jt} \in \mathbb{R}_{\geq 0}$ referring to the power output of wind farm $j \in \mathcal{J}$, and $L_{nt} \in \mathbb{R}_{\geq 0}$ representing the demand at node $n \in \mathcal{N}$. Network power flows at the day-ahead stage are restricted by the transmission capacity limits $\bar{f}_{nm} \in \mathbb{R}_{\geq 0}$ in (13.2c), with $\delta_{nt} \in \mathbb{R}$ being voltage angle at node n . Constraints (13.2d)-(13.2e) model the minimum online and offline time of conventional units based on commitment variable $u_{it} \in \{0, 1\}$, while parameters τ_g^1 and τ_g^0 are defined as $\tau^1 = \min\{t + \mathcal{T}_g^1 - 1, T\}$ and $\tau^0 = \min\{t + \mathcal{T}_g^0 - 1, T\}$, where $\mathcal{T}_g^1 \in \mathbb{R}_{\geq 0}$ and $\mathcal{T}_g^0 \in \mathbb{R}_{\geq 0}$ denote the duration of time for which unit i should remain online and offline, respectively. Constraint (13.2f) models the start-up of conventional units using the binary variables $y_{it} \in \{0, 1\}$. The scheduled energy production is bounded by the minimum and maximum generation limits in (13.2g). The set of constraints (13.2h)-(13.2j) captures the frequency dynamics of the system and imposes RoCoF thresholds. In contrast to Section 12.4, equality (13.2h) defines $k_{it} \in \mathbb{R}_{\geq 0}$ as the ratio of the installed power capacity of generator i and the total system capacity multiplied by the binary unit commitment variable u_{it} . Expression (13.2i)

introduces the average system variable for inertia, while (13.2j) enforces the RoCoF limit dependent on the predefined parameter $f_{\text{lim}} \in \mathbb{R}_{\geq 0}$ prescribed by the system operator [152]. Finally, (13.2k) declares the decision variables.

13.2.2.2 Frequency-Constrained UC with Virtual Inertia

With the addition of virtual inertia, the optimization problem (13.2) is augmented as follows:

$$\min_{\Phi} \sum_{t \in \mathcal{T}} \sum_{i \in \mathcal{I}} (C_i^{\text{SU}} y_{it} + C_i p_{it}) + \sum_{t \in \mathcal{T}} \sum_{v \in \mathcal{V}} C_v^{\text{VI}} h_{vt} \quad (13.3a)$$

$$\text{s.t. } \forall t \in \mathcal{T}, \forall i \in \mathcal{I}, \forall v \in \mathcal{V}, \forall n \in \mathcal{N}, \forall m : (n, m) \in \mathcal{L}, \quad (13.2b)-(13.2k),$$

$$k_{vt} = \frac{p_{vt}}{\sum_{v \in \mathcal{V}} P_v^{\text{cap}}}, \quad (13.3b)$$

$$h_{it} = 2H_i P_i^{\text{cap}} u_{it}, \quad (13.3c)$$

$$h_{vt} = 2H_v p_{vt}, \quad (13.3d)$$

$$M_t^{\text{SG}} = \sum_{i \in \mathcal{I}} 2H_i k_{it}, \quad (13.3e)$$

$$M_t^{\text{VI}} = \sum_{v \in \mathcal{V}} 2H_v k_{vt}, \quad (13.3f)$$

$$M_t = \frac{M_t^{\text{SG}} \sum_{i \in \mathcal{I}} P_i^{\text{cap}} + M_t^{\text{VI}} \sum_{v \in \mathcal{V}} P_v^{\text{cap}}}{\sum_{i \in \mathcal{I}} P_i^{\text{cap}} + \sum_{v \in \mathcal{V}} P_v^{\text{cap}}}, \quad (13.3g)$$

$$h_{it} \geq 0, p_{vt}, k_{vt}, h_{vt} \geq 0, M_t^{\text{SG}}, M_t^{\text{VI}} \geq 0, \quad (13.3h)$$

with $\Phi = \{p_{it}, u_{it}, y_{it}, k_{it}, h_{it}, \forall i, t; \delta_{nt}, \forall n, t; p_{vt}, k_{vt}, h_{vt}, \forall v, t; M_t, M_t^{\text{SG}}, M_t^{\text{VI}}, \forall t\}$ being the set of optimization variables and $C_v^{\text{VI}} \in \mathbb{R}_{\geq 0}$ reflecting the unit cost of virtual inertia for each unit $v \in \mathcal{V} \subseteq \mathcal{J}$.

Expression (13.3b) defines the power scaling factors $k_{vt} \in \mathbb{R}_{\geq 0}$ of wind generators providing VI² as a function of their power output $p_{vt} \in \mathbb{R}_{\geq 0}$, whereas constraints (13.3c)-(13.3d) describe the individual inertia constants³ of each traditional generator and virtual inertia device, respectively. The aggregate inertia contributions from synchronous and VI-based generators

² Note that the VI scaling factors k_{vt} are conceptually different from the SG scaling factors k_{it} in (13.2h), since the time-variant aspect comes from the active power output p_{vt} of the VI device and not the binary decision variable u_{vt} . This is justified by the fact that the VI devices are assumed to always be online (i.e., available for FFR provision) and hence $u_{vt} = 1, \forall v, t$.

³ Due to discrete nature of the objective function (13.3a), the inertia constants h_{it} and h_{vt} are expressed in MW s^2 .

Scenario	Total cost	Start-up cost	Energy cost
w/o inertia requirements	407 500	600	406 900
w/ inertia requirements	569 600	3 500	566 100

TABLE 13.1: Breakdown of UC costs [€] with and without inertia requirements.

are accounted for in (13.3e)-(13.3f), (13.3g) defines the global system inertia as a weighted average of inertia gains provided by SG and VI units, while (13.3h) declares the new decision variables.

13.3 ECONOMIC VALUATION OF INERTIA

13.3.1 *Value of Inertia for the TSO*

The consideration of minimum inertia requirements for a TSO raises the question of how much these requirements will cost. To assess the economic value of inertia, the UC results can be used to determine the difference in system costs with and without inertia requirements, which would in turn provide an upper bound of the value of inertia for the TSO.

As an illustrative example, Table 13.1 shows the breakdown of UC costs for the modified IEEE RTS-96 system described in Chapter 12, for cases with and without inertia requirements. Several conclusions can be drawn from Table 13.1. First of all, it is clear that the inclusion of inertia requirements has significant impact on the system cost, with the total commitment costs increasing by 162 100 €. Secondly, the 460 % increase in start-up costs indicates that the newly committed SGs are needed solely for satisfying the inertia requirements. Finally, a large increase in generator dispatch costs reflects the energy produced by the SGs additionally committed for inertia purposes, thus suggesting that they are operating at their technical minimum.

It can be concluded from the aforementioned results that the difference in cost between these two cases of 162 100 € can be used as an indicator for defining the price at which the TSO values inertia. In other words, this sum represents the maximum amount of money the TSO would be willing to pay for procuring inertia from other units.

13.3.2 *Inertia Substitution*

Authors in [316] and [317] employ the method of adding “free” inertia to a frequency-constrained unit commitment and defining the decrease in total costs resulting from this addition as the value of inertia. Such concept displaces the more expensive inertia provided by synchronous generators with the cheap inertia and simultaneously preserves the total system-level inertia constant. While adding free inertia to the system is an effective tool for understanding the marginal inertia cost of the traditional synchronous generation portfolio, it does not reflect the cost of inertia provision for converter-interfaced generators. Building on a similar approach, the technique used in this work is to include the continuous inertia slack variable $M_t^+ \in \mathbb{R}_{\geq 0}$ in the RoCoF constraint of the UC problem, with an associated cost $C^+ \in \mathbb{R}_{\geq 0}$ present in the objective function. The RoCoF constraint (13.2j) is thus reformulated as

$$\frac{\dot{f}_{\text{lim}}}{f_0}(M_t + M_t^+) \geq |\Delta P_t|, \quad \forall t, \quad (13.4)$$

whereas the objective function (13.2a) is transformed accordingly:

$$\min_{\Phi} \sum_{t \in \mathcal{T}} \sum_{i \in \mathcal{I}} (C_i^{\text{SU}} y_{it} + C_i p_{it}) + \sum_{t \in \mathcal{T}} C^+ M_t^+. \quad (13.5)$$

It should be noted that the virtual inertia is not considered in this case, as it will later replace the slack variable. Using the described method, a certain price C^+ for which the additional inertia is no longer profitable can be found, reflected by the optimizer deciding to commit conventional generators instead.

For illustration purposes, the UC is ran on the previously described test case for a wide range of C^+ values. For each run, the amount of extra inertia purchased by the system is recorded, with the final results illustrated in Fig. 13.1. Interestingly, the correlation between M^+ and C^+ is reminiscent of a demand curve and it can be interpreted in a similar fashion. The main difference compared to a traditional demand curve lies in the fact that the total amount of system inertia does not change for different values of M^+ . More precisely, the RoCoF constraint ensures that the minimum amount of inertia needed for system stability is obtained, and including cheaper inertia does not increase the total inertia in the system but rather substitutes more expensive inertia provided by conventional synchronous generators instead. This effect is clearly reflected by distinctive steps in the extra inertia cost curve, with each step corresponding to an SG being displaced by a unit with cheaper inertia provision. Eventually, at $M^+ \approx 8 \text{ MW s}^2$ the system does not

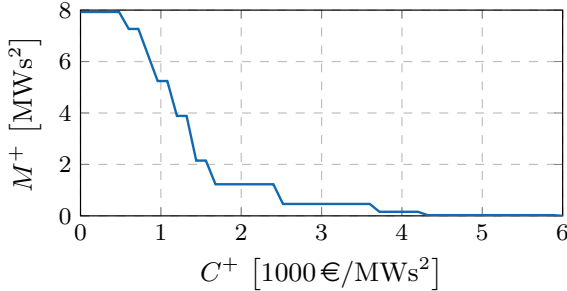


FIGURE 13.1: Cost curve of additional inertia provision.

purchase any more slack inertia despite it being free. This is justified by the fact that all expensive SGs, initially committed solely for providing inertia and meeting the frequency requirements, have now been decommissioned and replaced by addition of cheap inertia. Similarly, the extra inertia will not be procured at a cost higher than 6000 €/MW s^2 , since it is more expensive than having all necessary SGs come online.

It can be concluded that once the inertia requirements are set by the TSO - in this case by imposing upper limits on RoCoF - the system inertia will always be equal to the minimum amount needed to satisfy those requirements. Avoiding the dispatch of expensive SGs by procuring inertia at a cheaper cost creates value for the TSO. This is especially true in times of low load and high wind power, when a number of online SG units and hence the total inertia are at their operational minimum.

13.4 INERTIA PRICING AND PAYMENT METHODS

In this section, three novel methods for pricing and payment of inertia are proposed. In particular, the prices are derived from the UC model by obtaining the dual variables of the respective constraints. Nonetheless, this procedure requires to relax the original MILP form of the UC problem into a Linear Program (LP) whose dual variables are defined explicitly. For instance, the price of energy is determined as the dual of the power balance constraint, and there are three alternative price models for obtaining this dual [325]: (i) the restricted model; (ii) the dispatchable model; and (iii) the convex hull model.

In the restricted model, binary variables u are set to the optimal value u^* according to the solution of the preceding MILP, and the optimization problem

is solved again in the LP form. In contrast, the pricing in the dispatchable model is obtained by allowing binary variables to vary continuously in the range $0 \leq u \leq 1$. Finally, the convex hull model seeks to approximate the non-convex aggregate cost function with a convex hull function [325]. This work will solely focus on employing the restricted model for price determination, given that the main goal of this work is to investigate alternative inertia pricing schemes and not to focus on the non-convex nature of the UC problem. Indeed, while the convex hull method sidesteps the non-convexity issues, it is also very computationally intensive, whereas the dispatchable model introduces errors in the calculation of inertia based on variable u .

13.4.1 *Issues Pertaining to Negative SG Profits*

The inclusion of inertia requirements in the UC forces a dispatch of additional SGs solely for the purpose of providing rotational inertia, which in turn preserves the frequency deviation within prescribed limits after a fault. Under such circumstances, the expensive SGs are started up and operated at their technical minimum to ensure grid stability. Nonetheless, with extra units suddenly coming online the total generator profits get affected, which needs to be studied and proper reimbursement mechanisms should be put into place.

The increase in the number of online SGs can potentially lead to negative profits for units committed solely for inertia purposes, as they are dispatched out of the energy merit order. Indeed, the hourly price of energy is determined as the marginal cost of supplying the load. However, new generators coming online and operating at their technical minimum are not necessarily included in the energy market and their marginal cost is not reflected in the energy price. Hence, their fuel costs remain above the market price which eventually leads to negative revenue. In addition to the loss in the Energy-Only Market (EOM), they also face losses from the start-up costs. The issue of generators facing negative profits⁴ is important as there is no incentive for them to

⁴ We provide a small example in order to illustrate this statement. Let us consider a traditional UC problem with two generators (G_1 and G_2) and the respective power capacities of 50 MW and 20 MW. Both units are characterized by a technical minimum of 10 MW, with G_1 having a marginal cost of 20 €/MWh and G_2 having a marginal cost of 30 €/MWh. The power demand is set at 50 MW for the first and 55 MW for the second hour. According to the UC results, G_1 will supply 50 MW in the first hour while G_2 will remain offline. In the second hour, G_1 will be forced to reduce its power output to 45 MW in order to accommodate the technical minimum of 10 MW from G_2 to supply the load. However, when looking at the dual of the power balance, the energy price for both hours is equal to 20 €/MWh, corresponding to the marginal cost of G_1 ; G_2 is operating at a technical

come online for inertia provision. The TSO must therefore create payment mechanisms to reimburse SGs and encourage cheaper and more efficient technologies to provide inertia.

13.4.2 *Limitations of Obtaining Duals from RoCoF Constraint*

In any optimization problem, the shadow prices are obtained as the duals of certain constraints. In this specific case, in order to obtain a price for inertia and create payments to units providing it, the constraint of interest is the upper bound on RoCoF imposed in (13.2j). Due to non-convexity issues, obtaining a dual from such constraint is not straightforward. When considering SG units, the cost of providing inertia is linked to both the start-up costs and the fuel costs. The former costs depend on the binary commitment variables which complicates the extraction of the dual variables. Indeed, when only considering inertia provided by SGs, the RoCoF constraint is satisfied by committing a certain amount of generators. However, since the inertia comes in steps due to the binary nature of the problem, the constraint will be satisfied once the threshold is exceeded, but it will (almost) never be equal to the exact limit. Therefore, the dual of the RoCoF constraint would be zero in this particular case.

The main issue to be addressed in order to extract a meaningful RoCoF dual is the discrete online/offline characteristic of SGs and the fact that they do not provide inertia in a continuous manner. Hence, a straightforward approach to obtain a RoCoF dual variable would be to set the SG inertia as a continuous variable and rewrite constraint (13.2h) as

$$0 \leq k_{it} \leq \frac{P_i^{\text{cap}}}{\sum_{i \in \mathcal{I}} P_i^{\text{cap}}} u_{it}, \quad \forall i, t. \quad (13.6)$$

The aggregate inertia remains equal to

$$M_t = \sum_{i \in \mathcal{I}} 2H_i k_{it}, \quad \forall t, \quad (13.7)$$

and is therefore transformed into a continuous variable.

While such formulation enables SGs to artificially provide inertia in a continuous fashion, it still does not yield a meaningful RoCoF dual. More precisely, the problem lies in the fact that there is no direct cost associated with M_t in the objective (13.2a). Duals represent how a change in the

minimum and is not represented in the energy price. This is due to the non-convex nature of the unit commitment problem.

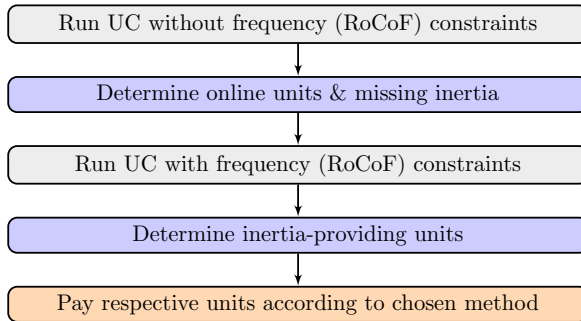


FIGURE 13.2: Proposed methodology for determining inertia payments.

respective constraint would affect the value of the objective function. However, the cost of inertia provision from SGs is not explicitly included in the objective function, but it is in fact “hidden” in the start-up and fuel costs.

On the other hand, when considering virtual inertia in the UC, a non-zero dual variable can be obtained for RoCoF constraint. Nevertheless, it only takes the bid-in cost C_v^{VI} of converter-interfaced units into account, since the objective (13.3a) has an explicit cost term $C_v^{VI}h_{vt}$ for purchasing VI. This however does not resolve the aforementioned issue pertaining to traditional SG units providing inertia, as their costs are still not captured in the existing price setting mechanism. Hence, alternative pricing methods must be developed instead.

13.4.3 Proposed Inertia Pricing and Payment Methods

Three novel methods for pricing and payment of inertia for all participating units are developed in this chapter, all using the same two-step UC algorithm described in Fig. 13.2. The main purpose of such algorithm is to differentiate between the units being online for energy purposes and the ones committed additionally solely for inertia provision. This breakdown allows payment schemes to reimburse units in a fair manner according to their individual participation. Moreover, the proposed two-step process is similar to the well-known two-step reliability commitment process [325]. The proposed pricing methods are described in detail in the remainder of this sections.

13.4.3.1 Method 1: Ex-Post Price Calculation

The first pricing method is based on *ex-post* calculation of the inertia price. Motivated by a common clearing price determination in an EOM, this method aims at setting the price of inertia provision as the cost of the most expensive unit supplying the inertia demand.

Let us assume obtaining a dual $\lambda_t^H, \forall t$ from the RoCoF constraint (13.2j), which would in this case represent the cost of procuring virtual inertia. In order to include the costs incurred to SGs providing rotational inertia into analysis, the following price structure is introduced:

$$\hat{\lambda}_t^H = \max \{ \lambda_t^H, \lambda_t^{SG} \}, \quad \forall t \in \mathcal{T}, \quad (13.8)$$

with $\hat{\lambda}_t^H$ being the desired marginal value of inertia provision at hour t and

$$\lambda_t^{SG} = \max_{i \in \mathcal{M}^+} \left\{ \frac{(\max_{i \in \mathcal{M}^+} \{ C_i - \mu_t, 0 \} p_{it} + C_i^{SU}) u_{it}}{h_{it}} \right\}, \quad \forall t \in \mathcal{T} \quad (13.9)$$

determining the cost of the most expensive SG unit $i \in \mathcal{M}^+$ online (and hence providing inertia); $\mathcal{M}^+ \in \mathbb{Z}_{>0}$ represents the set of additional SGs committed in the second UC run and $\mu_t, \forall t$ is the dual of the power balance constraint corresponding to the energy price.

According to (13.8), the price of inertia is defined as the cost of the most expensive unit (VI or SG) supplying inertia. The SG costs are obtained by combining the EOM losses, assuming the generator is in fact facing any, together with the start-up costs, and subsequently dividing it by the amount of inertia provided. Once the price is determined, units get reimbursed through Inertia Payments (IP) based on the previously determined price $\hat{\lambda}_t^H$ and the quantity of inertia that they provide (h_{it} for SGs and h_{vt} for VI providers), scaled accordingly as follows:

$$IP_{it} = \hat{\lambda}_t^H \frac{h_{it} \sum_{i \in \mathcal{I}} P_i^{\text{cap}}}{\sum_{i \in \mathcal{I}} P_i^{\text{cap}} + \sum_{v \in \mathcal{V}} P_v^{\text{cap}}}, \quad \forall i, t, \quad (13.10a)$$

$$IP_{vt} = \hat{\lambda}_t^H \frac{h_{vt} \sum_{v \in \mathcal{V}} P_v^{\text{cap}}}{\sum_{i \in \mathcal{I}} P_i^{\text{cap}} + \sum_{v \in \mathcal{V}} P_v^{\text{cap}}}, \quad \forall v, t. \quad (13.10b)$$

13.4.3.2 Method 2: Utility Function

In Section 13.3.1 it was shown that the financial resources the TSO would be willing to spend on inertia can be quantified. Indeed, for the given test system, this value corresponds to 162 100 € for procuring 8 MW s² and can

be defined as the utility of inertia for the TSO, thus providing information on how to price the inertia in the system.

In the same vein, this method aims to obtain the relevant pricing information from the UC by subtracting the utility term $U^H \sum_t M_t$ from the objective function (13.3a), which results in the objective of the form

$$\min_{\Phi} \sum_{t \in \mathcal{T}} \sum_{i \in \mathcal{I}} (C_i^{\text{SU}} y_{it} + C_i p_{it}) + \sum_{t \in \mathcal{T}} \sum_{v \in \mathcal{V}} C_v^{\text{VI}} h_{vt} - U^H \sum_t M_t. \quad (13.11)$$

Here, $U^H \in \mathbb{R}_{\geq 0}$ denotes the utility of inertia for the entire scheduling horizon. The cumulative value of U^H is calculated by running the UC twice for certain inertia demand: once without frequency constraints (denoted by “w/o FC”) and once with frequency constraints and no VI provision (denoted by “w/ FC”). Such procedure yields the lower and upper bound on system cost, respectively. The utility of inertia is then determined by

$$U^H = \frac{C_{\text{total}}^{\text{w/ FC}} - C_{\text{total}}^{\text{w/o FC}}}{H_{\text{dem}}}, \quad (13.12)$$

with $C_{\text{total}} \in \mathbb{R}_{\geq 0}$ referring to the total UC cost. It should be noted that by inertia demand $H_{\text{dem}} \in \mathbb{R}_{\geq 0}$ we consider the amount of additional inertia needed to satisfy the frequency requirements after the first UC run. Since the inertia costs of both VI and SG units are explicitly included in the objective function, a price for inertia can be obtained as the dual variable λ_t^H of the RoCoF constraint, i.e., $\hat{\lambda}_t^H := \lambda_t^H$. The units would subsequently be reimbursed for inertia provision through the same payment mechanism described in (13.10).

13.4.3.3 Method 3: Uplift Payments

The authors in [296] build on the concept of uplift payments or “commitment ticket price” for generators providing inertia, previously introduced in [327]. They define the additional payments to the units as

$$\pi_{it} = C_i^{\text{SU}} - \bar{\nu}_{it} P_i^{\text{max}} + \underline{\nu}_{it} P_i^{\text{min}}, \quad \forall i, t, \quad (13.13)$$

where $\bar{\nu}_{it}, \forall i, t$ and $\underline{\nu}_{it}, \forall i, t$ are the duals of the maximum and minimum unit generation constraints, respectively. The authors then suggest to include the product $\text{IP}_{it} = \pi_{it} y_{it}$ to the amount paid to the generators. The main drawback of the suggested payment lies in the fact that SGs are only compensated during start-up hours, as the payment is only made when $y_{it} > 0$. It implies that the generators facing losses due to energy prices being lower than their

marginal costs are not reimbursed during operating hours. Furthermore, an additional pricing mechanism for VI units must be implemented. Therefore, we propose a modified version of such scheme in order to resolve the above limitations.

The proposition in this work is to alter the uplift payment such that

$$\pi_{it} = C_i^{\text{SU}} y_{it} + \underline{\nu}_{it} P_i^{\text{min}}. \quad (13.14)$$

In contrast to (13.13), the modified uplift method allows the generators to receive payments for start-up costs as well as for all time periods in which they face EOM losses, and not only during the start-up hour. Indeed, the start-up decision variable y_{it} has been incorporated into (13.14) to reflect the incurred start-up costs, but SGs will receive additional compensation when operating at the technical minimum reflected by the expression $\underline{\nu}_{it} P_i^{\text{min}}$. The expression $\bar{\nu}_{it} P_i^{\text{max}}$ is omitted from (13.14) for simplicity, since the probability of all additionally committed SGs operating at their technical maximum is rather negligible. However, the aforementioned term can be easily incorporated into (13.14) if needed. Note however that the case studies and results presented in the remainder of the chapter are not affected by this term. Nevertheless, (13.14) is not sufficient for accurately capturing the costs of VI units. Hence, the VI providers will be reimbursed according to the dual λ_t^{H} of the RoCoF constraint obtained from the optimization, which still reflects the cost of inertia coming from such units. This dual represents in fact the VI common clearing price used to reimburse all virtual inertia units. The uplift payment method thus distinguishes between a standard shadow price mechanism for VI units and a reimbursement method based on (13.14) for traditional SG units.

13.5 CASE STUDIES

This section investigates and compares the performance of all three payment methods in terms of fairness for all unit types participating in inertia provision. Two test systems are considered and the analysis of every payment method is done individually for each system, with the results subsequently compared between the payment schemes. Moreover, the scenarios with and without virtual inertia are also taken into consideration throughout the course of this study.

Unit	$\bar{P}_{i/v}/\underline{P}_{i/v}$ [MW]	C_i [€/MWh]	C_i^{SU} [€]	$H_{i/v}$ [s]
G_1	160/10	10	0	4
G_2	100/10	12	300	4
G_3	80/10	11	200	4
B_1	10/0	–	–	10
B_2	20/0	–	–	10
B_3	30/0	–	–	10

TABLE 13.2: Small test system description.

13.5.1 *Small Test System*

In order to gain basic understanding of the proposed pricing methodologies as well as the economic interactions in a UC, we first consider a simple system comprising three conventional SGs, fixed amount of wind generation with constant power output, and three batteries offering VI capabilities. The most relevant unit parameters including their normalized inertia constants H_i and H_v are given in Table 13.2. Note that the cost of batteries is not included as their bid-in cost for inertia (C_v^{VI}) is the only cost considered and assumed to be determined by the operators of VI units. For cases where battery costs are not a varying parameter, we assume that all batteries bid-in at a fixed price of $C_v^{\text{VI}} = 50 \text{ €/MW s}^2$. This allows for dispatching of VI without completely removing the need for SGs, thus making the comparison between payment methods more comprehensive.

We consider an 8-hour scheduling horizon with the load demand varying between 180 MWh and 200 MWh, and a constant wind energy output of 150 MWh at each hour. The inertia demand is dictated by the requirement for withstanding a predefined change in active power of $\Delta P = (1, 1, 15, 25, 33, 33, 30, 10) \times 10^{-3}$ p.u. throughout the scheduling horizon, with smaller values indirectly corresponding to a lower disturbance probability.

13.5.2 *Large Test System*

For a more comprehensive test case, we focus on the IEEE RTS-96 system [308] previously introduced in Chapter 12, modified into a low-inertia system for the purposes of this study by adding a large amount of wind generation. For the analysis of virtual inertia pricing, four VI-controlled batteries are included

Unit	Origin	P_v^{cap} [MW]	H_v [s]	C_v^{VI} [€/MW s ²]
B_1	B102	70	12	10
B_2	B114	50	12	11
B_3	B202	100	12	12
B_4	B212	40	12	13

TABLE 13.3: Parameters of VI battery units in the large system.

in the system, with relevant parameters⁵ provided in Table 13.3. The costs shown are the bid-in costs for virtual inertia, as it is assumed throughout this work that the battery operators make decisions on which markets to participate in and thus select the appropriate bid-in costs to ensure profitable operation. In our case the battery operators enter the inertia provision market with a specific bid-in cost and are dispatched only if it is financially viable for the system. The given costs are not necessarily kept constant throughout this study and will occasionally be changed for certain test cases.

The scheduling horizon is taken as a typical 24-hour day-ahead time period. Demand and wind production profiles are taken from [308]. Moreover, the system is required to be able to maintain frequency within prescribed thresholds after a disturbance of $\Delta P = 0.1$ p.u. at each hour of the day.

The following sections will present the performance of each pricing method on both the small and the large test system, as well as with and without the inclusion of virtual inertia.

13.5.3 Method 1: Ex-Post Price Calculation

13.5.3.1 Small test system

Without enforcing constraints on inertia, only G_1 is needed to supply the demand. The total UC cost is 3360€ and G_1 makes zero profit since it is the only generator online and thus sets the EOM price (equal to 10€/MWh). With the addition of inertia requirements, units G_2 and G_3 come online for 3 hours each, resulting in 590€ increase in UC cost. Due to EOM price remaining the same, both units face losses from the EOM and start-up costs, leading to negative profits of -360€ and -230€ for G_2 and G_3 respectively. Table 13.4 provides more insights regarding the revenue, costs, payments and profits for G_2 and G_3 over the 8-hour scheduling horizon.

⁵ The *origin* reflects the location of the battery unit in the IEEE RTS-96 system (see Fig. 12.4).

Unit	Cost	H_1	H_2	H_3	H_4	H_5	H_6	H_7	H_8
G_2	EOM	-	-	-	-	-20	-20	-20	-
	SU	-	-	-	-	-300	0	0	-
	IP	-	-	-	-	320	20	20	-
	Total	-	-	-	-	0	0	0	-
G_3	EOM	-	-	-	-10	-10	-10	-	-
	SU	-	-	-	-200	0	0	-	-
	IP	-	-	-	210	65.6	39.5	-	-
	Total	-	-	-	0	55.6	29.5	-	-

TABLE 13.4: Breakdown of hourly UC costs [€] for *Method 1*.

At hour 4, G_3 turns on to provide inertia, and its start-up and EOM losses are covered by the inertia payments. Moreover, it turns on before G_2 due to its lower operating and start-up costs. Nevertheless, in the next hour G_2 also comes online, thus becoming the most expensive unit providing inertia. Inertia payments therefore cover its losses, resulting in G_3 making positive profit as it is no longer the most expensive unit providing inertia. Similar situation occurs at hour 6. Finally, in the next hour G_3 turns off and inertia payments cover the losses of generator G_2 . Overall, G_2 and G_3 now have respective profits of 0€ and 85.1€. The proposed payment method is thus successful in resolving negative profit issues and ensures that all units receive a common clearing inertia price.

13.5.3.2 Large test system

We investigate the performance of *Method 1* on a larger system by analyzing the hourly profits of all 20 generators given in Table 13.5, with green and red fields indicating positive and negative hourly profits respectively. The effectiveness of the payment scheme is clearly reflected in the vast majority of SG units achieving positive profits for most of the hours. The generators facing negative profits at some instances are the units participating in the EOM that suffer losses due to a decrease in energy price. More precisely, the inertia requirements and changed commitment of the system result in lower EOM prices and therefore reduced profits for units (see Fig. 13.3). This decrease in energy price is caused by the generators having to reduce their energy output to accommodate the extra energy in the system due to additional generators, mostly operating at their technical minimum, coming

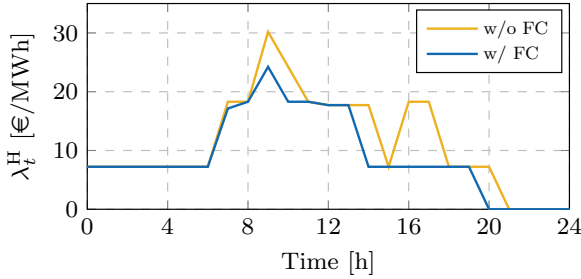


FIGURE 13.3: EOM price with and without frequency constraints.

online. At certain times, this reduction of energy output is large enough to cause a reduction in price.

13.5.3.3 Inclusion of Virtual Inertia

The proposed method performs well with the addition of virtual inertia, but issues appear once the cost of VI provision becomes too expensive for the system. As an illustrative example, let us consider the small test system and assume a simple case where all VI units bid-in at the same cost for inertia. According to (13.8), as this cost increases so do the corresponding inertia payments. However, a price threshold exists at which these payments exceed

$H \setminus G$	G_1	G_2	G_3	G_4	G_5	G_6	G_7	G_8	G_9	G_{10}	G_{11}	G_{12}	G_{13}	G_{14}	G_{15}	G_{16}	G_{17}	G_{18}	G_{19}	G_{20}
H_1	915	915	926	1164	891	0	0	0	1531	0	915	915	926	1164	891	0	0	0	1531	959
H_2	211	211	214	0	346	0	0	0	394	73	211	211	214	0	346	0	0	0	394	504
H_3	211	211	214	0	346	0	0	0	394	73	211	211	214	0	346	0	0	0	394	504
H_4	211	211	214	0	346	0	0	0	394	73	211	211	214	0	346	0	0	0	394	504
H_5	211	211	214	0	346	0	0	0	394	73	211	211	214	0	346	0	0	0	394	504
H_6	211	211	214	0	346	0	0	0	394	73	211	211	214	0	346	0	0	0	394	504
H_7	75	75	214	-161	116	0	3966	3966	69	0	75	75	-46	-96	116	0	3966	3966	69	171
H_8	-143	-143	0	338	94	0	4424	4424	39	0	65	65	0	274	94	0	4424	4424	39	145
H_9	-143	-143	0	338	94	0	4424	4424	39	0	65	65	0	338	94	0	4424	4424	39	145
H_{10}	-143	-143	0	338	94	0	4424	4424	39	0	65	65	0	338	94	0	4424	4424	39	145
H_{11}	65	65	0	338	94	0	4424	4424	39	0	65	65	0	338	94	0	4424	4424	39	145
H_{12}	70	70	-23	0	105	0	4195	4195	54	0	70	70	217	0	105	0	4195	4195	54	158
H_{13}	70	70	-23	0	105	0	4195	4195	54	0	70	70	217	0	105	0	4195	4195	54	158
H_{14}	166	166	-442	-1091	313	0	0	0	325	0	166	166	167	-1091	313	0	0	0	325	401
H_{15}	211	211	-442	0	346	0	0	0	394	73	211	211	214	0	346	0	0	0	394	504
H_{16}	211	211	-442	0	346	0	0	0	394	73	211	211	214	0	346	0	0	0	394	504
H_{17}	211	211	-442	0	346	0	0	0	394	73	211	211	214	0	346	0	0	0	394	504
H_{18}	211	211	214	0	346	0	0	0	394	73	211	211	214	0	346	0	0	0	394	504
H_{19}	211	211	214	0	346	0	0	0	394	73	211	211	214	0	346	0	0	0	394	504
H_{20}	464	464	377	0	631	0	-723	-723	872	378	464	464	377	0	631	0	-723	-723	872	1107
H_{21}	464	464	377	0	631	0	-723	-723	872	378	464	464	377	0	631	0	-723	-723	872	1107
H_{22}	464	464	377	0	631	0	-723	-723	872	378	464	464	377	0	631	0	-723	-723	872	1107
H_{23}	464	464	377	0	631	0	-723	-723	872	378	464	464	377	0	631	0	-723	-723	872	1107
H_{24}	464	464	377	0	631	0	-723	-723	872	378	464	464	377	0	631	0	-723	-723	872	1107

TABLE 13.5: Hourly SG profits [€] under *Method 1* pricing scheme.

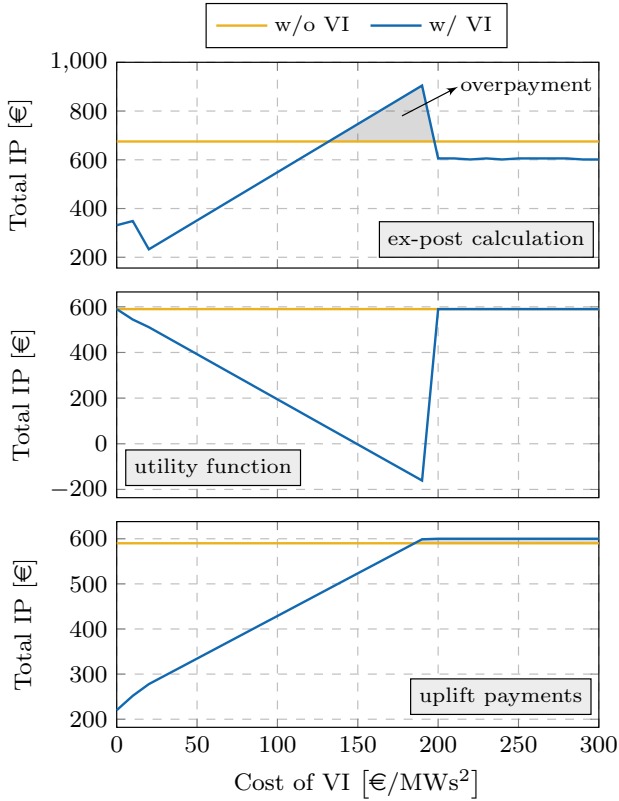


FIGURE 13.4: Impact of virtual inertia on total inertia payments under different bid-in prices and payment mechanisms: (i) *ex-post* calculation; (ii) utility function; and (iii) uplift payments.

the corresponding amount for a respective case without any VI units in the system, as indicated in Fig. 13.4. While counter-intuitive at first, such effect can be justified by the fact that at certain hours the virtual inertia is cheaper than the start-up costs of a generator, and the TSO would rather employ VI instead of committing a conventional SG. However, the VI costs lead to higher duals in the subsequent hours and therefore higher total payments for inertia.

Unit	Cost	H_1	H_2	H_3	H_4	H_5	H_6	H_7	H_8
G_2	EOM	–	–	–	–	–20	–20	–20	–
	SU	–	–	–	–	–300	0	0	–
	IP	–	–	–	–	152	61	144	–
	Total	–	–	–	–	–168	41	124	–
G_3	EOM	–	–	–	–10	–10	–10	–	–
	SU	–	–	–	–200	0	0	–	–
	IP	–	–	–	80	31	122	–	–
	Total	–	–	–	–130	21	112	–	–

TABLE 13.6: Breakdown of hourly UC costs [€] for *Method 2*.

13.5.4 *Method 2: Utility Function*

13.5.4.1 *Small test system*

Similar to the analysis of *Method 1*, Table 13.6 showcases the revenue, costs, payments and profits for generators 2 and 3 in the small test system under the payment scheme of *Method 2*. For the entire scheduling horizon the profits of G_2 and G_3 are -3€ and 3€ respectively. Despite having opposite profits, the issue of larger negative profits due to inertia requirements is resolved by the proposed payment method. Indeed, if the opposite profits were to be redistributed *ex-post*, then both G_2 and G_3 would break even and thus be indifferent to being committed for inertia provision. This symmetry in profits for SGs coming online for inertia provision is a specific characteristics of the utility function method and will be elaborated in more detail in the remainder of this section.

13.5.4.2 *Large test system*

By analyzing the total hourly profits of individual generators given in Table 13.7, we can conclude that in a larger system more units face negative profits compared to *Method 1*. There are two explanations for such outcome: (i) the issue of symmetry already observed in the small system; (ii) the utility function payment method does not provide compensation for reduced EOM revenue due to a decrease in energy price. Indeed, as shown previously in Fig. 13.3, the inertia requirements and changed commitment of the system result in lower EOM prices and therefore reduced unit profits. Such effect

$H \setminus G$	G_1	G_2	G_3	G_4	G_5	G_6	G_7	G_8	G_9	G_{10}	G_{11}	G_{12}	G_{13}	G_{14}	G_{15}	G_{16}	G_{17}	G_{18}	G_{19}	G_{20}
H_1	168	168	134	-153	324	0	0	0	364	-1222	168	168	134	-153	324	0	0	0	364	-784
H_2	28	28	20	-321	208	0	0	0	109	-225	28	28	20	-321	208	0	0	0	109	79
H_3	28	28	20	-321	208	0	0	0	109	-225	28	28	20	-321	208	0	0	0	109	79
H_4	28	28	20	-321	208	0	0	0	109	-225	28	28	20	-321	208	0	0	0	109	79
H_5	28	28	20	-321	208	0	0	0	109	-225	28	28	20	-321	208	0	0	0	109	79
H_6	28	28	20	-321	208	0	0	0	109	-225	28	28	20	-321	208	0	0	0	109	79
H_7	-52	-52	79	-96	20	0	3966	3966	-130	-208	-52	-52	-46	-161	20	0	3966	3966	-130	-126
H_8	-1	-1	0	274	44	0	4424	4424	-63	-107	-143	-143	0	338	44	0	4424	4424	-63	-8
H_9	-106	-106	0	338	-36	0	4424	4424	-228	-280	-143	-143	0	338	-36	0	4424	4424	-228	-254
H_{10}	-13	-13	0	338	34	0	4424	4424	-83	-128	-143	-143	0	338	34	0	4424	4424	-83	-38
H_{11}	12	12	0	338	53	0	4424	4424	-44	-87	12	12	0	338	53	0	4424	4424	-44	21
H_{12}	-1	-1	-23	0	51	0	4195	4195	-57	-116	-1	-1	142	0	51	0	4195	4195	-57	-8
H_{13}	-1	-1	-23	0	51	0	4195	4195	-57	-116	-1	-1	142	0	51	0	4195	4195	-57	-8
H_{14}	-85	-85	-442	-1091	122	0	0	0	-67	-410	-85	-85	-100	-1091	122	0	0	0	-67	-185
H_{15}	30	30	-442	-319	209	0	0	0	111	-223	30	30	22	-319	209	0	0	0	111	82
H_{16}	-23	-23	-442	-412	169	0	0	0	29	-309	-23	-23	-34	-412	169	0	0	0	29	-41
H_{17}	-29	-29	-442	-422	164	0	0	0	20	-319	-29	-29	-40	-422	164	0	0	0	20	-55
H_{18}	28	28	20	-321	208	0	0	0	109	-225	28	28	20	-321	208	0	0	0	109	79
H_{19}	28	28	20	-321	208	0	0	0	109	-225	28	28	20	-321	208	0	0	0	109	79
H_{20}	8	8	-107	-804	285	0	-723	-723	160	-367	8	8	-107	-804	285	0	-723	-723	160	44
H_{21}	75	75	-36	-686	336	0	-723	-723	265	-258	75	75	-36	-686	336	0	-723	-723	265	200
H_{22}	75	75	-36	-686	336	0	-723	-723	265	-258	75	75	-36	-686	336	0	-723	-723	265	200
H_{23}	75	75	-36	-686	336	0	-723	-723	265	-258	75	75	-36	-686	336	0	-723	-723	265	200
H_{24}	75	75	-36	-686	336	0	-723	-723	265	-258	75	75	-36	-686	336	0	-723	-723	265	200

TABLE 13.7: Hourly SG profits [€] under *Method 2* pricing scheme.

is not captured by this method and certain generators will inevitably face negative profits and not receive proper reimbursement.

The reason why payments to inertia providers lead to some generators making the exact opposite profits lies in the fact that the TSO reimburses them according to the exact amount at which it values the inertia at each hour, which is the cost of having those generators online in case no cheaper inertia is available. There is thus a single price for inertia at each hour, which does not necessarily correspond to the marginal inertia price (most expensive unit online), but to a total price that will be distributed among providers. Since generators provide different amounts of inertia, some units will receive higher payments than others during the redistribution of inertia provision revenue. This problem can be resolved by assigning the exact amount of inertia provided by each generator *ex-post*, such that no generator is facing losses. Nevertheless, it is hard to find a systematic way in which this procedure should be conducted. This is in fact a main distinction compared to *Method 1*, where the price of inertia is calculated *ex-post* as the cost of the most expensive unit coming online for inertia purposes.

13.5.4.3 Inclusion of Virtual Inertia

The addition of virtual inertia creates issues for reimbursement under the utility function method. More precisely, with the addition of VI units the dual of the RoCoF constraint yields $\lambda_t^H = U_t^H - C_v^{VI}$, which could have negative

$H \setminus G$	G_1	G_2	G_3	G_4	G_5	G_6	G_7	G_8	G_9	G_{10}	G_{11}	G_{12}	G_{13}	G_{14}	G_{15}	G_{16}	G_{17}	G_{18}	G_{19}	G_{20}
H_1	0	0	0	0	0	0	0	0	0	0	0	0	0	0	0	0	0	0	0	0
H_2	0	0	0	0	0	0	0	0	0	0	0	0	0	0	0	0	0	0	0	0
H_3	0	0	0	0	0	0	0	0	0	0	0	0	0	0	0	0	0	0	0	0
H_4	0	0	0	0	0	0	0	0	0	0	0	0	0	0	0	0	0	0	0	0
H_5	0	0	0	0	0	0	0	0	0	0	0	0	0	0	0	0	0	0	0	0
H_6	0	0	0	0	0	0	0	0	0	0	0	0	0	0	0	0	0	0	0	0
H_7	0	0	0	0	0	0	3966	3966	0	0	0	0	0	0	0	0	3966	3966	0	0
H_8	0	0	0	338	0	0	4424	4424	0	0	0	0	0	274	0	0	4424	4424	0	0
H_9	0	0	0	338	0	0	4424	4424	0	0	0	0	0	338	0	0	4424	4424	0	0
H_{10}	0	0	0	338	0	0	4424	4424	0	0	0	0	0	338	0	0	4424	4424	0	0
H_{11}	0	0	0	338	0	0	4424	4424	0	0	0	0	0	338	0	0	4424	4424	0	0
H_{12}	0	0	0	0	0	0	4195	4195	0	0	0	0	0	0	0	0	4195	4195	0	0
H_{13}	0	0	0	0	0	0	4195	4195	0	0	0	0	0	0	0	0	4195	4195	0	0
H_{14}	0	0	0	0	0	0	0	0	0	0	0	0	0	0	0	0	0	0	0	0
H_{15}	0	0	0	0	0	0	0	0	0	0	0	0	0	0	0	0	0	0	0	0
H_{16}	0	0	0	0	0	0	0	0	0	0	0	0	0	0	0	0	0	0	0	0
H_{17}	0	0	0	0	0	0	0	0	0	0	0	0	0	0	0	0	0	0	0	0
H_{18}	0	0	0	0	0	0	0	0	0	0	0	0	0	0	0	0	0	0	0	0
H_{19}	0	0	0	0	0	0	0	0	0	0	0	0	0	0	0	0	0	0	0	0
H_{20}	0	0	0	0	0	0	0	0	0	0	0	0	0	0	0	0	0	0	0	0
H_{21}	0	0	0	0	0	0	0	0	0	0	0	0	0	0	0	0	0	0	0	0
H_{22}	0	0	0	0	0	0	0	0	0	0	0	0	0	0	0	0	0	0	0	0
H_{23}	0	0	0	0	0	0	0	0	0	0	0	0	0	0	0	0	0	0	0	0
H_{24}	0	0	0	0	0	0	0	0	0	0	0	0	0	0	0	0	0	0	0	0

TABLE 13.8: Hourly SG profits [€] under *Method 3* pricing scheme.

values for large enough C_v^{VI} and result in units paying to provide inertia. In other words, as virtual inertia becomes more expensive, less payments will be made to units offering inertia which goes against the basic market intuition. Such phenomena can also be seen in Fig. 13.4 on the example of a small test system and assuming all VI units bid-in at the same cost. Furthermore, for $C_v^{\text{VI}} \in [150, 200]$ €/MWs² the dual becomes negative which is conceptually problematic.

A possible solution could simply be to set the dual to $\lambda_t^{\text{H}} = U_t^{\text{H}}$, with the TSO always paying U^{H} regardless of which technology is providing inertia and at which price. This would encourage cheaper technologies to enter the market with the potential for high profits. Such solution is not necessarily a disadvantage for the TSO. As a matter of fact, the operator could opt for paying a fixed price for inertia in order to encourage units with cheaper inertia provision to penetrate the system; once this is achieved, the TSO can reduce inertia payments.

13.5.5 *Method 3: Uplift Payments*

Applying the uplift method to the small system yields total inertia payments of 590 €, with losses on the EOM and start-up costs both covered. Therefore, G_2 and G_3 are left with zero profits. Similar conclusions can be drawn from

System performance metric	Method 1	Method 2	Method 3
Optimal UC solution [€]	569 610	569 610	569 610
Total inertia payments [€]	258 160	162 124	187 948
# units with negative profits	0/18	5/18	0/18
# units with positive profits	18/18	13/18	6/18

TABLE 13.9: Comparison of different inertia payment methods.

the hourly profit analysis for the larger test case given in Table. 13.8, where negative profits of all SGs have been reduced to zero.

Adding virtual inertia does not have any negative impact on the payments through *Method 3*. SGs still receive compensation in order to bring their profits to zero and batteries are reimbursed for VI provision based on their bids. Inertia payments will always be lower compared to the case without virtual inertia, as indicated in Fig. 13.4.

13.5.6 Comparison of Payment Methods

We now compare the three payment methods and evaluate them on a large test system based on several metrics of performance. Table 13.9 shows the comparison of total system costs and inertia payments for each pricing scheme, as well as the number of units facing negative or positive profits. Understandably, all methods result in the same UC costs and distinguish only between the amount of final inertia payments. Moreover, they yield the same commitment and dispatch schedule for all generators. *Method 2* is the most affordable for the TSO, with lower inertia payments compared to the other two mechanisms.

Some interesting observations can be made when studying different levels of virtual inertia in the system provided in Table 13.10. In particular, as the VI penetration increases the payments from *Method 1* and *Method 3* decrease, while *Method 2* remains unaffected. As a result, the uplift payments become more advantageous for the TSO. Furthermore, by agreeing to pay a fixed amount with the utility function method, this payment scheme can become more expensive as more VI units enter the system. Nonetheless, it is important to keep in mind that the TSO can choose to re-evaluate the inertia payments under such circumstances.

Finally, Table 13.11 highlights the main policy implications for all stakeholders involved in the inertia provision. It is clear that all three methods

could improve frequency stability and aid the operator in ensuring system reliability. On the other hand, the policy implications to different inertia providers might vary between the payment schemes. Nevertheless, taking all aspects into account, the uplift payments appear to be the most beneficial and practical method of the three. This can be justified on several grounds: (i) the fundamental concepts are already familiar to certain operators; (ii) the method does not require additional *ex-post* calculations; (iii) such payment scheme does not alter the standard UC formulation; and (iv) it prevents excessively high payments to inertia providers.

13.6 CONCLUSION

This chapter proposes three novel inertia pricing schemes, as well as the appropriate methods for reimbursement of respective inertia providers in a transparent and fair manner according to their individual participation. In particular, the focus is set on applying the *ex-post* calculation, utility function and uplift payments, respectively, for determining the appropriate market price for inertial response. A two-step approach based on frequency-constrained unit commitment formulation is employed, which co-optimizes the provision of energy and inertia services while accounting for their complementary properties and differentiating between the units being online for energy purposes and the ones committed additionally solely for inertia provision. The analysis includes both traditional synchronous generators and converter-based units providing virtual inertia, and gives insights into the impact of each pricing scheme on total system cost and its potential for attracting more affordable providers of inertial response.

The results indicate that all three methods could have a beneficial impact on frequency stability and aid the operator in ensuring system reliability. While the policy implications to different inertia providers might vary between

VI installation	Method 1	Method 2	Method 3
0 %	258 160	162 124	187 948
10 %	245 195	162 124	162 938
20 %	156 725	162 124	138 231
35 %	135 849	162 124	116 765

TABLE 13.10: Comparison of total inertia payments [€] under different levels of VI installation in the system.

Perspective	Ex-Post Price	Utility Function	Uplift Payments
TSO	Incentives for provision of virtual inertia	Clear financial expectations due to fixed rates for inertia services	Low payments whenever more affordable inertia is available
	Large inertia payments	Same expenses regardless of the available inertia resources, unless tailor-made utility function is used	Does not incentivize investment in more efficient inertia technologies
SGs	High profits	—	—
	—	Possible negative profits	—
VI units	High profits	Clear income expectations	Clear market understanding
	—	Fixed income for inertia provision	Low profitability

TABLE 13.11: Policy implications of proposed payment methods with distinctive advantages (green) and disadvantages (red).

the payment schemes, the uplift payments appear to be the most beneficial and practical method of the three, as the fundamental concepts are already familiar to certain operators and the method does not require additional *ex-post* calculations. Moreover, such payment scheme does not alter the standard UC formulation and prevents excessively high payments to inertia providers. This also opens the avenue for future work on integration of inertia provision in the existing ancillary service offering and understanding its impact on other services such as primary frequency response, which could eventually aid creation of an appropriate market for inertia.

IMPACT OF INVERTER-BASED GENERATION ON ISLANDING DETECTION SCHEMES IN DISTRIBUTION NETWORKS

This chapter studies the impact of inverter-based generation on islanding detection schemes. One of the most frequently used interface protections for distributed generators is the Loss of Mains (LoM) protection. It detects the formation of an island at the connection point and disconnects the DG to protect the unit, the system and the personnel. The increased penetration of inverter-interfaced DGs, in combination with the decommissioning of synchronous generators, reduces the system inertia and leads to faster changing and larger voltage and frequency deviations. Therefore, modern grid codes require inverter-based DGs to provide support to the grid by modifying their active and reactive power injection based on local measurements. However, this leads to complex inverter-grid interactions and modifies the islanded system behavior, thus disturbing the operation of LoM protections that rely mainly on local voltage and frequency measurements. In this work, we propose an improved analytical formulation for estimating the Non-Detection Zone (NDZ) of LoM protection devices in the presence of grid-feeding inverters, as well as novel NDZ approximations for grid-supporting and grid-forming inverter-based services. We verify the analytical results with detailed EMT simulations and comment on the impact that the new inverter requirements have on the performance of LoM protections. The chapter is based on [328].

14.1 INTRODUCTION

The growing penetration of distributed generation in power systems poses new challenges related to protection and control of these units. One of the most important aspects and a primary concern for operators in such systems is the occurrence of unintentional islanding or so-called loss of mains, where a DG unit is disconnected from the main utility grid but continues to operate and energize an isolated portion of the system. Such operating

conditions are highly undesirable as they complicate the orderly reconnection of the utility network and pose a hazard to the utility system and personnel, other customers, and to the DG itself. In addition to its normal function of protection and control of the DG, a state-of-the-art converter control scheme should be able to provide reliable islanding detection and cease to energize the area, typically within two seconds of the islanding instance, as prescribed by the IEEE 1547 standard [329].

With the share of distributed renewable generation steadily increasing, the degree of DG capacity is becoming sufficiently large to supply the local load demand and therefore reduce the power drawn from the grid. Under such circumstances the risk of LoM detection failure becomes particularly high, with the protection inputs - usually related to frequency and voltage deviations - not being large enough for detecting islanding within a prescribed time period. The NDZ is frequently used as a protection performance index defined in terms of active/reactive ($\Delta P/\Delta Q$) power mismatch between the DG inverter and the load. In particular, NDZ determines the minimum values of power mismatch between local load and generation that would trigger the LoM protection schemes. The islanding detection algorithm with the smallest NDZ is thus considered the most effective.

The existing anti-islanding techniques can be categorized into local and remote, with local schemes being further classified into active and passive [330–333]. Active schemes are generally based on the concept of perturb and observe [332, 334], where an external signal is injected into the system for the purpose of perturbing the DG output parameters up to a significant level upon islanding occurrence. While this deviation is relatively insignificant in normal operation, it would drastically enlarge in case of LoM and trip the protection relays. Passive methods use only local voltage and current sensing to detect abnormal operation while monitoring system characteristics such as Over/Under- Voltage (OV/UV) and Frequency (OF/UF), RoCoF, and voltage phase jumps [333]. Therefore, they possess a larger NDZ compared to active methods. However, while generally more effective, the active schemes are also slower, more expensive, tend to deteriorate power quality, reduce efficiency of parallel inverters, and may potentially have adverse impact on grid dynamics and lead to instability [335]. Finally, remote LoM methods connect the DGs directly to the feeder relays through inter-tripping mechanisms and are the most accurate and robust. However, they require protection-grade communication infrastructure and advanced signal processing techniques for every DG, which is usually not available and expensive to install. Despite having negligible NDZ and high reliability in comparison with local schemes,

high cost, complexity, and implementation problems lead to local schemes being more preferable [331]. Therefore, in this work we solely focus on local passive protection schemes, in particular the detection algorithms based on over/under-voltage and over/under-frequency measurements [336].

The existing literature focuses solely on anti-islanding protection of grid-feeding inverters [336–341], and the suggested approximations of NDZs tend to be imprecise due to unjustified physical assumptions. In particular, the proposed analytical expressions yield a rectangular NDZ (e.g., see [336–338]), whereas the simulations and real-world measurements indicate a rather trapezoidal-shaped non-detection region. Such imprecision is a consequence of often neglected dependencies between the active power and frequency, i.e., reactive power and voltage, respectively, which simplifies the mathematical analysis of the problem at hand. Moreover, considering that the more compelling converter control modes such as grid-forming and grid-supporting are gradually emerging [62], the compatibility of traditional LoM detection schemes needs to be re-evaluated.

This study tackles the weaknesses of the existing analytical NDZ approximations applied to passive UV/OV and UF/OF anti-islanding protection schemes of grid-feeding inverters in [336–341], and proposes a more accurate formulation which achieves an almost perfect match with the simulations. Moreover, we extend the framework onto more complex inverter control schemes, namely grid-forming and grid-supporting, and derive the analytical approximations for their respective NDZs. Such comprehensive formulation has not yet been presented in the literature. Finally, the theoretical results have been verified through EMT simulations using a detailed inverter control model from Chapter 2 connected to a distribution grid, as prescribed by industry standards.

The rest of the chapter is structured as follows. In Section 14.2, the standard anti-islanding testing conditions are presented, together with the existing practice for deriving the analytical NDZ approximation of grid-feeding inverters. Subsequently, the improved mathematical formulation for grid-feeding NDZ is introduced in Section 14.3, followed by the derivation of novel NDZ expressions for grid-forming and grid-supporting operation modes. Section 14.4 discusses the modeling and implementation of different converter control schemes as well as the design and settings of LoM protection schemes. The proposed theoretical approach is validated through time-domain simulations in Section 14.5, whereas Section 14.6 discusses the outlook of the study and concludes the chapter.

14.2 THEORETICAL PRELIMINARIES AND EXISTING PRACTICE

All of the variables used throughout this study are defined as scalars ($\in \mathbb{R}$), and hence the vector declaration is omitted for brevity. Moreover, unlike the majority of the thesis that is described in per unit, the notation in this chapter is expressed in SI.

14.2.1 *Anti-Islanding Testing Conditions*

A generic system traditionally used for LoM studies is illustrated in Fig. 14.1, as defined by the IEEE 1547 standard. Testing conditions of the *RLC* load are as follows: (i) resonant load frequency is the same as grid frequency; (ii) load quality factor¹ is set to $Q_f = 2.5$; and (iii) power generated by DG should match the power consumed by the load, i.e., $\Delta P = \Delta Q = 0$ when switch S_2 is closed. Under such conditions, the opening of switch S_2 results in resonance at nominal voltage and frequency between the islanded DG and load. The DG operating with unity power factor (i.e., $Q_G = 0$) yields a worst-case scenario for islanding detection and will therefore be considered as benchmark in this study.

In reality, there is always some power mismatch ($\Delta P, \Delta Q$) between the DG output and the load, compensated by the network when operating in grid-connected mode. Therefore, after the grid disconnection, the voltage and frequency in the system are forced to new values \hat{V} and \hat{f} , respectively. In case of a large power mismatch, these values might exceed the permissible ranges of the voltage and frequency protection schemes, which would in turn trip the switch S_1 to prevent continued islanded operation. The general relationship between the power mismatch and the voltage/frequency thresholds can be expressed as follows:

$$g(V, V_{\max}, \Delta Q) \leq \frac{\Delta P}{P_G} \leq g(V, V_{\min}, \Delta Q), \quad (14.1a)$$

$$h(f, f_{\min}, Q_f, \Delta P) \leq \frac{\Delta Q}{P_G} \leq h(f, f_{\max}, Q_f, \Delta P), \quad (14.1b)$$

where V_{\min} , V_{\max} , f_{\min} and f_{\max} are the respective UV/OV and UF/OF thresholds, typically defined as percentages of nominal voltage and frequency, and P_G is the DG's active power before the islanding event used as a normalization constant. The area formed in the $\Delta P - \Delta Q$ plane by the expressions

¹ The quality factor is defined as the ratio of the reactive power stored in the L and C elements and the active power consumed by the resistance R .

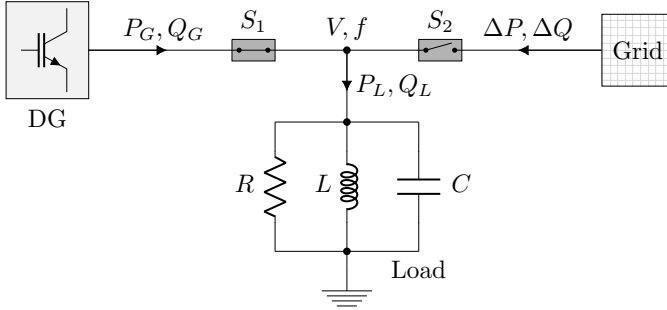


FIGURE 14.1: Generic system for studying anti-islanding detection schemes. Both switches are originally closed, with the opening of switch S_2 reflecting the islanding operation and activation of the LoM protection.

in (14.1) is defined as NDZ, and it indicates a set of power mismatches for which an island may be formed without being detected. More precisely, for any power mismatch within the specified thresholds the resulting voltage and frequency in the system will remain within the nominal range, even after a grid disconnection, thus failing to trigger the LoM protection.

14.2.2 Existing Practice

The existing literature is confined within the scope of DGs controlled as a constant power source, i.e., interfaced to the grid via an inverter operating in a so-called grid-feeding mode [336–341] (see Section 2.2.1). This implies that the injected power from a DG remains the same before and after an islanding event, which drastically simplifies the analysis. Moreover, the $\Delta P - f$ and $\Delta Q - V$ dependencies are often neglected, resulting in a rectangular NDZ approximation with vertical and horizontal lines coming from the voltage and frequency thresholds in (14.1a) and (14.1b), respectively. Such analytical formulation can be derived by looking at the power balance before and after the grid disconnection, as previously described in [336–338] and derived hereinafter.

Let us denote by $(\hat{\cdot})$ the quantities after the LoM event. Having in mind that $\hat{P}_G = \hat{P}_L$ and $\hat{Q}_G = \hat{Q}_L$, one obtains:

$$\Delta P := P_L - P_G = \Delta P_G - \Delta P_L, \quad (14.2a)$$

$$\Delta Q := Q_L - Q_G = \Delta Q_G - \Delta Q_L, \quad (14.2b)$$

where $\Delta P_i := \hat{P}_i - P_i$ and $\Delta Q_i := \hat{Q}_i - Q_i, \forall i \in \{G, L\}$. For the grid-feeding case at hand, the DG power after the event remains (or almost instantaneously restores to) the same power, i.e., $\Delta P_G = \Delta Q_G = 0$. On the other hand, the load consumption varies due to a change in voltage and frequency:

$$P_L = \frac{V^2}{R}, \quad Q_L = V^2 \left(\frac{1}{\omega L} - \omega C \right), \quad (14.3a)$$

$$\hat{P}_L = \frac{\hat{V}^2}{R}, \quad \hat{Q}_L = \hat{V}^2 \left(\frac{1}{\hat{\omega} L} - \hat{\omega} C \right), \quad (14.3b)$$

with $\omega = 2\pi f$ and $\hat{\omega} = 2\pi \hat{f}$. Since $\Delta P_G = 0$ and $P_G = \hat{P}_G = \hat{P}_L$, one can describe the $\Delta P/P_G$ term using the expressions in (14.3) by

$$\frac{\Delta P}{P_G} = -\frac{\Delta P_L}{P_G} = -\frac{\Delta P_L}{\hat{P}_L} = \frac{(V^2 - \hat{V}^2)/R}{\hat{V}^2/R} = \frac{V^2}{\hat{V}^2} - 1. \quad (14.4)$$

Therefore, for the voltage \hat{V} to be kept within $[V_{\min}, V_{\max}]$ limits, the following condition must be satisfied:

$$\frac{V^2}{V_{\max}^2} - 1 \leq \frac{\Delta P}{P_G} \leq \frac{V^2}{V_{\min}^2} - 1, \quad (14.5)$$

which yields two vertical lines in the $\Delta P - \Delta Q$ NDZ plane, as previously discussed.

A slightly different approach is taken for deriving the reactive power mismatch bounds. Since the DG power factor is assumed to be 1, we can set $Q_G = 0$ and therefore $\Delta Q = Q_L$. Moreover, according to the IEC 62116:2014 standard [342] and without loss of generality, the load is initialized at resonant frequency $f = 1/(2\pi\sqrt{L_0C_0})$, where L_0 and C_0 are the respective resonant frequency components and the quality factor is equal to $Q_f = RL_0/C_0$. Subsequently, either L or C load component is changed to accommodate for $\Delta Q \neq 0$, which holds as long as $Q_f \geq \Delta Q/P_G$. For the purposes of this study, we will assume that the capacitive element yields the complete reactive power mismatch, i.e.,

$$L = L_0, \quad C = C_0 + \Delta C = C_0 - \frac{\Delta Q}{2\pi f V^2}, \quad (14.6)$$

which together with (14.3) and the fact that $\Delta Q = Q_L$ results in

$$\Delta Q = V^2 \left(\frac{1}{2\pi f L} - 2\pi f C \right) = V^2 \left(\frac{1}{2\pi f L_0} - 2\pi f (C_0 + \Delta C) \right). \quad (14.7)$$

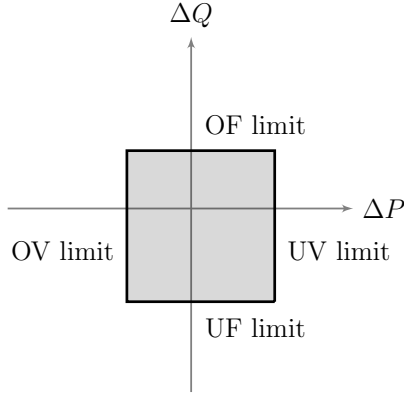


FIGURE 14.2: Graphical illustration of the (traditional) NDZ approximation widely used in the literature.

By combining the expressions (14.2b)-(14.3b), (14.6) and (14.7), and conducting a set of trivial mathematical operations, one obtains:

$$\frac{\Delta Q}{P_G} = Q_f \left(1 - \frac{f^2}{\hat{f}^2} \right), \quad (14.8)$$

which gives the NDZ bounds on the reactive power mismatch of the form:

$$Q_f \left(1 - \frac{f^2}{f_{\min}^2} \right) \leq \frac{\Delta Q}{P_G} \leq Q_f \left(1 - \frac{f^2}{f_{\max}^2} \right). \quad (14.9)$$

The thresholds in (14.9) define two horizontal lines in the $\Delta P - \Delta Q$ plane and together with (14.5) complete the rectangular-shaped NDZ illustrated in Fig. 14.2, characteristic of grid-feeding DG units. However, while widely used in the literature, such approximation tends to be inaccurate when compared to simulations and experimental studies, as previously pointed out in [336]. The imprecision mostly arises from simplifications based on ignoring the $\Delta P - f$ and $\Delta Q - V$ dependencies. Furthermore, the existing NDZ formulation is applicable only to a single mode of operation. With grid-feeding control design being replaced by more complex grid-forming and grid-supporting control schemes [62], a need for a comprehensive analytical NDZ evaluation that encompasses all potential DG control modes is rapidly increasing. In the remainder of this section, we will introduce the aforementioned inverter operation modes, followed by a novel formulation of NDZ thresholds for each inverter mode respectively.

14.3 ANALYTICAL APPROXIMATION OF NDZ

14.3.1 Converter Operation Modes

The classification of different converter control schemes and respective operation modes has been thoroughly discussed in Chapter 2. Here, we will briefly recap the main distinctions pertaining to system-level control and redefine the underlying notation for the purposes of this chapter.

Depending on their operation in a system, power converters can be classified into grid-forming and grid-following, with the latter category further distinguishing between grid-feeding and grid-supporting units [62]. The conceptual differences come mostly from the power control design (i.e., the outer control loop) and the input/output characteristic of the respective controller, as illustrated in Fig. 14.3. In particular, grid-forming converters can be represented as an ideal AC voltage source with a low-output impedance, setting the voltage amplitude V and frequency f at the connection terminal by adjusting the predefined power setpoints (P_G^*, Q_G^*) using a droop control law of the form:

$$\hat{f}^* := f^* + R_P (P_G^* - \hat{P}_G) = f^* - R_P \Delta P, \quad (14.10a)$$

$$\hat{V}^* := V^* + R_Q (Q_G^* - \hat{Q}_G) = V^* - R_Q \Delta Q, \quad (14.10b)$$

with \hat{f}^* and \hat{V}^* denoting the internally computed frequency and voltage references, and R_P and R_Q being the active and reactive power droop gains respectively. Therefore, these converters are capable of operating in an islanded network without the presence of traditional synchronous generators.

On the other hand, the grid-following power converters are mainly designed to deliver power to an energized grid. They can be represented as an ideal current source connected to the grid in parallel with a high impedance. While the grid-feeding mode acts as a constant power source with a fixed power output $P_G = P_G^*$ and $Q_G = Q_G^*$, the grid-supporting operation in addition regulates the current and voltage at the converter output in order to keep the grid frequency and voltage amplitude close to the nominal values, as follows:

$$\hat{P}_G^* := P_G^* + R_f (f^* - \hat{f}) = P_G^* - R_f \Delta f, \quad (14.11a)$$

$$\hat{Q}_G^* := Q_G^* + R_V (V^* - \hat{V}) = Q_G^* - R_V \Delta V, \quad (14.11b)$$

where \hat{P}_G^* and \hat{Q}_G^* are the adjusted power output references, and R_f and R_V denote the frequency and voltage-related droop gains. The operation of grid-following converters is contingent on having a stiff frequency signal

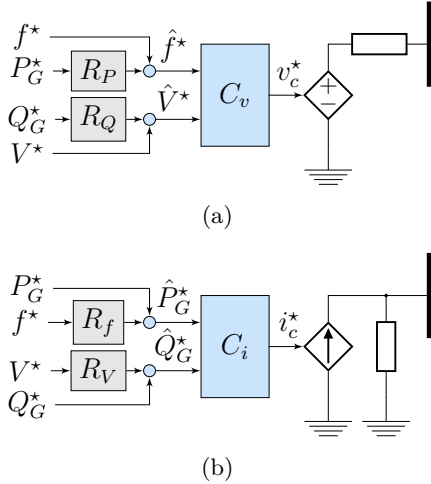


FIGURE 14.3: Simplified representation of grid-connected power converters with characteristic setpoint input and internally computed reference output: (a) grid-forming mode; and (b) grid-following mode.

at the connection terminal, which is then measured via a PLL and used for power regulation. Hence, these converter units do not possess standalone capabilities.

The system-level controllers C_v and C_i combine the signals and provide respective reference vectors $v_c^* \in \mathbb{R}^2$ and $i_c^* \in \mathbb{R}^2$ to device-level control, that adjusts the converter output accordingly. Therefore, in steady state, the equalities $\hat{f} = \hat{f}^*$ and $\hat{V} = \hat{V}^*$ hold for the grid-forming converter, i.e., $\hat{P}_G = \hat{P}_G^*$ and $\hat{Q}_G = \hat{Q}_G^*$ for the grid-following converter. Understandably, the device-level control (i.e., inner control loop) design also varies between different operation modes. In particular, the grid-forming mode comprises a cascade of voltage and current PI controllers, whereas the grid-following mode only employs the current control. More details on both the system- and device-level control are provided in Chapter 2.

14.3.2 NDZ Approximation for Grid-Following DGs

In this section, we focus on deriving the analytical expressions for NDZ approximation of a DG controlled through a grid-following inverter. In particular, we will focus on the grid-supporting mode, since a corresponding

approximation for the grid-feeding case can be easily obtained by setting the droop gains R_f and R_V to zero. Based on the previously introduced notation and according to (14.11), we can determine the change in DG's active and reactive power as

$$\Delta P_G = -R_f \Delta f, \tag{14.12a}$$

$$\Delta Q_G = -R_V \Delta V. \tag{14.12b}$$

Combining it with (14.3) and using the same procedure as in Section 14.2.2, the expression for normalized active power change $\Delta P/P_G$ is obtained:

$$\frac{\Delta P}{P_G} = \frac{V^2}{\hat{V}^2} - 1 - \frac{V^2 R_f (\hat{f} - f)}{\hat{V}^2 P_G}. \tag{14.13}$$

The approach for deriving the reactive power mismatch bounds is again similar to the one presented in Section 14.2.2, i.e., we assume a unity DG power factor and therefore set $Q_G = 0$ and $\Delta Q = Q_L$. Accordingly, using (14.3b) and (14.11a) we derive

$$R_V \Delta V = -\hat{V}^2 \left(\frac{1}{2\pi \hat{f} L_0} - 2\pi \hat{f} (C_0 + \Delta C) \right), \tag{14.14}$$

which substituted into (14.6) yields

$$\frac{\Delta Q}{P_G} = \left(1 + \frac{\Delta P}{P_G} \right) \left(Q_f \left(1 - \frac{f^2}{\hat{f}^2} \right) - R R_V \frac{f \Delta V}{\hat{f} \hat{V}^2} \right). \tag{14.15}$$

The formulation in (14.13) and (14.15) clearly corresponds to (14.4) and (14.8) from Section 14.2.2. However, unlike (14.4) and (14.8), the expressions in (14.13) and (14.15) are dependent on \hat{V} and \hat{f} respectively, which is not in accordance with the definition of $g(\cdot)$ and $h(\cdot)$ in (14.1). Therefore, relationships describing $\hat{f}(V, \hat{V})$ and $\hat{V}(f, \hat{f})$ have to be derived and substituted into (14.13) and (14.15).

Let us rewrite (14.13) and (14.14) using (14.2)-(14.3), as follows:

$$R_f \Delta f = -\frac{\hat{V}^2}{R} + P_G, \tag{14.16a}$$

$$R_V \Delta V = -\hat{V}^2 \left(\frac{1}{2\pi \hat{f} L} - 2\pi \hat{f} C \right). \tag{14.16b}$$

By solving (14.16a) for \hat{f} and (14.16b) for \hat{V} , and embedding the power output limits, we obtain

$$\hat{f}(V, \hat{V}) = \frac{1}{4\pi C} \left(\frac{R_V \Delta V}{\hat{V}^2} + \sqrt{\left(\frac{R_V \Delta V}{\hat{V}^2} \right)^2 + 4 \frac{C}{L}} \right), \quad (14.17a)$$

$$\hat{V}(f, \hat{f}) = \sqrt{R \left(\min \left\{ P_{\text{nom}}, \max \{ 0, P_G - R_f \Delta f \} \right\} \right)}, \quad (14.17b)$$

where P_{nom} denotes the nominal (rated) power of the inverter and “min” and “max” terms ensure that the DG power output is within the permissible range $\hat{P}_G \in [0, P_{\text{nom}}]$. Interestingly enough, the relationship in (14.17a) somewhat resembles the definition of “islanding pulsation” from [332] and [337].

The next step towards a general formulation (14.1) is to eliminate the load parameters from (14.17). Each RLC combination reflects a different power mismatch between the load and DG prior to the LoM event. Hence, NDZ is simulated through small perturbations of load parameters and evaluating whether the protection is able to detect the islanding for each scenario. For simplicity and without loss of generality, we assume that the inductive load element provides the complete inductive power mismatch. Substituting $\Delta C = 0$ into (14.7) and solving for L yields

$$L = \frac{1}{2\pi f} \left(\frac{\Delta Q}{V^2} + 2\pi f C_0 \right)^{-1}, \quad (14.18)$$

which in turn transforms (14.17a) into

$$\hat{f}(V, \hat{V}, \Delta Q) = \frac{\beta_V + \sqrt{\beta_V^2 + 8\pi f C_0 \left(\frac{\Delta Q}{V^2} + 2\pi f C_0 \right)}}{4\pi C_0}, \quad (14.19)$$

with the introduction of new variable $\beta_V = R_V \frac{\Delta V}{V^2}$. Note that the load is initialized at resonant frequency $f = \frac{1}{2\pi\sqrt{L_0 C_0}}$.

As for the resistive component, by combining (14.2a) and (14.3a) we can describe the load resistance by

$$R = \frac{V^2}{\Delta P + P_G}, \quad (14.20)$$

which substituted into (14.17b) gives

$$\hat{V}(f, \hat{f}, \Delta P) = \sqrt{\frac{V^2}{\Delta P + P_G} \left(\min \left\{ P_{\text{nom}}, \max \{ 0, P_G - R_f \Delta f \} \right\} \right)}. \quad (14.21)$$

Again, similarly to (14.17b), the active power output of the DG after the disconnection is bounded by $\hat{P}_G \in [0, P_{\text{nom}}]$.

The NDZ approximation can therefore be represented by the following inequalities:

$$\min_{\hat{V}} g(V, \hat{V}, \Delta Q) \leq \frac{\Delta P}{P_G} \leq \max_{\hat{V}} g(V, \hat{V}, \Delta Q), \quad (14.22a)$$

$$\min_{\hat{f}} h(f, \hat{f}, \Delta P) \leq \frac{\Delta Q}{P_G} \leq \max_{\hat{f}} h(f, \hat{f}, \Delta P), \quad (14.22b)$$

where $g(\cdot)$ and $h(\cdot)$ are obtained by substituting (14.19) into (14.13) and (14.21) into (14.15), respectively. Such mathematical procedure finalizes the NDZ approximation and yields

$$\frac{V^2}{V_{\text{max}}^2} - 1 - \frac{V^2 R_f \Delta f_1}{V_{\text{max}}^2 P_G} \leq \frac{\Delta P}{P_G} \leq \frac{V^2}{V_{\text{min}}^2} - 1 - \frac{V^2 R_f \Delta f_2}{V_{\text{min}}^2 P_G}, \quad (14.23a)$$

$$\xi_{\text{min}} \leq \frac{\Delta Q}{P_G} \leq \xi_{\text{max}}, \quad (14.23b)$$

with the NDZ bounds for reactive power described by

$$\xi_{\text{min}} := \left(1 + \frac{\Delta P}{P_G}\right) \left(Q_f \left(1 - \frac{f^2}{f_{\text{min}}^2}\right) - RR_V \frac{f \Delta V_1}{f_{\text{min}} \hat{V}_1^2}\right), \quad (14.24a)$$

$$\xi_{\text{max}} := \left(1 + \frac{\Delta P}{P_G}\right) \left(Q_f \left(1 - \frac{f^2}{f_{\text{max}}^2}\right) - RR_V \frac{f \Delta V_2}{f_{\text{max}} \hat{V}_2^2}\right). \quad (14.24b)$$

The deviation terms in (14.23) are defined $\forall i \in \{1, 2\}$ as

$$\Delta f_i := \hat{f}_i - f, \quad (14.25a)$$

$$\Delta V_i := \hat{V}_i - V, \quad (14.25b)$$

whereas the newly introduced variables are of the form

$$\hat{f}_1 := \hat{f}(V, V_{\text{max}}, \Delta Q), \quad \hat{f}_2 := \hat{f}(V, V_{\text{min}}, \Delta Q), \quad (14.26a)$$

$$\hat{V}_1 := \hat{V}(f, f_{\text{min}}, \Delta P), \quad \hat{V}_2 := \hat{V}(f, f_{\text{max}}, \Delta P). \quad (14.26b)$$

The mathematical justification for selecting $g_{\text{min}}(\cdot, V_{\text{max}})$, $g_{\text{max}}(\cdot, V_{\text{min}})$ and $h_{\text{min}}(\cdot, f_{\text{min}})$, $h_{\text{max}}(\cdot, f_{\text{max}})$ is based on the monotonic properties of the nonlinear functions $g(\cdot)$ and $h(\cdot)$ and is given in Appendix B.6. Unlike the traditional practice presented in Section 14.2.2, where only $\Delta P - V$ and $\Delta Q - f$ dependencies are considered when approximating the NDZ, the

proposed formulation also captures the impact of one power mismatch on another, i.e., incorporates the correlation between the $(\Delta P, f)$ and $(\Delta Q, V)$ terms.

Revisiting the conceptual differences between the grid-feeding and grid-supporting mode of operation elaborated in Section 14.3.1, one can easily approximate the NDZ of a grid-feeding converter by setting $R_f = R_V = 0$ in (14.23), which results in

$$\frac{V^2}{V_{\max}^2} - 1 \leq \frac{\Delta P}{P_G} \leq \frac{V^2}{V_{\min}^2} - 1, \quad (14.27a)$$

$$\left(1 + \frac{\Delta P}{P_G}\right) Q_f \left(1 - \frac{f^2}{f_{\min}^2}\right) \leq \frac{\Delta Q}{P_G} \leq \left(1 + \frac{\Delta P}{P_G}\right) Q_f \left(1 - \frac{f^2}{f_{\max}^2}\right). \quad (14.27b)$$

Comparing the analytical bounds in (14.27) to (14.5) and (14.9) respectively, we can conclude that the proposed formulation improves the approximation of the under/over-frequency thresholds of a grid-feeding inverter. In particular, it introduces a $(1 + \Delta P/P_G)$ term and therefore a linear dependency between the frequency and active power mismatch described in (14.27b), which breaks the traditional hierarchy of rectangular-shaped NDZs that do not accurately capture the realistic system conditions. More precisely, (14.27b) introduces a gradient in the bounds describing the UF/OF triggers in the $\Delta P - \Delta Q$ plane, which in turn yields a trapezoidal NDZ, as will be shown in Section 14.5.

14.3.3 NDZ Approximation for Grid-Forming DGs

While conceptually different in operation principles, the mathematical representation of the outer control loops of the grid-forming and grid-supporting converters has many similarities due to a droop-based control law. As a matter of fact, by comparing (14.10a) and (14.11a), i.e., (14.10b) and (14.11b), we can conclude that the two sets of expressions are identical if $R_P = R_f^{-1}$ and $R_Q = R_V^{-1}$. Therefore, the analytical approximation of NDZ for the grid-forming mode of operation can be obtained through minor alteration of the previously derived formulation for the grid-supporting converter. Indeed, the bounds of the non-detection region can also be expressed by (14.23), where R_f and R_V are replaced by R_P^{-1} and R_Q^{-1} respectively. Hence, the

analytical approximation of the NDZ for a grid-forming inverter is of the form:

$$\frac{V^2}{V_{\max}^2} - 1 - \frac{\Delta f_1}{R_P P_G} \leq \frac{\Delta P}{P_G} \leq \frac{V^2}{V_{\min}^2} - 1 - \frac{\Delta f_2}{R_P P_G}, \quad (14.28a)$$

$$\gamma_{\min} \leq \frac{\Delta Q}{P_G} \leq \gamma_{\max}, \quad (14.28b)$$

where the NDZ bounds for reactive power are defined by

$$\gamma_{\min} := \left(1 + \frac{\Delta P}{P_G}\right) \left(Q_f \left(1 - \frac{f^2}{f_{\min}^2}\right) - \frac{Rf\Delta V_1}{R_Q f_{\min} \hat{V}_1^2}\right), \quad (14.29a)$$

$$\gamma_{\max} := \left(1 + \frac{\Delta P}{P_G}\right) \left(Q_f \left(1 - \frac{f^2}{f_{\max}^2}\right) - \frac{Rf\Delta V_2}{R_Q f_{\max} \hat{V}_2^2}\right). \quad (14.29b)$$

The exploration of monotonic properties of $g(\cdot)$ and $h(\cdot)$ for the grid-supporting mode, discussed in Appendix B.6, applies to the grid-forming control mode as well.

14.4 MODELING AND IMPLEMENTATION

14.4.1 *OF/UF Protection Design*

The modeling of frequency protection follows the guidelines from [343] and uses additional information provided in [344–348]. There are several techniques for determining the frequency signal, namely the zero-crossing methods for obtaining the electrical speed of the synchronous generator [346], approaches based on carrying out continuous Fourier transformation on voltage waveform [347] and PLL-based techniques [348]. A PLL provides fast and robust frequency estimates for balanced three-phase systems and has been widely used for frequency estimation, and is therefore also employed in this study for computing the frequency of the voltage phasor at the connection terminal.

If the frequency signal is not within the prescribed limits $[f_{\min}, f_{\max}]$ and the magnitude of the terminal voltage is larger than the minimum voltage setting V_{\min} , the frequency relay sends a trip signal to the generator's circuit breaker. The addition of a voltage amplitude test - a so-called "under-voltage interlock" function - usually ensures the absence of false alarms and restrains the actuation of frequency relays during non-islanding situations such as generator start-up and short circuits [345]. However, since the UV/OV protection schemes are also implemented in this work and the system is in

steady state prior to the LoM event, the voltage amplitude test is redundant and therefore neglected. Moreover, frequency relays can be operated with a time delay in order to avoid false protection tripping during LoM-unrelated transients, since the frequency might exceed the prescribed limits for a short period of time. Under such circumstances, the tripping conditions must persist during a pre-determined period to trigger the relay. Finally, both the protection signal delay, corresponding to circuit breaker opening time, as well as the internal measuring window delay are taken into account [345].

14.4.2 *OV/UV Protection Design*

The generic computational model of the voltage relay employed in this work is similar to the one presented in [347]. First, the voltage of each phase is measured by the PLL and transformed into a synchronously-rotating reference frame, with the phasor amplitude corresponding to the absolute value of the line-to-line Root Mean Square (RMS) voltage. Voltage relays usually calculate the RMS value of the nodal voltage considering a measurement window over a few cycles, and the resulting signal is then low-pass filtered and checked for any violations of the UV/OV settings. However, similarly to the frequency signal, the voltage can also be prone to transient phenomena not produced by an LoM event. Hence, a duration block examining whether the limits are consistently exceeded is incorporated in the model, together with the internal measurement delay and circuit breaker opening time.

14.4.3 *Protection Settings*

For the protection settings, international standards and typical regulations of several countries were followed. The report of British Standard [343] suggests that the frequency response must be activated within 2s, and therefore frequency protection should be able to successfully recognize any LoM event within that time period. It should be noted that in some cases there is a presence of multiple OF/UF protection relays with different delay settings. However, those additional protection layers are primarily designed for extremely narrow limits with significantly higher time duration blocks, corresponding to signals that continuously exceed the predefined thresholds for a duration of up to 30 min. Such example is the United Kingdom, where the 47.5 Hz under-frequency threshold with 20s delay and the 51.5 Hz over-frequency threshold with 90s delay are enforced. As such protection designs require average windows drastically greater than the ones needed for LoM

Country	OV [p.u.]	UV [p.u.]	OF [Hz]	UF [Hz]	Trip delay [s]			
					OV	UV	OF	UF
Austria	1.15	0.8	51	47	0.2			
Belgium	1.1	0.8	51.5	47.5	–			
Cyprus	1.1	0.9	52	47	0.5			
Czech Republic	1.15	0.85	52	47.5	0.2		0.5	
Estonia	1.1	0.85	50.5	48	1.5	1.5	0.5	0.3
Finland	1.1	0.85	51.5	47.5	0.2			
Italy	1.15	0.85	50.5	49.5	0.2	0.4	0.1	0.1
Netherlands	1.1	0.8	51	48	2			
Slovenia	1.1	0.85	51	47	1.5		0.2	
Sweden	1.15	0.85	51	47	0.2		0.5	

TABLE 14.1: Frequency and voltage protection settings prescribed by the operators of different European countries.

detection, they were not considered in this study. Similar multi-stage OV/UV concepts are also employed for voltage protection, but with settings again mostly outside of the scope of this study.

A list of standard protection settings prescribed by different European system operators according to [343] is provided in Table 14.1. While it is clear that there is no unique parametrization for the underlying LoM protection scheme, the significance and wide use of OV/UV and OF/UF protections is reflected. A particular discrepancy can be observed in the permitted tripping delays between different TSOs. Additionally, recent studies introduce new requirements in terms of permissible delay in the LoM protection response, which differ from the standards in Table 14.1. For instance, [345] suggests that the protection should be able to detect an LoM event within 250 – 350 ms. The protection settings used in this work have been selected according to the provided data and are listed in Table 14.2.

Protection setting type	Frequency	Voltage
Upper threshold (OF/OV)	50.5 Hz	1.1 p.u.
Lower threshold (UF/UV)	49.3 Hz	0.88 p.u.
Internal delay (measuring window)	100 ms	100 ms
Signal delay (breaker opening time)	40 μ s	40 μ s

TABLE 14.2: Employed frequency and voltage protection settings.

14.5 VALIDATION OF NDZ APPROXIMATION

14.5.1 Test Case Setup

The proposed analytical approximations are validated through EMT simulations in MATLAB Simulink. The appropriate OF/UF and OV/UV detection schemes presented in Section 14.4 have been incorporated into the detailed EMT model previously described in Chapter 2, with the protection settings given in Table 14.2. A single-line diagram of the investigated test system is illustrated in Fig. 14.4. It comprises a 2 kW DG interfaced via converter to the distribution network, a load supplied locally by the DG at the connection terminal, as well as the step-up transformer and distribution feeder connecting the DG to the main grid. The DG operates at 50 % of its rated power and at the nominal voltage of 400 V. All network components are represented by three-phase models, with feeder and transformer implemented as series impedances. Moreover, the load is modeled as constant RLC load, as this type of load leads to the most conservative islanding detection performance of frequency and voltage-based relays.

The simulated NDZs are obtained in a discretized fashion, as the simulations require re-initialization of the system for different load parameters and result in a binary (i.e., triggered or not) signal output for each protection type. Discrete boundaries of simulated NDZs will be depicted using dots and extrapolated into continuous regions, whereas analytical approximations of the respective thresholds will be represented by full lines. The standard procedure requires 5 % step-changes in load power in order to evaluate the protection. However, for the purposes of sufficiently accurate comparison, the steps simulated in this study are occasionally significantly smaller and vary from one case to another.

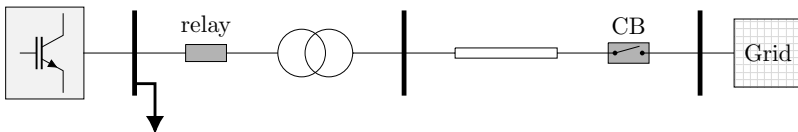


FIGURE 14.4: Single-line diagram of the test system under investigation.

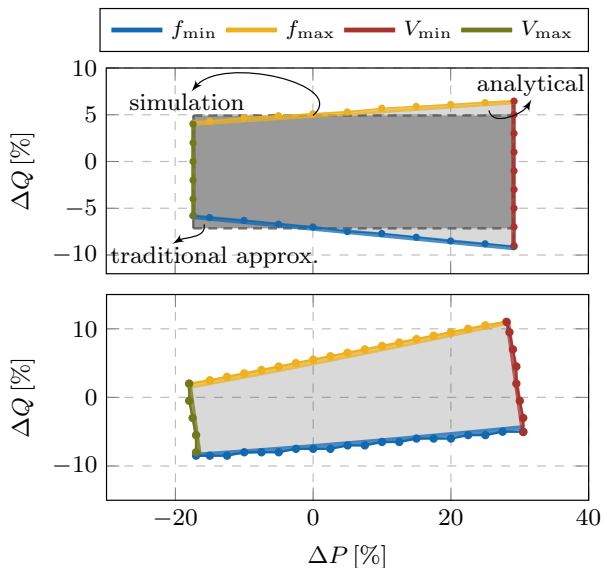


FIGURE 14.5: Comparison of analytical and simulated NDZs in case of grid-following converters: grid-feeding mode (top) and grid-supporting mode (bottom). Dark rectangular region represents an NDZ of the grid-feeding inverter obtained through a traditional approximation.

14.5.2 NDZ Validation for Grid-Following DGs

The comparisons between the analytical and simulated NDZs for both the grid-feeding and grid-supporting inverter mode are depicted in Fig. 14.5. For the grid-feeding case, the power mismatch increments ($\Delta P, \Delta Q$) were set to (5, 0.2) % for frequency protection validation and (0.2, 2) % for voltage protection analysis, whereas the values used for the grid-supporting mode of operation correspond to (2.5, 0.5) % and (0.5, 2.5) %, respectively. The lower discretization is employed in the second case in order to reduce the computational time, as NDZs of grid-supporting DG units are generally larger and greater parameter regions need to be swept. Moreover, the droop gains for the grid-supporting converter type were set to $R_f = 0.7$ p.u. and $R_V = 0.3$ p.u.

It is clear that for both operation modes we achieve a perfect matching between the simulations and the analytical formulation, indicated by the overlap between the full and dotted lines. As previously elaborated in Section 14.3,

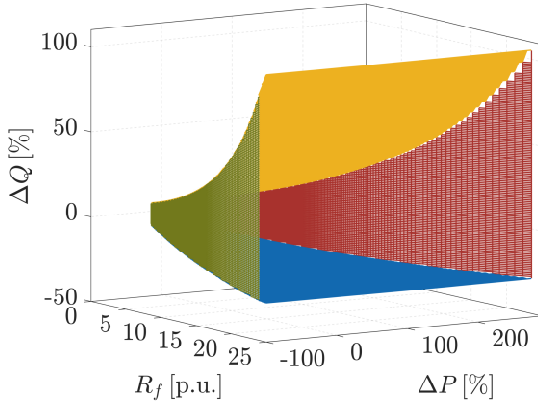


FIGURE 14.6: Analytical NDZ in case of grid-supporting converters for a wide range of frequency droop gains $R_f \in [0 - 25]$ p.u.

the lines representing the bounds for frequency protection of grid-feeding converters are also dependent on ΔP and therefore not vertical anymore, resulting in a trapezoidal NDZ. This significantly improves the performance of our approximation compared to the traditional NDZ estimation approach, described by (14.5) and (14.9) and indicated by the dark shaded rectangle in Fig. 14.5. The simulations also validate the accuracy of the novel and more complex NDZ formulation for the grid-supporting converter, with all four NDZ limits being functions of both active and reactive power mismatches. This is particularly important, as grid-supporting requirements are becoming an industry standard and such converter types are rapidly being employed, making the existing NDZ approximations obsolete. Nonetheless, the NDZs of such converter units tend to enlarge dramatically with the increase in droop gains, thus making the LoM protection ineffective. The aforementioned characteristic can be observed in Fig. 14.6, where the NDZ boundary is presented in the $\Delta P - R_f - \Delta Q$ space for a wide range of frequency droop gains $R_f \in [0 - 25]$ p.u. It can therefore be concluded that the passive anti-islanding detection schemes based on frequency and voltage triggers might be inadequate for future power systems with high penetration of very responsive grid-supporting DGs, i.e., DG units interfaced through power converters with high droop gains.

Understandably, the LoM protection settings have a crucial impact on the size of NDZ. We investigate this notion by comparing the NDZs for grid-supporting DGs obtained under two different types of protection triggers: (i)

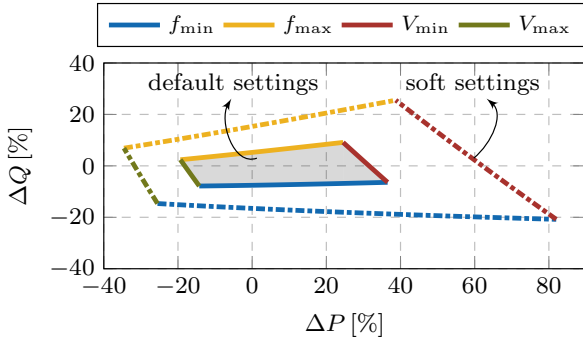


FIGURE 14.7: Analytical NDZ in case of grid-supporting converters for different LoM protection settings.

the *default* settings adopted from Table 14.2; and (ii) the *soft* settings with the OF/UF and OV/UV thresholds drastically relaxed compared to the default tuning. In particular, the soft LoM protection permits the voltage magnitude in the range $V \in [0.8, 1.2]$ p.u. and the frequency within $f \in [48.5, 51.5]$ Hz bounds. According to the results depicted in Fig. 14.7, the computed NDZ is substantially larger under the soft protection settings, with the main contributors to the increase being the UF/UV bounds. This suggests that the problem of large NDZs for grid-supporting units with high droop gains could be resolved through appropriate readjustment of the LoM protection triggers.

14.5.3 NDZ Validation for Grid-Forming DGs

On the other hand, the grid-forming mode is characterized by the fact that for conventional droop gains of $(R_P, R_Q) < (0.1, 0.01)$ p.u. the NDZ is rotated by $\approx 90^\circ$ counterclockwise compared to the zones of other inverter modes, as illustrated in Fig. 14.8. In other words, although typically having $\Delta P - V$ and $\Delta Q - f$ dependencies, the frequency and voltage protection of grid-forming units is mostly affected by the change in ΔP and ΔQ , respectively. However, it should be noted that under traditional droop tuning the non-detection region is extremely large and almost any type of islanding would go by undetected. This in fact is not a downside, as grid-forming DGs have standalone capabilities by design and should keep energizing the system even after the disconnection from the main grid. Nevertheless, the sole purpose of

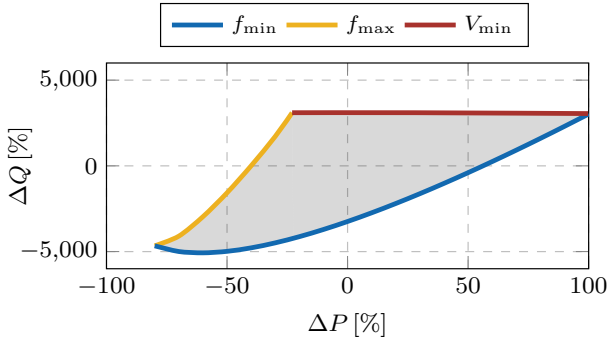


FIGURE 14.8: Analytical NDZ in case of grid-forming converters with conventional droop gain tuning of $(R_P, R_Q) = (0.05, 0.005)$ p.u.

LoM detection schemes in the presence of grid-forming units is questionable and must be reassessed in the future.

In order to evaluate the proposed analytical approximation for grid-forming DGs, we simulate NDZs for somewhat unconventional droop values of $(0.125, 0.75)$ p.u. and $(0.05, 0.1)$ p.u., since the voltage protection would otherwise never be triggered and the frequency protection would only be activated for a power imbalance of $\Delta P \approx \pm 50\%$. The power mismatch steps are set to 5% in the first and 2.5% in the second case, and the results are presented in Fig. 14.9. We can confirm that the proposed analytical expressions approximate the corresponding NDZs with sufficient accuracy, as the underlying mismatch is a sole consequence of a less discrete simulation sequence. An interesting observation can be made from the second case study, as the NDZ starts rotating with the droop gains approaching traditionally lower values, implying that only frequency protection preserves sensitivity towards islanding instances.

14.6 CONCLUSION

This chapter addresses the problem of LoM protection in modern distribution grids, in particular the NDZ approximation of passive anti-islanding detection methods based on OF/UF and OV/UV thresholds. For this purpose, we propose an improved analytical formulation for estimating the NDZ of LoM protection devices in the presence of grid-feeding inverters, which alleviates the imprecision of the existing methods pertaining to the coupling between the frequency and active power mismatch. Furthermore, novel approxima-

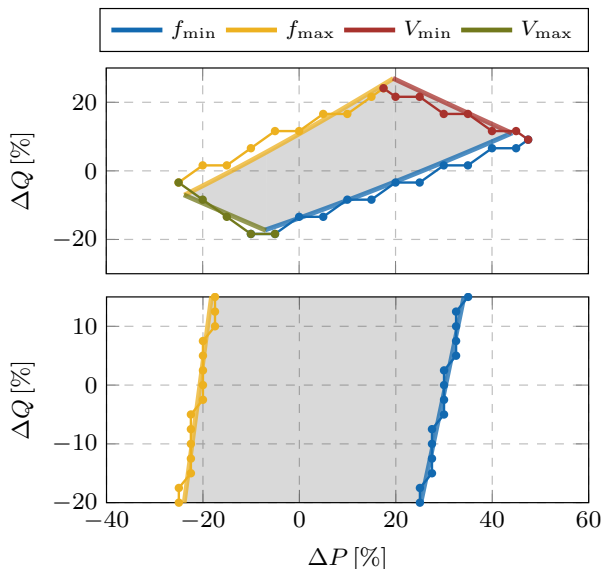


FIGURE 14.9: Comparison of analytical and simulated NDZs in case of grid-forming converters with unconventional droop gain tuning: scenario $(R_P, R_Q) = (0.125, 0.75)$ p.u. (top) and scenario $(R_P, R_Q) = (0.05, 0.1)$ p.u. (bottom).

tions for emerging grid-supporting and grid-forming inverter-based services are also introduced. The analytical results are validated through detailed EMT simulations, suggesting a high accuracy of the proposed formulation. Moreover, some interesting observations regarding the impact of new inverter requirements on the performance of LoM protections have been drawn.

The future work will extend the theoretical analysis onto other passive protection schemes. Although OF/UF and OV/UV protection schemes are very common and adopted by many countries, other passive protection schemes such as anti-islanding detection methods based on RoCoF and voltage phase jumps are also widely employed. The former one enforces a limit on the angle change of the voltage at the converter terminal, which can be dramatically increased in case of an LoM event, whereas the latter one uses the RoCoF measurement (averaged over several cycles) as a protection trigger. Another interesting avenue for further research is the parallel operation of DGs operating in grid-forming and grid-following modes. Typically, during intentional islanding operation in systems with parallel inverter-interfaced

generation, at least one of the DG units has grid-forming capabilities and the rest are operated in a grid-following mode. In such cases, the voltage and frequency response after the LoM event could be studied using the analytical results from this chapter.

CONCLUSIONS AND OUTLOOK

This chapter summarizes the content of the thesis (Section 15.1), draws conclusions based on the presented methods and results (Section 15.2), and provides suggestions for future work (Section 15.3).

15.1 SUMMARY

This thesis investigates the modeling and dynamics of converter-dominated power systems, and the potential of providing novel control and optimization methods for reliable and resilient operation of such networks.

The first part of the thesis focuses on modeling and stability of Power Electronics (PE)-based power systems. Chapter 2 presents the most promising grid-forming and grid-following control strategies and studies their compatibility in low-inertia systems. Motivated by the timescale separation between the fast and slow dynamics in an inverter-based power system, Chapter 3 proposes a hybrid model-order reduction method that preserves the slow system dynamics of the full-order model while simultaneously capturing the impact of the removed fast states on slow variables. Finally, Chapter 4 presents new insights into stability properties of power systems with large-scale integration of Renewable Energy Sources (RES) by characterizing the maximum permissible penetration levels of inverter-based generation and the nature of the associated unstable modes.

The second part of the thesis studies the frequency dynamics and various Fast Frequency Control (FFC) applications in low-inertia grids. In particular, Chapter 5 develops a uniform frequency response model of a generic low-inertia system and derives analytical expressions for frequency metrics of interest. This model is then applied to the adaptive Virtual Synchronous Machine (VSM) control design in Chapter 5 and Chapter 6, where the virtual inertia and damping constants are adjusted according to the frequency disturbance in the system. Subsequently, Chapter 7 develops both centralized and decentralized Model Predictive Control (MPC) methods for converter-interfaced generators that exploit their responsiveness through FFC provision. Chapter 8 completes this part of the thesis by introducing a method for combined sizing of DC-side storage capacity and tuning of controller gains of

grid-forming converters, which accounts for the coupling between installation planning and operation parameters of the storage and ensures sufficient energy and power capacity for containing a predefined power imbalance.

The third part of the thesis provides various methods for improving reliability and performance of networks with high converter penetration. More specifically, Chapter 9 presents a novel control strategy for synchronization of grid-connected converters based on emulating the physical properties of an induction machine and taking advantage of its inherent grid-friendly properties. The topic of time delay and its impact in low-inertia power systems is tackled in Chapter 10, both from the standpoint of a unique stability analysis and the design of the delay-robust wide-area oscillation damping controller. In contrast, Chapter 11 proposes a method for allocation of inertia and damping in an inverter-dominated power system by combining the detailed system representation from Chapter 2 and the analytical formulation from Chapter 5 with an iterative eigensensitivity-based optimization framework. The topic of Unit Commitment (UC) is dealt with in Chapter 12 and Chapter 13. The former one presents the UC problem formulation in a power network with low levels of rotational inertia by including the frequency-related constraints into a two-stage stochastic process, whereas the latter one investigates the financial side of the problem, i.e., the procurement and pricing of inertial response, and introduces three novel pricing and payment schemes that reimburse inertia providers in a transparent and fair manner. Finally, Chapter 14 studies the impact of inverter-based generation on islanding detection schemes and proposes an improved analytical formulation for estimating the non-detection zone of loss of mains protection devices in the presence of PE-interfaced generation.

15.2 CONCLUSIONS

The main conclusions and findings of this thesis are summarized as follows:

- Future power systems require sufficiently detailed modeling of converter control schemes in order to capture the fast timescales of PE-interfaced generation.
- The most promising grid-forming converter controls showcase compatibility in converter-dominated power networks, as well as small-signal equivalence under certain trivial conditions.
- Appropriate reduced-order models of power converters are needed for tractable and accurate large-scale simulations during transients.

- The sole definition and classification of converter operation modes must be improved, as it lacks foundation and tends to drastically differentiate between different operators and industries.
- Stability of a low-inertia power system might be more vulnerable and harder to ensure compared to a 100 % converter-based network.
- Transmission line dynamics, traditionally neglected in dynamic power system studies, must be taken into account when studying networks with low rotational inertia.
- Maximum permissible penetration levels of converter-interfaced generation cannot be quantified with a single system metric.
- MPC and adaptive VSM controls can significantly improve the frequency response of a low-inertia system during disturbances.
- Measurement and actuation delays can deteriorate the performance of PE devices, especially in a wide-area control infrastructure.
- Allocation of inertia and damping is a complex problem that must be tackled together from the optimization, control and stability perspective.
- Novel pricing and payment mechanisms are needed for fair and transparent reimbursement of inertia providers according to their individual participation in the ancillary service market.
- Presence of PE-interfaced generators and their respective control schemes must be taken into account when approximating the non-detection zone of islanding detection schemes in distribution networks.

15.3 OUTLOOK

There are various avenues for future work and possibilities to extend the topics addressed in this thesis. In the following, the most important questions that remain unanswered or require further investigation are pointed out:

- The modeling in Chapter 2 primarily focuses on the converter's AC-side and subsumes the DC-side energy source within a controllable current source. While justified from the perspective of system coupling and underlying timescales, such approach hardly distinguishes between different energy technologies (e.g., wind, solar, battery storage etc.) and their unique dynamical characteristics. It is therefore important to

provide more comprehensive DC-side models in order to capture the necessary level of detail.

- The topic of low-inertia power systems presents a multifaceted problem that combines the fields of power systems, control theory and power electronics. However, only the first two fields have been thoroughly considered throughout this thesis, whereas some important aspects of power electronics (e.g., detailed switching and modular multilevel converter designs) have been neglected for simplicity and tractability. In order to have a profound understanding of system dynamics during faults and transients, the level of detail pertaining to the modeling of power converter devices should be enhanced.
- The uniform frequency model proposed in Chapter 5 considers only the Center-of-Inertia (CoI) frequency. It has been shown throughout this thesis (specifically in Chapters 5-8 and Chapters 11-13) that the analytical formulation of most relevant CoI frequency metrics can be easily incorporated into various optimization and control design problems. However, depending on the type and location of the disturbance in the system, the frequencies of individual generators at different nodes across the network could significantly deviate from the CoI frequency and lead to inadequate control performance. Therefore, the proposed frequency model should be improved and extended onto individual nodes in the network, which could potentially lead to computational issues on larger scale.
- Besides the validation studies in Chapter 2, the vast majority of this thesis focuses on improving the system performance under stepwise disturbances in active power (e.g., load change and generation loss). Nevertheless, the system conditions and transient performance under more extreme faults such as short circuits have not been thoroughly studied in this work.
- The inertia and damping allocation method proposed in Chapter 11 combines the iterative optimization method and respective eigenvalue sensitivities with the \mathcal{H}_2 and \mathcal{H}_∞ system norms. However, the norms are computed *ex-post*, i.e., they are not explicitly included in the objective function. While the final results clearly indicate a significant reduction of system norms, the optimality of such reduction cannot be guaranteed without a more comprehensive problem formulation.

- As previously described in Chapter 13, only the Rate-of-Change-of-Frequency (RoCoF) constraint was included into the UC formulation for determining the corresponding inertia prices. This was justified by the fact that it is easier to extract meaningful information pertaining to inertia pricing from a constraint dependent on a single variable, compared to dealing with multi-variable expressions. In particular, the nadir constraint is not well-suited for obtaining pricing information, especially considering the difficulties related to linearizing the nadir expression and determining the binding variable of such constraint. A valuable extension of this work would be the inclusion of additional frequency-related constraints into the UC problem and definition of appropriate pricing and payment schemes for inertia provision.
- Although over- and under-frequency/voltage protection schemes studied in Chapter 14 are very common and adopted by many countries, other passive protection schemes such as anti-islanding detection methods based on RoCoF and voltage phase jumps are also widely employed and should be taken into consideration. Another interesting avenue for further research is the parallel operation of distributed generators operating in grid-forming and grid-following modes.

APPENDIX A - PROOFS

A.1 PROOF OF PROPOSITION 6.3.1

Proof. We start the proof by finding an appropriate candidate Lyapunov function of a given nonlinear open-loop system. Similar to the stability analysis of a synchronous generator in [27], we calculate the respective energy function by neglecting the $\dot{\omega}$ term associated to damping in the second equation of (6.3), and multiply the whole expression by $M\dot{\omega}$ in order to express energy:

$$M\dot{\omega}\ddot{\omega} + \frac{1}{T}((D + R_g)\omega - \Delta P)\dot{\omega} = 0. \quad (\text{A.1})$$

Integrating the product from the first equilibrium point x_1^* to any point on the system transient trajectory yields the following Lyapunov function:

$$\begin{aligned} V &= E_k + E_p \\ &= \int_0^{\dot{\omega}} M\dot{\omega} \, d\dot{\omega} + \frac{1}{T} \int_{\omega_{ss}}^{\omega} ((D + R_g)\omega - \Delta P) \, d\omega \\ &= \frac{1}{2}M\dot{\omega}^2 - \frac{1}{T} \left[\Delta P(\omega - \omega_{ss}) - \frac{1}{2}(D + R_g)(\omega^2 - \omega_{ss}^2) \right], \end{aligned} \quad (\text{A.2})$$

where $V(\omega, \dot{\omega})$ represents the transient energy of the system in $(\omega, \dot{\omega})$ coordinates after a step disturbance ΔP .

Let us now consider the adaptive approach with $M(\omega, \dot{\omega})$ and $D(\omega, \dot{\omega})$ being functions of state variables through VSM feedback control described in (6.4). By analyzing the gradient ∇V of the proposed Lyapunov function we can determine its stationary points:

$$\begin{bmatrix} \frac{\partial V}{\partial \omega} \\ \frac{\partial V}{\partial \dot{\omega}} \end{bmatrix} = \begin{bmatrix} \frac{1}{2} \frac{\partial M}{\partial \omega} \dot{\omega}^2 - \frac{1}{T} \left(\Delta P - \frac{1}{2} \frac{\partial D}{\partial \omega} \Delta \omega^2 - \omega(D + R_g) \right) \\ \frac{1}{2} \frac{\partial M}{\partial \omega} \dot{\omega}^2 + M\dot{\omega} + \frac{1}{2T} \frac{\partial D}{\partial \omega} \Delta \omega^2 \end{bmatrix}, \quad (\text{A.3})$$

with $\Delta \omega^2 := \omega^2 - \omega_{ss}^2$. It is trivial to shown that the proposed Lyapunov function has a stationary point at the system equilibrium x_2^* , i.e., $\nabla V(x_2^*) = 0_2$, which satisfies the first condition of Lyapunov stability. The second

condition states that it must be positive definite in the vicinity of the equilibrium point. This can be verified using the Hessian matrix

$$\mathcal{H} = \begin{bmatrix} \frac{\partial^2 V}{\partial \omega^2} & \frac{\partial^2 V}{\partial \omega \partial \dot{\omega}} \\ \frac{\partial^2 V}{\partial \dot{\omega} \partial \omega} & \frac{\partial^2 V}{\partial \dot{\omega}^2} \end{bmatrix} = \begin{bmatrix} \frac{1}{T}(D + R_g - 2K_d\omega) & -K_m\dot{\omega} \\ -K_m\dot{\omega} & M - 2\hat{K}_m\dot{\omega} \end{bmatrix},$$

which yields the following expression at the aforementioned equilibrium x_2^* :

$$\mathcal{H}(x_2^*) = \begin{bmatrix} \frac{1}{T}(D + R_g - \frac{2\hat{\kappa}}{D^* + R_g}) & 0 \\ 0 & M \end{bmatrix}. \quad (\text{A.4})$$

Here, $\hat{\kappa} \in \mathbb{R}_{>0}$ denotes the product $K_d\Delta P$, always positive by the nature of our control design. Having in mind that M , D and R_g are also positive, according to Sylvester's theorem $\mathcal{H}(x_2^*) > 0$ holds, and thus V is a valid Lyapunov candidate function.

In order to guarantee asymptotic stability, $\partial V/\partial t$ has to be negative semidefinite $\forall t \in [0, \infty)$, i.e., the condition

$$\begin{aligned} \partial V/\partial t &= \frac{\partial V}{\partial \dot{\omega}} \frac{\partial \dot{\omega}}{\partial t} + \frac{\partial V}{\partial \omega} \frac{\partial \omega}{\partial t} + \frac{\partial V}{\partial M} \frac{\partial M}{\partial t} + \frac{\partial V}{\partial D} \frac{\partial D}{\partial t} \\ &= - \left(\frac{M}{T} + D + F_g \right) \dot{\omega}^2 + \underbrace{\frac{1}{2} \frac{\partial M}{\partial t} \dot{\omega}^2}_{\nu_M(t)} + \underbrace{\frac{1}{2T} \frac{\partial D}{\partial t} (\omega^2 - \omega_{ss}^2)}_{\nu_D(t)} \leq 0 \end{aligned} \quad (\text{A.5})$$

needs to be met. Let us compare the last two terms of (A.5) by considering their ratio

$$\frac{\nu_M(t)}{\nu_D(t)} = \frac{T \frac{\partial M}{\partial t} \dot{\omega}^2}{\frac{\partial D}{\partial t} (\omega^2 - \omega_{ss}^2)} = \frac{T \dot{\omega}^2}{\omega^2 - \omega_{ss}^2} \frac{K_M^\top \frac{\partial x}{\partial t}}{K_D^\top \frac{\partial x}{\partial t}}, \quad (\text{A.6})$$

where $x = (\omega, \dot{\omega}) \in \mathbb{R}^2$. Based on the LQR design and the respective cost factor selection, we can assume the approximation $R_M K_M \approx R_D K_D$ and hence the expression in (A.6) can be transformed into

$$\frac{\nu_M(t)}{\nu_D(t)} \approx \frac{T R_D \dot{\omega}^2}{R_M (\omega^2 - \omega_{ss}^2)}. \quad (\text{A.7})$$

Considering that $\frac{R_D}{R_M} = \left(\frac{\dot{\omega}_{\max}}{\omega_{\max}} \right)^2$ in (6.17), (A.7) is rewritten as

$$\frac{\nu_M(t)}{\nu_D(t)} \approx T \underbrace{\frac{\omega_{\max}^2 \dot{\omega}^2}{\dot{\omega}_{\max}^2 (\omega^2 - \omega_{ss}^2)}}_{\sigma(t)}. \quad (\text{A.8})$$

We can observe that $\sigma(t) > 1$ for high values of $\nu_M(t)$ and $\nu_D(t)$ during the initial transients, whereas $\nu_M(t) \approx \nu_D = 0$ in steady state. Therefore, it is valid to assume $\nu_M(t) + \nu_D(t) \approx \nu_M(t)$ and neglect the last term in (A.5), leading to the following condition for system stability:

$$\frac{M}{T} + D + F_g \geq \frac{1}{2} \frac{\partial M}{\partial t} = \frac{1}{2} (-K_m \dot{\omega} - \hat{K}_m \ddot{\omega}), \quad (\text{A.9})$$

with the left hand side lower bounded by

$$\frac{M}{T} + D + F_g \geq \frac{M^*}{T} + D^* + F_g. \quad (\text{A.10})$$

As for the right-hand side of (A.9), we know that both $\dot{\omega}$ and $\ddot{\omega}$ are decaying oscillations as well as that during the initial stages of the response, when $\frac{\partial M}{\partial t}$ is relatively large, $-K_m \dot{\omega} > 0$ and $-\hat{K}_m \ddot{\omega} < 0$ hold. Hence, one could neglect the $-\hat{K}_m \ddot{\omega}$ term and upper bound the right-hand side by

$$-\frac{1}{2} K_m \dot{\omega}_{\max} = -\frac{1}{2} K_m \dot{\omega}(0) > \frac{1}{2} (-K_m \dot{\omega} - \hat{K}_m \ddot{\omega}). \quad (\text{A.11})$$

From (A.9)-(A.11), a sufficient condition for asymptotic stability is derived as

$$\frac{M^*}{T} + D^* + F_g \geq -\frac{1}{2} K_m \dot{\omega}_{\max}, \quad (\text{A.12})$$

where

$$\dot{\omega}_{\max} := \frac{M^* - \sqrt{M^{*2} - 4\hat{K}_m \Delta P}}{2\hat{K}_m}. \quad (\text{A.13})$$

Substituting (A.13) into (A.12) yields the stability condition in (6.18) and concludes the proof. $\square\square\square$

A.2 PROOF OF PROPOSITION 5.3.1

Proof. As previously shown in Appendix A.1, the expression (A.2) represents the appropriate Lyapunov candidate function of the second-order system in (5.3) with the inclusion of feedback control law in (5.16). Similarly, in order to guarantee stability in a closed-loop form, $\partial V/\partial t$ has to be negative semidefinite $\forall t \in [0, \infty)$, i.e.,

$$\begin{aligned} \dot{V} &= \frac{\partial V}{\partial \dot{\omega}} \frac{\partial \dot{\omega}}{\partial t} + \frac{\partial V}{\partial \omega} \frac{\partial \omega}{\partial t} + \frac{\partial V}{\partial M} \frac{\partial M}{\partial t} + \frac{\partial V}{\partial D} \frac{\partial D}{\partial t} \\ &= - \left(\frac{M}{T} + D + F_g \right) \dot{\omega}^2 + \underbrace{\frac{1}{2} \frac{\partial M}{\partial t} \dot{\omega}^2}_{\nu_M(t)} + \underbrace{\frac{1}{2T} \frac{\partial D}{\partial t} (\omega^2 - \omega_{\text{ss}}^2)}_{\nu_D(t)} \leq 0, \end{aligned} \quad (\text{A.14})$$

Interval	$\nu_M(t)$	$\nu_D(t)$
pre-disturbance	$0 \mapsto (\partial M/\partial t = 0)$	$0 \mapsto (\partial D/\partial t = 0)$
disturbance	$> 0 \mapsto (\partial M/\partial t \uparrow)$	$0 \mapsto (\omega^2 - \omega_{ss}^2 \approx 0)$
pre-nadir	$0 \mapsto (\partial M/\partial t = 0)$	$0 \mapsto (\partial D/\partial t = 0)$
nadir	$0 \mapsto (\partial \omega/\partial t \approx 0)$	$0 \mapsto (\partial D/\partial t = 0)$
post-nadir	$0 \mapsto (\partial M/\partial t = 0)$	$\hat{\nu}_D(t)$

TABLE A.1: Values of ν_M and ν_D throughout the response.

which is conservatively subsumed in $\nu_M(t) + \nu_D(t) \leq 0, \forall t \in [0, \infty)$.

Unlike the control design in Appendix A.1, the interval-based controller has discontinuities due to explicit switching instances throughout the response. The non-smooth characteristic of $\nu_M(t)$ and $\nu_D(t)$ can be resolved by observing different segments of the response indicated in Table A.1, and subsequently approximating $\partial M/\partial t$ by its average value (i.e., $\Delta M_c^*/T$) at the points of switching, which implies the first condition (5.18a). Furthermore, it suggests that ensuring $\hat{\nu}_D(t) \leq 0$ after the frequency nadir has been reached would guarantee stability, thus resulting in an inequality condition of the form

$$\hat{\nu}_D(t) = \frac{1}{2T} \frac{\Delta D_c^*}{\omega_{\max} - \omega_{ss}} \dot{\omega}(t) (\omega(t)^2 - \omega_{ss}^2) \leq 0, \quad (\text{A.15})$$

with the damping component $k_D \ddot{\omega}(t) \approx 0$ considered negligible. Since $\dot{\omega}(t)$ and $(\omega_{\max} - \omega_{ss})$ terms are of opposite signs, the problem in (A.15) corresponds to $|\omega(t)| \geq |\omega_{ss}|$, i.e., the system being critically damped or overdamped throughout the post-nadir interval. Mathematically speaking, the damping ratio in (5.4) must satisfy the condition $\zeta(t) \geq 1, \forall t \in [t_m, \infty)$. Considering that during this interval $\partial D/\partial t < 0$ and $T \geq M/D(t)$, as well as $R_g \approx F_g$, one can observe that $\zeta(t)$ is a decaying function, i.e.,

$$\frac{\partial \zeta}{\partial t} = \sqrt{\frac{T}{M}} \frac{\partial D}{\partial t} \frac{TD(t) + T(2R_g - F_g) - M}{4(D(t) + R_g)^{3/2}} < 0.$$

Therefore, combining $\zeta(t_m) \geq \zeta(t_{ss}) \geq 1$ with (5.4) yields the second stability condition (5.18b) and concludes the proof. □□□

A.3 PROOF OF PROPOSITION 10.3.1

Proof. Let us recall the definition of upper LFT of matrix $M \in \mathbb{R}^{(m+n) \times (m+n)}$ with respect to $\delta_t \in \mathbb{R}^{m \times m}$:

$$F_u(M, \delta_t) = M_{22} + M_{21}\delta_t(I - M_{11}\delta_t)^{-1}M_{12}, \quad (\text{A.16})$$

where $M_{11} \in \mathbb{R}^{m \times m}$, $M_{12} \in \mathbb{R}^{m \times n}$, $M_{21} \in \mathbb{R}^{n \times m}$, $M_{22} \in \mathbb{R}^{n \times n}$ and $I = \text{diag}(1_m)$ is the identity matrix of order m . Considering that

$$M = \begin{bmatrix} M_{11} & M_{12} \\ M_{21} & M_{22} \end{bmatrix} = \begin{bmatrix} -ba^{-1} & a^{-1} \\ -ba^{-1} & a^{-1} \end{bmatrix}, \quad (\text{A.17})$$

given by (10.3.1) for $m = n = 1$, (A.16) can be rewritten by substituting (A.17), as follows:

$$\begin{aligned} F_u(M, \delta_t) &= a^{-1} + (-ba^{-1})\delta_t(1 - (-ba^{-1})\delta_t)^{-1}a^{-1} \\ &= a^{-1} - (b^{-1}a^2\delta_t^{-1} + a)^{-1} \\ &= \frac{a + b\delta_t}{a^2 + ab\delta_t} - \frac{b\delta_t}{a^2 + ab\delta_t} \\ &= \frac{1}{a + b\delta_t}, \end{aligned}$$

which clearly yields $F_u(M, \delta_t) = \tau^{-1}$ and concludes the proof. $\square\square\square$

A.4 PROOF OF PROPOSITION 10.5.2

Proof. The proof is based on a combination of the stability analysis conducted in [242] with the control design approach using the descriptor method in [229] and the change of variables proposed in [243]. Consider the positive definite augmented Lyapunov-Krasovskii functional [242]

$$V(x_s, \dot{x}_s, t) = V_1 + V_2 + V_3, \quad (\text{A.18})$$

where

$$V_1 = \begin{bmatrix} x_s \\ \int_{t-h_1}^t x_s(s) ds \\ \int_{t-h_2}^{t-h_1} x_s(s) ds \end{bmatrix}^T P \begin{bmatrix} x_s \\ \int_{t-h_1}^t x_s(s) ds \\ \int_{t-h_2}^{t-h_1} x_s(s) ds \end{bmatrix}, \quad (\text{A.19a})$$

$$V_2 = \int_{t-h_1}^t x_s^\top(s) S_1 x_s(s) ds + \int_{t-h_2}^{t-h_1} x_s^\top(s) S_2 x_s(s) ds, \tag{A.19b}$$

$$\begin{aligned} V_3 &= h_1 \int_{-h_1}^0 \int_{t+\phi}^t \dot{x}_s^\top(s) R_1 \dot{x}_s(s) ds d\phi \\ &\quad + h_{12} \int_{-h_2}^{-h_1} \int_{t+\phi}^t \dot{x}_s^\top(s) R_2 \dot{x}_s(s) ds d\phi, \end{aligned} \tag{A.19c}$$

$P > 0, S_1 > 0, S_2 > 0, R_1 > 0, R_2 > 0$, and $h_{12} = h_2 - h_1$ (see (10.56) for more details on the notation). Then, by invoking [229, Lemma 4.3], the design objectives in Problem 10.5.1 are equivalent to the following constrained optimization problem:

$$\min \quad \gamma \tag{A.20a}$$

$$\text{s.t.} \quad \dot{V}((x_s, \dot{x}_s, t) - (\gamma^2 \|w(t)\|_2^2 - \|z(t)\|_2^2) \leq -\varrho (\|x_s(t)\|_2^2 + \|w(t)\|_2^2), \tag{A.20b}$$

where \dot{V} denotes the time-derivative of the Lyapunov-Krasovskii functional V in (A.18), $\|\cdot\|_2$ is the Euclidean norm and ϱ is some positive constant.

As shown in [242], the differentiation of V along the trajectories of the system (10.54) yields

$$\dot{V} = \dot{V}_1 + \dot{V}_2 + \dot{V}_3, \tag{A.21}$$

with

$$\begin{aligned} \dot{V}_1 &= \begin{bmatrix} x_s \\ \int_{t-h_1}^t x_s(s) ds \\ \int_{t-h_2}^{t-h_1} x_s(s) ds \end{bmatrix}^\top P \begin{bmatrix} \dot{x}_s \\ x_s - x_s(t-h_1) \\ x_s(t-h_1) - x_s(t-h_2) \end{bmatrix} \\ &\quad + \begin{bmatrix} \dot{x}_s \\ x_s - x_s(t-h_1) \\ x_s(t-h_1) - x_s(t-h_2) \end{bmatrix}^\top P \begin{bmatrix} x_s \\ \int_{t-h_1}^t x_s(s) ds \\ \int_{t-h_2}^{t-h_1} x_s(s) ds \end{bmatrix}, \end{aligned} \tag{A.22a}$$

$$\begin{aligned} \dot{V}_2 &= x_s^\top(t) S_1 x_s(t) - x_s^\top(t-h_1) S_1 x_s(t-h_1) \\ &\quad + x_s^\top(t-h_1) S_2 x_s(t-h_1) - x_s^\top(t-h_2) S_2 x_s(t-h_2), \end{aligned} \tag{A.22b}$$

$$\begin{aligned} \dot{V}_3 &= h_1^2 \dot{x}_s^\top(t) R_1 \dot{x}_s(t) + h_{12}^2 \dot{x}_s^\top(t) R_2 \dot{x}_s(t) \\ &\quad - h_1 \int_{t-h_1}^t \dot{x}_s^\top(s) R_1 \dot{x}_s(s) ds - h_{12} \int_{t-h_2}^{t-h_1} \dot{x}_s^\top(s) R_2 \dot{x}_s(s) ds. \end{aligned} \tag{A.22c}$$

Inspired by [242], we introduce the vector

$$\zeta(t) = \left[x_s^\top(t), \dot{x}_s^\top(t), x_s^\top(t-h_1), x_s^\top(t-\tau), x_s^\top(t-h_2), \frac{1}{h_1} \int_{t-h_1}^t x_s^\top(s) ds, \frac{1}{\tau-h_1} \int_{t-\tau}^{t-h_1} x_s^\top(s) ds, \frac{1}{h_2-\tau} \int_{t-h_2}^{t-\tau} x_s^\top(s) ds, w^\top \right]^\top. \tag{A.23}$$

Then, by using G_0 and $G_1(\tau)$ from (10.56), we obtain

$$\begin{bmatrix} x_s \\ \int_{t-h_1}^t x_s(s) ds \\ \int_{t-h_2}^{t-h_1} x_s(s) ds \end{bmatrix} = G_1(\tau)\zeta(t), \quad \begin{bmatrix} \dot{x}_s \\ x_s - x_s(t-h_1) \\ x_s(t-h_1) - x_s(t-h_2) \end{bmatrix} = G_0\zeta(t) \tag{A.24}$$

and \dot{V}_1 can be compactly written as

$$\dot{V}_1 = \zeta^\top \left(G_0^\top P G_1(\tau) + G_1^\top(\tau) P G_0 \right) \zeta. \tag{A.25}$$

Next, consider \dot{V}_3 in (A.22). Applying the improved integral inequality, i.e., [242, Lemma 2.1], gives

$$\begin{aligned} -h_1 \int_{t-h_1}^t \dot{x}_s^\top(s) R_1 \dot{x}_s(s) ds &\leq - \left[\begin{array}{c} x_s - x_s(t-h_1) \\ x_s + x_s(t-h_1) - \frac{2}{h_1} \int_{t-h_1}^t x_s(s) ds \end{array} \right]^\top \\ &\quad \begin{bmatrix} R_1 & 0 \\ 0 & 3R_1 \end{bmatrix} \begin{bmatrix} x_s - x_s(t-h_1) \\ x_s + x_s(t-h_1) - \frac{2}{h_1} \int_{t-h_1}^t x_s(s) ds \end{bmatrix}. \end{aligned} \tag{A.26}$$

Furthermore, as shown in [242], combining [242, Lemma 2.1] and [242, Lemma 2.2] allows us to obtain

$$-h_{12} \int_{t-h_2}^{t-h_1} \dot{x}_s^\top(s) R_2 \dot{x}_s(s) ds \leq -\zeta^\top \Gamma^\top \psi_2 \Gamma \zeta, \tag{A.27}$$

where Γ is given in (10.56), X is a matrix variable and

$$\psi_2 = \begin{bmatrix} \hat{R}_2 & X \\ * & \hat{R}_2 \end{bmatrix}, \quad \hat{R}_2 = \begin{bmatrix} R_2 & 0 \\ 0 & 3R_2 \end{bmatrix}. \tag{A.28}$$

Then, in contrast from the analysis conditions presented in [242], for the purpose of deriving a controller synthesis we employ the descriptor method,

see [229, Chapter 3]. Let P_2 and P_3 be matrix variables and introduce the following expression

$$0 = 2 \left[x_s^\top P_2^\top + \dot{x}_s^\top P_3^\top \right] [Ax_s - B_u K C_y x_s(t - \tau) + B_w w - \dot{x}_s]. \quad (\text{A.29})$$

Then, summing up (A.29), (A.25), \dot{V}_2 , the first two terms in \dot{V}_3 in (A.22) and (A.27), considering the output performance z in (10.54), and following the procedure in [229, Section 4.3.2] gives

$$\begin{aligned} & \dot{V}(x_s, \dot{x}_s, t) - (\gamma^2 \|w(t)\|_2^2 - \|z(t)\|_2^2) \leq \\ & \zeta^\top \left(\psi_{11} + G_0^\top(\tau) P G_1 + G_1^\top P G_0(\tau) - \Gamma^\top \psi_3 \Gamma + \psi_2^\top \psi_2 \right) \zeta, \end{aligned} \quad (\text{A.30})$$

where ψ_{11} is defined by

$$\psi_{11} = \begin{bmatrix} P_2^\top A + A^\top P_2 + S_1 - 4R_1 & -P_2^\top + A^\top P_3 & -2R_1 & -P_2^\top B_u K C_y & 0 & 6R_1 & 0 & 0 & P_2^\top B_w \\ * & -P_3^\top - P_3 + h_1^2 R_1 + h_1^2 R_2 & 0 & -P_3^\top B_u K C_y & 0 & 0 & 0 & 0 & P_3^\top B_w \\ * & * & -S_1 + S_2 - 4R_1 & 0 & 0 & 6R_1 & 0 & 0 & 0 \\ * & * & * & 0 & 0 & 0 & 0 & 0 & 0 \\ * & * & * & * & -S_2 & 0 & 0 & 0 & 0 \\ * & * & * & * & * & -12R_1 & 0 & 0 & 0 \\ * & * & * & * & * & * & 0 & 0 & 0 \\ * & * & * & * & * & * & * & 0 & 0 \\ * & * & * & * & * & * & * & * & -\gamma^2 I \end{bmatrix}, \quad (\text{A.31})$$

ζ is given in (A.23), $G_0(\tau)$, G_1 and Γ are given in (10.56), ψ_3 is defined in (A.28) and $\psi_2^\top = [C_z, 0, 0, -D_u K C_y, 0, 0, 0, 0, D_w]$. The right hand-side of (A.30), being negative for $\zeta \neq 0$, is through use of the Schur complement [229] equivalent to

$$\begin{bmatrix} \psi_1(\tau) & \psi_2 \\ * & -I \end{bmatrix} < 0, \quad (\text{A.32})$$

where $\psi_1 = \psi_{11} + G_0^\top(\tau) P G_1 + G_1^\top P G_0(\tau) - \Gamma^\top \psi_3 \Gamma$.

Due to the presence of the terms $P_2^\top B_u K C_y$ and $P_3 B_u K C_y$, the matrix ψ_{11} in (A.31) is bilinear in the decision variables P_2 , P_3 and K . To overcome this drawback, we choose

$$P_3 = \epsilon P_2, \quad W = P_2^{-1}, \quad (\text{A.33})$$

where ϵ is a tuning scalar. We perform a congruence transformation on the matrix in (A.32) by multiplying it by $\text{diag}(W, W, W, W, W, W, W, W, I, I)$

and its corresponding transpose from the right and left, respectively. We also define the matrices

$$[\bar{S}_1, \bar{S}_2, \bar{R}_1, \bar{R}_2] = W^\top [S_1, S_2, R_1, R_2] W, \quad (\text{A.34a})$$

$$\bar{P} = \text{diag}(W, W, W)^\top P \text{diag}(W, W, W), \quad (\text{A.34b})$$

$$\bar{X} = \text{diag}(W, W)^\top X \text{diag}(W, W) \quad (\text{A.34c})$$

and, following [243, W-Problem], introduce new matrix variables M and N satisfying the following equality conditions:

$$MC_y = C_y W, \quad K = NM^{-1}. \quad (\text{A.35})$$

By defining $\bar{\gamma} = \gamma^2$ we obtain (10.56), which is an LMI in the auxiliary controller variables N and M , as well as in the variables $\bar{\gamma}$, \bar{P} , \bar{R}_1 , \bar{R}_2 , \bar{X} , \bar{S}_1 and \bar{S}_2 , with additional (fixed) tuning parameter ε .

Finally, since $\bar{\psi}_1(\tau)$ in (10.56) is affine with respect to τ , a necessary and sufficient condition for $\bar{\psi}_1(\tau) < 0, \forall \tau \in [h_1, h_2]$ is that $\bar{\psi}_1(\tau = h_1) < 0$ and $\bar{\psi}_1(\tau = h_2) < 0$ hold simultaneously, see e.g., [242]. Hence, under the made assumptions, all conditions of [229, Lemma 4.3] are satisfied. This completes the proof.

□□□

B

APPENDIX B - EXAMPLES AND DERIVATIONS

B.1 VECTOR FORMULATION OF CIRCUIT DYNAMICS

We derive the dq -vector formulation for a general RL circuit described by the per-unit series resistance $r \in \mathbb{R}_{>0}$ and inductance $\ell \in \mathbb{R}_{>0}$. Let us consider such series impedance, with three-phase voltages $v_1^{abc} \in \mathbb{R}^3$ and $v_2^{abc} \in \mathbb{R}^3$ at the respective ends and the three-phase current $i^{abc} \in \mathbb{R}^3$ flowing through it. Assuming a base angular velocity $\omega_b \in \mathbb{R}_{>0}$, the current dynamics are described in per-unit by

$$\frac{d}{dt}i^{abc} = -\frac{\omega_b}{\ell} \left(v_1^{abc} - v_2^{abc} \right) - \frac{r}{\ell} \omega_b i^{abc}. \quad (\text{B.1})$$

Moreover, let us denote by $X(\theta_r) = T(\theta_r)^{-1}$ the inverse of the power-variant dq -transform in (2.4). Assuming a balanced three-phase system and, given a reference angle $\theta_r \in [-\pi, \pi)$ of the dq -frame, expression (B.1) can be rewritten as

$$\frac{d}{dt} \left(X i^{dq} \right) = -\frac{\omega_b}{\ell} X \left(v_1^{dq} - v_2^{dq} \right) - \frac{r}{\ell} \omega_b X i^{dq}. \quad (\text{B.2})$$

Considering that $\frac{d}{dt}\theta_r = \omega_b \omega_r$ and that $j := \mathcal{R}(\pi/2)$ can be interpreted as an embedding of the complex imaginary unit $\sqrt{-1}$ into \mathbb{R}^2 , the term on the left-hand side of (B.2) can be further expressed as

$$\frac{d}{dt} \left(X i^{dq} \right) = \frac{d}{dt} (X) i^{dq} + X \frac{d}{dt} i^{dq} = j \omega_b \omega_r i^{dq} + X \frac{d}{dt} \left(i^{dq} \right). \quad (\text{B.3})$$

Substituting (B.3) into (B.2) and conducting a set of trivial mathematical operations yields

$$\frac{d}{dt} i^{dq} = \frac{\omega_b}{\ell} \left(v_1^{dq} - v_2^{dq} \right) - \left(\frac{r}{\ell} \omega_b + j \omega_b \omega_r \right) i^{dq}. \quad (\text{B.4})$$

B.2 MATHEMATICAL EQUIVALENCE BETWEEN DROOP AND VSM CONTROL

Let us consider the active power droop control given by (2.14) and (2.15):

$$\omega_c = \omega_c^* + \lambda\theta(s)(p_c^* - p_c) = \omega_c^* + R_c^p \frac{\omega_z}{\omega_z + s} (p_c^* - p_c). \quad (\text{B.5})$$

By ignoring the low-pass filtering of active power setpoint p_c^* , and employing some trivial mathematical operations, we can rewrite (B.5) as

$$\frac{1}{\omega_z R_c^p} \dot{\omega}_c = \frac{1}{R_c^p} (\omega_c^* - \omega_c) + p_c^* - p_c + \frac{1}{\omega_z R_c^p} \dot{\omega}_c^* + \frac{1}{\omega_z} \dot{p}_c^*. \quad (\text{B.6})$$

On the other hand, without any simplifications, the swing equation model (2.17) can be expressed in per-unit as

$$M_c \dot{\omega}_c = \frac{p_c^* - p_c}{\omega_c} - D_c (\omega_c - \omega_c^*). \quad (\text{B.7})$$

Assuming small frequency deviations around the nominal value (i.e., $\omega_c \approx 1$ p.u.) and constant power and frequency setpoints (i.e., $\dot{\omega}_c^* = \dot{p}_c^* = 0$), (B.6) and (B.7) can be transformed into

$$\frac{1}{\omega_z R_c^p} \dot{\omega}_c = \frac{1}{R_c^p} (\omega_c^* - \omega_c) + p_c^* - p_c, \quad (\text{B.8a})$$

$$M_c \dot{\omega}_c = D_c (\omega_c^* - \omega_c) + p_c^* - p_c, \quad (\text{B.8b})$$

respectively, which is equivalent under the following condition:

$$M_c = \frac{1}{\omega_z R_c^p}, \quad D_c = \frac{1}{R_c^p}. \quad (\text{B.9})$$

B.3 FREQUENCY CONTROL LOOP OF A GRID-FORMING CONVERTER IN A MULTI-MACHINE SYSTEM

Let us consider an index set \mathcal{N}_g representing all interconnected grid-forming converters with the droop-based active power control (2.15)-(2.14) described by

$$\tau_z \dot{\omega}_{c_j} = \omega_{c_j}^* - \omega_{c_j} + R_c^p (p_{c_j}^* - p_{c_j}), \quad \forall j \in \mathcal{N}_g. \quad (\text{B.10})$$

Here, $\tau_z = \omega_z^{-1}$ is the time constant of the low-pass filter and the remaining notation is preserved from Chapter 2. Having in mind that $\dot{\theta}_{c_j} = \omega_b \omega_{c_j}$, one can transform (B.10) into

$$\tau_z \ddot{\theta}_{c_j} = -\dot{\theta}_{c_j} + \omega_b \omega_{c_j}^* + \omega_b R_c^p (p_{c_k}^* - p_{c_k}). \quad (\text{B.11})$$

The converter's output power p_{c_j} can be described as the sum of all powers flowing across the transmission lines connecting VSC j to the adjacent converter units $k \in \mathcal{K}_j$:

$$p_{c_j} = \sum_{k \in \mathcal{K}_j} p_{jk} = \sum_{k \in \mathcal{K}_j} v_{c_j}^\top i_{jk}, \quad (\text{B.12})$$

with $v_{c_j} := v_{f_j}$ corresponding to the filter output voltage of the respective converter $j \in \mathcal{N}_g$, i_{jk} being the vector of the current flowing through the line between converters j and k , and $\theta_{jk} := \theta_{c_j} - \theta_{c_k}$. Furthermore, considering line parameters of the form $(r_{jk}, \ell_{jk}) \in \mathbb{R}_{>0}$, we express the electromagnetic dynamics of the line current in a dq -frame by (see Appendix B.1)

$$\dot{i}_{jk} = \frac{\omega_b}{\ell_{jk}}(v_{c_j} - v_{c_k}) - \left(\frac{r_{jk}}{\ell_{jk}} \omega_b + j\omega_b \omega_0 \right) i_{jk}, \quad (\text{B.13})$$

which is subsequently transformed into frequency (Laplace) domain as

$$i_{jk} = \frac{v_{c_j} - v_{c_k}}{r_{jk} + j\omega_0 \ell_{jk} + s\ell_{jk}/\omega_b}. \quad (\text{B.14})$$

Let us define $i_{jk}^0 \in \mathbb{R}^2$ as the nominal current flowing through the line (r_{jk}, ℓ_{jk}) with the end voltages $v_{c_j} \in \mathbb{R}^2$ and $v_{c_k} \in \mathbb{R}^2$, i.e.,

$$i_{jk}^0 = \frac{v_{c_j} - v_{c_k}}{r_{jk} + j\omega_0 \ell_{jk}}. \quad (\text{B.15})$$

Substituting (B.15) into (B.14) yields

$$i_{jk} = \frac{i_{jk}^0}{1 + \underbrace{s\ell_{jk}/(r_{jk} + j\omega_0 \ell_{jk})}_{\sigma_l} \omega_b}. \quad (\text{B.16})$$

Note that σ_l can be expressed using SI terms as

$$\sigma_l = \frac{s\ell_{jk}}{(r_{jk} + j\omega_0 \ell_{jk}) \omega_b} = \frac{sL_{jk}}{R_{jk} + j\omega_0 L_{jk}} = \frac{sT_{jk}}{1 + j\omega_0 T_{jk}}, \quad (\text{B.17})$$

with $T_{jk} = \frac{L_{jk}}{R_{jk}}$ being the transmission line time constant. Considering that $\frac{X_l}{R_{jk}} \approx 10$, we can assume $T_{jk} \approx 0.03$ s. Therefore, it is reasonable to assume that $\sigma_l \ll 1$ holds for modes evolving on the timescales shorter than the line time constant T_{jk} [16]. By performing a first-order Taylor series expansion

$$\frac{1}{1 + \sigma_l} \approx 1 - \sigma_l, \quad (\text{B.18})$$

we can rewrite (B.20) as

$$i_{jk} \approx i_{jk}^0 - \frac{s\ell_{jk}}{\omega_b (r_{jk} + j\omega_0\ell_{jk})} i_{jk}^0, \quad (\text{B.19})$$

and transform it back into the time-domain form

$$i_{jk} \approx i_{jk}^0 - \frac{\ell_{jk}}{\omega_b (r_{jk} + j\omega_0\ell_{jk})^2} (\dot{v}_{c_j} - \dot{v}_{c_k}). \quad (\text{B.20})$$

Assuming nominal voltage magnitudes and small angle deviations between the nodes, i.e., $\|v_{c_j}\| \approx 1$ p.u. and $\theta_{jk} \approx 0, \forall j \in \mathcal{N}_g, \forall k \in \mathcal{K}_j$, we can compute the time derivatives of voltage vectors and subsequently the total active power injection as

$$\begin{aligned} p_{c_j} &= \sum_{k \in \mathcal{K}_j} \left(\frac{\omega_0\ell_{jk}}{\omega_b (r_{jk}^2 + \omega_0^2\ell_{jk}^2)} \theta_{c_j} + \frac{2r_{jk}\ell_{jk}^2}{\omega_b (r_{jk}^2 + \omega_0^2\ell_{jk}^2)} \dot{\theta}_{c_j} \right) \\ &= B_j\theta_{c_j} + B'_j\dot{\theta}_{c_j}. \end{aligned} \quad (\text{B.21})$$

Substituting (B.21) into (B.10) yields the frequency dynamics of an individual inverter of the form

$$\tau_z \ddot{\theta}_{c_j} + (1 - \omega_b R_c^p B'_j) \dot{\theta}_{c_j} + \omega_b R_c^p B_j \theta_{c_j} + C_j = 0, \quad (\text{B.22})$$

with $C_j = \omega_b \omega_{c_j}^* + \omega_b R_c^p p_{c_j}^*$.

B.4 DERIVATION OF SATURATED FREQUENCY SLIP

Let us recall the expressions for the minimum and maximum of two variables from (9.31):

$$\min\{a, b\} = \frac{a + b - |b - a|}{2}, \quad (\text{B.23a})$$

$$\max\{a, b\} = \frac{a + b + |b - a|}{2}. \quad (\text{B.23b})$$

The goal is to impose the lower and upper saturation limits $(\underline{\omega}_\nu, \bar{\omega}_\nu)$ on an unsaturated frequency slip signal $\tilde{\omega}_\nu$, i.e., to obtain a new signal ω_ν such that $\omega_\nu \in [\underline{\omega}_\nu, \bar{\omega}_\nu]$. This is equivalent to finding the maximum of the underlying signal and its lower bound (let us denote it by $\hat{\omega}_\nu$), and subsequently finding the minimum of that signal and the upper bound. In other words,

$$\hat{\omega}_\nu = \max\{\tilde{\omega}_\nu, \underline{\omega}_\nu\}, \quad (\text{B.24a})$$

$$\omega_\nu = \min\{\hat{\omega}_\nu, \bar{\omega}_\nu\}. \quad (\text{B.24b})$$

We can rewrite (B.24) as

$$\hat{\omega}_\nu = \frac{1}{2} (\tilde{\omega}_\nu + \underline{\omega}_\nu + |\underline{\omega}_\nu - \tilde{\omega}_\nu|), \quad (\text{B.25a})$$

$$\omega_\nu = \frac{1}{2} (\hat{\omega}_\nu + \bar{\omega}_\nu - |\bar{\omega}_\nu - \hat{\omega}_\nu|), \quad (\text{B.25b})$$

and subsequently substitute (B.25b) into (B.25a), resulting in the expression given by (9.32).

B.5 CLARIFICATION OF PWL FORMULATION

For clarity, here we present in more detail the mathematical formulation of how the PWL optimization problem (12.2) in Chapter 12 is solved. With $|\mathcal{V}| = 4$, the inner “max” operator can be eliminated from the objective function (12.2) by defining the following terms:

$$t_3 := \max \left\{ t_2, a_4 R_g^{(\eta)} + b_4 F_g^{(\eta)} + c_4 M^{(\eta)} + d_4 \right\}, \quad (\text{B.26a})$$

$$t_2 := \max \left\{ t_1, a_3 R_g^{(\eta)} + b_3 F_g^{(\eta)} + c_3 M^{(\eta)} + d_3 \right\}, \quad (\text{B.26b})$$

$$t_1 := \max \left\{ a_2 R_g^{(\eta)} + b_2 F_g^{(\eta)} + c_2 M^{(\eta)} + d_2, a_1 R_g^{(\eta)} + b_1 F_g^{(\eta)} + c_1 M^{(\eta)} + d_1 \right\} \quad (\text{B.26c})$$

and reformulating the complete optimization problem in (12.2) as

$$\min_{\Psi} \sum_{\eta \in \mathcal{H}} \left(t_3 \left(R_g^{(\eta)}, F_g^{(\eta)}, M^{(\eta)} \right) - \Delta f_{\max} \left(R_g^{(\eta)}, F_g^{(\eta)}, M^{(\eta)} \right) \right)^2 \quad (\text{B.27a})$$

$$\text{s.t. } \forall \eta \in \mathcal{H},$$

$$a_1 R_g^{(\eta)} + b_1 F_g^{(\eta)} + c_1 M^{(\eta)} + d_1 \leq t_1, \quad (\text{B.27b})$$

$$t_1 \leq a_1 R_g^{(\eta)} + b_1 F_g^{(\eta)} + c_1 M^{(\eta)} + d_1 + v_1 A, \quad (\text{B.27c})$$

$$a_2 R_g^{(\eta)} + b_2 F_g^{(\eta)} + c_2 M^{(\eta)} + d_2 \leq t_1, \quad (\text{B.27d})$$

$$t_1 \leq a_2 R_g^{(\eta)} + b_2 F_g^{(\eta)} + c_2 M^{(\eta)} + d_2 + (1 - v_1) A, \quad (\text{B.27e})$$

$$t_1 \leq t_2 \leq t_1 + v_2 A, \quad (\text{B.27f})$$

$$a_3 R_g^{(\eta)} + b_3 F_g^{(\eta)} + c_3 M^{(\eta)} + d_3 \leq t_2, \quad (\text{B.27g})$$

$$t_2 \leq a_3 R_g^{(\eta)} + b_3 F_g^{(\eta)} + c_3 M^{(\eta)} + d_3 + (1 - v_2) A, \quad (\text{B.27h})$$

$$t_2 \leq t_3 \leq t_2 + v_3 A, \quad (\text{B.27i})$$

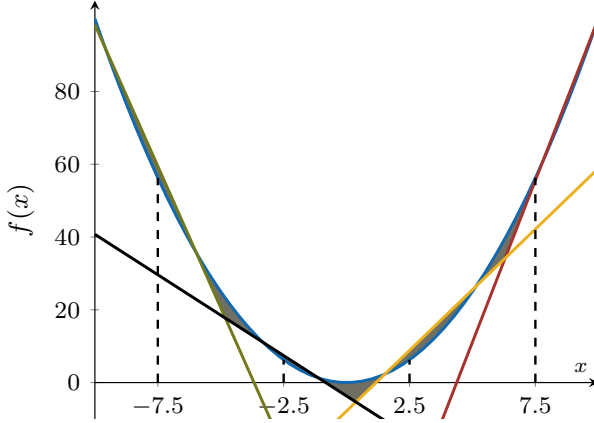


FIGURE B.1: Illustration of the PWL method on a 2-D function.

$$a_4 R_g^{(\eta)} + b_4 F_g^{(\eta)} + c_4 M^{(\eta)} + d_4 \leq t_3, \tag{B.27j}$$

$$t_3 \leq a_4 R_g^{(\eta)} + b_4 F_g^{(\eta)} + c_4 M^{(\eta)} + d_4 + (1 - v_3)A, \tag{B.27k}$$

where $(v_1, v_2, v_3) \in \{0, 1\}$ are binary variables and $A \in \mathbb{R}_{>0}$ is a sufficiently large scalar.

We visually illustrate how the PWL optimization problem (B.27) is solved using a simple 2-D example depicted in Fig. B.1. There are $|\mathcal{H}| = 4$ evaluation points set at $x^{(1)} = -7.5$, $x^{(2)} = -2.5$, $x^{(3)} = 2.5$ and $x^{(4)} = 7.5$, and the respective function $f : \mathbb{R} \mapsto \mathbb{R}$ is approximated by $|\mathcal{V}| = 4$ segments. At each evaluation point $\eta \in \mathcal{H}$, the model identifies the segment closest to the original curve, and subsequently aims to minimize the overall shaded area. The proposed technique can then be expanded and employed on a function of three variables, as we have done with the expression for frequency nadir in (12.1a).

B.6 MONOTONIC PROPERTIES OF NDZ BOUNDS

We explore the monotonic properties of nonlinear functions $g(\cdot)$ and $h(\cdot)$ in Section 14.3.2 by analyzing their first derivatives. Let us start with $g(\cdot)$ in (14.22a) by taking the partial derivative of the right-hand side in (14.13) with respect to \hat{V} :

$$\frac{\partial}{\partial \hat{V}} g(V, \hat{V}, \Delta Q) = -2 \frac{V^2}{\hat{V}^3} - \frac{R_f}{P_G} \frac{\partial}{\partial \hat{V}} \hat{f}(V, \hat{V}, \Delta Q). \tag{B.28}$$

The expression for $\rho = \frac{\partial}{\partial \hat{V}} \hat{f}(V, \hat{V}, \Delta Q)$ can be obtained from (14.19) as

$$\rho = \frac{VR_V}{4\pi C_0 \hat{V}^3} \left(1 + \frac{\beta_V}{2\sqrt{\beta_V^2 + 8\pi f C_0 \left(\frac{\Delta Q}{\hat{V}^2} + 2\pi f C_0 \right)}} \right). \quad (\text{B.29})$$

It can be shown that $\rho \geq 0, \forall \hat{V} \in \mathbb{R}_{>0}$, therefore implying that $\frac{\partial}{\partial \hat{V}} g(V, \hat{V}, \Delta Q) < 0$, i.e., $g(V, \hat{V}, \Delta Q)$ is monotonically decreasing. Hence, for $V_{\min} \leq \hat{V} \leq V_{\max}$ we can state that

$$g_{\min}(V, V_{\max}, \Delta Q) \leq \frac{\Delta P}{P_G} \leq g_{\max}(V, V_{\min}, \Delta Q), \quad (\text{B.30})$$

which confirms the inequality in (14.23a).

As for the permissible limits on reactive power mismatch, the partial derivative $\frac{\partial}{\partial \hat{f}} h(f, \hat{f}, \Delta P)$ can be derived from (14.15) and (14.21) accordingly:

$$\begin{aligned} \frac{\partial}{\partial \hat{f}} h(f, \hat{f}, \Delta P) = & \left(1 + \frac{\Delta P}{P_G} \right) \left(\frac{RR_V f}{\hat{f}^2 \hat{V}(f, \hat{f}, \Delta P)^2} (\hat{V}(f, \hat{f}, \Delta P) - V) \right. \\ & \left. \left(1 + \frac{\frac{\partial}{\partial \hat{f}} \hat{V}(f, \hat{f}, \Delta P)}{\hat{V}(f, \hat{f}, \Delta P)} \right) + 2Q_f \frac{f^2}{\hat{f}^3} \right). \end{aligned} \quad (\text{B.31})$$

However, unlike the expression in (B.28), (B.31) is not monotonic for every system initialization, i.e., it is strictly positive only for $V > \hat{V}$. Nevertheless, after conducting some trivial mathematical transformations, it can be shown that $\frac{\partial}{\partial \hat{f}} h(f, \hat{f}, \Delta P) \geq 0, \forall V \in \mathbb{R}_{>0}$ as long as the following inequality holds:

$$2Q_f \frac{f}{\hat{f}} > -\frac{\hat{Q}_G}{\hat{P}_G} \left(1 + \frac{\frac{\partial}{\partial \hat{f}} \hat{V}(f, \hat{f}, \Delta P)}{\hat{V}(f, \hat{f}, \Delta P)} \right). \quad (\text{B.32})$$

Since typically in practice $\hat{P}_G > \hat{Q}_G$, $0.8 < f/\hat{f} < 1.2$ and $Q_f = 2.5$, the condition in (B.32) will be satisfied for any realistic DG unit and distribution network under investigation. Therefore, the function $h(f, \hat{f}, \Delta P)$ is monotonically increasing on the interval $\hat{f} \in [f_{\min}, f_{\max}]$, which implies that

$$h_{\min}(f, f_{\min}, \Delta P) \leq \frac{\Delta Q}{Q_G} \leq h_{\max}(f, f_{\max}, \Delta P), \quad (\text{B.33})$$

and hence validates the inequality in (14.23b).

BIBLIOGRAPHY

- [1] W. Winter, K. Elkington, G. Bareux, and J. Kostevc. “Pushing the Limits: Europe’s New Grid: Innovative Tools to Combat Transmission Bottlenecks and Reduced Inertia”. In: *IEEE Power and Energy Magazine* 13.1 (2015), 60.
- [2] Australian Energy Market Operator. *Black System South Australia 28 September 2016 - Final Report*. Tech. rep. Mar. 2017.
- [3] Svenska kraftnät, Statnett, Fingrid and Energinet.dk. *Challenges and Opportunities for the Nordic Power System*. Tech. rep. 2016.
- [4] J. Matevosyan and P. Du. “Wind Integration in ERCOT”. In: *Integration of Large-Scale Renewable Energy into Bulk Power Systems*. Springer, 2017, 1.
- [5] G. Denis, T. Prevost, M. S. Debry, F. Xavier, X. Guillaud, and A. Menze. “The Migrate project: the challenges of operating a transmission grid with only inverter-based generation. A grid-forming control improvement with transient current-limiting control”. In: *IET Renewable Power Generation* 12.5 (2018), 523.
- [6] F. Milano, F. Dörfler, G. Hug, D. J. Hill, and G. Verbič. “Foundations and Challenges of Low-Inertia Systems”. In: *Power Systems Computation Conference (PSCC)*. June 2018.
- [7] A. Ulbig, S. T. Borsche, and G. Andersson. “Impact of low rotational inertia on power system stability and operation”. In: *IFAC Proceedings Volumes* 47.3 (2014), 7290.
- [8] EirGrid and Soni. *DS3: System Services Review TSO Recommendations*. Tech. rep. EirGrid, 2012.
- [9] B. Kroposki, B. B. Johnson, Y. Zhang, V. Gevorgian, P. Denholm, B-M. Hodge, and B. Hannegan. “Achieving a 100% Renewable Grid: Operating Electric Power Systems with Extremely High Levels of Variable Renewable Energy”. In: *IEEE Power and Energy Magazine* 15.2 (2017), 61.
- [10] A. Tayyebi, D. Großand A. Anta, and F. Dörfler. “Interactions of Grid-Forming Power Converters and Synchronous Machines - A Comparative Study”. In: *arXiv:1902.10750* (2019).

- [11] *Final Report - Queensland and South Australia system separation on 25 August 2018*. Tech. rep. AEMO, 2019.
- [12] U. Markovic, O. Stanojev, E. Vrettos, P. Aristidou, Duncan Callaway, and G. Hug. “Understanding Stability of Low-Inertia Systems”. In: *IEEE Transactions on Power Systems* (Nov. 2020).
- [13] N. W. Miller, M. Shao, S. Pajic, and R. D’Aquila. *Western wind and solar integration study phase 3—frequency response and transient stability*. Tech. rep. National Renewable Energy Lab.(NREL), Golden, CO (United States); GE Energy Management, Schenectady, NY (United States), 2014.
- [14] T. Qoria, Q. Cossart, C. Li, X. Guillaud, F. Colas, F. Gruson, and X. Kestelyn. *Local control and simulation tools for large transmission systems*. Tech. rep. Deliverable D3.2, MIGRATE WP3, 2018.
- [15] S. Curi, D. Groß, and F. Dörfler. “Control of low-inertia power grids: A model reduction approach”. In: *IEEE Conference on Decision and Control (CDC)*. 2017, 5708.
- [16] P. Vorobev, P. Huang, M. Al Hosani, J. L. Kirtley, and K. Turitsyn. “High-Fidelity Model Order Reduction for Microgrids Stability Assessment”. In: *IEEE Transactions on Power Systems* 33.1 (Jan. 2018), 874.
- [17] D. Groß, M. Colombino, J-S. Brouillon, and F. Dörfler. “The effect of transmission-line dynamics on grid-forming dispatchable virtual oscillator control”. In: *IEEE Transactions on Control of Network Systems* (2019).
- [18] U. Markovic, P. Aristidou, and G. Hug. “Stability Performance of Power Electronic Devices with Time Delays”. In: *2017 PowerTech*. June 2017.
- [19] U. Markovic, N. Früh, P. Aristidou, and G. Hug. “Interval-Based Adaptive Inertia and Damping Control of a Virtual Synchronous Machine”. In: *2019 PowerTech*. June 2019.
- [20] U. Markovic, J. Zhang, D. Rodriguez Flores, O. Stanojev, P. Aristidou, and G. Hug. “Impact of Measurement Delays on Stability and Performance of Inverter-Dominated Power Systems”. In: *IEEE Transactions on Power Systems* (under review).

- [21] U. Markovic, D. Groß, P. Aristidou, F. Colas, T. Qoria, T. Prevost, G. Denis, M. Debry, X. Guillaud, and G. Hug. “Compatibility of Grid-Forming Control Strategies in 100% Converter-Based Power Systems”. In: *IEEE Transactions on Power Delivery* (under review).
- [22] U. Markovic, J. Vorwerk, P. Aristidou, and G. Hug. “Stability Analysis of Converter Control Modes in Low-Inertia Power Systems”. In: *2018 ISGT-Europe*. Oct. 2018.
- [23] R. Ofir, U. Markovic, P. Aristidou, and G. Hug. “Droop vs. Virtual Inertia: Comparison from the Perspective of Converter Operation Mode”. In: *2018 ENERGYCON*. June 2018.
- [24] U. Markovic, O. Stanojev, P. Aristidou, and G. Hug. “Partial Grid Forming Concept for 100% Inverter-Based Transmission Systems”. In: *2018 PES General Meeting*. Aug. 2018.
- [25] P. M. Anderson and M. Mirheydar. “A low-order system frequency response model”. In: *IEEE Transactions on Power Systems* 5.3 (1990), 720.
- [26] P. Kundur. *Power System Stability and Control*. McGraw-Hill, 1994.
- [27] J. Machowski, J. W. Bialek, and J. R. Bumby. *Power System Dynamics: Stability and Control*. Wiley, 2008.
- [28] A. Yazdani and R. Iravani. *Voltage-Sourced Converters in Power Systems: Modeling, Control, and Applications*. John Wiley & Sons, 2010.
- [29] M. F. M. Arani and E. F. El-Saadany. “Implementing Virtual Inertia in DFIG-Based Wind Power Generation”. In: *IEEE Transactions on Power Systems* 28.2 (May 2013), 1373.
- [30] M. P. N. van Wesenbeeck, S. W. H. de Haan, P. Varela, and K. Visscher. “Grid tied converter with virtual kinetic storage”. In: *2009 IEEE Bucharest PowerTech*. June 2009.
- [31] F. Díaz-González, A. Sumper, O. Gomis-Bellmunt, and R. Villafáfila-Robles. “A review of energy storage technologies for wind power applications”. In: *Renewable and Sustainable Energy Reviews* 16.4 (2012), 2154.
- [32] Q-C. Zhong and T. Hornik. *Control of power inverters in renewable energy and smart grid integration*. Vol. 97. John Wiley & Sons, 2012.
- [33] T.C. Green and M. Prodanovic. “Control of inverter-based microgrids”. In: *Electric Power Systems Research* 77.9 (2007). Distributed Generation, 1204.

- [34] Q.-C. Zhong, P. L. Nguyen, Z. Ma, and W. Sheng. “Self-Synchronized Synchronverters: Inverters Without a Dedicated Synchronization Unit”. In: *IEEE Transactions on Power Electronics* 29.2 (2014), 617.
- [35] G. Denis, T. Prevost, P. Panciatici, X. Kestelyn, F. Colas, and X. Guillaud. “Review on potential strategies for transmission grid operations based on power electronics interfaced voltage sources”. In: *IEEE Power Energy Society General Meeting*. 2015.
- [36] M.-S. Debry, G. Denis, T. Prevost, F. Xavier, and A. Menze. “Maximizing the Penetration of Inverter-Based Generation on Large Transmission Systems: the MIGRATE Project”. In: *6th Solar Integration Workshop*. 2017.
- [37] T. Qoria, F. Gruson, F. Colas, X. Guillaud, M. Debry, and T. Prevost. “Tuning of Cascaded Controllers for Robust Grid-Forming Voltage Source Converter”. In: *Power Systems Computation Conference*. 2018.
- [38] I. A. Hiskens and E. M. Fleming. “Control of inverter-connected sources in autonomous microgrids”. In: *American Control Conference*. 2008.
- [39] J. Schiffer, R. Ortega, A. Astolfi, J. Raisch, and T. Sezi. “Conditions for stability of droop-controlled inverter-based microgrids”. In: *Automatica* 50.10 (2014), 2457.
- [40] B. B. Johnson, S. V. Dhople, A. O. Hamadeh, and P. T. Krein. “Synchronization of nonlinear oscillators in an LTI electrical power network”. In: *IEEE Transactions on Circuits and Systems I: Regular Papers* 61.3 (2014), 834.
- [41] F. Dörfler, J. W. Simpson-Porco, and F. Bullo. “Breaking the hierarchy: Distributed control and economic optimality in microgrids”. In: *IEEE Transactions on Control of Network Systems* 3.3 (2016), 241.
- [42] G. Peponides, P. Kokotovic, and J. Chow. “Singular perturbations and time scales in nonlinear models of power systems”. In: *IEEE Transactions on Circuits and Systems* 29.11 (1982), 758.
- [43] J. Schiffer, D. Zonetti, R. Ortega, A. M. Stanković, T. Sezi, and J. Raisch. “A survey on modeling of microgrids—From fundamental physics to phasors and voltage sources”. In: *Automatica* 74 (2016), 135.
- [44] L. Luo and S. V. Dhople. “Spatiotemporal Model Reduction of Inverter-Based Islanded Microgrids”. In: *IEEE Transactions on Energy Conversion* 29.4 (Dec. 2014), 823.

- [45] O. Ajala, A. D. Domínguez-García, and P. W. Sauer. *A Hierarchy of Models for Inverter-Based Microgrids*. Tech. rep. available at: www.entsoe.eu. Union for the co-ordination of transmission of electricity, 2017.
- [46] Y. Lin, B. B. Johnson, V. Gevorgian, V. Purba, and S. Dhople. “Stability assessment of a system comprising a single machine and inverter with scalable ratings”. In: *2017 North American Power Symposium (NAPS)*. Sept. 2017.
- [47] D. Ramasubramanian, V. Vittal, and J. M. Undrill. “Transient stability analysis of an all converter interfaced generation WECC system”. In: *Power Systems Computation Conference (PSCC)*. Genova, Italy, 2016.
- [48] M. C. Chandorkar, D. M. Divan, and R. Adapa. “Control of parallel connected inverters in standalone AC supply systems”. In: *IEEE Transactions on Industry Applications* 29.1 (Jan. 1993), 136.
- [49] Q. C. Zhong and G. Weiss. “Synchronverters: Inverters That Mimic Synchronous Generators”. In: *IEEE Transactions on Industrial Electronics* 58.4 (Apr. 2011), 1259.
- [50] S. D’Arco and J. A. Suul. “Equivalence of Virtual Synchronous Machines and Frequency-Droops for Converter-Based MicroGrids”. In: *IEEE Transactions on Smart Grid* 5.1 (2014), 394.
- [51] S. D’Arco, J. A. Suul, and O. B. Fosso. “Small-signal modelling and parametric sensitivity of a Virtual Synchronous Machine”. In: *2014 Power Systems Computation Conference*. Aug. 2014.
- [52] B. B. Johnson, S. V. Dhople, A. O. Hamadeh, and P. T. Krein. “Synchronization of parallel single-phase inverters with virtual oscillator control”. In: *IEEE Transactions on Power Electronics* 29.11 (2014), 6124.
- [53] M. Colombino, D. Groß, J-S. Brouillon, and F. Dörfler. “Global phase and magnitude synchronization of coupled oscillators with application to the control of grid-forming power inverters”. In: *IEEE Transactions on Automatic Control* (2019).
- [54] I. Cvetkovic, D. Boroyevich, R. Burgos, C. Li, and P. Mattavelli. “Modeling and control of grid-connected voltage-source converters emulating isotropic and anisotropic synchronous machines”. In: *IEEE 16th Workshop on Control and Modeling for Power Electronics (COMPEL)*. Vancouver, BC Canada, 2015.

- [55] I. Cvetkovic, D. Boroyevich, R. Burgos, Y-H. Hsieh, F. C. Lee, C. Li, and P. Mattavelli. "Experimental verification of a virtual synchronous generator control concept". In: *IEEE 17th Workshop on Control and Modeling for Power Electronics (COMPEL)*. Trondheim, Norway, 2016.
- [56] L. Huang, H. Xin, Z. Wang, K. Wu, H. Wang, J. Hu, and C. Lu. "A Virtual Synchronous Control for Voltage-Source Converters Utilizing Dynamics of DC-Link Capacitor to Realize Self-Synchronization". In: *IEEE Journal of Emerging and Selected Topics in Power Electronics* 5.4 (Dec. 2017), 1565.
- [57] T. Jouini, C. Arghir, and F. Dörfler. "Grid-friendly matching of synchronous machines by tapping into the DC storage". In: *IFAC Workshop on Distributed Estimation and Control in Networked Systems (NecSys)*. 2016, 192.
- [58] C. Arghir, T. Jouini, and F. Dörfler. "Grid-forming control for power converters based on matching of synchronous machines". In: *Automatica* 95 (2018), 273.
- [59] G. M. Foglia, L. Frosio, M. F. Iacchetti, and R. Perini. "Control loops design in a grid supporting mode inverter connected to a microgrid". In: *European Conference on Power Electronics and Applications (EPE)*. 2015.
- [60] A. Engler. "Applicability of droops in low voltage grids". In: *International Journal of Distributed Energy Resources* 1.1 (2005), 1.
- [61] K. De Brabandere, B. Bolsens, J. Van den Keybus, A. Woyte, J. Driesen, and R. Belmans. "A Voltage and Frequency Droop Control Method for Parallel Inverters". In: *IEEE Transactions on Power Electronics* 22.4 (July 2007), 1107.
- [62] J. Rocabert, A. Luna, F. Blaabjerg, and P. Rodríguez. "Control of Power Converters in AC Microgrids". In: *IEEE Transactions on Power Electronics* 27.11 (Nov. 2012), 4734.
- [63] M. A. A. Murad, A. Ortega, and F. Milano. "Impact on power system dynamics of PI control limiters of VSC-based devices", in *Power Systems Computation Conference (PSCC)*. Dublin, Ireland, June 2018.
- [64] P. W. Sauer and M. A. Pai. *Power system dynamics and stability*. Prentice Hall, 1997.

- [65] G. Pinares. “Analysis of the DC dynamics of VSC-HVDC systems connected to weak AC grids using a frequency domain approach”. In: *2014 Power Systems Computation Conference*. Aug. 2014.
- [66] S. D’Arco, J. A. Suul, and O. B. Fosso. “Virtual synchronous machines - Classification of implementations and analysis of equivalence to droop controllers for microgrids”. In: *2013 IEEE Grenoble Conference*. June 2013.
- [67] N. Pogaku, M. Prodanovic, and T. C. Green. “Modeling, Analysis and Testing of Autonomous Operation of an Inverter-Based Microgrid”. In: *IEEE Transactions on Power Electronics* 22.2 (Mar. 2007), 613.
- [68] S. Chung. “A phase tracking system for three phase utility interface inverters”. In: *IEEE Transactions on Power Electronics* 15.3 (May 2000), 431.
- [69] G. S. Misyris, J. A. Mermet-Guyennet, S. Chatzivasileiadis, and T. Weckesser. “Grid Supporting VSCs in Power Systems with Varying Inertia and Short-Circuit Capacity”. In: *2019 IEEE Milan PowerTech*. June 2019.
- [70] S. D’Arco and J. A. Suul. “Small-Signal analysis of an isolated power system controlled by a virtual synchronous machine”. In: *IEEE International Power Electronics and Motion Control Conference (PEMC)*. Sept. 2016, 462.
- [71] S. F. Zarei, H. Mokhtari, M. A. Ghasemi, S. Peyghami, P. Davari, and F. Blaabjerg. “Control of Grid-Following Inverters under Unbalanced Grid Conditions”. In: *IEEE Transactions on Energy Conversion* (2019), 1.
- [72] J. C. Vasquez, J. M. Guerrero, A. Luna, P. Rodriguez, and R. Teodorescu. “Adaptive Droop Control Applied to Voltage-Source Inverters Operating in Grid-Connected and Islanded Modes”. In: *IEEE Transactions on Industrial Electronics* 56.10 (Oct. 2009), 4088.
- [73] V. Mariani, F. Vasca, J. C. Vásquez, and J. M. Guerrero. “Model Order Reductions for Stability Analysis of Islanded Microgrids With Droop Control”. In: *IEEE Transactions on Industrial Electronics* 62.7 (July 2015), 4344.
- [74] J. W. Simpson-Porco, F. Dörfler, and F. Bullo. “Voltage Stabilization in Microgrids via Quadratic Droop Control”. In: *IEEE Transactions on Automatic Control* 62.3 (Mar. 2017), 1239.

- [75] H. P. Beck and R. Hesse. “Virtual synchronous machine”. In: *2007 9th International Conference on Electrical Power Quality and Utilisation*. Oct. 2007.
- [76] J. Driesen and K. Visscher. “Virtual synchronous generators”. In: *2008 IEEE Power and Energy Society General Meeting - Conversion and Delivery of Electrical Energy in the 21st Century*. July 2008.
- [77] S. D’Arco, J. A. Suul, and O. B. Fosso. “A Virtual Synchronous Machine implementation for distributed control of power converters in SmartGrids”. In: *Electric Power Systems Research* 122 (2015), 180.
- [78] G. Seo, I. Subotic, B. Johnson, M. Colombino, D. Groß, and F. Dörfler. “Dispatchable Virtual Oscillator Control for Decentralized Inverter-Dominant Power Systems – Analysis of Droop Characteristic and Verification”. In: *Applied Power Electronics Conference (APEC)*. 2019.
- [79] L. A. B. Tôrres, J. P. Hespanha, and J. Moehlis. “Synchronization of Identical Oscillators Coupled Through a Symmetric Network With Dynamics: A Constructive Approach With Applications to Parallel Operation of Inverters”. In: *IEEE Transactions on Automatic Control* 60.12 (2015), 3226.
- [80] M. Sinha, F. Dörfler, B. B. Johnson, and S. V. Dhople. “Uncovering Droop Control Laws Embedded Within the Nonlinear Dynamics of Van der Pol Oscillators”. In: *IEEE Transactions on Control of Network Systems* 4.2 (2017), 347.
- [81] M. Ashabani and Y. A. I. Mohamed. “Novel Comprehensive Control Framework for Incorporating VSCs to Smart Power Grids Using Bidirectional Synchronous-VSC”. In: *IEEE Transactions on Power Systems* 29.2 (2014), 943.
- [82] I. Cvetkovic, D. Boroyevich, R. Burgos, C. Li, and P. Mattavelli. “Modeling and control of grid-connected voltage-source converters emulating isotropic and anisotropic synchronous machines”. In: *IEEE Workshop on Control and Modeling for Power Electronics (COMPEL)*. 2015.
- [83] E. Pajuelo, R. Gokaraju, and M. S. Sachdev. “Coordination of overexcitation limiter, field overcurrent protection and generator control”. In: *IEEE PES General Meeting*. July 2010, 1.
- [84] M. E. Baran and N. R. Mahajan. “Overcurrent Protection on Voltage-Source-Converter-Based Multiterminal DC Distribution Systems”. In: *IEEE Transactions on Power Delivery* 22.1 (Jan. 2007), 406.

- [85] P. M. Anderson. *Power System Protection*. New York: IEEE Press, 1999.
- [86] J. Jia, G. Yang, and A. H. Nielsen. “A Review on Grid-Connected Converter Control for Short-Circuit Power Provision Under Grid Unbalanced Faults”. In: *IEEE Transactions on Power Delivery* 33.2 (2018), 649.
- [87] A. Junyent-Ferre, O. Gomis-Bellmunt, T. C. Green, and D. E. Soto-Sanchez. “Current Control Reference Calculation Issues for the Operation of Renewable Source Grid Interface VSCs Under Unbalanced Voltage Sags”. In: *IEEE Transactions on Power Electronics* 26.12 (2011), 3744.
- [88] I. Sadeghkhani, M. E. Hamedani Golshan, J. M. Guerrero, and A. Mehrizi-Sani. “A Current Limiting Strategy to Improve Fault Ride-Through of Inverter Interfaced Autonomous Microgrids”. In: *IEEE Transactions on Smart Grid* 8.5 (2017), 2138.
- [89] H. Xin, L. Huang, L. Zhang, Z. Wang, and J. Hu. “Synchronous Instability Mechanism of P-f Droop-Controlled Voltage Source Converter Caused by Current Saturation”. In: *IEEE Transactions on Power Systems* 31.6 (2016), 5206.
- [90] J. He and Y. W. Li. “Analysis, Design, and Implementation of Virtual Impedance for Power Electronics Interfaced Distributed Generation”. In: *IEEE Transactions on Industry Applications* 47.6 (2011), 2525.
- [91] A. D. Paquette and D. M. Divan. “Virtual Impedance Current Limiting for Inverters in Microgrids With Synchronous Generators”. In: *IEEE Transactions on Industry Applications* 51.2 (2015), 1630.
- [92] G. Denis, T. Prevost, M-S. Debry, F. Xavier, X. Guillaud, and A. Menze. “The Migrate project: the challenges of operating a transmission grid with only inverter-based generation. A grid-forming control improvement with transient current-limiting control”. In: *IET Renewable Power Generation* 12.5 (2018), 523.
- [93] D. Groß and F. Dörfler. “Projected grid-forming control for current-limiting of power converters”. In: *2019 57th Annual Allerton Conference on Communication, Control, and Computing (Allerton)*. Sept. 2019, 326.
- [94] T. Qoria, U. Markovic, T. Jouini, D. Groß, G. Denis, and T. Prevost. *Data underlying the research of a 3 bus model for full inverter system - Migrate WP3*. 2018.

- [95] ENTSO-E. *Documentation on controller tests in test grid configurations*. Tech. rep. Nov. 2013.
- [96] J. M. Uudrill. “Dynamic Stability Calculations for an Arbitrary Number of Interconnected Synchronous Machines”. In: *IEEE Transactions on Power Apparatus and Systems* PAS-87.3 (Mar. 1968), 835.
- [97] C. Spanias and I. Lestas. “A system reference frame approach for stability analysis and control of power grids”. In: *ArXiv e-prints* (Sept. 2018).
- [98] G. Diaz, C. Gonzalez-Moran, J. Gomez-Aleixandre, and A. Diez. “Complex-Valued State Matrices for Simple Representation of Large Autonomous Microgrids Supplied by PQ and Vf Generation”. In: *IEEE Transactions on Power Systems* 24.4 (Nov. 2009), 1720.
- [99] I. Caduff, U. Markovic, C. Roberts, G. Hug, and E. Vrettos. “Reduced-Order Modeling of Inverter-Based Generation using Hybrid Singular Perturbation”. In: *2020 PSCC*. June 2020.
- [100] H. K. Khalil. *Nonlinear systems*. 3rd. ed. Prentice Hall, 2002.
- [101] K. Kodra, Ningfan Zhong, and Z. Gajić. “Model order reduction of an islanded microgrid using singular perturbations”. In: *ACC*. 2016.
- [102] V. Mariani, F. Vasca, and J. M. Guerrero. “Analysis of droop controlled parallel inverters in islanded microgrids”. In: *2014 IEEE International Energy Conference (ENERGYCON)*. May 2014.
- [103] S. V. Iyer, M. N. Belur, and M. C. Chandorkar. “A Generalized Computational Method to Determine Stability of a Multi-inverter Microgrid”. In: *IEEE Transactions on Power Electronics* 25.9 (Sept. 2010), 2420.
- [104] M. Rasheduzzaman, J. A. Mueller, and J. W. Kimball. “Reduced-Order Small-Signal Model of Microgrid Systems”. In: *IEEE Transactions on Sustainable Energy* 6.4 (2015), 1292.
- [105] P. Kokotovic, H. K. Khali, and J. O’Reilly. *Singular perturbation methods in control: analysis and design*. Vol. 25. Siam, 1999.
- [106] Q. Cossart, F. Colas, and X. Kestelyn. “Model reduction of converters for the analysis of 100 % power electronics transmission systems”. In: *International Conference on Industrial Technology (ICIT)*. 2018.
- [107] I. J. Perez-Arriaga, G. C. Verghese, and F. C. Schweppe. “Selective Modal Analysis with Applications to Electric Power Systems, Part I: Heuristic Introduction”. In: *IEEE Power Engineering Review* PER-2.9 (1982), 29.

- [108] D. Mondal, A. Chakrabarti, and A. Sengupta. *Power System Small Signal Stability Analysis and Control*. Elsevier - Academic Press, 2014.
- [109] O. Mo, S. D'Arco, and J. A. Suul. "Evaluation of Virtual Synchronous Machines With Dynamic or Quasi-Stationary Machine Models". In: *IEEE Transactions on Industrial Electronics* 64.7 (July 2017), 5952.
- [110] E. A. A. Coelho, P. C. Cortizo, and P. F. D. Garcia. "Small-signal stability for parallel-connected inverters in stand-alone AC supply systems". In: *IEEE Transactions on Industry Applications* 38.2 (Mar. 2002), 533.
- [111] X. Guo, Z. Lu, B. Wang, X. Sun, L. Wang, and J. M. Guerrero. "Dynamic Phasors-Based Modeling and Stability Analysis of Droop-Controlled Inverters for Microgrid Applications". In: *IEEE Transactions on Smart Grid* 5.6 (Nov. 2014), 2980.
- [112] J. W. Simpson-Porco, F. Dörfler, and F. Bullo. "Synchronization and power sharing for droop-controlled inverters in islanded microgrids". In: *Automatica* 49.9 (2013), 2603.
- [113] J. W. Simpson-Porco, F. Dörfler, and F. Bullo. "Voltage Stabilization in Microgrids via Quadratic Droop Control". In: *52nd IEEE Conference on Decision and Control* (2013).
- [114] S. Leitner, M. Yazdani, A. Mehrizi-Sani, and A. Muetze. "Small-Signal Stability Analysis of an Inverter-Based Microgrid With Internal Model-Based Controllers". In: *IEEE Transactions on Smart Grid* 9.5 (Sept. 2018), 5393.
- [115] I. P. Nikolakakos, H. H. Zeineldin, M. S. El-Moursi, and N. D. Hatziargyriou. "Stability Evaluation of Interconnected Multi-Inverter Microgrids Through Critical Clusters". In: *IEEE Transactions on Power Systems* 31.4 (July 2016), 3060.
- [116] Q. Peng, Q. Jiang, Y. Yang, T. Liu, H. Wang, and F. Blaabjerg. "On the Stability of Power Electronics-Dominated Systems: Challenges and Potential Solutions". In: *IEEE Transactions on Industry Applications* (2019), 1.
- [117] M. Zhao, X. Yuan, J. Hu, and Y. Yan. "Voltage Dynamics of Current Control Time-Scale in a VSC-Connected Weak Grid". In: *IEEE Transactions on Power Systems* 31.4 (July 2016), 2925.

- [118] H. Yuan, X. Yuan, and J. Hu. “Modeling of Grid-Connected VSCs for Power System Small-Signal Stability Analysis in DC-Link Voltage Control Timescale”. In: *IEEE Transactions on Power Systems* 32.5 (Sept. 2017), 3981.
- [119] EirGrid and SONI. *DS3: System Services Review TSO Recommendations*. Tech. rep. EirGrid, May 2013.
- [120] “PSLF”, GE Energy Consulting. URL: <http://www.geenergyconsulting.com/practice-area/software-products/pslf>.
- [121] “TSAT”, Powertech Labs Inc. URL: <https://www.dsatools.com/tsat/>.
- [122] “PSS®E”, Siemens PTI. URL: <https://new.siemens.com/global/en/products/energy/services/transmission-distribution-smart-grid/consulting-and-planning/pss-software/pss-e.html>.
- [123] P. Pourbeik, J. J. Sanchez-Gasca, J. Senthil, J. D. Weber, P. S. Zadehkhosht, Y. Kazachkov, S. Tacke, J. Wen, and A. Ellis. “Generic Dynamic Models for Modeling Wind Power Plants and Other Renewable Technologies in Large-Scale Power System Studies”. In: *IEEE Transactions on Energy Conversion* 32.3 (Sept. 2017), 1108.
- [124] J.G. Slootweg and W.L. Kling. “The impact of large scale wind power generation on power system oscillations”. In: *Electric Power Systems Research* 67.1 (2003), 9.
- [125] A. Mendonca and J. A. P. Lopes. “Impact of large scale wind power integration on small signal stability”. In: *2005 International Conference on Future Power Systems*. Nov. 2005.
- [126] D. Gautam, V. Vittal, and T. Harbour. “Impact of Increased Penetration of DFIG-Based Wind Turbine Generators on Transient and Small Signal Stability of Power Systems”. In: *IEEE Transactions on Power Systems* 24.3 (Aug. 2009), 1426.
- [127] P. N. Papadopoulos and J. V. Milanović. “Probabilistic Framework for Transient Stability Assessment of Power Systems With High Penetration of Renewable Generation”. In: *IEEE Transactions on Power Systems* 32.4 (July 2017), 3078.
- [128] X. Xi, H. Geng, and G. Yang. “Small signal stability of weak power system integrated with inertia tuned large scale wind farm”. In: *2014 IEEE Innovative Smart Grid Technologies - Asia (ISGT ASIA)*. May 2014.

- [129] R. Elliott, R. Byrne, A. Ellis, and L. Grant. “Impact of increased photovoltaic generation on inter-area oscillations in the Western North American power system”. In: *2014 IEEE PES General Meeting / Conference Exposition*. July 2014.
- [130] F. Katiraei, M. R. Irvani, and P. W. Lehn. “Small-signal dynamic model of a micro-grid including conventional and electronically interfaced distributed resources”. In: *IET Generation, Transmission Distribution* 1.3 (May 2007), 369.
- [131] E. Ekomwenrenren, H. Alharbi, T. Elgorashi, J. Elmirghani, and P. Aristidou. “A stabilising control strategy for Cyber-Physical Power Systems”. In: *engrXiv e-prints* (May 2018).
- [132] P. Kundur, J. Paserba, V. Ajjarapu, G. Andersson, A. Bose, C. Canizares, N. Hatziargyriou, D. Hill, A. Stankovic, C. Taylor, T. Van Cutsem, and V. Vittal. “Definition and classification of power system stability IEEE/CIGRE joint task force on stability terms and definitions”. In: *IEEE Transactions on Power Systems* 19.3 (Aug. 2004), 1387.
- [133] P. Vorobev, P. Huang, M. A. Hosani, J. L. Kirtley, and K. Turitsyn. “A framework for development of universal rules for microgrids stability and control”. In: *IEEE 56th Annual Conference on Decision and Control (CDC)*. Dec. 2017.
- [134] W. Du, R. H. Lasseter, and A. S. Khalsa. “Survivability of Autonomous Microgrid during Overload Events”. In: *IEEE Transactions on Smart Grid* (Apr. 2018).
- [135] A. S. Ahmadyar, S. Riaz, G. Verbič, A. Chapman, and D. J. Hill. “A Framework for Assessing Renewable Integration Limits With Respect to Frequency Performance”. In: *IEEE Transactions on Power Systems* 33.4 (July 2018), 4444.
- [136] M. J. Gibbard and D. J. Vowles. “SIMPLIFIED 14-GENERATOR MODEL OF THE SE AUSTRALIAN POWER SYSTEM”. In: 2010.
- [137] A. Moeini, I. Kamwa, P. Brunelle, and G. Sybille. “Open data IEEE test systems implemented in SimPowerSystems for education and research in power grid dynamics and control”. In: *2015 50th International Universities Power Engineering Conference (UPEC)*. Sept. 2015, 1.

- [138] S. Püschel-Løvengreen and P. Mancarella. “Frequency Response Constrained Economic Dispatch with Consideration of Generation Contingency Size”. In: *2018 Power Systems Computation Conference (PSCC)*. June 2018, 1.
- [139] B. K. Poolla, D. Groß, and F. Dörfler. “Placement and Implementation of Grid-Forming and Grid-Following Virtual Inertia and Fast Frequency Response”. In: *IEEE Transactions on Power Systems* (2019 (forthcoming)).
- [140] U. Markovic, Z. Chu, P. Aristidou, and G. Hug. “LQR-Based Adaptive Virtual Synchronous Machine for Power Systems with High Inverter Penetration”. In: *IEEE Transactions on Sustainable Energy* 10.3 (July 2019), 1501.
- [141] G. Delille, B. Francois, and G. Malarange. “Dynamic Frequency Control Support by Energy Storage to Reduce the Impact of Wind and Solar Generation on Isolated Power System’s Inertia”. In: *IEEE Transactions on Sustainable Energy* 3.4 (Oct. 2012), 931.
- [142] U. Tamrakar, D. Shrestha, M. Manisha, B. P. Bhattarai, T. M. Hansen, and R. Tonkoski. *Virtual Inertia: Current Trends and Future Directions*. MDPI, 2017.
- [143] M. Ashabani and Y. A. R. I. Mohamed. “Novel Comprehensive Control Framework for Incorporating VSCs to Smart Power Grids Using Bidirectional Synchronous-VSC”. In: *IEEE Transactions on Power Systems* 29.2 (Mar. 2014), 943.
- [144] J. Fang, X. Li, and Y. Tang. “Grid-connected power converters with distributed virtual power system inertia”. In: *2017 IEEE Energy Conversion Congress and Exposition (ECCE)*. Oct. 2017, 4267.
- [145] J. Morren, S. W. H. de Haan, W. L. Kling, and J. A. Ferreira. “Wind turbines emulating inertia and supporting primary frequency control”. In: *IEEE Transactions on Power Systems* 21.1 (Feb. 2006), 433.
- [146] N. Soni, S. Doolla, and M. C. Chandorkar. “Improvement of Transient Response in Microgrids Using Virtual Inertia”. In: *IEEE Transactions on Power Delivery* 28.3 (July 2013), 1830.
- [147] M. A. Torres L., L. A. C. Lopes, L. A. Morán T., and J. R. Espinoza C. “Self-Tuning Virtual Synchronous Machine: A Control Strategy for Energy Storage Systems to Support Dynamic Frequency Control”. In: *IEEE Transactions on Energy Conversion* 29.4 (Dec. 2014), 833.

- [148] J. Alipoor, Y. Miura, and T. Ise. “Power System Stabilization Using Virtual Synchronous Generator With Alternating Moment of Inertia”. In: *IEEE Journal of Emerging and Selected Topics in Power Electronics* 3.2 (June 2015), 451.
- [149] D. Li, Q. Zhu, S. Lin, and X. Y. Bian. “A Self-Adaptive Inertia and Damping Combination Control of VSG to Support Frequency Stability”. In: *IEEE Transactions on Energy Conversion* 32.1 (Mar. 2017), 397.
- [150] H. Ahmadi and H. Ghasemi. “Security-Constrained Unit Commitment With Linearized System Frequency Limit Constraints”. In: *IEEE Transactions on Power Systems* 29.4 (2014), 1536.
- [151] ENTSO-E. *Frequency Measurement Requirements and Usage*. Tech. rep. RG-CE System Protection & Dynamics Sub Group, Jan. 2018.
- [152] RG-CE System Protection & Dynamics Sub Group. *Frequency Stability Evaluation Criteria for the Synchronous Zone of Continental Europe*. Tech. rep. ENTSO-E, 2016.
- [153] T. S. Borsche, T. Liu, and D. J. Hill. “Effects of Rotational Inertia on Power System Damping and Frequency Transients”. In: *IEEE Conference on Decision and Control (CDC)*. 2015, 5940.
- [154] D. Groß, S. Bolognani, B. K. Poolla, and F. Dörfler. “Increasing the Resilience of Low-inertia Power Systems by Virtual Inertia and Damping”. In: *Bulk Power Systems Dynamics and Control Symposium (IREP)*. Aug. 2017.
- [155] U. Markovic, Z. Chu, P. Aristidou, and G. Hug. “Fast Frequency Control Scheme through Adaptive Virtual Inertia Emulation”. In: *2018 ISGT-Asia*. May 2018.
- [156] S. Chandrapati. *Design and Implementation: Linear Quadratic Regulator*. LAP LAMBERT Academic Publishing, 2011.
- [157] *Typhoon HIL | Hardware in the Loop Testing Software and Hardware*. URL: <https://www.typhoon-hil.com/>.
- [158] Australian Energy Market Operator. *Initial operation of the Hornsdale Power Reserve Battery Energy Storage System*. Tech. rep. Apr. 2018.
- [159] *Virtual Hardware In The Loop (vHIL): Earlier and Better Testing for Automotive Applications*. URL: <http://johndayautomotiveelectronics.com/>.

- [160] O. Stanojev, U. Markovic, P. Aristidou, G. Hug, D. Callaway, and E. Vrettos. “MPC-Based Fast Frequency Control of Voltage Source Converters in Low-Inertia Power Systems”. In: *IEEE Transactions on Power Systems* (June 2020), 1.
- [161] J. Rawlings, D. Mayne, and M. Diehl. *Model Predictive Control: Theory, Computation, and Design*. Nob Hill, 2017.
- [162] A. M. Ersdal, L. Imsland, and K. Uhlen. “Model Predictive Load-Frequency Control”. In: *IEEE Transactions on Power Systems* 31.1 (Jan. 2016), 777.
- [163] M. Shiroei and A.M. Ranjbar. “Supervisory predictive control of power system load frequency control”. In: *International Journal of Electrical Power & Energy Systems* 61 (2014), 70.
- [164] A. N. Venkat, I. A. Hiskens, J. B. Rawlings, and S. J. Wright. “Distributed MPC Strategies With Application to Power System Automatic Generation Control”. In: *IEEE Transactions on Control Systems Technology* 16.6 (Nov. 2008), 1192.
- [165] A. Ulbig, T. Rinke, S. Chatzivasileiadis, and G. Andersson. “Predictive control for real-time frequency regulation and rotational inertia provision in power systems”. In: *52nd IEEE Conference on Decision and Control*. Dec. 2013.
- [166] L. Papangelis, M-S. Debry, T. Prevost, P. Panciatici, and T. Van Cutsem. “Decentralized model predictive control of voltage source converters for AC frequency containment”. In: *International Journal of Electrical Power & Energy Systems* 98 (2018), 342.
- [167] A. Fuchs, M. Imhof, T. Demiray, and M. Morari. “Stabilization of Large Power Systems Using VSC–HVDC and Model Predictive Control”. In: *IEEE Transactions on Power Delivery* 29.1 (Feb. 2014), 480.
- [168] Q. Hong, M. Nedd, S. Norris, I. Abdulhadi, M. Karimi, V. Terzija, B. Marshall, K. Bell, and C. Booth. “Fast frequency response for effective frequency control in power systems with low inertia”. In: *The Journal of Engineering* 2019.16 (2019), 1696.
- [169] L. Ljung. *System Identification: Theory for the User*. Prentice Hall, 1999.
- [170] L. Ljung. *System Identification Toolbox User’s Guide*. MathWorks. 2015. 904 pp.

- [171] A. Bemporad, F. Borrelli, and M. Morari. “Model predictive control based on linear programming - the explicit solution”. In: *IEEE Transactions on Automatic Control* 47.12 (Dec. 2002), 1974.
- [172] T. Athay, R. Podmore, and S. Virmani. “A Practical Method for the Direct Analysis of Transient Stability”. In: *IEEE Transactions on Power Apparatus and Systems* PAS-98.2 (Mar. 1979), 573.
- [173] A. Pai. *Energy Function Analysis for Power System Stability*. Springer, 1989.
- [174] J. Löfberg. “YALMIP : a toolbox for modeling and optimization in MATLAB”. In: *IEEE International Conf. on Robotics & Automation*. 2004.
- [175] M. Herceg, M. Kvasnica, C.N. Jones, and M. Morari. “Multi-Parametric Toolbox 3.0”. In: *Proc. of the European Control Conference*. Zürich, Switzerland, July 2013, 502.
- [176] U. Markovic, V. Häberle, D. Shchetinin, G. Hug, D. Callaway, and E. Vrettos. “Optimal Sizing and Tuning of Storage Capacity for Fast Frequency Control in Low-Inertia Systems”. In: *2019 SEST*. Sept. 2019.
- [177] O. Mégel, J. L. Mathieu, and G. Andersson. “Maximizing the potential of energy storage to provide fast frequency control”. In: *IEEE PES ISGT Europe 2013*. Oct. 2013.
- [178] U. Markovic, T. Jouini, and Dominic Groß. *MIGRATE WP3 - Control and Operation of a Grid with 100% Converter-Based Devices*. Tech. rep. Horizon 2020 - LCE-6, Dec. 2018.
- [179] V. Poullos, E. Vrettos, F. Kienzle, E. Kaffe, H. Luternauer, and G. Andersson. “Optimal placement and sizing of battery storage to increase the PV hosting capacity of low voltage grids”. In: *International ETG Congress 2015; Die Energiewende - Blueprints for the new energy age*. Nov. 2015.
- [180] H. Chen, T. N. Cong, W. Yang, C. Tan, Y. Li, and Y. Ding. “Progress in electrical energy storage system: A critical review”. In: *Progress in Natural Science* 19.3 (2009), 291.
- [181] U. Markovic, P. Aristidou, and G. Hug. “Virtual Induction Machine Strategy for Converters in Power Systems with Low Rotational Inertia”. In: *2017 IREP*. Aug. 2017.

- [182] U. Markovic, O. Stanojev, P. Aristidou, and G. Hug. “Improving Frequency Stability of Low-Inertia Systems using Virtual Induction Machine”. In: *IEEE Transactions on Power Systems* (under review).
- [183] S. M. Malik, X. Ai, Y. Sun, C. Zhengqi, and Z. Shupeng. “Voltage and frequency control strategies of hybrid AC/DC microgrid: a review”. In: *IET Generation, Transmission Distribution* 11.2 (2017), 303.
- [184] J. Svensson. “Synchronisation methods for grid-connected voltage source converters”. In: *IEE Proceedings - Generation, Transmission and Distribution* 148.3 (2001), 229.
- [185] M. Ciobotaru, R. Teodorescu, and F. Blaabjerg. “A New Single-Phase PLL Structure Based on Second Order Generalized Integrator”. In: *IEEE Power Electronics Specialists Conference*. 2006.
- [186] S. Shinnaka. “A Robust Single-Phase PLL System With Stable and Fast Tracking”. In: *IEEE Transactions on Industry Applications* 44.2 (2008), 624.
- [187] H. Karimi, M. Karimi-Ghartemani, and M. R. Iravani. “Estimation of frequency and its rate of change for applications in power systems”. In: *IEEE Transactions on Power Delivery* 19.2 (Apr. 2004), 472.
- [188] A. Nicastrì and A. Nagliero. “Comparison and evaluation of the PLL techniques for the design of the grid-connected inverter systems”. In: *2010 IEEE International Symposium on Industrial Electronics*. July 2010, 3865.
- [189] L. Harnefors, M. Bongiorno, and S. Lundberg. “Input-Admittance Calculation and Shaping for Controlled Voltage-Source Converters”. In: *IEEE Transactions on Industrial Electronics* 54.6 (Dec. 2007), 3323.
- [190] F. Blaabjerg, R. Teodorescu, M. Liserre, and A. V. Timbus. “Overview of Control and Grid Synchronization for Distributed Power Generation Systems”. In: *IEEE Transactions on Industrial Electronics* 53.5 (Oct. 2006), 1398.
- [191] J. Hu, S. Wang, W. Tang, and X. Xiong. “Full-Capacity Wind Turbine with Inertial Support by Adjusting Phase-Locked Loop Response”. In: *IET Renewable Power Generation* 11.1 (2017), 44.
- [192] Ö. Göksu, R. Teodorescu, C. L. Bak, F. Iov, and P. C. Kjær. “Instability of Wind Turbine Converters During Current Injection to Low Voltage Grid Faults and PLL Frequency Based Stability Solution”. In: *IEEE Transactions on Power Systems* 29.4 (July 2014), 1683.

- [193] F. Bizzarri, A. Brambilla, and F. Milano. “Analytic and Numerical Study of TCSC Devices: Unveiling the Crucial Role of Phase-Locked Loops”. In: *IEEE Transactions on Circuits and Systems I: Regular Papers* PP.99 (2017), 1.
- [194] L. Zhang, L. Harnefors, and H-P. Nee. “Power-Synchronization Control of Grid-Connected Voltage-Source Converters”. In: *IEEE Transactions on Power Systems* 25.2 (2010), 809.
- [195] M. Ashabani, F. D. Freijedo, S. Golestan, and J. M. Guerrero. “Inductors: PLL-Less Converters With Auto-Synchronization and Emulated Inertia Capability”. In: *IEEE Transactions on Smart Grid* 7.3 (May 2016), 1660.
- [196] P. Kundur. *Power System Stability And Control*. McGraw-Hill Education, 1994.
- [197] D. W. Novotny R. W. De Doncker. “The Universal Field Oriented Controller”. In: *IEEE Transactions on Industry Application* 30.1 (Jan. 1993), 92.
- [198] S. Golestan, F. D. Freijedo, A. Vidal, J. M. Guerrero, and J. Doval-Gandoy. “A Quasi-Type-1 Phase-Locked Loop Structure”. In: *IEEE Transactions on Power Electronics* 29.12 (Dec. 2014), 6264.
- [199] U. M. Ascher and L. R. Petzold. “The Numerical Solution of Delay-Differential-Algebraic Equations of Retarded and Neutral Type”. In: *SIAM Journal on Numerical Analysis* 32.5 (1995), 1635.
- [200] J. G. Ziegler and N. B. Nichols. “Optimum Settings for Automatic Controllers”. In: *Journal of Dynamic Systems, Measurement, and Control* (June 1993), 220.
- [201] D. Rodriguez Flores, U. Markovic, P. Aristidou, and G. Hug. “Robust Converter Control Design under Time-Delay Uncertainty”. In: *2019 PowerTech*. June 2019.
- [202] S. Alghamdi, U. Markovic, O. Stanojev, J. Schiffer, G. Hug, and P. Aristidou. “Wide-Area Oscillation Damping in Low-Inertia Grids under Time-Varying Communication Delays”. In: *2020 PSCC*. June 2020.
- [203] H. Jia, N. Guangyu, S. T. Lee, and P. Zhang. “Study on the impact of time delay to power system small signal stability”. In: *MELECON 2006 - 2006 IEEE Mediterranean Electrotechnical Conference*. May 2006.

- [204] H. Jia, X. Yu, Y. Yu, and C. Wang. “Power system small signal stability region with time delay”. In: *International Journal of Electrical Power & Energy Systems* 30.1 (2008), 16.
- [205] F. Milano and M. Anghel. “Impact of Time Delays on Power System Stability”. In: *IEEE Transactions on Circuits and Systems I: Regular Papers* 59.4 (2012), 889.
- [206] F. Milano. “Small-Signal Stability Analysis of Large Power Systems With Inclusion of Multiple Delays”. In: *IEEE Transactions on Power Systems* 31.4 (2016), 3257.
- [207] S. Ayasun and C. O. Nwankpa. “Probability of small-signal stability of power systems in the presence of communication delays”. In: *Electrical and Electronics Engineering, 2009. ELECO 2009. International Conference on*. IEEE. 2009, I.
- [208] T. Li, M. Wu, and Y. He. “Lyapunov-Krasovskii functional based power system stability analysis in environment of WAMS”. In: *Journal of Central South University of Technology* 17.4 (2010), 801.
- [209] D. P. Ke, C. Y. Chung, and Y. Xue. “An eigenstructure-based performance index and its application to control design for damping inter-area oscillations in power systems”. In: *IEEE Transactions on Power Systems* 26.4 (2011), 2371.
- [210] R. Shah, N. Mithulananthan, K. Y. Lee, et al. “Large-scale PV plant with a robust controller considering power oscillation damping”. In: *IEEE Transactions on Energy Conversion* 28.1 (2013), 106.
- [211] H. Wu, K. S. Tsakalis, and G. T. Heydt. “Evaluation of time delay effects to wide-area power system stabilizer design”. In: *IEEE Transactions on Power Systems* 19.4 (Nov. 2004), 1935.
- [212] T. Zabaiou, L-A. Dessaint, F-A. Okou, and R. Grondin. “Wide-area coordinating control of SVCs and synchronous generators with signal transmission delay compensation”. In: *Power and Energy Society General Meeting, 2010 IEEE*. IEEE. 2010, 1.
- [213] B. Chaudhuri, R. Majumder, and B. C. Pal. “Wide-area measurement-based stabilizing control of power system considering signal transmission delay”. In: *IEEE Transactions on Power Systems* 19.4 (2004), 1971.

- [214] P. Zhang, D. Y. Yang, K. W. Chan, and G. W. Cai. “Adaptive wide-area damping control scheme with stochastic subspace identification and signal time delay compensation”. In: *IET generation, transmission & distribution* 6.9 (2012), 844.
- [215] H. Othman, J. J. Sanchez-Gasca, M. A. Kale, and J. H. Chow. “On the design of robust power system stabilizers”. In: *Proc. of the 28th IEEE CDC*. 1989, 1853.
- [216] M. Klein, G. J. Rogers, S. Moorthy, and P. Kundur. “Analytical investigation of factors influencing power system stabilizers performance”. In: *IEEE Transactions on Energy Conversion* 7.3 (1992), 382.
- [217] A. Mesanovic, U. Münz, and C. Heyde. “Comparison of \mathcal{H}_∞ , \mathcal{H}_2 , and pole optimization for power system oscillation damping with remote renewable generation”. In: *IFAC* 49.27 (2016), 103.
- [218] A. Mesanovic, D. Unseld, U. Münz, C. Ebenbauer, and R. Findeisen. “Parameter Tuning and Optimal Design of Decentralized Structured Controllers for Power Oscillation Damping in Electrical Networks”. In: *ACC*. 2018, 3828.
- [219] I. Kamwa, J. Beland, G. Trudel, R. Grondin, C. Lafond, and D. McNabb. “Wide-area monitoring and control at Hydro-Quebec: past, present and future”. In: *IEEE PES General Meeting*. 2006.
- [220] G. J. Rogers. “The application of power system stabilizers to a multi-generator plant”. In: *IEEE Transactions on Power Systems* 15 (2000), 350.
- [221] F. Dörfler, M. R. Jovanović, M. Chertkov, and F. Bullo. “Sparsity-Promoting Optimal Wide-Area Control of Power Networks”. In: *IEEE Transactions on Power Systems* 29.5 (2014), 2281.
- [222] S. Schuler, U. Münz, and F. Allgöwer. “Decentralized state feedback control for interconnected systems with application to power systems”. In: *Journal of Process Control* 24.2 (2014), 379.
- [223] Y. Wang, P. Yemula, and A. Bose. “Decentralized Communication and Control Systems for Power System Operation”. In: *IEEE Transactions on Smart Grid* 6.2 (2015), 885.
- [224] P. Kansal and A. Bose. “Smart grid communication requirements for the high voltage power system”. In: *IEEE PES General Meeting*. 2011.
- [225] Y. Ghaedsharaf, C. Somarakis, F. Dörfler, and N. Motee. “Wide-Area Control of Power Networks with Time-Delay”. In: *IFAC* 51.23 (2018), 277.

- [226] E. Ekomwenrenren, H. Alharbi, T. Elgorashi, J. Elmirghani, and P. Aristidou. “Stabilising control strategy for cyber-physical power systems”. In: *IET Cyber-Physical Systems: Theory & Applications* (2019).
- [227] J. M. Thangaiah and R. Parthasarathy. “Delay-dependent stability analysis of power system considering communication delays”. In: *International Transactions on Electrical Energy Systems* 27.3 (2017).
- [228] E. Fridman. “Tutorial on Lyapunov-based methods for time-delay systems”. In: *European Journal of Control* 20.6 (2014), 271.
- [229] E. Fridman. *Introduction to Time-Delay Systems: Analysis and Control*. Birkhäuser, 2014.
- [230] J. P. Hespanha, P. Naghshtabrizi, and Y. Xu. “A survey of recent results in networked control systems”. In: *Proc. of the IEEE* 95.1 (2007), 138.
- [231] H. K. Khalil. *Nonlinear systems*. Vol. 3. Prentice Hall, 2002.
- [232] J. Li, Z. Chen, D. Cai, W. Zhen, and Q. Huang. “Delay-dependent stability control for power system with multiple time-delays”. In: *IEEE Transactions on Power Systems* 31.3 (2016), 2316.
- [233] S. Wang, X. Meng, and T. Chen. “Wide-Area Control of Power Systems Through Delayed Network Communication”. In: *IEEE Transactions on Control Systems Technology* 20.2 (2012), 495.
- [234] B. Yang and Y. Sun. “Damping Factor Based Delay Margin for Wide Area Signals in Power System Damping Control”. In: *IEEE Transactions on Power Systems* 28.3 (2013), 3501.
- [235] S. Qiang, A. Haiyun, J. Hongjie, Y. Xiaodan, W. Chengshan, W. Wei, M. Zhiyu, Z. Yuan, Z. Jinli, and L. Peng. “An improved power system stability criterion with multiple time delays”. In: *IEEE PES General Meeting*. 2009.
- [236] M. Singh, A. Allen, E. Muljadi, and V. Gevorgian. “Oscillation damping: A comparison of wind and photovoltaic power plant capabilities”. In: *IEEE PEMWA*. 2014.
- [237] L. Zacharia, L. Hadjidemetriou, and E. Kyriakides. “Integration of Renewables Into the Wide Area Control Scheme for Damping Power Oscillations”. In: *IEEE Transactions on Power Systems* 33.5 (2018).

- [238] C. Liu, G. Cai, W. Ge, D. Yang, C. Liu, and Z. Sun. “Oscillation Analysis and Wide-Area Damping Control of DFIGs for Renewable Energy Power Systems Using Line Modal Potential Energy”. In: *IEEE Transactions on Power Systems* 33.3 (2018), 3460.
- [239] X. Wu, F. Dörfler, and M. R. Jovanović. “Input-Output Analysis and Decentralized Optimal Control of Inter-Area Oscillations in Power Systems”. In: *IEEE Transactions on Power Systems* 31.3 (2016), 2434.
- [240] A. Mesanovic, U. Münz, J. Bamberger, and R. Findeisen. “Controller Tuning for the Improvement of Dynamic Security in Power Systems”. In: *2018 IEEE PES ISGT-Europe*. 2018.
- [241] M. Li and Y. Chen. “A Wide-Area Dynamic Damping Controller Based on Robust \mathcal{H}_∞ Control for Wide-Area Power Systems With Random Delay and Packet Dropout”. In: *IEEE Transactions on Power Systems* 33.4 (2018).
- [242] A. Seuret, F. Gouaisbaut, and E. Fridman. “Stability of systems with fast-varying delay using improved Wirtinger’s inequality”. In: *52nd IEEE CDC*. 2013, 946.
- [243] C. A. R. Crusius and A. Trofino. “Sufficient LMI conditions for output feedback control problems”. In: *IEEE Transactions on Automatic Control* 44.5 (1999), 1053.
- [244] I. A. Hiskens. “Power system modeling for inverse problems”. In: *IEEE Transactions on Circuits and Systems I: Regular Papers* 51.3 (2004), 539.
- [245] W. Michiels and S-I. Niculescu. *Stability and Stabilization of Time-Delay Systems (Advances in Design & Control)*. Society for Industrial and Applied Mathematics, 2007.
- [246] G. A. Baker Jr. and P. Graves-Morris. *Padé Approximants-Part I: Basic Theory*. Reading, MA, USA: Addison-Wesley, 1981.
- [247] A. Bellen and S. Maset. “Numerical solution of constant coefficient linear delay differential equations as abstract Cauchy problems”. In: *Numerische Mathematik* 84.3 (2000), 351.
- [248] A. Bellen and M. Zennaro. *Numerical Methods for Delay Differential Equations*. Oxford: Oxford University Press, 2003.
- [249] D. Breda, S. Maset, and R. Vermiglio. “Pseudospectral approximation of eigenvalues of derivative operators with non-local boundary conditions”. In: *Applied Numerical Mathematics* 56.3 (2006), 318.

- [250] E. A. Butcher, H. Ma, E. Bueler, V. Averina, and Z. Szabo. “Stability of linear time-periodic delay-differential equations via Chebyshev polynomials”. In: *International Journal for Numerical Methods in Engineering* 59.7 (2004), 895.
- [251] D. Breda. “Solution operator approximations for characteristic roots of delay differential equations”. In: *Applied Numerical Mathematics* 56.3 (2006). Selected Papers, The Third International Conference on the Numerical Solutions of Volterra and Delay Equations, 305.
- [252] E. Bueler. “Error Bounds for Approximate Eigenvalues of Periodic-Coefficient Linear Delay Differential Equations”. In: *SIAM Journal on Numerical Analysis* 45.6 (2007), 2510.
- [253] K. Engelborghs and D. Roose. “Numerical computation of stability and detection of Hopf bifurcations of steady state solutions of delay differential equations”. In: *Advances in Computational Mathematics* 10.3 (May 1999), 271.
- [254] K. Engelborghs, T. Luzyanina, and D. Roose. “Numerical Bifurcation Analysis of Delay Differential Equations Using DDE-BIFTOOL”. In: *ACM Transactions on Mathematical Software* 28.1 (Mar. 2002), 1.
- [255] K. Engelborghs and D. Roose. “On Stability of LMS Methods and Characteristic Roots of Delay Differential Equations”. In: *SIAM J. Numer. Anal.* 40.2 (Feb. 2002), 629.
- [256] H. B. Phillips. “Review: E. J. Townsend, Functions of a Complex Variable”. In: *Bull. Amer. Math. Soc.* 23.4 (Jan. 1917), 184.
- [257] S. Skogestad and I. Postlethwaite. *Multivariable feedback control: analysis and design*. Vol. 2. Wiley New York, 2007.
- [258] K-Z. Liu and Y. Yao. *Robust control: theory and applications*. John Wiley & Sons, 2016.
- [259] H. Kwakernaak. “Robustness optimization of linear feedback systems”. In: *The 22nd IEEE Conference on Decision and Control*. Dec. 1983, 618.
- [260] M. Verma and E. Jonckheere. “ L_∞ compensation with mixed sensitivity as a broadband matching problem”. In: *Systems & Control Letters* 4.3 (1984), 125.
- [261] H. Kwakernaak. “MIXED SENSITIVITY DESIGN”. In: *IFAC Proceedings Volumes* 35.1 (2002). 15th IFAC World Congress, 61.

- [262] B. Barmish. “Stabilization of uncertain systems via linear control”. In: *IEEE Transactions on Automatic Control* 28.8 (1983), 848.
- [263] W. M. Haddad and D. S. Bernstein. “Parameter-dependent Lyapunov functions, constant real parameter uncertainty, and the Popov criterion in robust analysis and synthesis. 1”. In: *Decision and Control, 1991., Proceedings of the 30th IEEE Conference on*. IEEE. 1991, 2274.
- [264] P. Apkarian and P. Gahinet. “A convex characterization of gain-scheduled \mathcal{H}_∞ controllers”. In: *IEEE Transactions on Automatic Control* 40.5 (May 1995), 853.
- [265] M. Chilali, P. Gahinet, and P. Apkarian. “Robust pole placement in LMI regions”. In: *IEEE transactions on Automatic Control* 44.12 (1999), 2257.
- [266] J. Lofberg. “YALMIP: A toolbox for modeling and optimization in MATLAB”. In: *Computer Aided Control Systems Design, 2004 IEEE International Symposium on*. IEEE. 2004, 284.
- [267] J. F. Sturm. “Using SeDuMi 1.02, a MATLAB toolbox for optimization over symmetric cones”. In: *Optimization methods and software* 11.1-4 (1999), 625.
- [268] K-C. Toh, M. J. Todd, and R. H. Tütüncü. “SDPT3—a MATLAB software package for semidefinite programming, version 1.3”. In: *Optimization methods and software* 11.1-4 (1999), 545.
- [269] J. Schiffer, E. Fridman, R. Ortega, and J. Raisch. “Stability of a class of delayed port-Hamiltonian systems with application to microgrids with distributed rotational and electronic generation”. In: *Automatica* 74 (2016), 71.
- [270] J. Schiffer, F. Dörfler, and E. Fridman. “Robustness of distributed averaging control in power systems: Time delays & dynamic communication topology”. In: *Automatica* 80 (2017), 261.
- [271] S. Alghamdi, J. Schiffer, and E. Fridman. “Conditions for Delay-Robust Consensus-Based Frequency Control in Power Systems with Second-Order Turbine-Governor Dynamics”. In: *CDC*. 2018, 786.
- [272] MOSEK ApS. *The MOSEK optimization toolbox for MATLAB manual. Version 8.1.0.51*. 2017.
- [273] A. Venkatraman, U. Markovic, D. Shchetinin, E. Vrettos, P. Aristidou, and G. Hug. “Improving Dynamic Properties of Low-Inertia Systems through Eigensensitivity Optimization”. In: *IEEE Transactions on Power Systems* (under review).

- [274] P. Tielens and D. Van Hertem. “The relevance of inertia in power systems”. In: *Renewable and Sustainable Energy Reviews* 55 (2016), 999.
- [275] R. Yan, T. K. Saha, N. Modi, N-A. Masood, and M. Mosadeghy. “The combined effects of high penetration of wind and PV on power system frequency response”. In: *Applied Energy* 145 (2015), 320.
- [276] H. Bevrani, T. Ise, and Y. Miura. “Virtual synchronous generators: A survey and new perspectives”. In: *International Journal of Electrical Power and Energy Systems* 54.C (2014), 244.
- [277] T. V. Van, K. Visscher, J. Diaz, V. Karapanos, A. Woyte, M. Albu, J. Bozelie, T. Loix, and D. Federenciuc. “Virtual synchronous generator: An element of future grids”. In: *2010 IEEE PES Innovative Smart Grid Technologies Conference Europe (ISGT Europe)*. Oct. 2010.
- [278] M. Torres and L. A. C. Lopes. “Virtual synchronous generator control in autonomous wind-diesel power systems”. In: *2009 IEEE Electrical Power Energy Conference (EPEC)*. Oct. 2009, 1.
- [279] B. K. Poolla, S. Bolognani, and F. Dörfler. “Optimal placement of virtual inertia in power grids”. In: *IEEE Transactions on Automatic Control* 62.12 (2017), 6209.
- [280] E. Rakhshani, D. Remon, A. Mir Cantarellas, and P. Rodriguez. “Analysis of derivative control based virtual inertia in multi-area high-voltage direct current interconnected power systems”. In: *IET Generation, Transmission Distribution* 10.6 (2016), 1458.
- [281] T. S. Borsche and F. Dörfler. “On Placement of Synthetic Inertia with Explicit Time-Domain Constraints”. In: *arXiv preprint arXiv:1705.03244* (2017).
- [282] L. Xiong, P. Li, F. Wu, and J. Wang. “Stability enhancement of power systems with high DFIG-wind turbine penetration via virtual inertia planning”. In: *IEEE Transactions on Power Systems* 34.2 (2018), 1352.
- [283] A. Ademola-Idowu and B. Zhang. “Optimal design of virtual inertia and damping coefficients for virtual synchronous machines”. In: *2018 IEEE Power & Energy Society General Meeting (PESGM)*. IEEE. 2018, 1.
- [284] M. Pirani, E. Hashemi, B. Fidan, and J. W. Simpson-Porco. “ H_∞ Performance of Mechanical and Power Networks”. In: *IFAC-PapersOnLine* 50.1 (2017). 20th IFAC World Congress, 5196.

- [285] F. Paganini and E. Mallada. “Global performance metrics for synchronization of heterogeneously rated power systems: The role of machine models and inertia”. In: *2017 55th Annual Allerton Conference on Communication, Control, and Computing (Allerton)*. Oct. 2017, 324.
- [286] K. Zhou, J. C. Doyle, and K. Glover. *Robust and Optimal Control*. Upper Saddle River, NJ, USA: Prentice-Hall, Inc., 1996.
- [287] B. Datta. *Numerical methods for linear control systems*. Academic Press, Dec. 2003.
- [288] S. Boyd, V. Balakrishnan, and P. Kabamba. “A bisection method for computing the H_∞ norm of a transfer matrix and related problems”. In: *Mathematics of Control, Signals and Systems 2.3* (1989), 207.
- [289] J. C. Doyle, K. Glover, P. P. Khargonekar, and B. A. Francis. “State-space solutions to standard H_2 and H_∞ control problems”. In: *IEEE Transactions on Automatic Control* 34.8 (Aug. 1989), 831.
- [290] N.A. Bruinsma and M. Steinbuch. “A fast algorithm to compute the H infinity norm of a transfer function matrix”. In: *Systems and Control Letters* 14.4 (1990), 287.
- [291] G. Kuster. “ H_∞ Norm Calculation via a State Space Formulation”. MA thesis. Blacksburg, Virginia: Virginia Polytechnic Institute and State University, Dec. 2012.
- [292] MATLAB. *version 9.5.0.944444 (R2018b)*. Natick, Massachusetts: The MathWorks Inc., Aug. 2018.
- [293] M. Paturet, U. Markovic, S. Delikaraoglou, E. Vrettos, P. Aristidou, and G. Hug. “Stochastic Unit Commitment in Low-Inertia Grids”. In: *IEEE Transactions on Power Systems* 35.5 (Sept. 2020), 3448.
- [294] EirGrid and SONI. *DS3 System Services: Review TSO Recommendations*. Tech. rep. EirGrid, May 2013.
- [295] EirGrid and SONI. *DS3 System Services: Portfolio Capability Analysis*. Tech. rep. EirGrid, Nov. 2014.
- [296] E. Davarinejad, M. R. Hesamzadeh, and H. Chavez. *Incorporating Inertia Constraints into the Power Market*. Tech. rep. Energiforsk, 2017.
- [297] F. Pérez-Illanes, E. Álvarez-Miranda, C. Rahmann, and C. Campos-Valdés. “Robust Unit Commitment Including Frequency Stability Constraints”. In: *Energies* 9.11 (2016), 957.

- [298] P. Daly, D. Flynn, and N. Cunniffe. “Inertia considerations within unit commitment and economic dispatch for systems with high non-synchronous penetrations”. In: *PowerTech, 2015 IEEE Eindhoven*. 2015.
- [299] F. Teng, V. Trovato, and G. Strbac. “Stochastic Scheduling With Inertia-Dependent Fast Frequency Response Requirements”. In: *IEEE Transactions on Power Systems* 31.2 (Mar. 2016), 1557.
- [300] L. Badesa, F. Teng, and G. Strbac. “Optimal Scheduling of Frequency Services Considering a Variable Largest-Power-Infeed-Loss”. In: *2018 IEEE Power Energy Society General Meeting (PESGM)*. Aug. 2018.
- [301] M. Brito, E. Gil, and I. Calle. “Unit Commitment with Primary Frequency Control Requirements for Low-Inertia Systems”. In: *2018 IEEE Power Energy Society General Meeting (PESGM)*. Aug. 2018.
- [302] V. Trovato, A. Bialecki, and A. Dallagi. “Unit Commitment With Inertia-Dependent and Multispeed Allocation of Frequency Response Services”. In: *IEEE Transactions on Power Systems* 34.2 (Mar. 2019), 1537.
- [303] D. Lee Hau Aik. “A General-Order System Frequency Response Model Incorporating Load Shedding: Analytic Modeling and Applications”. In: *IEEE Transactions on Power Systems* 21 (June 2006), 709.
- [304] A. Ahmadi-Khatir, A. J. Conejo, and R. Cherkaoui. “Multi-Area Energy and Reserve Dispatch Under Wind Uncertainty and Equipment Failures”. In: *IEEE Transactions on Power Systems* 28 (2013), 4373.
- [305] R. N. Allan and R. Billinton. *Reliability Evaluation of Power Systems*. Springer Science & Business Media, 2013.
- [306] A. J. Conejo, M. Carrión, and J. M. Morales. *Decision making under uncertainty in electricity markets*. Vol. 1. Springer, 2010.
- [307] S. Delikaraoglou and P. Pinson. “High-quality wind power scenario forecasts for decision-making under uncertainty in power systems”. In: *13th IEEE International Workshop on Large-Scale Integration of Wind Power and Transmission Networks (WIW 2014)*. 2014.
- [308] H. Pandzic, Y. Dvorkin, T. Qiu, Y. Wang, and D. Kirschen. Unit Commitment under Uncertainty - GAMS Models, Library of the Renewable Energy Analysis Lab (REAL), University of Washington, Seattle, USA. [Online]. Available at: http://www.ee.washington.edu/research/real/gams_code.html.

- [309] Y. Dvorkin, H. Pandžić, M. A. Ortega-Vazquez, and D. S. Kirschen. “A hybrid stochastic/interval approach to transmission-constrained unit commitment”. In: *IEEE Transactions on Power Systems* 30.2 (2014), 621.
- [310] M. Paturet, U. Markovic, S. Delikaraoglou, E. Vrettos, P. Aristidou, and G. Hug. “Economic Valuation and Pricing of Inertia in Inverter-Dominated Power Systems”. In: *IEEE Transactions on Power Systems* (under review).
- [311] P. Tielens and D. Van Hertem. “Grid inertia and frequency control in power systems with high penetration of renewables”. In: *Young Researchers Symposium in Electrical Power Engineering* (2012).
- [312] B. Hartmann, I. Vokony, and I. Táci. “Effects of decreasing synchronous inertia on power system dynamics - Overview of recent experiences and marketisation of services”. In: *International Transactions on Electrical Energy Systems* n/a.n/a (July 2019), e12128.
- [313] National Grid. *Product Roadmap for Frequency Response and Reserve*. Tech. rep. National Grid, 2017.
- [314] ENTSO-E - Inertia2020. *Technical Requirements for Fast Frequency Reserve Provision in the Nordic Synchronous Area*. Tech. rep. 2019.
- [315] EirGrid and SONI. *Operational Constraints Update*. Tech. rep. EirGrid, Mar. 2019.
- [316] T. Xu, W. Jang, and T. Overbye. “An economic evaluation tool of inertia services for systems with integrated wind power and fast-acting storage resources”. In: *System Sciences (HICSS), 2016 49th Hawaii International Conference on*. IEEE. 2016, 2456.
- [317] L. Badesa, F. Teng, and G. Strbac. “Economic value of inertia in low-carbon power systems”. In: *Innovative Smart Grid Technologies Conference Europe (ISGT-Europe), 2017 IEEE PES*. IEEE. 2017.
- [318] E. Ela, V. Gevorgian, A. Tuohy, B. Kirby, M. Milligan, and M. O’Malley. “Market Designs for the Primary Frequency Response Ancillary Service—Part I: Motivation and Design”. In: *IEEE Transactions on Power Systems* 29.1 (Jan. 2014), 421.
- [319] T. Greve, F. Teng, M. G. Pollitt, and G. Strbac. “A system operator’s utility function for the frequency response market”. In: *Applied energy* 231 (2018), 562.

- [320] L. Badesa, F. Teng, and G. Strbac. “Pricing inertia and Frequency Response with diverse dynamics in an MISOCP formulation”. In: *arXiv preprint:1909.06671* (2019).
- [321] W. Li, P. Du, and N. Lu. “Design of a New Primary Frequency Control Market for Hosting Frequency Response Reserve Offers From Both Generators and Loads”. In: *IEEE Transactions on Smart Grid* 9.5 (Sept. 2018), 4883.
- [322] E. Ela, V. Gevorgian, A. Tuohy, B. Kirby, M. Milligan, and M. O’Malley. “Market Designs for the Primary Frequency Response Ancillary Service—Part II: Case Studies”. In: *IEEE Transactions on Power Systems* 29.1 (Jan. 2014), 432.
- [323] B. K. Poolla, S. Bolognani, N. Li, and F. Dörfler. “A Market Mechanism for Virtual Inertia”. In: *IEEE Transactions on Smart Grid* 11.4 (2020), 3570.
- [324] H. Thiesen, C. Jauch, and A. Gloe. “Design of a System Substituting Today’s Inherent Inertia in the European Continental Synchronous Area”. In: *Energies* 9.8 (2016), 1.
- [325] P. R. Gribik, W. H. Hogan, and S. L. Pope. “Market-clearing electricity prices and energy uplift”. In: *Cambridge, MA* (2007).
- [326] Australian Energy Market Commission. *National Electricity Amendment (Inertia Ancillary Service Market) Rule 2017*. Sept. 2017.
- [327] W. W. Hogan and B. J. Ring. “On minimum-uplift pricing for electricity markets”. In: *Electricity Policy Group* (2003).
- [328] U. Markovic, D. Chrysostomou, P. Aristidou, and G. Hug. “Impact of Inverter-Based Generation on Islanding Detection Schemes in Distribution Networks”. In: *2020 PSCC*. June 2020.
- [329] “IEEE Standard for Interconnection and Interoperability of Distributed Energy Resources with Associated Electric Power Systems Interfaces”. In: *IEEE Std 1547-2018 (Revision of IEEE Std 1547-2003)* (Apr. 2018).
- [330] D. Velasco, C. L. Trujillo, G. Garcerá, and E. Figueres. “Review of anti-islanding techniques in distributed generators”. In: *Renewable and sustainable energy reviews* 14.6 (2010), 1608.
- [331] S. K. G. Manikonda and D. N. Gaonkar. “Comprehensive review of IDMs in DG systems”. In: *IET Smart Grid* 2 (1 Mar. 2019), 11.

- [332] F. De Mango, M. Liserre, A. Dell'Aquila, and A. Pigazo. "Overview of Anti-Islanding Algorithms for PV Systems. Part I: Passive Methods". In: *12th International Power Electronics and Motion Control Conf.* Aug. 2006.
- [333] F. De Mango, M. Liserre, and A. Dell'Aquila. "Overview of Anti-Islanding Algorithms for PV Systems. Part II: ActiveMethods". In: *12th International Power Electronics and Motion Control Conference.* Aug. 2006.
- [334] A. Pouryektā et al. "Boundary Detection and Enhancement Strategy for Power System Bus Bar Stabilization - Investigation under Fault Conditions for Islanding Operation". In: *Energies* 11.4 (Apr. 2018), 1.
- [335] S-J. Huang and F-S. Pai. "A New Approach to Islanding Detection of Dispersed Generators with Self-Commutated Static Power Converters". In: *IEEE Transactions on Power Delivery* 15.2 (2000), 500.
- [336] Z. Ye, A. Kolwalkar, Y. Zhang, P. Du, and R. Walling. "Evaluation of Anti-Islanding Schemes Based on Nondetection Zone Concept". In: *IEEE Transactions on Power Electronics* 19.5 (2004), 1171.
- [337] R. Teodorescu, M. Liserre, and P. Rodriguez. *Grid Converters for Photovoltaic and Wind Power Systems*. Vol. 29. John Wiley & Sons, 2011.
- [338] X. Zhu, C. Du, G. Shen, M. Chen, and D. Xu. "Analysis of the Non-detection Zone with Passive Islanding Detection Methods for Current Control DG System". In: *2009 Twenty-Fourth Annual IEEE Applied Power Electronics Conference and Exposition*. Feb. 2009.
- [339] H. Sun, L. A. C. Lopes, and Z. Luo. "Analysis and comparison of islanding detection methods using a new load parameter space". In: *30th Annual Conference of IEEE Industrial Electronics Society, 2004. IECON 2004*. Vol. 2. Nov. 2004.
- [340] M. Bakhshi, R. Noroozian, and G. B. Gharehpetian. "Capability improvement of over/under frequency relays by using a hybrid islanding detection method for synchronous based DG units". In: *2012 Proceedings of 17th Conference on Electrical Power Distribution*. May 2012.
- [341] M. Yingram and S. Premrudeepreechacharn. "Over/Undervoltage and Undervoltage Shift of Hybrid Islanding Detection Method of Distributed Generation." In: *Scientific World Journal* (Mar. 2015).

- [342] *BS EN 62116:2014, Utility-interconnected photovoltaic inverters - Test procedure of islanding prevention measures*. Tech. rep. London: British-Standard-Institution, 2014.
- [343] *BS EN 50438:2013, Requirements for micro-generating plants to be connected in parallel with public low-voltage distribution networks*. Tech. rep. London: British-Standard-Institution, 2013.
- [344] J. C. M. Vieira, W. Freitas, W. Xu, and A. Morelato. “Performance of frequency relays for distributed generation protection”. In: *IEEE transactions on power delivery* 21.3 (2006), 1120.
- [345] A. A. M. Hassan and T. A. Kandeel. “Effectiveness of frequency relays on networks with multiple distributed generation”. In: *Journal of Electrical Systems and Information Technology* 2.1 (2015), 75.
- [346] C. M. Affonso, W. Freitas, W. Xu, and L. C. P. da Silva. “Performance of ROCOF relays for embedded generation applications”. In: *IEE Proceedings - Generation, Transmission and Distribution* 152.1 (Jan. 2005), 109.
- [347] J. C. M. Vieira, W. Freitas, A. Morelato, and J. C. Leao. “Dynamic models of frequency and voltage based relays for distributed generation protection”. In: *2005 IEEE Russia Power Tech*. IEEE. 2005, 1.
- [348] V. Kaura and V. Blasko. “Operation of a phase locked loop system under distorted utility conditions”. In: *IEEE Transactions on Industry Applications* 33.1 (Jan. 1997), 58.

CURRICULUM VITAE

PERSONAL DATA

Name	Uroš Marković
Date of Birth	September 20, 1990
Place of Birth	Belgrade, Serbia
Citizen of	Serbia

EDUCATION

09/2013 – 11/2015	MSc in Electrical Engineering and Information Technology ETH Zurich, Switzerland <i>Major:</i> Energy systems and power electronics
09/2009 – 07/2013	BSc in Electrical Engineering and Information Technology University of Belgrade, Serbia <i>Major:</i> Electric power systems
09/2005 – 06/2009	High School Diploma Mathematical Grammar School, Belgrade, Serbia

EMPLOYMENT

03/2016 – 02/2020	Research assistant at ETH Zurich, Switzerland Power Systems Laboratory <i>Advisor:</i> Prof. Dr. Gabriela Hug
05/2019 – 08/2019	Visiting researcher at University of California, Berkeley, USA Energy and Resources Group <i>Advisor:</i> Prof. Dr. Duncan Callaway
05/2015 – 01/2016	Internship at EWZ, Zurich, Switzerland R&D Smart Grids Group <i>Advisor:</i> Dr. Florian Kienzle

- 01/2015 – 05/2015 Internship at ABB Corporate Research Center,
Baden, Switzerland
R&D Power Semiconductors Group
Advisor: Dr. Jürgen Schuderer
- 10/2014 – 01/2015 Teaching assistant at ETH Zurich, Switzerland
Power Electronic Systems Laboratory
Advisor: Prof. Dr. Johann W. Kolar